Quantum Criticality in Heavy Fermion Systems

A real-frequency numerical perspective

Andreas Gleis

Munich 2024

Quantum Criticality in Heavy Fermion Systems

A real-frequency numerical perspective

Andreas Gleis

A dissertation submitted

to the Faculty of Physics at the

Ludwig–Maximilians–Universität München

for the degree of

DOCTOR RERUM NATURALIUM

Munich, May 23, 2024

Zusammenfassung (Summary in German)

Schwerfermionenmetalle sind eine Klasse von stark korrelierten Materialien. Sie enthalten seltene Erden wie Ytterbium oder Cer, deren lokalisierte f-Schalen zur Bildung lokaler Momente neigen. In Verbindung mit den ebenfalls vorhandenen delokalisierten Leitungsbändern führen die lokalen Momente bei ausreichend niedrigen Temperaturen zu interessanten, stark korrelierten Phasen. Ein gut verstandenes Beispiel ist die so genannte schwere Fermi-Flüssigkeit, in welcher die kollektive Verschränkung zwischen Elektronen in den Leitungsbändern und lokalen Momenten zu einer Fermi-Flüssigkeit mit Quasiteilchenmassen von mehr als 1000 Elektronenmassen führt. Faszinierenderweise führt diese kollektive Verschränkung zu einer Mobilisierung der lokalen Momente und somit zu einer so genannten großen Fermi-Fläche. Diese berücksichtigt sowohl die Leitungselektronen als auch die f-Momente und kann experimentell z. B. durch eine entsprechende Änderung der Hall-Zahl nachgewiesen werden. Inzwischen wurde gezeigt, dass diese effektive Delokalisierung der f-Momente aus allgemeinen Gründen zu erwarten ist.

Überaschenderweise zeigen jedoch einige Verbindungen, z. B. YbRh$_2$Si$_2$ und CeCoIn$_5$, Fermi-Flüssigkeits-ähnliche Phasen, in denen die f-Momente lokalisiert zu sein scheinen. Diese Phasen sind durch eine so genannte kleine Fermi-Fläche gekennzeichnet, die nur Leitungselektronen berücksichtigt, was wiederum durch Messungen der Hall-Zahl beobachtet werden kann. Besonders interessant sind sogenannte Kondo-Zusammenbruchsphasenübergänge zwischen Phasen mit kleiner und großer Fermi-Fläche. Ein Kennzeichen von Kondo-Zusammenbrüchen ist eine plötzliche Rekonstruktion der Fermi-Fläche, die als Sprung in der Hall-Zahl beobachtet werden kann. Trotzdem scheinen Kondo-Zusammenbrüche kontinuierliche Quantenphasenübergänge zu sein. Darüber hinaus weisen der quantenkritische Punkt des Kondo-Zusammenbruchs und der zugehörige quantenkritische Bereich typischerweise ein "seltsames Metall"-Verhalten (strange metal behavior) auf. Dazu gehören eine lineare Temperaturabhängigkeit des Widerstandes, dynamisches Skalierungsverhalten von Suszeptibilitäten und das scheinbare Fehlen von Quasiteilchen. Viele der Phänomene, die bei Kondo-Zusammenbrüchen beobachtet werden, sind noch nicht vollständig verstanden, insbesondere die Phasen mit kleinen Fermi-Flächen und das seltsame Metallverhalten im quantenkritischen Bereich. Das Hauptziel dieser Arbeit ist es, diese Phänomene mit Hilfe numerischer Methoden zu untersuchen.

Der erste Teil dieser Arbeit befasst sich hauptsächlich mit der Verbesserung von Matrix-Produkt-Zustands (MPS)-Algorithmen. Dort entwickeln wir ein Verfahren zur kontrollierten Verbindungserweiterung (CBE), das die günstigen Konvergenzeigenschaften der weit verbreiteten 2-Gitterplatz-Aktualisierung aufweist, aber mit einem Rechenaufwand welcher nur geringfügig höher ist als der einer 1-Gitterplatz-Aktualisierung. Eine anschließende Anwendung von CBE auf die MPS-Grundzustandssuche für ein Kondo-Heisenberg-Modell auf einem 4-schenkligen Zylinder, einem paradigmatischen Schwerfermionmodell, zeigte, dass in diesem Modell zwei Phasen existieren, die durch eine kleine bzw. eine große Fermi-Fläche gekennzeichnet sind. Die Untersuchung eines mutmaßlichen Kondo-Zusammenbruchs zwischen diesen Phasen wird zukünftigen Arbeiten überlassen.

Im zweiten Teil untersuchten wir das periodische Anderson-Modell, ein weiteres paradigmatisches Schwerfermionmodell. Unter Verwendung der 2-Gitterplatz zellulären dynamischen Molekularfeldtheorie zusammen mit der numerischen Renormierungsgruppe (NRG) als Störstellenlöser, waren wir in der Lage, einen Kondo-Zusammenbruchsphasenübergang in diesem

Modell zu identifizieren und gründlich zu untersuchen. Dank der Fähigkeit der NRG, exponentiell kleine Energie- und Temperaturskalen aufzulösen, erzielten wir mehrere neue Erkenntnisse, insbesondere über die Phase mit kleiner Fermi-Fläche und über den quantenkritischen Bereich, in welchem wir seltsames metallisches Verhalten finden und untersuchen. Mehrere Vergleiche zwischen numerischen Ergebnissen und experimentellen Daten zeigen eine bemerkenswert gute qualitative Übereinstimmung.

Summary

Heavy fermion metals are a class of strongly correlated materials. They typically contain rare earth elements like Ytterbium or Cerium which host localized f shells that tend towards local moment formation. In conjunction with itinerant conduction bands which are also present in these metals, the local moments give rise to interesting strongly correlated phases at sufficiently low temperatures. A well-understood example is the so-called heavy Fermi liquid, where collective entanglement between electrons in the conduction bands and local moments gives rise to a Fermi liquid with quasiparticle masses in excess of 1000 bare electron masses. A captivating property of the heavy Fermi liquid is that this collective entanglement effectively renders the local moments mobile. This leads to a so-called large Fermi surface which accounts for both the conduction electrons and the f moments and is experimentally detected for instance by a corresponding change of the Hall number. By now, it is well understood that this effective delocalization of the f moments is expected on general grounds.

It is therefore surprising that some compounds, for instance $YbRh_2Si_2$ and $CeCoIn_5$, host Fermi-liquid-like phases in which the f moments appear to be localized. These phases are characterized by a so-called small Fermi surface which only accounts for the conduction electrons, again observable via measurements of the Hall number. Particularly interesting are so-called Kondo breakdown quantum phase transitions between small and large Fermi surface phases. A hallmark of Kondo breakdown transitions is a sudden reconstruction of the Fermi surface, observable as a jump in the Hall number. Despite that, Kondo breakdown transitions appear to be continuous quantum phase transitions. Furthermore, the Kondo breakdown quantum critical point and the associated quantum critical region typically exhibit strange metal behavior. This includes phenomena such as linear-in-temperature resistivity, dynamical scaling of susceptibilities, and the apparent absence of quasiparticles. Many of the phenomena observed around Kondo breakdown transitions are not fully understood yet, particularly the small Fermi surface phases and the strange metal behavior in the quantum critical region. The main goal of this thesis is to shed light on these phenomena using numerical methods.

The first part of this thesis is mainly focused on improving matrix product state (MPS) algorithms. There, we develop a controlled bond expansion (CBE) scheme that exhibits the favorable convergence properties of the widely used 2-site update, but at a reduced computational cost, only marginally higher than that of a 1-site update. A subsequent application of CBE to MPS ground-state search for a Kondo-Heisenberg model on a 4-leg cylinder, a paradigmatic heavy-fermion model, showed that this model hosts two phases, characterized by a small and a large Fermi surface, respectively. An investigation of a putative Kondo breakdown transition between those phases was left for future work.

In the second part, we studied of the periodic Anderson model (PAM), another paradigmatic toy model to describe heavy fermions. Using 2-site cellular dynamical mean-field theory (2CDMFT) together with the numerical renormalization group (NRG) as an impurity solver, we were able to identify and thoroughly study a Kondo breakdown quantum phase transition in this model. Facilitated by the ability of NRG to resolve exponentially small energy and temperature scales, we were able to obtain several new insights on the small Fermi surface phase and especially on the quantum critical region, where we find and study strange metal behavior. Repeated comparison between numerical results and experimental data shows remarkably good qualitative agreement.

(Summary in English)

Publications

This dissertation is based on the following journal articles, listed in the order they appear in this thesis:

P1 *Projector formalism for kept and discarded spaces of matrix product states*
Andreas Gleis, Jheng-Wei Li, and Jan von Delft
Sec. 2.4.2 / arXiv:2207.13161   Phys. Rev. B **106**, 195138 (2022)

P2 *Controlled Bond Expansion for Density Matrix Renormalization Group Ground State Search at Single-Site Costs*
Andreas Gleis, Jheng-Wei Li, and Jan von Delft
Sec. 2.5.2 / arXiv:2207.14712   Phys. Rev. Lett. **130**, 246402 (2023)

P3 *Time-dependent variational principle with controlled bond expansion for matrix product states*
Jheng-Wei Li, **Andreas Gleis** and Jan von Delft
Sec. 2.5.3 / arXiv:2208.10972   submitted to Physical Review Letters

P4 *Emergent Properties of the Periodic Anderson Model: a High-Resolution, Real-Frequency Study of Heavy-Fermion Quantum Criticality*
Andreas Gleis, Seung-Sup B. Lee, Gabriel Kotliar and Jan von Delft
Sec. 3.2 / arXiv:2310.12672   submitted to Physical Review X

P5 *Dynamical scaling and Planckian dissipation due to heavy-fermion quantum criticality*
Andreas Gleis, Seung-Sup B. Lee, Gabriel Kotliar and Jan von Delft
Sec. 3.3 / arXiv:2404.14079   submitted to Physical Review Letters

Acknowledgements

First of all, I would like to thank Jan von Delft for the great opportunity to pursue my PhD in his group and for initiating and supervising numerous fascinating research projects. I am especially grateful for his patience in allowing me the freedom to explore ideas not directly related to our ongoing projects, even though these explorations were often unproductive. I further deeply appreciate the many discussions with other researchers that he facilitated, the trips to conferences, and the visits to other research groups that he made possible. His dedication to improving presentations and polishing manuscripts is truly impressive, and I learned a great deal about presenting my research from his insightful feedback.

I am also especially grateful to Gabriel Kotliar for agreeing to co-referee my thesis, for proposing the heavy fermion project, and for the many insightful discussions on this project. I find our collaboration truly inspiring and rewarding, and I gained significant insights into many-body physics from it. I also enjoyed my stay at Rutgers in August 2023, where we had numerous enlightening discussions.

I am deeply grateful to Seung-Sup Lee for providing the exceptionally well-documented NRG code used in this thesis and for his extensive help, experience, and expert insights, especially regarding DMFT plus NRG calculations. Our numerous discussions on both physics and numerics, particularly during our time together in Munich and continuing afterward, were incredibly helpful. I learned many valuable tricks and insights from these conversations that are not available in the literature.

I also extend my gratitude to Fabian Kugler for the many discussions we had during our time in Munich and afterward. His repeated advice on various matters was always very helpful. Additionally, I am thankful for his efforts in initiating and organizing the visit to the Flatiron Institute in August 2023.

Special thanks to Jheng-Wei Li for introducing me to hands-on MPS calculations with QSpace and for our fruitful collaboration on controlled bond expansion. Furthermore, I would like to thank Andreas Weichselbaum for providing the QSpace tensor library, without which the projects in this thesis would not have been possible. I also appreciate Katharina Stadler for introducing me to NRG, even though this was during my Bachelor's thesis.

I also want to thank my colleagues for the great time in and around the office. I enjoy the current projects with Ming Huang, Sasha Kowalska, Mathias Pelz, and Oleg Yevtushenko, as well as the inspiring non-MPS discussions in our office, with Anxiang Ge, Nepomuk Ritz, and Benedikt Schneider. I appreciate numerous discussions with Markus Frankenbach, Marcel Gievers, Gün Günal, Toni Guthardt, Johannes Halbinger, Sebastian Huber, Boheng Niu, Frederik Pfeiffer, Marc Ritter, Björn Sbierski, Markus Scheb, Jeongmin Shim, Julian Thönniß, Elias Walter, Changkai Zhang, and with the occasional visitor from Antarctica. Special thanks also go to Kathrin Higgen for being an extraordinary secretary.

I'm also deeply grateful for my family's constant support. A special thanks to Julia for her constant presence and support, regardless of the circumstances.

Contents

1 Introduction

This chapter provides some basic background on heavy fermion (HF) materials and the concepts involved when attempting to understand them. Section 1.1 provides an overview of basic notions in HF systems, focusing on a motivation of simple toy models and how we can understand the emergence of a heavy Fermi liquid from those models. Section 1.2 then provides an introduction to quantum criticality in HF systems, starting with Hertz-Millis-Moriya theory in Sec. 1.2.1. Finally, an overview of Kondo breakdown quantum criticality is given, focusing on experimental phenomena in Sec. 1.2.2 followed by an overview of theoretical approaches to explain these phenomena in Sec. 1.2.3.

1.1 Heavy fermion systems – basic concepts

Heavy fermion systems are intermetallic compounds that typically contain elements with partially filled, localized f shells [Ste84, Col07] like Cerium or Ytterbium. At low temperatures, some of these compounds host rather extreme Fermi liquids (FL) with quasiparticle (QP) masses several orders of magnitude larger than for instance copper. This was first observed experimentally in $CeAl_3$ [AGO75], where at low temperatures, a paramagnetic state with properties consistent with an FL was observed. $CeAl_3$ has a specific heat coefficient $\gamma = C/T = 1620 \, \text{mJ/mole} \, \text{K}^2$, more than 3 orders of magnitude larger than that of copper ($\gamma < 1 \, \text{mJ/mole} \, \text{K}^2$ [BLJF70]). Since γ is directly proportional to the effective mass m^* in a FL [GV05], $CeAl_3$ hosts extremely heavy QP, hence the name "heavy fermion" [SAB$^+$79]. Similar extreme enhancement is found in the $\sim T^2$ coefficient of the resistivity and the magnetic susceptibility of $CeAl_3$ [AGO75]. Subsequent work has uncovered many more heavy fermion materials [Ste84, Col07], for instance $CeCu_6$ [SFW84] or the heavy fermion superconductors $CeCu_2Si_2$ [SAB$^+$79] or UBe_{13} [ORFS83]. Of special interest to this thesis are compounds which show so-called Kondo breakdown quantum critical points (c.f. Sec. 1.2.2 and 1.2.3) like $YbRh_2Si_2$ [TGM$^+$00] or the so-called Ce-115 family including $CeRhIn_5$ [SSHO05, JCK$^+$15] or $CeCoIn_5$ [MEC$^+$22].

1.1.1 Simple models

The key ingredient in heavy fermion compounds is the presence of partially filled, localized f shells from rare-earth elements like Cerium or Ytterbium which hybridize with broad, itinerant conduction bands [Col15]. The heavy-fermion compounds most relevant for this thesis contain trivalent Ce^{3+} or Yb^{3+} ions, which have a [Xe] $4f^1$ or [Xe] $4f^{13}$ configuration, respectively. The interesting strong correlation effects observed in heavy fermion compounds like $CeCoIn_5$ or $YbRh_2Si_2$, reviewed in subsequent sections of this introduction, emerge due to the presence of the $4f$ electron or hole, respectively. The $4f$ states in both Ce^{3+} and Yb^{3+} are subject to relatively strong spin-orbit coupling, which leads two sectors with total angular momenta $j = 5/2$ and $j = 7/2$. In Ce^{3+}, the $j = 5/2$ sector is lower in energy by $\sim 0.3\text{eV}$ [HYK10, JGK$^+$22], which corresponds to a temperature of $\sim 3500\text{K}$, i.e. this temperature scale is not relevant for solid-state experiments and we can therefore focus on $j = 5/2$ sector. The situation is similar in Yb^{3+}, but there the $j = 7/2$ sector is lower in
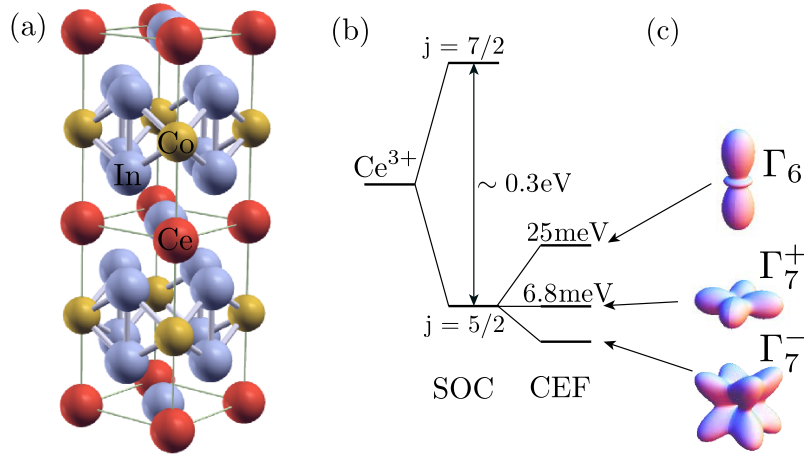
Figure 1.1 (a) Crystal structure of $CeCoIn_5$. Red, yellow, and blue balls denote Ce, Co, and In atoms, respectively. Adapted from Fig. 12 of Ref. [HYK10]. (b) Energy level structure of the $4f$ shell of Ce^{3+} in $CeCoIn_5$. The spin-orbit coupling (SOC) splits the energy levels into a high-energy $j = 7/2$ sector and a low-energy $j = 5/2$ sector, with an energy difference of $\sim 0.3\,\mathrm{eV}$ [JGK$^+$22]. The crystal electric field (CEF) leads to a further splitting of the $j = 5/2$ sector into three Kramers doublets, denoted Γ_7^-, Γ_7^+ and Γ_6. The excitation energy of Γ_7^+ is $6.8\,\mathrm{meV}$, that of Γ_6 is $25\,\mathrm{meV}$ [SAS$^+$19]. (c) Shapes of the Γ_7^-, Γ_7^+ and Γ_6 orbitals. Adapted from Fig. 4 of Ref. [SAS$^+$19].

energy and the energy difference between the two sectors exceeds 1eV [Nor05, LIK07], i.e. it is even larger than for Ce^{3+}.

The tetragonal crystal structure of e.g. $CeCoIn_5$ or $YbRh_2Si_2$ further splits the low-energy $j = 5/2$ (Ce^{3+}) or $j = 7/2$ (Yb^{3+}) angular momentum sectors due to the crystal electric field (CEF). For the Ce^{3+} ion, this leads to three Kramers doublets, denoted Γ_7^+, Γ_7^- and Γ_6 [HYK10]. The Γ_7^- orbital is usually lowest in energy, followed by Γ_7^+ and Γ_6. The energy difference between Γ_6 and Γ_7^- is around 25–30meV for Ce-115 compounds like $CeCoIn_5$ [SAS$^+$19], which corresponds to a temperature scale around 300–350K, i.e. roughly room temperature. Since the temperature range where heavy fermion metals like $CeCoIn_5$ show interesting strongly correlated phenomena is considerably lower (typically $T < 100$K or less), the Γ_6 orbital is not expected to be highly relevant for those. On the other hand, the energy difference to Γ_7^+ is rather small and around 5–10meV [SAS$^+$19], which corresponds to a temperature scale of around 60–120K. In $CeCoIn_5$ for instance, the crystal field splitting between Γ_7^- and Γ_7^+ is 6.8meV [SAS$^+$19], corresponding to a temperature scale of 78.9K. Since emergent strongly correlated phenomena like strange metal behavior emerge at an even lower scale around $\simeq 40$K [MEC$^+$22], an effective description of the $4f$ shell in terms of only the Γ_7^- Kramers doublet can be expected to be sufficient to describe such emergent phenomena qualitatively. The situation in $CeCoIn_5$ described above is illustrated in Fig. 1.1, and the situation in other tetragonal Ce-based HF compounds like $CeRhIn_5$ or $CeIrIn_5$ is similar.

In $YbRh_2Si_2$, the CEF splits the $j = 7/2$ states into four Kramers doublets, with an energy splitting between the two lowest-energy doublets of 17meV [SKF$^+$06, LIK07], which corresponds to almost 200K. Due to that, low-temperature emergent phenomena like strange-metal behavior in $YbRh_2Si_2$ should be well described by a model considering only the lowest energy Kramers doublet.

The $4f$ orbitals are comparably narrow and tightly bound to the nucleus [Col15]. As a result, the $4f$ electrons in the lowest-energy Kramers doublet are localized and subject

to strong Coulomb repulsion, which promotes local moment formation in the $4f$ orbitals. Further, the $4f$ electrons are subject to hybridization with itinerant *spd*-bands present in HF compounds like $CeCoIn_5$ or $YbRh_2Si_2$.

Periodic Anderson model

A basic toy model that contains the key ingredients described above is the periodic Anderson model (PAM),

$$H_{\mathrm{PAM}} = \sum_{i\sigma} \epsilon_f \, f_{i\sigma}^\dagger f_{i\sigma} + U \sum_i f_{i\uparrow}^\dagger f_{i\downarrow}^\dagger f_{i\downarrow} f_{i\uparrow} \quad + V \sum_{i\sigma} [f_{i\sigma}^\dagger c_{i\sigma} + \mathrm{h.c.}] + \sum_{\mathbf{k}\sigma} \epsilon_{c\mathbf{k}} \, c_{\mathbf{k}\sigma}^\dagger c_{\mathbf{k}\sigma} . \quad (1.1)$$

Here, $f_{i\sigma}$ and $c_{\mathbf{k}\sigma}$ annihilate a spin-σ electron in the narrow f or the itinerant c band at site i or momentum $\mathbf{k}$, respectively. The spin σ should be regarded as an effective spin, accounting for the 2-fold degeneracy of the lowest-energy Kramers doublet. From here on, we will use the terms f electrons or c electrons to refer to the localized f band or the itinerant c band. The f band is completely flat with energy ϵ_f while the c band has a dispersion $\epsilon_{c\mathbf{k}}$ with some bandwidth W. The f and c electrons are subject to local hybridization with strength V. U is a local Hubbard-type interaction on the f band and is typically the largest scale in the system, i.e. $W, V \ll U$. Realistic values of U are typically of the order of several eV, which means double occupation only occurs in terms of virtual transitions at the energy scales of interest. In this thesis, we will usually pick $\epsilon_f \simeq -U/2$, such that the f band is approximately half-filled such that also the empty state only occurs in virtual transitions. This leaves only the spin degree of freedom of the f band active, i.e. the f-electrons form local moments at temperatures and energy scales where the Hamiltonian (1.1) is reasonably applicable.

Kondo-Heisenberg model

The local doubly-occupied or empty states $\{|0\rangle_i, |\uparrow\downarrow\rangle_i\}$ (from now on referred to as charge fluctuation sector) are of order U higher in energy than the local moment sector $\{|\uparrow\rangle_i, |\downarrow\rangle_i\}$. Because the interaction energy U is large, the charge fluctuations in the f band of the periodic Anderson model (1.1) are often (approximately) integrated out [SW66, Col15, LvDW17b]. The result is an effective low-energy Hamiltonian where the f band is described as local spin-1/2 degrees of freedom. Remarkably, this means we have cooked down the full $4f$ orbital of Yb^{3+} or Ce^{3+} with a local many-body Hilbert space of dimension $4^7 = 16384$ to its bare minimum, an effective 2-dimensional Hilbert space. The resulting model is known as the Kondo-Heisenberg model (KHM),

$$H_{\mathrm{KHM}} = J_{\mathrm{H}} \sum_{\langle i,j \rangle} \mathbf{S}_i \cdot \mathbf{S}_j + J_{\mathrm{K}} \sum_i \mathbf{S}_i \cdot \mathbf{s}_i + \sum_{\mathbf{k}\sigma} \epsilon_{c\mathbf{k}} c_{\mathbf{k}\sigma}^\dagger c_{\mathbf{k}\sigma} , \quad (1.2)$$

where $\mathbf{S}_i$ are spin-1/2 operators describing the f local moments and $\mathbf{s}_i = \sum_{ss'} c_{is}^\dagger \sigma_{ss'} c_{is'}$ are the local c-electron spin operators, with σ Pauli matrices. J_{K} is a local antiferromagnetic Kondo coupling between f spins and c-electrons while J_{H} is an antiferromagnetic Heisenberg interaction between nearest-neighbor f local moments. It should be emphasized that both H_{PAM} and H_{KHM} are expected to describe the same universal phenomena at low energies, where they should provide a good qualitative description of the otherwise more complicated $4f$ shells and their hybridization with the itinerant *spd* bands in real heavy-fermion compounds. Which Hamiltonian to use is mostly a matter of convenience.

1.1.2 Hybridization, Fermi surface and heavy Fermi liquid

A striking aspect of HF metals is the emergence of a heavy Fermi liquid with extremely large QP masses, as discussed for $CeAl_3$ [AGO75] at the beginning of this section. The emergence of this heavy FL is a result of c-f hybridization. At high temperatures, the f-electron local moments are subject to thermal fluctuations, resulting in a Curie-like magnetic susceptibility [Col15]. As the temperature is lowered, the thermal fluctuations of the local moments gradually become insufficient to overcome the hybridization between c and f electrons, which promotes c-f singlet formation. The heavy FL finally emerges at low temperatures, when thermal fluctuations become weak enough to allow collective Kondo singlet formation [Col07], similar to the Kondo singlet formation in the single impurity Kondo or Anderson models [Hew93]. The QPs in this heavy FL are composed of both c and f electrons, the local nature and strong interactions of the latter result in a large effective QP mass. The f electrons thus effectively become mobile charge carriers which contribute to the charge density in the valence band. In Ce-based HF metals, for instance, the heavy FL formation can be thought of as a crossover in the valence of the Ce ion from Ce^{3+} at high temperatures where the f electron should be regarded as a core electron, to Ce^{4+} in the low-temperature heavy FL where the f electron contributes as a valence electron [Col15]. This valence change leads to a corresponding change in Fermi surface (FS) volume [Lut60, Osh00, Dzy03, CNHC18, NCHC18, HB20] and the Hall number n_H [GV05], both of which are proportional to the charge density in an FL. From here on, an FS whose volume includes the f-electron density will be called a large FS, the converse will be referred to as a small FS.

It can be argued using basic conservation laws that the large FS, i.e. the case where the f electrons contribute as valence electrons, should be the rule at sufficiently low temperatures. This is known as the Luttinger sum rule [Lut60, Osh00]. Some materials appear to disregard this rule, e.g. $YbRh_2Si_2$ and $CeCoIn_5$, and seem to have a small FS at low temperatures, at least in some areas of their phase diagram. How this rule can be circumvented is a major theoretical challenge, and it is one of the main goals of this thesis to improve our understanding of this.

Periodic Anderson model

The effect of hybridization and the emergence of the heavy FL can be qualitatively understood from the PAM. At high temperatures, the PAM exhibits local-moment behavior. This can be qualitatively understood from the $V = 0$ limit with $U \gg T > 0$ and $\epsilon_f = -U/2$ such that there are thermally fluctuating local moments on the f site which are decoupled from the c electrons. As a result, the FS is determined by the c-electrons alone and is therefore small. Non-zero V will lead to scattering of the c-electrons off the local moments and thus to a broadening of spectral features, but the qualitative picture at high temperatures remains unchanged.

As the temperature is lowered, the c-electron scattering amplitude increases with decreasing temperature [Hew93]. Since the scattering phase shifts are subject to strong fluctuations, scattering events at different sites do not develop phase coherence. The scattering described here has some similarities to the scattering from dilute Anderson or Kondo impurities, which also leads to a resistivity that increases with temperature (and finally saturates at low temperatures) [Hew93]. There is however a very important difference between the periodic Anderson model and dilute Anderson impurities. In the dilute case, what matters is the scattering amplitude while phase coherence between scattering events is not of importance because the scatterers are far apart and randomly distributed. In the periodic case, phase incoherence of scattering events is key since it prevents the formation of coherent Bloch

waves.

At low temperatures, the scattering phase shift fluctuations eventually become weaker, and scattering eventually becomes elastic and coherent. A simple way to model this situation is to just consider a periodic arrangement of non-interacting resonant levels with energy ϵ_f. This corresponds to the PAM with $U = 0$ and $V \neq 0$. It has a two-band structure with dispersions $E_{\mathbf{k}}^\pm = \frac{1}{2}\left(\epsilon_{c\mathbf{k}} + \epsilon_f \pm \sqrt{(\epsilon_{c\mathbf{k}} - \epsilon_f)^2 + 4V^2}\right)$. There is a gap between the bands of order $|V|$, referred to as the hybridization gap (c.f. Fig. 1.2). If the chemical potential is within the gap, the system is an insulator, referred to as a Kondo insulator in the HF context. In this thesis, we will usually deal with situations where the chemical potential is within one of the two bands, say in the $+$ band. In these cases, the Fermi surface is shifted from its $V = 0$ position and determined by $E_{\mathbf{k}}^+ = 0$. Thus, the FS is now large and determined by both the c and f electrons and the single-particle excitations in the vicinity of the FS are now hybrid c-f particles. Compared to $\epsilon_{c\mathbf{k}}$, the QP dispersion is relatively flat, a feature inherited by the localized f electrons. This means they have a large effective mass. Including interaction effects further renormalizes the band structure and leads to QPs with an even larger effective mass. If interactions do not trigger a phase transition, the qualitative picture will remain the same at low temperatures.

Kondo-Heisenberg model

Both the local moment and heavy FL regimes can be described from the perspective of the KHM. The high-temperature local moment regime can be understood by considering the $J_{\mathrm{H}} = J_{\mathrm{K}} = 0$ limit. The qualitative picture is similar to the PAM and will not be further discussed here.

On the other hand, the emergence of the heavy FL is not quite as simple. The heavy FL in the KHM can be derived as a mean-field solution involving auxiliary fermions. Since this approach is quite instructive, it will be shortly outlined here. We will thereby follow chapters 29-31 of Ref. [Sac23] and chapters 16 and 17 of Ref. [Col15]. For simplicity, we will only consider the $J_{\mathrm{H}} = 0$ case.

As a first step, we represent the f-spins in terms of fermions, $\mathbf{S}_i = \frac{1}{2} f_{is}^\dagger \sigma_{ss'} f_{is'}$, with the constraint $\sum_s f_{is}^\dagger f_{is} = 1$. Using $\sigma_{ab} \cdot \sigma_{cd} = 2\delta_{ad}\delta_{bc} - \delta_{ab}\delta_{cd}$, we can rewrite the Kondo interaction as

$$J_{\mathrm{K}}\mathbf{S}_i \cdot \mathbf{s}_i = -\frac{J_{\mathrm{K}}}{2}\sum_{a,b} f_{ia}^\dagger c_{ia} c_{ib}^\dagger f_{ib} - \frac{J_{\mathrm{K}}}{4}\underbrace{\sum_a f_{ia}^\dagger f_{ia}}_{=1}\sum_b c_{ib}^\dagger c_{ib}\,. \tag{1.3}$$

The second term proportional to $J_{\mathrm{K}}/4$ can be lumped together with the chemical potential of the c-electrons and will therefore be ignored from here on. We can then write the partition function of the KHM as a path integral (suppressing time arguments on all fields),

$$\mathcal{Z}_{\mathrm{KHM}} = \int \mathcal{D}\lambda_i \mathcal{D}f_{i\sigma} \mathcal{D}c_{i\sigma} \exp\left[-\int_0^\beta \mathrm{d}\tau\,(\mathcal{L}_0 + \mathcal{L}_{\mathrm{K}})\right], \tag{1.4}$$

$$\mathcal{L}_0 = \sum_{\mathbf{k}} \bar{c}_{\mathbf{k}\sigma}\left(\partial_\tau + \epsilon_{c\mathbf{k}}\right)c_{\mathbf{k}\sigma} + \sum_{i\sigma} \bar{f}_i(\partial_\tau + \mathrm{i}\lambda_i)f_{i\sigma} - \mathrm{i}\sum_i \lambda_i\,, \tag{1.5}$$

$$\mathcal{L}_{\mathrm{K}} = -\frac{J_{\mathrm{K}}}{2}\sum_i \bar{f}_{i\sigma} c_{i\sigma} \bar{c}_{i\sigma'} f_{i\sigma'}\,, \tag{1.6}$$

where sums over repeated σ-indices are implied. The expression for $\mathcal{Z}_{\mathrm{KHM}}$ above is exact

because the constraint $\overline{f}_{i\sigma} f_{i\sigma} = 1$ is implemented exactly, using the identity

$$\delta \left(\overline{f}_{i\sigma} f_{i\sigma} - 1 \right) = \int \mathcal{D}\lambda_i \exp \left[\mathrm{i}\lambda_i \left(\overline{f}_{i\sigma} f_{i\sigma} - 1 \right) \right] . \tag{1.7}$$

It should be emphasized that λ_i is a τ-dependent field whose real part is fluctuating, i.e., integrated over. Therefore, even when $J_\mathrm{K} = J_\mathrm{H} = 0$, the action of the KHM is not quadratic since $\mathcal{L}_0$ contains coupling term between the f spinon fields and λ_i. We can choose a constant imaginary offset for λ_i which is not integrated over, without changing $\mathscr{Z}_\mathrm{KHM}$.

For our mean-field analysis, we perform a Hubbard-Stratonovic decoupling of the Kondo interaction,

$$\mathscr{Z}_\mathrm{KHM} = \int \mathcal{D}\lambda_i \mathcal{D}P_i \mathcal{D}f_{i\sigma} \mathcal{D}c_{i\sigma} \exp \left[- \int_0^\beta \mathrm{d}\tau \left(\mathcal{L}_0 + \mathcal{L}_P \right) \right] , \tag{1.8}$$

$$\mathcal{L}_P = \sum_i \left[\frac{2}{J_\mathrm{K}} \overline{P}_i P_i - P_i \overline{f}_{i\sigma} c_{i\sigma} - \overline{P}_i \overline{c}_{i\sigma} f_{i\sigma} \right] . \tag{1.9}$$

Following the standard procedure (c.f. Ch. 6 of [AS10]), integrating over $c_{i\sigma}$ and $f_{i\sigma}$ and minimizing the effective action for the bosonic fields yields the mean-field equations,

$$\langle \overline{f}_{i\sigma} f_{i\sigma} \rangle_\mathrm{MF} = 1 , \quad P = \frac{J_\mathrm{K}}{2} \langle \overline{c}_{i\sigma} f_{i\sigma} \rangle_\mathrm{MF} , \tag{1.10}$$

where we assume uniform, τ-independent, isotropic and real mean-field solutions for P_i, denoted P and $\langle \cdot \rangle_\mathrm{MF}$ is the average w.r.t. the mean-field action. For λ_i, we choose a τ-independent and uniform imaginary part $\widetilde{\lambda}$ such that the single occupancy constraint is fulfilled on average at the mean-field level. The real part of λ_i should be zero at the saddle point. Otherwise, $\langle \overline{f}_{i\sigma} f_{i\sigma} \rangle_\mathrm{MF}$ is generically not real. This mean-field theory becomes exact in the limit of a large number of spin flavors σ [Sac23].

The heavy FL corresponds to a mean-field solution with $P \neq 0$, which always exists if $J_\mathrm{H} = 0$ [Sac23]. The analytically continued Matsubara Green's functions for f and c at the mean-field level are

$$\begin{pmatrix} G_{f\mathbf{k}}(z) & G_{fc\mathbf{k}}(z) \\ G_{fc\mathbf{k}}(z) & G_{c\mathbf{k}}(z) \end{pmatrix} = \begin{pmatrix} z + \widetilde{\lambda} & -P \\ -P & z - \epsilon_{c\mathbf{k}} \end{pmatrix}^{-1} , \tag{1.11}$$

where $z \in \mathbb{C}$. Thus, the picture that emerges from the auxiliary particle mean-field theory of the KHM is qualitatively the same as that discussed for the PAM at $U = 0$. In particular, as for the PAM, we get a bandstructure featuring two bands with dispersions $E_\mathbf{k}^\pm = \frac{1}{2} \left(\epsilon_{c\mathbf{k}} - \widetilde{\lambda} \pm \sqrt{(\epsilon_{c\mathbf{k}} + \widetilde{\lambda})^2 + 4P^2} \right)$, a hybridization gap in the c-electron density of states, and a large FS whose volume accounts for both the c and f densities.

The physics of the KHM from a mean-field perspective is illustrated in Fig. 1.2. There, we consider a cubic lattice with c-electron dispersion $\epsilon_{c\mathbf{k}} = -\frac{1}{6}[\cos(k_x) + \cos(k_y) + \cos(k_z)] - \mu$, where $\mu = 0.2$. The band structure and FS of the c electrons (without Kondo spins) are shown in Fig. 1.2(a). As expected, it features a single band, and the (small) FS is centered around $\mathbf{k} = \Pi = (\pi, \pi, \pi)$ since the model is slightly electron doped. Figure 1.2(b) shows the corresponding local spectral function, obtained by $\mathbf{k}$-integrating the imaginary part of the retarded Green's function, $A_c(\omega) = -\frac{1}{\pi} \mathrm{Im} \int_\mathbf{k} G_{c\mathbf{k}}(\omega^+)$ with $\omega^+ = \omega + \mathrm{i}0^+$ and $\omega \in \mathbb{R}$. Figure 1.2(c) shows the band structure of the mean-field solution with $J_\mathrm{K} = 0.4$. In stark contrast to Fig. 1.2(a), the band structure now features two bands, separated by a hybridization gap. Further, the FS is reconstructed and centered around $\mathbf{k} = \Gamma = (0, 0, 0)$,
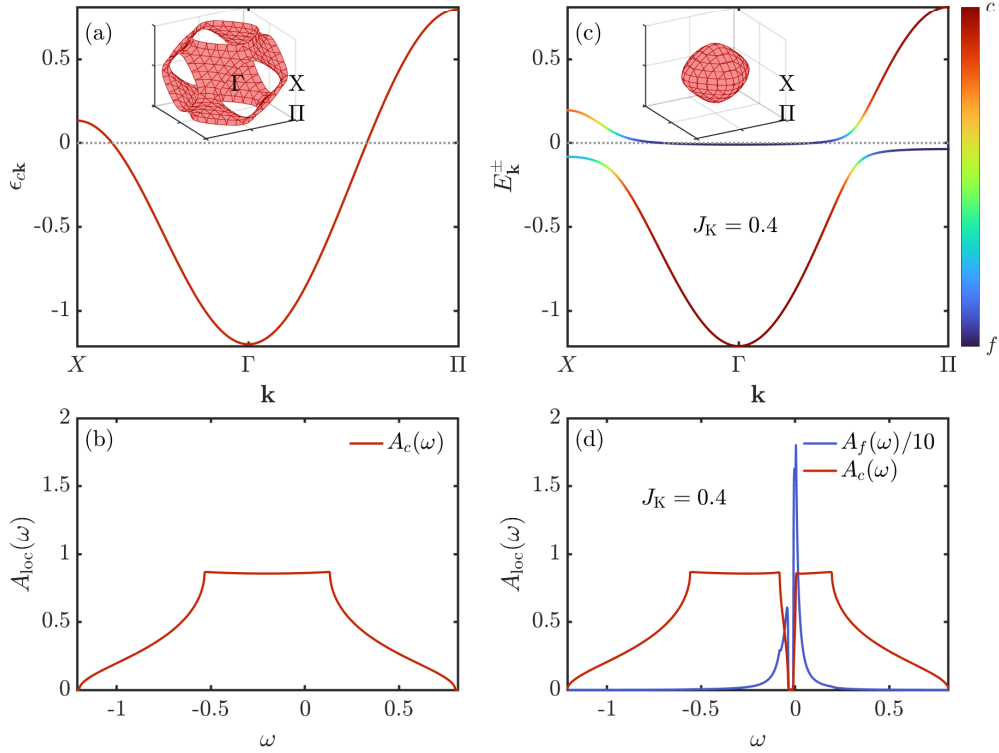
Figure 1.2 (a) Band structure of the c electrons on a three-dimensional cubic lattice. The inset shows the (small) Fermi surface plotted in the first Brillouin zone. The labeled **k**-points correspond to $\Gamma = (0, 0, 0)$, $X = (0, \pi, \pi)$ and $\Pi = (\pi, \pi, \pi)$. (b) Corresponding local spectral function. (c) Mean-field band structure of the KHM on a cubic lattice. The color scale shows the c (red) or f (blue) character of the bands. The inset shows the (large) Fermi surface in the first Brillouin zone. (d) Local spectral functions of the c electrons (red) and f spinons (blue), corresponding to the band structure in (c). Note that the f-electron spectral function has been divided by a factor of 10.

counting both c and f electrons, i.e. the FS is large. At the Fermi level, the band structure is flat compared to $\epsilon_{c\mathbf{k}}$ and is mostly f-electron-like (blue). Thus, QPs at the Fermi surface have a large effective mass. Figure 1.2(d) shows the corresponding local spectral functions. In contrast to the bare c-electron case in Fig. 1.2(b), the c-electron spectral function now features a hybridization gap at small negative frequencies. At high frequencies on the other hand, the c-electron spectral function is almost completely unaltered, illustrating that the heavy FL is a low-energy phenomenon. The f-electron spectral weight is concentrated around $\omega = 0$ (note that $A_f(\omega)$ has ben rescaled by a factor of 10). It also shows a hybridization gap and sharp features in the flat regions of the QP bands.

1.2 Quantum criticality in heavy fermion systems

In Sec. 1.1.2, we have seen that the emergence of the heavy FL is due to collective Kondo singlet formation, driven by J_K, and in the mean-field theory described by a non-zero expectation value of the bosonic field P. The Kondo temperature T_K, i.e. the energy scale for Kondo singlet formation, scales exponentially with the Kondo coupling, $T_K \propto e^{-1/(J_K \rho_c(0))}$ [Hew93, Sac23], where $\rho_c(0)$ is the free c-electron density of states at the Fermi level. In a Kondo lattice, the c electrons mediate an effective, dynamically generated interaction between the f spins, known as Rudermann-Kittel-Kasuya-Yosida (RKKY) [RK54, Kas56, Yos57] interaction. To leading order in the Kondo coupling, $J_{RKKY} \propto J_K^2 \rho_c(0)$ [Col07, Col15], and

this interaction is predominantly antiferromagnetic if the c electrons are approximately half-filled. In the KHM, the RKKY interaction is often included by hand in terms of the Heisenberg interaction J_H. Since J_{RKKY} is a polynomial of J_K, in contrast to T_K with its exponential dependence, we expect that the large-J_K regime is dominated by Kondo correlations while the small-J_K regime is governed by RKKY correlations. This competition was initially pointed out by S. Doniach [Don77], who concluded that this should drive a second-order quantum phase transition between an RKKY-correlated antiferromagnetic and a Kondo-correlated paramagnetic state. That was explicitly confirmed on Doniach's "Kondo necklace model" [Don77], an XY chain with a local Kondo coupling to an array of local moments [JFD77a, JFD77b].

Quantum criticality in HF systems is a several decades-old problem and is still an active field of experimental and theoretical research [Ste01, LRVW07, Ste01, KPC+20]. There is by now a large number of HF compounds that can be tuned through quantum critical points, for instance by varying magnetic fields, pressure, or doping. In some materials, the quantum critical behavior can be understood as a spin density wave (SDW) instability of the heavy FL, described by Hertz-Millis-Moriya (HMM) theory [Her76, Mor85, Mil93, Sac11], see Sec. 1.2.1. Many HF materials on the other hand show a so-called Kondo breakdown (KB) QCP [SRIS01, CPSR01, CP02], which does not fit the description in terms of HMM theory. At KB–QCPs, it seems like the lattice Kondo effect, responsible for the heavy FL with a large FS, breaks down, leading to a sudden reconstruction of the FS. An overview of experimental phenomena at the KB-QCP is given in Sec. 1.2.2 and the main theoretical approaches to describe it are briefly summarized in Sec. 1.2.3.

1.2.1 Hertz-Millis-Moriya theory

Hertz-Millis-Moriya (HMM) theory [Her76, Mor85, Mil93, Sac11] describes ordering of a FL. In HF materials, we are mostly concerned with magnetic order, which is what we will focus on here. To describe such a transition, we decouple the Heisenberg interaction of the KHM with $J_H > 0$ [SSV03] or alternatively the Hubbard interaction of the PAM [Her76] in the magnetic channel, with a real-valued, three component field ϕ_i^α [LRVW07, AS10, Sac11] representing a fluctuating magnetic field. Integrating out the fermions leads to an effective action for ϕ_i^α, which is expanded to fourth order in the field [Her76, Mil93, LRVW07, Sac11],

$$\mathcal{S}_\phi \simeq \int_{\mathbf{q}} T \sum_{\omega_n} \left[u_2 + \mathbf{q}^2 + |\omega_n|/\gamma \right] |\phi(\mathbf{q}, \omega_n)|^2 + u_4 \int_{\mathbf{r}} \int_0^\beta \mathrm{d}\tau \left[|\phi(\mathbf{r}, \tau)|^2 \right]^2 , \qquad (1.12)$$

where the first term is obtained by expanding the magnetic susceptibility of the (free) fermions for small frequencies ω_n and small wavevectors $\mathbf{q}$ around the ordering wavevector. Here, we assumed antiferromagnetic ordering [Her76, LRVW07]. The constant u_2, which depends on the static susceptibility of the fermions and the interaction strength, can be tuned through zero. $u_2 = 0$ marks the position of the QCP at the mean-field level. The quartic term is in principle non-local and retarded, and determined by the 4-point spin correlation function of the fermions. In the HMM approach, it is approximated as local in time and space [Her76].

To make progress on the relevance of the ϕ^4 or even higher order terms compared to the ϕ^2 term at long distances and times, we perform a scaling analysis by rescaling [Sac11]

$$\mathbf{r} \to \mathbf{r} \, \mathrm{e}^{-\lambda}, \quad \tau \to \tau \, \mathrm{e}^{-z\lambda}, \quad \phi(x, \tau) \to \phi(x, \tau) \, \mathrm{e}^{\frac{d+z-2}{2}\lambda} , \qquad (1.13)$$

such that the kinetic ($\propto \mathbf{q}^2$) and dynamical ($\propto |\omega_n|$) terms [Her76] of the Gaussian part of the action remain invariant under the scaling ($u_2 = 0$ at the QCP where we expect scale invariance). The dynamical critical exponent z also rescales the upper cutoff of the τ integrals,

$\beta \to \mathrm{e}^{-z\lambda}\beta$. At $T > 0$ where $\beta = 1/T$ is finite, this eventually scales the time dimension to zero. As a result, the action becomes classical and we are dealing with a classical phase transition. At $T = 0$ on the other hand, the time dimension is an additional dimension with infinite extent, and it counts as z effective dimensions [Her76]. In the present case, $z = 2$ makes sure that the rescaling of the $\mathbf{q}^2$ and $|\omega_n|$ matches. Note also that at $T = 0$, the Matsubara sum becomes an integral. The quartic interaction then scales as

$$u_4 \to u_4 \, \mathrm{e}^{4-d-z} \, , \tag{1.14}$$

i.e. whenever $4 - d - z < 0$, it is reasonable to expect that the quartic term is irrelevant and we are left with a Gaussian theory at long distances and times. Since $z = 2$, this is the case for $d > 2$. Higher order ϕ^n interactions are naively expected to scale with $u_n \to u_n \, \mathrm{e}^{n - \frac{n-2}{2}(d+z)}$. Thus, for $d + z \geq 3$, higher order terms become less relevant the larger n, i.e. we can ignore $n > 4$ terms from a simple naive scaling perspective.

In $d = 3$ dimensions and with dynamical critical exponent $z = 2$ (i.e. antiferromagnetic ordering), $4 - d - z = -1 < 0$, i.e. the u_4 interaction is irrelevant. In this case, the antiferromagnetic SDW–QCP described by HMM theory is Gaussian at long distances and times. A more careful analysis confirms the naive scaling argument [Sac11]. The fermions in HMM theory are mostly mere spectators, and quasiparticles remain stable at and across the transition. In particular, no sudden changes of the FS are expected. The FS will reconstruct due to elastic scattering off the order parameter in the ordered phase, but that reconstruction is gradual at a second order transition since the scattering amplitude depends on the size of the order parameter. Further, since the theory is Gaussian, ω/T scaling of dynamical susceptibilities, a clear sign of an interacting fixed point [Sac11], is not expected in the HMM theory in $d = 3$.

It should be emphasized that potential problems with the arguments outlined in this section arise not so much because the naive scaling analysis of the ϕ^4 theory is insufficient (instead of properly integrating out long wavelength fluctuations, e.g. using some perturbative momentum shell renormalization group). Instead, issues tend to arise when the fermions are integrated out and the effective action is expanded in ϕ. At this step, we assume that nothing dramatic happens to the fermions [Mil93, Sac11], i.e. we assume that the fermions remain stable quasiparticles that are not seriously affected by the QCP. In $d = 2$ for instance, this premise does not hold and HMM theory breaks down and a more elaborate analysis which includes the fermionic degrees of freedom is necessary [AC00, AC04, MS10a, MS10b, Sac11, HP21].

1.2.2 Kondo breakdown: experimental phenomena

Intriguingly, there is a large number of HF materials with QCPs not compatible with an itinerant SDW transition and show so-called KB-QCPs [SRIS01, CPSR01, CP02]. The most prominent examples are compounds from the Ce-115 family like $CeRhIn_5$ [SSHO05, JCK$^+$15] and $CeCoIn_5$ [MEC$^+$22], $YbRh_2Si_2$ [TGM$^+$00, PLW$^+$04, GSS08, CGW$^+$03] or $CeCu_{6-x}Au_x$ [LSSW96]. Observations on these materials indicate that the effective c-f hybridization, i.e. the Kondo correlations described for instance by P in Sec. 1.1.2, appears to break down across the QCP, hence the name KB-QCP. The decoupling of c and f electrons at low energies means that the f electrons do not contribute to the FS volume anymore, which means there is a sudden reconstruction from a large to a small FS, which is indeed observed as outlined below. Since the f electrons do not contribute as mobile charge carriers in the small FS phase, they can be considered as effectively localized. The KB–QCP therefore marks a transition from delocalized (large FS) to localized (small FS) f electrons. Below, key experimental observations on HF materials undergoing a KB transition are listed, focusing

on universal phenomena.

The following discussion of experiments associated with KB quantum criticality is an extended version of parts of the introduction of Ref. [P4].

Fermi surface reconstruction at $T = 0$

Most of the HF materials showing a KB transition feature heavy FL behavior below some low-temperature scale T_{FL}. This seems to be the case on either side of the QCP, though the RKKY correlated small FS phase is often magnetically ordered. The observed heavy FL behavior is qualitatively similar to that discussed for CeAl$_3$ in Sec. 1.1, i.e. $\sim T^2$ behavior of the resistivity and $\sim T$ behavior of the specific heat is usually observed [GCG$^+$02, CGW$^+$03, GSS08, SS11]. Remarkable, the RKKY correlated and Kondo correlated FLs differ in their FS volume, which has been established in many experiments.

Hall number.— An important quantity to distinguish large from small FS is the Hall number $n_H \sim 1/R_H$, where R_H is the Hall coefficient. The Hall number is proportional to the number of mobile charge carriers per unit cell in the system. A sudden change in n_H may thus be interpreted as a sign of a sudden FS reconstruction. The Hall number has been measured in several HF compounds. Some of the most impressive experimental results have arguably been obtained on YbRh$_2$Si$_2$ [PLW$^+$04, FOW$^+$10], where a clear jump in n_H has been measured if tuned across its KB–QCP. Recent measurements on CeCoIn$_5$ show a sharp crossover of the Hall coefficient as a function of Sn doping, c.f. Ref. [MEC$^+$22], Fig. 1(c). While the Hall number of CeCoIn$_5$ is consistent with that of LaCoIn$_5$, the analogue compound of CeCoIn$_5$ without f electrons, substituting less than 1% of In by Sn leads to a Hall number consistent with an additional electron per unit cell, see Figs. 1(b,c) of Ref. [MEC$^+$22]. Thus, CeCoIn$_5$ appears to be located close to a KB–QCP, though on the RKKY side of the transition.

Quantum oscillations.— Quantities like the magnetic susceptibility of the resistivity oscillate as functions of the inverse of an applied magnetic field. The period of the oscillations depends on the size and shape of the FS; quantum oscillation measurements are therefore a standard tool to map out Fermi surfaces [AM76]. Oscillations of the magnetic susceptibility versus magnetic field, called de Haas–van Alphen (dHvA) frequencies, have been measured mostly in the Ce-115 compounds CeRhIn$_5$ and CeCoIn$_5$. When CeRhIn$_5$ [SSHO05, JCK$^+$15] is tuned across its KB–QCP by varying pressure or magnetic field, dHvA frequencies exhibit a jump. This shows that the FS reconstructs at the KB–QCP. At ambient pressure, where CeRhIn$_5$ is in its RKKY correlated phase, the dHvA frequencies are almost identical to those of LaRhIn$_5$. This strongly suggests that the Ce $4f$ electrons do not contribute to the FS and may thus be considered localized. Similarly, such a jump has also been observed in CeCoIn$_5$ [MEC$^+$22]. A comparison of the experimental dHvA frequencies [SSI$^+$01] to ab initio calculations with and without including the f electrons for CeCoIn$_5$ indicate a localization of the f electrons across the KB–QCP [MEC$^+$22]. Note that there are conflicting conclusions from dHvA measurements regarding the localized or itinerant nature of f electrons in pure CeCoIn$_5$ at ambient conditions, with earlier studies concluding an itinerant nature [SSI$^+$01, SSA$^+$02] while a recent study concludes localized behavior [MEC$^+$22]. For YbRh$_2$Si$_2$, dHvA measurements are only available in Kondo-correlated large FS phase [RML$^+$08]. The reason is that quite small magnetic fields ($\lesssim 0.7\,\mathrm{T}$) induce a KB transition in YbRh$_2$Si$_2$, from a low-field RKKY-correlated phase to a high-field Kondo-correlated phase [PLW$^+$04].

Angle resolved photoemission.— An even more direct way to map out the FS is provided by angle-resolved photoemission (ARPES) measurements [KPC$^+$20], which by now have become possible for HF materials at the relevant temperatures. These experiments are typically done at ambient pressures and without a magnetic field. Thus, the evolution of the FS across the

QCP is usually not observed.

For CeCoIn$_5$, ARPES measurements have led to conflicting conclusions, similar to dHvA experiments. Early studies concluded that the f electrons are predominantly localized [KOE$^+$09, KBI$^+$08]. However, these studies also found indications of c-f hybridization and concluded that f electrons are not fully localized in CeCoIn$_5$. By contrast, later studies concluded a more itinerant character of the f electrons [CXN$^+$17, JDA$^+$20]. We note here that pure CeCoIn$_5$ at ambient conditions does *not* show any signs of FL behavior. CeCoIn$_5$ shows strange metal behavior below $\simeq$ 40K and becomes superconducting below $T_c \simeq 2.3$K directly out of this strange metal state [KPC$^+$20]. The above-mentioned ARPES and dHvA experiments on CeCoIn$_5$ were thus conducted in a quantum critical non-Fermi-liquid (NFL) state where the distinction between localized and itinerant f electrons may indeed not be clear-cut.

The situation is somewhat clearer for RKKY correlated HF compounds CeRhIn$_5$ and YbRh$_2$Si$_2$, but nevertheless puzzling. In CeRhIn$_5$ for instance, ARPES measurements show an FS compatible with localized f electrons [CXN$^+$18], as also clearly inferred from dHvA measurements. However, the same ARPES experiments also show clear signs of c-f hybridization [CXN$^+$18] and the formation of Kondo resonances.

For YbRh$_2$Si$_2$, ARPES measurements indicate that the c-electron FS in the RKKY regime is slightly enlarged due to small but finite c-f hybridization [DVK$^+$11]. Further, c-f hybridization seems to lead to strong renormalization of the band structure in the vicinity of the FS. A later ARPES study further found that the size of this slightly enlarged FS seems to be remarkable stable under variation of temperature [KPC$^+$15]. In Ref. [PFW$^+$16], this peculiar behavior was explained by arguing that the ARPES measurements had been performed at temperatures too high to represent the $T \to 0$ limit with a well-defined FS. At the temperatures considered in the aforementioned experiments [DVK$^+$11, KPC$^+$15], YbRh$_2$Si$_2$ is in the quantum critical region, where spectral weight from critical QP is suspected at both the small and large FS. The missing spectral weight at the small FS was attributed in Ref. [PFW$^+$16] to the small photoemission intensity of the c electrons.

For YbCo$_2$Si$_2$, which has an antiferromagnetic ground state with localized f electrons, the expected small FS has been observed in ARPES studies [GKP$^+$14]. Interestingly, this study also found weak but finite c-f hybridization, which however does not lead to an increase of the FS volume.

Continuous suppression of the FL scale to zero

As outlined above, the KB transition appears to be a transition between FLs with different FS volumes. It appears to be a continuous quantum phase transition because the FL scale T_{FL} continuously decreases to zero at the QCP [CGW$^+$03, SS11]. This is further underpinned by evidence that the QP mass diverges when approaching the KB–QCP from either side [GCG$^+$02, SSHO05, LSSW96].

Onset scale for hybridization

The reconstruction from a large to a small FS across the KB–QCP suggests the assumption that c and f electrons do not hybridize in the small FS phase. However, hybridization between c and f electrons, signaled by the presence of a hybridization gap and f-electron spectral weight close to the Fermi level, sets in at an energy scale much higher than T_{FL}. Following the notation used in Refs. [P4] and [P5], we will call this scale T_{NFL} from here on, since it marks the scale below which typically non-Fermi liquid (NFL) behavior emerges. Interestingly, T_{NFL} is typically almost unaltered across the KB–QCP, as is for instance seen in ARPES studies, which were discussed above.

Scanning tunneling spectroscopy.— Apart from ARPES, information on single-particle properties in both the Kondo and RKKY regimes is provided by scanning tunneling spectroscopy (STS) experiments [KPC$^+$20]. STS data on CeCoIn$_5$ [AdSNG$^+$12], CeRhIn$_5$ [HPT$^+$19] and YbRh$_2$Si$_2$ [EKK$^+$11, SJK$^+$18] show the formation of a hybridization gap, a clear sign of c-f hybridization. Interestingly, the hybridization gap seems to form around temperatures scales where NFL behavior (see below) begins to set in. The hybridization gap appears to form irrespective of whether the $T \to 0$ phase has a small or large FS. It deepens as temperature is lowered, showing that c-f hybridization increases as temperature decreases. This is the case even for clearly RKKY correlated compounds like YbRh$_2$Si$_2$ and CeRhIn$_5$. The experiments on CeRhIn$_5$ [HPT$^+$19] showed that the deepening of the hybridization gap even continues in its antiferromagnetically ordered RKKY regime where the FS is small.

Optical conductivity.— Measurements of the optical conductivity in YbRh$_2$Si$_2$ [KNS$^+$04, KSF$^+$06], CeRhIn$_5$ [MvdMS05], CeCoIn$_5$ [SBBM02, MvdMS05] and CeCu$_{6-x}$Au$_x$ [MW90] all show a hybridization gap regardless of the FS volume at $T = 0$, further supporting the findings by ARPES and STS discussed above.

Possible absence of magnetic ordering

The KB-QCP is not necessarily associated with magnetic ordering [FWB$^+$09, ZZL$^+$19, MEC$^+$22]. CeCoIn$_5$ orders only away from the KB–QCP in the RKKY-dominated small FS phase [MEC$^+$22]. Further, in YbRh$_2$Si$_2$, the location of the AFM–QCP and the KB–QCP can be detuned by chemical pressure [FWB$^+$09]. The latter changes the location of the AFM–QCP but leaves the location of the KB–QCP almost unchanged. Thus, the jump in n_{H} can be tuned to either occur in the paramagnetic or in the ordered phase. Moreover, the compound CeRh$_6$Ge$_4$ hosts a ferromagnetic QCP that exhibits characteristics consistent with a KB–QCP [SZK$^+$20]. However, the hallmark Fermi surface reconstruction typical of a KB-QCP has yet to be observed in CeRh$_6$Ge$_4$. Therefore, antiferromagnetic ordering is apparently not a universal feature of the KB–QCP [Si06, FWB$^+$09, YS10, Si10].

Strange metal behavior

Close to the KB–QCP, a quantum critical region emerges in the temperature region $T_{\mathrm{FL}} < T < T_{\mathrm{NFL}}$. In this quantum critical region, strange metal behavior [PHA22, HM22, CGPS22, Zaa04, CBC$^+$24] is usually observed. A hallmark feature of the strange metal is a linear-in-T resistivity, which is observed for all of the above-mentioned materials featuring a KB–QCP [TGM$^+$00, PLM$^+$20, vL96, PTH$^+$03, MEC$^+$22, MTK$^+$01, SZK$^+$20]. Additionally, YbRh$_2$Si$_2$ [TGM$^+$00, CGW$^+$03], CeCu$_{6-x}$Au$_x$ [LSSW96, vL96], CeCoIn$_5$ [BMV$^+$03] and CeRh$_6$Ge$_4$ [SZK$^+$20] feature a $\sim T \ln(T)$ dependence of the specific heat. Further, recent measurements on YbRh$_2$Si$_2$ nanowires find strongly suppressed shot noise in the strange metal region [CLB$^+$22], indicating that well-defined QPs are absent.

Further, dynamical susceptibilities exhibit ω/T scaling [VLSR$^+$89] in the quantum critical region, in stark contrast to expectations from HMM theory, as discussed in Sec. 1.2.1. This was initially observed for the dynamical magnetic susceptibilites in UCu$_{5-x}$Pd$_x$ [AOR$^+$95], CeCu$_{6-x}$Au$_x$ [SAC$^+$00] and CeCu$_{6-x}$Ag$_x$ [PLW$^+$19] and very recently also for the optical conductivites of both YbRh$_2$Si$_2$ [PLM$^+$20] and CeCu$_{6-x}$Au$_x$ [YPZ$^+$20]. Note that ω/T scaling is a clear sign for a non-Gaussian QCP [Sac11], i.e. the critical fixed point is an interacting one. Particularly interesting, too, are the recent observations of ω/T scaling for the optical conductivity, as it shows that the critical behavior is not limited to the magnetic degrees of freedom only, but also includes the charge degrees of freedom.

1.2.3 Kondo breakdown: theoretical description

The experimental observations discussed in Sec. 1.2.2 above are inconsistent with the HMM theory discussed in Sec. 1.2.1. Below, we first outline the challenges to theory that arise from these observations, followed by an outline of routes to overcome those challenges.

The following discussion of theoretical aspects of the KB–QCP is an extended version of parts of the introduction of Ref. [P4].

Challenges to theory

Description of the strange metal.— Arguably the most challenging aspect of the KB–QCP is the strange metal behavior at finite temperatures above the QCP. There are by now various routes to microscopically realize NFL behavior, see Ref. [CGPS22] for an extensive recent review. Rigorous results on NFL physics can for instance be obtained from Sachdev-Ye-Kitaev (SYK) models [CGPS22] or from impurity models featuring quantum phase transitions [Voj06], e.g. multi-channel Kondo impurities [TW84, Tsv85, EK92, CIT95] or multi-impurity models [Gan95, SSK90, SS92, FHLS03, LF04, SLO⁺96, AL92, ALJ95, Jon07, WK23b, WK23a]. Despite considerable recent progress [ETS21, ES21, PGES23], it is to date not fully clarified to what extent known routes to NFL physics connect to the strange metal behavior observed experimentally in HF materials.

Description of the Fermi surface reconstruction.— Another challenging issue is to explain how the FS can change its size in the first place. The volume of the FS is fixed to be proportional to the particle number by the Luttinger sum rule [Lut60, Osh00], which involves the combined particle number of the c and f electrons [Osh00]. While the FS volume matches the Luttinger sum rule prediction in the Kondo correlated phase, this is not the case in the RKKY correlated phase where the f electrons seem to be missing from the FS volume. A theoretical description of the KB–QCP also needs to correctly describe both the Kondo and RKKY correlated phases, which is far from straightforward in the latter case. Nevertheless, this aspect of the KB–QCP is better understood and intuitively more accessible than the strange metal physics.

Numerically exact approaches

Significant progress on physical phenomena can be made based on numerically exact solutions, even if they are only available for simplified models. From such exact solutions, one can then either gain direct insight into the problem at hand or the corresponding solutions can for instance be used as benchmarks for approximate solutions which are also applicable to more realistic settings. So far, simulations of the KHM with the goal of capturing KB phenomena have mostly been done using Quantum Monte Carlo (QMC) methods [Ass99, Ass04, CA01, BLST19, PTSA19, RA20, DVAG20, DLAR21, RDA22, DVGA22, FLA⁺23, LFJ⁺23], some of which have reported evidence of a Kondo breakdown [RDA22, DVGA22].

Due to the sign problem, QMC simulations are only available at particle-hole symmetry. At particle-hole symmetry, the KH model has a charge gap and thus no FS [Ass99, CA01]; KB quantum criticality was thus not obtained in early studies [Ass04]. Recently, progress has been made by resorting to dimensional mismatch, i.e. by coupling D-dimensional free fermions to a $(D-1)$-dimensional spin system [DLAR21, DVGA22, FLA⁺23, LFJ⁺23]. Due to the dimensional mismatch, the spin system is not able to open a charge gap and metallic quantum criticality can be investigated. Indeed, it was shown in references [RDA22] and [DVGA22] that Dirac fermions in two dimensions, Kondo-coupled to a Heisenberg chain, exhibit a KB–QCP. However, no transport properties have been reported so far. In references [FLA⁺23]

and [LFJ$^+$23] a two-dimensional Heisenberg model, Kondo-coupled to three-dimensional electrons, was investigated. It was shown that this model does not exhibit a KB–QCP, but rather a SDW–QCP [LFJ$^+$23]. Interestingly, a $\sim T$ resistivity perpendicular to the two-dimensional Heisenberg model was found [FLA$^+$23] at the QCP.

The KHM can also be simulated with the Density Matrix Renormalization Group (DMRG), which is not constrained to particle-hole symmetry but to quasi-one-dimensional geometries. Thus, most DMRG simulations of the KHM were done in one dimension [MJRG01, MJRG02, SSMS09, KAH$^+$18], but without focusing on possible KB physics. As a part of this thesis, the KHM has been studied with DMRG on a cylinder [P2]. There, we found two phases differing in their FS volumes, indicating a KB–QCP in between.

Auxiliary particle approaches

Considerable conceptual progress on KB physics has been achieved using auxiliary-particle approaches [Col84, BGG02, SSV03, SVS04, PÓ5, Voj10, Sac23]. These approaches decompose the degrees of freedom of the PAM or the KLM in terms of additional auxiliary fermionic or bosonic degrees of freedom which are subject to constraints, to ensure the mapping is exact [Col84, PÓ7, BGG02, SSV03, SVS04, Voj10, ACPA22]. An explicit example of an auxiliary particle approach to the KHM is given in Sec. 1.1.2, where we have represented the spin in terms of auxiliary fermions with a half-filling constraint. There, we have also seen that the auxiliary particle decomposition does not render the model exactly solvable. However, the auxiliary particle decomposition allows for much more flexibility in constructing approximate solutions. For instance, in the example in Sec. 1.1.2, it allowed us to describe the heavy FL in terms of f spinons hybridizing with the c electrons. Without an auxiliary particle decomposition of the f spins, a mean-field description of the heavy FL in the KHM would not have been possible. Indeed, the mean-field solution of the KHM presented in Sec. 1.1.2 is the starting point for studying KB physics using auxiliary particle methods.

In Sec. 1.1.2, we have seen that the heavy FL in the KHM is due to a condensed bosonic field, denoted P there, which effectively hybridizes f spinons and c electrons and enlarges the FS volume. By adding a non-zero Heisenberg interaction and choosing a suitable mean-field decoupling, it turns out that the KHM can undergo a (non-symmetry breaking) phase transition to a phase with $P = 0$, i.e. where the Kondo boson is not condensed [SSV03, SVS04, Voj10, Sac23]. The f and c electrons are then no longer hybridized at low energies, leading to a small FS formed by the c electrons which coexists with an f-electron spin liquid. This spin liquid hosts fractionalized, possibly topological excitations which account for the missing FS volume [SSV03, SVS04, BCPP16, Sac23], coining the term fractionalized FL (FL*). Thus, it is possible to describe a continuous transition between Kondo and RKKY correlated phases [SVS04, Sac23], including an FS reconstruction accompanied by a jump in the Hall coefficient [CMS05].

Early work on the KB using auxiliary particles mainly focused on the large-N approach discussed in Sec. 1.1.2, where the number of spin labels of the fermions is large, but the Kondo and Heisenberg interactions are decoupled with a single boson flavor per site or link, respectively. Due to that, feedback between the large number N of fermion flavors and critical bosonic fluctuations are suppressed by $1/N$. As a result, the large-N limit is non-interacting and does not describe strange metal behavior [ACPA22]. Recently, a different large-N approach was considered which introduces an artificial large-N flavor index for *both* bosons and fermions while considering two spin flavors per artificial flavor [ACPA22]. The Yukawa coupling between bosons and fermions is then approximated as random, which allows for an exact solution within the Yukawa-SYK approach [ACPA22, PGES23]. This approach is capable of describing a strange-metal-like $\sim T \ln T$ resistivity if a spatially random Yukawa

coupling or anisotropic solutions are considered [ACPA22, PGES23].

Dynamical mean-field approaches

Dynamical mean-field theory (DMFT) [GKKR96, KSH$^+$06] and its extensions [KSPB01, MJPH05, RHT$^+$18] have been successfully used in many studies on HF systems [SRIS01, SK03, dMGKB05, SK05b, SKK$^+$19, HCS20, Ov17, THKD11, DLCK08b, DLCK08a] and have lead to valuable new insights. DMFT methods treat lattice models by mapping them on self-consistent impurity models.

The most prominent approach, which has led to many insights, is the extended DMFT (EDMFT) approach to KHM [SSI99, SS00, SRIS01, SRIS03, SK03, ZGS03, GI07, CYH$^+$20, HCC$^+$21, HCCS21, KHSI22, HCS22a, HCS22b]. EDMFT maps the KHM on a self-consistent Bose-Fermi-Kondo (BFK) impurity model and is able to capture a KB–QCP due to the local competition between Kondo screening and magnetic fluctuations. One of the main successes of EDMFT is the explanation of ω/T scaling of the dynamical spin structure factor in CeCu$_{6-x}$Au$_x$ [SAC$^+$00] at the KB–QCP. However, to the best of our knowledge, predictions of other thermodynamic and transport properties, like the linear-in-T resistivity or the $T \ln T$ dependence of the specific heat, are lacking to date. It is therefore still unclear whether the EDMFT approach correctly describes the experimentally observed strange metal behavior.

A downside of the EDMFT approach is that full self-consistency leads to a first-order phase transition [SK03, SK05a] at $T > 0$. A continuous transition can be recovered by insisting on a featureless fermionic density of states (DOS) [SZG05], at the cost of giving up self-consistency of the fermionic degrees of freedom. This is routinely done in KB–QCP studies using EDMFT [ZGS03, GI07, HCC$^+$21].

This downside of EDMFT has led to the proposal of using 2-site cellular DMFT (CDMFT) [KSPB01] to study Kondo breakdown physics in the PAM [SK05b]. Using exact diagonalization (ED) as an impurity solver, it was shown that a 2-site CDMFT treatment of the PAM can describe the KB–QCP as an orbital selective Mott transition (OSMT) at $T = 0$ [DLCK08b, DLCK08a], where the f electrons localize while the c electrons remain itinerant. Similar studies with QMC impurity solvers [MA08, MBA10, THKD11] were however not able to find signs of a KB–QCP in the temperature range studied. Since ED suffers from limited frequency resolution while QMC has trouble reaching low temperatures, it was not clear prior to the work reported in this thesis to what extent CDMFT can describe KB physics. The ED study was further not able to establish conclusively whether the transition is first or second order.

1.3 Scope and outline

The main goal of this thesis is to shed light on the emergent phenomena associated with KB-QCPs and the phases in their vicinity, primarily relying on numerical methods. To achieve this, we focused on both improving methods and applying methods to examine concrete heavy fermion models. The structure of the thesis is outlined below.

In Chapter 2, we provide an overview of the methods employed in this thesis. Section 2.1 covers DMFT and its cluster extensions, including techniques for performing momentum integrals for Green's functions in Section 2.1.3, and numerically more stable alternatives to the Dyson equation to computing the hybridization function in DMFT in Section 2.1.4. Section 2.2 introduces the numerical renormalization group (NRG), which we use as an impurity solver for DMFT. Sections 2.1 and 2.2 provide the necessary methodological background for the results presented in Chapter 3.

Section 2.3 introduces MPS methods, focusing on subspace structures implied by the isometries of an MPS. There, we also introduce the tangent space projector and its 2-site generalization. Section 2.3.1 offers an MPS perspective on NRG. Sections 2.3.2 and 2.3.3 introduce the density matrix renormalization group (DMRG) for MPS ground-state search and the time-dependent variational principle (TDVP) for MPS time evolution, respectively. Section 2.4 presents Ref. [P1], where the subspace structure implied by the isometries of an MPS is fleshed out in detail and n-site generalizations of the tangent space projector is derived. In Sec. 2.5, we present Refs. [P2] and [P3], where the insights from Ref. [P1] are used to arrive at a scheme called controlled bond expansion (CBE). CBE is intended as a computationally cheap alternative to the widely used 2-site update, and we show in Refs. [P2] and [P3] that its application to DMRG and TDVP is highly successful. Using CBE–DMRG, Ref. [P2] also shows that the KHM on a 4-leg cylinder hosts two phases with different FS volumes.

Chapter 3 presents Refs. [P4] and [P5], which contain an extensive 2-site CDMFT plus NRG study of KB quantum criticality in the PAM. There, we identify a KB–QCP in the PAM and thoroughly study its properties, gaining new insights, especially into the RKKY phase and the quantum critical region, where we find strange metal behavior.

Chapter 4 concludes the thesis and offers an outlook on future research directions to further explore the phenomena surrounding the KB-QCP beyond the achievements of this thesis.

2 Methods

This chapter provides an overview of the numerical methods that have been used in this thesis. Section 2.1 provides a brief overview of dynamical mean-field theory (DMFT) and its most widely used cluster extensions, the cellular DMFT (CDMFT) and the dynamical cluster approximation (DCA). In Sec. 2.1.3, a comparison of different momentum integration methods for Green's functions is given, which is an essential ingredient when solving DMFT equations. Section 2.1.4 further provides a numerically more stable method to extract the dynamical mean-field $\Delta(\omega)$ in the case of limited accuracy of momentum-integrated Green's functions. In Section 2.2, the numerical renormalization group (NRG) is introduced, which we use as an impurity solver in our DMFT calculations. Matrix product states (MPS) are introduced in Sec. 2.3, including a brief overview of the structure of the MPS manifold and its tangent space. Sections 2.3.2 and 2.3.3 introduce the density matrix renormalization group (DMRG) for MPS ground state search and the time-dependent variational principle (TDVP) for MPS time evolution, respectively.

2.1 Dynamical mean-field theory

This section provides an introduction to DMFT and its most commonly used cluster extensions, the cellular DMFT (CDMFT) and the dynamical cluster approximation (DCA). DMFT has been used with great success in the past, for instance by shedding light on the Mott metal-to-insulator transition [GKKR96] or as a powerful tool in electronic structure calculations [KSH$^+$06]. By now, DMFT has evolved into a standard tool to approach various phenomena in strongly correlated metals and is used by many researchers worldwide. Similar to other mean-field theories, DMFT has a controlled large-N limit, namely the limit of large coordination number [GKKR96]. In contrast to many other large-N limits, the limit of a large coordination number does not render the action Gaussian. The DMFT approximation instead leads to an action equivalent to the action of an effective impurity model, i.e. a single interacting site hybridizing with an effective non-interacting bath. DMFT thereby neglects non-local correlation effects, which can, however, be of qualitative importance in certain situations. In HF metals, for instance, the competition between local and non-local correlations is thought to drive the Kondo breakdown transition as discussed in the introduction. To include short-ranged non-local correlation effects, cluster extensions to DMFT [MJPH05] like CDMFT [KSPB01] and DCA [HTZJ$^+$98, HMJK00] have been developed. These methods approximate the lattice model by mapping it to an effective cluster impurity model, with multiple interacting lattice sites hybridizing with an effective non-interacting bath.

2.1.1 Single-site dynamical mean-field theory: brief overview

The idea behind DMFT originated from foundational work by Metzner and Vollhardt [MV89], followed up by Georges and Kotliar [GK92], who considered the Hubbard model in infinite dimensions and realized its connection to the single-impurity Anderson model (SIAM). In infinite dimensions, correlations become purely local, reflected by an entirely local self-energy,

$$\Sigma_{ij}(\omega) = \delta_{ij}\Sigma(\omega) \leftrightarrow \Sigma_{\mathbf{k}}(\omega) = \Sigma(\omega)\,. \tag{2.1}$$

Assuming a purely local self-energy, also in finite dimensions, and exploiting the simplifications that arise from this approximation is at the heart of DMFT [GKKR96]. It should be emphasized that the simplifications that arise assuming a purely local self-energy also require a purely local bare interaction vertex U. In DMFT, non-local parts of U are truncated and treated in a static mean-field approximation.

The DMFT equations can be conveniently derived using the Baym-Kadanoff formalism [BK61, Bay62], which formulates the many-body problem as a variational optimization of the grand potential as a functional of the Green's function G and the bare interaction vertex U [AGD63],

$$\Omega[G, U] = \Phi[G, U] + T \sum_{n, \mathbf{k}, \sigma} \left[\ln G_{\mathbf{k}}(i\omega_n) - \Sigma_{\mathbf{k}}(i\omega_n) G_{\mathbf{k}}(i\omega_n) \right]. \tag{2.2}$$

Here, $\Phi[G, U]$ is the Luttinger-Ward (LW) functional [LW60]. Variation of $\Phi[G, U]$ provides the self-energy as a functional of G and U,

$$\frac{\delta \Phi[G, U]}{\delta G_{\mathbf{k}}(i\omega_n)} = T \Sigma_{\mathbf{k}}[G, U](i\omega_n). \tag{2.3}$$

Demanding stationarity of $\Omega[G, U]$ w.r.t variation of G gives the stationarity condition

$$\frac{\delta \Omega[G, U]}{\delta G_{\mathbf{k}}(i\omega_n)} = T \Sigma_{\mathbf{k}}[G, U](i\omega_n) + T G_{\mathbf{k}}^{-1}(i\omega_n) - T \mathcal{G}_{\mathbf{k}}^{-1}(i\omega_n) \stackrel{!}{=} 0 \quad \forall \mathbf{k}, \tag{2.4}$$

where $\mathcal{G}_{\mathbf{k}}(i\omega_n)$ is the non-interacting Green's function and we have used Dyson's equation, $\Sigma_{\mathbf{k}}(i\omega_n) = \mathcal{G}_{\mathbf{k}}^{-1}(i\omega_n) - G_{\mathbf{k}}^{-1}(i\omega_n)$. We can now reshuffle the stationarity condition (2.4),

$$G_{\mathbf{k}}(i\omega_n) = \frac{1}{\mathcal{G}_{\mathbf{k}}^{-1}(i\omega_n) - \Sigma_{\mathbf{k}}[G, U](i\omega_n)} \quad \forall \mathbf{k}, \tag{2.5}$$

which provides us with a self-consistency condition for G. Since both $\Phi[G, U]$ and $\Sigma_{\mathbf{k}}[G, U](i\omega_n)$ are generically not known, approximations are required to make progress. For instance, in self-consistent n-th order perturbation theory, the functional $\Sigma_{\mathbf{k}}[G, U](i\omega_n)$ is expanded to order n in the interaction vertex U and the self-consistency equation (2.5) is then iterated until convergence.

DMFT uses a non-perturbative approximation which assumes that the self-energy as a functional of G is (i) $\mathbf{k}$-independent and (ii) depends only on U_{loc}, the local part of the interaction vertex (in Hubbard models, $U = U_{\mathrm{loc}}$),

$$\Sigma_{\mathbf{k}}[G, U](i\omega_n) \xrightarrow{\mathrm{DMFT}} \Sigma[G, U_{\mathrm{loc}}](i\omega_n). \tag{2.6}$$

For the LW functional, this implies that it only depends on the $\mathbf{k}$-averaged or, in other words, local Green's functions, $G_{ii}(i\omega_n) = \frac{1}{N} \sum_{\mathbf{k}} G_{\mathbf{k}}(i\omega_n)$,

$$\Sigma[G, U_{\mathrm{loc}}](i\omega_n) = \frac{\delta \Phi[G_{ii}, U_{\mathrm{loc}}]}{\delta G_{\mathbf{k}}(i\omega_n)} = \frac{1}{N} \sum_i \frac{\delta \Phi[G_{ii}, U_{\mathrm{loc}}]}{\delta G_{ii}(i\omega_n)} = \Sigma[G_{ii}, U_{\mathrm{loc}}](i\omega_n). \tag{2.7}$$

By $\mathbf{k}$-averaging Eq. (2.5), we get a self-consistency condition for G_{ii},

$$G_{ii}(i\omega_n) = \frac{1}{N} \sum_{\mathbf{k}} \frac{1}{\mathcal{G}_{\mathbf{k}}^{-1}(i\omega_n) - \Sigma[G_{ii}, U_{\mathrm{loc}}](i\omega_n)}. \tag{2.8}$$

We now need a way to evaluate $\Sigma[G_{ii}, U_{\mathrm{loc}}](i\omega_n)$ for a given G_{ii}. In DMFT, this is done via a

reference impurity model with bare interaction vertex U_{loc}, LW functional $\phi[G_{\mathrm{imp}}, U_{\mathrm{loc}}]$ and Ω-functional

$$\Omega_{\mathrm{imp}}[G_{\mathrm{imp}}, U_{\mathrm{loc}}] = \phi[G_{\mathrm{imp}}, U_{\mathrm{loc}}] - T\sum_{n\sigma}\left[\ln G_{\mathrm{imp}}(\mathrm{i}\omega_n) - \Sigma(\mathrm{i}\omega_n)G_{\mathrm{imp}}(\mathrm{i}\omega_n)\right], \qquad (2.9)$$

with $\Sigma(\mathrm{i}\omega_n) = \mathcal{G}_{\mathrm{imp}}^{-1}(\mathrm{i}\omega_n) - G_{\mathrm{imp}}^{-1}(\mathrm{i}\omega_n)$. Since the DMFT approximation to the lattice LW functional is then given by $\Phi[G, U_{\mathrm{loc}}] = \sum_i \phi[G_{ii}, U_{\mathrm{loc}}]$, solving the impurity model and computing its Green's function $G_{\mathrm{imp}}(\mathrm{i}\omega_n)$ self-energy $\Sigma_{\mathrm{imp}}(\mathrm{i}\omega_n)$ allows us to evaluate the DMFT Σ-functional, $\Sigma[G_{\mathrm{imp}}, U_{\mathrm{loc}}](\mathrm{i}\omega_n) = \Sigma_{\mathrm{imp}}(\mathrm{i}\omega_n)$. Since we want to evaluate the functional at G_{ii} to solve Eq. (2.8), a second self-consistency condition between impurity model and lattice model is required,

$$G_{\mathrm{imp}}(\mathrm{i}\omega_n) = G_{ii}(\mathrm{i}\omega_n), \qquad (2.10)$$

which is used to adjust the non-interacting Green's function of the impurity model, $\mathcal{G}_{\mathrm{imp}}(\mathrm{i}\omega_n)$. The latter can be written as $\mathcal{G}_{\mathrm{imp}}^{-1}(\mathrm{i}\omega_n) = \mathrm{i}\omega_n + \mu - \epsilon_0 - \Delta(\mathrm{i}\omega_n)$, where ϵ_0 is the local on-site energy of the lattice model and the hybridization function $\Delta(\mathrm{i}\omega_n)$ describes the influence of the bath on the impurity model.

The DMFT equations (2.8) and (2.10) are solved in an iterated self-consistency cycle, initialized by some guess for $\Sigma(\mathrm{i}\omega_n)$:

(i) Compute $G_{\mathrm{loc}}(\mathrm{i}\omega_n) = \frac{1}{N}\sum_{\mathbf{k}}\left[\mathcal{G}_{\mathbf{k}}^{-1}(\mathrm{i}\omega_n) - \Sigma(\mathrm{i}\omega_n)\right]^{-1}$

(ii) Using $G_{\mathrm{imp}}(\mathrm{i}\omega_n) \overset{!}{=} G_{\mathrm{loc}}(\mathrm{i}\omega_n)$, update the hybridization function via $\Delta(\mathrm{i}\omega_n) = \mathrm{i}\omega_n + \mu - \epsilon_0 - \Sigma(\mathrm{i}\omega_n) - G_{\mathrm{loc}}^{-1}(\mathrm{i}\omega_n)$.

(iii) Solve the impurity model with the updated $\Delta(\mathrm{i}\omega_n)$ from step (ii) to obtain an updated $\Sigma(\mathrm{i}\omega_n)$, repeat with step (i) until convergence.

After the cycle has converged, $G_{\mathrm{imp}}(\mathrm{i}\omega_n) = G_{ii}(\mathrm{i}\omega_n)$ and Eq. (2.8) is fulfilled. Usually, the DMFT cycle converges without major issues. Convergence can be accelerated using mixing methods [Žit09b]. These can also help to stabilize the DMFT cycle in the rare cases where it does not converge.

2.1.2 Cluster extensions of DMFT

DMFT approximates the self-energy as entirely local/$\mathbf{k}$-independent and therefore neglects non-local correlation effects. To overcome this shortcoming of DMFT, there are by now several different approaches, which can largely be divided into two subclasses: (i) cluster extensions of DMFT [MJPH05] and (ii) diagrammatic extensions of DMFT [RHT+18].

Diagrammatic extensions aim to extend the self-consistency of DMFT on the single-particle level to the n-particle level, where $n = 2$ is currently computationally feasible. This allows us to deal with e.g. long-ranged spin, pairing, and charge fluctuations and their feedback on the electronic spectral function. The reference system remains a single lattice site hybridizing with an effective bath. Diagrammatic extensions are expected to work well in cases with strong, long-ranged fluctuations, e.g. at magnetic (quantum) phase transitions. The dynamical vertex approximation [TKH07] has for instance been used to study the quantum phase transition between a Kondo insulator and an antiferromagnetic insulator in the PAM [SKK+19].

Cluster extensions on the other hand focus on short-ranged correlations and treat them on equal footing as local correlations. This is achieved by considering a cluster of multiple lattice sites hybridizing with an effective self-consistent bath. To date, there are two main

(a) CDMFT

(b) DCA
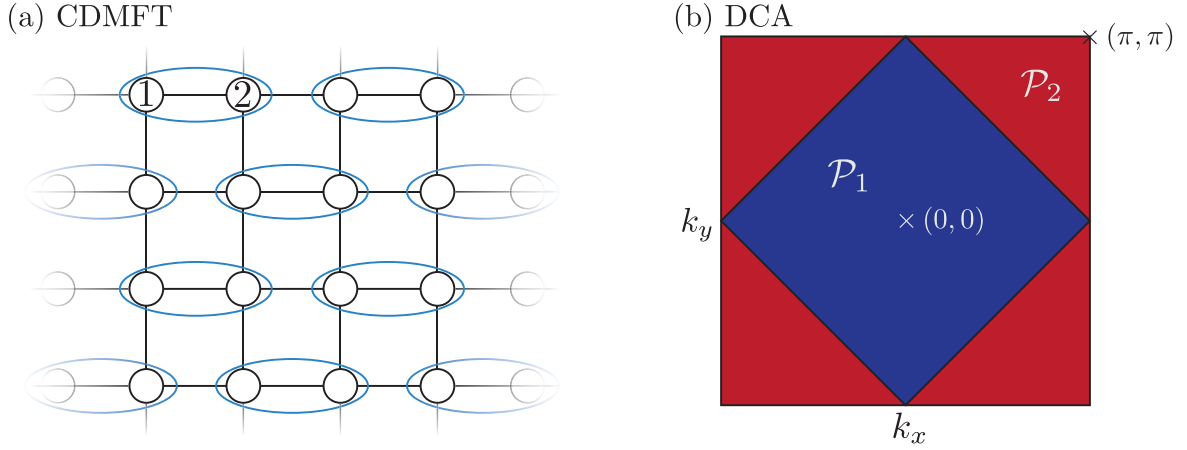
Figure 2.1 (a) Tiling of a 2-dimensional square lattice into $N_c = 2$-site unit cells (blue ellipses). CDMFT fully considers the self-energy within each cell but neglects self-energy contributions between cells. (b) Patching of the Brillouin zone of a 2-dimensional square lattice into $N_c = 2$ equally sized patches. DCA approximates the self-energy within each patch as **k**-independent, but the self-energy for different patches may differ.

methods, the cellular DMFT (CDMFT) [KSPB01] and the dynamical cluster approximation (DCA) [HTZJ⁺98, HMJK00]. Both methods are described in more detail below.

Cellular dynamical mean-field theory

CDMFT takes a real-space approach by tiling the lattice into a superlattice of unit cells containing N_c sites, c.f. Fig. 2.1(a). The method then takes the intra-cell self-energy fully into account but neglects any inter-cell self-energy contributions. As a result, the translation symmetry of the original lattice is broken and only the translation symmetry of the superlattice remains. We therefore have to work in the Brillouin zone of the superlattice, corresponding momenta will be denoted **K** to distinguish them from momenta **k** in the Brillouin zone of the original lattice. The self-energy $\boldsymbol{\Sigma}(\omega)$ is **K**-independent and is a matrix of the intra-cell site indices [1 and 2 in Fig. 2.1(a)]. In that way, short-ranged non-local correlations within each cell are taken into account, described for instance by $\Sigma_{12}(\omega)$ in the example shown in Fig. 2.1(a). The inter-cell hopping $\boldsymbol{\epsilon_K}$ is a **K**-dependent matrix of the intra-cell site indices.

Analogous to DMFT, CDMFT proceeds by iteratively solving the matrix-valued self-consistency equations,

$$\mathbf{G}_{ii}(\omega) = \frac{N_c}{N} \sum_{\mathbf{K}} \left[\boldsymbol{\mathcal{G}}_{\mathbf{K}}^{-1}(\omega) - \boldsymbol{\Sigma}[\mathbf{G}_{\mathrm{imp}}, U_{\mathrm{cl}}](\omega) \right]^{-1} , \tag{2.11}$$

$$\mathbf{G}_{\mathrm{imp}}(\omega) = \mathbf{G}_{ii}(\omega) , \tag{2.12}$$

where $\boldsymbol{\mathcal{G}}_{\mathbf{K}}^{-1}(\omega) = \omega + \mu - \boldsymbol{\epsilon}_{\mathrm{cl}} - \boldsymbol{\epsilon_K}$, $\boldsymbol{\epsilon}_{\mathrm{cl}}$ describes intra-cell hopping and on-site energies and N is the number of lattice sites in the original lattice and U_{cl} is the bare interaction vertex truncated to the cluster. $\mathbf{G}_{\mathrm{imp}}$ is the Green's function of a reference impurity model, used to non-perturbatively evaluate the functional $\boldsymbol{\Sigma}[\mathbf{G}, U_{\mathrm{cl}}](\omega)$. This reference impurity model now contains N_c impurities, with the impurity Hamiltonian mirroring the intra-cell Hamiltonian, and a non-interacting Green's function $\boldsymbol{\mathcal{G}}_{\mathrm{imp}}(\omega)$ which is also matrix-valued. Except for the complication that everything is matrix-valued, the self-consistency cycle is analogous to the DMFT self-consistency cycle. The non-interacting impurity Green's function can again be written as $\boldsymbol{\mathcal{G}}_{\mathrm{imp}}^{-1}(\omega) = \omega + \mu - \boldsymbol{\epsilon}_{\mathrm{cl}} - \boldsymbol{\Delta}(\omega)$, where $\boldsymbol{\Delta}(\omega)$ is a matrix-valued hybridization

function that determines the influence of the bath on the cluster impurity model.

In many cases, it is possible to diagonalize the local self-energy and Green's function matrices, with a unitary transformation independent of ω. For instance, in the example shown in Fig. 2.1(a), if we assume that sites 1 and 2 are equivalent, such that $\Sigma_{11}(\omega) = \Sigma_{22}(\omega)$ and $\Sigma_{21}(\omega) = \Sigma_{12}(\omega)$ (and the same also for cluster Green's functions), the unitary

$$U_H = \frac{1}{\sqrt{2}} \begin{pmatrix} 1 & 1 \\ 1 & -1 \end{pmatrix}$$

diagonalizes all intra-cell Green's functions and self-energies. However, it is generically not possible to diagonalize $\epsilon_{\mathbf{K}}$ independent of $\mathbf{K}$, meaning that the integrand in Eq. (2.11) remains matrix-valued.

Dynamical cluster approximation

The DMFT approximation can also be approached from a $\mathbf{k}$-space coarse-graining approach, by averaging the bare interaction vertex U over the Brillouin zone [MH89, MJPH05]. The DCA is motivated from the perspective of this $\mathbf{k}$-space coarse-graining perspective. DCA partitions the Brillouin zone into N_c patches $\mathcal{P}_i$ of equal size (the shape of the patches can otherwise be chosen arbitrarily), see Fig. 2.1(b). The bare interaction vertex is now only averaged over the patches, the coarse-grained vertex $\overline{U}$ now retains a coarse momentum dependence and in particular also inter-patch momentum conservation [MJPH05]. As a result, the LW functional depends only on the patch-averaged Green's functions,

$$\overline{G}_i(\omega) = \frac{N_c}{N} \sum_{\mathbf{k} \in \mathcal{P}_i} G_{\mathbf{k}}(\omega) \,, \tag{2.13}$$

and the same goes for the Σ-functional. This leads to self-consistency equations for $\overline{G}_i$

$$\overline{G}_i(\omega) = \frac{N_c}{N} \sum_{\mathbf{k} \in \mathcal{P}_i} \frac{1}{\mathcal{G}_{\mathbf{k}}^{-1} - \Sigma_i[G_{\mathrm{imp},i}, \overline{U}](\omega)} \,, \tag{2.14}$$

$$G_{\mathrm{imp},i}(\omega) = \overline{G}(\omega) \,, \tag{2.15}$$

where G_{imp} is the Green's function of an N_c-site reference impurity model with bare interaction vertex $\overline{U}$. The iterative solution of the self-consistency equations is analogous to DMFT and CDMFT.

2.1.3 Momentum integrals of Green's functions

To solve the DMFT, CDMFT, or DCA self-consistency equations, it is generically necessary to perform momentum integrals to determine the local or patch-averaged Green's functions. If one works with real frequencies, ω^+, the integrands are often close to singular. I describe here methods to deal with such $\mathbf{k}$ integrals efficiently. It should be noted that efficiency is of importance since the integrals typically have to be performed for $\mathcal{O}(10^3$–$10^4)$ ω-points. Even though parallelization over ω-points is, of course, possible, it is desirable to not require additional cores just for the integration task (the NRG impurity solver typically parallelizes well with ~ 10 cores). Thus, we would like to perform $\mathcal{O}(10^3$–$10^4)$ $\mathbf{k}$ integrals on ~ 10 cores within a time window of a few minutes. This means the integrator should be able to solve a single $\mathbf{k}$ integral within $\mathcal{O}(10^{-1}\,\mathrm{sec})$.

Below, three methods to perform momentum integrals will be presented, (i) the adaptive linear tetrahedron (ALT) method, (ii) iterated adaptive integration (IAI) [KBB+23] and (iii)
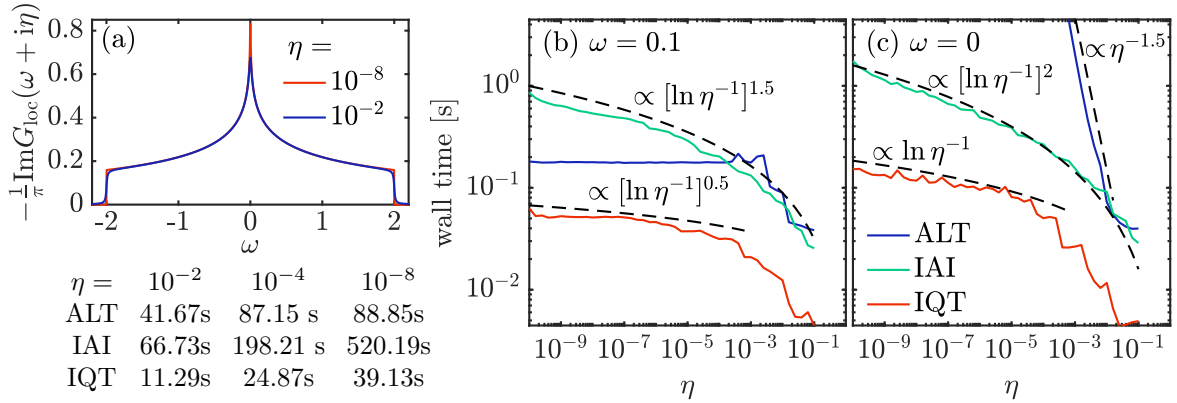
Figure 2.2 (a) Imaginary part of the local Green's function for $\eta = 10^{-2}$ and 10^{-8}, respectively, evaluated on a linear frequency grid with 10^3 grid points, evenly spaced between $-2.2 \leq \omega \leq 2.2$ $(\min |\omega| = 2.2 \times 10^{-3})$. All three methods, ALT, IAI, and IQT meet the absolute accuracy criterion of $\epsilon = 10^{-3}$. The curves in (a) produced by all three methods are identical on the scale shown there. The table below panel (a) shows the total wall time needed by the integrators (all calculations were done on a single core of an Intel Core i7-9750H CPU) versus η to compute $G_{\text{loc}}(\omega + i\eta)$ on the frequency grid used in (a). (b) Scaling of the wall time versus η away from the van Hove singularity at $\omega = 0.1$. As described in the text, ALT has constant scaling with η since the **k**-dependence of the inverse Green's function at the relevant **k**-points is reasonably well captured by a linear function. IAI has $[\ln \eta^{-1}]^\alpha$ scaling, with $\alpha \simeq 1.5 < d = 2$ smaller than the expected worst scaling. IQT is by far the fastest of the three methods and scales with $[\ln \eta^{-1}]^{\alpha-1}$ (see text). (c) Scaling of the wall time versus η at the van Hove singularity at $\omega = 0$. ALT now has power law scaling, $\eta^{-1.5}$, since the **k**-dependence of the inverse Green's function at the relevant **k**-points is quadratic and therefore never well captured by linear approximations. IAI has $[\ln \eta^{-1}]^\alpha$ scaling, with $\alpha = d = 2$ saturated at the expected worst scaling. IQT has again by far the best performance and scales with $[\ln \eta^{-1}]^{\alpha-1}$, as expected.

iterated adaptive integration with the adaptive quadratic tetrahedron method as the initial integrator [iterated quadratic tetrahedron (IQT)]. All of these methods are tested on the non-interacting Green's function of a two-dimensional square lattice with nearest-neighbor hopping,

$$G_{\text{loc}}(\omega + i\eta) = \int_{-\pi}^{\pi} \frac{dk_x}{2\pi} \int_{-\pi}^{\pi} \frac{dk_y}{2\pi} \, G_{\mathbf{k}}(\omega + i\eta) \tag{2.16}$$

$$G_{\mathbf{k}}(\omega + i\eta) = \frac{1}{\omega + i\eta + \cos k_x + \cos k_y} \,. \tag{2.17}$$

Runtime and accuracy will be compared for different η, which controls the sharpness of the features of $G_{\mathbf{k}}(\omega + i\eta)$.

The results are shown and compared in Fig. 2.2 and are discussed below. The main message is the following: away from van Hove singularities, ALT performs very well and runtime is approximately constant as a function of η. Very close to van Hove singularities, however, ALT has very unfavorable $\mathcal{O}(\eta^a)$ scaling, with $a \simeq 1.5$ in the present case. IAI scales as $\mathcal{O}([\log \eta^{-1}]^\alpha)$, with $\alpha \leq d$ bounded by the dimension d of the the integration area, i.e. $d = 2$ for $G_{(k_x, k_y)}(\omega + i\eta)$. The exponent α seems to saturate (i.e. $\alpha = 2$) at the van Hove singularity, while away from the van Hove singularity, the scaling is more favorable with $\alpha < d$. IQT performs by far the best and scales as $\mathcal{O}([\log \eta^{-1}]^{\alpha-1})$, where α is the same exponent as that for IAI. For more details, see the discussion of the three methods below.

Adaptive linear tetrahedron method

The integration method used for most of the results in this thesis is the linear tetrahedron method [LV84, BJA94, Kap12], with an adaptive **k**-grid to improve performance and allow us to control the accuracy [adaptive linear tetrahedron (ALT)]. When integrating Green's functions over momenta, the integrals can typically written in the form

$$I = \int_{\mathcal{A}} d\mathbf{k} \frac{f(\mathbf{k})}{g(\mathbf{k})}, \tag{2.18}$$

where both $f(\mathbf{k})$ and $g(\mathbf{k})$ are smooth functions of $\mathbf{k}$ and $\mathcal{A}$ is the integration area. The idea behind the linear tetrahedron method is now to tile the integration area into tetrahedra $\mathcal{T}_i$ (triangles in 2 dimensions or lines in 1 dimension), approximate both $f(\mathbf{k})$ and $g(\mathbf{k})$ as linear functions within each tetrahedron, $f(\mathbf{k}) \simeq a_i + \mathbf{b}_i \cdot \mathbf{k}$ and $g(\mathbf{k}) \simeq c_i + \mathbf{d}_i \cdot \mathbf{k}$, and then solve the integral over each $\mathcal{T}_i$ exactly and sum up all contributions,

$$I \simeq \sum_i \int_{\mathcal{T}_i} d\mathbf{k} \frac{a_i + \mathbf{b}_i \cdot \mathbf{k}}{c_i + \mathbf{d}_i \cdot \mathbf{k}}. \tag{2.19}$$

To achieve accuracy control, we can tile each tetrahedron into smaller tetrahedra, $\tau_{ij} \in \mathcal{T}_i$. To check whether an absolute error threshold ε is satisfied, we use the global criterion

$$\left| \sum_i \int_{\mathcal{T}_i} d\mathbf{k} \frac{a_i + \mathbf{b}_i \cdot \mathbf{k}}{c_i + \mathbf{d}_i \cdot \mathbf{k}} - \sum_i \sum_j \int_{\tau_{ij}} d\mathbf{k} \frac{a_{ij} + \mathbf{b}_{ij} \cdot \mathbf{k}}{c_{ij} + \mathbf{d}_{ij} \cdot \mathbf{k}} \right| < \varepsilon. \tag{2.20}$$

If the global criterion is not met, tetrahedra $\mathcal{T}_i$ are fine-grained if they do not meet the local criterion

$$\left| \int_{\mathcal{T}_i} d\mathbf{k} \frac{a_i + \mathbf{b}_i \cdot \mathbf{k}}{c_i + \mathbf{d}_i \cdot \mathbf{k}} - \sum_j \int_{\tau_{ij}} d\mathbf{k} \frac{a_{ij} + \mathbf{b}_{ij} \cdot \mathbf{k}}{c_{ij} + \mathbf{d}_{ij} \cdot \mathbf{k}} \right| < \varepsilon \frac{\mathcal{V}_i}{\mathcal{V}_{\mathcal{A}}}, \tag{2.21}$$

where $\mathcal{V}_{\mathcal{A}}$ is the volume of the integration area and $\mathcal{V}_i$ is the volume of $\mathcal{T}_i$. The tetrahedra $\mathcal{T}_i$ that do not meet the local accuracy criterion are fine-grained by promoting the finer tetrahedra to coarse tetrahedra, $\tau_{ij} \to \mathcal{T}_\ell$, followed by fine-graining the newly promoted $\mathcal{T}_\ell$ into even finer tetrahedra $\tau_{\ell j}$. This is iterated until the global accuracy criterion is passed. More information on the adaptive linear tetrahedron method, especially also on how to deal with matrix-valued integrands, can be found in my Master's thesis [Gle19], Ch. 5.

For instance, in the example (2.16), $g(\mathbf{k}) = \omega + i\eta + \cos k_x + \cos k_y$ and $f(\mathbf{k}) = 1$, i.e. both functions are smooth and do not contain sharp features. The main contributions to the integral (2.16) are due to **k**-space regions where $\mathrm{Re}\, g(\mathbf{k}) = 0$. In most cases, $g(\mathbf{k})$ can be very well represented with a piecewise linear function, and the tetrahedron method is expected to converge quickly in these cases. The runtime depends only on the number of **k**-points needed to obtain a reliable piecewise linear interpolation around **k**-points with $\mathrm{Re}\, g(\mathbf{k}) = 0$. For small η, we therefore expect that the runtime is approximately independent of η, provided that a reliable piecewise linear interpolation around **k**-points with $\mathrm{Re}\, g(\mathbf{k}) = 0$ can be found.

Our expectations are confirmed in Fig. 2.2(a). ALT performs the integral (2.16) for 10^3 frequency points in less than 1.5 minutes, i.e. every frequency point requires less than 0.1s on average. Further, $\eta = 10^{-4}$ and $\eta = 10^{-8}$ require almost the same amount of time, confirming the η-independnece claimed above. This is further illustrated in Fig. 2.2(b), which shows the time required to compute $G_{\mathrm{loc}}(0.1 + i\eta)$. At small η, the time required by ALT does not depend on η, since $g(\mathbf{k})$ can be sufficiently well represented by a linear interpolation in the

momentum region satisfying $\cos k_x + \cos k_y = -0.1$.

However, $g(\mathbf{k})$ also contains saddle points where the gradient $\nabla_\mathbf{k}\, g(\mathbf{k})$ vanishes, for instance at $(k_x, k_y) = (0, \pm\pi)$. At these points in the BZ, piecewise linear interpolation of $g(\mathbf{k})$ cannot be expected to be very reliable. Thus, whenever $\mathrm{Re}\, g(\mathbf{k}) = 0$ and $\nabla_\mathbf{k}\, g(\mathbf{k}) = 0$, (which leads to van Hove singularities in $G_{\mathrm{loc}}(\omega + \mathrm{i}\eta)$), we expect ALT to converge slowly. An example is the evaluation of (2.16) at $\omega = 0$. As can be seen in Fig. 2.2(c), ALT has very unfavorable $\eta^{-1.5}$ scaling there and performs considerably worse than IAI or IQT. In principle, this issue could be cured by choosing a piecewise quadratic interpolation on every tetrahedron. Unfortunately, the integrals over the tetrahedra are then generically not analytically solvable. An exception is in one dimension, which will be the basis for IQT, together with insights from IAI presented below.

Iterated adaptive integration

Another efficient way to deal with integrals over Green's functions is iterated adaptive integration (IAI) [KBB+23]. The idea behind iterated integration is to perform the integrals over different dimensions in series. For the integral (2.16) for instance,

$$F(k_x) = \int_{-\pi}^{\pi} \frac{\mathrm{d}k_y}{2\pi}\, G_\mathbf{k}(\omega + \mathrm{i}\eta) \tag{2.22}$$

$$G_{\mathrm{loc}}(\omega + \mathrm{i}\eta) = \int_{-\pi}^{\pi} \frac{\mathrm{d}k_x}{2\pi}\, F(k_x)\,, \tag{2.23}$$

where the integrals (2.22) and (2.23) is evaluated with a standard adaptive integrator, e.g. adaptive Gauss quadrature [KBB+23]. For a given k_x, the integrand in Eq (2.22) contains, in the present example, two sharp features as a function of k_y, where $\mathrm{Re}\, G_\mathbf{k}^{-1}(\omega + \mathrm{i}\eta) = 0$. The sharpness of the features is controlled by η. Using an adaptive grid, such a sharp feature can be resolved with $\mathcal{O}(\log \eta^{-1})$ k_y-points; evaluating Eq. (2.22) therefore scales with $\mathcal{O}(\log \eta^{-1})$.

To ease the discussion of Eq. (2.23), we exploit the fact that in the simple case of the example (2.16), $F(k_x)$ is known exactly,

$$F(k_x) = \frac{1}{\sqrt{(\omega + \mathrm{i}\eta + \cos k_x)^2 - 1}}\,. \tag{2.24}$$

$F(k_x)$ also contains a small set of sharp features, in the example (2.16) located where $|\omega + \cos k_x| = 1$, with their sharpness again controlled by η. Thus, evaluation of Eq. (2.23) generically requires $\mathcal{O}(\log \eta^{-1})$ evaluations of $F(k_x)$, which in turn requires $\mathcal{O}(\log \eta^{-1})$ evaluations of $G_\mathbf{k}(\omega + \mathrm{i}\eta)$. We therefore expect that IAI requires $\mathcal{O}([\log \eta^{-1}]^2)$ to evaluate the 2-dimensional integral (2.16). The scaling $\mathcal{O}([\log \eta^{-1}]^2)$ should be regarded as a worst-case scenario. Typically, the sharpness of features in $F(k_x)$ are more well-behaved w.r.t. η than those in $G_\mathbf{k}(\omega + \mathrm{i}\eta)$, which means we can expect $\mathcal{O}([\log \eta^{-1}]^\alpha)$ scaling, with $1 \leq \alpha \leq 2$. For instance, $F(k_x)$ in Eq. (2.24) scales with $\eta^{-1/2}$ close to its singularities, while $G_\mathbf{k}(\omega + \mathrm{i}\eta)$ scales with η^{-1}. In general, α is expected to be upper bounded by d, where d is the dimension of the integral [KBB+23].

The scaling and performance of IAI are illustrated in Fig. 2.2. We have used MATLAB's `integral2` function with the option "`'method','iterated'`" to produce the data there. In the table below Fig. 2.2(a), we can see that IAI takes longer than ALT to produce the curves in Fig. 2.2(a), reflecting the $\mathcal{O}([\log \eta^{-1}]^\alpha)$ scaling of IAI versus the constant scaling of ALT for generic frequency points [note that $\omega = 0$ is *not* part of the frequency grid used in Fig. 2.2(a)]. The $\mathcal{O}([\log \eta^{-1}]^\alpha)$ scaling is further illustrated in Fig. 2.2(b), where $\alpha = 1.5 < 2$ for a generic frequency point which is not at a van Hove singularity. Figure 2.2(c) shows that at the van

Hove singularity at $\omega = 0$ in our example, the exponent $\alpha = 2$ saturates, showing that such points are most challenging for IAI. Importantly, IAI scales reasonably both away from a van Hove singularity and at a van Hove singularity. In that sense, IAI is more suitable as a general-purpose integrator, but ALT will in most cases be faster.

Iterated quadratic tetrahedron method

As we have seen in the discussions above, ALT is usually a very fast Green's function integration routine. An exception is van Hove singularities, where it performs very poorly because $g(\mathbf{k})$ cannot be represented reliably using a piecewise linear interpolation. A fix for this issue would be piecewise quadratic interpolation, but an analytic expression for the integral can only be obtained in one dimension. IAI on the other hand performs worse than ALT for generic cases, but it has a much more favorable performance at van Hove singularities. The performance of IAI is most severely influenced by the initial integral [Eq. (2.22)], whose integrand is more singular than e.g. the integral Eq. (2.23). Here, I present a new method that combines the advantages of both IAI and ALT, which I call iterated quadratic thetrahedron (IQT) method.

The main idea is to proceed as in IAI, but using the adaptive quadratic tetrahedron method to perform the initial integral (2.22). As for ALT, we assume an integrand of the form $f(\mathbf{k})/g(\mathbf{k})$, with f and g smooth functions. We proceed by performing the integral

$$F(k_x) = \int \mathrm{d}k_y \frac{f(k_x, k_y)}{g(k_x, k_y)} \simeq \sum_i \int_{\mathcal{L}_i} \mathrm{d}k_y \frac{a_i(k_x) + b_i(k_x)k_y + c_i(k_x)k_y^2}{\alpha_i(k_x) + \beta_i(k_x)k_y + \gamma_i(k_x)k_y^2}, \qquad (2.25)$$

where we have partitioned the integration domain in k_y-direction into lines $\mathcal{L}_i$ and have chosen a quadratic interpolation on every $\mathcal{L}_i$. The integral over $\mathcal{L}_i$ is easy to evaluate analytically, summing over the contributions gives $F(k_x)$. Error control is achieved analogous to ALT. The remaining procedure is analogous to IAI, i.e. we use a standard adaptive integrator (in this thesis: MATLAB's `integral` function) to integrate $F(k_x)$.

We expect that the integral (2.25) has constant scaling with η, regardless of whether we are close to a van Hove singularity or not. Similar to ALT, this is because $g(k_x, k_y)$ can be represented well with piecewise quadratic interpolation, requiring only a small number of k_y points. In contrast to ALT, this now works also close to van Hove singularities because the interpolation is now *quadratic* opposed to linear. Using the same arguments as for IAI, we therefore expect that IQT scales with $\mathcal{O}([\log \eta^{-1}]^{\alpha-1})$, where α is the same exponent as in IAI. The reason is that IQT is using a much more efficient integration routine to evaluate Eq. (2.22) (for IAI, this step had a scaling of $\mathcal{O}(\log \eta^{-1})$, opposed to constant for IQT).

Figure 2.2 illustrates the performance of IQT. To produce the curves in Fig. 2.2, IQT takes between around $1/2$ and $1/10$ the time of the other two methods. Figures 2.2(b,c) confirm the expected scaling and illustrate that the exceptionally good performance of IQT holds both away and at a van Hove singularity.

2.1.4 Improved estimators for $\Delta(\omega)$

The evaluation of the local Green's function G_{loc} by numerical integration is is subject to an integration error ϵ. When computing the hybridization function in DMFT via the Dyson equation,

$$\Delta(\omega) = \omega + \mu - \Sigma(\omega) - G_{\mathrm{loc}}^{-1}(\omega), \qquad (2.26)$$

a relatively small error $\epsilon \simeq 10^{-3}$ can lead to a much larger error for $\Delta(\omega)$, because (i) G_{loc} is inverted and (ii) Eq. (2.26) contains a subtraction. By computing additional functions,

$$F_{\mathrm{loc}}(\omega) = \int_{\mathbf{k}} \epsilon_{\mathbf{k}}\, G_{\mathbf{k}}(\omega)\,, \qquad I_{\mathrm{loc}}(\omega) = \int_{\mathbf{k}} \epsilon_{\mathbf{k}}^2\, G_{\mathbf{k}}(\omega)\,, \qquad (2.27)$$

numerically more stable formulas for the hybridization function can be obtained:

$$\Delta^{\mathrm{FG}}(\omega) = F_{\mathrm{loc}}(\omega) G_{\mathrm{loc}}^{-1}(\omega)\,, \qquad (2.28)$$

$$\Delta^{\mathrm{IFG}}(\omega) = I_{\mathrm{loc}}(\omega) - F_{\mathrm{loc}}(\omega) G_{\mathrm{loc}}^{-1}(\omega) F_{\mathrm{loc}}(\omega)\,. \qquad (2.29)$$

The formula for Δ^{IFG} came up in a discussion with Fabian Kugler, and both formulas also appear in Ref. [KK22], while Δ^{IFG} also appears in Ref. [BSB22]. Here, the purpose is to show that Δ^{FG} and Δ^{IFG} provide numerically more stable alternatives to Eq. (2.26), the precise context in Refs. [KK22, BSB22] is different. Further, similar formulas also appear in the literature as more stable alternatives to the Dyson equation for computing the single-particle irreducible self-energy $\Sigma(\omega)$ [BHP98, Kug22]. A derivation of Eqs. (2.28) and (2.29) can be found in the supplemental material of Ref. [KK22] and will not be repeated here. We will denote Δ computed via Eq. (2.26) by Δ^{G} in this subsection, to clearly distiguish it from Δ^{FG} and Δ^{IFG}. If $|\Delta(\omega)| \ll |\Sigma(\omega)| \simeq |G_{\mathrm{loc}}^{-1}(\omega)|$, Eq. (2.26) involves the subtraction of two almost equal numbers which are subject to numerical inaccuracies, which leads to much larger relative inaccuracies in their difference, $\Delta(\omega)$. Eqs. (2.28) and (2.29) avoid subtracting almost equal numbers and are therefore expected to be numerically more stable.

As an example, consider the Hubbard model on a cubic lattice,

$$H = \sum_{\mathbf{k}\sigma} (\epsilon_{\mathbf{k}} - \mu) c_{\mathbf{k}\sigma}^{\dagger} c_{\mathbf{k}\sigma} + U \sum_i n_{i\uparrow} n_{i\downarrow}\,, \qquad (2.30)$$

with dispersion $\epsilon_{\mathbf{k}} = -\frac{1}{6}(\cos k_x + \cos k_y + \cos k_z)$, $\mu = U/2$ and $U = 2.2$ at temperature $T = 10^{-6}$. The single-site DMFT spectral function, obtained by DMFT plus NRG is shown in Fig. 2.3(a). We use the ALT method to compute the one-dimensional density of states integrals,

$$G_{\mathrm{loc}}(\omega) = \int_{-1}^{1} \mathrm{d}\epsilon \frac{\rho(\epsilon)}{\omega + \mu - \epsilon - \Sigma(\omega)}\,, \qquad F_{\mathrm{loc}}(\omega) = \int_{-1}^{1} \mathrm{d}\epsilon \frac{\epsilon \rho(\epsilon)}{\omega + \mu - \epsilon - \Sigma(\omega)}\,, \qquad (2.31)$$

$$I_{\mathrm{loc}}(\omega) = \int_{-1}^{1} \mathrm{d}\epsilon \frac{\epsilon^2 \rho(\epsilon)}{\omega + \mu - \epsilon - \Sigma(\omega)}\,, \qquad \rho(\epsilon) = \int_{\mathrm{BZ}} \frac{\mathrm{d}\mathbf{k}}{(2\pi)^3} \delta(\epsilon - \epsilon_{\mathbf{k}})\,, \qquad (2.32)$$

where $\rho(\epsilon)$ is the non-interacting density of states the cubic lattice (which was precomputed with high accuracy and stored in the past).

Figure 2.3(b) shows the imaginary parts of Σ, G_{loc}^{-1} and Δ. The latter is a reference curve, obtained by a high-accuracy computation of G_{loc}, F_{loc} and I_{loc} (error less than 10^{-12}) and using Eq. (2.29). Around $\omega \simeq 10^{-1}$, we find $-\mathrm{Im}\Sigma \simeq \mathrm{Im}G_{\mathrm{loc}}^{-1} \gg -\mathrm{Im}\Delta$ (note that the y-axis of Fig. 2.3(b) is in log scale!). In this region, obtaining $-\mathrm{Im}\Delta$ via Eq. (2.26) is therefore prone to numerical errors, and Eqs. (2.28) and (2.29) are significantly more stable. This is illustrated in Fig. 2.3(c), which shows $-\mathrm{Im}\Delta$ obtained via Eq. (2.26) (blue, unstable) versus Eq. (2.29) (red dashed, stable), with the integrals now performed with a more practical accuracy of 10^{-3}. We have checked that Eq. (2.28) and Eq. (2.29) yield identical results on the scales shown in Fig. 2.3(c). Around $\omega \simeq 10^{-1}$, $-\mathrm{Im}\Delta^{\mathrm{G}}$ has clearly visible artifacts, which are not present in $-\mathrm{Im}\Delta^{\mathrm{IFG}}$. In Figures 2.3(d,e,f), we show the error of Δ^{G}, Δ^{FG} and Δ^{IFG} for different integration accuracies ε w.r.t the high-accuracy reference curve. Both Δ^{FG}
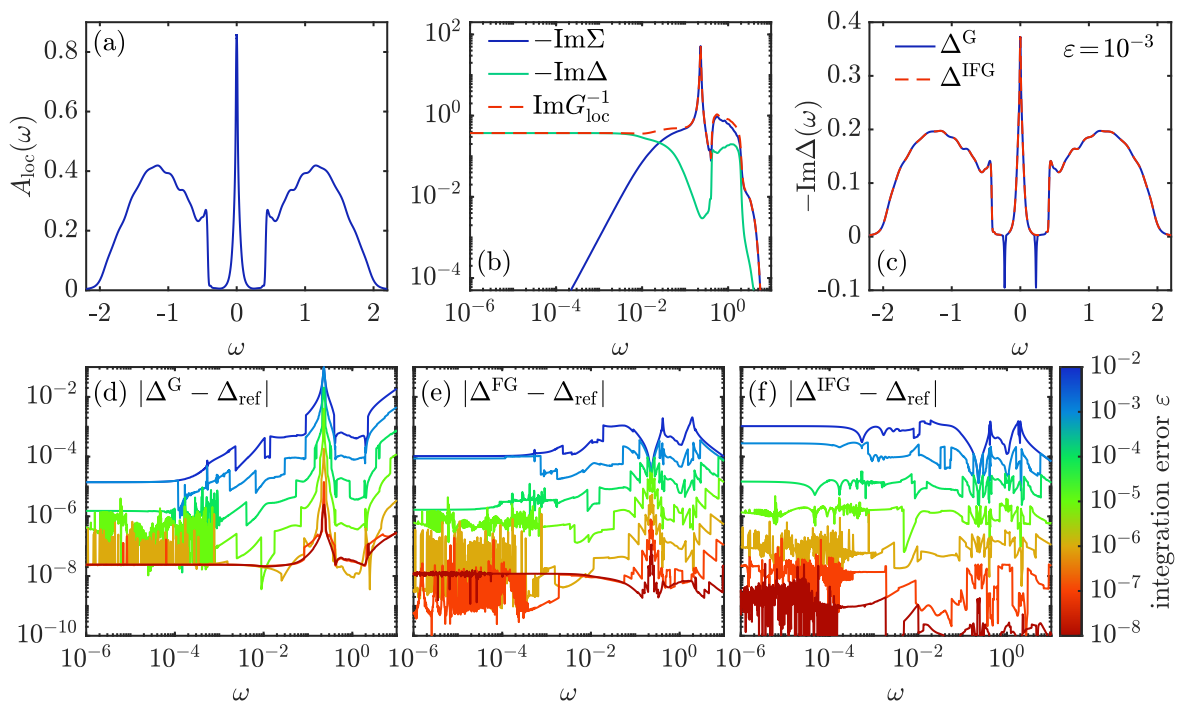
Figure 2.3 (a) Local spectral function of the Hubbard model on a cubic lattice in the single-site DMFT approximation at $U = 2.2$ and $T = 10^{-6}$. (b) Corresponding imaginary parts of the self-energy $\Sigma(\omega)$, hybridization function $\Delta(\omega)$ and inverse local Green's function $G_{\text{loc}}(\omega)$. $G_{\text{loc}}(\omega)$ and $\Delta(\omega)$ have been evaluated using an integration accuracy of $\epsilon = 10^{-12}$. (c) Imaginary part of the hybridization function $\Delta(\omega)$ using the Dyson equation (2.26) (Δ^{G}, blue) and using the improved estimator (2.29) (Δ^{IFG}, red dashed), respectively. A practical integration accuracy of $\epsilon = 10^{-3}$ has been used. Δ^{G} has clearly visible artifacts where $-\text{Im}\,\Delta^{\text{G}}$ becomes negative. (d-f) Absolute errors of the estimates Δ^{G}, Δ^{FG} and Δ^{IFG} to the reference curve shown in (b). Both Δ^{FG} and Δ^{IFG} come with an acceptable error ($< 10^{-3}$) at moderate integration accuracies ($\epsilon \geq 10^{-4}$) while Δ^{G} needs smaller $\epsilon \simeq 10^{-6}$ to achieve an error of less than 10^{-3}.

and Δ^{IFG} have an error of order at most ε, while the error of Δ^{G} significantly exceeds the integration error in some frequency region.

To conclude, Eqs. (2.28) and (2.29) offer a numerically much more stable alternative to Eq. (2.26), at the expense of requiring the evaluation of one or two additional integrals, respectively. From current experience, Δ^{FG} is the best choice since it requires only one additional integral while performing similarly to Δ^{IFG} in terms of accuracy. It should also be emphasized that the parameters chosen in this section were picked such that Δ^{G} is prone to numerical inaccuracies. In many cases, Δ^{G} is accurate for a reasonable integration accuracy of say $\varepsilon = 10^{-3}$, but Δ^{FG} and Δ^{IFG} offer a safer alternative which also work when Eq. (2.26) is unstable. Also, while we have concluded here that Δ^{FG} and Δ^{IFG} are equally accurate for the problem in this section, there is no guarantee that this generically the case.

2.2 Numerical Renormalization Group

In this thesis, we have employed the Numerical Renormalization Group (NRG) as an impurity solver to within the DMFT self-consistency equations. NRG is a non-perturbative, real-frequency impurity solver with unparalleled low-frequency and temperature resolution [BCP08]. The original ideas for the NRG algorithm were published by Wilson [Wil75] in 1975 as a solution to the Kondo problem. Back then, NRG could not compute Green's

functions or self-energies, a prerequisite for applying it in the DMFT context. This problem was solved by subsequent work [FO86, CHZ94, BHP98, Hof00, WvD07, Kug22]. Important developments on the way to its current status were (i) the construction of a complete basis using NRG by F. B. Anders and A. Schiller [AS05, AS06], (ii) the subsequent development of the full density matrix NRG (fdm-NRG) by A. Weichselbaum and J. von Delft [WvD07] for sum-rule conserving spectral functions at arbitrary temperatures, and (iii) the computation of self-energies via equations of motion by R. Bulla *et. al.* [BHP98] and F. B. Kugler [Kug22]. In the following, a brief overview of NRG is provided. The NRG code used to produce the results in this thesis was implemented by S.-S. B. Lee and is based on A. Weichselbaum's QSpace tensor library [Wei12, Wei20, Wei24], which allows the exploitation of Abelian and non-Abelian symmetries.

NRG uses a Hamiltonian formulation of the impurity model,

$$H = H_{\text{imp}} + H_{\text{hyb}} + H_{\text{bath}}, \quad H_{\text{hyb}} = \sum_{\alpha\lambda} V_{\alpha\lambda} f_\alpha^\dagger c_\lambda + \text{h.c.}, \quad H_{\text{bath}} = \sum_\lambda \epsilon_\lambda c_\lambda^\dagger c_\lambda, \quad (2.33)$$

where f_α are annihilation operators on the impurity with flavor α (spin, orbital, etc.), c_λ are annihilation operators for bath flavor λ and H_{imp} is the local impurity Hamiltonian, which can be an arbitrary function of f_α but does not depend on c_λ. The number of impurity flavors N_α, is assumed to be small. NRG can, at the moment, reasonably deal with 4 spinful fermionic orbitals ($N_\alpha = 8$) if symmetries can be exploited. On the other hand, the number of bath flavors λ is usually infinite, and the energies ϵ_λ are continuous.

The influence of the bath on the impurity is described by the hybridization function $\Delta(z)$,

$$\Delta_{\alpha\beta}(z) = \sum_\lambda \frac{V_{\alpha\lambda} V_{\beta\lambda}^*}{z - \epsilon_\lambda}, \quad \Gamma_{\alpha\beta}(\omega) = \sum_\lambda V_{\alpha\lambda} V_{\beta\lambda}^* \delta(\omega - \epsilon_\lambda), \quad (2.34)$$

where the Hermitian matrix $\Gamma(\omega)$ is the spectral function of $\Delta(z)$. In the following, we assume that $\Gamma_{\alpha\beta}(\omega) \propto \delta_{\alpha\beta}$ is diagonal, since this is the case in all situations considered in this thesis. To make progress with Hamiltonian-based methods, the bath usually needs to be discretized by approximating $\Gamma(\omega)$ by a discrete set of spectral peaks,

$$\Gamma_\alpha(\omega) \simeq \Gamma_\alpha^{\text{disc}}(\omega) = \sum_{n,\zeta=\pm} |\gamma_\alpha^{n\zeta}|^2 \delta(\omega - \xi_\alpha^{n\zeta}). \quad (2.35)$$

In NRG, a logarithmic discretization is used [Wil75, BCP08], which allows us to resolve features at different frequency scales with equal accuracy. There, the support of $\Gamma_\alpha(\omega)$, $[-D_\alpha^-, D_\alpha^+]$, is partitioned into intervals $\mathcal{I}_\alpha^{n+} = D_\alpha^+[\Lambda^{-n-1}, \Lambda^{-n}]$ and $\mathcal{I}_\alpha^{n-} = -D_\alpha^-[\Lambda^{-n}, \Lambda^{-n-1}]$, where $\Lambda > 1$ is a discretization parameter. A single peak at a representative energy $\xi_\alpha^{n\zeta} \in \mathcal{I}_\alpha^{n\zeta}$ and weight $|\gamma_\alpha^{n\zeta}|^2$ is chosen per interval and impurity flavor α. The weights $|\gamma_\alpha^{n\zeta}|^2$ are chosen such that the total weight of the hybridization spectrum in $\mathcal{I}_\alpha^{n\zeta}$ is conserved, $|\gamma_\alpha^{n\zeta}|^2 = \int_{\mathcal{I}_\alpha^{n\zeta}} \Gamma_\alpha(\omega)$. For the representative energies, $\xi_\alpha^{n\zeta}$, we use a scheme invented by R. Žitko and T. Pruschke [ŽP09, Žit09a] and whose stable implementation was achieved by K. M. Stadler, c.f. Sec. 2.2.3 of Ref. [Sta19]. The corresponding discretized bath and hybridization Hamiltonians are

$$H_{\text{bath}}^{\text{disc}} = \sum_{\alpha,n,\zeta} \xi_\alpha^{n\zeta} a_{\alpha n\zeta}^\dagger a_{\alpha n\zeta}, \quad H_{\text{hyb}}^{\text{disc}} = \sum_{\alpha,n,\zeta} \gamma_\alpha^{n\zeta} a_{\alpha n\zeta}^\dagger f_\alpha + \text{h.c.}. \quad (2.36)$$

In the next step, the bath is transformed into a semi-infinite chain using Lanczos tridiagonal-

ization, known as Wilson chain [Wil75],

$$H_{\text{bath}}^{\text{chain}} = \sum_\alpha \left[\sum_{\ell=1}^\infty \left(t_{\ell\alpha} d_{\ell-1\alpha}^\dagger d_{\ell\alpha} + \text{h.c.} \right) + \sum_{\ell=0}^\infty \epsilon_{\ell\alpha} d_{\ell\alpha}^\dagger d_{\ell\alpha} \right], \quad H_{\text{hyb}}^{\text{chain}} = \sum_\alpha t_{0\alpha} d_{0\alpha}^\dagger f_\alpha + \text{h.c.} \quad (2.37)$$

Due to the logarithmic discretization, the hopping matrix elements $t_{\ell\alpha}$ and on-site energies $\epsilon_{\ell\alpha}$ decay as $\propto \Lambda^{-\ell/2}$ and $\propto \Lambda^{-\ell}$, respectively. The problem has therefore been separated into energy scales, with

$$H_{\mathscr{L}}^{\text{chain}} = H_{\text{imp}} + \sum_\alpha \left[t_{0\alpha} d_{1\alpha}^\dagger f_\alpha + \text{h.c.} + \sum_{\ell=1}^{\mathscr{L}} \left(t_{\ell\alpha} d_{\ell-1\alpha}^\dagger d_{\ell\alpha} + \text{h.c.} \right) + \sum_{\ell=0}^{\mathscr{L}} \epsilon_{\ell\alpha} d_{\ell\alpha}^\dagger d_{\ell\alpha} \right] \quad (2.38)$$

describing the spectrum with a resolution of order $\Lambda^{-\mathscr{L}/2}$. NRG then uses iterative diagonalization to obtain a full approximate spectrum of $\lim_{\mathscr{L} \to \infty} H_{\mathscr{L}}^{\text{chain}}$. The chain is successively extended, $H_{\mathscr{L}}^{\text{chain}} \to H_{\mathscr{L}+1}^{\text{chain}}$, thereby improving energy resolution by a factor $\Lambda^{-1/2}$, but also increasing the Hilbert space size by a factor 2^{N_α}. To keep the problem computationally feasible, the high-energy part of the spectrum of $H_{\mathscr{L}}^{\text{chain}}$ is discarded and $H_{\mathscr{L}}^{\text{chain}}$ is projected to its low-energy kept sector before extending the chain. Thus, the high-energy discarded states $|s\rangle_{\mathscr{L}}^{\text{D}}$ are not further fine-grained and therefore computed with resolution $\Lambda^{-\mathscr{L}/2}$, while the low-energy kept states $|s\rangle_{\mathscr{L}}^{\text{K}}$ are further fine-grained. Because $t_{\mathscr{L}+1} \ll t_{\mathscr{L}}$, $H_{\mathscr{L}+1}^{\text{chain}}$ is not expected to strongly mix $|s\rangle_{\mathscr{L}}^{\text{K}}$ and $|s\rangle_{\mathscr{L}}^{\text{D}}$, which justifies the truncation. Typically, the approximate eigenenergies $E_s^{\mathscr{L}}$ are shifted by the ground state energy $E_0^{\mathscr{L}}$ and rescaled by the scale $\Lambda^{-\mathscr{L}/2}$. This helps to avoid small numbers and identify crossovers and fixed points in the low-energy spectra, but is conceptionally not necessary. The iterative diagonalization is halted at some length $\mathscr{L}_{\text{max}}$ after a certain desired energy resolution $\Lambda^{-\mathscr{L}_{\text{max}}/2}$ has been reached. In fdm-NRG, this resolution is set by the temperature, $\Lambda^{-\mathscr{L}_{\text{max}}/2} \simeq T$ [WvD07, Wei12].

As was pointed out by Anders and Schiller [AS05, AS06], the iterative diagonalization generates a complete approximate eigenbasis of $H_{\mathscr{L}_{\text{max}}}^{\text{chain}}$,

$$H_{\mathscr{L}_{\text{max}}}^{\text{chain}} |s\rangle_{\mathscr{L}}^{\text{D}} \otimes |e\rangle_{\mathscr{L}} \simeq E_s^{\mathscr{L}} |s\rangle_{\mathscr{L}}^{\text{D}} \otimes |e\rangle_{\mathscr{L}}, \quad (2.39)$$

where $|e\rangle_{\mathscr{L}} = |\sigma_{\mathscr{L}+1}\rangle \otimes \cdots \otimes |\sigma_{\mathscr{L}_{\text{max}}}\rangle$ is some product state on sites $\mathscr{L}+1$ to $\mathscr{L}_{\text{max}}$. Thus, the energy level $E_s^{\mathscr{L}}$ has, by construction, a degeneracy of $2^{N_\alpha(\mathscr{L}_{\text{max}}-\mathscr{L})}$, which reflects that the discarded states have not been fine-grained further. In the fdm-NRG scheme, the approximate eigenstates are used to set up a full approximate eigenbasis, construct a thermal density matrix and compute spectral functions using the Lehmann representation [WvD07, Wei12].

Since we have discretized the originally continuous bath, the spectral functions computed with fdm-NRG consist of discrete δ-peaks with an exponentially increasing density towards $\omega = 0$, reflecting the exponentially fine energy resolution of fdm-NRG around $\omega = 0$. These discrete spectral peaks are broadened using a log-Gaussian kernel [LW16] to mimic the effect of the bath modes which have been truncated by the logarithmic discretization.

To improve the resolution of NRG, several calculations with shifted discretization grids can be performed, known as z-averaging. For that, several, (usually equally-spaced) parameters $z \in [0, 1)$ are chosen to define shifted discretization intervals $\mathcal{I}_\alpha^{n+}(z) = D_\alpha^+[\Lambda^{-n-1-z}, \Lambda^{-n-z}]$ and $\mathcal{I}_\alpha^{n-}(z) = -D_\alpha^-[\Lambda^{-n-z}, \Lambda^{-n-1-z}]$. The results from separate fdm-NRG calculations with different z are in the end averaged to achieve higher resolution, especially at high frequencies [OO94, ŽP09]. By considering the effect of an infinitesimal z-shift on the spectra, it is further possible to adaptively adjust the widths of the log-Gaussian broadening kernels, which further improves high-frequency resolution [LW16, LvDW17a].

The z-shifting trick can also be used to reduce the computational cost if N_α is large, known

as interleaved NRG (iNRG) [MGWF$^+$14, SMvDW16]. For that, different shift parameters z_α are used for the different impurity flavors α, which introduces an artificial scale separation between flavors. Due to that, different flavors can be added in series during the iterative diagonalization, which reduces the Hilbert space dimension at every diagonalization step and thus the computational cost.

2.3 Matrix product states

This section introduces matrix product states (MPS), which offer a very efficient representation of one-dimensional quantum states. For reviews on MPS, see Refs. [Sch11, CPGSV21]. The discussion which follows is partially based on parts of Ref. [P1] and extensively uses the notation developed there. Consider a quantum state

$$|\Psi\rangle = \sum_{\sigma_1,\dots,\sigma_{\mathscr{L}}} \Psi^{\sigma_1\dots\sigma_{\mathscr{L}}} |\sigma_1 \dots \sigma_{\mathscr{L}}\rangle, \qquad (2.40)$$

where $\{|\sigma_\ell\rangle\}$ are basis vectors of some local, low-dimensional Hilbert space $\mathbb{v}_\ell$ with dimension d, e.g. a local moment or a spinful fermionic orbital. In general, the wavefunction $\Psi^{\sigma_1\dots\sigma_{\mathscr{L}}}$ can be decomposed as a product of matrices $M_\ell^{\sigma_\ell}$, known as MPS representation,

$$\Psi^{\sigma_1\dots\sigma_{\mathscr{L}}} = M_1^{\sigma_1}\dots M_{\mathscr{L}}^{\sigma_{\mathscr{L}}} = \quad \text{[graphical notation]} \quad . \qquad (2.41)$$

Here, we have used a graphical notation that represents the tensors M_ℓ as circles with legs representing tensor indices. Connected legs are summed over. The MPS representation is useful if the rank of $M_\ell^{\sigma_\ell}$ is small (say at most D, called bond dimension), or if a controlled low-rank approximation can be found. In that case, the number of parameters needed to represent the wavefunction has been reduced dramatically, from initially $\mathcal{O}(d^{\mathscr{L}})$ to $\mathcal{O}(\mathscr{L}D^2d)$. The existence of a controlled low-rank approximation can be proven for ground states of one-dimensional gapped local Hamiltonians [Has07, ECP10, AKLV13, BH15]. In general, the MPS representation is very efficient for one-dimensional systems, even if they are critical [VC06, PMTM09]. For this reason, MPS algorithms are arguably the most powerful numerical tools available to date to treat (quasi-) one-dimensional systems. An important class of effectively one-dimensional systems are impurity models, as we have seen for NRG in Sec. 2.2 where we have mapped the impurity model on a Wilson chain. As discussed in Sec. 2.3.1, NRG can be formulated as an MPS method [Wei12]. Apart from NRG, other impurity solvers based on MPS [WMPS14, WMS14, WGM$^+$15, FH17, BBLG$^+$23, CLSP24] or more general loopless tensor network states [BZT$^+$17, GWK$^+$24] are becoming increasingly popular in the DMFT community.

The MPS representation is not unique since we can insert some invertible matrix X and its inverse between two MPS matrices, $M_\ell^{\sigma_\ell} M_{\ell+1}^{\sigma_{\ell+1}} = M_\ell^{\sigma_\ell} X X^{-1} M_{\ell+1}^{\sigma_{\ell+1}} = \widetilde{M}_\ell^{\sigma_\ell} \widetilde{M}_{\ell+1}^{\sigma_{\ell+1}}$, with $\widetilde{M}_\ell^{\sigma_\ell} = M_\ell^{\sigma_\ell} X$ and $\widetilde{M}_{\ell+1}^{\sigma_{\ell+1}} = X^{-1} M_{\ell+1}^{\sigma_{\ell+1}}$. Since M and $\widetilde{M}$ represent the same state, an MPS has a gauge freedom. A very convenient gauge is the so-called bond-canonical form,

$$\Psi^\sigma = \quad \text{[graphical notation]} \quad , \qquad (2.42)$$

where the bond matrix Λ_ℓ ($\bigcirc$) is called isometry center and $A_{\tilde{\ell}}$ ($\searrow$) and $B_{\tilde{\ell}'}$ ($\diagdown$) are left

and right isometries, respectively. They fulfill the isometry conditions

$$
\bar{\alpha}\,\underset{A_{\tilde{\ell}}^{*}}{\overset{A_{\tilde{\ell}}}{\bigcup}}\,{}_{\alpha}^{\alpha'} = \Big(\,{}_{\alpha}^{\alpha'} = [\mathbb{1}_{\tilde{\ell}}^{\mathrm{K}}]_{\alpha\alpha'}\,, \qquad \underset{B_{\tilde{\ell}'}^{*}}{\overset{B_{\tilde{\ell}'}}{\underset{\alpha'}{\overset{\alpha}{\bigcap}}}}\,\bar{\alpha} = {}_{\alpha'}^{\alpha}\Big) = [\mathbb{1}_{\tilde{\ell}'-1}^{\mathrm{K}}]_{\alpha\alpha'}\,, \tag{2.43}
$$

where lines denote identities and K stands for kept space, denoted $\mathbb{V}_{\tilde{\ell}}^{\mathrm{K}}$ and $\mathbb{W}_{\tilde{\ell}'}^{\mathrm{K}}$, respecively. The isometry $A_{\tilde{\ell}}$ is an orthogonal map from the parent space $\mathbb{V}_{\tilde{\ell}}^{\mathrm{P}} = \mathbb{V}_{\tilde{\ell}-1}^{\mathrm{K}} \otimes \mathrm{v}_{\tilde{\ell}}$ to the kept space $\mathbb{V}_{\tilde{\ell}}^{\mathrm{K}}$, and likewise for $B_{\tilde{\ell}'}$. The kept spaces are spanned by the kept states

$$
|\Psi_{\tilde{\ell}\alpha}^{\mathrm{K}}\rangle = \sum_{\sigma_1\ldots\sigma_{\tilde{\ell}}} [\Psi_{\tilde{\ell}\alpha}^{\mathrm{K}}]^{\sigma_1\ldots\sigma_{\tilde{\ell}}}|\sigma_1\ldots\sigma_{\tilde{\ell}}\rangle\,, \qquad |\Phi_{\tilde{\ell}'\alpha'}^{\mathrm{K}}\rangle = \sum_{\sigma_{\tilde{\ell}'}\ldots\sigma_{\mathscr{L}}} [\Phi_{\tilde{\ell}'\alpha'}^{\mathrm{K}}]^{\sigma_{\tilde{\ell}'}\ldots\sigma_{\mathscr{L}}}|\sigma_{\tilde{\ell}'}\ldots\sigma_{\mathscr{L}}\rangle \tag{2.44}
$$

$$
\Psi_{\tilde{\ell}\alpha}^{\mathrm{K}} = \;\;\overset{A_1 \quad A_{\tilde{\ell}}}{\star\!\!\curlyvee\!\curlyvee\!\curlyvee}\,\alpha \qquad\qquad\qquad \Phi_{\tilde{\ell}'\alpha'}^{\mathrm{K}} = \;\alpha'\overset{B_{\tilde{\ell}'} \quad B_{\mathscr{L}}}{\curlywedge\!\curlywedge\!\curlywedge\!\star}\,, \tag{2.45}
$$

which form an orthonormal basis due to the isometry condition (2.43). Using the kept states and the bond matrix $\Lambda_{\tilde{\ell}}$ (chosen to be diagonal), we obtain a Schmidt decomposition of $|\Psi\rangle$,

$$
|\Psi\rangle = \sum_{\alpha} [\Lambda_{\ell}]_{\alpha\alpha}|\Psi_{\ell\alpha}^{\mathrm{K}}\rangle \otimes |\Phi_{\ell+1\alpha}^{\mathrm{K}}\rangle\,. \tag{2.46}
$$

We can also define orthogonal complements to $A_{\tilde{\ell}}$ and $B_{\tilde{\ell}'}$, denoted by $\overline{A}_{\tilde{\ell}}$ ($\curlywedge$) and $\overline{B}_{\tilde{\ell}'}$ ($\curlyvee$). They also fulfill isometry conditions and they are orthogonal to $A_{\tilde{\ell}}$ and $B_{\tilde{\ell}'}$,

$$
\overline{A}_{\tilde{\ell}}^{\dagger}\overline{A}_{\tilde{\ell}} = \mathbb{1}_{\tilde{\ell}}^{\mathrm{D}}\,, \;\; A_{\tilde{\ell}}^{\dagger}\overline{A}_{\tilde{\ell}} = 0\,, \;\; \overline{B}_{\tilde{\ell}'}\overline{B}_{\tilde{\ell}'}^{\dagger} = \mathbb{1}_{\tilde{\ell}'-1}^{\mathrm{D}}\,, \;\; \overline{B}_{\tilde{\ell}'}B_{\tilde{\ell}'}^{\dagger} = 0\,,
$$

$$
\underset{\tilde{\ell}}{\bigcup} = \Big(= \mathbb{1}_{\tilde{\ell}}^{\mathrm{D}}\,, \;\; \underset{\tilde{\ell}}{\bigcup} = 0\,, \;\; \underset{\tilde{\ell}'}{\bigcap} = \Big) = \mathbb{1}_{\tilde{\ell}'-1}^{\mathrm{D}}\,, \;\; \underset{\tilde{\ell}'}{\bigcap} = 0\,, \tag{2.47}
$$

where D stands for discarded space, denoted $\mathbb{V}_{\tilde{\ell}}^{\mathrm{D}}$ and $\mathbb{W}_{\tilde{\ell}'}^{\mathrm{D}}$. The discarded spaces are such that together with the kept space, they span the full parent space, i.e. $\mathbb{V}_{\tilde{\ell}}^{\mathrm{K}} \oplus \mathbb{V}_{\tilde{\ell}}^{\mathrm{D}} = \mathbb{V}_{\tilde{\ell}}^{\mathrm{P}}$ and $\mathbb{W}_{\tilde{\ell}'}^{\mathrm{K}} \oplus \mathbb{W}_{\tilde{\ell}'}^{\mathrm{D}} = \mathbb{W}_{\tilde{\ell}'}^{\mathrm{P}}$. Thus, the direct sum of $A_{\tilde{\ell}}$ and $\overline{A}_{\tilde{\ell}}$, $A_{\tilde{\ell}} \oplus \overline{A}_{\tilde{\ell}} = \curlyvee \oplus \curlywedge$ is a unitary on the parent space $\mathbb{V}_{\tilde{\ell}}^{\mathrm{P}} = \mathbb{V}_{\tilde{\ell}-1}^{\mathrm{K}} \otimes \mathrm{v}_{\tilde{\ell}}$, and likewise for $B_{\tilde{\ell}'}$ and $\overline{B}_{\tilde{\ell}'}$. Similar to the kept states, we can use the isometries to write down wavefunctions for the discarded states,

$$
|\Psi_{\tilde{\ell}\alpha}^{\mathrm{D}}\rangle = \sum_{\sigma_1\ldots\sigma_{\tilde{\ell}}} [\Psi_{\tilde{\ell}\alpha}^{\mathrm{D}}]^{\sigma_1\ldots\sigma_{\tilde{\ell}}}|\sigma_1\ldots\sigma_{\tilde{\ell}}\rangle\,, \qquad |\Phi_{\tilde{\ell}'\alpha'}^{\mathrm{D}}\rangle = \sum_{\sigma_{\tilde{\ell}'}\ldots\sigma_{\mathscr{L}}} [\Phi_{\tilde{\ell}'\alpha'}^{\mathrm{D}}]^{\sigma_{\tilde{\ell}'}\ldots\sigma_{\mathscr{L}}}|\sigma_{\tilde{\ell}'}\ldots\sigma_{\mathscr{L}}\rangle \tag{2.48}
$$

$$
\Psi_{\tilde{\ell}\alpha}^{\mathrm{D}} = \;\;\overset{A_1 \quad \overline{A}_{\tilde{\ell}}}{\star\!\!\curlyvee\!\curlyvee\!\curlywedge}\,\alpha\,, \qquad\qquad\qquad \Phi_{\tilde{\ell}'\alpha'}^{\mathrm{D}} = \;\alpha'\overset{\overline{B}_{\tilde{\ell}'} \quad B_{\mathscr{L}}}{\curlyvee\!\curlywedge\!\curlywedge\!\star}\,, \tag{2.49}
$$

which span the discarded spaces $\mathbb{V}_{\tilde{\ell}}^{\mathrm{D}}$ and $\mathbb{W}_{\tilde{\ell}'}^{\mathrm{D}}$, respectively.

Another convenient gauge, the so-called site-canonical gauge, can be obtained by contracting $C_{\ell} = A_{\ell}\Lambda_{\ell}$ in Eq. (2.42),

$$
\Psi^{\sigma} = \;\;\overset{A_1 \qquad\qquad A_{\ell-1} \;\; C_{\ell} \;\; B_{\ell+1} \qquad\qquad B_{\mathscr{L}}}{\star\!\underset{\sigma_1}{\curlyvee}\!\underset{D_{\ell-2}}{\;}\!\underset{\sigma_{\ell-1}}{\curlyvee}\!\underset{D_{\ell-1}}{\;}\!\underset{\sigma_{\ell}}{\circ}\!\underset{D_{\ell}}{\;}\!\underset{\sigma_{\ell+1}}{\curlywedge}\!\underset{D_{\ell+1}}{\;}\!\underset{\sigma_{\mathscr{L}}}{\curlywedge}\!\star}\,. \tag{2.50}
$$

Shifting the isometry center or finding the canonical form can be done using singular value decompositions (SVD) or QR decompositions as usual, c.f. for instance Eq.(7) of Ref. [P1] or Ref. [Sch11].

The set of MPS with bond-dimension D forms a submanifold of the full space $\mathbb{V} = \mathbb{v}_1 \otimes \cdots \otimes \mathbb{v}_{\mathscr{L}}$, denoted $\mathcal{M}_{\text{D-MPS}}$ [HOV13, HMOV14]. It is not a vector space since for instance adding two bond-dimension D MPS generally leads to an MPS with bond dimension $2D$, i.e. the result is not in $\mathcal{M}_{\text{D-MPS}}$. The tangent space $\mathcal{T}_\Psi \mathcal{M}_{\text{D-MPS}} \subset \mathbb{V}$ denotes the space of 1-site changes of $|\Psi\rangle \in \mathcal{M}_{\text{D-MPS}}$. A projector to $\mathcal{T}_\Psi \mathcal{M}_{\text{D-MPS}}$, denoted $\mathcal{P}^{1s}$, can be written down using the kept and discarded isometries of $|\Psi\rangle$ [LOV15, HLO$^+$16, P1],

$$\mathcal{P}^{1s} = \sum_{\ell=1}^{\mathscr{L}} \underset{\ell}{\vcenter{\hbox{\includegraphics{fig}}}} + \underset{1 \qquad \mathscr{L}}{\vcenter{\hbox{\includegraphics{fig}}}} \tag{2.51}$$

$$= \sum_{\ell=1}^{\mathscr{L}} \underbrace{\underset{\ell}{\vcenter{\hbox{\includegraphics{fig}}}}}_{\mathcal{P}_\ell^{1s}} - \sum_{\ell=1}^{\mathscr{L}-1} \underbrace{\underset{\ell}{\vcenter{\hbox{\includegraphics{fig}}}}}_{\mathcal{P}_\ell^{b}}, \tag{2.52}$$

where we have defined single-site and bond projectors $\mathcal{P}_\ell^{1s}$ and $\mathcal{P}_\ell^{b}$, respectively. A generic tangent vector $|\partial\Psi\rangle \in \mathcal{T}_\Psi \mathcal{M}_{\text{D-MPS}}$ does not have a bond-dimension D MPS representation. Thus, taking macroscopic steps within the tangent space will in general result in a state that is not in $\mathcal{M}_{\text{D-MPS}}$, which reflects that this manifold has a curvature. There are, however, subspaces of $\mathcal{T}_\Psi \mathcal{M}_{\text{D-MPS}}$ within which we can take macroscopic steps while remaining on $\mathcal{M}_{\text{D-MPS}}$ ($\mathcal{M}_{\text{D-MPS}}$ is therefore flat in these directions, i.e. the (non-uniform) MPS manifold is a ruled manifold [HMOV14]). These are for instance the images of the single-site projectors $\mathcal{P}_\ell^{1s}$ (denoted $\mathbb{V}_\ell^{1s}$) and bond projectors $\mathcal{P}_\ell^{b}$ (denoted $\mathbb{V}_\ell^{b}$), i.e. $|\Psi\rangle + a\mathcal{P}_\ell^{1s}|\partial\Psi\rangle \in \mathcal{M}_{\text{D-MPS}}$ and likewise for $\mathcal{P}_\ell^{b}$. Further, $|\Psi\rangle \in \mathbb{V}_\ell^{1s}$ and $|\Psi\rangle \in \mathbb{V}_\ell^{b}$. As a result, we can manipulate an MPS within the subspaces $\mathbb{V}_\ell^{1s}$ and $\mathbb{V}_\ell^{b}$ at will without leaving $\mathcal{M}_{\text{D-MPS}}$. This is for instance used in ground-state search, c.f. Sec. 2.3.2. The tangent space projector can be decomposed into projectors to $\mathbb{V}_\ell^{1s}$ and $\mathbb{V}_\ell^{b}$, c.f. Eq. (2.52) [HLO$^+$16]. This convenient decomposition is used in time evolution within $\mathcal{M}_{\text{D-MPS}}$, c.f. Sec. 2.3.3.

Another important projector is the 2-site generalization of $\mathcal{P}^{1s}$ [HLO$^+$16, P1],

$$\mathcal{P}^{2s} = \sum_{\ell=1}^{\mathscr{L}-1} \underbrace{\underset{\ell}{\vcenter{\hbox{\includegraphics{fig}}}}}_{\mathcal{P}_\ell^{2s}} - \sum_{\ell=2}^{\mathscr{L}-1} \underbrace{\underset{\ell}{\vcenter{\hbox{\includegraphics{fig}}}}}_{\mathcal{P}_\ell^{1s}} . \tag{2.53}$$

For an n-site generalization, see Ref. [P1].

Similar to states, we can represent operators like the Hamiltonian $\widehat{H}$ as matrix product operators (MPO),

$$\widehat{H} = \sum_{\sigma,\sigma'} |\sigma_1 \ldots \sigma_{\mathscr{L}}\rangle H^{\sigma_1 \ldots \sigma_{\mathscr{L}}}_{\sigma'_1 \ldots \sigma'_{\mathscr{L}}} \langle \sigma'_1 \ldots \sigma'_{\mathscr{L}}|, \tag{2.54}$$

$$H^{\sigma_1 \ldots \sigma_{\mathscr{L}}}_{\sigma'_1 \ldots \sigma'_{\mathscr{L}}} = [W_1]^{\sigma_1}_{\sigma'_1} \ldots [W_{\mathscr{L}}]^{\sigma_{\mathscr{L}}}_{\sigma'_{\mathscr{L}}} = \vcenter{\hbox{\includegraphics{fig}}} \quad , \tag{2.55}$$

with an MPO bond dimension denoted w. Important for ground-state search and time evolution are the bond, 1-site and 2-site projections of $\widehat{H}$,

$$H_\ell^{b} = \underset{\ell \quad \ell+1}{\vcenter{\hbox{\includegraphics{fig}}}}, \quad H_\ell^{1s} = \underset{\ell-1 \; \ell \; \ell+1}{\vcenter{\hbox{\includegraphics{fig}}}}, \quad H_\ell^{2s} = \underset{\ell-1 \; \ell \;\; \ell+1 \; \ell+2}{\vcenter{\hbox{\includegraphics{fig}}}}, \tag{2.56}$$

with the left and right environments

$$L_\ell = \begin{array}{c}\text{[diagram]}\\ \ell\end{array} = \begin{array}{c}\text{[diagram]}\\ 1 \qquad \ell\end{array} = \begin{array}{c}\text{[diagram]}\\ L_{\ell-1}\ \ell\end{array}\ , \quad R_\ell = \begin{array}{c}\text{[diagram]}\end{array} = \begin{array}{c}\text{[diagram]}\\ \ell \qquad \mathscr{L}\end{array} = \begin{array}{c}\text{[diagram]}\\ \ell\ R_{\ell+1}\end{array}\ . \quad (2.57)$$

2.3.1 Numerical renormalization group as an MPS method

The kept and discarded states in NRG are naturally generated as MPS [Wei12]. Consider the situation where we have iteratively diagonalized the Wilson chain up to site $\tilde{\ell}-1$, i.e. we have computed the kept and discarded states $|s\rangle^{\mathrm{K}}_{\tilde{\ell}-1}$ and $|s\rangle^{\mathrm{D}}_{\tilde{\ell}-1}$, respectively. Since the discarded states are not further fine-grained, we project $H^{\mathrm{chain}}_{\tilde{\ell}}$ to the subspace $\mathbb{V}^{\mathrm{P}}_{\tilde{\ell}} = \mathrm{span}\{|s\rangle^{\mathrm{K}}_{\tilde{\ell}-1}\otimes|\sigma_{\tilde{\ell}}\rangle\}$, called parent space in the parlace of Sec. 2.3. We now proceed by diagonalizing the projected Hamiltonian,

$$\left[H^{\mathrm{chain}}_{\tilde{\ell}}\right]^{\mathrm{P}} = \sum_{s\sigma_{\tilde{\ell}}}\sum_{s'\sigma'_{\tilde{\ell}}}|s^{\mathrm{K}}_{\tilde{\ell}-1}\sigma_{\tilde{\ell}}\rangle\underbrace{\langle s^{\mathrm{K}}_{\tilde{\ell}-1}\sigma_{\tilde{\ell}}|H^{\mathrm{chain}}_{\tilde{\ell}}|s'^{\mathrm{K}}_{\tilde{\ell}-1}\sigma'_{\tilde{\ell}}\rangle}_{\left[H^{\mathrm{chain}}_{\tilde{\ell}}\right]_{s\sigma_{\tilde{\ell}},s'\sigma'_{\tilde{\ell}}}}\langle s'^{\mathrm{K}}_{\tilde{\ell}-1}\sigma'_{\tilde{\ell}}| \overset{\mathrm{diag}}{=} \sum_{\tilde{s}}|\tilde{s}\rangle^{\mathrm{X}}_{\tilde{\ell}}E^{\tilde{\ell}}_{\tilde{s}}\langle\tilde{s}|^{\mathrm{X}}_{\tilde{\ell}}\ , \quad (2.58)$$

$$|\tilde{s}\rangle^{\mathrm{X}}_{\tilde{\ell}} = \sum_{s\sigma_{\tilde{\ell}}}U^{\sigma_{\tilde{\ell}}}_{s\tilde{s}}|s^{\mathrm{K}}_{\tilde{\ell}-1}\sigma_{\tilde{\ell}}\rangle\ , \quad (2.59)$$

where X is a placeholder for K or D and U is the unitary which diagonalizes the matrix $\left[H^{\mathrm{chain}}_{\tilde{\ell}}\right]_{s\sigma_{\tilde{\ell}},s'\sigma'_{\tilde{\ell}}}$. The states $|\tilde{s}\rangle^{\mathrm{X}}_{\tilde{\ell}}$ are now split into kept (K) and discarded (D) based on their energy $E^{\tilde{\ell}}_{\tilde{s}}$, which amounts to splitting the unitary U into kept and discarded isometries $A_{\tilde{\ell}}$ ($\searrow$) and $\overline{A}_{\tilde{\ell}}$ ($\searrow$), respectively. Thus, we can write the kept and discarded states as

$$|\tilde{s}\rangle^{\mathrm{K}}_{\tilde{\ell}} = \sum_{s\sigma_{\tilde{\ell}}}[A^{\sigma_{\tilde{\ell}}}_{\tilde{\ell}}]_{s\tilde{s}}|s^{\mathrm{K}}_{\tilde{\ell}-1}\sigma_{\tilde{\ell}}\rangle\ , \qquad\qquad |\tilde{s}\rangle^{\mathrm{D}}_{\tilde{\ell}} = \sum_{s\sigma_{\tilde{\ell}}}[\overline{A}^{\sigma_{\tilde{\ell}}}_{\tilde{\ell}}]_{s\tilde{s}}|s^{\mathrm{K}}_{\tilde{\ell}-1}\sigma_{\tilde{\ell}}\rangle\ . \quad (2.60)$$

Representing the K states from earlier shells $\tilde{\ell}' < \tilde{\ell}$ in the same way leads to an MPS representation of both kept and discarded states,

$$|\tilde{s}\rangle^{\mathrm{K}}_{\tilde{\ell}} = \sum_{\sigma_1...\sigma_{\tilde{\ell}}}\underbrace{[A^{\sigma_1}_1...A^{\sigma_{\tilde{\ell}}}_{\tilde{\ell}}]_{1\tilde{s}}}_{A_1 \quad A_{\tilde{\ell}}}|\sigma_1...\sigma_{\tilde{\ell}}\rangle\ , \quad |\tilde{s}\rangle^{\mathrm{D}}_{\tilde{\ell}} = \sum_{\sigma_1...\sigma_{\tilde{\ell}}}\underbrace{[A^{\sigma_1}_1...A^{\sigma_{\tilde{\ell}-1}}_{\tilde{\ell}-1}\overline{A}^{\sigma_{\tilde{\ell}}}_{\tilde{\ell}}]_{1\tilde{s}}}_{A_1 \quad \overline{A}_{\tilde{\ell}}}|\sigma_1...\sigma_{\tilde{\ell}-1}\sigma_{\tilde{\ell}}\rangle\ . \quad (2.61)$$

Using this MPS representation is very convenient for bookkeeping, and the computation of thermal expectation values, spectral weights, etc. can be nicely formulated in terms of tensor network diagrams [Wei12].

2.3.2 Denstiy matrix renormalization group

The density matrix renormalization group (DMRG) [Sch05, Sch11] is currently the standard algorithm for MPS ground-state search. It was invented by S. R. White in 1992 [Whi92, Whi93], but its connection to MPS was realized only later by S. Östlund and S. Rommer [OR95, RO97, VPC04]. Given a Hamiltonian $\widehat{H}$, DMRG is designed to find an optimal bond-dimension D MPS by minimizing the cost function

$$E(\Psi) = \frac{\langle\Psi|\widehat{H}|\Psi\rangle}{\langle\Psi|\Psi\rangle} \quad (2.62)$$

with $|\Psi\rangle \in \mathcal{M}_{\text{D-MPS}}$. To achieve that, DMRG uses that $\mathcal{M}_{\text{D-MPS}}$ is ruled. Thus no matter where $|\Psi\rangle$ is on $\mathcal{M}_{\text{D-MPS}}$, there is a large number of directions, $\mathbb{V}_\ell^{1s} \subset \mathcal{T}_\Psi \mathcal{M}_{\text{D-MPS}}$, in which $\mathcal{M}_{\text{D-MPS}}$ is completely flat. Thus, we can search for the optimal solution of $E(\Psi)$ in $\mathbb{V}_\ell^{1s}$ without having to worry about leaving $\mathcal{M}_{\text{D-MPS}}$. Since $\mathbb{V}_\ell^{1s}$ is a subspace of $\mathcal{T}_\Psi \mathcal{M}_{\text{D-MPS}}$ and therefore a vector space, we can search for the optimal solution using conventional linear algebra operations. In the present case, we can find the optimal solution in $\mathbb{V}_\ell^{1s}$ by finding the ground state of $\widehat{H}$ projected to this space, $H_\ell^{1s} = \mathcal{P}_\ell^{1s} \widehat{H} \mathcal{P}_\ell^{1s}$ [c.f. Eq. (2.56)], i.e. we have to solve for the ground state of the eigenvalue problem

$$H_\ell^{1s} C_\ell = E\, C_\ell\,, \qquad \underset{\ell-1\;\;\ell\;\;\ell+1}{\boxed{}} = E\; \underset{\ell}{}\;, \qquad (2.63)$$

where C_ℓ is the isometry center in the bond-canonical form (2.50). Solving for the ground state Eq. (2.64) comes with a computational cost of $\mathcal{O}(D^3 dw)$ if an iterative eigensolver is used, see [Sch11] for more details. This concludes a local DMRG optimization step, called single-site (1s) update since a single-site tensor of the MPS is updated. Global optimization of $E(\Psi)$ is achieved by iteratively moving from site to site and updating $|\Psi\rangle$, called sweeping. Sweeping is repeated until changes of $E(\Psi)$ are below some convergence threshold. An important property of the tangent space is that it is completely covered by the flat directions, $\mathcal{T}_\Psi \mathcal{M}_{\text{D-MPS}} = \cup_\ell \mathbb{V}_\ell^{1s}$. Due to that, the DMRG algorithm does not miss any directions, which may otherwise constrain the solution to some submanifold of $\mathcal{M}_{\text{D-MPS}}$.

It should be noted that the manifold of *uniform* MPS (uMPS) with bond dimension D, $\mathcal{M}_{\text{D-uMPS}}$, is *not* ruled [HMOV14]. This is because changing a single tensor in a uMPS generally leads to a non-uniform MPS which is not in $\mathcal{M}_{\text{D-uMPS}}$. For that reason, optimizing uMPS is usually more complicated, and is done for instance either by using retractions to remain on $\mathcal{M}_{\text{D-uMPS}}$ [HDH21] or by leaving $\mathcal{M}_{\text{D-uMPS}}$ during optimization, followed by a projection back on $\mathcal{M}_{\text{D-uMPS}}$. The latter strategy is for instance used by the variational uMPS (VUMPS) algorithm [ZSVF$^+$18].

In practical applications, precisely sticking to $\mathcal{M}_{\text{D-MPS}}$ turns out to be not very useful. First, D may be too small to reliably approximate the true ground state of the system. In that case, we would like to adjust D accordingly. Generically, since DMRG scales with $\mathcal{O}(D^3)$, it is advantageous to start with some small D and gradually increase it while sweeping. Second, when exploiting symmetries, the MPS manifold is not fully classified by D, but we further need information on the sizes of the symmetry sectors (labeled by quantum numbers q) at bond ℓ, D_ℓ^q. Thus, the set $\{D_\ell^q\}$ determines our MPS manifold and we would like to choose an optimal manifold at a given bond dimension $D_\ell = \sum_q D_\ell^q$. Third, even if the bond dimension and quantum number sectors do not need further adjustment, it can be advantageous for convergence to search for an optimal solution in a slightly larger space and then project back on $\mathcal{M}_{\text{D-MPS}}$.

The standard extension of 1s DMRG to meet the demands above is 2-site (2s) DMRG, which can grow the bond dimension, adjust the sizes of quantum number sectors, and in general venture away from $\mathcal{M}_{\text{D-MPS}}$ to accelerate convergence. Instead of solving for the ground state of H_ℓ^{1s} during the update, 2-site DMRG updates the state by finding the ground state of $H_\ell^{2s} = \mathcal{P}_\ell^{2s} \widehat{H} \mathcal{P}_\ell^{2s}$, see also Eq. (2.56). For that, we have to solve for the ground state of the eigenvalue problem

$$H_\ell^{2s} \Psi_\ell^{2s} = E\, \Psi_\ell^{2s}\,, \qquad \underset{\ell-1\;\;\ell\;\;\ell+1\;\ell+2}{\boxed{}} = E\; \underset{\ell\;\;\;\ell+1}{}\;, \qquad (2.64)$$

where $\Psi_\ell^{2s} = A_\ell \Lambda_\ell B_{\ell+1}$ is the 2-site wavefunction. Before we can move on from site ℓ to $\ell + 1$, we have to decompose Ψ_ℓ^{2s} into the isometries A_ℓ and $B_{\ell+1}$ and the bond matrix Λ_ℓ using SVD. In general, Λ_ℓ will be a $Dd \times Dd$ matrix, which means the newly optimized MPS is not in $\mathcal{M}_{\text{D-MPS}}$. To project it back on $\mathcal{M}_{\text{D-MPS}}$, we truncate the small eigenvalues of $\Lambda_\ell^\dagger \Lambda_\ell$ (or equivalently the small singular values of Ψ_ℓ^{2s}), which amounts to finding the state on $\mathcal{M}_{\text{D-MPS}}$ which has the largest overlap with the state directly after 2-site optimization. In general, the quantum number sectors of the state after optimization and truncation will have different sizes than before optimization, i.e. the 2-site update adjusts the relative sizes of quantum number sectors. Further, we can decide not to fully truncate down to bond dimension D, which allows us to control the bond dimension. Typically, one monitors the truncated weight of $\Lambda_\ell^\dagger \Lambda_\ell$ to determine whether the bond dimension is adequate or not. The truncation step concludes the 2-site update. Otherwise, 2-site DMRG functions analogous to single-site DMRG. Due to exploring a larger space, the 2-site update comes with an increased computational cost of $\mathcal{O}(D^3 d^2 w)$ for the iterative eigensolver and $\mathcal{O}(D^3 d^3)$ for the SVD (the latter has a smaller prefactor than the former).

In many cases, 2-site DMRG converges very well and, despite the increased computational cost, is preferred over 1-site DMRG, for the reasons discussed above. There are however cases where 2-site DMRG has convergence problems. For such situations, mixing methods like density matrix perturbation [Whi05] or DMRG3S [HMSW15] have been developed. These mixing methods can also be used together with the 1-site update, which would lead to 1-site computational cost. In practice, convergence is faster if one uses mixing with the 2-site update, which is what is often done nowadays [SW12]. In Ref. [P2], we have developed a so-called controlled bond expansion (CBE) algorithm which has very similar convergence properties as the 2-site update, but at a reduced computational cost of $\mathcal{O}(D^3 d w)$, i.e. 1-site cost. Using the CBE update together with mixing provides a computationally cheap algorithm with excellent convergence properties.

2.3.3 Time-dependent variational principle for MPS

Apart from ground state search, another important application of MPS is time evolution. For an overview of MPS time evolution methods, see Ref. [PKS$^+$19]. Here, we focus on the time-dependent variational principle (TDVP) [Dir30, McL64] for MPS, which aims to solve the time-dependent Schrödinger equation constrained to the manifold $\mathcal{M}_{\text{D-MPS}}$ [HCO$^+$11]. For that, we have to solve the differential equation [HLO$^+$16]

$$\frac{\mathrm{d}|\Psi(t)\rangle}{\mathrm{d}t} = -\mathrm{i}\mathcal{P}_{\Psi(t)}^{1s} \widehat{H} |\Psi(t)\rangle \,, \tag{2.65}$$

where $|\Psi(t)\rangle \in \mathcal{M}_{\text{D-MPS}}$ is a bond-dimension D MPS and $\mathcal{P}_{\Psi(t)}^{1s}$ is its tangent-space projector (2.52). We have indicated $\Psi(t)$ as a subscript of the projector to convey that it inherits a time dependence from $|\Psi(t)\rangle$. Due to the time dependence of the projector, Eq. (2.65) amounts to quite an intimidating set of non-linear coupled differential equations [HCO$^+$11]. These can be conveniently dealt with using the projector splitting integrator of C. Lubich and I. V. Oseledets [LO13]. This approach uses the decomposition (2.52) of the tangent space projector in terms of $\mathcal{P}_\ell^{1s}$ and $\mathcal{P}_\ell^{b}$. To first order in a small timestep δt, this leads to a set of first-order linear differential equations for the site tensors C_ℓ and bond matrices Λ_ℓ [HLO$^+$16],

$$\frac{\mathrm{d}C_\ell(t)}{\mathrm{d}t} = -\mathrm{i}H_\ell^{1s} C_\ell(t) \,, \quad \frac{\mathrm{d}\Lambda_\ell(t)}{\mathrm{d}t} = \mathrm{i}H_\ell^{b} \Lambda_\ell(t) \,. \tag{2.66}$$

These are then solved in series, i.e. by sweeping from site 1 to $\mathscr{L}$ and updating $C_\ell(t) \to C_\ell(t+\delta t)$, followed by an update of $\Lambda_\ell(t) \to \Lambda_\ell(t+\delta t)$. Integrating each individual contribution to Eq. (2.66) can be done by exponentiating H_ℓ^{1s} and H_ℓ^{b} (usually by means of a Lanczos scheme). The projector splitting approach again uses the fact that $\mathcal{M}_{\text{D-MPS}}$ is completely flat when projecting to $\mathbb{V}_\ell^{1s}$ or $\mathbb{V}_\ell^{b}$, which allows us to stay on $\mathcal{M}_{\text{D-MPS}}$ without having to worry about any curvature. We have to pick δt since the projector splitting approach has an error of $\mathcal{O}(\delta t^2)$. Higher-order integration schemes can be used which introduce an error of $\mathcal{O}(\delta t^{n+1})$, but also require more sweeps.

Similar to 1-site DMRG, $\mathcal{M}_{\text{D-MPS}}$ is usually too restrictive to achieve reliable time evolution. In Ref. [HLO$^+$16], a 2-site TDVP algorithm based on Eq. (2.53) has been proposed. It amounts to iteratively solving the differential equations

$$\frac{\mathrm{d}\Psi_\ell^{2s}(t)}{\mathrm{d}t} = -\mathrm{i}H_\ell^{2s}\Psi_\ell^{2s}(t)\,, \quad \frac{\mathrm{d}C_\ell(t)}{\mathrm{d}t} = \mathrm{i}H_\ell^{1s}C_\ell(t)\,, \qquad (2.67)$$

for a small timestep δt. Here, $\Psi_\ell^{2s}(t) = A_\ell(t)\Lambda_\ell(t)B_{\ell+1}(t)$ is again the 2-site wavefunction. Similar to 2-site DMRG, it has to be decomposed into isometries A_ℓ and $B_{\ell+1}$ and the bond matrix Λ_ℓ using SVD, followed by truncation to keep the bond dimension manageable. In that way, 2-site TDVP can dynamically adjust the bond dimension and change the sizes of quantum number sectors.

As for DMRG, the 1-site TDVP algorithm has a cost of $\mathcal{O}(D^3 dw)$ while the 2-site algorithm comes at a cost of $\mathcal{O}(D^3 d^2 w)$ (not including the SVD). For that reason, multiple bond expansion schemes to reduce the cost of 2-site TDVP have been proposed [YPZ$^+$20, DC21, XXX$^+$22]. In Ref. [P3], we show that the CBE scheme we developed for DMRG in Ref. [P2] also works very well for TDVP.

2.4 n-site generalization of the tangent space projector

2.4.1 Overview

In Sec. 2.3, we have introduced the tangent space projector (2.52), which was an important conceptional ingredient of the single-site DMRG and TDVP algorithms. In Eq. (2.53), we have further introduced its 2-site generalization, which is conceptionally important for the 2-site generalizations of DMRG and TDVP. The construction of these projectors was based on the kept and discarded isometries discussed in Sec. 2.3.

In Ref. [P1], we use the diagrammatic notation for the kept and discarded isometries introduced there (which was also used in Sec. 2.3) to explicitly construct n-site generalizations of the tangent space projector (2.52), denoted $\mathcal{P}^{ns}$. We further reveal a nested structure of these projectors. An n-site projector $\mathcal{P}^{ns}$ can be decomposed into an $(n-1)$-site projector $\mathcal{P}^{ns}$ and an irreducible n-site projector $\mathcal{P}^{n\perp}$. These irreducible projectors are mutually orthogonal, $\mathcal{P}^{n\perp}\mathcal{P}^{n'\perp} = \delta_{n,n'}\mathcal{P}^{n\perp}$. As a result, the n-site projectors can be decomposed into irreducible $n \geq n'$-site contributions, $\mathcal{P}^{ns} = \sum_{n'=0}^{n} \mathcal{P}^{n'\perp}$, with $\mathcal{P}^{0\perp} = |\Psi\rangle\langle\Psi|$. Since $\mathcal{P}^{\mathscr{L}s} = \mathbb{1}$ is the identity on the full Hilbert space, the irreducible projectors induce a complete orthogonal decomposition of the identity, $\mathbb{1} = \sum_{n'=0}^{\mathscr{L}} \mathcal{P}^{n'\perp}$.

This decomposition of the identity is particularly convenient when computing connected equal-time correlation functions,

$$\langle \mathcal{A}\mathcal{B}\rangle_c = \langle\Psi|\mathcal{A}\mathcal{B}|\Psi\rangle - \langle\Psi|\mathcal{A}|\Psi\rangle\langle\Psi|\mathcal{B}|\Psi\rangle = \langle\Psi|\mathcal{A}\underbrace{\left(\mathbb{1} - |\Psi\rangle\langle\Psi|\right)}_{\sum_{n'=1}^{\mathscr{L}} \mathcal{P}^{n'\perp}}\mathcal{B}|\Psi\rangle = \sum_{n'=1}^{\mathscr{L}} \langle \mathcal{A}\mathcal{B}\rangle_c^{n'}\,, \quad (2.68)$$

where $\langle \mathcal{A}\mathcal{B}\rangle_c^{n'} = \langle\Psi|\mathcal{A}\,\mathcal{P}^{n'\perp}\,\mathcal{B}|\Psi\rangle$ is the irreducible n'-site contribution the connected correlation function. It is in general numerically more stable to compute the connected correlation function via orthogonal projectors instead of subtracting expectation values, especially if $\langle \mathcal{A}\mathcal{B}\rangle_c \ll \langle\Psi|\mathcal{A}\mathcal{B}|\Psi\rangle$. Further, if either $\mathcal{A}$ or $\mathcal{B}$ are sums of operators which act non-trivially only on at most ℓ consecutive sites, it is easy to show that $\langle \mathcal{A}\mathcal{B}\rangle_c^n = 0$ if $n > \ell$. Since this is the case in many situations of interest, it usually suffices to compute a small number of contributions $\langle \mathcal{A}\mathcal{B}\rangle_c^n$. An important example is the case where $\mathcal{A} = \mathcal{B} = \widehat{H}$, i.e. the computation of the energy variance. Up to $n = 2$, this was first considered in Ref. [HHS18]. In Ref. [P1], we generalize this to arbitrary n.

Projector formalism for kept and discarded spaces of matrix product states

Andreas Gleis ⬤, Jheng-Wei Li ⬤, and Jan von Delft ⬤

Arnold Sommerfeld Center for Theoretical Physics, Center for NanoScience, and Munich Center for
Quantum Science and Technology, Ludwig-Maximilians-Universität München, 80333 Munich, Germany

Any matrix product state $|\Psi\rangle$ has a set of associated kept and discarded spaces, needed for the description of $|\Psi\rangle$, and changes thereof, respectively. These induce a partition of the full Hilbert space of the system into mutually orthogonal spaces of irreducible n-site variations of $|\Psi\rangle$. Here, we introduce a convenient projector formalism and diagrammatic notation to characterize these n-site spaces explicitly. This greatly facilitates the formulation of MPS algorithms that explicitly or implicitly employ discarded spaces. As an illustration, we derive an explicit expression for the n-site energy variance and evaluate it numerically for a model with long-range hopping. We also describe an efficient algorithm for computing low-lying n-site excitations above a finite MPS ground state.

I. INTRODUCTION

Matrix product states (MPS) are widely used for the numerical description of quantum systems defined on one- or two-dimensional lattices. Well-known MPS-based algorithms include ground-state searches and time evolution using the density matrix renormalization group (DMRG and tDMRG) [1–6], time-evolving block decimation (TEBD) methods [7–9], or the time-dependent variational principle (TDVP) [10–14]; and the computation of spectral information using the numerical renormalization group (NRG) [15–17], DMRG [18–21], or so-called post-MPS approaches [14,22]; see Refs. [23–25] for reviews.

All such algorithms involve update steps: a quantum state of interest, $|\Psi\rangle$, is represented in MPS form, and its constituent tensors are updated, e.g., during optimization or time evolution. During an update, highly relevant information is *kept* (κ) and less relevant information *discarded* (D). A sequence of updates thereby endows the full Hilbert space of the system $\mathbb{V}$ with a structure of intricately nested κ or D subspaces, changing with each update, containing states from $\mathbb{V}$, which either do (κ) or do not (D) contribute to the description of $|\Psi\rangle$.

The nested structure of $\mathbb{V}$ is rarely made explicit in the formulation of MPS algorithms. A notable exception is NRG, where D states are used to construct a complete basis [26] of approximate energy eigenstates for $\mathbb{V}$, facilitating the computation of time evolution or spectral information [16,17]. For the computation of local multipoint correlators [27] using NRG, it has proven useful to elucidate the structure of κ and D subspaces by introducing projectors having these subspaces as their images. The orthogonality properties of κ and D projectors bring structure and clarity to the description of rather complex algorithmic strategies.

Inspired by the convenience of κ and D projectors in the context of NRG, we here introduce an analogous but more

general κ, D projector formalism and diagrammatic conventions suitable for the description of arbitrary MPS algorithms. In particular, our κ, D projectors offer a natural language for the formulation of algorithms that explicitly or implicitly employ discarded spaces; this includes algorithms evoking the notion of tangent spaces [10,12–14,22] and generalizations thereof, as will be described later.

To formulate the goals of this paper, we here briefly indicate how the nested subspaces mentioned above come about. Concrete constructions follow in later sections.

An MPS $|\Psi\rangle$ written in canonical form is defined by a set of isometric tensors [23]. The image space of an isometric tensor, its *kept* space, is needed for the description of $|\Psi\rangle$. The orthogonal complement of the kept space, its *discarded* space, is not needed for $|\Psi\rangle$ itself, but for the description of changes of $|\Psi\rangle$ due to an update step, e.g., during variational optimization, time evolution, or the computation of excitations above the ground state. Any such change can be assigned to one of the subspaces $\mathbb{V}^{ns}$ in the nested hierarchy

$$\mathbb{V}^{0s} \subset \mathbb{V}^{1s} \subset \mathbb{V}^{2s} \subset \cdots \subset \mathbb{V}^{\mathscr{L}s} = \mathbb{V}, \qquad (1)$$

where $\mathbb{V}$ is the full Hilbert space of a system of $\mathscr{L}$ sites, $\mathbb{V}^{ns}$ the subspace spanned by all n-site (ns) variations of $|\Psi\rangle$, and $\mathbb{V}^{0s} = \text{span}\{|\Psi\rangle\}$ the one-dimensional space spanned by the reference MPS itself. The orthogonality of kept and discarded spaces induces a partition of each $\mathbb{V}^{ns}$ into nested orthogonal subspaces [6,28], such that

$$\mathbb{V}^{ns} = \oplus_{n'=0}^{n} \mathbb{V}^{n'\perp}, \qquad (2)$$

where $\mathbb{V}^{n\perp}$ is the subspace of $\mathbb{V}^{ns}$ spanned by all irreducible ns variations not expressible through n's variations with $n' < n$, and $\mathbb{V}^{0\perp} = \mathbb{V}^{0s}$. In particular, the full Hilbert space can be represented as $\mathbb{V} = \oplus_{n=0}^{\mathscr{L}} \mathbb{V}^{n\perp}$.

The subspaces defined above underlie, implicitly or explicitly, all MPS algorithms. $\mathbb{V}^{1s}$ is the so-called tangent space

of $|\Psi\rangle$, i.e., the space of all one-site (1s) variations of $|\Psi\rangle$. It plays an explicit role in numerous recent MPS algorithms, such as TDVP time-evolution, or the description of translationally invariant MPS and their excitations [13,14,28]. It also features implicitly in MPS algorithms formulated using 1s update schemes, such as the 1s formulation of DMRG [23], because 1s updates explore states from $\mathbb{V}^{1s}$. Likewise, the space $\mathbb{V}^{2s}$ implicitly underlies all 2s MPS algorithms such as 2s DMRG ground-state search, 2s time-dependent DMRG (tDMRG), or 2s TDVP, in that 2s updates explore states from $\mathbb{V}^{2s}$. Moreover, $\mathbb{V}^{1\perp}$ and $\mathbb{V}^{2\perp}$ are invoked explicitly when computing the 2s energy variance, an error measure for MPS ground-state searches introduced in Ref. [6]. Finally, $\mathbb{V}^{ns}$ is implicitly invoked in MPS algorithms defining excited states of translationally invariant MPS through linear combinations of local excitations defined on n sites [22].

The construction of a basis for $\mathbb{V}^{ns}$ and $\mathbb{V}^{n\perp}$ is well known for $n = 1$ [12], and for $n = 2$ it is outlined in Ref. [6]. However, we are not aware of a general, explicit construction for $n > 2$, as needed, e.g., to compute the ns energy variance. Here, we explicitly construct projectors, $\mathcal{P}^{ns}$ and $\mathcal{P}^{n\perp}$, having $\mathbb{V}^{ns}$ and $\mathbb{V}^{n\perp}$ as images, respectively. For $n = 1$, this amounts to a construction of a basis for the tangent space $\mathbb{V}^{1s}$. More generally, our κ,D projector formalism used to construct $\mathcal{P}^{ns}$ and $\mathcal{P}^{n\perp}$ greatly facilitates the formulation of MPS algorithms that explicitly or implicitly employ discarded spaces. As an illustration, we derive an explicit expression for the n-site energy variance, generalizing the error measure proposed in Ref. [6], and evaluate it numerically for a model with long-range hopping, the Haldane-Shastry model. We also show how the multiparticle ns excitations proposed in Ref. [22] are formulated in our scheme, and propose a strategy for computing them explicitly, for any n.

We expect that the κ, D projector formalism developed here will be particularly useful for improving the efficiency of MPS algorithms by incorporating information from $\mathbb{V}^{n\perp}$ into suitably expanded versions of $\mathbb{V}^{(n' < n)s}$ without fully computing $\mathbb{V}^{n\perp}$. For example, we have recently developed a scheme, called controlled bond expansion, which incorporates 2s information into 1s updates for DMRG ground-state search [29] and TDVP time evolution [30], in a manner requiring only 1s costs.

This paper is structured as follows. In Sec. II we collect some well-known facts about MPSs, and formally define the associated kept and discarded spaces and corresponding projectors. Section III, the heart of this paper, describes the construction of the $\mathcal{P}^{ns}$ and $\mathcal{P}^{n\perp}$ projectors for general n. As applications of our projector formalism, we compute the ns energy variance of the Haldane-Shastry model in Sec. IV, and describe the construction and computation of ns excitations in Sec. V. We end with a brief outlook in Sec. VI.

II. MPS BASICS

This section offers a concise, tutorial-style summary of MPS notation and the associated diagrammatics. Moreover, we formalize the notion of kept spaces, needed to describe an MPS $|\Psi\rangle$, and discarded spaces, needed to describe changes to it at specified sites. We also recapitulate the definition of

local bond, 1s and 2s projectors routinely used in 1s and 2s MPS algorithms.

A. Basic MPS notation

Consider a quantum chain with sites labeled $\ell = 1, ..., \mathscr{L}$. Let each site be represented by a d-dimensional Hilbert space v_ℓ with local basis states $|\sigma_\ell\rangle$, $\sigma_\ell = 1, ..., d$. The full Hilbert space is $\mathbb{V} = \prod_{\otimes \ell} \mathrm{v}_\ell = \mathrm{span}\{|\boldsymbol{\sigma}\rangle\}$, with basis states $|\boldsymbol{\sigma}\rangle = |\sigma_1\rangle|\sigma_2\rangle\cdots|\sigma_\mathscr{L}\rangle$. Any state $|\Psi\rangle = |\boldsymbol{\sigma}\rangle\Psi^{\boldsymbol{\sigma}} \in \mathbb{V}$ can be written as an open boundary MPS, with wavefunction of the form

$$\Psi^{\boldsymbol{\sigma}} = [M_1]_{1\alpha_1}^{\sigma_1}[M_2]_{\alpha_1\alpha_2}^{\sigma_2}\cdots[M_\mathscr{L}]_{\alpha_{\mathscr{L}-1}1}^{\sigma_\mathscr{L}}$$

$$= \underset{1}{\overset{M_1}{\underset{\sigma_1}{\big|}}} \underset{\alpha_1}{\overset{M_2}{\underset{\sigma_2}{\big|}}} \underset{\alpha_2}{} \quad \quad \quad \underset{\alpha_{\mathscr{L}-1}}{\overset{M_\mathscr{L}}{\underset{\sigma_\mathscr{L}}{\big|}}} \underset{1}{}. \quad (3)$$

(This diagram depicts both the wavefunction Ψ and the corresponding state $|\Psi\rangle$.) For clarity, we do not use ellipses in our MPS diagrams, but instead draw them for some small choice of $\mathscr{L}$, e.g., $\mathscr{L} = 7$ above. Sums over repeated indices are implied throughout, and depicted diagrammatically by bonds. Each M_ℓ is a three-leg tensor with elements $[M_\ell]_{\alpha_{\ell-1}\alpha_\ell}^{\sigma_\ell}$. Its physical and virtual bond indices, σ_ℓ and $\alpha_{\ell-1}$, α_ℓ, have dimensions d and $D_{\ell-1}$, D_ℓ, respectively. The outermost bonds, to dummy sites represented by crosses, have $D_0 = D_\mathscr{L} = 1$. The bond dimensions D_ℓ are adjustable parameters, controlling the amount of entanglement an MPS can encode. (In the literature, it is common practice to drop the subscript on D_ℓ for brevity, understanding that D can nevertheless vary from bond to bond.) Likewise, a Hamiltonian acting within $\mathbb{V}$, $\mathcal{H} = |\boldsymbol{\sigma}\rangle H^{\boldsymbol{\sigma\sigma}'}\langle\boldsymbol{\sigma}'|$, can be expressed as an MPO, with

$$H^{\boldsymbol{\sigma\sigma}'} = [W_1]_{1\nu_1}^{\sigma_1\sigma_1'}[W_2]_{\nu_1\nu_2}^{\sigma_2\sigma_2'}\cdots[W_\mathscr{L}]_{\nu_{\mathscr{L}-1}1}^{\sigma_\mathscr{L}\sigma_\mathscr{L}'},$$

$$= \underset{1}{\overset{\sigma_1'}{\underset{\sigma_1}{\overset{W_1}{\square}}}} \underset{\nu_1}{\overset{\sigma_2'}{\underset{\sigma_2}{\overset{W_2}{\square}}}} \underset{\nu_2}{} \quad \quad \quad \underset{\nu_{\mathscr{L}-1}}{\overset{\sigma_\mathscr{L}'}{\underset{\sigma_\mathscr{L}}{\overset{W_\mathscr{L}}{\square}}}} \underset{1}{}, \quad (4)$$

where the four-leg tensors W_ℓ have elements $[W_\ell]_{\nu_{\ell-1}\nu_\ell}^{\sigma_\ell\sigma_\ell'}$, and the virtual bond indices ν_ℓ have dimensions w_ℓ.

Any MPS wavefunction can be brought into canonical form with respect to an "orthogonality center" at site $\ell \in [1, \mathscr{L}]$, or with respect to bond ℓ connecting sites ℓ and $\ell + 1$,

$$\Psi^{\boldsymbol{\sigma}} = \underset{\sigma_1}{\overset{A_1}{\underset{}{\big\backslash}}} \quad \underset{\sigma_{\ell-1}}{\overset{A_{\ell-1}}{\underset{D_{\ell-1}}{\big\backslash}}} \underset{}{\overset{C_\ell}{\underset{D_\ell}{\big\circ}}} \underset{\sigma_{\ell+1}}{\overset{B_{\ell+1}}{\underset{D_{\ell+1}}{\big/}}} \quad \underset{\sigma_\mathscr{L}}{\overset{B_\mathscr{L}}{\big/}}, \quad (5)$$

where we indicated some of the bond dimensions. Here, $A_{\tilde{\ell}}$ and $B_{\tilde{\ell}'}$ (with $1 \leqslant \tilde{\ell} < \ell < \tilde{\ell}' \leqslant \mathscr{L}$) satisfy the relations

$$[A_{\tilde{\ell}}^\dagger]_{\alpha\bar{\alpha}}^\sigma[A_{\tilde{\ell}}]_{\bar{\alpha}\alpha'}^\sigma = [\mathbb{1}_{\tilde{\ell}}^\kappa]_{\alpha\alpha'}, \quad [B_{\tilde{\ell}'}]_{\alpha\bar{\alpha}}^\sigma[B_{\tilde{\ell}'}^\dagger]_{\bar{\alpha}\alpha'}^\sigma = [\mathbb{1}_{\tilde{\ell}'-1}^\kappa]_{\alpha\alpha'},$$

$$\bar{\alpha}\underset{A_{\tilde{\ell}}^*}{\overset{A_{\tilde{\ell}}}{\bigcirc}}\alpha' = \left(\underset{\alpha}{\overset{\alpha'}{=}} [\mathbb{1}_{\tilde{\ell}}^\kappa]_{\alpha\alpha'}\right), \quad \underset{\alpha'}{\overset{\alpha}{\underset{B_{\tilde{\ell}'}^*}{\overset{B_{\tilde{\ell}'}}{\bigcirc}}}}\bar{\alpha} = \underset{\alpha'}{\overset{\alpha}{=}}\right) = [\mathbb{1}_{\tilde{\ell}'-1}^\kappa]_{\alpha\alpha'}, \quad (6)$$

or $A_{\tilde{\ell}}^\dagger A_{\tilde{\ell}} = \mathbb{1}_{\tilde{\ell}}^\kappa$, $B_{\tilde{\ell}'} B_{\tilde{\ell}'}^\dagger = \mathbb{1}_{\tilde{\ell}'-1}^\kappa$ for short, where $\mathbb{1}_{\tilde{\ell}}^\kappa$ denotes a $D_{\tilde{\ell}} \times D_{\tilde{\ell}}$ unit matrix. (The superscript κ stands for "kept", for reasons explained below.) The open triangles representing $A_{\tilde{\ell}}$ and $B_{\tilde{\ell}'}$ are oriented such that their diagonals face left or right, respectively. The orthogonality center can be shifted left or

right by using singular value decomposition (SVD) to express it as $C_\ell = U_{\ell-1} S_{\ell-1} B_\ell$ or $C_\ell = A_\ell S_\ell V_\ell^\dagger$,

$$
\begin{aligned}
\overset{A_{\ell-1}\quad C_\ell}{\vee\quad\circ} &= \overset{A_{\ell-1}\quad U_{\ell-1}\quad S_{\ell-1}\quad B_\ell}{\vee\quad\square\quad\diamond\quad\triangledown} = \overset{C_{\ell-1}\quad B_\ell}{\circ\quad\triangledown}, \\
\overset{C_\ell\quad B_{\ell+1}}{\circ\quad\triangledown} &= \overset{A_\ell\quad S_\ell\quad V_\ell^\dagger\quad B_{\ell+1}}{\vee\quad\diamond\quad\square\quad\triangledown} = \overset{A_\ell\quad C_{\ell+1}}{\vee\quad\circ}.
\end{aligned} \tag{7}
$$

Here $U_{\ell-1}$, $V_\ell^\dagger$, $S_{\ell-1}$, S_ℓ are square matrices, the former two unitary, the latter two diagonal and containing SVD singular values. (Shifting can be combined with truncation, if desired, by discarding some small singular values and correspondingly reducing the bond dimension.) By renaming $V_\ell^\dagger B_{\ell+1}$ as $B_{\ell+1}$ and defining $\Lambda_\ell = S_\ell$, we can also express Ψ^σ in "bond-canonical" form with respect to bond ℓ,

$$
\overset{A_1 \qquad\qquad A_{\ell-1}\; A_\ell \qquad \Lambda_\ell \qquad B_{\ell+1} \qquad\qquad B_{\mathscr{L}}}{\ast\!-\!\vee\!-\!-\!-\!\vee\!-\!\vee\!-\!\circ\!-\!\triangledown\!-\!-\!-\!\triangledown\!-\!\ast} . \tag{8}
$$

The fact that the same MPS can be written in many different but equivalent ways reflects the gauge freedom of MPS representations.

B. Kept spaces

Given an MPS $|\Psi\rangle$ in canonical form, its constituent tensors can be used to define a set of state spaces defined on parts of the chain, and a sequence of isometric maps between these state spaces. Let us make this explicit to reveal the underlying structures.

The $A_{\tilde{\ell}}$ tensors for sites 1 to $\tilde{\ell}$ can be used to define a set of left *kept* (κ) states $|\Psi^{\textsc{k}}_{\tilde{\ell}\alpha}\rangle$, and the $B_{\tilde{\ell}'}$ tensors for sites $\tilde{\ell}'$ to $\mathscr{L}$ can be used to define right κ states $|\Phi^{\textsc{k}}_{\tilde{\ell}'\alpha'}\rangle$, with wavefunctions of the form

$$
\Psi^{\textsc{k}}_{\tilde{\ell}\alpha} = \overset{A_1\quad A_{\tilde{\ell}}}{\ast\!-\!\vee\!\vee\!\vee}\alpha, \qquad \Phi^{\textsc{k}}_{\tilde{\ell}'\alpha'} = \alpha'\overset{B_{\tilde{\ell}'}\quad B_{\mathscr{L}}}{\triangledown\!\triangledown\!\triangledown\!-\!\ast}. \tag{9}
$$

These states are called *kept*, since they are building blocks of $|\Psi\rangle$. Their spans define left and right κ spaces,

$$
\mathbb{V}^{\textsc{k}}_{\tilde{\ell}} = \mathrm{span}\big\{\big|\Psi^{\textsc{k}}_{\tilde{\ell}\alpha}\big\rangle\big\} \;\subset\; \mathbb{v}_1 \otimes \dots \otimes \mathbb{v}_{\tilde{\ell}}, \tag{10}
$$

$$
\mathbb{W}^{\textsc{k}}_{\tilde{\ell}'} = \mathrm{span}\big\{\big|\Phi^{\textsc{k}}_{\tilde{\ell}'\alpha'}\big\rangle\big\} \subset \mathbb{v}_{\tilde{\ell}'} \otimes \dots \otimes \mathbb{v}_{\mathscr{L}}, \tag{11}
$$

of dimension $D_{\tilde{\ell}}$ and $D_{\tilde{\ell}'-1}$, respectively. The dummy sites 0 and $\mathscr{L}+1$ are represented by one-dimensional spaces, $\mathbb{V}^{\textsc{k}}_0$ and $\mathbb{W}^{\textsc{k}}_{\mathscr{L}+1}$.

Each $A_{\tilde{\ell}}$ and $B_{\tilde{\ell}'}$ tensor defines an isometric map, from a *parent* (P) space involving a direct product of a κ space and a local space, to an adjacent κ space,

$$
A_{\tilde{\ell}} : \mathbb{V}^{\textsc{k}}_{\tilde{\ell}-1} \otimes \mathbb{v}_{\tilde{\ell}} \to \mathbb{V}^{\textsc{k}}_{\tilde{\ell}}, \quad \big|\Psi^{\textsc{k}}_{\tilde{\ell}-1,\alpha}\big\rangle|\sigma_{\tilde{\ell}}\rangle [A_{\tilde{\ell}}]^{\sigma_{\tilde{\ell}}}_{\alpha\alpha'} = \big|\Psi^{\textsc{k}}_{\tilde{\ell}\alpha'}\big\rangle,
$$

$$
B_{\tilde{\ell}'} : \mathbb{v}_{\tilde{\ell}'} \otimes \mathbb{W}^{\textsc{k}}_{\tilde{\ell}'+1} \to \mathbb{W}^{\textsc{k}}_{\tilde{\ell}'}, \quad [B_{\tilde{\ell}'}]^{\sigma_{\tilde{\ell}'}}_{\alpha\alpha'} |\sigma_{\tilde{\ell}'}\rangle \big|\Phi^{\textsc{k}}_{\tilde{\ell}'+1,\alpha'}\big\rangle = \big|\Phi^{\textsc{k}}_{\tilde{\ell}'\alpha}\big\rangle.
$$

(To connect sites 1 and $\mathscr{L}$ to their neighboring dummy sites, we define $\Psi^{\textsc{k}}_{0,1} = 1$, $\Phi^{\textsc{k}}_{\mathscr{L}+1,1} = 1$.) We orient the triangles depicting $A_{\tilde{\ell}}$ and $B_{\tilde{\ell}'}$ such that equal-length legs point to parent spaces and 90-degree angles to kept spaces. The dimensions of left or right kept and parent spaces satisfy $D_{\tilde{\ell}} \leqslant D_{\tilde{\ell}-1} d$ or $D_{\tilde{\ell}'-1} \leqslant d D_{\tilde{\ell}'}$, respectively. If a kept space is smaller than its parent space, it has an orthogonal complement, called

discarded (D) space, discussed in Sec. II D below. The fact that the maps $A_{\tilde{\ell}}$ and $B_{\tilde{\ell}'}$ are *isometries* follows from Eqs. (6). These ensure that the left and right κ basis states form orthonormal sets,

$$
\langle \Psi^{\textsc{k}}_{\tilde{\ell}\alpha} | \Psi^{\textsc{k}}_{\tilde{\ell}\alpha'} \rangle = \big[\mathbb{1}^{\textsc{k}}_{\tilde{\ell}}\big]_{\alpha\alpha'}, \qquad \langle \Phi^{\textsc{k}}_{\tilde{\ell}'\alpha} | \Phi^{\textsc{k}}_{\tilde{\ell}'\alpha'} \rangle = \big[\mathbb{1}^{\textsc{k}}_{\tilde{\ell}'-1}\big]_{\alpha\alpha'},
$$

$$
\underset{1\qquad\tilde{\ell}\qquad\;\mathbb{1}^{\textsc{k}}_{\tilde{\ell}}}{\boxed{\,\!}\,} = (\,, \qquad \underset{\tilde{\ell}'\qquad\mathscr{L}\quad\;\mathbb{1}^{\textsc{k}}_{\tilde{\ell}'-1}}{\,\boxed{\,\!}} =)\,. \tag{12}
$$

The basis states can be used to build projectors onto the left or right κ spaces $\mathbb{V}^{\textsc{k}}_{\tilde{\ell}}$ or $\mathbb{W}^{\textsc{k}}_{\tilde{\ell}'}$, depicted as

$$
\mathcal{P}^{\textsc{k}}_{\tilde{\ell}} = \sum_\alpha |\Psi^{\textsc{k}}_{\tilde{\ell}\alpha}\rangle\langle\Psi^{\textsc{k}}_{\tilde{\ell}\alpha}| = \underset{1\qquad\tilde{\ell}}{\overset{\triangle\triangle\triangle}{\ast\!\Vert\Vert\Vert}}, \tag{13a}
$$

$$
\mathcal{Q}^{\textsc{k}}_{\tilde{\ell}'} = \sum_{\alpha'} |\Phi^{\textsc{k}}_{\tilde{\ell}'\alpha'}\rangle\langle\Phi^{\textsc{k}}_{\tilde{\ell}'\alpha'}| = \underset{\tilde{\ell}'\qquad\mathscr{L}}{\overset{\triangleright\triangleright\triangleright}{\Vert\Vert\Vert\!\ast}}, \tag{13b}
$$

with $\mathcal{P}^{\textsc{k}}_0 = 1$, $\mathcal{Q}^{\textsc{k}}_{\mathscr{L}+1} = 1$, and $(\mathcal{P}^{\textsc{k}}_{\tilde{\ell}})^2 = \mathcal{P}^{\textsc{k}}_{\tilde{\ell}}$, $(\mathcal{Q}^{\textsc{k}}_{\tilde{\ell}'})^2 = \mathcal{Q}^{\textsc{k}}_{\tilde{\ell}'}$,

$$
\underset{\tilde{\ell}}{\boxed{\,\!}} = \underset{\tilde{\ell}}{(\,}, \qquad \underset{\tilde{\ell}'}{\boxed{\,\!}} = \underset{\tilde{\ell}'}{\,)}. \tag{14}
$$

C. Bond, 1s and 2s projectors

The above projectors can, in turn, be used to construct bond, 1s and 2s projectors acting on the full chain,

$$
\mathcal{P}^{\mathrm{b}}_\ell = \mathcal{P}^{\textsc{k}}_\ell \otimes \mathcal{Q}^{\textsc{k}}_{\ell+1} = \underset{\ell\quad\ell+1}{\overset{\triangle\triangle\;\;\triangleright\triangleright}{\ast\!\Vert\Vert\;\Vert\Vert\!\ast}}, \tag{15a}
$$

$$
\mathcal{P}^{\mathrm{1s}}_\ell = \mathcal{P}^{\textsc{k}}_{\ell-1} \otimes \mathbb{1}_d \otimes \mathcal{Q}^{\textsc{k}}_{\ell+1} = \underset{\ell-1\;\;\ell\;\;\ell+1}{\overset{\triangle\triangle\;|\;\triangleright\triangleright}{\ast\!\Vert\Vert\;|\;\Vert\Vert\!\ast}}, \tag{15b}
$$

$$
\mathcal{P}^{\mathrm{2s}}_\ell = \mathcal{P}^{\textsc{k}}_{\ell-1} \otimes \mathbb{1}_d \otimes \mathbb{1}_d \otimes \mathcal{Q}^{\textsc{k}}_{\ell+2} = \underset{\ell-1\;\ell\;\ell+1\;\ell+2}{\overset{\triangle\triangle\;|\;|\;\triangleright\triangleright}{\ast\!\Vert\Vert\;|\;|\;\Vert\Vert\!\ast}}, \tag{15c}
$$

defined for $\ell\in[0,\mathscr{L}]$, $\ell\in[1,\mathscr{L}]$ and $\ell\in[1,\mathscr{L}-1]$, respectively. They mutually commute and satisfy $(\mathcal{P}^{\textsc{x}}_\ell)^2 = \mathcal{P}^{\textsc{x}}_\ell$, as follows from Eqs. (12) and (14). For example,

$$
(\mathcal{P}^{\mathrm{b}}_\ell)^2 = \underset{\ell}{\boxed{\,\!}}\;\underset{\ell}{\boxed{\,\!}} = \underset{\ell}{(\,}\;\underset{\ell}{\,)} = \mathcal{P}^{\mathrm{b}}_\ell.
$$

The projectors $\mathcal{P}^{\mathrm{b}}$, $\mathcal{P}^{\mathrm{1s}}$, and $\mathcal{P}^{\mathrm{2s}}$ map the full $\mathbb{V}$ into the subspaces $\mathbb{V}^{\textsc{k}}_\ell \otimes \mathbb{W}^{\textsc{k}}_{\ell+1}$, $\mathbb{V}^{\textsc{k}}_{\ell-1} \otimes \mathbb{v}_\ell \otimes \mathbb{W}^{\textsc{k}}_{\ell+1}$, and $\mathbb{V}^{\textsc{k}}_{\ell-1} \otimes \mathbb{v}_\ell \otimes \mathbb{v}_{\ell+1} \otimes \mathbb{W}^{\textsc{k}}_{\ell+2}$. These spaces offer three equivalent representations of the same state $|\Psi\rangle$, in bond-, 1s- or 2s-canonical form,

$$
|\Psi\rangle = \big|\Psi^{\textsc{k}}_{\ell\alpha}\big\rangle\big|\Phi^{\textsc{k}}_{\ell+1,\alpha'}\big\rangle\big[\psi^{\mathrm{b}}_\ell\big]_{\alpha\alpha'} \tag{16a}
$$

$$
= \big|\Psi^{\textsc{k}}_{\ell-1,\alpha}\big\rangle|\sigma_\ell\rangle\big|\Phi^{\textsc{k}}_{\ell+1,\alpha'}\big\rangle\big[\psi^{\mathrm{1s}}_\ell\big]^{\sigma_\ell}_{\alpha\alpha'} \tag{16b}
$$

$$
= \big|\Psi^{\textsc{k}}_{\ell-1,\alpha}\big\rangle|\sigma_\ell\rangle|\sigma_{\ell+1}\rangle\big|\Phi^{\textsc{k}}_{\ell+2,\alpha'}\big\rangle\big[\psi^{\mathrm{2s}}_\ell\big]^{\sigma_\ell\sigma_{\ell+1}}_{\alpha\alpha'}, \tag{16c}
$$

$$
\psi^{\mathrm{b}}_\ell = \Lambda_\ell, \quad \psi^{\mathrm{1s}}_\ell = C_\ell, \quad \psi^{\mathrm{2s}}_\ell = A_\ell \Lambda_\ell B_{\ell+1}. \tag{16d}
$$

These forms emphasize the tensors describing bond ℓ, site ℓ or sites $(\ell, \ell+1)$ and the bond in between, respectively. For example, Eqs. (16a) and (16b) are depicted as

The projections of the Hamiltonian into these spaces, $\mathcal{H}_\ell^x = \mathcal{P}_\ell^x \mathcal{H} \mathcal{P}_\ell^x$, have matrix elements of the form

with left and right environments for sites $\ell \pm 1$ given by

Here the first equalities define L_ℓ and R_ℓ, the second equalities show how they can be computed recursively, starting from $L_0 = 1$, $R_{\mathscr{L}+1} = 1$. The open triangles on L_ℓ and R_ℓ signify that they are computed using left- or right-normalized A or B tensors.

The above matrix elements are standard ingredients in numerous MPS algorithms. To give a specific example, we briefly recall their role in DMRG ground-state searches. These seek approximate ground-state solutions to $\mathcal{H}|\Psi\rangle = E|\Psi\rangle$ through a sequence of local optimization steps. Focusing on bond ℓ, or site ℓ, or sites $(\ell, \ell+1)$, one updates Λ_ℓ, or C_ℓ, or $A_\ell \Lambda_\ell B_{\ell+1}$, by finding the ground-state solution of, respectively,

$$(H_\ell^b - E)\psi_\ell^b = 0, \qquad \text{(19a)}$$

$$(H_\ell^{1s} - E)\psi_\ell^{1s} = 0, \qquad \text{(19b)}$$

$$(H_\ell^{2s} - E)\psi_\ell^{2s} = 0, \qquad \text{(19c)}$$

One then uses Eq. (7) to shift the orthogonality center to the neighboring bond or site, optimizes it, and sweeps back and forth through the chain until the ground-state energy has converged. These three schemes are known as 0s or bond DMRG, 1s and 2s DMRG, respectively. They differ regarding their flexibility for increasing ("expanding") virtual bond dimensions, which increases the size of the variational space and hence the accuracy of the converged ground-state energy. 0s and 1s DMRG offer no way of doing this, because the tensors Λ_ℓ or C_ℓ have the same dimensions after the update as before. By contrast, 2s DMRG does offer a way of expanding

bond dimensions: the bonds connecting the updated tensors A_ℓ, Λ_ℓ, and $B_{\ell+1}$ have dimensions $d \min(D_{\ell-1}, D_{\ell+1})$, which is $\geq D_\ell$; one may thus expand bond ℓ by retaining more than D_ℓ singular values in Λ_ℓ. However, this comes at a price. The numerical cost is $\mathcal{O}(D^3 d^2 w)$ for applying H^{2s} to ψ^{2s} during the iterative solution of the eigenvalue problem Eq. (19c), and $\mathcal{O}(D^3 d^3)$ for SVDing the resulting eigenstate to identify the updated A, Λ, and B. By contrast, for 1s DMRG the costs are lower: $\mathcal{O}(D^3 d w)$ for applying H^{1s} to C, and $\mathcal{O}(D^3 d)$ for SVDing C to shift to the next site. Various schemes have been proposed for achieving 2s accuracy at 1s costs; see Refs. [4,5,29].

D. Discarded spaces

In this section, we define discarded spaces as the orthogonal complements of kept spaces, and introduce their corresponding isometries and discarded space projectors.

As mentioned above, the kept spaces $\mathbb{V}_{\tilde{\ell}}^K$ and $\mathbb{W}_{\tilde{\ell}'}^K$ have dimensions smaller than the parent spaces $\mathbb{V}_{\tilde{\ell}-1}^K \otimes \mathbb{v}_{\tilde{\ell}}$ and $\mathbb{v}_{\tilde{\ell}} \otimes \mathbb{W}_{\tilde{\ell}'+1}^K$ from which they are constructed. Their orthogonal complements are the above-mentioned discarded spaces, to be denoted $\mathbb{V}_{\tilde{\ell}}^D$ and $\mathbb{W}_{\tilde{\ell}'}^D$, respectively, of dimension $\overline{D}_{\tilde{\ell}}^A = D_{\tilde{\ell}-1} d - D_{\tilde{\ell}}$ and $\overline{D}_{\tilde{\ell}'}^B = D_{\tilde{\ell}'} d - D_{\tilde{\ell}'-1}$. By definition, $\text{span}\{\mathbb{V}_{\tilde{\ell}}^K, \mathbb{V}_{\tilde{\ell}}^D\}$ and $\text{span}\{\mathbb{W}_{\tilde{\ell}'}^K, \mathbb{W}_{\tilde{\ell}'}^D\}$ yield the full parent spaces, respectively. Let $\overline{A}_{\tilde{\ell}}$ and $\overline{B}_{\tilde{\ell}'}$ be isometries from the parent to the discarded spaces,

$$\overline{A}_{\tilde{\ell}} : \mathbb{V}_{\tilde{\ell}-1}^K \otimes \mathbb{v}_{\tilde{\ell}} \to \mathbb{V}_{\tilde{\ell}}^D, \quad |\Psi_{\tilde{\ell}-1,\alpha}^K\rangle |\sigma_{\tilde{\ell}}\rangle [\overline{A}_{\tilde{\ell}}]_{\alpha\alpha'}^{\sigma_{\tilde{\ell}}} = |\Psi_{\tilde{\ell}\alpha'}^D\rangle,$$

$$\overline{B}_{\tilde{\ell}'} : \mathbb{v}_{\tilde{\ell}'} \otimes \mathbb{W}_{\tilde{\ell}'+1}^K \to \mathbb{W}_{\tilde{\ell}'}^D, \quad [\overline{B}_{\tilde{\ell}'}]_{\alpha\alpha'}^{\sigma_{\tilde{\ell}'}} |\sigma_{\tilde{\ell}'}\rangle |\Phi_{\tilde{\ell}'+1,\alpha'}^K\rangle = |\Phi_{\tilde{\ell}'\alpha}^D\rangle.$$

Then $A_{\tilde{\ell}} \oplus \overline{A}_{\tilde{\ell}}$ and $B_{\tilde{\ell}'} \oplus \overline{B}_{\tilde{\ell}'}$ are unitary maps on the parent spaces, and Eq. (6) is complemented by relations expressing orthonormality and completeness,

$$\overline{A}_{\tilde{\ell}}^\dagger \overline{A}_{\tilde{\ell}} = \mathbb{1}_{\tilde{\ell}}^D, \quad A_{\tilde{\ell}}^\dagger \overline{A}_{\tilde{\ell}} = 0, \quad \overline{B}_{\tilde{\ell}'} \overline{B}_{\tilde{\ell}'}^\dagger = \mathbb{1}_{\tilde{\ell}'-1}^D, \quad \overline{B}_{\tilde{\ell}'} B_{\tilde{\ell}'}^\dagger = 0,$$

$$\text{(20)}$$

$$A_{\tilde{\ell}} A_{\tilde{\ell}}^\dagger + \overline{A}_{\tilde{\ell}} \overline{A}_{\tilde{\ell}}^\dagger = \mathbb{1}_{\tilde{\ell}}^P, \qquad B_{\tilde{\ell}'}^\dagger B_{\tilde{\ell}'} + \overline{B}_{\tilde{\ell}'}^\dagger \overline{B}_{\tilde{\ell}'} = \mathbb{1}_{\tilde{\ell}'-1}^P,$$

$$\text{(21)}$$

Here, left- or right-oriented grey triangles denote the complements $\overline{A}_{\tilde{\ell}}$ and $\overline{B}_{\tilde{\ell}'}$ associated with discarded spaces. The orthogonality relations (6) and (20) state that K meeting K or D meeting D yield unity, whereas K meeting D yields zero. We will use them often below. For the completeness relations (21), $\mathbb{1}_{\tilde{\ell}}^P = \mathbb{1}_{\tilde{\ell}-1}^K \otimes \mathbb{1}_d$ and $\mathbb{1}_{\tilde{\ell}'-1}^P = \mathbb{1}_d \otimes \mathbb{1}_{\tilde{\ell}'}^K$ are identity matrices on the parent spaces, with $\mathbb{1}_d$ a $d \times d$ unit matrix. In numerical practice, it desirable to avoid the explicit computation of $\overline{A}_{\tilde{\ell}} \overline{A}_{\tilde{\ell}}^\dagger$ or $\overline{B}_{\tilde{\ell}'}^\dagger \overline{B}_{\tilde{\ell}'}$, since these are huge objects. Instead, one can always use Eq. (21) to express them as $\mathbb{1}_{\tilde{\ell}}^P - A_{\tilde{\ell}} A_{\tilde{\ell}}^\dagger$ or $\mathbb{1}_{\tilde{\ell}'-1}^P - B_{\tilde{\ell}'}^\dagger B_{\tilde{\ell}'}$.

Equations (21) imply additional identities that will likewise be useful below:

$$\supset \Big|_{\ell} \mathsf{c} \;=\; \text{(diagram)} + \text{(diagram)} \;=\; \supset \text{(diagram)} + \supset \text{(diagram)}, \qquad (22a)$$

$$\supset \Big|_{\ell} \Big|_{\ell+1} \mathsf{c} = \text{(diagram)} + \text{(diagram)} + \text{(diagram)} + \text{(diagram)}, \quad (22b)$$

$$\text{(diagram)}_{\ell}\,\text{(diagram)}_{\ell+1} = \supset \big| \quad \big| \mathsf{c} - \supset \text{(diagram)} - \text{(diagram)}\big|\mathsf{c} + \text{(diagram)}. \quad (22c)$$

The first two lines can be used to express 1s or 2s projectors through bond projectors, as elaborated below. The third line follows from the first two. The two equivalent forms on the right of Eq. (22a) arise from combining the physical state space of site ℓ with virtual state spaces on either the left or the right, yielding either left- or right-normalized parent spaces.

In complete analogy to Eqs. (9)–(13), the complement isometries can be used to define orthonormal bases states for the left and right discarded spaces $\mathbb{V}_{\tilde{\ell}}^{\mathrm{D}}$ and $\mathbb{W}_{\tilde{\ell}'}^{\mathrm{D}}$,

$$\Psi_{\tilde{\ell}\alpha}^{\mathrm{D}} = \underset{1 \qquad \tilde{\ell}}{\overset{A_1 \quad \overline{A}_{\tilde{\ell}}}{\text{(diagram)}}}\alpha, \quad \Phi_{\tilde{\ell}'\alpha'}^{\mathrm{D}} = \alpha'\underset{\tilde{\ell}' \qquad \mathscr{L}}{\overset{\overline{B}_{\tilde{\ell}'} \quad B_{\mathscr{L}}}{\text{(diagram)}}}, \quad (23)$$

satisfying the orthonormality relations

$$\underset{1 \qquad \tilde{\ell}}{\text{(diagram)}} = \Big(_{\mathbb{1}_{\tilde{\ell}}^{\mathrm{D}}}, \qquad \underset{\tilde{\ell}' \qquad \mathscr{L}}{\text{(diagram)}} = \Big)_{\mathbb{1}_{\tilde{\ell}'-1}^{\mathrm{D}}}, \quad (24a)$$

$$\underset{1 \qquad \tilde{\ell}}{\text{(diagram)}} = 0\,, \qquad \underset{\tilde{\ell}' \qquad \mathscr{L}}{\text{(diagram)}} = 0\,. \quad (24b)$$

The corresponding projectors are defined as

$$\mathcal{P}_{\tilde{\ell}}^{\mathrm{D}} = \sum_{\alpha} |\Psi_{\tilde{\ell}\alpha}^{\mathrm{D}}\rangle\langle\Psi_{\tilde{\ell}\alpha}^{\mathrm{D}}| \;=\; \underset{1 \qquad \tilde{\ell}}{\text{(diagram)}}, \quad (25)$$

$$\mathcal{Q}_{\tilde{\ell}'}^{\mathrm{D}} = \sum_{\alpha'} |\Phi_{\tilde{\ell}'\alpha'}^{\mathrm{D}}\rangle\langle\Phi_{\tilde{\ell}'\alpha'}^{\mathrm{D}}| \;=\; \underset{\tilde{\ell}' \qquad \mathscr{L}}{\text{(diagram)}}, \quad (26)$$

with $\mathcal{P}_0^{\mathrm{D}} = \mathcal{Q}_{\mathscr{L}+1}^{\mathrm{D}} = 0$. They obey orthonormality relations,

$$\mathcal{P}_{\tilde{\ell}}^{\mathrm{x}}\mathcal{P}_{\tilde{\ell}}^{\overline{\mathrm{x}}} = \delta^{\mathrm{x}\overline{\mathrm{x}}}\mathcal{P}_{\tilde{\ell}}^{\mathrm{x}}, \quad \mathcal{Q}_{\tilde{\ell}'}^{\mathrm{x}}\mathcal{Q}_{\tilde{\ell}'}^{\overline{\mathrm{x}}} = \delta^{\mathrm{x}\overline{\mathrm{x}}}\mathcal{Q}_{\tilde{\ell}'}^{\overline{\mathrm{x}}}, \quad (27)$$

where here and henceforth, $\mathrm{x}, \overline{\mathrm{x}} \in \{\mathrm{K}, \mathrm{D}\}$. Moreover, Eq. (21) implies the completeness relations

$$\mathcal{P}_{\tilde{\ell}}^{\mathrm{K}} + \mathcal{P}_{\tilde{\ell}}^{\mathrm{D}} = \mathcal{P}_{\tilde{\ell}-1}^{\mathrm{K}} \otimes \mathbb{1}_d, \quad \mathcal{Q}_{\tilde{\ell}'}^{\mathrm{K}} + \mathcal{Q}_{\tilde{\ell}'}^{\mathrm{D}} = \mathbb{1}_d \otimes \mathcal{Q}_{\tilde{\ell}'+1}^{\mathrm{K}}, \quad (28)$$

stating that the kept and discarded projectors of a given site together form a projector for their parent space. These will play a crucial role in subsequent sections.

To conclude this section, we apply the projector identity (22b) to the open legs of the state $\mathcal{H}_{\ell}^{2s}\psi_{\ell}^{2s}$ appearing in the 2s

Schrödinger (19c). We obtain

$$(29)$$

If only the first term is retained, the 2s Schrödinger Eq. (19c) reduces to the bond Schrödinger Eq. (19a), sandwiched between A_ℓ and $B_{\ell+1}$,

$$A_\ell(H_\ell^{\mathrm{b}} - E)\Lambda_\ell B_{\ell+1} = 0. \quad (30a)$$

The first term together with the second or third term reduces to the 1s Schrödinger Eq. (19b) for sites $\ell+1$ or ℓ, left or right contracted with A_ℓ and $B_{\ell+1}$, respectively,

$$A_\ell\big(H_{\ell+1}^{1s} - E\big)C_{\ell+1} = 0, \quad (30b)$$

$$\big(H_\ell^{1s} - E\big)C_\ell B_{\ell+1} = 0. \quad (30c)$$

All four terms together of course give the full 2s Schrödinger Eq. (19c),

$$\big(H_\ell^{2s} - E\big)A_\ell \Lambda_\ell B_{\ell+1} = 0. \quad (30d)$$

Evidently, the fourth term in Eq. (29), involving a DD projector pair, is beyond the reach of 1s schemes. A strategy for nevertheless computing its most important contributions with 1s costs, called controlled bond expansion, has recently been formulated by us in Ref. [29].

III. CONSTRUCTION OF $\mathcal{P}^{ns}$ AND $\mathcal{P}^{n\perp}$

As discussed in the introduction, each site of an MPS $|\Psi\rangle$ induces a splitting of the local Hilbert space into K and D sectors. This induces a partition of the full vector space $\mathbb{V}$ into intricately nested orthogonal subspaces [6]. It is useful to identify orthogonal projectors for these subspaces. Gauge invariance—the existence of many equivalent representations of $|\Psi\rangle$—makes this a nontrivial task. It can be accomplished systematically by Gram-Schmidt orthogonalization, formulated in projector language. The following three sections are devoted to this endeavor.

In the present section, we define a set of projectors, $\mathcal{P}_{\ell\bar{\ell}}^{\mathrm{x}\overline{\mathrm{x}}}$, $\mathrm{x}, \overline{\mathrm{x}} \in \{\mathrm{K}, \mathrm{D}\}$, involving kept and/or discarded sectors at sites $\ell, \bar{\ell}$. These serve as building blocks for all projectors introduced thereafter. Then, in Sec. III B, we define generalized *local n-site* (ns) projectors $\mathcal{P}_\ell^{ns}$ describing variations of $|\Psi\rangle$ involving up to n contiguous sites. In Sec. III C, we add them up to obtain *global n*s projectors $\mathcal{P}^{ns}$; and in Sec. III D we orthogonalize these to obtain *irreducible* global ns projectors $\mathcal{P}^{n\perp}$ not expressible through combinations of variations on subsets of $n' < n$ sites. They are useful for various purposes, including the computation of the energy variance [6], and the formulation of MPS algorithms based on the notion of tangent spaces [11–14,30] and generalizations thereof. Throughout, we concisely summarize the properties of the various projectors encountered along the way.

A. Projectors for kept and discarded sectors $\mathcal{P}_{\ell\bar{\ell}}^{\mathrm{X}\bar{\mathrm{X}}}$

We start by introducing kept and discarded space projectors defined on the full Hilbert space $\mathbb{V}$. To this end, we supplement $\mathcal{P}_\ell^{\mathrm{X}}$ and $\mathcal{Q}_\ell^{\mathrm{X}}$ by right or left environments (E) comprising the entire rest of the chain, and define

$$\mathcal{P}_\ell^{\mathrm{XE}} = \mathcal{P}_\ell^{\mathrm{X}} \otimes \mathbb{1}_d^{\otimes \mathscr{L}-\ell}, \qquad \mathcal{P}_\ell^{\mathrm{EX}} = \mathbb{1}_d^{\otimes \ell-1} \otimes \mathcal{Q}_\ell^{\mathrm{X}},$$

$$\mathcal{P}_\ell^{\mathrm{KE}} = \cdots, \quad \mathcal{P}_\ell^{\mathrm{EK}} = \cdots,$$

$$\mathcal{P}_\ell^{\mathrm{DE}} = \cdots, \quad \mathcal{P}_\ell^{\mathrm{ED}} = \cdots. \tag{31}$$

with $\ell \in [0, \mathscr{L}]$ for $\mathcal{P}_\ell^{\mathrm{XE}}$ and $\ell \in [1, \mathscr{L}+1]$ for $\mathcal{P}_\ell^{\mathrm{EX}}$. Equations (12) and (24) imply orthogonality relations for projectors with E on the same side (both right or both left),

$$\mathcal{P}_\ell^{\mathrm{XE}}\mathcal{P}_{\bar{\ell}}^{\bar{\mathrm{X}}\mathrm{E}} = \delta^{\ell<\bar{\ell}}\delta_{\mathrm{XK}}\mathcal{P}_{\bar{\ell}}^{\bar{\mathrm{X}}\mathrm{E}} + \delta^{\ell\bar{\ell}}\delta_{\mathrm{X}\bar{\mathrm{X}}}\mathcal{P}_\ell^{\mathrm{XE}} + \delta^{\ell>\bar{\ell}}\mathcal{P}_\ell^{\mathrm{XE}}\delta_{\mathrm{K}\bar{\mathrm{X}}}, \tag{32a}$$

$$\mathcal{P}_\ell^{\mathrm{EX}}\mathcal{P}_{\bar{\ell}}^{\mathrm{E}\bar{\mathrm{X}}} = \delta^{\ell<\bar{\ell}}\mathcal{P}_\ell^{\mathrm{EX}}\delta_{\mathrm{K}\bar{\mathrm{X}}} + \delta^{\ell\bar{\ell}}\delta_{\mathrm{X}\bar{\mathrm{X}}}\mathcal{P}_\ell^{\mathrm{EX}} + \delta^{\ell>\bar{\ell}}\delta_{\mathrm{XK}}\mathcal{P}_{\bar{\ell}}^{\mathrm{E}\bar{\mathrm{X}}}. \tag{32b}$$

The δ symbols indicate that the first, second, and third terms contribute only for $\ell < \bar{\ell}$, $\ell = \bar{\ell}$, and $\ell > \bar{\ell}$, respectively. Thus, same-site projectors are orthonormal; different-site products with Es on the same side, of the type $\mathcal{P}_\ell^{\mathrm{XE}}\mathcal{P}_{\bar{\ell}}^{\bar{\mathrm{X}}\mathrm{E}}$ (or $\mathcal{P}_\ell^{\mathrm{EX}}\mathcal{P}_{\bar{\ell}}^{\mathrm{E}\bar{\mathrm{X}}}$), vanish if the earlier (later) site hosts a D; if it hosts a K, they yield the projector from the other site. We depict two cases of Eq. (32a) below:

$$\mathcal{P}_\ell^{\mathrm{DE}}\mathcal{P}_{\ell}^{\mathrm{DE}} = \cdots = \cdots = \mathcal{P}_\ell^{\mathrm{DE}}.$$

$$\mathcal{P}_\ell^{\mathrm{KE}}\mathcal{P}_{\bar{\ell}}^{\mathrm{DE}} = \cdots = \cdots = \mathcal{P}_{\bar{\ell}}^{\mathrm{DE}}.$$

Equation (32a) was first written down in that form in Ref. [27], Eq. (29), in the context of NRG. There, one deals exclusively with left-normalized states, and sites to the right of the orthogonality center are treated purely as environmental degrees of freedom, described by product states. Equation (32b) is the counterpart of (32a) for right-normalized states.

Projector products with Es in the middle, $\mathcal{P}_\ell^{\mathrm{XE}}\mathcal{P}_{\bar{\ell}}^{\mathrm{E}\bar{\mathrm{X}}}$, and $\ell < \bar{\ell}$, again yield projectors. We denote them by

$$\mathcal{P}_{\ell\bar{\ell}}^{\mathrm{X}\bar{\mathrm{X}}} = \mathcal{P}_\ell^{\mathrm{XE}}\mathcal{P}_{\bar{\ell}}^{\mathrm{E}\bar{\mathrm{X}}} \quad (0 \leq \ell < \bar{\ell} \leq \mathscr{L}+1),$$

$$\mathcal{P}_{\ell\bar{\ell}}^{\mathrm{KK}} = \cdots, \quad \mathcal{P}_{\ell\bar{\ell}}^{\mathrm{KD}} = \cdots,$$

$$\mathcal{P}_{\ell\bar{\ell}}^{\mathrm{DK}} = \cdots, \quad \mathcal{P}_{\ell\bar{\ell}}^{\mathrm{DD}} = \cdots. \tag{33}$$

They have local unit operators on $n = \bar{\ell} - (\ell+1)$ contiguous sites, sandwiched between any combination of K and D projectors to the left and right. In this sense, they generalize Eqs. (15) and will be called generalized *local n*s projectors.

They fulfill numerous orthogonality relations following directly from Eqs. (32). For example,

$$\mathcal{P}_{\ell\bar{\ell}}^{\mathrm{X}\bar{\mathrm{X}}}\mathcal{P}_{\ell\bar{\ell}}^{\mathrm{X}'\bar{\mathrm{X}}'} = \delta^{\mathrm{XX}'}\delta^{\bar{\mathrm{X}}\bar{\mathrm{X}}'}\mathcal{P}_{\ell\bar{\ell}}^{\mathrm{X}\bar{\mathrm{X}}}, \tag{34a}$$

$$\forall \ell < \ell': \ \mathcal{P}_{\ell\bar{\ell}}^{\mathrm{D}\bar{\mathrm{X}}}\mathcal{P}_{\ell'\bar{\ell}'}^{\mathrm{X}'\bar{\mathrm{X}}'} = 0, \quad \forall \bar{\ell} < \bar{\ell}': \ \mathcal{P}_{\ell\bar{\ell}}^{\mathrm{X}\bar{\mathrm{X}}}\mathcal{P}_{\ell'\bar{\ell}'}^{\mathrm{X}'\mathrm{D}} = 0, \tag{34b}$$

$$\mathcal{P}_{\ell\bar{\ell}}^{\mathrm{D}\bar{\mathrm{X}}}\mathcal{P}_{\ell'\bar{\ell}'}^{\mathrm{D}\bar{\mathrm{X}}'} \sim \delta_{\ell\ell'}, \quad \mathcal{P}_{\ell\bar{\ell}}^{\mathrm{XD}}\mathcal{P}_{\ell'\bar{\ell}'}^{\mathrm{X}'\mathrm{D}} \sim \delta_{\bar{\ell}\bar{\ell}'}. \tag{34c}$$

Thus, two projectors having the same site indices are orthonormal; projector products involving a D on a site earlier or later than all other indexed sites vanish; those involving two Ds on the same side but different sites vanish, too. Some of these relations are illustrated below:

$$\mathcal{P}_{\ell\bar{\ell}}^{\mathrm{DK}}\mathcal{P}_{\ell\bar{\ell}}^{\mathrm{DK}} = \cdots = \cdots = \mathcal{P}_{\ell\bar{\ell}}^{\mathrm{DK}},$$

$$\mathcal{P}_{\ell\bar{\ell}}^{\mathrm{DK}}\mathcal{P}_{\ell'\bar{\ell}'}^{\mathrm{KK}} = \cdots = 0,$$

$$\mathcal{P}_{\ell\bar{\ell}}^{\mathrm{DK}}\mathcal{P}_{\ell\bar{\ell}'}^{\mathrm{DD}} = \cdots = \cdots = \mathcal{P}_{\ell\bar{\ell}'}^{\mathrm{DD}}.$$

Equation (28) implies another useful property (for $\bar{\ell}-\ell > 1$),

$$\mathcal{P}_{\ell\bar{\ell}}^{\mathrm{K}\bar{\mathrm{X}}} = \mathcal{P}_{\ell+1,\bar{\ell}}^{\mathrm{K}\bar{\mathrm{X}}} + \mathcal{P}_{\ell+1\bar{\ell}}^{\mathrm{D}\bar{\mathrm{X}}}, \quad \mathcal{P}_{\ell\bar{\ell}}^{\mathrm{XK}} = \mathcal{P}_{\ell,\bar{\ell}-1}^{\mathrm{XK}} + \mathcal{P}_{\ell,\bar{\ell}-1}^{\mathrm{XD}}, \tag{35}$$

reflecting Eq. (22b). Thus, a K on a given site ℓ (or $\bar{\ell}$) can be decomposed into K and D on the inner neighboring site $\ell + 1$ (or $\bar{\ell} - 1$), thereby expressing one projector through two that both target one less site. This decomposition will be used repeatedly below.

B. Local n-site projectors $\mathcal{P}_\ell^{n\mathrm{s}}$

The KK projectors merit special attention. For $\bar{\ell} - \ell = 1$, 2 or 3, they correspond to the bond, 1s and 2s projectors introduced in Eqs. (15). These can be expressed as

$$\mathcal{P}_\ell^{\mathrm{b}} = \mathcal{P}_{\ell,\ell+1}^{\mathrm{KK}}, \quad \mathcal{P}_\ell^{\mathrm{1s}} = \mathcal{P}_{\ell-1,\ell+1}^{\mathrm{KK}}, \quad \mathcal{P}_\ell^{\mathrm{2s}} = \mathcal{P}_{\ell-1,\ell+2}^{\mathrm{KK}}. \tag{36}$$

Generalizing the notation of (36), we define a set of local ns projectors (for $n \geq 0$ and $\ell \in [1, \mathscr{L}+1-n]$) as

$$\mathcal{P}_\ell^{n\mathrm{s}} = \mathcal{P}_{\ell-1,\ell+n}^{\mathrm{KK}} = \cdots. \tag{37}$$

Then $\mathcal{P}_\ell^{0\mathrm{s}} = \mathcal{P}_{\ell-1}^{\mathrm{b}}$, and for $n \geq 1$, these projectors span the spaces of variations of $|\Psi\rangle$ on n contiguous sites from ℓ to $\ell + n - 1$. However, projectors $\mathcal{P}_\ell^{n\mathrm{s}}$ and $\mathcal{P}_{\ell'}^{n\mathrm{s}}$ with $\ell \neq \ell'$ are not orthogonal. Instead, the following relations hold for all $\ell < \ell'$,

$$\mathcal{P}_\ell^{n\mathrm{s}}\mathcal{P}_{\ell'}^{n\mathrm{s}} = \mathcal{P}_{\ell+1}^{(n-1)\mathrm{s}}\mathcal{P}_{\ell'}^{n\mathrm{s}} = \mathcal{P}_\ell^{n\mathrm{s}}\mathcal{P}_{\ell'}^{(n-1)\mathrm{s}} = \mathcal{P}_{\ell+1}^{(n-1)\mathrm{s}}\mathcal{P}_{\ell'}^{(n-1)\mathrm{s}}, \tag{38}$$

as can be verified using Eqs. (32). For example, for

we obtain the same result in both cases. In particular, for $n \geqslant 1$, two ns projectors mismatched by one site yield an $(n-1)$-site projector,

$$\mathcal{P}_\ell^{ns}\mathcal{P}_{\ell+1}^{ns} = \mathcal{P}_{\ell+1}^{(n-1)s} \tag{39}$$

Orthogonalized versions of the $\mathcal{P}_\ell^{ns}$ projectors will be constructed in the next subsection. Here, we collect some properties, following from Eq. (32), that will be needed for that purpose,

$$\forall \ell < \ell': \ \mathcal{P}_{\ell\bar{\ell}}^{D\bar{X}}\mathcal{P}_{\ell'}^{ns} = 0, \tag{40a}$$

$$\forall (\ell+n) \leqslant \bar{\ell}': \ \mathcal{P}_\ell^{ns}\mathcal{P}_{\ell'\bar{\ell}'}^{X'D} = 0. \tag{40b}$$

Thus, $\mathcal{P}_\ell^{ns}$ is annihilated by a left D on its left or a right D on its right. For example,

$$\mathcal{P}_\ell^{ns}\mathcal{P}_{\ell'\bar{\ell}'}^{KD} = \quad = 0.$$

Using Eq. (35), $\mathcal{P}_\ell^{ns}$ can be expressed through two $(n-1)$s projectors,

$$\mathcal{P}_\ell^{ns} = \mathcal{P}_{\ell,\ell+n}^{KK} + \mathcal{P}_{\ell,\ell+n}^{DK} = \mathcal{P}_{\ell-1,\ell+n-1}^{KK} + \mathcal{P}_{\ell-1,\ell+n-1}^{KD}$$

$$= \mathcal{P}_{\ell+1}^{(n-1)s} + \mathcal{P}_{\ell,\ell+n}^{DK} = \mathcal{P}_\ell^{(n-1)s} + \mathcal{P}_{\ell-1,\ell+n-1}^{KD}$$

$$\tag{41}$$

The existence of two different decompositions of $\mathcal{P}_\ell^{ns}$, mimicking Eq. (22a), reflects the gauge freedom of MPSs. This can be exploited to write $\mathcal{P}_{\ell,\ell+n}^{DK}$ as $\mathcal{P}_\ell^{(n-1)s} + \mathcal{P}_{\ell-1,\ell-1+n}^{KD} - \mathcal{P}_{\ell+1}^{(n-1)s}$, converting DK to KD, or vice versa. Repeated use

yields an identity that will be useful below,

$$\sum_{\ell=\bar{\ell}}^{\ell'} \mathcal{P}_{\ell,\ell+n}^{DK} = \mathcal{P}_{\bar{\ell}}^{(n-1)s} + \sum_{\ell=\bar{\ell}}^{\ell'} \mathcal{P}_{\ell-1,\ell-1+n}^{KD} - \mathcal{P}_{\ell'+1}^{(n-1)s}. \tag{42}$$

C. Global ns projectors, $\mathcal{P}^{ns}$

We now are ready to define the ns spaces $\mathbb{V}^{ns}$. For $n = 0$, we define $\mathbb{V}^{0s} = \mathrm{span}\{|\Psi\rangle\}$. For $n \geqslant 1$, we define $\mathbb{V}^{ns}$ as the span of $|\Psi\rangle$ and all states $|\Psi'\rangle$ differing from it on at most n contiguous sites,

$$\mathbb{V}^{ns} = \mathrm{span}\left\{ \ \middle| \ \ell \in [1, \mathscr{L}+1-n] \right\}. \tag{43}$$

For $n = 1$, $\mathbb{V}^{1s}$ is the tangent space of $|\Psi\rangle$. More concretely, $\mathbb{V}^{ns}$ is defined as the image of all local ns projectors,

$$\mathbb{V}^{ns} = \mathrm{span}\{\mathrm{im}(\mathcal{P}_1^{ns}), \mathrm{im}(\mathcal{P}_2^{ns}), \ldots, \mathrm{im}(\mathcal{P}_{\mathscr{L}+1-n}^{ns})\}. \tag{44}$$

For any $n' \leqslant n$, the image $\mathrm{im}(\mathcal{P}_\ell^{n's})$ is by construction fully contained in the image $\mathrm{im}(\mathcal{P}_\ell^{ns})$, hence $\mathbb{V}^{n's}$ is a subspace of $\mathbb{V}^{ns}$, implying the nested hierarchy (1).

Let $\mathcal{P}^{ns}$ be the projector having $\mathbb{V}^{ns}$ as image; then, $\mathrm{im}(\mathcal{P}^{ns})$ contains $\mathrm{im}(\mathcal{P}_\ell^{ns})$ for all $\ell \in [1, \mathscr{L}+1-n]$. Formally, $\mathcal{P}^{ns}$ has the defining properties

$$\left(\mathcal{P}^{ns}\right)^2 = \mathcal{P}^{ns}, \quad \mathcal{P}^{ns}\mathcal{P}_\ell^{ns} = \mathcal{P}_\ell^{ns}, \tag{45a}$$

$$\mathcal{P}_\ell^{ns}|\Phi\rangle = 0 \ \forall \ell \Rightarrow \mathcal{P}^{ns}|\Phi\rangle = 0. \tag{45b}$$

Moreover, the nested structure of the $\mathbb{V}^{ns}$s implies

$$\forall n' < n: \quad \mathcal{P}^{ns}\mathcal{P}^{n's} = \mathcal{P}^{n's}. \tag{46}$$

Let us construct $\mathcal{P}^{ns}$ explicitly. Simply summing up the local projectors $\mathcal{P}_\ell^{ns}$ does not yield a projector because the images of $\mathcal{P}_\ell^{ns}$ and $\mathcal{P}_{\ell'}^{ns}$ are not orthogonal. A set of mutually orthogonal local projectors can be obtained by projecting out the overlap between $\mathcal{P}_\ell^{ns}$ and $\mathcal{P}_{\ell\pm1}^{ns}$. We thus define

$$\mathcal{P}_{\ell\lessgtr}^{ns} = \mathcal{P}_\ell^{ns}\left(\mathbb{1}_\mathbb{V} - \mathcal{P}_{\ell\pm1}^{ns}\right), \tag{47}$$

so that $\mathcal{P}_{\ell\lessgtr}^{ns}\mathcal{P}_{\ell'}^{ns} = 0$ holds for neighboring ℓ, ℓ' with $\ell \lessgtr \ell'$. It suffices to orthogonalize ns projectors mismatched by *one* site, since from these we can select a set of projectors mutually orthogonal on all sites. Indeed, Eqs. (39) and (41) yield $(n-1)$-site projectors containing Ds,

$$\mathcal{P}_{\ell<}^{ns} = \mathcal{P}_\ell^{ns} - \mathcal{P}_{\ell+1}^{(n-1)s} = \mathcal{P}_{\ell,\ell+n}^{DK}, \tag{48a}$$

$$\mathcal{P}_{\ell>}^{ns} = \mathcal{P}_\ell^{ns} - \mathcal{P}_\ell^{(n-1)s} = \mathcal{P}_{\ell-1,\ell-1+n}^{KD}, \tag{48b}$$

and the Ds ensure the orthonormality relations [cf. (34)]

$$\mathcal{P}_{\ell\lessgtr}^{ns}\mathcal{P}_{\ell'\lessgtr}^{ns} = \delta_{\ell\ell'}\mathcal{P}_{\ell\lessgtr}^{ns}, \tag{49a}$$

$$\forall \ell < \ell': \mathcal{P}_{\ell<}^{ns}\mathcal{P}_{\ell'>}^{ns} = 0, \tag{49b}$$

$$\forall \ell \lessgtr \ell': \mathcal{P}_{\ell\lessgtr}^{ns}\mathcal{P}_{\ell'}^{ns} = 0. \tag{49c}$$

These equations have a remarkable implication: for any choice of $\ell' \in [1, \mathscr{L}-n+1]$, the projectors $\mathcal{P}_{\ell<}^{ns}$ for $\ell \in [1, \ell'-1]$, $\mathcal{P}_{\ell'}^{ns}$, and $\mathcal{P}_{\ell>}^{ns}$ for $\ell \in [\ell'+1, \mathscr{L}+1-n]$ form an orthonormal set, and this set contains a $\mathcal{P}_\ell^{ns}$ (in projected form) for

every $\ell \in [1, \mathscr{L} + 1 - n]$. We define the global ns projector as their sum,

$$\mathcal{P}^{ns} = \sum_{\ell=1}^{\ell'-1} \mathcal{P}_{\ell<}^{ns} + \mathcal{P}_{\ell'}^{ns} + \sum_{\ell=\ell'+1}^{\mathscr{L}+1-n} \mathcal{P}_{\ell>}^{ns}$$

$$= \sum_{\ell=1}^{\ell'-1} \text{[diagram]}_{\ell} \quad \text{[diagram]}_{\ell+n} + \text{[diagram]}_{\ell'} \quad \text{[diagram]}_{\ell'+n}$$

$$+ \sum_{\ell=\ell'+1}^{\mathscr{L}+1-n} \text{[diagram]}_{\ell-1} \quad \text{[diagram]}_{\widetilde{\ell+n-1}}. \tag{50}$$

Here, ℓ' may be chosen freely as convenience dictates; different choices are equivalent, being related by Eqs. (41). The orthogonality relations (49) ensure the properties (45a). For example,

$$\mathcal{P}^{ns}\mathcal{P}_{\ell'}^{ns} = 0 + \mathcal{P}_{\ell'}^{ns}\mathcal{P}_{\ell'}^{ns} + 0 = \mathcal{P}_{\ell'}^{ns}. \tag{51}$$

The property (45b) is ensured by orthogonalizing $\mathcal{P}_\ell^{ns}$ with respect to each other and thus never including states with $\mathcal{P}_\ell^{ns}|\Phi\rangle = 0 \ \forall\ell$. This confirms that $\text{im}(\mathcal{P}^{ns})$ contains $\text{im}(\mathcal{P}_\ell^{ns})$ for all $\ell \in [1, \mathscr{L} + 1 - n]$; thus, $\mathcal{P}^{ns}$ indeed is the desired projector having $\mathbb{V}^{ns}$ as image. Evaluating Eq. (50) using the middle expressions from (48), we obtain

$$\mathcal{P}^{ns} = \sum_{\ell=1}^{\mathscr{L}+1-n} \mathcal{P}_\ell^{ns} - \sum_{\ell=1}^{\mathscr{L}-n} \mathcal{P}_{\ell+1}^{(n-1)s}$$

$$= \sum_{\ell=1}^{\mathscr{L}+1-n} \text{[diagram]}_{\ell} \quad \text{[diagram]}_{\ell+n} - \sum_{\ell=1}^{\mathscr{L}-n} \text{[diagram]}_{\ell+1} \quad \text{[diagram]}_{\ell+n}, \tag{52a}$$

expressing $\mathcal{P}^{ns}$ through local ns and $(n-1)$s projectors in a manner manifestly independent of ℓ', and not involving an D sectors. The occurrence of the first term, a sum over all $\mathcal{P}_\ell^{ns}$, is no surprise; the nontrivial part of the above construction was establishing the form of the second term, needed to ensure that $\mathcal{P}^{ns}$ is a projector. Note that Eq. (45a) directly implies property (45b). Alternatively, we can use the rightmost forms of (48) in (50) to obtain

$$\mathcal{P}^{ns} = \sum_{\ell=1}^{\ell'} \mathcal{P}_{\ell,\ell+n}^{\text{DK}} + \mathcal{P}_{\ell',\ell'+n}^{\text{KK}} + \sum_{\ell=\ell'}^{\mathscr{L}-n} \mathcal{P}_{\ell,\ell+n}^{\text{KD}}, \tag{52b}$$

now expressed purely through $(n-1)$s projectors, with all but one involving D sectors.

For $n = 1$, Eqs. (52) reproduce the well-known tangent space projector,

$$\mathcal{P}^{1s} = \sum_{\ell=1}^{\mathscr{L}} \mathcal{P}_\ell^{1s} - \sum_{\ell=1}^{\mathscr{L}-1} \mathcal{P}_\ell^{b}$$

$$= \sum_{\ell=1}^{\mathscr{L}} \text{[diagram]}_{\ell} \quad \text{[diagram]} - \sum_{\ell=1}^{\mathscr{L}-1} \text{[diagram]}_{\ell} \quad \text{[diagram]}, \tag{53a}$$

$$= \sum_{\ell=1}^{\ell'} \mathcal{P}_{\ell,\ell+1}^{\text{DK}} + \mathcal{P}_{\ell',\ell'+1}^{\text{KK}} + \sum_{\ell=\ell'}^{\mathscr{L}-1} \mathcal{P}_{\ell,\ell+1}^{\text{KD}}$$

$$= \sum_{\ell=1}^{\ell'} \text{[diagram]}_{\ell} \quad \text{[diagram]} + \text{[diagram]}_{\ell'} \quad \text{[diagram]}$$

$$+ \sum_{\ell=\ell'}^{\mathscr{L}-1} \text{[diagram]}_{\ell} \quad \text{[diagram]}. \tag{53b}$$

These expressions are widely used in MPS algorithms based on tangent space concepts, such as time evolution using the time-dependent variational principle (TDVP) [11–14,30]. The form (53a), or (53b) with the choice $\ell' = \mathscr{L} - 1$, was first given Lubich, Oseledts, and Vandereycken [11] (Theorem 3.1), and transcribed into MPS notation in Ref. [12]. In these papers, it was derived in a different manner than here, using arguments invoking gauge invariance. Our derivation has the advantage that it generalizes directly to ns projectors. For $n = 2$, our expression (52a) for $\mathcal{P}^{2s}$ reproduces the projector proposed in Ref. [12] for 2s TDVP:

$$\mathcal{P}^{2s} = \sum_{\ell=1}^{\mathscr{L}-1} \text{[diagram]}_{\ell} \quad \text{[diagram]} - \sum_{\ell=2}^{\mathscr{L}-1} \text{[diagram]}_{\ell} \quad \text{[diagram]}. \tag{54}$$

D. Irreducible global ns projectors $\mathcal{P}^{n\perp}$

Our final step is to orthogonalize the global $\mathcal{P}^{ns}$ projectors to obtain mutually *orthogonal* global ns projectors $\mathcal{P}^{n\perp}$. This step is inspired by the observation, made in Ref. [6], that a given MPS $|\Psi\rangle$ induces a decomposition of the full Hilbert space into mutually orthogonal subspaces,

$$\mathbb{V} = \oplus_{n=0}^{\mathscr{L}} \mathbb{V}^{n\perp}, \tag{55}$$

where $\mathbb{V}^{0\perp}$ is spanned by $|\Psi\rangle$, and for $n \geqslant 1$ each $\mathbb{V}^{n\perp}$ is the complement of $\mathbb{V}^{(n-1)s}$ in $\mathbb{V}^{ns} = \mathbb{V}^{(n-1)s} \oplus \mathbb{V}^{n\perp}$. Each $\mathbb{V}^{n\perp}$ is *irreducible*, comprising variations of $|\Psi\rangle$ defined on n contiguous sites that are not expressible through variations on subsets of $n' < n$ sites.

The decomposition (55) induces a decomposition of the identity on $\mathbb{V}$ into a sum of irreducible, mutually orthogonal projectors $\mathcal{P}^{n\perp}$, each with a $\mathbb{V}^{n\perp}$ as image,

$$\mathbb{1}_{\mathbb{V}} = \mathbb{1}_d^{\otimes\mathscr{L}} = \sum_{n=0}^{\mathscr{L}} \mathcal{P}^{n\perp}, \quad \mathcal{P}^{n\perp}\mathcal{P}^{n'\perp} = \delta^{nn'}\mathcal{P}^{n\perp}. \tag{56}$$

We now construct the $\mathcal{P}^{n\perp}$ projectors through a Gram-Schmidt procedure. For $n \geqslant 1$, we define $\mathcal{P}^{n\perp}$ by projecting out $\mathcal{P}^{(n-1)s}$ from $\mathcal{P}^{ns}$, using Eq. (46),

$$\mathcal{P}^{n\perp} = \mathcal{P}^{ns}(\mathbb{1}_{\mathbb{V}} - \mathcal{P}^{(n-1)s}) = \mathcal{P}^{ns} - \mathcal{P}^{(n-1)s}. \tag{57}$$

This scheme is initialized by the definition

$$\mathcal{P}^{0\perp} = \mathcal{P}^{0s} = |\Psi\rangle\langle\Psi| \tag{58a}$$

$$= \mathcal{P}^{0s}_{\mathscr{L}+1} = \mathcal{P}^{KK}_{\mathscr{L},\mathscr{L}+1} = \;[\text{diagram}]\;, \tag{58b}$$

$$= \mathcal{P}^{0s}_1 = \mathcal{P}^{KK}_{0,1} \quad = \;[\text{diagram}]. \tag{58c}$$

The two equivalent forms for $\mathcal{P}^{0\perp}$, (58b) and (58c), reflect MPS gauge invariance.

For $n = 1$, Eqs. (57) and (52a), with $\mathcal{P}^{0s} = \mathcal{P}^{0s}_1$, yield

$$\mathcal{P}^{1\perp} = \mathcal{P}^{1s} - \mathcal{P}^{0s} = \sum_{\ell=1}^{\mathscr{L}}\left[\mathcal{P}^{1s}_\ell - \mathcal{P}^{0s}_\ell\right]$$
$$= \sum_{\ell=1}^{\mathscr{L}}\left[\;[\text{diagram}]_\ell - [\text{diagram}]_\ell\;\right]. \tag{59a}$$

More compact forms are obtained by evaluating Eq. (57) using Eq. (52b), choosing either $\ell' = \mathscr{L}$ or 0 for $\mathcal{P}^{0s}$,

$$\mathcal{P}^{1\perp} = \sum_{\ell=1}^{\mathscr{L}} \mathcal{P}^{DK}_{\ell,\ell+1} = \sum_{\ell=1}^{\mathscr{L}}\;[\text{diagram}]_\ell\;, \tag{59b}$$

$$= \sum_{\ell=1}^{\mathscr{L}} \mathcal{P}^{KD}_{\ell-1,\ell} = \sum_{\ell=1}^{\mathscr{L}}\;[\text{diagram}]_\ell\;. \tag{59c}$$

Diagrammatically, the latter expressions also follow directly from (59a), using (22a). That two equivalent forms exist again reflects MPS gauge invariance.

For $n \geqslant 2$, Eqs. (57) and (52a) yield

$$\mathcal{P}^{n\perp} = \sum_{\ell=1}^{\mathscr{L}+1-n}\left[\mathcal{P}^{ns}_\ell - \mathcal{P}^{(n-1)s}_{\ell+1} - \mathcal{P}^{(n-1)s}_\ell + \mathcal{P}^{(n-2)s}_{\ell+1}\right]$$
$$= \sum_{\ell=1}^{\mathscr{L}+1-n}\Big[\;[\text{diagram}]_{\ell,\,\ell+n} - [\text{diagram}]_{\ell+1,\,\ell+n}$$
$$\quad -\;[\text{diagram}]_{\ell,\,\widetilde{\ell+n-1}} + [\text{diagram}]_{\widetilde{\ell+1},\,\widetilde{\ell+n-1}}\Big]. \tag{60a}$$

A more compact form is obtained by evaluating Eq. (57) using Eq. (52b), choosing $\ell' = \mathscr{L}+1-n$ for *both* terms,

$$\mathcal{P}^{n\perp} = \sum_{\ell=1}^{\mathscr{L}+1-n}\mathcal{P}^{DK}_{\ell,\ell+n} + \mathcal{P}^{KK}_{\mathscr{L}+1-n,\mathscr{L}+1}$$
$$\quad -\sum_{\ell=1}^{\mathscr{L}+1-n}\mathcal{P}^{DK}_{\ell,\ell+n-1} - \mathcal{P}^{KK}_{\mathscr{L}+1-n,\mathscr{L}} - \mathcal{P}^{KD}_{\mathscr{L}+1-n,\mathscr{L}}$$
$$= \sum_{\ell=1}^{\mathscr{L}-(n-1)}\mathcal{P}^{DD}_{\ell,\ell+n-1} = \sum_{\ell=1}^{\mathscr{L}-(n-1)}\;[\text{diagram}]_{\ell,\,\widetilde{\ell+n-1}}\;. \tag{60b}$$

We used the first and second relations in Eq. (35) to combine the $\sum_\ell$ sums and cancel the remaining terms. Diagrammatically, Eq. (60b) also follows directly from (60a), using a relation analogous to (22c) (with $n-2$ additional unit operator lines in the middle). Its form is very natural: $n-2$ unit operators are sandwiched between two DS, which project out contributions contained in n'-site projectors with $n' < n$. For future reference we also display the $n = 2$ projector

$$\mathcal{P}^{2\perp} = \sum_{\ell=1}^{\mathscr{L}-1}\mathcal{P}^{DD}_{\ell,\ell+1} = \sum_{\ell=1}^{\mathscr{L}-1}\;[\text{diagram}]_\ell\;. \tag{61}$$

This projector is implicitly used in Ref. [6] to compute the 2s variance, as will be recapitulated below. It also plays a key role in controlled bond expansion algorithms recently developed by us for performing DMRG ground-state searches [29] and TDVP time evolution [30] with 2s accuracy at 1s costs.

Equations (58) to (61), giving explicit formulas for $\mathcal{P}^{n\perp}$ for all n, are the main results of the last three sections.

The orthonormality of the $\mathcal{P}^{n\perp}$, guaranteed by construction, relies on gauge invariance. This is seen when verifying orthonormality explicitly. For example, $\mathcal{P}^{1\perp}\mathcal{P}^{0\perp} = 0$ can be shown in two ways, using either $\mathcal{P}^{DK}_{\ell,\ell+1}\mathcal{P}^{KK}_{\mathscr{L},\mathscr{L}+1} = 0$ or $\mathcal{P}^{KD}_{\ell-1,\ell}\mathcal{P}^{KK}_{0,1} = 0$ (both relations hold $\forall\ell \in [1,\mathscr{L}]$).

We continue with some remarks providing intuition about the structure of states in the image of $\mathcal{P}^{n\perp}$. The basis states for the spaces $\mathbb{V}^{n\perp}$ can be chosen such that they involve wavefunctions of the following forms:

$$\mathbb{V}^{0\perp}: \quad [\text{diagram}] \quad (\ell\in[0,\mathscr{L}]), \tag{62a}$$

$$\mathbb{V}^{1\perp}: \quad [\text{diagram}]_\ell \quad (\ell\in[1,\mathscr{L}]), \tag{62b}$$

$$\quad\quad [\text{diagram}]_\ell \quad (\ell\in[1,\mathscr{L}]), \tag{62c}$$

$$\mathbb{V}^{2\perp}: \quad [\text{diagram}]_\ell \quad (\ell\in[1,\mathscr{L}-1]), \tag{62d}$$

$$\mathbb{V}^{(n>2)\perp}: \quad [\text{diagram}]_{\ell,\,\widetilde{\ell+n-1}} \quad (\ell\in[1,\mathscr{L}-n+1]). \tag{62e}$$

Due to MPS gauge invariance, any choice of ℓ in Eq. (62a) for $\mathbb{V}^{0\perp}$ yields the *same* wavefunction Ψ. Gauge invariance also implies that the wavefunctions in Eqs. (62b) and (62c) for $\mathbb{V}^{1\perp}$ are not all independent; nevertheless, both forms are useful.

To explicitly construct a complete basis on $\mathbb{V}^{1\perp}$, we can for instance use the form Eq. (62b) and construct a complete set of mutually orthonormal bond matrices of dimension $\overline{D}^A_\ell \times D_\ell$ for every bond ℓ. ($\overline{D}^{A,B}_\ell$ are defined near the beginning of Sec. II D.) Note that we could have as well used the form Eq. (62c). Using this construction, we can also explicitly determine the dimension of $\mathbb{V}^{1\perp}$, $\dim\mathbb{V}^{1\perp} = \sum_{\ell=1}^{\mathscr{L}}\overline{D}^A_\ell D_\ell$. In the same way, a complete basis with states of the form Eq. (62d) for $\mathbb{V}^{2\perp}$ can be constructed by constructing a complete set of mutually orthonormal $\overline{D}^A_\ell \times \overline{D}^B_{\ell+1}$ bond matrices for every bond ℓ. Thus, we find $\dim\mathbb{V}^{2\perp} = \sum_{\ell=1}^{\mathscr{L}-1}\overline{D}^A_\ell \overline{D}^B_{\ell+1}$. A complete basis for $\mathbb{V}^{(n>2)\perp}$ may be characterized by finding, for every $\ell < \mathscr{L} - n + 1$, a complete set of mutually

orthogonal $(n-2)$-site MPS, which connect $\overline{A}_\ell$ and $\overline{B}_{\ell+n-1}$ in Eq. (62e). There are $\overline{D}_\ell^A d^{n-2} \overline{D}_{\ell+n-1}^B$ such MPSs for every ℓ, i.e., dim $\mathbb{V}^{(n>2)\perp} = \sum_{\ell=1}^{\mathscr{L}-n+1} \overline{D}_\ell^A d^{n-2} \overline{D}_{\ell+n-1}^B$.

The basis states for $\mathbb{V}^{(n>0)\perp}$ differ from the reference state $|\Psi\rangle$ in $\mathbb{V}^{0\perp}$ through the replacement of a kept by a discarded space involving precisely one site for $n=1$, and two adjacent sites for $n=2$. For $n>2$, they differ by two discarded spaces and $n-2$ contiguous sites sandwiched between them, involving virtual bond spaces orthogonal to those from $|\Psi\rangle$. Therefore, states from $\mathbb{V}^{n\perp}$ and $\mathbb{V}^{n'\perp}$ are manifestly mutually orthogonal if $n \neq n'$. This can be checked via Eqs. (24), e.g., for $\mathbb{V}^{0\perp}$ and $\mathbb{V}^{1\perp}$:

$$\text{(diagram)} = 0, \quad \text{(diagram)} = 0. \quad (63)$$

States of the form (62) yield a complete basis for $\mathbb{V}$. This is ensured by our Gram-Schmidt construction; but for $\mathcal{P}^{1\perp}$, the completeness is not self-evident. For example, consider a state $|\Psi'\rangle$ of the following form:

$$\Psi' = \text{(diagram)} , \quad \Psi = \text{(diagram)} , \quad (64)$$

$$\langle \Psi | \Psi' \rangle = \text{(diagram)} = \text{(diagram)} = 0 .$$

It differs from $|\Psi\rangle$ only in the κ space of bond of ℓ', having a bond matrix $\Lambda'_{\ell'}$ orthogonal to the $\Lambda_{\ell'}$ of $|\Psi\rangle$. Since $|\Psi'\rangle$ is orthogonal to $|\Psi\rangle$ it does not lie in $\mathbb{V}^{0\perp}$, but it is not immediately apparent that it lies in im($\mathcal{P}^{1\perp}$). To see that it does, we rewrite Eq. (59b) such that it contains DKs to the left of site ℓ and KDs to its right, using Eq. (42) (with $\bar{\ell}, \ell'$ there replaced by $\ell'+1, \mathscr{L}$),

$$\mathcal{P}^{1\perp} = \sum_{\ell=1}^{\ell'-1} \mathcal{P}_{\ell,\ell+1}^{\text{DK}} + \mathcal{P}_{\ell'}^{1s} + \sum_{\ell=\ell'+1}^{\mathscr{L}} \mathcal{P}_{\ell-1,\ell}^{\text{KD}} - \mathcal{P}_{\mathscr{L},\mathscr{L}+1}^{\text{KK}}. \quad (65)$$

When evaluating $\mathcal{P}^{1\perp}|\Psi'\rangle$ using this form, and recalling that $\mathcal{P}_{\mathscr{L},\mathscr{L}+1}^{\text{KK}} = |\Psi\rangle\langle\Psi|$, we find that all terms but the second yield zero, and the second yields $|\Psi'\rangle$, as claimed above. In this manner, one sees that the image of $\mathcal{P}^{1\perp}$ indeed contains all single-site and single-bond variations of $|\Psi\rangle$ that are orthogonal to $|\Psi\rangle$.

To conclude this section, we remark that the nested structure of $\mathbb{V}$ is an integral part for (thermo)dynamical computations using the NRG [16,17,24], although a slightly different structure from $\mathcal{P}^{n\perp}$ is used to systematically span the full Hilbert space. While the chain considered in NRG is in principle semi-infinite, this chain is in practice cut off naturally by thermal weights [17,24]. The resulting chain length $\mathscr{L}$ increases logarithmically with decreasing temperature. In NRG, the so-called Anders-Schiller basis [26] is routinely used, which decomposes the full identity as follows:

$$\mathbb{1}_{\mathbb{V}} = \sum_{\ell=1}^{\mathscr{L}} \text{(diagram)} . \quad (66)$$

Here, all states of the parent space associated with the last site $\mathscr{L}$ are considered discarded, i.e., the kept space of site $\mathscr{L}$ has dimension 0. The projectors occurring in Eq. (66) are constructed from approximate eigenstates of the Hamiltonian,

so that this decomposition of unity can be used, e.g., to explicitly construct time-evolution operators [26], full thermal density matrices [17,24], or evaluate Lehmann representations for two-point [17] or recently even multipoint [27,31] spectral functions.

IV. ENERGY VARIANCE

The decomposition of the identity $\mathbb{1}_{\mathbb{V}}$ into mutually orthogonal n-site projections can be used to similarly split the energy variance, $\Delta_E = \|(H-E)\Psi\|^2$, of a state with average energy $E = \langle\Psi|H|\Psi\rangle$ into n-site contributions. For $n=1$ and 2, these were given in Ref. [6]. Here, we extend their analysis to general n,

$$\Delta_E = \sum_{n=0}^{\mathscr{L}} \langle\Psi|(H-E)\mathcal{P}^{n\perp}(H-E)|\Psi\rangle = \sum_{n=1}^{\mathscr{L}} \Delta_E^{n\perp}, \quad (67a)$$

$$\Delta_E^{n\perp} = \|\mathcal{P}^{n\perp} H\Psi\|^2 \quad (67b)$$

$$= \begin{cases} \sum_{\ell=1}^{\mathscr{L}} \|\mathcal{P}_{\ell,\ell+1}^{\text{DK}} H\Psi\|^2 & (n=1), \\ \sum_{\ell=1}^{\mathscr{L}+1-n} \|\mathcal{P}_{\ell,\ell+n-1}^{\text{DD}} H\Psi\|^2 & (n \geqslant 2). \end{cases} \quad (67c)$$

In the first line, we used (56), $\mathbb{1}_{\mathbb{V}} = \sum_{n=0}^{\mathscr{L}} \mathcal{P}^{n\perp}$; since $\mathcal{P}^{0\perp} = |\Psi\rangle\langle\Psi|$ and $\mathcal{P}^{(n>0)\perp}|\Psi\rangle = 0$, the potentially large contributions linear and quadratic in E drop out. This convenient feature, emphasized in Ref. [6], significantly improves the accuracy of the determination of Δ_E. The cumulative ns variance is defined as $\Delta_E^{ns} = \sum_{n'=1}^{n} \Delta_E^{n'\perp}$.

Expressed diagrammatically, the 1s and ns variance are

$$\Delta_E^{1\perp} = \sum_{\ell=1}^{\mathscr{L}} \left\| \text{(diagram)} \right\|^2 = \sum_{\ell=1}^{\mathscr{L}} \left\| \text{(diagram)} \right\|^2, \quad (68a)$$

$$\Delta_E^{(n\geq2)\perp} = \sum_{\ell=1}^{\mathscr{L}-(n-1)} \left\| \text{(diagram)} \right\|^2 . \quad (68b)$$

The second equality in Eq. (68a) follows from Eq. (20). To compute these expressions in practice, the D projectors are expressed through κ projectors using Eq. (21), e.g.,

$$\Delta_E^{1\perp} = \sum_{\ell=1}^{\mathscr{L}} \left\| \text{(diagram)} - \text{(diagram)} \right\|^2 . \quad (69)$$

If the Hamiltonian contains only local and nearest-neighbor terms, all contributions with $n>2$ are zero [6], i.e., $\Delta_E = \Delta_E^{2s}$. However, it has been argued in Ref. [6] that even if long-range terms are present, Δ_E^{2s} is a reliable error measure. Here, we confirm this for the case of the spin-$\frac{1}{2}$ Haldane-Shastry model on a ring of length $\mathscr{L} = 40$, with Hamiltonian

$$\mathcal{H}_{\text{HS}} = \sum_{\ell<\ell'\leqslant\mathscr{L}} \frac{\pi^2 \mathbf{S}_\ell \cdot \mathbf{S}_{\ell'}}{\mathscr{L}^2 \sin^2 \frac{\pi}{\mathscr{L}}(\ell-\ell')} . \quad (70)$$

Figure 1 shows $\Delta_E^{n\perp}$ for $n \in \{1, 2, \ldots, 10\}$ and four choices of D^*. In all cases, $\Delta_E^{n\perp}$ is largest for $n=2$, and smaller by an order magnitude or more for $n>2$, with the decrease being stronger the larger D^*. For this model, therefore, $\Delta_E^{2\perp}$ by itself suffices to reliably estimate the energy error.

FIG. 1. The n-site variance $\Delta_E^{n\perp}$ of the $\mathscr{L} = 40$ Haldane-Shastry model for different D^*. $\Delta_E^{1\perp}$ can in principle always be converged to numerically zero (i.e., $\Delta_E^{1\perp} \lesssim 10^{-16}$) by extensive DMRG sweeping; this being the case here, we plot it symbolically at $\Delta_E^{1\perp} = 10^{-16}$. In practice it suffices to sweep until $\Delta_E^{1\perp} \ll \Delta_E^{2\perp}$, since the variance is dominated by $\Delta_E^{2\perp}$.

V. n-SITE EXCITATIONS

The ns projectors can be used as an Ansatz to compute low energy excitations. This so-called excitation Ansatz has been very successful in infinite systems [14,22,28,32,33] and lately also shown to be reliable on finite lattices [34]. Using our diagrammatic notation, we generalize the 1s Ansatz for finite systems used in Ref. [34] to n sites, similar to the ns Ansatz for infinite systems [22,28].

We seek an ns excitation Ansatz satisfying the condition $\mathcal{P}^{ns}|\Psi_{\text{ex}}^{ns}\rangle = |\Psi_{\text{ex}}^{ns}\rangle$. Let us choose $\ell' = \mathscr{L} - n + 1$ in Eq. (50), such that $\mathcal{P}^{ns} = \sum_{\ell=1}^{\mathscr{L}-n} \mathcal{P}_{\ell<}^{ns} + \mathcal{P}_{\ell'}^{ns}$. Then, the following Ansatz has the desired property:

$$|\Psi_{\text{ex}}^{ns}\rangle = \sum_{\ell=1}^{\mathscr{L}-n} \underbrace{\quad}_{\ell} \overbrace{\quad}^{T_1^\ell \quad T_n^\ell}_{\ell+n-1} + \underbrace{\quad}_{\ell} \overbrace{\quad}^{T_1^{\ell'} \quad T_n^{\ell'}}_{\ell'=\mathscr{L}-n+1}$$

$$= \sum_{\ell=1}^{\mathscr{L}-n+1} \underbrace{\quad}_{\ell} \overbrace{\quad}^{T_1^\ell \quad T_n^\ell}_{\ell+n-1} . \tag{71}$$

Here, $T_{i>1}^\ell$ ($\curlyvee$) are generic tensors of rank 3 and

$$T_1^\ell = \begin{cases} \text{\scriptsize $\blacktriangledown$} & \ell < \ell', \\ \text{\scriptsize $\curlyvee$} & \ell = \ell', \end{cases} \qquad \ell' = \mathscr{L} - n + 1 . \tag{72}$$

The two forms of T_1^ℓ reflect the presence or absence of a ᴅ projection associated with $\mathcal{P}_{\ell<}^{ns}$ or $\mathcal{P}_{\ell'}^{ns}$, respectively.

It seems that $|\Psi_{\text{ex}}^{ns}\rangle$ cannot be efficiently computed, since it involves a sum over $\mathscr{L} - n + 1$ (i.e., many!) terms, and performing MPS sums explicitly leads to increased bond dimensions. However, that can be avoided here. The isometries A_ℓ ($\triangledown$) and B_ℓ ($\triangledown$) flanking the modified sites reappear in every summand and only need to be saved once; hence, only the tensors T_i^ℓ need to be saved. In the case of $n = 1$ for example, we have to save $\mathscr{L}$ tensors of dimensions $D \times d \times D$, i.e., the same memory requirement as for an MPS with bond dimension D.

Moreover, Eq. (72) ensures that all summands are by construction mutually orthogonal, facilitating the computation of overlaps. Consider $|\Psi_{\text{ex}}^{ns}\rangle$ and $|\Psi_{\text{ex}}'^{ns}\rangle$, characterized by T_i^ℓ and $T_i'^\ell$, respectively. Due to Eq. (72), their overlap involves only $\mathscr{L} - n + 1$ terms (not that number squared), namely

$$\langle \Psi_{\text{ex}}'^{ns} | \Psi_{\text{ex}}^{ns} \rangle = \sum_{\ell=1}^{\mathscr{L}-n+1} \begin{array}{c} T_1^\ell \quad T_n^\ell \\ \hline T_1'^\ell \quad T_n'^\ell \end{array}, \tag{73}$$

while the computation of sums or differences can be done on the level of the T_i^ℓ, i.e.,

$$|\Psi_{\text{ex}}^{ns}\rangle + a|\Psi_{\text{ex}}'^{ns}\rangle \rightarrow \forall \ell : \underbrace{\overset{T_1^\ell \ T_n^\ell}{\quad}}_{\ell \quad \widehat{\ell+n-1}} + a \underbrace{\overset{T_1'^\ell \ T_n'^\ell}{\quad}}_{\ell \quad \widehat{\ell+n-1}} . \tag{74}$$

If $\prod_{i=1}^n T_i^\ell$ and $\prod_{i=1}^n T_i'^\ell$ are represented as MPSs, Eq. (74) in effect involves a sum of two ns MPS; this is manageable if n is not too large. In the case $n = 1$, there is only T_1^ℓ and $T_1'^\ell$, i.e. in this case, no MPS sums are required.

A further benefit of Eq. (72) is that it serves to fix the MPS gauge degree of freedom on the site hosting T_ℓ^1, improving numerical stability.

To determine the tensors T_i^ℓ for $|\Psi_{\text{ex}}^{ns}\rangle$ explicitly, one projects the Hamiltonian onto the space $\overline{\mathbb{V}}^{ns}$ and solves for low-energy states of

$$\mathcal{P}_{\text{ex}}^{ns} H \mathcal{P}_{\text{ex}}^{ns} |\Psi_{\text{ex}}^{ns}\rangle = E_{\text{ex}}^{ns} |\Psi_{\text{ex}}^{ns}\rangle \tag{75}$$

that are orthogonal to the ground state. This can be done using some iterative eigensolver like the Lanczos method, initialized by some appropriate initial wavefunction. Explicit orthogonalization with respect to to the ground state is required, since our Ansatz space $\mathcal{P}^{ns}$ contains the ground state, whose kept and discarded spaces span the image of $\mathcal{P}^{ns}$.

To run an iterative eigensolver, a scheme is needed for efficiently applying the projected Hamiltonian $\mathcal{P}^{ns} H \mathcal{P}^{ns}$ to the state $|\Psi_{\text{ex}}^{ns}\rangle$. The resulting state, say $|\overline{\Psi}_{\text{ex}}^{ns}\rangle = \mathcal{P}^{ns} H \mathcal{P}^{ns} |\Psi_{\text{ex}}^{ns}\rangle$, will again be of the form (71), but described by tensors $\overline{T}_i^\ell$. To find these, we compute the tensors

$$\overset{\widetilde{T}_1^\ell \ \overline{T}_2^\ell \ \overline{T}_n^\ell}{\quad} = \sum_{\ell'=1}^{\mathscr{L}-n+1} \left(\begin{array}{c} T_1^{\ell'} \quad T_n^{\ell'} \\ \hline 1 \qquad \ell \qquad \mathscr{L} \end{array} \right), \tag{76}$$

and project $\widetilde{T}_1^\ell$ to the discarded space to obtain $\overline{T}_1^\ell$,

$$\overset{\overline{T}_1^\ell}{\text{\scriptsize $\bullet$}} = \overset{\widetilde{T}_1^\ell}{\text{\scriptsize $\curlyvee$}} - (1 - \delta_{\ell,\mathscr{L}-n+1}) \underbrace{\begin{array}{c} \widetilde{T}_1^\ell \\ A_\ell^* \\ A_\ell \end{array}}, \tag{77}$$

such that Eq. (72) is fulfilled.

To evaluate Eq. (76), we split the sum $\sum_{\ell'}$ into terms with $\ell' < \ell$ and $\ell' \geqslant \ell$, and express these as follows:

$$\overset{\widetilde{T}_1^\ell \ \overline{T}_2^\ell \ \overline{T}_n^\ell}{\quad} = \sum_{m=1}^n \underbrace{\begin{array}{c} T_{m+1}^{\ell-m} \ T_n^{\ell-m} \\ \mathcal{L}_{\ell-1}^m \qquad \overline{R}_{\ell+n} \end{array}}_{\ell}$$

$$+ \sum_{m=0}^n \underbrace{\begin{array}{c} T_1^{\ell+m} \ T_{n-m}^{\ell+m} \\ L_{\ell-1} \qquad \mathcal{R}_{\ell+n}^m \end{array}}_{\ell} . \tag{78}$$

Next to the left and right environments L_ℓ and R_ℓ defined in Eq. (18), these expressions contain another set of environments, denoted by $\mathcal{L}_\ell^m$ and $\mathcal{R}_\ell^m$, each involving those m of the $T_i^{\ell'}$ tensors in Eq. (76) that do not face open physical legs. For $m = 0$, $m \in \{1, \ldots, n-1\}$ or $m = n$, they are defined by the left equalities below; the right equalities show how for each m, $\mathcal{L}_{\ell+1}^m$ and $\mathcal{R}_{\ell-1}^m$ can be computed recursively from $\mathcal{L}_\ell^m$ and $\mathcal{R}_\ell^m$, initialized with $\mathcal{L}_0^0 = 1$, $\mathcal{L}_0^{m>0} = 0$, $\mathcal{R}_{\mathscr{L}+1}^0 = 1$, $\mathcal{R}_{\mathscr{L}+1}^{m>0} = 0$:

$$\mathcal{L}_\ell^0 = \ \vcenter{\hbox{[diagram]}} \ , \qquad (79a)$$

$$\mathcal{L}_\ell^m = \ \vcenter{\hbox{[diagram]}} \ ,$$

$$\mathcal{L}_\ell^n = \ \vcenter{\hbox{[diagram]}} \ ,$$

$$\mathcal{R}_\ell^0 = \ \vcenter{\hbox{[diagram]}} \ , \qquad (79b)$$

$$\mathcal{R}_\ell^m = \ \vcenter{\hbox{[diagram]}} \ ,$$

$$\mathcal{R}_\ell^n = \ \vcenter{\hbox{[diagram]}} \ .$$

The solution of Eq. (75) using an iterative eigensolver has costs scaling with $\mathcal{O}(D^3 d^n w)$, the same as ns DMRG. However, because the Ansatz Eq. (71) is built from a sum over $\mathscr{L} - n + 1$ MPSs, states can be captured, which would need significantly larger bond dimensions if represented in standard fashion as an MPS. Because there are n summands in Eq. (71), which differ from the ground state at site ℓ (with corresponding tensors $T_1^\ell, \ldots, T_n^{\ell-n+1}$ at site ℓ), an MPS representation would need bond dimension $D(1 + n)$, assuming A_ℓ, B_ℓ, and T_i^ℓ are tensors of dimension $D \times d \times D$. Optimizing such an MPS with ns DMRG comes with $\mathcal{O}(D^3(n+1)^3 d^n w)$ costs, larger by $(n + 1)^3$ than the costs for optimizing the Ansatz Eq. (71). Of course, the latter Ansatz is much more restrictive than a generic MPS of bond dimension $D(1 + n)$. However, that should not be a limitation if the physics of interest involves single- or few-particle excitations, as is the case, e.g., when computing correlations functions of single- or few-particle operators.

We test the ns excitation Ansatz on a Haldane-Shastry model on a ring of length $\mathscr{L} = 40$ [see Eq. (70) for the Hamiltonian], for which we seek to compute the lowest energy excitation with total spin $S = 1$ above the total spin $S = 0$ ground state. For comparison, we have also computed this state by performing a DMRG ground-state search in the $S = 1$ sector.
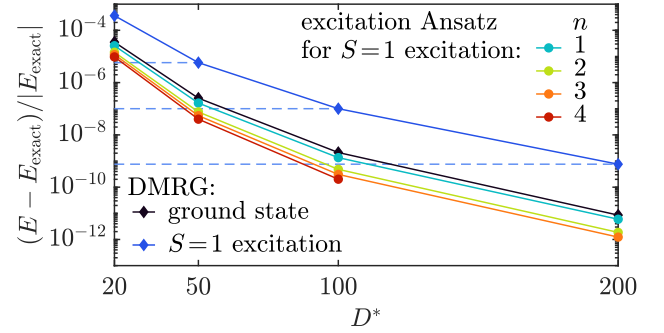
FIG. 2. Relative error in energy of the lowest-lying $S = 1$ excited state of the Haldane-Shastry model, computed using the n-site excitation Ansatz (circles), or using DMRG (blue diamonds). Black diamonds show DMRG results for the $S = 0$ ground state. The dashed-blue lines are guides to the eye.

Figure 2 shows the corresponding relative errors in energy versus the bond dimension D^*. As reference values, we use the exact energies $E_{\text{exact}}^{S=0} = -\pi^2(\mathscr{L} + 5/\mathscr{L})/24$ and $E_{\text{exact}}^{S=1} = -\pi^2(\mathscr{L} - 7/\mathscr{L})/24$ for the ground state and excited state [35–37], respectively. Remarkably, we find that for the same D^*, the $n = 1$ site excitation Ansatz yields an $S = 1$ excitation energy that is more accurate than that obtained from DMRG by one to two orders of magnitude, even though the computational cost of both approaches at the same D^* is comparable. In fact, the relative error obtained by the excitation Ansatz for the $S = 1$ state is comparable to (even slightly lower than) that obtained by DMRG for the $S = 0$ ground state.

The reason for the high accuracy of the excitation Ansatz is that the first excited state of the Haldane-Shastry model is essentially a superposition of local spin excitations, i.e., it fits Ansatz (71). The excitation Ansatz avoids representing this superposition as a single MPS, which would require about twice the bond dimension. Instead, it exploits the fact that each local excitation differs from the ground state only locally. This leads to a more economic Ansatz compared to DMRG, which needs about twice the bond dimension. This can also be seen in Fig. 2, where the relative error in energy of the 1s excitation Ansatz at some D^* almost coincides with the corresponding error of DMRG at $2D^*$. The latter error is slightly smaller than the former, because the $2D^*$ MPS Ansatz used by DMRG is less restrictive than the D^* excitation Ansatz, though this improvement is rather marginal.

The capability of the excitation Ansatz can be further improved by considering $n > 1$, leading to a reduction of the relative error in energy compared to $n = 1$, see Fig. 2. This reduction is rather small and further improvements seem to become ever smaller for ever larger n. However, with increasing n the costs for this Ansatz increase exponentially, as $\sim d^n$. Therefore, including information beyond $n = 1$ by brute force, i.e., by just going to $n > 1$, is not advisable. Nevertheless, we believe that valuable improvements of the Ansatz may be achievable, while circumventing the exponential d^n scaling, by including only those parts of the $n > 1$ sectors that contribute to the excited state with significant weight. It should be possible to identify these parts by generalizing the strategy proposed in our recent work on controlled bond

expansion in both DMRG ground-state search [29] and TDVP time evolution [30]. We leave this as a topic for future study.

More generally, we believe that the diagrammatics for the n-site excitation Ansatz and the projector formalism developed in this work will provide a solid foundation to construct systematic improvements to the 1-site excitation Ansatz without a significant increase in computational costs.

We conclude this section by noting that the above construction will not be able to find states that differ from a given ground state on an extensive number of sites. In particular, if the ground-state sector has a degeneracy, e.g., due to symmetry breaking or topological order, the excitation Ansatz on top of one of the ground states is not expected to reliably find the other ground states. Further, while the excitation Ansatz Eq. (71) can in principle be used for excitations at any energy, it is expected to perform less reliable the higher the energy of the excitation. Examples, where the Ansatz Eq. (71) should have problems, are excitations of multiple independent particles (i.e., the particles may be located far apart from each other) or excited states with a volume-law entanglement entropy.

VI. SUMMARY AND OUTLOOK

We have developed a projector formalism for kept and discarded spaces of MPS, together with a convenient diagrammatic notation. We use it to derive explicit expressions for global n-site projectors $\mathcal{P}^{n\mathrm{s}}$ and irreducible n-site projectors $\mathcal{P}^{n\perp}$. We then use our results to derive explicit formulas for the n-site variance and evaluate it for the Haldane-Shastry model, showing that indeed the 2-site contribution is the most dominant one. Further, we derive explicit diagrammatic formulas to perform excited state computations based on the n-site excitation Ansatz for finite, nontranslation invariant MPS.

The κ, ᴅ projector formalism and diagrammatic notation developed here proved very convenient for the applications considered in this paper. More generally, we expect them to provide a convenient tool for the development of new MPS algorithms that explicitly or implicitly utilize the properties of discarded spaces. The information contained in these is a *resource*, useful for describing changes or variations of a given MPS, and for algorithms exploiting this resource, the κ, ᴅ projector formalism facilitates book-keeping thereof. Indeed, we have developed the formalism presented here while working out a controlled bond expansion algorithm to perform both DMRG ground-state searches [29] and time evolutions using the time-dependent variational principle [30] with 2-site accuracy at 1-site computational cost. Moreover, our formalism provides the tools needed to efficiently implement the perspectives outlined in Refs. [14,22] for post-MPS applications, that build on a given MPS to compute low-energy excitation spectra.

As a final remark, we note that though we focused on MPSs in this paper, our formalism should be generalizable to any tensor network for which canonical forms are available, such as tensor networks without loops.

ACKNOWLEDGMENTS

[1] S. R. White, Density Matrix Formulation for Quantum Renormalization Groups, Phys. Rev. Lett. **69**, 2863 (1992).

[2] S. R. White, Density-matrix algorithms for quantum renormalization groups, Phys. Rev. B **48**, 10345 (1993).

[3] A. J. Daley, C. Kollath, U. Schollwöck, and G. Vidal, Time-dependent density-matrix renormalization-group using adaptive effective Hilbert spaces, J. Stat. Mech. (2004) P04005.

[4] S. R. White, Density matrix renormalization group algorithms with a single center site, Phys. Rev. B **72**, 180403(R) (2005).

[5] C. Hubig, I. P. McCulloch, U. Schollwöck, and F. A. Wolf, Strictly single-site DMRG algorithm with subspace expansion, Phys. Rev. B **91**, 155115 (2015).

[6] C. Hubig, J. Haegeman, and U. Schollwöck, Error estimates for extrapolations with matrix-product states, Phys. Rev. B **97**, 045125 (2018).

[7] G. Vidal, Efficient Classical Simulation of Slightly Entangled Quantum Computations, Phys. Rev. Lett. **91**, 147902 (2003).

[8] G. Vidal, Efficient Simulation of One-Dimensional Quantum Many-Body Systems, Phys. Rev. Lett. **93**, 040502 (2004).

[9] G. Vidal, Classical Simulation of Infinite-Size Quantum Lattice Systems in One Spatial Dimension, Phys. Rev. Lett. **98**, 070201 (2007).

[10] J. Haegeman, J. I. Cirac, T. J. Osborne, I. Pižorn, H. Verschelde, and F. Verstraete, Time-Dependent Variational Principle for Quantum Lattices, Phys. Rev. Lett. **107**, 070601 (2011).

[11] C. Lubich, I. V. Oseledets, and B. Vandereycken, Time integration of tensor trains, SIAM J. Numer. Anal. **53**, 917 (2015).

[12] J. Haegeman, C. Lubich, I. Oseledets, B. Vandereycken, and F. Verstraete, Unifying time evolution and optimization with matrix product states, Phys. Rev. B **94**, 165116 (2016).

[13] V. Zauner-Stauber, L. Vanderstraeten, M. T. Fishman, F. Verstraete, and J. Haegeman, Variational optimization algorithms for uniform matrix product states, Phys. Rev. B **97**, 045145 (2018).

[14] L. Vanderstraeten, J. Haegeman, and F. Verstraete, Tangent-space methods for uniform matrix product states, SciPost Phys. Lect. Notes **7** (2019).

[15] K. G. Wilson, The renormalization group: Critical phenomena and the Kondo problem, Rev. Mod. Phys. **47**, 773 (1975).

[16] R. Peters, T. Pruschke, and F. B. Anders, Numerical renormalization group approach to Green's functions for quantum impurity models, Phys. Rev. B **74**, 245114 (2006).

[17] A. Weichselbaum and J. von Delft, Sum-Rule Conserving Spectral Functions from the Numerical Renormalization Group, Phys. Rev. Lett. **99**, 076402 (2007).

[18] K. A. Hallberg, Density-matrix algorithm for the calculation of dynamical properties of low-dimensional systems, Phys. Rev. B **52**, 9827(R) (1995).

[19] T. D. Kühner and S. R. White, Dynamical correlation functions using the density matrix renormalization group, Phys. Rev. B **60**, 335 (1999).

[20] E. Jeckelmann, Dynamical density-matrix renormalization-group method, Phys. Rev. B **66**, 045114 (2002).

[21] A. Holzner, A. Weichselbaum, I. P. McCulloch, U. Schollwöck, and J. von Delft, Chebyshev matrix product state approach for spectral functions, Phys. Rev. B **83**, 195115 (2011).

[22] J. Haegeman, T. J. Osborne, and F. Verstraete, Post-matrix product state methods: To tangent space and beyond, Phys. Rev. B **88**, 075133 (2013).

[23] U. Schollwöck, The density-matrix renormalization group in the age of matrix product states, Ann. Phys. **326**, 96 (2011).

[24] A. Weichselbaum, Tensor networks and the numerical renormalization group, Phys. Rev. B **86**, 245124 (2012).

[25] S. Paeckel, T. Köhler, A. Swoboda, S. R. Manmana, U. Schollwöck, and C. Hubig, Time-evolution methods for matrix-product states, Ann. Phys. **411**, 167998 (2019).

[26] F. B. Anders and A. Schiller, Real-Time Dynamics in Quantum-Impurity Systems: A Time-Dependent Numerical Renormalization-Group Approach, Phys. Rev. Lett. **95**, 196801 (2005).

[27] Seung-Sup B. Lee, F. B. Kugler, and J. von Delft, Computing Local Multipoint Correlators Using the Numerical Renormalization Group, Phys. Rev. X **11**, 041007 (2021).

[28] J. Haegeman, S. Michalakis, B. Nachtergaele, T. J. Osborne, N. Schuch, and F. Verstraete, Elementary Excitations in Gapped Quantum Spin Systems, Phys. Rev. Lett. **111**, 080401 (2013).

[29] A. Gleis, J.-W. Li, and J. von Delft, Controlled bond expansion for DMRG ground state search at single-site costs, arXiv:2207.14712.

[30] J.-W. Li, A. Gleis, and J. von Delft, Time-dependent variational principle with controlled bond expansion for matrix product states, arXiv:2208.10972.

[31] F. B. Kugler, Seung-Sup B. Lee, and J. von Delft, Multipoint Correlation Functions: Spectral Representation and Numerical Evaluation, Phys. Rev. X **11**, 041006 (2021).

[32] J. Haegeman, B. Pirvu, D. J. Weir, J. I. Cirac, T. J. Osborne, H. Verschelde, and F. Verstraete, Variational matrix product ansatz for dispersion relations, Phys. Rev. B **85**, 100408(R) (2012).

[33] W.-L. Tu, H.-K. Wu, N. Schuch, N. Kawashima, and J.-Y. Chen, Generating function for tensor network diagrammatic summation, Phys. Rev. B **103**, 205155 (2021).

[34] M. Van Damme, R. Vanhove, J. Haegeman, F. Verstraete, and L. Vanderstraeten, Efficient matrix product state methods for extracting spectral information on rings and cylinders, Phys. Rev. B **104**, 115142 (2021).

[35] T. Yamamoto, Y. Saiga, M. Arikawa, and Y. Kuramoto, Exact Dynamical Structure Factor of the Degenerate Haldane-Shastry Model, Phys. Rev. Lett. **84**, 1308 (2000).

[36] T. Yamamoto, Y. Saiga, M. Arikawa, and Y. Kuramoto, Exact dynamics of the SU(K) Haldane-Shastry model, J. Phys. Soc. Jpn. **69**, 900 (2000).

[37] Y.-H. Wu, L. Wang, and H.-H. Tu, Tensor Network Representations of Parton Wave Functions, Phys. Rev. Lett. **124**, 246401 (2020).

[38] A. Weichselbaum, Non-abelian symmetries in tensor networks: A quantum symmetry space approach, Ann. Phys. **327**, 2972 (2012).

[39] A. Weichselbaum, X-symbols for non-Abelian symmetries in tensor networks, Phys. Rev. Res. **2**, 023385 (2020).

2.5 Controlled bond expansion

2.5.1 Overview

Even though the 2-site update for DMRG or TDVP is more expensive than the 1-site update, the former is almost always preferred over the latter due to its superior convergence properties (c.f. also Secs. 2.3.2 and 2.3.3). In Ref. [P2], we develop a controlled bond expansion (CBE) scheme that mirrors the properties of the 2-site update, though at a computational cost that is only slightly larger than that of a 1-site update. We achieve this by locally expanding the tangent space (2.52) by a small number of directions orthogonal to it. Since the number of added directions is small, the increase in computational cost is only marginal.

In Ref. [P2], we use CBE in the context of DMRG and thoroughly benchmark CBE–DMRG on several models, ranging from free fermions on a chain to a doped Hubbard model on a width 6 cylinder. As an interesting application, we use CBE–DMRG on a Kondo-Heisenberg model on a width 4 cylinder and show that this model has two phases that differ in their FS volumes. We therefore expect a KB–QCP which separates these two phases. A thorough investigation especially of the small FS RKKY phase and the QCP is left as a promising direction for future work.

In Ref. [P3], we then apply CBE to TDVP. CBE–TDVP is benchmarked and tested in multiple applications, ranging from a simple domain wall in an XY model to the challenging application of adiabatic spinon pumping through a chiral spin liquid.

P2 *Controlled Bond Expansion for Density Matrix Renormalization Group Ground State Search at Single-Site Costs*
Andreas Gleis, Jheng-Wei Li, and Jan von Delft
Phys. Rev. Lett. **130**, 246402 (2023)
DOI: 10.1103/PhysRevLett.130.246402
© 2023 American Physical Society
reprinted on pages pages 53–60
supplemental material reprinted on pages pages 61–71

P3 *Time-dependent variational principle with controlled bond expansion for matrix product states*
Andreas Gleis, Jheng-Wei Li, and Jan von Delft
© 2022 The Authors
arXiv:2208.10972
reproduced on pages pages 72–81

Controlled Bond Expansion for Density Matrix Renormalization Group Ground State Search at Single-Site Costs

Andreas Gleis, Jheng-Wei Li, and Jan von Delft
Arnold Sommerfeld Center for Theoretical Physics, Center for NanoScience,
and Munich Center for Quantum Science and Technology, Ludwig-Maximilians-Universität München,
80333 Munich, Germany

DMRG ground state search algorithms employing symmetries must be able to expand virtual bond spaces by adding or changing symmetry sectors if these lower the energy. Traditional single-site DMRG does not allow bond expansion; two-site DMRG does, but at much higher computational costs. We present a controlled bond expansion (CBE) algorithm that yields two-site accuracy and convergence per sweep, at single-site costs. Given a matrix product state Ψ defining a variational space, CBE identifies parts of the orthogonal space carrying significant weight in $H\Psi$ and expands bonds to include only these. CBE-DMRG uses no mixing parameters and is fully variational. Using CBE-DMRG, we show that the Kondo-Heisenberg model on a width 4 cylinder features two distinct phases differing in their Fermi surface volumes.

DOI: 10.1103/PhysRevLett.130.246402

Introduction.—A powerful tool for studying ground state properties of one- and two-dimensional quantum systems is the density martrix renormalization group (DMRG) [1–7]. Prominent two-dimensional applications include the *t-J* [8–11] and Hubbard [12–18] models, and quantum magnets [19–22]. Because of their high numerical costs, such studies are currently limited to either small finite-sized systems or cylinders with small circumference. Progress towards computationally cheaper DMRG ground state search algorithms would clearly be welcome.

In this Letter, we address this challenge. A DMRG ground state search explores a variational space spanned by matrix product states [23,24]. If symmetries are exploited, the algorithm must be able to expand the auxiliary spaces associated with virtual bonds by adjusting symmetry sectors if this lowers the energy. Traditional single-site (1*s*) DMRG, which variationally updates one site at a time, does not allow such bond expansions. As a result, it often gets stuck in metastable configurations having quantum numbers different from the actual ground state. Two-site (2*s*) DMRG naturally leads to bond expansion, but carries much higher computational costs.

Hence, schemes have been proposed for achieving bond expansions at sub-2*s* costs, such as density matrix perturbation [25] or strictly single-site DMRG (DMRG3S) [26]. However, in these schemes, the degree of subspace expansion per local update is controlled by a heuristic mixing factor. Depending on its value, some subspace expansion updates increase, rather than decrease, the energy.

Here, we present a controlled bond expansion (CBE) algorithm which lowers the energy with each step and yields 2*s* accuracy and convergence per sweep, at 1*s* costs.

Given a matrix product state Ψ defining a variational space, our key idea is to identify parts of the 2*s* orthogonal space that carry significant weight in $H\Psi$, and to include only these parts when expanding the virtual bonds of a 1*s* Hamiltonian. Remarkably, these parts can be found via a projector that can be constructed at 1*s* costs.

Using CBE–DMRG we study the Kondo–Heisenberg model on a width 4 cylinder and show that it features two phases differing in their Fermi surface volumes. We thereby further advance the understanding of this highly debated model using a controlled method.

MPS basics.—We briefly recall some standard MPS concepts [5], adopting the diagrammatic conventions of Ref. [27]. Consider an $\mathscr{L}$-site system with an open boundary MPS wave function Ψ having dimensions d for physical sites and D for virtual bonds. Ψ can be written in bond-canonical form with respect to any bond ℓ,

$$\Psi = \overset{A_1 \quad A_2 \qquad A_\ell \quad \Lambda_\ell \quad B_{\ell+1} \qquad B_{\mathscr{L}-1} \quad B_{\mathscr{L}}}{\underset{d \ D \ D \ d}{\rule{0pt}{0pt}}} . \quad (1)$$

The tensors Λ_ℓ ($\diamond$), A_ℓ ($\triangledown$) and B_ℓ ($\triangledown$) are variational parameters. They are linked by gauge relations, $A_\ell \Lambda_\ell = \Lambda_{\ell-1} B_\ell$, useful for shifting the bond tensor Λ_ℓ to neighboring bonds. A_ℓ and B_ℓ are left- and right-sided isometries, respectively, projecting Dd-dimensional *parent* (P) spaces to D-dimensional *kept* (K) image spaces [27]; they satisfy

$$A_\ell^\dagger A_\ell = \overset{A_\ell}{\underset{A_\ell^*}{\ominus}} = \big(= \mathbb{1}^{\text{K}}_\ell, \qquad B_\ell B_\ell^\dagger = \overset{B_\ell}{\underset{B_\ell^*}{\ominus}} = \big) = \mathbb{1}^{\text{K}}_{\ell-1}. \quad (2)$$

The Hamiltonian can similarly be expressed as a matrix product operator (MPO) with virtual bond dimension w,

$$H = \text{(diagram)} \quad \text{(3)}$$

For $2s$ or $1s$ DMRG, the energy of Ψ is lowered by projecting H to a local variational space associated with sites $(\ell, \ell+1)$ or ℓ, respectively, and using its ground state (GS) within that space to locally update Ψ. The effective $2s$ and $1s$ Hamiltonians can be computed recursively using

$$H_\ell^{2s} = \text{(diagram)}, \quad \text{(4a)}$$

$$H_\ell^{1s} = \text{(diagram)}. \quad \text{(4b)}$$

To perform $2s$ or $1s$ updates, one replaces $\psi_\ell^{2s} = A_\ell \Lambda_\ell B_{\ell+1}$ or $\psi_\ell^{1s} = C_\ell = A_\ell \Lambda_\ell (\text{◌})$ by the GS solutions of

$$(H_\ell^{2s} - E)\psi_\ell^{2s} = 0, \quad \text{(diagram)} = E \frac{A_\ell \, \Lambda_\ell \, B_{\ell+1}}{\text{(diagram)}}, \quad \text{(5a)}$$

$$(H_\ell^{1s} - E)\psi_\ell^{1s} = 0, \quad \text{(diagram)} = E \frac{C_\ell}{\text{(diagram)}}. \quad \text{(5b)}$$

Updating site by site, one sweeps back and forth through the MPS until the GS energy converges.

The local variational space is larger for $2s$ than $1s$ DMRG by a factor d, $\mathcal{O}(D^2 d^2)$ vs. $\mathcal{O}(D^2 d)$. This enables $2s$ DMRG to increase ("expand") the bond dimension during updates by including new states (and symmetry sectors) from the $2s$ space. $1s$ DMRG cannot do this, and hence often fails to yield accurate GS energies. The better performance of $2s$ vs $1s$ has its price: much higher numerical costs, $\mathcal{O}(D^3 d^3 + D^3 d^2 w)$ vs $\mathcal{O}(D^3 dw)$ [5].

Discarded spaces.—To track those parts of $2s$ spaces not contained in $1s$ spaces, we introduce orthogonal complements of A_ℓ and B_ℓ, denoted $\overline{A}_\ell (\text{◥})$ and $\overline{B}_\ell (\text{◤})$. These isometries have image spaces, called *discarded* (D) spaces [27], of dimension $\overline{D} = D(d-1)$, orthogonal to the kept images of A_ℓ and B_ℓ. Thus $A_\ell^{\mathbb{1}}(\text{◣}) = A_\ell \oplus \overline{A}_\ell$ and $B_\ell^{\mathbb{1}}(\text{◢}) = B_\ell \oplus \overline{B}_\ell$ are unitaries on their parent spaces, with

$$\frac{A_\ell}{D \text{◥} D} \oplus \frac{\overline{A}_\ell}{D \text{◥} \overline{D}} = \frac{A_\ell^{\mathbb{1}}}{D \text{◣} Dd}, \quad \frac{B_\ell^{\mathbb{1}}}{Dd \text{◢} D} = \frac{B_\ell}{D \text{◤} D} \oplus \frac{\overline{B}_\ell}{\overline{D} \text{◤} D}. \quad \text{(6)}$$

The unitarity conditions for $A_\ell^{\mathbb{1}}$ and $B_\ell^{\mathbb{1}}$ imply orthonormality and completeness relations complementing Eq. (2),

$$\text{(diagram)} = (= \mathbb{1}_\ell^{\text{D}}, \quad \text{(diagram)} = 0, \quad \text{(diagram)} =) = \mathbb{1}_{\ell-1}^{\text{D}}, \quad \text{(diagram)} = 0 \quad \text{(7a)}$$

$$\text{(diagram)} + \text{(diagram)} = \supset \Big|_\ell = \mathbb{1}_\ell^{\text{P}}, \quad \text{(diagram)} + \text{(diagram)} = \Big|_\ell \subset = \mathbb{1}_{\ell-1}^{\text{P}}. \quad \text{(7b)}$$

If the unitary maps $A_\ell^{\mathbb{1}\dagger}$ and $B_{\ell+1}^{\mathbb{1}\dagger}$ of Eq. (6) are applied to some of the open indices of $H_\ell^{1s}\psi_\ell^{1s}$, $H_{\ell+1}^{1s}\psi_{\ell+1}^{1s}$, and $H_\ell^{2s}\psi_\ell^{2s}$ as indicated below, they map the diagrams of Eqs. (5) to

$$H_\ell^{1s}\psi_\ell^{1s} \to \text{(diagram)} = \text{(diagram)} = \text{(diagram)} \oplus \text{(diagram)},$$

$$H_{\ell+1}^{1s}\psi_{\ell+1}^{1s} \to \text{(diagram)} = \text{(diagram)} = \text{(diagram)} \oplus \text{(diagram)},$$

$$H_\ell^{2s}\psi_\ell^{2s} \to \text{(diagram)} \oplus \text{(diagram)} \oplus \text{(diagram)} \oplus \text{(diagram)}.$$

The first three terms from the third line also appear in the first two lines, but the fourth, involving ◢◣, does not. Let DD denote the image of the orthogonal complements $\overline{A}_\ell \otimes \overline{B}_{\ell+1} (\text{◥} \otimes \text{◤})$, then DD is orthogonal to the variational space explored by $1s$ DMRG on sites $(\ell, \ell+1)$. DD is much larger than the latter, of dimension $\overline{D}^2 = D^2(d-1)^2$ vs $2D^2 d$, and (importantly) may contain new symmetry sectors. Thus DD is the $2s$ ingredient lacking in $1s$ schemes.

This can also be seen considering the energy variance $\Delta_E = \|(H - E)\Psi\|^2$. By expanding it into contributions involving orthogonal projections on one, two, or more sites [28], $\Delta_E = \Delta_E^{1\perp} + \Delta_E^{2\perp} + \cdots$, one obtains [27]

$$\Delta_E^{1\perp} = \sum_{\ell=1}^{\mathscr{L}} \left\| \text{(diagram)} \right\|^2, \quad \Delta_E^{2\perp} = \sum_{\ell=1}^{\mathscr{L}-1} \left\| \text{(diagram)} \right\|^2. \quad \text{(8)}$$

$1s$ DMRG minimizes only $\Delta_E^{1\perp}$, $2s$ minimizes $\Delta_E^{1\perp}$ *and* $\Delta_E^{2\perp}$. We thus seek to expand the K image of ◥ or ◤ at the expense of the D image of ◥ or ◤. This transfers weight from $\Delta_E^{2\perp}$ to $\Delta_E^{1\perp}$, making it accessible to $1s$ minimization.

Controlled bond expansion.—The CBE algorithm rests on two new insights, substantiated by the quality of its results. The first insight is that the subspace of DD relevant for lowering the GS energy is relatively small: it is the subspace on which $H_\ell^{2s}\psi_\ell^{2s}$ and hence $\Delta_E^{2\perp}$ have significant weight. When expanding a bond, it thus suffices to add only this small subspace (hence the moniker *controlled bond expansion*), or only part of it, to be called relevant DD (rDD) [29]. Since DD is the image of $\overline{A}_\ell \otimes \overline{B}_{\ell+1} (\text{◥} \otimes \text{◤})$,

$$\mathcal{C}_1 = \left\| \begin{matrix} w \\ \overline{D}\,\overline{D}\,\overline{D} \\ \overline{D}\,d \quad d\,\overline{D} \end{matrix} - \begin{matrix} w \\ \widetilde{D}\,\overline{D}\,\overline{D} \\ \widetilde{D}\,d \quad d\,\overline{D} \end{matrix} \right\|,$$

$$\mathcal{C}_2 \parallel$$

$$\left\| \begin{matrix} D \quad D \\ w \quad w \\ \overline{D}\,d \quad d\,\overline{D} \\ \overline{D}\,d \quad d\,\overline{D} \end{matrix} - \begin{matrix} D \quad \widehat{D} \quad D'\,D \\ d \quad w \quad w'\,d \end{matrix} \right\|, \qquad \left\| \begin{matrix} w \\ \overline{D}\,\widehat{D}\,\overline{D}\,\overline{D} \\ \overline{D}\,d \quad d\,\overline{D} \end{matrix} - \begin{matrix} w \\ \widetilde{D}\,\overline{D}\,\overline{D} \\ \widetilde{D}\,d \quad d\,\overline{D} \end{matrix} \right\|.$$

$$\mathcal{C}_3 \parallel$$

FIG. 1. Shrewd selection for a right-to-left sweep: Ideally, the truncated complement $\widetilde{A}_\ell^{\text{tr}}(\blacktriangledown)$ should be found by minimizing the cost function $\mathcal{C}_1$, but that would involve 2s cost, $\mathcal{O}(D^3 d^2 w)$. To achieve 1s cost, $\mathcal{O}(D^3 dw)$, we instead use *shrewd selection*, involving two separate truncations: The first truncation (*preselection*) truncates $\overline{A}_\ell(\blacktriangledown)$ to $\widehat{A}_\ell^{\text{pr}}(\blacktriangledown)$ by minimizing the cost function $\mathcal{C}_2$. The second truncation (*final selection*) further truncates $\widehat{A}_\ell^{\text{pr}}(\blacktriangledown) \to \widetilde{A}_\ell^{\text{tr}}(\blacktriangledown)$ by minimizing the cost function $\mathcal{C}_3$. For details, see Fig. S-2 in Sec. S-1 of the Supplemental Material [30].

rDD can be viewed as the image of $\widetilde{A}_\ell^{\text{tr}} \otimes \overline{B}_{\ell+1}(\blacktriangledown \otimes \blacktriangleright)$ or $\overline{A}_\ell \otimes \widetilde{B}_{\ell+1}^{\text{tr}}(\blacktriangledown \otimes \blacktriangleright)$, where the isometries $\widetilde{A}_\ell^{\text{tr}}(\blacktriangledown)$ or $\widetilde{B}_{\ell+1}^{\text{tr}}(\blacktriangleright)$ are *truncated* versions of $\overline{A}_\ell$ or $\overline{B}_{\ell+1}$ and have image dimensions $\widetilde{D}$, say. It turns out that one may choose $\widetilde{D} < D$, independent of d, thus rDD, of dimension $\widetilde{D}\overline{D}$, is indeed much smaller than DD. The second insight is that $\widetilde{A}_\ell^{\text{tr}}$ or $\widetilde{B}_{\ell+1}^{\text{tr}}$ can be constructed at 1s costs using a novel scheme explained in Fig. 1. We call it *shrewd selection* since it is cheap, efficient and practical, though not strictly optimal (that would require 2s costs).

Shrewd selection.—Ideally, $\widetilde{A}_\ell^{\text{tr}}$ should minimize the cost function $\mathcal{C}_1$ (Fig. 1, top), the difference between applying the projectors $\overline{A}_\ell \overline{A}_\ell^\dagger$ or $\widetilde{A}_\ell^{\text{tr}} \widetilde{A}_\ell^{\text{tr}\dagger}$ to $H_\ell^{2s} \psi_\ell^{2s} \overline{B}_{\ell+1}^\dagger \overline{B}_{\ell+1}$. However, exact minimization of $\mathcal{C}_1$ would involve 2s costs (feasible if d, w, and D are comparatively small, but in general undesirable). To maintain 1s costs, $\mathcal{O}(D^3 dw)$, we instead use *shrewd selection*, involving two separate truncations, depicted schematically in Fig. 2 and explained in detail in Sec. S-1 of the Supplemental Material [30]. The first truncation (*preselection*) truncates the central MPS bond from $D \to D'$ (specified below) in the presence of its environment by minimizing the cost function $\mathcal{C}_2$ (Fig. 1, bottom left); this replaces the full complement by a preselected complement, $\overline{A}_\ell \blacktriangledown \to \widehat{A}_\ell^{\text{pr}} \blacktriangledown$, with reduced image dimension, $\overline{D} \to \widehat{D} = D'w$ [44]. The second truncation (*final selection*) minimizes the cost function $\mathcal{C}_3$ (Fig. 1, bottom right) with central MPO bond closed as appropriate for $H_\ell^{2s} \psi_\ell^{2s}$: it further truncates $\widehat{A}_\ell^{\text{pr}}$ to yield the final truncated complement, $\widetilde{A}_\ell^{\text{tr}}$, $\blacktriangledown \to \blacktriangledown$, $\widehat{D} \to \widetilde{D} < D$. To ensure 1s costs for final selection we need $\widehat{D} = D$, and thus choose $D' = D/w$ for preselection.

CBE update.—A CBE update of bond ℓ proceeds in four substeps. We describe them for a right-to-left sweep for building $\widetilde{A}_\ell^{\text{tr}}$ and updating $C_{\ell+1}$ (left-to-right sweeps,
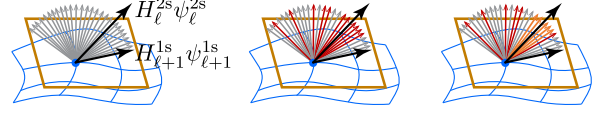
FIG. 2. The projection $H_\ell^{2s} \psi_\ell^{2s} \overset{A_\ell^\dagger}{\mapsto} H_{\ell+1}^{1s} \psi_{\ell+1}^{1s}$ to the tangent space (yellow) of the MPS manifold (blue) discards information from DD (depicted by gray arrows for DD basis vectors). *Relevant* information is recovered at 1s cost by constructing rDD through preselection (red), then final selection (orange).

building $\widetilde{B}_{\ell+1}^{\text{tr}}$ and updating C_ℓ, are analogous). (i) Compute $\widetilde{A}_\ell^{\text{tr}}(\blacktriangledown)$ using shrewd selection. (ii) Expand bond ℓ from dimension D to $D + \widetilde{D}$ by replacing A_ℓ by an expanded isometry $A_\ell^{\text{ex}}(\blacktriangledown) = A_\ell \oplus \widetilde{A}_\ell^{\text{tr}}$, and $C_{\ell+1}$ by an expanded tensor initialized as $C_{\ell+1}^{\text{ex,i}}(\blacktriangledown)$, defined such that $A_\ell^{\text{ex}} C_{\ell+1}^{\text{ex,i}} = A_\ell C_{\ell+1}$:

$$\begin{matrix} A_\ell \\ D\,\blacktriangledown\,D \\ d \end{matrix} \oplus \begin{matrix} \widetilde{A}_\ell^{\text{tr}} \\ D\,\blacktriangledown\,\widetilde{D} \\ d \end{matrix} = \begin{matrix} A_\ell^{\text{ex}} \\ D\,\blacktriangledown\,(D+\widetilde{D}) \\ d \end{matrix} \begin{matrix} C_{\ell+1}^{\text{ex,i}} \\ (D+\widetilde{D})\,\blacktriangledown\,D \\ d \end{matrix} = \begin{matrix} C_{\ell+1} \\ \boxed{}_{\ell+1} \end{matrix}. \tag{9}$$

Also construct an expanded *one-site* Hamiltonian, defined in a variational space of dimension $D(D + \widetilde{D})d$:

$$H_{\ell+1}^{1s,\text{ex}} = \begin{matrix} \boxed{}\;\boxed{} \\ {}_{\ell+1} \end{matrix} = \begin{matrix} D+\widetilde{D} \\ \boxed{}\,d\,D \\ {}_{\ell+1} \end{matrix}. \tag{10}$$

(iii) Update $C_{\ell+1}^{\text{ex}}$ variationally by using an iterative eigensolver, as usual in DMRG, to find the GS solution of $(H_{\ell+1}^{1s,\text{ex}} - E) C_{\ell+1}^{\text{ex}} = 0$, starting from $C_{\ell+1}^{\text{ex,i}}$. (We employ a Lanczos eigensolver.) This has costs of $\mathcal{O}(D^3 dw)$. Thus, $C_{\ell+1}^{\text{ex}}$ can be updated at 1s costs, while including only the most relevant 2s information via the contribution of $\widetilde{A}_\ell^{\text{tr}}$. (iv) Shift the isometry center from site $\ell + 1$ to site ℓ using a singular value decomposition (SVD) and truncate (*trim*) bond ℓ from dimension $D + \widetilde{D}$ back to D, removing low-weight states. The discarded weight, say ξ, of this bond trimming serves as an error measure [30].

The energy minimization based on $H_{\ell+1}^{1s,\text{ex}}$ is variational, hence each CBE update strictly lowers the GS energy. Though shrewd selection involves severe bond reductions, it yields rDDs suitable for efficiently lowering the GS energy (in step (iii)). Moreover, although CBE explores a much smaller variational space than 2s DMRG, it converges at the same rate and accuracy (see below and Ref. [30]), since it focuses on the subspace that really matters for energy reduction. Section S-1 in [30] illustrates this by analyzing singular value spectra. All in all, CBE is a 1s cost version of the 2s update, compatible with established DMRG parallelization schemes [45]. Similar to

$2s$ [7], CBE can also be combined with mixing during the initial few sweeps (see Ref. [30], Sec. S-3).

We note that bond expansion using a truncated DD has been proposed before [26,46]. But our $A_\ell^{\mathrm{ex}}(\triangledown)$ outperforms that of DMRG3S [26] (see below and Ref. [30]); and we find $A_\ell^{\mathrm{ex}}(\triangledown)$ at $1s$ costs, whereas Ref. [46] (on variational uniform MPS [47]) uses an SVD requiring $2s$ costs.

Sweeping.—Our computations exploit $\mathrm{U}(1)_{\mathrm{ch}} \otimes \mathrm{SU}(2)_{\mathrm{sp}}$ charge and spin symmetries using QSpace [48,49], with bond dimensions D^* (or D) counting symmetry multiplets (or states). Usually, D^* is increased with each update during sweeping, from an initial D_{i}^* to a final $D_{\mathrm{f}}^* = \alpha D_{\mathrm{i}}^*$, with $\alpha > 1$. To achieve this with CBE we (i,ii) use $D'^* \simeq D_{\mathrm{f}}^*/w^*$, $\widehat{D}^* = D_{\mathrm{f}}^*$ (cf. Fig. 1) and expand from D_{i}^* to $D_{\mathrm{i}}^* + \widetilde{D}^* = D_{\mathrm{f}}^*(1 + \delta)$, (iii) call the iterative eigensolver, and (iv) truncate back to D_{f}^* when shifting the isometry center. We use $\delta = 0.1$ for CBE, unless stated otherwise.

Benchmarks.—As a first benchmark, we consider the 1D Hubbard-Holstein (HH) model [31–35], described by

$$H_{\mathrm{HH}} = -\sum_{\ell\sigma}(c_{\ell\sigma}^\dagger c_{\ell+1\sigma} + \mathrm{H.c.}) + 0.8\sum_\ell n_{\ell\uparrow}n_{\ell\downarrow}$$
$$+ 0.5\sum_\ell b_\ell^\dagger b_\ell + \sqrt{0.2}\sum_\ell(n_{\ell\uparrow} + n_{\ell\downarrow} - 1)$$
$$\times (b_\ell^\dagger + b_\ell). \tag{11}$$

Here, $c_{\ell\sigma}^\dagger$ creates an electron and $b_\ell^\dagger$ a phonon at site ℓ, and $n_{\ell\sigma} = c_{\ell\sigma}^\dagger c_{\ell\sigma}$. We search for the GS with $N = \mathscr{L} = 50$, total spin $S = 0$, and restrict the maximum local number of excited phonons to $N_{\mathrm{ph}}^{\mathrm{max}}$. Then, $d^*[d] = 3(N_{\mathrm{ph}}^{\mathrm{max}} + 1)$ $[4(N_{\mathrm{ph}}^{\mathrm{max}} + 1)]$. Figure 3(a) shows the relative error in energy vs number of half-sweeps n_s for different D_{max}^* at fixed $d^* = 12$, comparing CBE and $2s$ DMRG schemes. The convergence with n_s is similar for CBE and $2s$. Figure 3(b) compares the CPU time (measured on a single core of an Intel Core i7-9750H CPU) per sweep for CBE and $2s$ for different d^* at fixed D_{max}^*. Linear and quadratic fits confirm the expected d^* ($1s$) or d^{*2} ($2s$) scaling, respectively, highlighting the speedup from CBE.

Next, we consider $\mathscr{L}_x \times \mathscr{L}_y = 10 \times 4$ and 10×6 Hubbard cylinders (HC), described by (following Ref. [28])

$$H_{\mathrm{HC}} = -\sum_{\langle\ell,\ell'\rangle,\sigma}(c_{\ell\sigma}^\dagger c_{\ell'\sigma} + \mathrm{H.c.}) + 8\sum_\ell n_{\ell\uparrow}n_{\ell\downarrow}. \tag{12}$$

Here, $\ell = (x, y)$ is a 2D site index and $\sum_{\langle\ell,\ell'\rangle}$ a nearest-neighbor sum. We search for the GS with total filling $N = 0.9\mathscr{L}_x\mathscr{L}_y$ and spin $S = 0$. We use a real-space MPO, not the hybrid-space MPO [13,50] used in Ref. [28]. Figures 3(c) and 3(d) benchmarks CBE (black) against $2s$ DMRG (red); their accuracies match (same GS energy for given D^*). CBE-DMRG yields controlled convergence
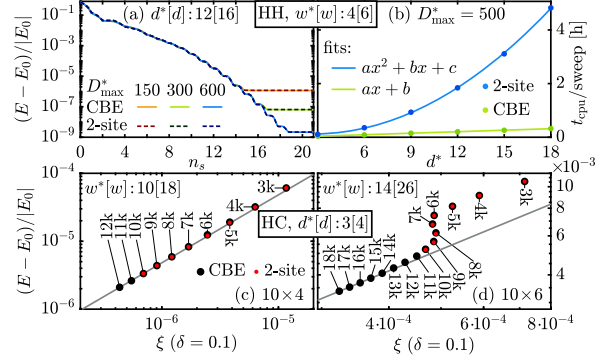
FIG. 3. Hubbard-Holstein (HH) model: (a) Convergence of the GS energy versus number of half-sweeps n_s at fixed $d^* = 3(N_{\mathrm{ph}}^{\mathrm{max}} + 1)$. E_0 was obtained by linear ξ extrapolation of data from $D_{\mathrm{max}}^* \in [1000, 1200]$. (b) CPU time per sweep for various d^* at fixed D_{max}^*, showing d^* (CBE) vs d^{*2} ($2s$) scaling. Hubbard cylinders (HC): Error in GS energy vs ξ for (c) 10×4 and (d) 10×6 HCs, obtained with CBE (black) and $2s$ (red) DMRG, for various D_{max}^* (legends). Since $2s$ CPU times far exceed those of CBE, $2s$ data is only shown for $D_{\mathrm{max}}^* \leq 10k$. Reference energies $E_0 = -27.881\,694\,2$ (10×4) and $-41.747\,496\,1$ (10×6) are obtained by linear ξ extrapolation of the four most accurate CBE results to $\xi = 0$ (gray line).

for sufficiently large D^*, where the energy error decreases linearly with ξ. DMRG3S does not reach $2s$ accuracy for this model, as is clear from the data shown in Ref. [28] Sec. V E.

Further benchmarks and comparison to DMRG3S are shown in Ref. [30], Secs. S-2,3. We find that CBE has similar run time per sweep but converges faster than DMRG3S [26]: for given D_{max}^*, the energy converges in fewer sweeps and less run time, and reaches a lower value.

Kondo-Heisenberg cylinders.—Finally, to include some new physics results in this Letter, we study the Kondo-Heisenberg (KH) lattice model on a cylinder. The KH model is believed to describe the essential physics of heavy-fermion (HF) materials [36,51–53], which feature many interesting phenomena. One of the most intriguing is the so-called Kondo breakdown (KB) quantum critical point (QCP) [38,42,54], where collective Kondo singlets [42] formed at strong coupling break up, leading to a FS reconstruction [55–58] at $T = 0$. Strange metal behavior is observed at finite temperatures with, e.g., $\sim T$ resistivity [58–62] or $\sim T \log T$ specific heat [61–64].

Theoretical understanding of the KB-QCP is still incomplete, in part due to scarceness of numerical simulations. Prior numerical studies used dynamical mean-field theory [65–69] and Monte Carlo methods [70–73], but we are not aware of DMRG results on the KB-QCP. Here, we take first steps in this direction by studying FS reconstruction on a KH cylinder: we show that at $T = 0$, there are two distinct phases featuring different Fermi surfaces.
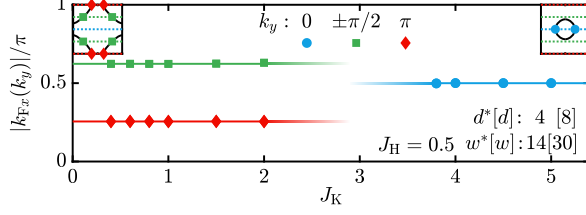
FIG. 4. Kondo-Heisenberg (KH) cylinder: Fermi wave vectors $|k_{Fx}(k_y)|$ for a 40×4 KH cylinder for various values of J_K. Symbols are data points (error bars are below symbol size), lines are guides to the eye. In the insets, black lines sketch the presumed FS for $\mathscr{L}_y \to \infty$, dotted lines show the k_y values allowed for $\mathscr{L}_y = 4$.

We study a $\mathscr{L}_x \times \mathscr{L}_y = 40 \times 4$ KH cylinder, described by

$$H_{KH} = - \sum_{\langle \boldsymbol{\ell}, \boldsymbol{\ell}' \rangle, \sigma} (c^\dagger_{\boldsymbol{\ell}\sigma} c_{\boldsymbol{\ell}'\sigma} + \text{H.c.}) + J_K \sum_{\boldsymbol{\ell}} \boldsymbol{S}_{\boldsymbol{\ell}} \cdot \boldsymbol{s}_{\boldsymbol{\ell}}$$
$$+ \frac{1}{2} \sum_{\langle \boldsymbol{\ell}, \boldsymbol{\ell}' \rangle} \boldsymbol{S}_{\boldsymbol{\ell}} \cdot \boldsymbol{S}_{\boldsymbol{\ell}'}.$$

Here, $\boldsymbol{s}_{\boldsymbol{\ell}} = \frac{1}{2}\sum_{\sigma\sigma'} c^\dagger_{\boldsymbol{\ell}\sigma} \boldsymbol{\sigma}_{\sigma\sigma'} c_{\boldsymbol{\ell}\sigma'}$ and $\boldsymbol{S}_{\boldsymbol{\ell}}$ are electron and local moment spin-$\frac{1}{2}$ operators at site $\boldsymbol{\ell}$. We search for the GS with total filling $N = 1.25 \mathscr{L}_x \mathscr{L}_y$ and spin $S = 0$.

For a $\mathscr{L}_y = 4$ cylinder, the Brillouin zone consists of four lines, since $k_y \in \{0, \pm(\pi/2), \pi\}$ is discrete. If such a line cuts the $\mathscr{L}_y \to \infty$ FS, that defines a "Fermi point," with Fermi momentum $(k_{Fx}(k_y), k_y)$. We have extracted the corresponding $k_{Fx}(k_y)$ values from CBE-DMRG results for the single-particle density matrix (see Ref. [30], Sec. S-4 B for details; Fig. S-13 shows controlled convergence of this quantity). Figure 4 shows the results for various values of J_K. There are clearly two distinct phases with qualitatively different Fermi points $k_{Fx}(k_y)$. At small $J_K \leq 2$, we find Fermi points at $(|k_{Fx}|, |k_y|) = (0.625\pi, \pi/2)$ and $(0.256\pi, \pi)$, matching the free-electron values at $J_K = 0$. By contrast, at large $J_K \geq 2.8$, we find Fermi points only at $(\pi/2, 0)$, suggesting a FS reconstruction at some J_{Kc} in between. Note also that $k_{Fx}(k_y)$ remains J_K independent in each of the two regimes. This is expected from Luttinger's sum rule [39,41], which links the effective number n_{eff} of mobile charge carriers (defined modulo 2, i.e., up to filled bands) to the FS volume (see Ref. [30], Sec. S-4 C for details). For small $J_K \leq 0.75$, we find $n_{\text{eff}} = 1.25$, consistent with 25% electron doping. By contrast, at large $J_K \geq 2.8$ we find $n_{\text{eff}} = 0.25 = 2.25 \mod 2$, consistent with the spins becoming mobile charge carriers by "binding" to the electrons [42]. Pinpointing and studying a possible KB-QCP separating the two phases is left for future work.

Summary and outlook.—CBE expands bonds by adding subspaces on which Δ^{2s}_E, the $2s$ contribution to the energy variance, has significant weight, thus making these subspaces accessible to $1s$ energy minimization. CBE is fully variational and has $1s$ costs, since the variational space is only slightly expanded relative to $1s$ DMRG.

By significantly saving costs, CBE opens the door to studying challenging models of current interest at higher accuracy (larger D) than previously possible, or tackling more complex models, with d or w so large that they were hitherto out of reach. Examples are multiband models with several different type of couplings, in particular in two-dimensional settings, models involving bosonic excitations, and quantum-chemical applications. We have made a first step in this direction by showing that the KH model on a width 4 cylinder features two phases with distinct FS volumes. Our study of the KH model opens the door to investigate this model in more depth; for example, follow-up work may aim to sort out the range of applicability of existing approximate approaches, e.g., parton mean-field theories [74,75] or DMFT based studies [65–69].

More generally, CBE can be used for any variational MPS optimization task. Besides energy minimization, an example is approximating a given Ψ by a Ψ' with smaller bond dimension through minimization of $\|\Psi' - \Psi\|$. CBE can also be used to build Krylov spaces with $2s$ accuracy at $1s$ costs, relevant for all of the many MPS methods relying on Krylov methods. For example, in a follow-up paper [76] we focus on MPS time evolution using the time-dependent variational principle (TDVP), and use CBE to achieve dramatic improvements in performance. Finally, analogous statements hold for variational optimization or time evolution of MPOs. Thus, CBE will become a widely used, indispensable tool in the MPS/MPO toolbox.

[1] S. R. White, Density Matrix Formulation for Quantum Renormalization Groups, Phys. Rev. Lett. **69**, 2863 (1992).

[2] S. R. White, Density-matrix algorithms for quantum renormalization groups, Phys. Rev. B **48**, 10345 (1993).

[3] F. Verstraete, D. Porras, and J. I. Cirac, Density Matrix Renormalization Group and Periodic Boundary Conditions: A Quantum Information Perspective, Phys. Rev. Lett. **93**, 227205 (2004).

[4] U. Schollwöck, The density-matrix renormalization group, Rev. Mod. Phys. **77**, 259 (2005).

[5] U. Schollwöck, The density-matrix renormalization group in the age of matrix product states, Ann. Phys. (Amsterdam) **326**, 96 (2011).

[6] S. R. White, Spin Gaps in a Frustrated Heisenberg Model for CaV_4O_9, Phys. Rev. Lett. **77**, 3633 (1996).

[7] E. Stoudenmire and S. R. White, Studying two-dimensional systems with the density matrix renormalization group, Annu. Rev. Condens. Matter Phys. **3**, 111 (2012).

[8] S. R. White and D. J. Scalapino, Density Matrix Renormalization Group Study of the Striped Phase in the 2d $t-J$ Model, Phys. Rev. Lett. **80**, 1272 (1998).

[9] S. R. White and D. J. Scalapino, Checkerboard patterns in the $t-J$ model, Phys. Rev. B **70**, 220506(R) (2004).

[10] S. R. White and D. J. Scalapino, Pairing on striped t-t'-J lattices, Phys. Rev. B **79**, 220504(R) (2009).

[11] S. Jiang, D. J. Scalapino, and S. R. White, Ground-state phase diagram of the t-t'-J model, Proc. Natl. Acad. Sci. U.S.A. **118**, e2109978118 (2021).

[12] J. P. F. LeBlanc *et al.* (Simons Collaboration on the Many-Electron Problem), Solutions of the Two-Dimensional Hubbard Model: Benchmarks and Results from a Wide Range of Numerical Algorithms, Phys. Rev. X **5**, 041041 (2015).

[13] G. Ehlers, S. R. White, and R. M. Noack, Hybrid-space density matrix renormalization group study of the doped two-dimensional Hubbard model, Phys. Rev. B **95**, 125125 (2017).

[14] B.-X. Zheng, C.-M. Chung, P. Corboz, G. Ehlers, M.-P. Qin, R. M. Noack, H. Shi, S. R. White, S. Zhang, and G. K.-L. Chan, Stripe order in the underdoped region of the two-dimensional Hubbard model, Science **358**, 1155 (2017).

[15] E. W. Huang, C. B. Mendl, H.-C. Jiang, B. Moritz, and T. P. Devereaux, Stripe order from the perspective of the Hubbard model, npj Quantum Mater. **3**, 22 (2018).

[16] M. Qin, C.-M. Chung, H. Shi, E. Vitali, C. Hubig, U. Schollwöck, S. R. White, and S. Zhang (Simons Collaboration on the Many-Electron Problem), Absence of Superconductivity in the Pure Two-Dimensional Hubbard Model, Phys. Rev. X **10**, 031016 (2020).

[17] Y.-F. Jiang, J. Zaanen, T. P. Devereaux, and H.-C. Jiang, Ground state phase diagram of the doped Hubbard model on the four-leg cylinder, Phys. Rev. Res. **2**, 033073 (2020).

[18] H.-C. Jiang and S. A. Kivelson, Stripe order enhanced superconductivity in the Hubbard model, Proc. Natl. Acad. Sci. U.S.A. **119**, e2109406119 (2022).

[19] S. Yan, D. A. Huse, and S. R. White, Spin-liquid ground state of the $S=1/2$ kagome Heisenberg antiferromagnet, Science **332**, 1173 (2011).

[20] S. Depenbrock, I. P. McCulloch, and U. Schollwöck, Nature of the Spin-Liquid Ground State of the $S=1/2$ Heisenberg Model on the Kagome Lattice, Phys. Rev. Lett. **109**, 067201 (2012).

[21] F. Kolley, S. Depenbrock, I. P. McCulloch, U. Schollwöck, and V. Alba, Phase diagram of the J_1-J_2 Heisenberg model on the kagome lattice, Phys. Rev. B **91**, 104418 (2015).

[22] Y.-C. He, M. P. Zaletel, M. Oshikawa, and F. Pollmann, Signatures of Dirac Cones in a DMRG Study of the Kagome Heisenberg Model, Phys. Rev. X **7**, 031020 (2017).

[23] S. Östlund and S. Rommer, Thermodynamic Limit of Density Matrix Renormalization, Phys. Rev. Lett. **75**, 3537 (1995).

[24] S. Rommer and S. Östlund, Class of ansatz wave functions for one-dimensional spin systems and their relation to the density matrix renormalization group, Phys. Rev. B **55**, 2164 (1997).

[25] S. R. White, Density matrix renormalization group algorithms with a single center site, Phys. Rev. B **72**, 180403(R) (2005).

[26] C. Hubig, I. P. McCulloch, U. Schollwöck, and F. A. Wolf, Strictly single-site DMRG algorithm with subspace expansion, Phys. Rev. B **91**, 155115 (2015).

[27] A. Gleis, J.-W. Li, and J. von Delft, Projector formalism for kept and discarded spaces of matrix product states, Phys. Rev. B **106**, 195138 (2022).

[28] C. Hubig, J. Haegeman, and U. Schollwöck, Error estimates for extrapolations with matrix-product states, Phys. Rev. B **97**, 045125 (2018).

[29] If $2s$ DMRG has converged to an optimal MPS Ψ_D with *fixed* bond dimension D, the size of rDD is zero. Because Ψ_D is already optimal (at *fixed* D), *any* state in DD is less relevant than those already present in the kept space of Ψ_D. As a result, Ψ_D cannot be further optimized unless D is increased. Away from convergence, the size of rDD is usually still much smaller than the already somewhat optimized kept space, which in turn is much smaller than DD. Expanding by rDD (CBE) instead of DD ($2s$) is similar in spirit to using an iterative eigensolver for Eqs. (5a) and 5(b) instead of full diagonalization.

[30] See Supplemental Material at http://link.aps.org/supplemental/10.1103/PhysRevLett.130.246402 for a detailed analysis of shrewd selection; a pseudocode for shrewd selection; additional simple benchmarks; a comparison to DMRG3S; and more details on the analysis of the Kondo-Heisenberg model on a 4-leg cylinder. The Supplemental Material includes Refs. [32–44].

[31] E. Jeckelmann and S. R. White, Density-matrix renormalization-group study of the polaron problem in the Holstein model, Phys. Rev. B **57**, 6376 (1998).

[32] M. Tezuka, R. Arita, and H. Aoki, Phase diagram for the one-dimensional Hubbard-Holstein model: A density-matrix renormalization group study, Phys. Rev. B **76**, 155114 (2007).

[33] H. Fehske, G. Hager, and E. Jeckelmann, Metallicity in the half-filled Holstein-Hubbard model, E. J. Phys. **84**, 57001 (2008).

[34] S. Ejima and H. Fehske, DMRG analysis of the sdw-cdw crossover region in the 1d half-filled Hubbard-Holstein model, J. Phys. Conf. Ser. **200**, 012031 (2010).

[35] T. E. Reinhard, U. Mordovina, C. Hubig, J. S. Kretchmer, U. Schollwöck, H. Appel, M. A. Sentef, and A. Rubio, Density-matrix embedding theory study of the one-dimensional Hubbard-Holstein model, J. Chem. Theory Comput. **15**, 2221 (2019).

[36] P. Coleman, Heavy fermions: Electrons at the edge of magnetism, in *Handbook of Magnetism and Advanced Magnetic Materials*, edited by H. Kronmüller and S. Parkin (Wiley, New York, 2007), Vol. 1, pp. 95–148.

[37] M. Ye, H.-H. Kung, P. F. S. Rosa, E. D. Bauer, K. Haule, and G. Blumberg, Anisotropy of Kondo-lattice coherence in momentum space for $CeCoIn_5$, arXiv:2202.09642.

[38] P. Coleman, C. Pépin, Q. Si, and R. Ramazashvili, How do Fermi liquids get heavy and die?, J. Phys. Condens. Matter **13**, R723 (2001).

[39] J. M. Luttinger, Fermi surface and some simple equilibrium properties of a system of interacting fermions, Phys. Rev. **119**, 1153 (1960).

[40] D. Sénéchal, An introduction to bosonization, arXiv: cond-mat/9908262.

[41] M. Oshikawa, Topological Approach to Luttinger's Theorem and the Fermi Surface of a Kondo Lattice, Phys. Rev. Lett. **84**, 3370 (2000).

[42] Q. Si, J. H. Pixley, E. Nica, S. J. Yamamoto, P. Goswami, R. Yu, and S. Kirchner, Kondo destruction and quantum criticality in Kondo lattice systems, J. Phys. Soc. Jpn. **83**, 061005 (2014).

[43] Y. Nishikawa, O. J. Curtin, A. C. Hewson, and D. J. G. Crow, Magnetic field induced quantum criticality and the Luttinger sum rule, Phys. Rev. B **98**, 104419 (2018).

[44] We could achieve the desired reduction $\overline{D} \to \tilde{D}$ already during preselection by choosing $D' = \tilde{D}/w$ there, so that $\hat{D} = \tilde{D}$; however, that would neglect the information that in $H^{2s}\psi^{2s}$ the central MPO bond is closed. Final selection serves to include that information.

[45] E. M. Stoudenmire and S. R. White, Real-space parallel density matrix renormalization group, Phys. Rev. B **87**, 155137 (2013).

[46] V. Zauner-Stauber, L. Vanderstraeten, M. T. Fishman, F. Verstraete, and J. Haegeman, Variational optimization algorithms for uniform matrix product states, Phys. Rev. B **97**, 045145 (2018).

[47] L. Vanderstraeten, J. Haegeman, and F. Verstraete, Tangent-space methods for uniform matrix product states, SciPost Phys. Lect. Notes **7** (2019).

[48] A. Weichselbaum, Non-Abelian symmetries in tensor networks: A quantum symmetry space approach, Ann. Phys. (Amsterdam) **327**, 2972 (2012).

[49] A. Weichselbaum, X-symbols for non-Abelian symmetries in tensor networks, Phys. Rev. Res. **2**, 023385 (2020).

[50] J. Motruk, M. P. Zaletel, R. S. K. Mong, and F. Pollmann, Density matrix renormalization group on a cylinder in mixed real and momentum space, Phys. Rev. B **93**, 155139 (2016).

[51] S. Kirchner, S. Paschen, Q. Chen, S. Wirth, D. Feng, J. D. Thompson, and Q. Si, Colloquium: Heavy-electron quantum criticality and single-particle spectroscopy, Rev. Mod. Phys. **92**, 011002 (2020).

[52] H. v. Löhneysen, A. Rosch, M. Vojta, and P. Wölfle, Fermi-liquid instabilities at magnetic quantum phase transitions, Rev. Mod. Phys. **79**, 1015 (2007).

[53] G. R. Stewart, Non-Fermi-liquid behavior in d- and f-electron metals, Rev. Mod. Phys. **73**, 797 (2001).

[54] P. Coleman and C. Pépin, What is the fate of the heavy electron at a quantum critical point?, Physica (Amsterdam) **312–313B**, 383 (2002).

[55] S. Paschen, T. Lühmann, S. Wirth, P. Gegenwart, O. Trovarelli, C. Geibel, F. Steglich, P. Coleman, and Q. Si, Hall-effect evolution across a heavy-fermion quantum critical point, Nature (London) **432**, 881 (2004).

[56] H. Shishido, R. Settai, H. Harima, and Y. Ōnuki, A drastic change of the Fermi surface at a critical pressure in CeRhIn$_5$: dHvA study under pressure, J. Phys. Soc. Jpn. **74**, 1103 (2005).

[57] S. Friedemann, N. Oeschler, S. Wirth, C. Krellner, C. Geibel, F. Steglich, S. Paschen, S. Kirchner, and Q. Si, Fermi-surface collapse and dynamical scaling near a quantum-critical point, Proc. Natl. Acad. Sci. U.S.A. **107**, 14547 (2010).

[58] N. Maksimovic et al., Evidence for a delocalization quantum phase transition without symmetry breaking in CeCoIn$_5$, Science **375**, 76 (2022).

[59] V. Martelli, A. Cai, E. M. Nica, M. Taupin, A. Prokofiev, C.-C. Liu, H.-H. Lai, R. Yu, K. Ingersent, R. Küchler, A. M. Strydom, D. Geiger, J. Haenel, J. Larrea, Q. Si, and S. Paschen, Sequential localization of a complex electron fluid, Proc. Natl. Acad. Sci. U.S.A. **116**, 17701 (2019).

[60] L. Prochaska, X. Li, D. C. MacFarland, A. M. Andrews, M. Bonta, E. F. Bianco, S. Yazdi, W. Schrenk, H. Detz, A. Limbeck, Q. Si, E. Ringe, G. Strasser, J. Kono, and S. Paschen, Singular charge fluctuations at a magnetic quantum critical point, Science **367**, 285 (2020).

[61] O. Trovarelli, C. Geibel, S. Mederle, C. Langhammer, F. M. Grosche, P. Gegenwart, M. Lang, G. Sparn, and F. Steglich, YbRh$_2$Si$_2$: Pronounced non-Fermi-Liquid Effects Above a Low-Lying Magnetic Phase Transition, Phys. Rev. Lett. **85**, 626 (2000).

[62] H. Zhao, J. Zhang, M. Lyu, S. Bachus, Y. Tokiwa, P. Gegenwart, S. Zhang, J. Cheng, Y.-f. Yang, G. Chen, Y. Isikawa, Q. Si, F. Steglich, and P. Sun, Quantum-critical phase from frustrated magnetism in a strongly correlated metal, Nat. Phys. **15**, 1261 (2019).

[63] H. Löhneysen, M. Sieck, O. Stockert, and M. Waffenschmidt, Investigation of non-fermi-liquid behavior in CeCu$_{6-x}$Au$_x$, Physica (Amsterdam) **223–224B**, 471 (1996).

[64] H. von Löhneysen, Non-fermi-liquid behaviour in the heavy-fermion system CeCu$_{6-x}$Au$_x$, J. Phys. Condens. Matter **8**, 9689 (1996).

[65] L. De Leo, M. Civelli, and G. Kotliar, Cellular dynamical mean-field theory of the periodic Anderson model, Phys. Rev. B **77**, 075107 (2008).

[66] L. De Leo, M. Civelli, and G. Kotliar, $T = 0$ Heavy-Fermion Quantum Critical Point as an Orbital-Selective Mott Transition, Phys. Rev. Lett. **101**, 256404 (2008).

[67] D. Tanasković, K. Haule, G. Kotliar, and V. Dobrosavljević, Phase diagram, energy scales, and nonlocal correlations in the Anderson lattice model, Phys. Rev. B **84**, 115105 (2011).

[68] Q. Si, S. Rabello, K. Ingersent, and J. L. Smith, Locally critical quantum phase transitions in strongly correlated metals, Nature (London) **413**, 804 (2001).

[69] Q. Si, S. Rabello, K. Ingersent, and J. L. Smith, Local fluctuations in quantum critical metals, Phys. Rev. B **68**, 115103 (2003).

[70] F. F. Assaad, Quantum Monte Carlo Simulations of the Half-Filled Two-Dimensional Kondo Lattice Model, Phys. Rev. Lett. **83**, 796 (1999).

[71] S. Capponi and F. F. Assaad, Spin and charge dynamics of the ferromagnetic and antiferromagnetic two-dimensional half-filled Kondo lattice model, Phys. Rev. B **63**, 155114 (2001).

[72] F. Parisen Toldin, T. Sato, and F. F. Assaad, Mutual information in heavy-fermion systems, Phys. Rev. B **99**, 155158 (2019).

[73] B. Danu, Z. Liu, F. F. Assaad, and M. Raczkowski, Zooming in on heavy fermions in Kondo lattice models, Phys. Rev. B **104**, 155128 (2021).

[74] T. Senthil, S. Sachdev, and M. Vojta, Fractionalized Fermi Liquids, Phys. Rev. Lett. **90**, 216403 (2003).

[75] T. Senthil, M. Vojta, and S. Sachdev, Weak magnetism and non-Fermi liquids near heavy-fermion critical points, Phys. Rev. B **69**, 035111 (2004).

[76] J.-W. Li, A. Gleis, and J. von Delft, Time-dependent variational principle with controlled bond expansion for matrix product states, arXiv:2208.10972.

This supplement offers additional material on five issues: in Sec. S-1, details on the implementation of shrewd selection, including pseudocode, and a detailed analysis of preselection and final selection; in Sec. S-2, a simple additional benchmark of CBE–DMRG on free Fermions; in Sec. S-3, a comparison to DMRG3S; and in Sec. S-4, more details on the analysis of the Kondo-Heisenberg model on a 4-leg cylinder.

S-1. SHREWD SELECTION

Figures 1 and 2 in the main text introduce a novel scheme needed for CBE, called *shrewd selection*. In this section, we discuss it in detail. Section S-1 A provides algorithmic details; Sec. S-1 B discusses various options for choosing the parameters involved in perselection and final selection; Secs. S-1 C and S-1 D discusses the properties of the singular values and singular vectors obtained; and
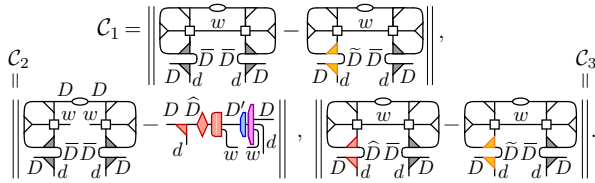
FIG. S-1. Shrewd selection (concept). During a right-to-left CBE sweep, bond ℓ is expanded from $A_\ell(\searcharrow)$ to $A_\ell \oplus \widetilde{A}_\ell^{\mathrm{tr}}(\searcharrow \oplus \searcharrow)$, where $\widetilde{A}_\ell^{\mathrm{tr}}(\searcharrow)$, with image dimension $\widetilde{D}$, is a truncation of $\overline{A}_\ell(\searcharrow)$, with image dimension $\overline{D} = D(d-1)$. This expansion will reduce Δ_E^{2s} significantly if $\widetilde{A}_\ell^{\mathrm{tr}} \oplus \overline{B}_{\ell+1}(\searcharrow \otimes \searcharrow)$ targets rDD, a $\widetilde{D}\overline{D}$-dimensional subspace of the $\overline{D}^2$-dimensional space DD on which $H_\ell^{2s}\psi_\ell^{2s}$ has significant weight. As explained in the main text, ideally, $\widetilde{A}_\ell^{\mathrm{tr}}(\searcharrow)$ should minimize the cost function $\mathcal{C}_1$. To achieve this at 1s costs, we instead find $\widetilde{A}_\ell^{\mathrm{tr}}(\searcharrow)$ using shrewd selection, involving two separate truncations. The first truncation (*preselection*) truncates the central MPS bond from $D \to D'$ in the presence of its environment by minimizing $\mathcal{C}_2$; this replaces the full complement by a preselected complement, $\overline{A}_\ell\searcharrow \to \widehat{A}_\ell^{\mathrm{pr}}\searcharrow$, with reduced image dimension, $\overline{D} \to \widehat{D} = D'w$ [31]. The second truncation (*final selection*) minimizes $\mathcal{C}_3$ with central MPO bond closed as appropriate for $H_\ell^{2s}\psi_\ell^{2s}$: it further truncates $\widehat{A}_\ell^{\mathrm{pr}}$ to yield the final truncated complement, $\widetilde{A}_\ell^{\mathrm{tr}}$, $\searcharrow \to \searcharrow$, $\widehat{D} \to \widetilde{D} < D$. To ensure 1s costs for final selection we need $\widehat{D} = D$, and thus choose $D' = D/w$ for preselection. The truncations underlying preselection and final selection are explained in detail in Fig. S-2.

Sec. S-1 E discusses the convergence rate per sweep.

A. Algorithmic details

For convenience, Fig. 1 of the main text is shown again in Fig. S-1, with a caption summarizing the main ideas underlying shrewd selection. Its two ingredients, preselection and final selection, are explained in detail in Fig. S-2 using tensor network diagrams. Table I provides pseudocode for the tensor network diagrams in Fig. S-2.

In the remainder of this section we discuss preselection and final selection in more detail, and illustrate their effects on the properties of various singular value spectra
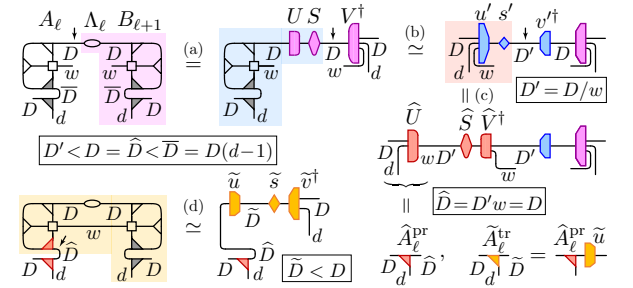
FIG. S-2. Shrewd selection (details). Computation of (a-c) the preselected complement $\widehat{A}_\ell^{\mathrm{pr}}(\searcharrow)$ to minimize $\mathcal{C}_2$, and (d) the final truncated complement $\widetilde{A}_\ell^{\mathrm{tr}}(\searcharrow)$ to minimize $\mathcal{C}_3$, using four SVDs, all with at most 1s costs. For each, an arrow indicates a bond being opened before doing the SVD, shading and symbols in matching colors indicate the SVD input and output, and the latter is written as $USV^\dagger$ or $usv^\dagger$ when involving no or some truncation, respectively. Importantly, we express $\overline{A}_\ell\overline{A}_\ell^\dagger$ and $\overline{B}_{\ell+1}^\dagger\overline{B}_{\ell+1}$ (grey) as $\mathbb{1}_\ell^{\mathrm{P}} - A_\ell A_\ell^\dagger$ and $\mathbb{1}_\ell^{\mathrm{P}} - B_{\ell+1}^\dagger B_{\ell+1}$ (Eq. (7b)), avoiding the computation of $\overline{A}_\ell$ and $\overline{B}_{\ell+1}$. (a) The first SVD canonicalizes the right side of the diagram, assigning its weights to the central MPS bond. (b) The second SVD and truncation reduces the dimension of this bond, $D \to D' = D/w$. (c) The third SVD regroups indices to combine the truncated MPS bond and the MPO bond into a composite bond of dimension $\widehat{D} = D'w = D$, yielding the preselected complement $\widehat{A}_\ell^{\mathrm{pr}} = \widehat{U}(\searcharrow)$. Nominally, step (c) would require no truncation if exact arithmetic were used, but in practice (numerically) zero singular values, of order $\mathcal{O}(10^{-16})$, may arise; these must be discarded to ensure $A_\ell^\dagger \widehat{A}_\ell^{\mathrm{pr}} = 0$. (d) The fourth SVD and truncation yields the final truncated complement $\widetilde{A}_\ell^{\mathrm{tr}} = \widehat{A}_\ell^{\mathrm{pr}} \widetilde{u}(\searcharrow)$, with bond reduction $\widehat{D} \to \widetilde{D} < D$. Table I gives a pseudocode for shrewd selection.

Algorithm 1 Computation of truncated complement using shrewd selection

---

Input: 2s Hamiltonian $H_\ell^{2s} = L_{\ell-1}W_\ell W_{\ell+1}R_{\ell+2}$, 2s wavefunction $\psi^{2s} = A_\ell \Lambda_\ell B_{\ell+1}$ in bond-canonical form, preselection bond dimension D', truncated complement dimension $\widetilde{D}$

Output: truncated complement $\widetilde{A}_\ell^{\mathrm{tr}}$ (◥)

1: **function** GETRORTH($R_{\ell+2},W_{\ell+1},B_{\ell+1},\Lambda_\ell$)
2:      Compute $R_{\ell+1}^{\mathrm{tmp}} = \Lambda_\ell B_{\ell+1}W_{\ell+1}R_{\ell+2}$
3:      Compute $R_{\ell+1}^{\mathrm{orth}} = R_{\ell+1}^{\mathrm{tmp}} - R_{\ell+1}^{\mathrm{tmp}}B_{\ell+1}^\dagger B_{\ell+1}$
4:      **return** $R_{\ell+1}^{\mathrm{orth}}$
5: **end function**
6: (Fig. S-2(a)): SVD ℓ-bond of $R_{\ell+1}^{\mathrm{orth}} = USV^\dagger$
7: **function** GETLORTH($L_{\ell-1},W_\ell,A_\ell,U,S$)
8:      Compute $L_\ell^{\mathrm{tmp}} = L_{\ell-1}W_\ell US$
9:      Compute $L_\ell^{\mathrm{orth}} = L_\ell^{\mathrm{tmp}} - A_\ell A_\ell^\dagger L_\ell^{\mathrm{tmp}}$
10:      **return** L_ℓ^{orth}
11: **end function**
12: (Fig. S-2(b)): SVD $L_\ell^{\mathrm{orth}} = U'S'V'^\dagger$ and truncate all except the largest D' singular values in S': $U'S'V'^\dagger \overset{\mathrm{trunc}}{\Rightarrow} u's'v'^\dagger$
13: (Fig. S-2(c)): Redirect the MPO-leg of $u's'$ and perform an SVD on its combined MPO- and ℓ-bond, $u's' = \widehat{U}\widehat{S}\widehat{V}^\dagger$. Truncate all singular values in $\widehat{S}$ which are numerically zero to ensure $A_\ell^\dagger \widehat{U} = 0$. ▷ **warning:** $A_\ell^\dagger \widehat{U} = 0$ is crucial and *must* be ensured!
14: (Optional): safety orthogonalization of $\widehat{U}$ by SVD on $\widehat{U} - A_\ell A_\ell^\dagger \widehat{U}$ plus truncation of small singular values.
15: Assign $\widehat{A}_\ell^{\mathrm{pr}} = \widehat{U}$ (◥)
16: **function** GETCORTH($L_{\ell-1},W_\ell,W_{\ell+1},R_{\ell+2},A_\ell,\Lambda_\ell,{}_{\mathrm{B}_{\ell+1}},\widehat{A}_\ell^{\mathrm{pr}}$)
17:      Compute $L_\ell^{\mathrm{pr}} = (\widehat{A}_\ell^{\mathrm{pr}})^\dagger L_{\ell-1}W_\ell A_\ell$
18:      Compute $C_{\ell+1}^{\mathrm{tmp}} = L_\ell^{\mathrm{pr}}\Lambda_\ell B_{\ell+1}W_{\ell+1}R_{\ell+2}$
19:      Compute $C_{\ell+1}^{\mathrm{orth}} = C_{\ell+1}^{\mathrm{tmp}} - C_{\ell+1}^{\mathrm{tmp}}B_{\ell+1}^\dagger B_{\ell+1}$
20:      **return** $C_{\ell+1}^{\mathrm{orth}}$
21: **end function**
22: (Fig. S-2(d)): SVD $C_{\ell+1}^{\mathrm{orth}} = \widetilde{U}\,\widetilde{S}\,\widetilde{V}^\dagger$ and truncate all except the largest $\widetilde{D}$ singular values: $\widetilde{U}\,\widetilde{S}\,\widetilde{V}^\dagger \overset{\mathrm{trunc}}{\Rightarrow} \widetilde{u}\,\widetilde{s}\,\widetilde{v}^\dagger$
23: Compute $\widetilde{A}_\ell^{\mathrm{tr}} = \widehat{A}_\ell^{\mathrm{pr}}\widetilde{u}$ (◥)

TABLE I. Pseudocode for computing the truncated complement $\widetilde{A}_\ell^{\mathrm{tr}}$ using shrewd selection.

and singular vectors. We here write bond dimensions with $*$, indicating numbers of multiplets (not states), since these determine computational complexities and truncation thresholds and are the quantities shown in the figures. Relations such as $\widehat{D} = D'w$, exact for Abelian symmetries where all symmetry multiplets have dimension 1, become approximate, $\widehat{D}^* \simeq D'^*w^*$, when written for non-Abelian symmetries.

B. Options for preselection and final selection

The key idea of CBE is to expand the isometry A_ℓ (◥), whose image (the kept space) initially has dimension D_{i}^*, through a direct sum with a so-called truncated comple-

ment, an isometry with image dimension $\widetilde{D}^* (< D_{\mathrm{i}}^*)$. The latter is obtained through a suitable truncation of the full complement, $\overline{A}_\ell$(◥), whose image (the discarded space) initially has dimension $\overline{D}^* \simeq D_{\mathrm{i}}^*(d^*-1)$. Figure 1 defines three cost functions, $\mathcal{C}_1$, $\mathcal{C}_2$ and $\mathcal{C}_3$, relevant for constructing the truncated complement. The optimal choice for the truncated complement, to be denoted $\overline{A}_\ell^{\mathrm{tr}}$(◥) here, is obtained by exact minimization of $\mathcal{C}_1$, but that requires 2s costs. Therefore, the main text proposes an alternative two-step strategy, requiring only 1s costs. First perform preselection: obtain a preselected complement $\widehat{A}_\ell^{\mathrm{pr}}$ (◥), with image dimension $\widehat{D}^* \simeq D'^*w^*$, through minimization of $\mathcal{C}_2$ (Fig. S-2, steps (a-c)). Then perform final selection: obtain the desired truncated complement, denoted $\widetilde{A}_\ell^{\mathrm{tr}}$ (◥), through minimization of $\mathcal{C}_3$ (Fig. S-2, step (d)).

The minimization of the cost functions $\mathcal{C}_1$ and $\mathcal{C}_3$ defined in Fig. 1 involves performing SVDs and truncations of the following two tensors, respectively:

$$\overline{M}^{\mathrm{full}} = \text{(diagram)} = \text{(diagram)} \simeq \text{(diagram)}, \quad \text{(S1a)}$$

$$\widehat{M}^{\mathrm{pr}} = \text{(diagram)} = \text{(diagram)} \simeq \text{(diagram)}. \quad \text{(S1b)}$$

They differ only in one ingredient, $\overline{A}_\ell^\dagger$(◢) vs. $\widehat{A}_\ell^{\mathrm{pr}\dagger}$(◢), but since these have vastly different open leg dimensions, $\overline{D}^*$ vs. $\widehat{D}^*$, the SVD costs differ vastly too, 2s vs. 1s. The isometries $\overline{u}$(◗) or $\widetilde{u}$(◗) obtained from the above SVDs and truncations, both with image dimension $\widetilde{D}^*$, can then be used to construct $\overline{A}_\ell^{\mathrm{tr}}$(◥) or $\widetilde{A}_\ell^{\mathrm{tr}}$(◥) as follows:

$$\overline{A}_\ell^{\mathrm{tr}} \ / \ D^* \searrow \widetilde{D}^* \ = \ \overline{A}_\ell \overline{u}, \quad \text{(S2a)}$$

$$\widetilde{A}_\ell^{\mathrm{tr}} \ / \ D^* \searrow \widetilde{D}^* \ = \ \widehat{A}_\ell^{\mathrm{pr}}\widetilde{u}. \quad \text{(S2b)}$$

Both $\overline{A}_\ell^{\mathrm{tr}}$(◥) and $\widetilde{A}_\ell^{\mathrm{tr}}$(◥) have image dimension $\widetilde{D}^*$; the former serves as reference (equivalent to using no preselection, $D'^* = D^*$, the latter is an approximation to the former. An even cruder approximation is obtained if one performs preselection without final selection: for that, truncate $\widehat{U} \simeq \widehat{u}$ in step (c) of Fig. S-2 using $\widehat{D}^* = \widetilde{D}^*$ (not D'^*w^*), and use the resulting isometry, $\widehat{A}_\ell^{\mathrm{tr}}$(◥) $= \widehat{u}$, as approximation for $\overline{A}_\ell^{\mathrm{tr}}$(◥), omitting step (d) altogether:

$$\widehat{A}_\ell^{\mathrm{tr}} \ / \ D^* \searrow \widetilde{D}^* \ = \ \widehat{u}. \quad \text{(S2c)}$$

To illustrate the effects of preselection, we will compare four settings: (I) the reference, $\overline{A}^{\mathrm{tr}}$(◥); or three

versions of preselection with $D'^* = D_f^*/w^*$, $0.1D_f^*/w^*$ or 1, to be called (II) *moderate*, (III) *severe* or (IV) *extreme* preselection, respectively, all followed by final selection, yielding three versions of $\widetilde{A}^{\mathrm{tr}}(\searrow)$. Here, D_f^* is the final bond dimension after an update, obtained by expanding the bond from dimension D_i^* to $D_i^* + \widetilde{D}^* = D_f^*(1+\delta)$, then trimming it back to D_f^*. To illustrate the importance of final selection we also consider a fifth setting: (V) moderate preselection and $\widehat{U} \simeq \widehat{u}$ truncation, without final selection, yielding $\widehat{\widetilde{A}}_\ell^{\mathrm{tr}}(\searrow)$.

In the main text, we recommended performing CBE updates using moderate preselection followed by final selection. We showed (Fig. 4(a)) that this yields equally fast convergence per sweep for the GS energy as 2s update. Below, we elucidate why moderate preselection works so well. To this end, we analyze various singular value spectra (Sec. S-1 C) and left singular vectors (Sec. S-1 D), with $D_f^* = D_{\max}^*$ fixed. We also show that severe and even extreme preselection likewise yield full convergence, albeit at slower rates, by comparing various convergence rates per sweep while increasing D_f^* (Sec. S-1 E).

C. Singular values

We start by comparing the singular values of the tensors $\overline{M}^{\mathrm{full}}$ and $\widehat{M}^{\mathrm{pr}}$, i.e. the diagonal elements of the diagonal matrices $\overline{S}(\diamond)$ and $\widetilde{S}(\diamond)$ in Eqs. (S1), denoted $\overline{s}_i$ ($i = 1, \ldots, \overline{D}^*$) and $\widetilde{s}_i$ ($i = 1, \ldots, \widehat{D}^*$), respectively. They differ strongly in number, but if the largest $\widetilde{s}_i$ values roughly mimic the largest $\overline{s}_i$ values, serving as reference, then preselection is "efficient", in that it yields essentially optimal results for the dominant singular values.

Figure S-3 compares $\overline{s}_i$ (grey) and $\widetilde{s}_i$ (orange: moderate or brown: severe preselection) for bond $\ell = \mathscr{L}/2$ of both the least and most challenging models considered in this work: (a,b) the free fermion chain of Fig. 3, and (c,d) the KHH cylinder of Fig. S-10. Here, we consider the case that D_f^* has reached $D_{\max}^*$ and is not grown further, and hence choose $\widetilde{D}^* = D_f^* \delta$ (with $\delta = 0.1$), so that $D_i^* = D_f^*$.

For (II) moderate preselection ($D'^* = D_f^*/w^*$) the $\widetilde{s}_i$ (orange) and $\overline{s}_i$ (grey) values coincide quite well in the range where they are largest, and eventually drift apart as they get smaller. Especially for the largest $\widetilde{D}^* = D_f^* \delta$ ($\delta = 0.1$) singular values, i.e. the ones that survive final selection and are used for bond expansion, the agreement is rather good (Figs. S-3 (b,d)). This is a very important finding—it indicates that moderate preselection is efficient. By contrast, (III) severe preselection ($D'^* = 0.1D_f^*/w^*$), shown only in Fig. S-3 (a,b), yields $\overline{s}_i$ (brown) values that differ substantially from their $\widetilde{s}_i$ (grey) counterparts, even in the range of largest values. Therefore, in this case preselection is too severe to be very efficient.

(We note in passing that when using severe preselection, the corresponding final selection involves almost no further
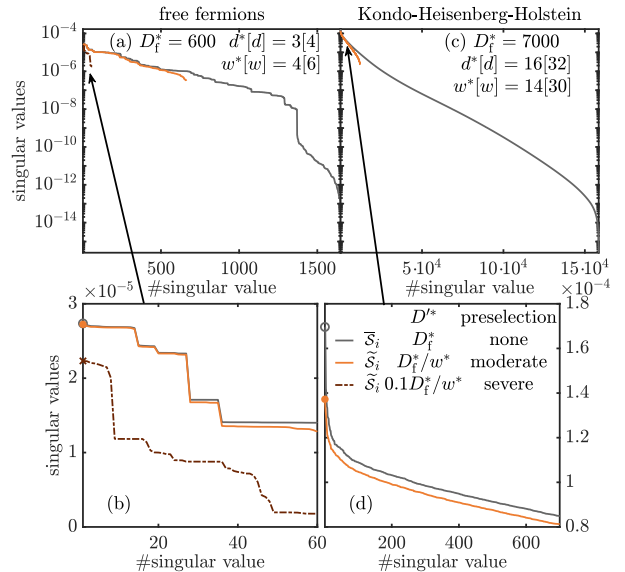
FIG. S-3. Comparison of singular values for three truncation settings (I-III) defined in Sec. S-1 B: the singular values $\overline{s}_i$ of the tensor $\overline{M}^{\mathrm{full}}$, obtained (I) without preselection (reference, grey); and the singular values $\widetilde{s}_i$ of the tensor $\widehat{M}^{\mathrm{pr}}$, obtained using (II) moderate preselection ($D'^* = D_f^*/w^*$, orange) and (III) severe preselection ($D'^* = 0.1D_f^*/w^*$, brown), all followed by final selection with $\widetilde{D}^* = 0.1D_f^*$. They are all computed for bond $\ell = \mathscr{L}/2$ of (a,b) the free fermion chain of Fig. 3, and (c,d) the KHH cylinder of Fig. S-10(d). (b,d) Subsets of the data from (a,c), shown on linear scales, focusing on the range of the largest $\widetilde{D}^* = D_f^* \delta$ singular values $\overline{s}_i$ and $\widetilde{s}_i$ (with $\delta = 0.1$). This range contains all singular vectors comprising the truncated complement $\widetilde{A}^{\mathrm{tr}}(\searrow)$ obtained after final selection and used for bond expansion. The singular values found with moderate (orange) or no (grey) preselection agree rather well, but those from severe preselection (brown) differ significantly from these.

truncation, since $\widehat{D}^*$ (given by $\simeq D'^* w^* = 0.1D^*$) is almost equal to $\widetilde{D}^*$ (given by $D^*\delta$). For the present example, we have $\widehat{D}^* = 63$ and $\widetilde{D}^* = 60$.)

In Figs. S-3 (a,b), the length of the grey vs. orange lines visually illustrates the main rationale for our CBE strategy: the number of $\overline{s}_i$ values is generally very much larger than needed for successful bond expansion, $\overline{D}^* \gg \widetilde{D}^*$. Thus, the 2s full complement subspace (obtained by excluding the 1s variational space from the 2s variational space), is likewise much larger than needed for energy minimization—only a small subspace thereof really matters. CBE aims to identify parts of that small subspace; shrewd selection offers a cheap way of doing so, yielding a notable speedup when computing the truncated complement.

FIG. S-4. Comparison of weights (S3) with which reference singular vectors $\overline{\mathcal{S}}_i$ from $\overline{A}_\ell^{\mathrm{tr}}$ (◥) are supported in truncated spaces obtained with three truncation settings (II-IV) defined in Sec. S-1 B: $\widetilde{w}_i$ gives the weight of $|\overline{\mathcal{S}}_i\rangle$ in span$\{|\widetilde{\mathcal{S}}_j\rangle\}$, the image of $\widetilde{A}_\ell^{\mathrm{tr}}$ (◥), computed through shrewd selection, using either (II) moderate (orange dots) or (III) severe (brown crosses) preselection; and $\widehat{w}_i$ gives the weight of $|\overline{\mathcal{S}}_i\rangle$ in span$\{|\widehat{\mathcal{S}}_j\rangle\}$, the image of $\widehat{A}_\ell^{\mathrm{pr}}$ (◥), computed using (IV) moderate preselection without final selection (pink circles). Both panels show the same data, on (a) a linear and (b) a log scale.

D. Singular vectors

We next turn to a comparison of singular vectors to further quantify the benefits of using (II) moderate rather than (III) severe preselection, and of using final selection.

For the latter purpose, we consider a truncation scheme (V) involving moderate preselection but no final selection: after the minimization of the cost function $\mathcal{C}_2$ (see Fig. S-2(c)), we directly truncate $\widehat{U}\,\widehat{S}\,\widehat{V}^\dagger \simeq \widehat{u}\,\widehat{s}\,\widehat{v}^\dagger$ from $\widehat{D}^*$ to $\widetilde{D}^*$, and define the truncated complement as $\widehat{A}_\ell^{\mathrm{tr}} = \widehat{u}$ (◥), with singular vectors $|\widehat{\mathcal{S}}_i\rangle$.

To compare singular vectors we compute the weights

$$\widetilde{w}_i = \sum_{j=1}^{\widetilde{D}^*} |\langle \widetilde{\mathcal{S}}_j | \overline{\mathcal{S}}_i \rangle|^2 = \quad, \tag{S3a}$$

$$\widehat{w}_i = \sum_{j=1}^{\widetilde{D}^*} |\langle \widehat{\mathcal{S}}_j | \overline{\mathcal{S}}_i \rangle|^2 = \quad. \tag{S3b}$$

Here, $\widetilde{w}_i$ is the weight with which a singular vector $|\overline{\mathcal{S}}_i\rangle$ (ordered by size of corresponding singular value) from the image of $\overline{A}_\ell^{\mathrm{tr}}$ (◥) is supported in the subspace span$\{|\widetilde{\mathcal{S}}_j\rangle\}$, the image of $\widetilde{A}_\ell^{\mathrm{tr}}$ (◥); and $\widehat{w}_i$ gives its weight in span$\{|\widehat{\mathcal{S}}_j\rangle\}$, the image of $\widehat{A}_\ell^{\mathrm{tr}}$ (◥). In less technical

terms, the weights characterize how well reference singular vectors can be represented in these truncated spaces.

These weights are shown in Fig. S-4 for the free fermion data corresponding to Fig. S-3(a). For (II) moderate preselection plus final selection ($\widetilde{w}_i$, orange dots), all weights are close to one. Thus, this truncation scheme almost perfectly captures that part of the 2s subspace most relevant for minimizing the GS energy. By contrast, for both (III) severe preselection plus final selection ($\widetilde{w}_i$, brown crosses) and (V) moderate preselection without final selection ($\widehat{w}_i$, pinc circles), most weights are significantly smaller than 1; four are numerically zero. Thus, both these schemes discard a significant part of the space relevant for minimizing the GS energy.

The above analysis illustrates that final selection includes valuable additional information for the $\widehat{D}^* \to \widetilde{D}^*$ truncation, which is not available when truncating $\widehat{S}$ from $\widehat{D}^* \to \widetilde{D}^*$ directly after preselection. This is because the central MPO bond, open during preselection, is *closed* during final selection (compare their cost functions, $\mathcal{C}_2$ and $\mathcal{C}_3$ in Fig. 1). Closing the central MPO bond, as appropriate for $H_\ell^{2s}\psi_\ell^{2s}$, brings in additional information. The SVD in step (d) of Fig. S-2 involves an additional rotation (encoded in $\widetilde{u}$) before the $\widehat{D}^* \to \widetilde{D}^*$ truncation, incorporating this additional information.

E. Convergence rate per sweep

The weights obtained for severe preselection ($D'^* = \delta D^*/w^*$) in Fig. S-4 pose the question whether D'^* can be too small to give converged results. In this case, preselection would not only be inefficient, but actually unsuccessful. To explore this, Fig. S-5 compares the CBE–DMRG convergence rate for several choices of D'^*, corresponding to (II) moderate (red), (III) severe (green), and (IV) extreme (blue) preselection.

As expected, convergence slows down with smaller D'^*. Remarkably, however, once convergence has been reached, the converged results agree (even for $D'^* = 1$, a truly extreme choice!). In this sense, the preselection strategy is robust—converged results don't depend on D'^*. Note, though, that the computation time does not depend significantly on D'^* (provided it is clearly smaller than D^*). On the other hand, it obviously does depend on the number of sweeps, and the time per sweep can be very large for expensive models. Therefore, D'^* should not be chosen too small, to avoid a time-costly increase in the number of sweeps.

To summarize: a bond expansion is *efficient*, yielding a significant reduction in GS energy and therefore quick convergence, if D'^* is large enough that the "most important" states $|\overline{\mathcal{S}}_i\rangle$, i.e. those with the largest singular values $\overline{s}_i$, are well represented in the expanded space, i.e. have weights $\widetilde{w}_i \simeq 1$.

FIG. S-5. Influence of preselection on CBE–DMRG convergence rate, for a half-filled free-fermion chain ($\mathscr{L} = N = 20$). The GS energy is plotted as a function of the number of half-sweeps, n_s, for three values of D'^*, used for preselection. We start from a $D_i^* = 1$ valence bond state, set $\delta = 0.1$, increase D^* using $\alpha = 1.1$ until $D^* = 300$ is reached, and continue sweeping with $\alpha = 1$ thereafter.

However, even if D'^* is so small that most of the important states $|\overline{\mathcal{S}}_i\rangle$ are represented with small weights, a bond expansion can nevertheless be *successful*, in the sense of adding some relevant new states, provided that these weights are non-zero, $\widetilde{w}_i \neq 0$. The reason is that the states $|\widetilde{\mathcal{S}}_i\rangle$ added to $A_\ell(\text{≠})$ contain information about the optimal states $|\overline{\mathcal{S}}_i\rangle$ with finite $\widetilde{w}_i$, i.e. those $|\overline{\mathcal{S}}_i\rangle$ are not orthogonal to the expanded kept space. As long as this information is available, subsequent 1s updates will optimize the kept sector accordingly; the states $|\widetilde{\mathcal{S}}_i\rangle$ just offer a somewhat less optimal starting point for that than the $|\overline{\mathcal{S}}_i\rangle$.

Note that it is of utmost importance for successful bond expansion that information on the *most important* $|\overline{\mathcal{S}}_i\rangle$ is included. Since only a small set of states is in the end used for expansion, the most important states must be prioritized; otherwise, inferior information is included in the kept space, rendering the bond expansion unsuccessful: Subsequent 1s updates may then optimize towards a suboptimal kept sector, as the optimal one may not be available to the 1s update, e.g. due to symmetry constraints. The energy will still decrease due to the unsuccessful bond expansion plus 1s update, but not as much as if the correct information on the most important $|\overline{\mathcal{S}}_i\rangle$ is correctly included. The result will be a suboptimal final state at the desired finite bond dimension $D_{\max}^*$, i.e. we have wasted resources.

Fig. S-5 shows that CBE–DMRG correctly includes information on the most optimal states when expanding the bond, independent of D'^*. Even with extreme preselection ($D'^* = 1$), it does not get stuck with some sub-optimal state at $D_{\max}^* = 300$, but eventually converges (albeit slowly) to the same GS as found with larger choices of $D_{\max}$.
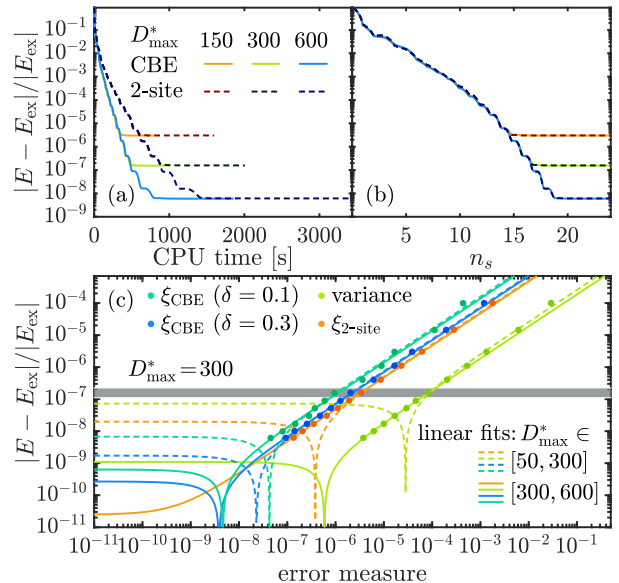
FIG. S-6. Benchmark results for free fermions. Relative error in GS energy vs. (a) CPU time xt and (b) number of half-sweeps n_s, for CBE and 2s DMRG. E_{ex} is the exact GS energy. (c) Quality of linear extrapolation of the GS energy using various error measures. Dashed (solid) lines show linear fits to data points lying on or above (on or below) the grey bar, computed using $D_{\max}^* \leq 300$ (≥ 300), representing intermediate (high) accuracy calculations; when these lines touch zero, the extrapolated error changes sign.

S-2. SIMPLE BENCHMARK: FREE FERMIONS

In this section, we benchmark CBE–DMRG for free fermions in one dimension (1D). The main purpose is to evaluate the validity of the CBE discarded weight as an error measure usable for extrapolation on an exactly solvable model and compare it to other established error measures. All CPU time measurements were done on a single core of an Intel Core i7-9750H processor.

Consider a chain of spinful free fermions, exactly solvable but non-trivial for DMRG, with Hamiltonian $H_{\text{FF}} = -\sum_{i=1}^{\mathscr{L}-1} \sum_\sigma \left(c_{i\sigma}^\dagger c_{i+1\sigma} + \text{h.c.} \right)$ and $\mathscr{L} = 100$ sites. We exploit $\text{U}(1)_{\text{ch}} \otimes \text{SU}(2)_{\text{sp}}$ charge and spin symmetry, with local dimension $d^*[d] = 3[4]$. The MPO dimension is $w^*[w] = 4[6]$. We seek the GS in the sector with total spin $S = 0$, at half-filling, with particle number $N = \mathscr{L}$.

Figure S-6(a) plots the relative error in energy vs. CPU time for different $D_{\max}^*$ for both CBE and 2s schemes; Fig. S-6(b) plots it vs. the number of half-sweeps n_s. While convergence with n_s is comparable for CBE and 2s, CBE requires less CPU time than 2s by a factor of $\simeq 2$. (This speedup factor is less than $d^* = 3$, since d^* is quite small and steps not involving the iterative eigensolver have the same numerical cost for both CBE and 2s schemes.)

Figure S-6(c) shows linear-fit extrapolations of the energy in terms of the discarded weight ξ and the 2s variance

(the latter computed following Ref. [28]). The quality of the extrapolations is comparable for all considered methods: they all reduce the error in energy by roughly one order compared to the most accurate data point considered, as expected [25, 28]. The error is smaller for $\delta = 0.3$ than for $\delta = 0.1$, and its dependence on discarded weight is slightly less noisy (though this hardly affects the extrapolation).

S-3. COMPARISON OF CBE TO DMRG3S

In this section, we provide a comparison between DMRG3S and CBE–DMRG. First, we formulate DMRG3S in terms of the kept-discarded (KD) space language developed by us in Ref. 27 and also used in this paper. Based on that, we then discuss to what extent the bond-expansion term in DMRG3S is different to that occurring in CBE-DMRG. We then compare the performance of DMRG3S and CBE–DMRG based on two models.

A. DMRG3S in KD language

In case of a right-to-left sweep, DMRG3S expands and truncates the right isometry as follows:

$$(S4)$$

where ◀ represents a unitary, in analogy to Eq. (6) in the main text. Here, $C_{\ell+1}$ is direct-summed with the expansion term multiplied by a mixing parameter α, then (a) singular value decomposed and (b) truncated to bond dimension D, yielding the new isometry $B_{\ell+1}^{3S}$. Finally in steps (c) and (d), C_ℓ and H_ℓ^{1s} are "expanded", respectively, similar to CBE (DMRG3S first updates $C_{\ell+1}$ and then uses the mixing expansion of Eq. (S4) to expand $B_{\ell+1}$; by contrast, CBE first expands A_ℓ via Eq. (9), then updates $C_{\ell+1}$). Note that in step (c), $C_\ell^{3S,i}$ needs to be normalized explicitly because

$$(S5)$$

i.e. the kept space spanned by the old isometry $B_{\ell+1}$ is not fully contained in the new one, $B_{\ell+1}^{3S}$, since part of the kept space has been truncated. Finally, C_ℓ^{3S} is

updated with the GS of $H_\ell^{1s,3S}$ obtained with an iterative eigensolver (Lanczos in our case), initialized with $C_\ell^{3S,i}$.

Our CBE strategy differs from DMRG3S in the following ways:

(i) When constructing the expansion term, CBE considers $H_\ell^{2s}\psi_\ell^{2s}$, i.e. the action of the full 2s Hamiltonian on the 2s wavefunction. By contrast, DMRG3S only considers part of $H_\ell^{2s}\psi_\ell^{2s}$ (the right "half" in the right-to-left sweep discussed here). We found however that considering $H_\ell^{2s}\psi_\ell^{2s}$ fully is crucial to not experience convergence issues. Note that the expansion term in DMRG3S is more heuristic than that in CBE and does not have the interpretation of an effective Hamiltonian acting on a wavefunction.

(ii) CBE projects $H_\ell^{2s}\psi_\ell^{2s}$ fully to the DD sector, i.e. the image of the orthogonal complements $\overline{A}_\ell \otimes \overline{B}_{\ell+1}$ (▼ ⊗ ▶). This ensures that the kept space is not truncated during the bond expansion and crucially, the energy of the variational wavefunction remains the same. By contrast, DMRG3S does not involve any DD or D projections. Thus, part of the K sector is usually truncated during the DMRG3S bond expansion, raising the energy of the variational wavefunction. Thus, CBE–DMRG is fully variational (bond expansion does not lead to a less optimal wavefunction) while DMRG3S is not (see also the discussion of Fig. 1 of Ref. 26).

(iii) Because DMRG3S changes the variational wavefunction by truncating part of the K sector, the weight of the expansion term in DMRG3S has to be controlled by a heuristic mixing factor α to ensure the variational energy is not raised too much. This mixing factor has to be carefully adapted during the calculation to ensure reliable convergence and is model dependent (see Ref. 26 Sec. VI). By contrast, there is no such mixing parameter in CBE. In CBE, there is a parameter δ which controls the amount of bond expansion. We found however that CBE–DMRG is not at all sensitive to the value of δ and most important, δ is not model dependent. Indeed, we have set $\delta = 0.1$ in our CBE calculations independent of the model. Further, δ remains constant during the calculation.

Note that if 3S would include projections to the D sector and would not truncate part of the kept space during expansion, it would be similar to CBE without preselection and final selection. However, leaving out preselection is expensive while leaving out final selection is inefficient (see Sec. S-1).

B. Results

We now benchmark the accuracy and speed of DMRG3S against that of CBE–DMRG. For that, we use three models: a 1D Hubbard-Holstein model, spinful free fermions on a short 4-leg cylinder and a free fermion chain with only next-nearest neighbor hopping. All CPU time measurements were done on a single core of an Intel Core

FIG. S-7. Error in energy for the Hubbard-Holstein (HH) model versus (a) CPU time and (b) number of half-sweeps n_s, computed using CBE–DMRG (solid) or DMRG3S (dashed). E_0 is obtained via ξ-extrapolation of calculations done at $D^* \geq 1000$.

i7-9750H processor.

Hubbard-Holstein model.— We start our comparison with the 1D Hubbard-Holstein model [32–36], with Hamiltonian

$$H_{\mathrm{HH}} = -\sum_{i\sigma}\left(c_{i\sigma}^{\dagger}c_{i+1\sigma} + \mathrm{h.c.}\right) + U\sum_{i} n_{i\uparrow}n_{i\downarrow} \quad (\mathrm{S6})$$
$$+ \omega_{\mathrm{ph}}\sum_{i} b_{i}^{\dagger}b_{i} + g\sum_{i}\left(n_{i\uparrow} + n_{i\downarrow} - 1\right)\left(b_{i}^{\dagger} + b_{i}\right).$$

We chose $U = 0.8$, $g = \sqrt{0.2}$, $\omega_{\mathrm{ph}} = 0.5$, $\mathscr{L} = N = 100$, total spin $S = 0$, and restrict the maximum local number of excited phonons to $N_{\mathrm{ph}}^{\max} = 3$. Both CBE–DMRG and DMRG3S are initialized with the same $D^* = 1$ MPS with uniform charge distribution and the bond dimension is grown by a factor of $\sqrt{2}$ every half sweep, i.e. it is doubled every sweep. The DMRG3S mixing parameter is adapted according to the prescription described in Ref. 26, Sec. VI.

Figures S-7 (a) and (b) show a comparison between the error in energy versus CPU time and number of sweeps, respectively, for different bond dimensions. As a function of CPU time, the error in energy of DMRG3S initially converges at the same rate as CBE–DMRG. Subsequently, however, the convergence of 3S slows down compared to CBE, ultimately requiring significantly more CPU time to reach the final converged result. Further, the final converged 3S result is not as accurate as the CBE result, though this is more severe at small D^* than at large D^*. At $D^* = 150$, the relative error from 3S is about 1.3 times that of CBE.

Spinful free fermion cylinder.— For our next benchmark, we use free fermions on a $\mathscr{L}_x \times \mathscr{L}_y = 10 \times 4$ cylinder, described by $H_{\mathrm{cyl}} = -\sum_{\langle \boldsymbol{\ell}, \boldsymbol{\ell}' \rangle, \sigma}\left(c_{\boldsymbol{\ell}\sigma}^{\dagger}c_{\boldsymbol{\ell}'\sigma} + \mathrm{h.c.}\right)$. We search for the GS with $N = \mathscr{L}_x \cdot \mathscr{L}_y$ and $S = 0$. Again, we start with a $D^* = 1$ state with uniform charge distribution and increase the bond dimension by a factor of $\sqrt{2}$ every half-sweep.

Figures S-8 (a) and (b) show a comparison of the error in energy versus CPU time and the number of sweeps obtained with both CBE and 3S, respectively. Again,
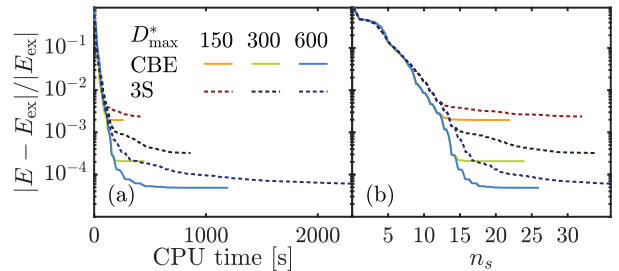
FIG. S-8. Error in energy for spinful free fermions on a 10×4 cylinder versus (a) CPU time and (b) number of half-sweeps n_s. E_{ex} is the exact ground-state energy.

CBE and 3S initially converge at the same rate w.r.t. CPU time, but DMRG3S eventually slows down and takes longer to reach final convergence compared to CBE. Further, for all considered bond dimensions, 3S converges now to a noticeably larger error, about 1.2 to >1.5 times that of CBE.

Next-nearest neighbor free fermion chain.— As a last model for our comparison, we choose free fermions on a chain with only next-nearest neighbor hopping, described by $H_{\mathrm{nnn}} = -\sum_{\ell=1}^{\mathscr{L}-2}(c_{\ell}^{\dagger}c_{\ell+2} + \mathrm{h.c.})$. Choosing $\mathscr{L} = 100$ and exploiting $\mathrm{U}(1)_{\mathrm{ch}}$ symmetry, we initialize DMRG with a half-filled product state consisting of a succession of two occupied sites followed by two empty sites.

As shown in Fig. S-9(a), this rather simple model initialized with the product state described above poses a serious challenge to 2s DMRG, which does not converge. The reason for the failure of 2s DMRG is that the initial state has $\Delta_E^{1\perp} = 0$ and $\Delta_E^{2\perp} = 0$ (c.f. Eq. (8)), implying that $H_{\ell}^{2\mathrm{s}}\psi_{\ell}^{2\mathrm{s}}$ is parallel to $\psi_{\ell}^{2\mathrm{s}}$. From the perspective of 2s DMRG, the initial state is therefore an eigenstate.

By contrast, both DMRG3S and CBE–DMRG do converge, with CBE–DMRG again reaching convergence faster in terms of number of sweeps and converging to a sightly lower energy than DMRG3S. During the initial few sweeps, CBE–DMRG lowers the energy somewhat
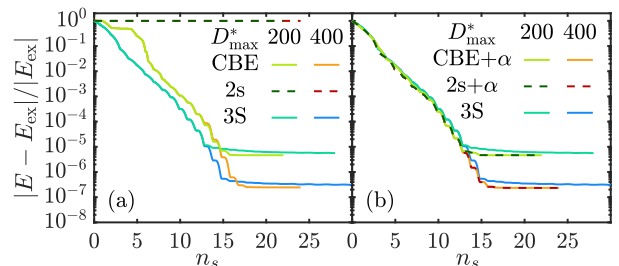
FIG. S-9. Error in energy for the next-nearest neighbor free fermion chain, computed using CBE and 2s, (a) without mixing, and (b) with mixing ($\alpha = 0.1$), during the initial 14 half-sweeps. DMRG3S results in (a) and (b) are the same data. E_{ex} is the exact ground-state energy.

more slowly than DMRG3S, reflecting the close relation between CBE–DMRG and 2s DMRG. In contrast to the latter, however, CBE–DMRG eventually does converge. The reason is that CBE expands the MPS bond from D to $D + \widetilde{D}$ even if the projection of $H_\ell^{2s}\psi_\ell^{2s}$ to DD yields zero — indeed, final selection (Fig. 2(d)) generates $\widetilde{D}$ additional states even if some or all of the associated singular values (from $\widetilde{s}$ in Fig. 2(d)) are numerically zero. This enlarges the kept space from D to $D + \widetilde{D}$, such that eventually $\Delta_E^{1\perp}$ becomes nonzero and the energy can be lowered during the CBE 1s update.

As suggested in Ref. 7, Section 3.1, adding noise terms in the spirit of DMRG3S or density matrix perturbation of Ref. 25 during the initial few sweeps can help 2s DMRG to converge. The same is true for CBE–DMRG, which also struggles during the initial sweeps in the present case, as mentioned above. To demonstrate this, we therefore performed 2s and CBE calculations combined with DMRG3S mixing, dubbed 2s+α and CBE+α, respectively. (For CBE+α, first the CBE expansion of A_ℓ according to Eq. (9) is used, then $C_{\ell+1}$ is updated, and finally a mixing expansion of $B_{\ell+1}$ according to Eq. (S4) is used.) We choose $\alpha = 0.1$ during the initial 7 sweeps (i.e. 14 half-sweeps) and then continue without mixing. Note that we do not need to fine-tune α, in contrast to DMRG3S. The results of this strategy are displayed in Fig. S-9(b), which shows that both 2s+α and CBE+α converge similarly w.r.t. the number of sweeps.

Summary of CBE to DMRG3S comparison.— CBE generically converges significantly faster w.r.t. number of sweeps than 3S but takes about the same CPU time per sweep. This leads to overall significantly faster convergence of CBE compared to 3S. Further, the accuracy of CBE is generically better than that of 3S at the same bond dimension, meaning that CBE uses variational resources more efficiently than 3S. This seems to be especially the case for more challenging models where single-site methods provide the most benefit due to reduced computational demands. An exception are situations where 2s DMRG fails entirely. In such cases, the convergence during the initial few sweeps is significantly slower for CBE than DMRG3S (though CBE eventually catches up, ultimately reaching a lower final energy than DMRG3S). The initial CBE convergence can be sped up, if desired, by including some mixing during the first few sweeps, using a mixing parameter that need not be fine-tuned. This strategy is the one we would recommend as standard practice when dealing with challenging models.

S-4. KONDO-HEISENBERG CYLINDERS

In this section, we provide supplementary information on the two most challenging models considered in this work, both defined on a 4-leg cylinder: the Kondo-Heisenberg (KH) model discussed in the main text, where

we presented evidence for Fermi surface (FS) reconstruction; and the Kondo-Heisenberg-Holstein (KHH) model, included here to demonstrate the feasibility of using CBE for tackling truly complex models.

The KH model is relevant for heavy-fermion materials, which consist of itinerant conduction electrons, hybridizing with localized f orbitals [37]. At low energies, only the spin degree of freedom of the f electrons remain, describable by a KH model,

$$H_{\mathrm{KH}} = - \sum_{\sigma=\uparrow,\downarrow} \sum_{\langle \boldsymbol{\ell},\boldsymbol{\ell}' \rangle} \left(c_{\boldsymbol{\ell}\sigma}^\dagger c_{\boldsymbol{\ell}'\sigma} + h.c. \right) \tag{S7}$$
$$+ J_{\mathrm{K}} \sum_{\boldsymbol{\ell}} \boldsymbol{S}_{\boldsymbol{\ell}} \cdot \boldsymbol{s}_{\boldsymbol{\ell}} + J_{\mathrm{H}} \sum_{\langle \boldsymbol{\ell},\boldsymbol{\ell}' \rangle} \boldsymbol{S}_{\boldsymbol{\ell}} \cdot \boldsymbol{S}_{\boldsymbol{\ell}'} \, .$$

Here, $c_{\boldsymbol{\ell}\sigma}^\dagger$ is a fermionic creation operator at site $\boldsymbol{\ell} = (x, y)$ with spin σ, $\boldsymbol{s}_{\boldsymbol{\ell}} = \frac{1}{2} \sum_{ss'} c_{\boldsymbol{\ell}s}^\dagger \boldsymbol{\sigma}_{ss'} c_{\boldsymbol{\ell}s'}$ is the corresponding electron spin operator and $\boldsymbol{S}_{\boldsymbol{\ell}}$ the spin operator of a spin-$\frac{1}{2}$ local moment, all for site $\boldsymbol{\ell}$.

The KHH model is obtained from the KH model by additionally including Holstein phonons, motivated by experimental data suggesting that phonons may play a role in heavy-fermion physics [38]:

$$H_{\mathrm{KHH}} = H_{\mathrm{KH}} + \omega_{\mathrm{ph}} \sum_{\boldsymbol{\ell}} b_{\boldsymbol{\ell}}^\dagger b_{\boldsymbol{\ell}} + g \sum_{\boldsymbol{\ell}\sigma} (n_{\boldsymbol{\ell}\sigma} - \tfrac{1}{2})(b_{\boldsymbol{\ell}}^\dagger + b_{\boldsymbol{\ell}}) \, . \tag{S8}$$

Here, $b_{\boldsymbol{\ell}}^\dagger$ is phonon creation operator for site $\boldsymbol{\ell}$. To deal with the infinite local phonon Hilbert space, we restrict the maximum number of local phonon excitations to $N_{\mathrm{ph}}^{\max}$ (specified below) in our DMRG calculations.

In Sec. S-4 A we first show stable convergence of CBE–DMRG for the KHH model on a 10×4 cylinder. Then, in Sec. S-4 B, we describe how to extract information on the FS in 40×4 KH cylinders from ground states computed with CBE–DMRG. Finally, in Sec. S-4 C, we show that our KH cylinder results are consistent with Luttinger's sum rule, relating the electron density to the FS volume.

A. Kondo-Heisenberg-Holstein cylinders: convergence

Our intention is to show that CBE–DMRG is stable for the KHH model, which is at the edge of what is possible with current DMRG techniques. To check the applicability of CBE–DMRG to the KHH model on a 10×4 cylinder, we use Kondo coupling $J_{\mathrm{K}} = 5$, Holstein coupling $g = 0.5$ to the phonons and optical phonon frequency $\omega_{\mathrm{ph}} = 0.5$. We considered two different values for $N_{\mathrm{ph}}^{\max} \in \{0, 3\}$ and the Heisenberg coupling $J_{\mathrm{H}} \in \{0, 0.5\}$.

We performed GS searches for $N = \mathscr{L}(1 + \frac{1}{4}) = 50$ and $S = 0$, i.e. at 25% electron doping. Figure S-10 shows the energy error vs. ξ for four parameter combinations
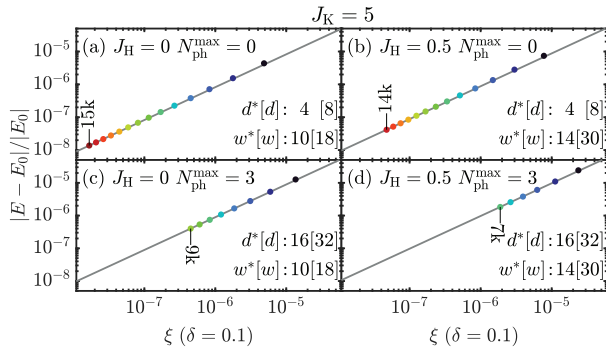
FIG. S-10. Error in GS energy versus discarded weight for the Kondo-Heisenberg-Holstein (KHH) model on a 10×4 cylinder, with (a) only Kondo coupling, (b) Kondo and Heisenberg coupling, (c) Kondo and Holstein coupling and (c) Kondo, Heisenberg and Holstein coupling. Legends state our choices for J_H and N_{ph}^{max}, and corresponding values of $d^*[d]$ and $w^*[w]$. For each panel, E_0 was obtained by linear ξ-extrapolation to $\xi = 0$ (grey line) using the four largest D^* values. The very largest D^* is shown next to its data point; D^* changes by 1k between adjacent data points.

(see legends). The linear ξ-dependence of E demonstrates proper convergence of CBE–DMRG. Very large D^* values are achievable despite the rather huge values of d and w. This is remarkable especially for $J_H = 0.5$ and $N_{ph}^{max} = 3$ (Fig. S-10(d)), where $d^*[d] = 16[32]$ and $w^*[w] = 14[30]$ are large, so that 2s schemes become excessively costly. These results encouragingly illustrate the potential of CBE for handling very complex models.

B. Kondo-Heisenberg cylinders: Fermi surface

Having established stable convergence of CBE–DMRG for the KHH model on a 10×4 cylinder, we turn to the Kondo-Heisenberg (KH) model on longer 40×4 cylinders. In this section, we provide some supplementary information on our discussion of the Fermi surface (FS) reconstruction in the KH model.

Heavy-fermion materials feature many interesting phenomena. One that is not so well understood is the so-called Kondo breakdown (KB) quantum critical point (QCP). When the system is tuned across this KB–QCP, the FS volume abruptly changes [39], leading to a violation of Luttinger's sum rule [40] and strange metal behavior at finite temperatures.

In Fig. 6 of the main text, we have shown strong evidence for the existence of two distinct phases with different FS volumes in the KH model on a 4-leg cylinder. This in turn strongly suggests the existence of a KB-QCP in the KH model on 4-leg cylinders, which can be studied in a non-perturbative, controlled and unbiased way using our newly developed CBE–DMRG method. Here, our goal is to explain in detail how we extracted the Fermi points from our CBE–DMRG data on the 40×4 KH cylinder,
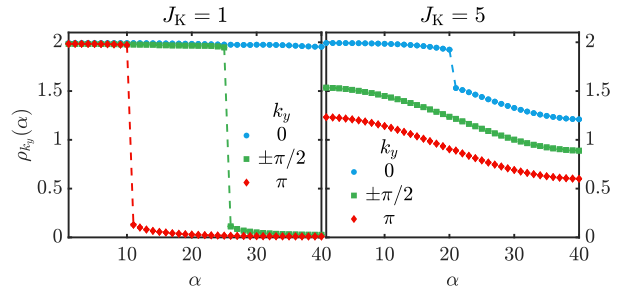
FIG. S-11. k_y-resolved eigenvalues, $\rho_{k_y}(\alpha)$ of the single-particle density matrix of the Kondo-Heisenberg (KH) model on a 40×4 cylinder at 25% electron doping, $J_H = 0.5$ and (a) $J_K = 0.5$ and (b) $J_K = 2.5$. Eigenvalues are extrapolated to truncation error $\xi \to 0$, error bars are below symbol sizes. Dashed lines highlight jumps in the spectra.

thereby establishing the two distinct phases reported in the main text. We leave the study and discussion of a possible KB–QCP and its rich physics to future work.

To illustrate our Fermi point extraction strategy, we here focus on $J_K = 1$ and $J_K = 5$, representative for the two phases with different Fermi surfaces at small and large J_K, respectively. We extract the Fermi points from the single-particle density matrix,

$$\rho_{k_y}(x, x') = \sum_\sigma \langle c^\dagger_{x k_y \sigma} c_{x' k_y \sigma} \rangle, \qquad (S9)$$

where $c_{x k_y \sigma} = \frac{1}{2} \sum_{y=1}^4 e^{i k_y y} c_{x y \sigma}$, with $k_y \in \{0, \pm\frac{\pi}{2}, \pi\}$, is the y-Fourier transform of the fermionic annihilation operator $c_{x y \sigma} = c_{\ell \sigma}$.

Figure S-11 shows the eigenvalues of $\rho_{k_y}(x, x')$, dubbed $\rho_{k_y}(\alpha)$, for given k_y (extrapolated to zero discarded weight ξ). The structure of the eigenvalue spectra for $J_K = 1$ and $J_K = 5$ differ qualitatively: For $J_K = 1$, they show a jump for $k_y = \pm\frac{\pi}{2}$ and $k_y = \pi$, but not for $k_y = 0$, while for $J_K = 5$ it is the other way around.

A jump in $\rho_{k_y}(\alpha)$ suggests that the corresponding k_y value is visited by the Fermi surface, i.e. there exists a point on the FS with Fermi wavevector $\mathbf{k}_F = (k_{Fx}(k_y), k_y)$. Note, however, that since we use open boundary conditions, the eigenbasis of ρ_{k_y} is not the Fourier basis. We
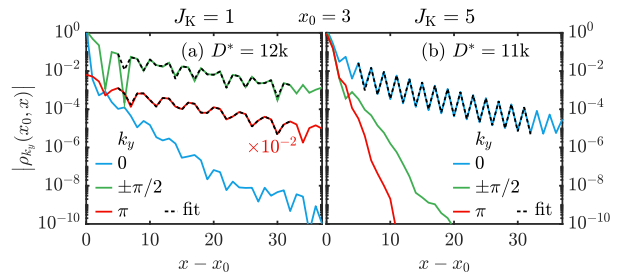
FIG. S-12. Absolute values of the off-diagonal elements of the single-particle density matrix of the Kondo-Heisenberg model on a 40×4 cylinder at 25% electron doping, for $J_H = 0.5$ and (a) $J_K = 1$, (b) $J_K = 5$. Solid lines are CBE–DMRG data; black dotted lines are fits to Eq. (S10) to extract λ and k_{Fx}.
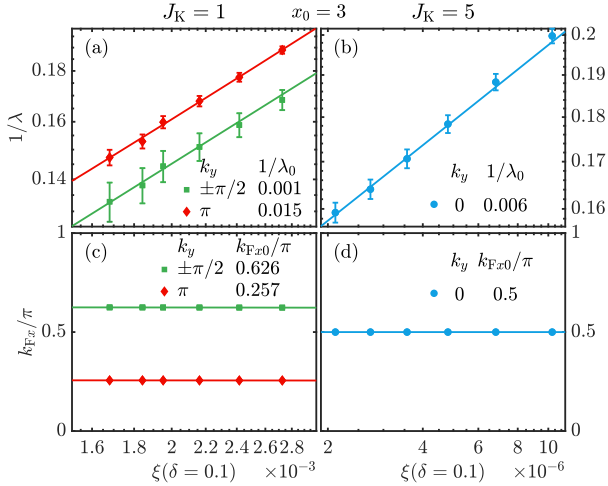
FIG. S-13. Discarded weight extrapolation of (a,b) the correlation length and (c,d) the corresponding Fermi wavevectors, obtained through the fits of $\rho_{k_y}(x_0, x)$ to Eq. (S10), as shown in Fig. S-12. Error bars indicate 68.2% confidence intervals (i.e. one standard deviation) for the fit parameters (below symbol size in (c,d)).

can therefore not rely on the eigenbasis of ρ_{k_y} to determine the corresponding x-direction Fermi wavevector $k_{Fx}(k_y)$. Instead, we use the off-diagonal elements $\rho_{x_0 x}(k_y)$ in the real space basis, for fixed $x_0 = 3$, and study the behaviour of $\rho_{k_y}(x_0, x)$ as a function of $|x - x_0|$. The expected behaviour in the case of a Fermi point can be parametrized by the Ansatz

$$\rho_{k_y}(x_0, x) \sim \cos\left(k_{Fx}(k_y)|x - x_0| + \phi\right) \frac{e^{-|x - x_0|/\lambda}}{|x - x_0|^\alpha} .$$
$$(S10)$$

Here, the exponent in the denominator is given by $\alpha = 1$ in case of a Fermi liquid (obtained by Fourier transforming a step function), or takes some non-universal, interaction-dependent value in the case of a Luttinger liquid [41]. Because CBE–DMRG approximates the true ground state by a MPS, the correlation length λ is finite. When $D^* \to \infty$, or equivalently when $\xi \to 0$, we expect $\lambda \to \infty$. In Fig. S-12, we show that a fit of $\rho_{k_y}(x_0, x)$ to Eq. (S10) indeed works well for those ρ_{k_y} with gapped spectrum (green, red curves in Fig. S-11(a), blue curve in Fig. S-11(b)). Note that such fits are not possible for the remaining cases.

Figures S-13(a,b) show the behaviour of the inverse correlation length $1/\lambda$ versus discarded weight ξ. In the cases where we have identified a possible Fermi wavevector $k_{Fx}(k_y)$, $1/\lambda$ indeed extrapolates to zero (i.e. $\lambda \to \infty$) within our numerical accuracy, consistent with expectations for either a Fermi or Luttinger liquid. In Fig. S-13(c,d), we show the corresponding Fermi wavevectors $k_{Fx}(k_y)$ plotted against discarded weight ξ. It turns out that $k_{Fx}(k_y)$ is almost independent of ξ, which means the determination of $k_{Fx}(k_y)$ is highly accurate.

Our way of extracting Fermi wavevectors from DMRG ground states using the single-particle density matrix is reliable and numerically robust. In Fig. 5 of the main text, we only presented Fermi wavevectors for values of J_K where we were able to converge the DMRG calculation with reasonable numerical effort ($D^* \leq 12k$ on the 40×4 cylinder). Closer to the putative KB-QCP, more numerical resources are needed. These more challenging calculations are beyond the scope of the current work (which mainly focuses on the development of the CBE method) and are left for the future.

C. Kondo-Heisenberg cylinders: Fermi volume and Luttinger's sum rule

The FS is especially interesting in the context of Luttinger's sum rule [40, 42],

$$n_{\text{eff}} = 2v_{\text{FS}} \qquad (S11)$$

(prefactor 2 for spin). It links the volume enclosed by the FS, v_{FS} (measured in terms of Brillouin zone volumes), to the effective number of mobile charge carriers n_{eff} (defined modulo 2, i.e. excluding filled bands).

An unambiguous definition of the volume of the FS must include a criterion distinguishing its inside and outside. The inside of the Fermi volume is usually defined as those momentum space states which are "filled", having $n_{\boldsymbol{k}} = \sum_\sigma \langle c^\dagger_{\boldsymbol{k}\sigma} c_{\boldsymbol{k}\sigma} \rangle \simeq 2$. We point out that the criterion based on $n_{\boldsymbol{k}}$ is only stringent in the non-interacting limit where $n_{\boldsymbol{k}} \in \{0, 2\}$ can only take two values, which is not the case for interacting systems. A stringent criterion for interacting systems can be formulated in terms of single-electron Green's functions (see, e.g., Ref. 44, Eq. (7)), but the computation of such dynamical quantities is beyond the scope of this work. Here, we take the heuristic approach based on $n_{\boldsymbol{k}}$.

To make progress on a formula for v_{FS} in 2D, we assume that single-electron states in the vicinity of $\boldsymbol{k} = (0, 0)$ are usually lower in energy than those in the vicinity of $\boldsymbol{k} = (\pi, \pi)$. Thus, we consider the states between $\in [-k_{Fx}(k_y), k_{Fx}(k_y)]$ filled. For an infinite 2D system, we can now compute

$$v_{\text{FS}} = \int_{-\pi}^{\pi} \frac{dk_y}{2\pi} \int_{-k_{Fx}(k_y)}^{k_{Fx}(k_y)} \frac{dk_x}{2\pi} = \int_{-\pi}^{\pi} \frac{dk_y}{2\pi} \frac{|k_{Fx}(k_y)|}{\pi} .$$
$$(S12)$$

Our KH cylinders at hand are however not infinite 2D systems due to the finite circumference of $\mathscr{L}_y = 4$ (the finite length $\mathscr{L}_x$ can in practice chosen large enough to not play a conceptionally problematic role). In this case, we replace the integral in Eq. (S12) by a sum to obtain

$$v_{\text{FS}} = \frac{1}{\mathscr{L}_y} \sum_{k_y} |k_{Fx}(k_y)|/\pi . \qquad (S13)$$

Note that we are now faced with the ambiguity of how to define $k_{\mathrm{F}x}(k_y)$ for those k_y values for which no Fermi points exist. The corresponding $k_{\mathrm{F}x}(k_y)$ could be either π or 0, depending on whether $n_{\boldsymbol{k}}$ is filled or empty for all k_x, respectively. For $\mathscr{L}_y \to \infty$, this can be decided based on continuity of $k_{\mathrm{F}x}(k_y)$. By contrast, for finite $\mathscr{L}_y$, where k_y takes only discrete values, the definition of $k_{\mathrm{F}x}(k_y)$ has to be based on heuristic arguments. To this end, we use the eigenvalues of the single-particle density matrix $\rho_{k_y}(\alpha)$ (see Fig. S-11) as a proxy for $n_{\boldsymbol{k}}$ (in the limit $\mathscr{L}_x \to \infty$, these quantities coincide). If the eigenvalues $\rho_{k_y}(\alpha)$ are close to (or not close to) 2 for *all* α, we take that as an indication that all states are filled (or empty), and accordingly define $k_{\mathrm{F}x}(k_y) = \pi$ (or $= 0$).

For $J_{\mathrm{K}} = 1$, only $k_{\mathrm{F}x}(k_y = 0)$ is undecided. Since $\rho_0(\alpha) \simeq 2$ (see Fig. S-11(a), blue dots), we define $k_{\mathrm{F}x}(0) = \pi$. Together with the Fermi points found at $k_y = \pm\frac{\pi}{2}, \pi$, we thus find $(|k_{\mathrm{F}x}|, |k_y|) = (\pi, 0)$, $(0.625\pi, \frac{\pi}{2})$ and $(0.256\pi, \pi)$, matching the free-electron values at $J_{\mathrm{K}} =$

0. Inserting these into Eq. (S13), we find $v_{\mathrm{FS}} = 0.627$ and $n_{\mathrm{eff}} = 1.25$, consistent with 25% electron doping.

By contrast, for $J_{\mathrm{K}} \geq 5$, we find Fermi points only at $(\frac{\pi}{2}, 0)$. For $k_y = \pm\frac{\pi}{2}, \pi$, we have to consult $\rho_{k_y}(\alpha)$ shown in Fig. S-11(b) (green squares and red diamonds). Since these are well below 2, we define $k_{\mathrm{F}x} = 0$ for these, so that $(|k_{\mathrm{F}x}|, |k_y|) = (0, \frac{\pi}{2})$ and $(0, \pi)$. Insertion into Eq. (S13) yields $v_{\mathrm{FS}} = 0.125$ and $n_{\mathrm{eff}} = 0.25 = 2.25 \bmod 2$ (n_{eff} is only defined modulo 2, i.e. up to filled bands). This is consistent with spins becoming mobile charge carriers by "binding" to the electrons [43] by forming collective Kondo singlets. These collective Kondo singlets break up when approaching the KB–QCP from $J_{\mathrm{K}} > J_{\mathrm{K,c}}$ (hence the name "Kondo breakdown") and cease to exist for $J_{\mathrm{K}} < J_{\mathrm{K,c}}$. The existence of collective Kondo singlets manifests in a pole in the single-electron self-energy. Due to this pole, the Fermi wavevector is shifted, leading to a FS consistent with spins counting as mobile charge carriers [42, 43].

Time-dependent variational principle with controlled bond expansion for matrix product states

Jheng-Wei Li,[1] Andreas Gleis,[1] and Jan von Delft[1]

[1] *Arnold Sommerfeld Center for Theoretical Physics, Center for NanoScience, and Munich Center for Quantum Science and Technology, Ludwig-Maximilians-Universität München, 80333 Munich, Germany*

We present a controlled bond expansion (CBE) approach to simulate quantum dynamics based on the time-dependent variational principle (TDVP) for matrix product states. Our method alleviates the numerical difficulties of the standard, fixed-rank one-site TDVP integrator by increasing bond dimensions on the fly to reduce the projection error. This is achieved in an economical, local fashion, requiring only minor modifications of standard one-site TDVP implementations. We illustrate the performance of CBE–TDVP with several numerical examples on finite quantum lattices.

DOI:

Introduction.— The time-dependent variational principle (TDVP) [1–4] is a standard tool for time-evolving the Schrödinger equation on a constrained manifold parametrizing the wave function. Tensor networks (TN) offer efficient parametrizations based on low-rank approximations [5–12]. Their combination, TN–TDVP, holds much potential for studying the dynamics of quantum lattice models [13–32], quantum field theories [33, 34], and quantum chemistry problems [35–40].

Here, we focus on matrix product states (MPSs), an elementary class of TN states. Their time evolution, pioneered in Refs. [41–43], can be treated using a variety of methods, reviewed in Refs. [8, 44]. Among these, MPS–TDVP [15, 18–22], which uses Lie-Trotter decomposition to integrate a train of tensors sequentially, arguably gives the best results regarding both physical accuracy and performance [44]: it (i) is applicable for long-ranged Hamiltonians, and its one-site (1s) version (1TDVP) ensures (ii) unitary time evolution, (iii) energy conservation [15, 45] and (iv) numerical stability [18, 21, 23].

A drawback of 1TDVP, emphasized in Refs. [46–48], is use of a *fixed*-rank integration scheme. This offers no way of dynamically adjusting the MPS rank (or bond dimension), as needed to track the entanglement growth typically incurred during MPS time evolution. For this, a rank-adaptive two-site (2s) TDVP (2TDVP) algorithm can be used [22], but it has much higher computational costs and in practice does not ensure properties (ii-iii).

To remedy this drawback, we introduce a rank-adaptive integrator for 1TDVP that is more efficient than previous ones [49–52]. It ensures properties (i-iv) at the same numerical costs as 1TDVP, with marginal overhead. Our key idea is to control the TDVP projection error [22, 49, 53] by adjusting MPS ranks on the fly via the controlled bond expansion (CBE) scheme of Ref. [54]. CBE finds and adds subspaces missed by 1s schemes but containing significant weight from $H\Psi$. When used for DMRG ground state searches, CBE yields 2s accuracy with faster convergence per sweep, at 1s costs [54]. CBE–

TDVP likewise comes at essentially 1s costs.

MPS basics.— Let us recall some MPS basics, adopting the notation of Refs. 54 and 55. For an $\mathscr{L}$-site system an open boundary MPS wave function Ψ having dimensions d for physical sites and D for virtual bonds can always be written in site-canonical form,

$$\Psi = \begin{array}{c} A_1 \quad A_2 \qquad A_{\ell-1} \; C_\ell \; B_{\ell+1} \qquad B_{\mathscr{L}-1} \; B_{\mathscr{L}} \\ \cdots \qquad \cdots \end{array}. \quad (1)$$

The tensors C_ℓ ($\curlywedge$), A_ℓ ($\triangledown$) and B_ℓ ($\triangledown$) are variational parameters. A_ℓ and B_ℓ are left and right-sided isometries, respectively, projecting Dd-dimensional *parent* (P) spaces to D-dimensional *kept* (K) images spaces; they obey

$$A_\ell^\dagger A_\ell = \begin{array}{c} A_\ell \\ A_\ell^* \end{array} = \Big(= \mathbb{1}_\ell^{\text{K}}, \qquad B_\ell B_\ell^\dagger = \begin{array}{c} B_\ell \\ B_\ell^* \end{array} = \Big) = \mathbb{1}_{\ell-1}^{\text{K}}. \quad (2)$$

The gauge relations $C_\ell = A_\ell \Lambda_\ell = \Lambda_{\ell-1} B_\ell$ ensure that Eq. (1) remains unchanged when moving the orthogonality center C_ℓ from one site to another.

The Hamiltonian can likewise be expressed as a matrix product operator (MPO) with virtual bond dimension w,

$$H = \begin{array}{c} W_1 \; W_2 \qquad\qquad W_\ell \qquad\qquad W_{\mathscr{L}-1} W_{\mathscr{L}} \\ \cdots \qquad d \; w \; d \qquad \cdots \end{array}. \quad (3)$$

Its projection to the effective local state spaces associated with site ℓ or bond ℓ yields effective one-site or zero-site Hamiltonians, respectively, computable recursively via

$$H_\ell^{1\text{s}} = \begin{array}{c} D \quad d \quad D \\ \ell-1 \; \ell \; \ell+1 \end{array} = \begin{array}{c} \\ 1 \qquad \ell-1 \; \ell \; \ell+1 \qquad \mathscr{L} \end{array}, \quad (4\text{a})$$

$$H_\ell^{\text{b}} = \begin{array}{c} D \qquad D \\ \ell \quad \ell+1 \end{array} = \begin{array}{c} \\ \ell-1 \; \ell \; \ell+1 \end{array} = \begin{array}{c} \\ \ell \; \ell+1 \; \ell+2 \end{array}. \quad (4\text{b})$$

These act on 1s or bond representations of the wave function, $\psi_\ell^{1\text{s}} = C_\ell$ ($\curlywedge$) or $\psi_\ell^{\text{b}} = \Lambda_\ell$ ($\diamond$), respectively.

Let $\overline{A}_\ell$ ($\triangledown$) and $\overline{B}_\ell$ ($\triangledown$) be isometries that are orthogonal complements of A_ℓ and B_ℓ, with *discarded* (D) image spaces of dimension $\overline{D} = D(d-1)$, obeying orthonormality and completeness relations complementing Eq. (2) [54]:

$$\begin{array}{llll} \text{(diagram)} = \text{(diagram)} = \mathbb{1}^{\mathrm{p}}_\ell\,, & \text{(diagram)} = 0\,, & \text{(diagram)} = \mathbb{1}^{\mathrm{p}}_{\ell-1}\,, & \text{(diagram)} = 0\,, \quad (5\mathrm{a}) \end{array}$$

$$\text{(diagram)}_\ell + \text{(diagram)}_\ell = \supset\big|_\ell = \mathbb{1}^{\mathrm{p}}_\ell\,, \qquad \text{(diagram)}_\ell + \text{(diagram)}_\ell = \big|_\ell \subset = \mathbb{1}^{\mathrm{p}}_{\ell-1}. \quad (5\mathrm{b})$$

Tangent space projector.— Next, we recapitulate the TDVP strategy. It aims to solve the Schrödinger equation, $\mathrm{i}\dot{\Psi}=H\Psi$, constrained to the manifold $\mathcal{M}$ of all MPSs of the form (1), with *fixed* bond dimensions. Since $H\Psi$ typically has larger bond dimensions than Ψ and hence does not lie in $\mathcal{M}$, the TDVP aims to minimize $\|\mathrm{i}\dot{\Psi}-H\Psi\|$ within $\mathcal{M}$. This leads to

$$\mathrm{i}\dot{\Psi}(t) = \mathcal{P}^{1\mathrm{s}}(t)H\Psi(t), \qquad (6)$$

where $\mathcal{P}^{1\mathrm{s}}(t)$ is the projector onto the tangent space of $\mathcal{M}$ at $\Psi(t)$, i.e. the space of all 1s variations of $\Psi(t)$:

$$\mathcal{P}^{1\mathrm{s}} = \sum_{\ell'=1}^{\mathscr{L}} \text{(diagram)} - \sum_{\ell'=1}^{\mathscr{L}-1} \text{(diagram)} \qquad (7)$$

$$= \sum_{\ell'=1}^{\bar{\ell}} \text{(diagram)} + \text{(diagram)} + \sum_{\ell'=\bar{\ell}+1}^{\mathscr{L}} \text{(diagram)}.$$

The form in the first line was derived by Lubich, Oseledts, and Vandereycken [21] (Theorem 3.1), and transcribed into MPS notation in Ref. [22]. For further explanations of its form, see Refs. [55, 56]. The second line, valid for any $\bar{\ell}=1,\dots,\mathscr{L}-1$, follows via Eq. (5b); Eq. (5a) implies that all its terms conveniently are mutually orthogonal, and that the projector property $(\mathcal{P}^{1\mathrm{s}})^2=\mathcal{P}^{1\mathrm{s}}$ holds [55].

One-site TDVP.— The 1TDVP algorithm [21, 22] represents Eq. (6) by $2\mathscr{L}-1$ coupled equations, $\mathrm{i}\dot{C}_\ell=H^{1\mathrm{s}}_\ell C_\ell$ and $\mathrm{i}\dot{\Lambda}_\ell=-H^{\mathrm{b}}_\ell\Lambda_\ell$, stemming, respectively, from the $\mathscr{L}$ single-site and $\mathscr{L}-1$ bond projectors of $\mathcal{P}^{1\mathrm{s}}$ (Eq. (7), first line). Evoking a Lie-Trotter decomposition, they are then decoupled and for each time step solved sequentially, for C_ℓ or Λ_ℓ (with all other tensors fixed). For a time step from t to $t'=t+\delta$ one repeatedly performs four substeps, e.g. sweeping right to left: (1) Integrate $\mathrm{i}\dot{C}_{\ell+1}=H^{1\mathrm{s}}_{\ell+1}C_{\ell+1}$ from t to t'; (2) QR factorize $C_{\ell+1}(t')=\Lambda_\ell(t')B_{\ell+1}(t')$; (3) integrate $\mathrm{i}\dot{\Lambda}_\ell=-H^{\mathrm{b}}_\ell\Lambda_\ell$ from t' to t; and (4) update $A_\ell(t)C_{\ell+1}(t)\to C_\ell(t)B_{\ell+1}(t')$, with $C_\ell(t)=A_\ell(t)\Lambda_\ell(t)$.

1TDVP has two leading errors. One is the Lie-Trotter decomposition error. It can be reduced by higher-order integration schemes [45, 57]; we use a third-order integrator with error $\mathcal{O}(\delta^3)$ [58]. The second error is the projection error from projecting the Schrödinger equation into the tangent space of $\mathcal{M}$ at $\Psi(t)$, quantified by $\Delta_P=\|(\mathbb{1}-\mathcal{P}^{1\mathrm{s}})H\Psi(t)\|^2$. It can be reduced brute force by increasing the bond dimension, as happens when using 2TDVP [22, 44, 47], or through global subspace expansion [50]. Here, we propose a local approach, similar in spirit to that of Ref. [52], but more efficient, with 1s costs, and without stochastic ingredients, in contrast to [40].

Controlled bond expansion.— Our key idea is to use CBE to reduce the 2s contribution in Δ_P, given by $\Delta^{2\perp}_P = \big\|\mathcal{P}^{2\perp}H\Psi\big\|^2$, where $\mathcal{P}^{2\perp}=\mathcal{P}^{2\mathrm{s}}(1-\mathcal{P}^{1\mathrm{s}})$. Here, $\mathcal{P}^{2\mathrm{s}}$ is the projector onto 2s variations of Ψ, and $\mathcal{P}^{2\perp}$ its component

orthogonal to the tangent space projector (see also [55]):

$$\mathcal{P}^{2\mathrm{s}} = \sum_{\ell=1}^{\mathscr{L}-1} \text{(diagram)} - \sum_{\ell=2}^{\mathscr{L}-1} \text{(diagram)}, \qquad (8\mathrm{a})$$

$$\mathcal{P}^{2\perp} = \sum_{\ell=1}^{\mathscr{L}-1} \text{(diagram)}, \quad \Delta^{2\perp}_P = \sum_{\ell=1}^{\mathscr{L}-1} \left\| \text{(diagram)} \right\|^2. \quad (8\mathrm{b})$$

Now note that $\Delta^{2\perp}_P$ is equal to $\Delta^{2\perp}_E=\|\mathcal{P}^{2\perp}(H-E)\Psi\|^2$, the 2s contribution to the energy variance [53–55]. In Ref. [54], discussing ground state searches via CBE–DMRG, we showed how to minimize $\Delta^{2\perp}_E$ at 1s costs: each bond ℓ can be expanded in such a manner that the added subspace carries significant weight from $\mathcal{P}^{2\perp}H\Psi$. This expansion removes that subspace from the image of $\mathcal{P}^{2\perp}$, thus reducing $\Delta^{2\perp}_E$ significantly. Consider, e.g., a right-to-left sweep and let $\widetilde{A}^{\mathrm{tr}}_\ell$ (diagram) be a truncation of $\overline{A}_\ell$ (diagram) having an image spanning such a subspace, of dimension $\widetilde{D}$, say. To expand bond ℓ from D to $D+\widetilde{D}$, we replace A_ℓ(diagram) by A^{ex}_ℓ(diagram), $C_{\ell+1}$(diagram) by $C^{\mathrm{ex}}_{\ell+1}$(diagram) and $H^{1\mathrm{s}}_{\ell+1}$ by $H^{1\mathrm{s,ex}}_{\ell+1}$, with expanded tensors defined as

$$\frac{A_\ell}{D\ \ D} \oplus \frac{\widetilde{A}^{\mathrm{tr}}_\ell}{D\ \widetilde{D}} = \frac{A^{\mathrm{ex}}_\ell}{D\ \ (D+\widetilde{D})} \quad \frac{C^{\mathrm{ex}}_{\ell+1}}{(D+\widetilde{D})\ D} = \text{(diagram)}\frac{C_{\ell+1}}{}, \quad (9)$$

$$H^{(1,\mathrm{ex})}_{\ell+1} = \text{(diagram)}_{\ell+1} = \ ^{D+\widetilde{D}}\text{(diagram)}_{\ell+1}{}^{D}. \qquad (10)$$

Note that Ψ remains unchanged, $A^{\mathrm{ex}}_\ell C^{\mathrm{ex}}_{\ell+1}=A_\ell C_{\ell+1}$.

Similarly, the projection error $\Delta^{2\perp}_P$ can be minimized through a suitable choice of the truncated complement $\widetilde{A}^{\mathrm{tr}}_\ell$ (diagram) [54]. We find $\widetilde{A}^{\mathrm{tr}}_\ell$ using the so-called *shrewd selection* strategy of Ref. [54] (Figs. 1 and 2 there); it avoids computation of (diagram) and has 1s costs regarding CPU and memory, thus becoming increasingly advantageous for large D and d. Shrewd selection involves two truncations ($D\to D'$ and $\widehat{D}\to\widetilde{D}$ in Ref. [54]). Here, we choose these to respect singular value thresholds of $\epsilon'=10^{-4}$ and $\widetilde{\epsilon}=10^{-6}$, respectively; empirically, these yield good results in the benchmark studies presented below.

CBE–TDVP.— It is straightforward to incorporate CBE into the 1TDVP algorithm: simply expand each bond ℓ from $D\to D+\widetilde{D}$ before time-evolving it. Concretely, when sweeping right-to-left, we add step (0): expand $A_\ell, C_{\ell+1}, H^{1\mathrm{s}}_{\ell+1} \to A^{\mathrm{ex}}_\ell, C^{\mathrm{ex}}_{\ell+1}, H^{1\mathrm{s,ex}}_{\ell+1}$ following Eq. (9) (and by implication also $\Lambda_\ell, H^{\mathrm{b}}_\ell \to \Lambda^{\mathrm{ex}}_\ell, H^{\mathrm{b,ex}}_\ell$). The other steps remain as before, except that in (2) we replace the QR factorization by an SVD. This allows us to reduce (trim) the bond dimension from $D+\widetilde{D}$ to a final value D_{f}, as needed in two situations [49, 51, 59]: First, while standard 1TDVP requires keeping and even padding small singular values in order to retain a fixed bond dimension [13, 18], that is not necessary here. Instead, for bond trimming, we discard small singular values below an empirically determined threshold $\epsilon=10^{-12}$. This keeps the MPS rank as low as possible, without impacting the accuracy [49]. Second, once $D+\widetilde{D}$ exceeds
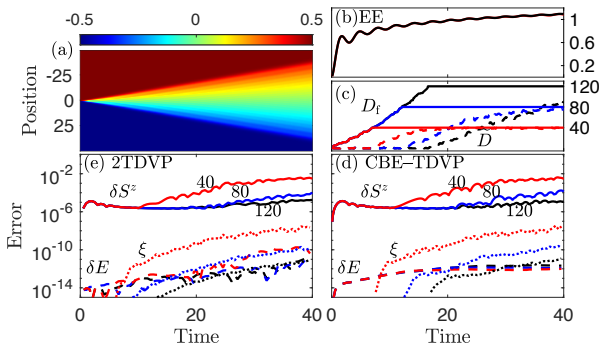
FIG. 1. 100-site XX spin chain: Time evolution of a domain wall, computed with time step $\delta = 0.05$ and U(1) spin symmetry. (a) Local magnetization profile $S_\ell^z(t)$. (b) Entanglement entropy EE(t) between the left and the right half of the chain. (c) Bond dimension $D_f(t)$ and its pre-trimming expansion $\widetilde{D}(t)$ per time step, for $D_{\max} = 120$. (d,e) Error analysis: magnetization $\delta S^z(t)$ (solid line),i.e., the maximum deviation (over ℓ) of $S_\ell^z(t)$ from the exact result, , energy $\delta E(t)$ (dashed line), and discarded weight $\xi(t)$ (dotted line) for $D_{\max} = 40$ (red), 80 (blue) and 120 (black), computed with (d) CBE–TDVP or (e) 2TDVP. Remarkably, the errors are comparable in size, although CBE–TDVP has much smaller computational costs.

$D_{\max}$, we trim it back down to $D_{\max}$ aiming to limit computational costs. The trimming error is characterized by its discarded weight, $\xi(t)$, which we either control or monitor. The TDVP properties of (ii) unitary evolution and (iii) energy conservation [51] hold to within order $\xi(t)$.

Results.— We now benchmark CBE–TDVP for three spin models, then illustrate its performance for large d using the Peierls–Hubbard model with $d = 36$. Our benchmark comparisons track the time evolution of the entanglement entropy EE(t) between the left and right halves of a chain, the bond dimensions $D_f(t)$ and $\widetilde{D}(t)$, the discarded weight $\xi(t)$, the deviations from exact results of spins expectation values, $\delta S(t)$, and the energy change, $\delta E(t)$, which should vanish for unitary time evolution.

XX model: domain wall motion.— We consider a spin chain with Hamiltonian $H_{XX} = \sum_\ell (S_\ell^x S_{\ell+1}^x + S_\ell^y S_{\ell+1}^y)$. We compute the time evolution of the local magnetization profile $S_\ell^z(t) = \langle \Psi(t)| \widehat{S}_\ell^z |\Psi(t)\rangle$, initialized with a sharp domain wall, $|\Psi(0)\rangle = |\uparrow\uparrow\ldots\uparrow\downarrow\downarrow\ldots\downarrow\rangle$. For comparison, the analytical solution for $\mathscr{L} \to \infty$ reads [60] $S_\ell^z(t) = -1/2 \sum_{n=1-\ell}^{\ell-1} J_n(t)^2$, for $\ell \geq 1$ (right half) and $S_\ell^z = -S_{1-\ell}^z$ otherwise, where $J_n(t)$ is the Bessel function of the first kind. The domain wall spreads with time [Fig. 1(a)], entailing a steady growth of the entanglement entropy (EE) between the left and right halves of the spin chain [Fig. 1(b)]. $D(t)$ and $\widetilde{D}(t)$ [Fig. 1(c)] start from 1 and 0. Initially, $\widetilde{D}$ remains remarkably small ($\lesssim 10$), while D_f increases in steps of $\widetilde{D}$ until reaching $D_{\max}$. Thereafter $\widetilde{D}$ increases noticeably, but remains below $D_{\max}$ for all times shown here. This reflects CBE
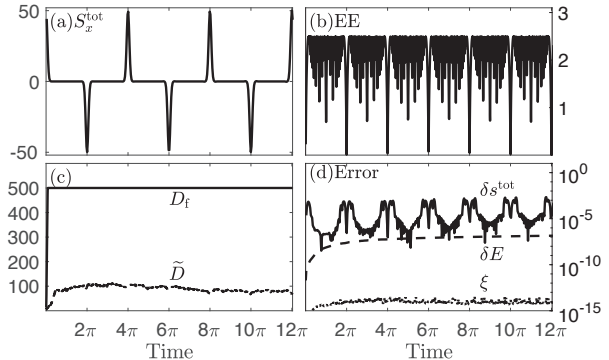
FIG. 2. 100-site one-axis twisting model: Time evolution of an initially x-polarized spin state, computed using $\delta = 0.01$ and $\mathbb{Z}_2$ spin symmetry. (a) Total spin $S_x^{\mathrm{tot}}(t)$, (b) entanglement entropy, and (c) bond dimensions. (d) Error analysis: error in total spin density $\delta s_x^{\mathrm{tot}}(t)$ (solid line), energy $\delta E(t)$ (dashed line), and discarded weight $\xi(t)$ (dotted line), for $D_{\max} = 500$.

frugality—bonds are expanded only as much as needed.

Figure 1(d) illustrates the effects of changing $D_{\max}$, following the error analysis of Ref. 61. The leading error is quantified by $\delta S^z(t)$ (solid line), the maximum deviation (over ℓ) of $S_\ell^z(t)$ from the exact result. Comparing the data for $D_{\max} = 40, 80, 120$, we observe a finite bond dimension effect: The error δS^z increases appreciably once the discarded weight ξ (dotted line) becomes larger than 10^{-11}. By contrast, the energy change (dashed line) stays small irrespective of the choice of $D_{\max}$. (For more discussion of error accumulation, see Ref. [56].) Figure 1(e) shows a corresponding error analysis for 2TDVP, computed using $D = D_{\max}$; its errors are comparable to those of CBE–TDVP, though the latter is much cheaper.

One-axis twisting (OAT) model: quantum revivals.— The OAT model has a very simple Hamiltonian, $H_{\mathrm{OAT}} = (\sum_\ell S_\ell^z)^2/2$, but its long-range interactions are a challenge for tensor network methods using real-space parametrizations. We study the evolution of $S_x^{\mathrm{tot}}(t) = \langle \Psi(t)| \sum_\ell \widehat{S}_\ell^x |\Psi(t)\rangle$, for an initial $|\Psi(0)\rangle$ having all spins x-polarized (an MPS with $D = 1$). The exact result, $S_x^{\mathrm{tot}}(t) = (L/2)\cos^{L-1}(t/2)$, exhibits periodic collapses and revivals [62]. Yang and White [50] have studied the short-time dynamics using TDVP with global subspace expansion, reaching times $t \leq 0.5$. CBE–TDVP is numerically stable for much longer times [Fig. 2(a)]; it readily reached $t = 12\pi$, completing three cycles. (More would have been possible with *linear* increase in computation time.) This stability is remarkable, since the rapid initial growth of the entanglement entropy, the finite time-step size, and the limited bond dimension [Fig. 2(b,c)] cause some inaccuracies, which remain visible throughout [Fig. 2(d)]. However, such numerical noise evidently does not accumulate over time and does not spoil the long-time dynamics: CBE–TDVP retains the treasured properties (i-iv) of 1TDVP, up to the trun-
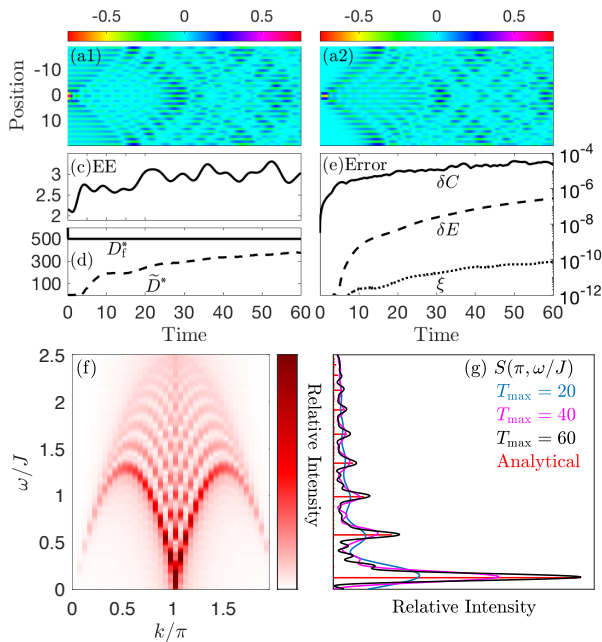
FIG. 3. 40-site SU(2) Haldane-Shastry model: (a-d) Time evolution of a spin excitation, computed with $\delta = 0.05$ and SU(2) spin symmetry. (a1,a2) Real and imaginary parts of $C(x,t)$, (b) entanglement entropy, and (c) bond dimensions. (d) Error analysis: $\delta C(t)$, the maximum of $\delta C(x,t)$ over x (solid line), energy $\delta E(t)$ (dashed line) and discarded weight $\xi(t)$ (dotted line), for $D_{\max} = 500$. (f) Normalized spectral function $S(k,\omega)/S(\pi,0)$, obtained using $t_{\max} = 60$. (g) $S(\pi,\omega)/S(\pi,0)$, obtained using $t_{\max} = 20, 40, 60$; red lines indicate exact peak heights.

cation tolerance governed by ξ.

SU(2) *Haldane-Shastry model: spectral function.*— Our final benchmark example is the SU(2) Haldane-Shastry model on a ring of length $\mathscr{L}$, with Hamiltonian

$$H_{\mathrm{HS}} = J \sum_{\ell < \ell' \leq \mathscr{L}} \frac{\pi^2 \mathbf{S}_\ell \cdot \mathbf{S}_{\ell'}}{\mathscr{L}^2 \sin^2 \frac{\pi}{\mathscr{L}}(\ell - \ell')}. \tag{11}$$

Its ground state correlator, $C(x,t) = \langle \Psi_0 | \widehat{\mathbf{S}}_x(t) \widehat{\mathbf{S}}_0(0) | \Psi_0 \rangle$, is related by discrete Fourier transform to its spectral function, $S(k,\omega)$, given by $(0 < \ell' < \ell \leq \mathscr{L}/2)$ [63, 64]

$$S\left(2(\ell + \ell')\frac{\pi}{\mathscr{L}}, \frac{\pi^2}{\mathscr{L}^2}((\ell + \ell')\mathscr{L} - 2(\ell^2 + \ell'^2) + \ell - \ell')\right) \tag{12}$$

$$= \frac{2\ell - 2\ell' - 1}{(2\ell - 1)(\mathscr{L} - 2\ell' - 1)} \prod_{\bar{\ell} = \ell' + 1}^{\ell - 1} \frac{2\bar{\ell}(\mathscr{L} - 2\bar{\ell})}{(2\bar{\ell} - 1)(\mathscr{L} - 2\bar{\ell} - 1)}.$$

Figures 3(a,b) show the real and the imaginary parts of $C(x,t)$, computed using CBE–TDVP. For early times $(t \leq 20)$, the local excitation introduced at $\ell = 0$, $t = 0$ spreads ballistically, as reported previously [28, 65, 66]. Once the counter-propagating wavefronts meet on the ring, an interference pattern emerges. Our numerical results remain accurate throughout, as shown by the error analysis in Fig. 3(e). Figure 3(f) shows the corresponding spectral function $S(k,\omega)$, obtained by discrete Fourier

transform of $C(x,t)$ using a maximum simulation time of $t_{\max}$. Figure 3(g) shows a cut along $k = \pi$: peaks can be well resolved by increasing $t_{\max}$, with relative heights in excellent agreement with the exact Eq. (12).

Peierls–Hubbard model: scattering dynamics.— Finally, we consider the scattering dynamics of interacting electrons coupled to phonons. This interaction leads to non-trivial low-energy physics involving polarons [67–79]; the numerical study of polaron dynamics is currently attracting increasing attention [69, 80–84]. Here, we consider the 1-dimensional Peierls–Hubbard model,

$$H_{\mathrm{PH}} = \sum_\ell U n_{\ell\uparrow} n_{\ell\downarrow} + \sum_\ell \omega_{\mathrm{ph}} b_\ell^\dagger b_\ell \tag{13}$$

$$+ \sum_{\ell\sigma}(c_{\ell\sigma}^\dagger c_{\ell+1\sigma} + \mathrm{h.c.})\left(-t + b_\ell^\dagger + b_\ell - b_{\ell+1}^\dagger - b_{\ell+1}\right).$$

Spinful electrons with onsite interaction strength U and hopping amplitude $t = 1$, and local phonons with frequency ω_{ph}, are coupled with strength g through a Peierls term modulating the electron hopping.

We consider two localized wave packets with opposite spins, average momenta $k = \pm\pi/2$ and width W [85, 86], initialized as $|\Psi_\pm\rangle = \sum_\ell A e^{-(\frac{x_\ell \mp x_0}{W})^2} e^{\mp ikx_\ell} c_{\ell\pm}^\dagger |0\rangle$, where $|0\rangle$ describes an empty lattice. Without electron-phonon coupling [$g = 0$, Fig. 4(a)], there is little dispersion effect through the time of flight, and the strong interaction causes an elastic collision. By contrast, for a sizable coupling in the nonperturbative regime [77, 79] [$g = 1$, Figs. 4(b-e)], phonons are excited by the electron motion [Fig. 4(c)]. After the two electrons have collided, they show a tendency to remain close to each other (though a finite distance apart, since U is large) [Fig. 4(b)]; they thus seem to form a bi-polaron, stabilized by a significant phonon density in the central region [Fig. 4(c)].

We limited the phonon occupancy to $n_{\max}^{\mathrm{ph}} = 8$ per site. Then, $d = 4(n_{\max}^{\mathrm{ph}} + 1) = 36$, and $\overline{D} = 35D_{\mathrm{f}}$ is so large that 2TDVP would be utterly unfeasible. By contrast, CBE–

FIG. 4. Peierls–Hubbard model: Real-space scattering of two electron wave packets, for $U = 10$ and $\omega_{\mathrm{ph}} = 3$, computed with $\delta = 0.05$, $n_{\max}^{\mathrm{ph}} = 8$ and U(1) spin symmetry. (a,b) Spin magnetic moment $S^z(x,t)$ for $g = 0$ and $g = 1$. (c) Phonon density $n^{\mathrm{ph}}(x,t)$, (d) bond dimensions, and (e) error analysis: energy $\delta E(t)$ (dashed line) and discarded weight $\xi(t)$ (dotted line), all computed for $g = 1$, with $D_{\max} = 500$.

TDVP requires a comparatively small bond expansion of only $\widetilde{D}(t) \leq 4D_{\max}$ for the times shown; after that, the discarded weight $\xi(t)$ becomes substantial [Figs. 4(d,e)].

Conclusions and outlook.— Among the schemes for MPS time evolution, 1TDVP has various advantages (see introduction), but its projection error is uncontrolled. 2TDVP remedies this, albeit at 2s costs, $\mathcal{O}(d^2wD^3)$, and is able to simulate dynamics reliably [44]. CBE–TDVP at 1s costs, $\mathcal{O}(dwD^3)$ achieves the same accuracy as 2TDVP. Moreover, CBE–TDVP comes with significantly slower growth of bond dimensions D in time, which speeds up the calculations further (see Ref. [56]).

Our benchmark tests of CBE–TDVP, on three exactly solvable spin models (two with long-range interactions), demonstrate its reliability. Our results on the Peierls–Hubbard model suggest that bi-polarons form during electron scattering—an effect not previously explored numerically. This illustrates the potential of CBE–TDVP for tracking complex dynamics in computationally very challenging models.

For applications involving the time evolution of MPSs defined on "doubled" local state spaces, with effective local bond dimensions $d_{\mathrm{eff}} = d^2$, the cost reduction of CBE–TDVP vs. 2TDVP, $\mathcal{O}(d^2wD^3)$ vs. $\mathcal{O}(d^4wD^3)$, will be particularly dramatic. Examples are finite temperature properties, treated by purification of the density matrix [87] or dissipation-assisted operator evolution [88]; and the dynamics of open quantum systems [89], described by Liouville evolution of the density matrix [90–92] or by an influence matrix approach [93].

[1] P. A. M. Dirac, Note on exchange phenomena in the Thomas atom, Math. Proc. Camb. Philos. Soc. **26**, 376 (1930).

[2] A. McLachlan, A variational solution of the time-dependent Schrodinger equation, Molecular Physics **8**, 39 (1964).

[3] H.-D. Meyer, U. Manthe, and L. Cederbaum, The multiconfigurational time-dependent Hartree approach, Chem. Phys. Lett. **165**, 73 (1990).

[4] E. Deumens, A. Diz, R. Longo, and Y. Öhrn, Time-dependent theoretical treatments of the dynamics of electrons and nuclei in molecular systems, Rev. Mod. Phys. **66**, 917 (1994).

[5] F. Verstraete, V. Murg, and J. Cirac, Matrix product states, projected entangled pair states, and variational renormalization group methods for quantum spin systems, Adv. Phys **57**, 143 (2008).

[6] J. I. Cirac and Frank Verstraete, Renormalization and tensor product states in spin chains and lattices, J. Phys. A Math. **42**, 504004 (2009).

[7] J. Eisert, M. Cramer, and M. B. Plenio, Colloquium: Area laws for the entanglement entropy, Rev. Mod. Phys. **82**, 277 (2010).

[8] U. Schollwöck, The density-matrix renormalization group in the age of matrix product states, Ann. Phys. **326**, 96 (2011).

[9] E. Stoudenmire and S. R. White, Studying two-dimensional systems with the density matrix renormalization group, Annu. Rev. Condens. Matter Phys. **3**, 111 (2012).

[10] J. C. Bridgeman and C. T. Chubb, Hand-waving and interpretive dance: an introductory course on tensor networks, J. Phys. A Math. **50**, 223001 (2017).

[11] R. Orús, Tensor networks for complex quantum systems, Nat. Rev. Phys. **1**, 538 (2019).

[12] P. Silvi, F. Tschirsich, M. Gerster, J. Jünemann, D. Jaschke, M. Rizzi, and S. Montangero, The tensor networks anthology: Simulation techniques for many-body quantum lattice systems, SciPost Phys. Lect. Notes , 8 (2019).

[13] O. Koch and C. Lubich, Dynamical low-rank approximation, SIAM J. Matrix Anal. Appl. **29**, 434 (2007).

[14] O. Koch and C. Lubich, Dynamical tensor approximation, SIAM J. Matrix Anal. Appl. **31**, 2360 (2010).

[15] J. Haegeman, J. I. Cirac, T. J. Osborne, I. Pižorn, H. Verschelde, and F. Verstraete, Time-dependent variational principle for quantum lattices, Phys. Rev. Lett. **107**, 070601 (2011).

[16] T. Koffel, M. Lewenstein, and L. Tagliacozzo, Entanglement entropy for the long-range Ising chain in a transverse field, Phys. Rev. Lett. **109**, 267203 (2012).

[17] P. Hauke and L. Tagliacozzo, Spread of correlations in long-range interacting quantum systems, Phys. Rev. Lett. **111**, 207202 (2013).

[18] C. Lubich and I. V. Oseledets, A projector-splitting integrator for dynamical low-rank approximation, BIT Numer. Math. **54**, 171 (2013).

[19] C. Lubich, T. Rohwedder, R. Schneider, and B. Vandereycken, Dynamical approximation by hierarchical Tucker and tensor-train tensors, SIAM J. Matrix Anal. Appl. **34**, 470 (2013).

[20] J. Haegeman, T. J. Osborne, and F. Verstraete, Post-matrix product state methods: To tangent space and beyond, Phys. Rev. B **88**, 075133 (2013).

[21] C. Lubich, I. V. Oseledets, and B. Vandereycken, Time integration of tensor trains, SIAM J. Numer. Anal. **53**, 917 (2015).

[22] J. Haegeman, C. Lubich, I. Oseledets, B. Vandereycken, and F. Verstraete, Unifying time evolution and optimization with matrix product states, Phys. Rev. B **94**, 165116 (2016).

[23] E. Kieri, C. Lubich, and H. Walach, Discretized dynamical low-rank approximation in the presence of small singular values, SIAM J. Numer. Anal. **54**, 1020 (2016).

[24] V. Zauner-Stauber, L. Vanderstraeten, M. T. Fishman, F. Verstraete, and J. Haegeman, Variational optimization algorithms for uniform matrix product states, Phys. Rev.

B **97**, 045145 (2018).

[25] L. Vanderstraeten, J. Haegeman, and F. Verstraete, Tangent-space methods for uniform matrix product states, SciPost Phys. Lect. Notes , 7 (2019).

[26] D. Bauernfeind and M. Aichhorn, Time Dependent Variational Principle for Tree Tensor Networks, SciPost Phys. **8**, 24 (2020).

[27] M. M. Rams and M. Zwolak, Breaking the entanglement barrier: Tensor network simulation of quantum transport, Phys. Rev. Lett. **124**, 137701 (2020).

[28] P. Secular, N. Gourianov, M. Lubasch, S. Dolgov, S. R. Clark, and D. Jaksch, Parallel time-dependent variational principle algorithm for matrix product states, Phys. Rev. B **101**, 235123 (2020).

[29] B. Kloss, D. R. Reichman, and Y. B. Lev, Studying dynamics in two-dimensional quantum lattices using tree tensor network states, SciPost Phys. **9**, 70 (2020).

[30] G. Ceruti, C. Lubich, and H. Walach, Time integration of tree tensor networks, SIAM J. Numer. Anal. **59**, 289 (2021).

[31] L. Kohn and G. E. Santoro, Efficient mapping for Anderson impurity problems with matrix product states, Phys. Rev. B **104**, 014303 (2021).

[32] M. Van Damme, R. Vanhove, J. Haegeman, F. Verstraete, and L. Vanderstraeten, Efficient matrix product state methods for extracting spectral information on rings and cylinders, Phys. Rev. B **104**, 115142 (2021).

[33] A. Milsted, J. Haegeman, and T. J. Osborne, Matrix product states and variational methods applied to critical quantum field theory, Phys. Rev. D **88**, 085030 (2013).

[34] E. Gillman and A. Rajantie, Topological defects in quantum field theory with matrix product states, Phys. Rev. D **96**, 094509 (2017).

[35] F. A. Y. N. Schröder and A. W. Chin, Simulating open quantum dynamics with time-dependent variational matrix product states: Towards microscopic correlation of environment dynamics and reduced system evolution, Phys. Rev. B **93**, 075105 (2016).

[36] J. del Pino, F. A. Y. N. Schröder, A. W. Chin, J. Feist, and F. J. Garcia-Vidal, Tensor network simulation of non-Markovian dynamics in organic polaritons, Phys. Rev. Lett. **121**, 227401 (2018).

[37] Y. Kurashige, Matrix product state formulation of the multiconfiguration time-dependent Hartree theory, J. Chem. Phys. **149**, 194114 (2018).

[38] B. Kloss, D. R. Reichman, and R. Tempelaar, Multiset matrix product state calculations reveal mobile Franck-Condon excitations under strong Holstein-type coupling, Phys. Rev. Lett. **123**, 126601 (2019).

[39] X. Xie, Y. Liu, Y. Yao, U. Schollwöck, C. Liu, and H. Ma, Time-dependent density matrix renormalization group quantum dynamics for realistic chemical systems, J. Chem. Phys. **151**, 224101 (2019).

[40] Y. Xu, Z. Xie, X. Xie, U. Schollwöck, and H. Ma, Stochastic adaptive single-site time-dependent variational principle, JACS Au **2**, 335 (2022).

[41] G. Vidal, Efficient simulation of one-dimensional quantum many-body systems, Phys. Rev. Lett. **93**, 040502 (2004).

[42] A. J. Daley, C. Kollath, U. Schollwöck, and G. Vidal, Time-dependent density-matrix renormalization-group using adaptive effective Hilbert spaces, J. Stat. Mech.: Theor. Exp. **P04005** (2004).

[43] S. R. White and A. E. Feiguin, Real-time evolution using the density matrix renormalization group, Phys. Rev. Lett. **93**, 076401 (2004).

[44] S. Paeckel, T. Köhler, A. Swoboda, S. R. Manmana, U. Schollwöck, and C. Hubig, Time-evolution methods for matrix-product states, Ann. Phys. **411**, 167998 (2019).

[45] E. Hairer, C. Lubich, and G. Wanner, *Geometric Numerical Integration* (Springer-Verlag, 2006).

[46] B. Kloss, Y. B. Lev, and D. Reichman, Time-dependent variational principle in matrix-product state manifolds: Pitfalls and potential, Phys. Rev. B **97**, 024307 (2018).

[47] S. Goto and I. Danshita, Performance of the time-dependent variational principle for matrix product states in the long-time evolution of a pure state, Phys. Rev. B **99**, 054307 (2019).

[48] T. Chanda, P. Sierant, and J. Zakrzewski, Time dynamics with matrix product states: Many-body localization transition of large systems revisited, Phys. Rev. B **101**, 035148 (2020).

[49] A. Dektor, A. Rodgers, and D. Venturi, Rank-adaptive tensor methods for high-dimensional nonlinear PDEs, J. Sci. Comput. **88**, 36 (2021).

[50] M. Yang and S. R. White, Time-dependent variational principle with ancillary Krylov subspace, Phys. Rev. B **102**, 094315 (2020).

[51] G. Ceruti, J. Kusch, and C. Lubich, A rank-adaptive robust integrator for dynamical low-rank approximation, BIT Numer. Math. (2022).

[52] A. J. Dunnett and A. W. Chin, Efficient bond-adaptive approach for finite-temperature open quantum dynamics using the one-site time-dependent variational principle for matrix product states, Phys. Rev. B **104**, 214302 (2021).

[53] C. Hubig, J. Haegeman, and U. Schollwöck, Error estimates for extrapolations with matrix-product states, Phys. Rev. B **97**, 045125 (2018).

[54] A. Gleis, J.-W. Li, and J. von Delft, Controlled bond expansion for DMRG ground state search at single-site costs, arXiv:2207.14712 [cond-mat.str-el] (2022).

[55] A. Gleis, J.-W. Li, and J. von Delft, Projector formalism for kept and discarded spaces of matrix product states, arXiv:2207.13161 [quant-ph] (2022).

[56] See Supplemental Material at [url] for: (S-1) an explanation of the structure of the tangent space projector $\mathcal{P}^{1s}$; (S-2) an analysis of the fidelity of CBE–TDVP: we show that under backward time evolution (implemented by changing the sign of H), the domain wall recontracts to a point; and (S-3) a comparison of the CPU time costs of CBE–TDVP vs. 2TDVP. The Supplemental Material includes Refs. [21, 22, 51].

[57] R. I. McLachlan, On the numerical integration of ordinary differential equations by symmetric composition methods, SIAM J. Sci. Comput **16**, 151 (1995).

[58] A first-order integrator, with error $\mathcal{O}(\delta)$, involves a single left-to-right sweep L_δ or right-to-left sweep R_δ through the entire chain. For 1TDVP, L_δ and R_δ are adjoint operations, with $L_{-\delta} \circ R_\delta = \mathbb{1}$, hence higher-order integrators can be obtained through symmetric compositions [57]. We use one of third order (error $\mathcal{O}(\delta^3)$): $L_{\delta/4} \circ R_{\delta/2} \circ L_{\delta/4}$, for one time step, $R_{\delta/4} \circ L_{\delta/2} \circ R_{\delta/4}$ for the next.

[59] B. Vanhecke, M. V. Damme, J. Haegeman, L. Vanderstraeten, and Frank Verstraete, Tangent-space methods for truncating uniform MPS, SciPost Phys. Core **4**, 4 (2021).

[60] T. Antal, Z. Rácz, A. Rákos, and G. M. Schütz, Transport in the XX chain at zero temperature: Emergence of flat magnetization profiles, Phys. Rev. E **59**, 4912 (1999).

[61] D. Gobert, C. Kollath, U. Schollwöck, and G. Schütz, Real-time dynamics in spin-1/2 chains with adaptive time-dependent density matrix renormalization group, Phys. Rev. E **71**, 036102 (2005).

[62] S. Dooley and T. P. Spiller, Fractional revivals, multiple-Schrödinger-cat states, and quantum carpets in the interaction of a qubit with n qubits, Phys. Rev. A **90**, 012320 (2014).

[63] T. Yamamoto, Y. Saiga, M. Arikawa, and Y. Kuramoto, Exact dynamical structure factor of the degenerate Haldane-Shastry model, Phys. Rev. Lett. **84**, 1308 (2000).

[64] T. Yamamoto, Y. Saiga, M. Arikawa, and Y. Kuramoto, Exact dynamics of the SU(K) Haldane-Shastry model, J. Phys. Soc. Japan **69**, 900 (2000).

[65] F. D. M. Haldane and M. R. Zirnbauer, Exact calculation of the ground-state dynamical spin correlation function of a $s = 1/2$ antiferromagnetic Heisenberg chain with free spinons, Phys. Rev. Lett. **71**, 4055 (1993).

[66] M. P. Zaletel, R. S. K. Mong, C. Karrasch, J. E. Moore, and F. Pollmann, Time-evolving a matrix product state with long-ranged interactions, Phys. Rev. B **91**, 165112 (2015).

[67] J. Bonča, T. Katrašnik, and S. A. Trugman, Mobile bipolaron, Phys. Rev. Lett. **84**, 3153 (2000).

[68] R. T. Clay and R. P. Hardikar, Intermediate phase of the one dimensional half-filled Hubbard-Holstein model, Phys. Rev. Lett. **95**, 096401 (2005).

[69] H. Fehske and S. A. Trugman, Numerical solution of the Holstein polaron problem, in *Polarons in Advanced Materials*, edited by A. S. Alexandrov (Springer Netherlands, Dordrecht, 2007) p. 393.

[70] J. P. Hague, P. E. Kornilovitch, J. H. Samson, and A. S. Alexandrov, Superlight small bipolarons in the presence of a strong Coulomb repulsion, Phys. Rev. Lett. **98**, 037002 (2007).

[71] R. P. Hardikar and R. T. Clay, Phase diagram of the one-dimensional Hubbard-Holstein model at half and quarter filling, Phys. Rev. B **75**, 245103 (2007).

[72] M. Tezuka, R. Arita, and H. Aoki, Phase diagram for the one-dimensional Hubbard-Holstein model: A density-matrix renormalization group study, Phys. Rev. B **76**, 155114 (2007).

[73] H. Fehske, G. Hager, and E. Jeckelmann, Metallicity in the half-filled Holstein-Hubbard model, Europhys Lett. **84**, 57001 (2008).

[74] D. J. J. Marchand, G. De Filippis, V. Cataudella, M. Berciu, N. Nagaosa, N. V. Prokof'ev, A. S. Mishchenko, and P. C. E. Stamp, Sharp transition for single polarons in the one-dimensional Su-Schrieffer-Heeger model, Phys. Rev. Lett. **105**, 266605 (2010).

[75] M. Hohenadler and F. F. Assaad, Excitation spectra and spin gap of the half-filled Holstein-Hubbard model, Phys. Rev. B **87**, 075149 (2013).

[76] M. Hohenadler, Interplay of site and bond electron-phonon coupling in one dimension, Phys. Rev. Lett. **117**, 206404 (2016).

[77] J. Sous, M. Chakraborty, R. V. Krems, and M. Berciu, Light bipolarons stabilized by Peierls electron-phonon coupling, Phys. Rev. Lett. **121**, 247001 (2018).

[78] T. E. Reinhard, U. Mordovina, C. Hubig, J. S. Kretchmer, U. Schollwöck, H. Appel, M. A. Sentef, and A. Rubio, Density-matrix embedding theory study of the one-dimensional Hubbard–Holstein model, J. Chem. Theory Comput. **15**, 2221 (2019).

[79] A. Nocera, J. Sous, A. E. Feiguin, and M. Berciu, Bipolaron liquids at strong Peierls electron-phonon couplings, Phys. Rev. B **104**, L201109 (2021).

[80] D. Golež, J. Bonča, and L. Vidmar, Dissociation of a Hubbard-Holstein bipolaron driven away from equilibrium by a constant electric field, Phys. Rev. B **85**, 144304 (2012).

[81] P. Werner and M. Eckstein, Phonon-enhanced relaxation and excitation in the Holstein-Hubbard model, Phys. Rev. B **88**, 165108 (2013).

[82] L. Chen, Y. Zhao, and Y. Tanimura, Dynamics of a one-dimensional Holstein polaron with the hierarchical equations of motion approach, J. Phys. Chem. Lett. **6**, 3110 (2015).

[83] J. H. Fetherolf, D. Golež, and T. C. Berkelbach, A unification of the Holstein polaron and dynamic disorder pictures of charge transport in organic crystals, Phys. Rev. X **10**, 021062 (2020).

[84] B. Pandey, G. Alvarez, and E. Dagotto, Excitonic wave-packet evolution in a two-orbital Hubbard model chain: A real-time real-space study, Phys. Rev. B **104**, L220302 (2021).

[85] K. A. Al-Hassanieh, F. A. Reboredo, A. E. Feiguin, I. González, and E. Dagotto, Excitons in the one-dimensional Hubbard model: A real-time study, Phys. Rev. Lett. **100**, 166403 (2008).

[86] A. Moreno, A. Muramatsu, and J. M. P. Carmelo, Charge and spin fractionalization beyond the Luttinger-liquid paradigm, Phys. Rev. B **87**, 075101 (2013).

[87] F. Verstraete, J. J. Garcia-Ripoll, and J. I. Cirac, Matrix product density operators: Simulation of finite-temperature and dissipative systems, Phys. Rev. Lett. **93**, 207204 (2004).

[88] T. Rakovszky, C. W. von Keyserlingk, and F. Pollmann, Dissipation-assisted operator evolution method for capturing hydrodynamic transport, Phys. Rev. B **105**, 075131 (2022).

[89] H. Weimer, A. Kshetrimayum, and R. Orús, Simulation methods for open quantum many-body systems, Rev. Mod. Phys. **93**, 015008 (2021).

[90] G. Lindblad, On the generators of quantum dynamical semigroups, Comm. Math. Phys. **48**, 119 (1976).

[91] F. Verstraete, J. J. García-Ripoll, and J. I. Cirac, Matrix product density operators: Simulation of finite-temperature and dissipative systems, Phys. Rev. Lett. **93**, 207204 (2004).

[92] M. Zwolak and G. Vidal, Mixed-state dynamics in one-dimensional quantum lattice systems: A time-dependent superoperator renormalization algorithm, Phys. Rev. Lett. **93**, 207205 (2004).

[93] A. Lerose, M. Sonner, and D. A. Abanin, Influence matrix approach to many-body floquet dynamics, Phys. Rev. X **11**, 021040 (2021).

[94] A. Weichselbaum, Non-Abelian symmetries in tensor networks: A quantum symmetry space approach, Ann. Phys. **327**, 2972 (2012).

[95] A. Weichselbaum, X-symbols for non-Abelian symmetries in tensor networks, Phys. Rev. Res. **2**, 023385 (2020).

Supplemental material: Time-dependent variational principle with controlled bond expansion for matrix product states

Jheng-Wei Li,[1] Andreas Gleis,[1] and Jan von Delft[1]

[1]*Arnold Sommerfeld Center for Theoretical Physics, Center for NanoScience, and Munich Center for Quantum Science and Technology, Ludwig-Maximilians-Universität München, 80333 Munich, Germany*

(Dated: August 24, 2022)

S-1. SINGLE SITE (FIXED RANK) TANGENT SPACE PROJECTOR

The structure (7) of the tangent space projector $\mathcal{P}^{1s}$ can be motivated by the following short-cut argument (equivalent to invoking gauge invariance [21, 22]). If Ψ is represented as an MPS, then its tangent vectors $\delta\Psi$ under the fixed-rank approximation can be expressed as a sum of MPSs each containing one derivative of a local tensor. This representation is not unique, but its gauge redundancy can be easily removed. To do so, let us first consider the variation of MPS in Eq. (1) on a single bond ℓ, i.e., $A_\ell C_{\ell+1} = A_\ell \Lambda_\ell B_{\ell+1}$, while the other tensors remain fixed (and hence are not depicted below). Its first order variation then gives us $\delta A_\ell \Lambda_\ell B_{\ell+1} + A_\ell \delta\Lambda_\ell B_{\ell+1} + A_\ell \Lambda_\ell \delta B_{\ell+1}$. By further rewriting $\delta A_\ell \Lambda_\ell$ as $A_\ell \Lambda'_\ell + \overline{A}_\ell \overline{\Lambda}'_\ell$ and $\Lambda_\ell \delta B_{\ell+1}$ as $\Lambda''_\ell B_{\ell+1} + \overline{\Lambda}''_\ell \overline{B}_{\ell+1}$, we obtain the following unique decomposition,

$$\delta\left(\underset{A_\ell \ \Lambda_\ell \ B_{\ell+1}}{\overset{}{\rightthreetimes\!\circ\!\looparrowright}}\right) = \underset{\overline{A}_\ell \ \overline{\Lambda}'_\ell \ B_{\ell+1}}{\overset{}{\rightthreetimes\!\circ\!\looparrowright}} + \underset{A_\ell \ \widetilde{\Lambda}_\ell \ B_{\ell+1}}{\overset{}{\rightthreetimes\!\circ\!\looparrowright}} + \underset{A_\ell \ \overline{\Lambda}''_\ell \ \overline{B}_{\ell+1}}{\overset{}{\rightthreetimes\!\circ\!\looparrowright}}, \quad \text{(S1)}$$

with $\widetilde{\Lambda}_\ell = \Lambda'_\ell + \delta\Lambda_\ell + \Lambda''_\ell$. The three terms on the right are mutually orthogonal to each other. Each of them belongs to the image space of one of the following three orthogonal projectors:

$$\rightthreetimes\ \looparrowright, \quad \rightthreetimes\ \looparrowright, \quad \rightthreetimes\ \looparrowright; \quad \text{(S2)}$$

their sum is a tangent space projector for $A_\ell \Lambda_\ell B_{\ell+1}$. Repeating the same argument for all the bonds, while avoiding double counting, i.e., including every term only once, we readily obtain $\mathcal{P}^{1s}$ given by the second line of Eq. (7).

Therefore, given an MPS of the form (1), $\mathcal{P}^{1s}$ is indeed the orthogonal projector onto its tangent space under the fixed-rank approximation. For real-time evolution, applying the Hamiltonian to $|\Psi\rangle$ leads the state out of its tangent space. In the 1TDVP scheme, $H|\Psi\rangle$ is approximated by $\mathcal{P}^{1s}H|\Psi\rangle$, its orthogonal projection onto the tangent space, leading to Eq. (6).

S-2. ANALYSIS OF CBE-TDVP ERROR PROPAGATION

The TDVP time evolution of an MPS under the fixed-rank approximation is unitary, with energy conservation if the Hamiltonian is time-independent. Expanding the tangent space does not spoil these desirable properties, provided that no truncations are performed. However, then the bond dimension would keep growing with time, which is not practical for studies of long-time dynamics.

With our CBE approach, we instead restrict the bond dimension growth by bond trimming using $\epsilon = 10^{-12}$, and also stopping the increase of D_f once it has reached a specified maximal value $D_{\max}$. Due to these truncations, the desirable TDVP properties are no longer satisfied exactly. However, *for each time step* they do hold within the truncation error, as shown by Ceruti, Kusch, and Lubich [51]. Thus, the time evolution per time step is almost unitary. Nevertheless, errors can accumulate with time, hence it is unclear *a priori* to what extent the desirable TDVP properties survive over long times.

To investigate this, we revisit our first benchmark example for the domain wall motion of the XX model. We use CBE–TDVP (while exploiting $U(1)$ spin symmetry) to compute the forward-backward fidelity [Fig. S-1(a)]

$$F(\bar{t}) = |\langle\Psi_-(\bar{t})|\Psi_+(t)\rangle|^2, \quad \bar{t} = t_{\max} - t \in [0, t_{\max}]. \quad \text{(S3)}$$

Here, $|\Psi_+(t)\rangle = e^{-iHt}|\Psi(0)\rangle$ is obtained through forward evolution for time t, and $|\Psi_-(\bar{t})\rangle = e^{iH\bar{t}}|\Psi_+(t_{\max})\rangle$ through forward evolution until time $t = t_{\max}$, then back-evolution for $\bar{t} = t_{\max} - t$ to get back to time t. The deviation of the fidelity from unity, $\delta F(\bar{t}) = 1 - F(\bar{t})$, equals zero for unitary evolution; increases with $\bar{t}$ if time evolution is computed using truncations; and tends to 1 for $\bar{t} \to t_{\max}$ if truncations are too severe.

Figure 1(b) shows the back-evolution of the domain wall described by $|\Psi_-(\bar{t})\rangle$ as $\bar{t}$ increases from 0 to $t_{\max} = 40$, where both $|\Psi_+(t)\rangle$ and $|\Psi_-(\bar{t})\rangle$ were computed using CBE–TDVP with the truncation parameters stated in the main text, namely $\widetilde{\epsilon} = 10^{-6}$ and $D_{\max} = 120$. The corresponding $\delta F(\bar{t})$ (Fig. 1(d), black dashes) shows initial transient growth, but then *saturates* at a remarkably small plateau value of 6.7×10^{-5}. Moreover, the corresponding bond expansion per update, $\widetilde{D}(\bar{t})$ (Fig. 1(e), black dots), increases only fairly slowly. For these truncation settings, the CBE–TDVP errors are thus clearly under good control and do not accumulate rapidly, so that long-time evolution can be computed accurately.

The fidelity becomes worse ($\delta F(\bar{t})$ increases) if the singular-value threshold for bond expansion, $\widetilde{\epsilon}$, is raised (Fig. 1(d), dashed lines). Nevertheless, even for $\widetilde{\epsilon}$ as large as 10^{-2} we find long-time plateau behavior for $\delta F(\bar{t})$, implying that the errors remain controlled. This illustrates

(a)

$|\langle\Psi_-(\bar t)|\Psi_+(t)\rangle|^2$

0   t t_{max}

t_{max} $\bar t = t_{max} - t$ 0

(b) CBE–TDVP

Position

-25

0

25

$\widetilde\epsilon = 10^{-6}$
$D_{max} = 120$

0.5

-0.5

(d)   1TDVP$_{D=120}$

10^{-0}

10^{-4}

$\widetilde\epsilon$ D_{max} 120 ∞

10^{-2}
10^{-4}
10^{-6}

10^{-8}

10^{-12}

(c) 1TDVP

Position

-25

0

25

0.5

-0.5

(e)

$D_f/5$

D_f

$\widetilde D$

250
200
150
100
50

0   20   40

$\bar t$

0   20   40

$\bar t$
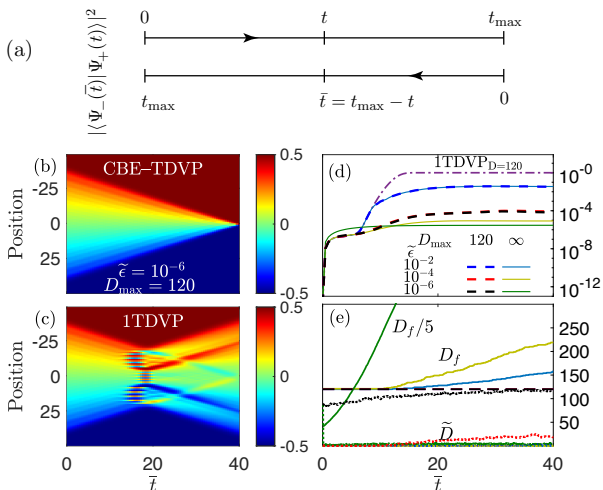
FIG. S-1. (a) Forward-backward time evolution for the computation of $F(t)$. (b,c) Back-evolution of the domain wall, described by $|\Psi_-(\bar t)\rangle$, computed using (b) CBE–TDVP and (c) 1TDVP. (d) Time evolution of $\delta F(\bar t) = 1 - F(\bar t)$, computed via 1TDVP with $D = 120$ (dash-dotted line), and via CBE–TDVP using three values of $\widetilde\epsilon$, and either with $D_{max} = 120$ (dashed lines) or $D_{max} = \infty$ (solid lines). (e) Time evolution of the corresponding bond dimensions $D_f(\bar t)$ (solid lines) and $\widetilde D(\bar t)$ (dots). (The solid green curve shows $D_f/5$.)

the robustness of CBE–TDVP. The plateau value can be decreased by increasing D_{max}, but the reduction becomes significant only if $\widetilde\epsilon$ is sufficiently small. Even for $D_{max} = \infty$ (Fig. 1(d), solid lines) the plateau reduction relative to $D_{max} = 120$ is modest, whereas the corresponding growth in D_f (Fig. 1(e), solid lines) becomes so rapid that this setting is not recommended in practice.

Finally, Figs. 1(c) and 1(d) (dash-dotted, purple line) also show 1TDVP results, computed with $D = 120$: the domain wall fails to recontract to a point, and the fidelity reaches zero ($\delta F(\bar t)$ reaches 1). This occurs even though 1TDVP uses no truncations besides the tangent space projection, and hence yields unitary time evolution. This poor performance illustrates a key limitation of 1TDVP when exploiting symmetries (as here): time evolution involves transitions to sectors having quantum numbers not yet present, but 1TDVP cannot include these, due to the fixed-rank nature of its tangent space projection. CBE–TDVP by construction lifts this restriction.

S-3. COMPARISON OF CPU TIME FOR CBE–TDVP AND 2TDVP

In this section, we compare the CPU time for CBE–TDVP and 2TDVP. As a demonstration, we use the one-axis twisting (OAT) model discussed in *Results* in the main text. All CPU time measurements were done on a single core of an Intel Core i7-9750H processor.

First, we compare the early-time behavior of CBE–TDVP and 2TDVP. From $t = 0$ to 1.5, both methods yield good accuracy as shown in Fig. S-2(a). The CPU

1   10 10^2 10^3

(a) $S_x^{tot}(t)$

30
20
10

CBE–TDVP
2TDVP
Exact

(c) 2TDVP

MPS bond

50
30
10

(b) CPU Time [10^4 sec]

20
15
10
5
0

2TDVP

CBE-TDVP

(d) CBE–TDVP

MPS bond

50
30
10

0   0.5   1   1.5

t

0   0.5   1   1.5

t
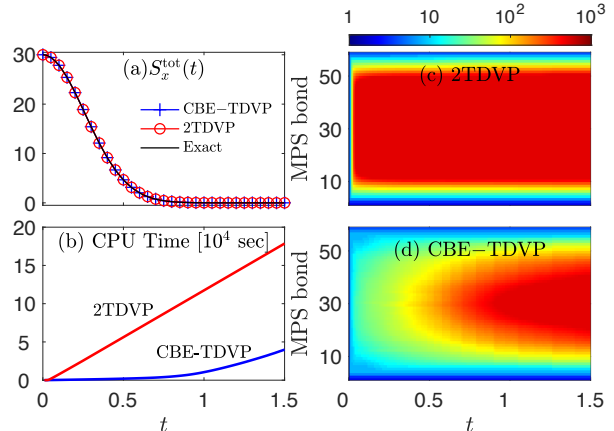
FIG. S-2. 60-site one-axis twisting model for spin $S = 1/2$: Time evolution of an initially x-polarized spin state, computed using $\delta = 0.01$, $D_{max} = 500$, and $\mathbb{Z}_2$ spin symmetry. (a) Total spin $S_x^{tot}(t)$ for CBE–TDVP (blue), 2TDVP (red) and the exact solution (black). (b) CPU time for CBE-TDVP (blue) and 2TDVP (red). (c,d) Color scale plot of the bond dimension as a function of time for all MPS bonds, for (c) 2TDVP and (d) CBE–TDVP.

time spent to achieve this, however, is quite different. In Fig. S-2(b), we see that while the 2TDVP takes about two days, CBE–TDVP accomplishes the same time span overnight.

The main reason for this difference does not lie in the 1s vs. 2s scaling of CBE–TDVP vs. 2TDVP (discussed below), because $d = 2$ (for $S = 1/2$) is small, and CBE involves some algorithmic overhead for determining the truncated complement $\widetilde A_\ell^{tr}(\blacktriangledown)$. Instead, the difference reflects the fact that the growth in MPS bond dimension $D(t)$ with time is much slower for CBE-TDVP than 2TDVP. This implies dramatic cost savings, since both methods have time complexity proportional to D^3. Figure S-2(c,d) show the time evolution of bond dimensions for all MPS bonds for CBE–TDVP and 2TDVP respectively. For 2TDVP [Fig. S-2(c)], the bond dimensions grow almost exponentially and quickly saturate to their specified maximal value, here $D_{max} = 500$. This saturation is reflected by the early onset of linear growth in the CPU time in Fig. S-2(b). By contrast, the bond dimensions of CBE–TDVP show a much slower growth [Fig. S-2(d)], yielding a strong reduction in CPU time compared to 2TDVP.

Second, we demonstrate that when D is fixed, the time complexity of CBE–TDVP vs. 2TDVP scales as d vs. d^2, implying 1s vs. 2s scaling. Figure S-3 shows this by displaying the CPU time per sweep for the OAT model for several different values of the spin S, with the MPS bond dimension fixed at $D_{max} = 500$.
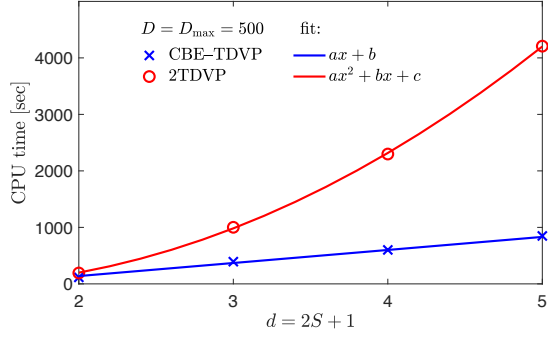
FIG. S-3. CPU time per sweep for the 20-site one-axis twisting model, computed for several values of S, at $D_{\max} = 500$.

3 Heavy-fermion quantum criticality in the periodic Anderson model

3.1 Overview

This chapter presents an extensive high-resolution study of heavy-fermion (HF) quantum criticality in the periodic Anderson model (PAM) using 2-site cellular dynamical mean-field theory (2CDMFT) with the numerical renormalization group (NRG) as an impurity solver. It is based on earlier studies of quantum criticality in the PAM using 2CDMFT with an exact diagonalization (ED) impurity solver [DLCK08a, DLCK08b].

The 2CDMFT plus ED studies [DLCK08a, DLCK08b] identified a Kondo breakdown (KB) QCP in the PAM, described in terms of an orbital selective Mott transition (OSMT). This OSMT features an FS reconstruction and a depletion of f-electron spectral weight at the Fermi level, suggesting a low-energy decoupling of the c and f electrons. Further, it was clarified that magnetic ordering at the transition should be interpreted as a byproduct of the OSMT [DLCK08b], in stark contrast to an itinerant magnetic transition as it is described for instance by Hertz-Millis-Moriya theory, c.f. Sec. 1.2.1. However, due to the coarse frequency resolution of the ED impurity solver, these studies left many questions unanswered or without a clear definitive answer. For instance, it was not clear whether the OSMT is continuous or a weakly first-order transition, or whether the FS undergoes a sudden jump, or whether the reconstruction is continuous, see e.g. Fig. 3 of Ref. [DLCK08b]. Further, it was not possible to properly resolve and access the quantum critical region governed by the QCP. Thus, it was not clear whether this region hosts non-Fermi liquid (NFL) behavior and whether it is consistent with the strange metal behavior found in many HF compounds.

The question regarding the quantum critical region is highly non-trivial. 2CDMFT maps the PAM on an effective two-impurity Anderson model (2IAM). This impurity model hosts an *unstable* impurity QCP with NFL behavior in its quantum critical region [FHLS03]. However, the effective 2IAM which arises in 2CDMFT is a priori subject to relevant perturbations that destabilize the impurity QCP. Therefore, it has been argued in Ref. [DLCK08a] that the KB transition found there using 2CDMFT plus ED is governed by the *proximity* to the impurity QCP, even though this QCP cannot be reached due to the presence of a relevant perturbation. This, of course, leaves open the question of how close the 2CDMFT solution gets to the impurity QCP, and how severely it is influenced by the impurity QCP.

It should also be noted that a later 2CDMFT study of the PAM using a quantum Monte Carlo (QMC) impurity solver did not find signs of KB quantum criticality [THKD11]. The same goes for a DCA study which also used QMC as an impurity solver [MBA10]. However, the 2CDMFT study reached temperatures of order 10^{-3} in terms of the c-electron bandwidth while the DCA study had to stick to even higher temperatures of order 10^{-2} in terms of the c-electron bandwidth. Thus, the temperatures considered in the QMC-based studies may have been too high for conclusive answers regarding the existence of a KB–QCP and its properties. Nevertheless, the absence of KB physics in the 2CDMFT or DCA plus QMC studies raises the question whether the KB transition found in the 2CDMFT plus ED studies [DLCK08a, DLCK08b] is due to the coarse frequency resolution of ED or a genuine feature of the 2CDMFT approximation to the PAM.

To shed light on the questions left open by earlier studies, we studied the PAM in Refs. [P4] and [P5] using 2CDMFT with NRG as an impurity solver. Due to the logarithmic frequency resolution and the ability to study arbitrary temperatures, NRG is perfectly suited to study quantum critical phenomena and is not faced by the limitations of ED (coarse frequency resolution) or QMC impurity solvers (limited by temperature).

In Ref. [P4], we show that 2CDMFT indeed captures a KB–QCP in terms of an OSMT, confirming this finding of the earlier 2CDMFT plus ED studies [DLCK08a, DLCK08b]. Due to the unprecedented low-frequency resolution of NRG, we can confirm that this transition is continuous and show that the FS indeed undergoes a discrete jump at zero temperature. Apart from that, we find several surprising aspects that go far beyond the early 2CDMFT plus ED work: First, we show that even though the FS jumps across the transition and is small in the RKKY phase, c and f electrons are *not* decoupled in the RKKY phase. This leads to the emergence of a *third* narrow QP band in the RKKY phase, which is surprising considering that the PAM has two orbitals (c and f) per site. Further, we find that the CDMFT self-consistency conditions stabilize a novel quantum critical NFL fixed point which governs the physics at the QCP and in the quantum critical region. This fixed point bears some similarities to the impurity fixed point mentioned above, but with the important difference that the former exists in the presence of perturbations which would render the latter unstable.

In Ref. [P5], we study the NFL behavior of the quantum critical fixed point in more detail. We uncover several intriguing aspects, including ω/T scaling of several dynamical susceptibilities. Interestingly, this includes the current susceptibility,[1] which implies ω/T scaling of the optical conductivity. We find that this ω/T scaling is with corresponding strange metal scaling in $YbRh_2Si_2$.

P4 *Emergent Properties of the Periodic Anderson Model: a High-Resolution, Real-Frequency Study of Heavy-Fermion Quantum Criticality*
Andreas Gleis, Seung-Sup B. Lee, Gabriel Kotliar, and Jan von Delft
© 2023 The Authors
arXiv:2310.12672
reproduced on pages pages 85–129

P5 *Dynamical scaling and Planckian dissipation due to heavy-fermion quantum criticality*
Andreas Gleis, Seung-Sup B. Lee, Gabriel Kotliar, and Jan von Delft
© 2024 The Authors
arXiv:2404.14079
reproduced on pages pages 130–145

---

[1]Note that the current operator is zero at the impurity QCP mentioned earlier. This is because single-particle hopping between impurities is a relevant perturbation that destabilizes this impurity QCP [FHLS03].

Emergent Properties of the Periodic Anderson Model: a High-Resolution, Real-Frequency Study of Heavy-Fermion Quantum Criticality

Andreas Gleis,[1, *] Seung-Sup B. Lee,[1, 2, 3, †] Gabriel Kotliar,[4, 5, ‡] and Jan von Delft[1, §]

[1] *Arnold Sommerfeld Center for Theoretical Physics, Center for NanoScience, and Munich Center for Quantum Science and Technology, Ludwig-Maximilians-Universität München, 80333 Munich, Germany*
[2] *Department of Physics and Astronomy, Seoul National University, Seoul 08826, Korea*
[3] *Center for Theoretical Physics, Seoul National University, Seoul 08826, Korea*
[4] *Condensed Matter Physics and Materials Science Department, Brookhaven National Laboratory, Upton, NY 11973, USA*
[5] *Department of Physics and Astronomy, Rutgers University, Piscataway, NJ 08854, USA*
(Dated: October 20, 2023)

We study paramagnetic quantum criticality in the periodic Anderson model (PAM) using cellular dynamical mean-field theory (CDMFT), with the numerical renormalization group (NRG) as a cluster impurity solver. The PAM describes itinerant c electrons hybridizing with a lattice of localized f electrons. At zero temperature, it exhibits a much-studied quantum phase transition from a Kondo phase to an RKKY phase when the hybridization is decreased through a so-called Kondo breakdown quantum critical point (KB–QCP). There, Kondo screening of f spins by c electrons breaks down, so that f excitations change their character from somewhat itinerant to mainly localized, while c excitations remain itinerant. Building on Phys. Rev. Lett. 101, 256404 (2008), which interpreted the KB transition as an orbital selective Mott transition, we here elucidate its nature in great detail by performing a high-resolution, real-frequency study of various dynamical quantities (susceptibilities, self-energies, spectral functions). NRG allows us to study the quantum critical regime governed by the QCP and located between two temperature scales, $T_{\mathrm{FL}} < T_{\mathrm{NFL}}$. In this regime we find fingerprints of non-Fermi-liquid (NFL) behavior in several dynamical susceptibilities. Surprisingly, CDMFT self-consistency is essential to stabilize the QCP and the NFL regime. The Fermi-liquid (FL) scale T_{FL} decreases towards and vanishes at the KB–QCP; at temperatures below T_{FL}, FL behavior emerges. At $T = 0$, we find the following properties. The KB transition is continuous. The f quasiparticle weight decreases continuously as the transition is approached from either side, vanishing only at the KB–QCP. Therefore, the quasiparticle weight of the f-band is nonzero not only in the Kondo phase but also in the RKKY phase; hence, the FL quasiparticles comprise c *and* f electrons in both phases. The Fermi surface (FS) volumes in the two phases differ, implying a FS reconstruction at the KB–QCP. Whereas the large-FS Kondo phase has a two-band structure as expected, the small-FS RKKY phase unexpectedly has a three-band structure. We provide a detailed analysis of quasiparticle properties of both the Kondo and, for the first time, also the RKKY phase and uncover their differences. The FS reconstruction is accompanied by the appearance of a Luttinger surface on which the f self-energy diverges. The volumes of the Luttinger and Fermi surfaces are related to the charge density by a generalized Luttinger sum rule. We interpret the small FS volume and the emergent Luttinger surface as evidence for f-electron fractionalization in the RKKY phase. Finally, we compute the temperature dependence of the Hall coefficient and the specific heat, finding good qualitative agreement with experiments.

I. INTRODUCTION

For more than twenty years, quantum criticality in heavy-fermion (HF) systems has remained a subject of ongoing experimental and theoretical research [1–3]. In this paper, we study several open theoretical questions within a canonical model for HF systems, the periodic Anderson model (PAM) in three dimensions. Our new insights are derived from real-frequency results with unprecedented energy resolution at arbitrarily low temperatures. To set the scene, we begin with a survey of the state of the field, focusing in particular on aspects relevant for the subsequent discussion of our own results. Readers well familiar with HF physics may prefer to skip directly to section I E, which offers an outline of our own work and results.

A. Heavy fermion compounds and phenomena

HF compounds are a class of strongly correlated systems. They contain partially filled, localized f orbitals featuring strong local Coulomb repulsion. These localized orbitals hybridize with weakly interacting itinerant conduction bands (c bands) [4]. Particularly interesting is the appearance of a so-called Kondo breakdown (KB) quantum critical point (QCP) [5, 6], which will be subject of this work. The most prominent HF compounds featuring a KB–QCP derive their f orbitals from Yb or Ce.

* andreas.gleis@lmu.de
† sslee@snu.ac.kr
‡ kotliar@physics.rutgers.edu
§ vondelft@lmu.de

Examples are YbRh$_2$Si$_2$, CeCu$_{6-x}$Au$_x$ or the so called Ce-115 family, including CeCoIn$_5$ or CeRhIn$_5$. In the following, we will first introduce HF materials in general and then focus on experimental and theoretical aspects of the KB–QCP.

In HF systems, the hybridization between c and f electrons in combination with the strong local repulsion of f electrons generates Kondo correlations [4]. The strong repulsion effectively leads to the formation of local moments in the f orbitals. These experience an effective antiferromagnetic interaction with the c electrons due to hybridization. This promotes singlet formation between c and f electrons, similar to the Kondo singlet formation in the single impurity Kondo or Anderson models [7]. At temperatures below some scale T_{FL}, these Kondo correlations ultimately lead to the formation of a Fermi liquid (FL) with quasiparticles (QP) composed of both c and f electrons. Due to the local nature of the f electrons, these QPs usually have a large effective mass, hence the name heavy fermions.

If Kondo correlations are strong, the f electrons effectively become mobile and contribute to the density of mobile charge carriers. This especially affects the Fermi surface (FS) volume [8–13] and the Hall number n_{H} [14], which are both proportional to the charge density in a FL.

Kondo correlations compete with Rudermann-Kittel-Kasuya-Yosida (RKKY) [15–18] correlations. The RKKY interaction is an effective exchange interaction between f electrons mediated by the c electrons. If the c band is close to half-filling, this interaction is antiferromagnetic and promotes f-f singlet formation. This competes with the aforementioned c-f singlet formation [19].

It is believed that quantum criticality in HF systems is largely driven by this competition between RKKY and Kondo correlations [4, 18, 19]. Many HF materials can be tuned through a QCP by varying, e.g., magnetic fields, pressure, or doping [1, 2]. At these QCPs, a transition from the Kondo correlated heavy FL to some other, often magnetically ordered phase occurs. In some HF materials, this quantum phase transition may be understood in terms of a spin density wave (SDW) instability of the heavy FL, i.e. a magnetic transition in an itinerant electron system, described by Hertz-Millis-Moriya theory [20–23]. The antiferromagnetic ordering occurring at this SDW–QCP leads to a doubling of the unit cell, but QPs remain intact across the transition. In particular, the charge density involved in charge transport does not change abruptly across the SDW–QCP. It is therefore expected that the Hall coefficient, which is sensitive to the carrier density, likewise does not abruptly change at such a QCP [5, 6]. Further, in $d = 3$ spatial dimensions, such a QCP is essentially described by a ϕ^4 theory above its upper critical dimension. The long wavelength order parameter fluctuations are therefore Gaussian. Due to that, ω/T scaling of dynamical susceptibilities, a clear sign of an interacting fixed point [23], is not expected at a SDW–QCP.

Interestingly however, there is a large class of HF materials which show QCPs not compatible with the spin density wave scenario [1]. Examples include YbRh$_2$Si$_2$ [24–27], CeCu$_{6-x}$Au$_x$ [28], CeRhIn$_5$ [29, 30] and CeCoIn$_5$ [31]. In these materials, experimental observations point towards a sudden localization of the f electrons as the QCP is crossed from the Kondo correlation dominated heavy FL phase. In contrast to the SDW scenario, QP seem to be destroyed at this QCP [5, 6, 27]. It thus seems that the Kondo correlations between f and c electrons suddenly break down at the QCP, hence the name KB–QCP.

B. Experimental phenomena at the KB–QCP

In the following, we briefly summarize some experimental results indicative of the sudden breakdown of Kondo correlations and a corresponding sudden localization of the f electrons. We first focus on results close to $T = 0$ that indicate that the f electrons localize. After that, we discuss some remarkable dynamical and finite temperature properties of the KB–QCP. We focus on universal phenomena and omit material-specific aspects.

Fermi liquid behavior at low T.— In most HF systems, FL behavior is observed at temperatures below some FL scale T_{FL}, on either side of the KB–QCP (on the RKKY side, the FL is often antiferromagnetically ordered). Below T_{FL}, $\sim T^2$ behavior of the resistivity and $\sim T$ behavior of the specific heat is usually observed [26, 27, 32, 33].

FS reconstruction at $T = 0$.— A smoking gun signal of a KB–QCP is a sudden reconstruction of the FS at $T = 0$. In a FL, the volume of the FS is connected to the density of charge carriers by Luttingers theorem [8, 9, 34, 35]. Thus, a sudden change in the FS volume is also a sign for partial localization of charge carriers. A sudden change in the carrier density has been observed in terms of a sudden jump of the Hall number $n_{\text{H}} \sim 1/R_{\text{H}}$ (where R_{H} is the Hall coefficient) in many HF materials, including YbRh$_2$Si$_2$ [25, 36], CeCu$_{6-x}$Au$_x$ [28] and CeCoIn$_5$ [31]. Further evidence for a FS reconstruction is due to de Haas–van Alphen (dHvA) frequency measurements, with sudden jumps of dHvA frequencies observed in CeRhIn$_5$ [29, 30] and CeCoIn$_5$ [31, 37, 38]. More direct access to the FS is provided by angle resolved photoemission (ARPES) measurements [3], which have by now been performed on several HF compounds like CeCoIn$_5$ [39–42], CeRhIn$_5$ [43], YbRh$_2$Si$_2$ [44–46] or YbCo$_2$Si$_2$ [47]. Close to criticality, ARPES data on HF compounds is to date not quite conclusive yet since low-temperature scans across the KB–QCP (often tuned by magnetic field or pressure) are challenging.

Possible absence of magnetic ordering.— The KB–QCP is not necessarily accompanied by magnetic ordering [31, 48, 49]. In CeCoIn$_5$, antiferromagnetic order only occurs well away from the KB–QCP inside the RKKY dominated phase where the f electrons are localized [31]. Further, while for pure YbRh$_2$Si$_2$ antiferromagnetic ordering sets

in at the KB–QCP, this may be changed by chemical pressure [48]. In this way, the jump of n_{H} can be tuned to occur either deep in the antiferromagnetic phase or deep in the paramagnetic phase. This fact suggests that the KB–QCP is not tied to magnetic ordering [48, 50].

Continuous suppression of the FL scale to zero.— The above mentioned sudden FS reconstruction suggests that the KB–QCP marks a transition between two FL phases with different densities of mobile carriers. Observations on various different materials suggests that this transition is continuous: The FL scale T_{FL} decreases continuously to zero at the KB–QCP [27, 33] and the QP mass at the QCP diverges in many compounds [28, 29, 32] from both sides of the transition.

Onset scale for c-f hybridization.— Besides the FL scale T_{FL}, another important scale in HF compounds is the scale below which c-f hybridization begins to build up. We denote this scale by T_{NFL}, for reasons explained later. (It is often also denoted T_0.) This scale is visible for instance in scanning tunneling spectroscopy (STS) experiments [3] or in optical conductivity measurements in terms of a distinct gap in the STS or optical spectra, called hybridization gap. T_{NFL} is then the temperature below which hybridization gap formation sets in. This scale has been determined in many different HF compounds via STS, for instance in CeCoIn$_5$ [51], CeRhIn$_5$ [52] and YbRh$_2$Si$_2$ [53, 54], or via optical conductivity measurements, e.g. in YbRh$_2$Si$_2$ [55, 56], CeRhIn$_5$ [57], CeCoIn$_5$ [57, 58] and CeCu$_{6-x}$Au$_x$ [59]. These experiments unambiguously show that T_{NFL} is virtually unaffected by the distance to the KB–QCP or whether the f electrons are (de-)localized at $T = 0$.

Strange metal behavior.— Close to the KB–QCP, there is a vast scale separation between T_{NFL} and the FL scale, giving rise to an intermediate quantum critical region with NFL behavior. In this NFL region, a linear in temperature resistivity is measured universally for all of the above mentioned materials [24, 31, 60–63]. Further, YbRh$_2$Si$_2$ [24, 27], CeCu$_{6-x}$Au$_x$ [28, 61] and CeCoIn$_5$ [64] feature a $\sim T\ln(T)$ dependence of the specific heat. Both observations are in stark contrast to the $\sim T^2$ dependence of the resistivity and $\sim T$ dependence of the specific heat expected from a FL [14]. Recent shot-noise measurements on YbRh$_2$Si$_2$ nanowires further indicate the absence of QP in the strange metal region [65].

Further, dynamical susceptibilities exhibit ω/T scaling [66] at the KB–QCP. This was initially observed for the dynamical magnetic susceptibilites in UCu$_{5-x}$Pd$_x$ [67], CeCu$_{6-x}$Au$_x$ [68] and CeCu$_{6-x}$Ag$_x$ [69] and very recently also for the optical conductivites of both YbRh$_2$Si$_2$ [60] and CeCu$_{6-x}$Au$_x$ [70]. Note that ω/T scaling is a clear sign for a non-Gaussian QCP [23], i.e. the critical fixed point is an interacting one. Particularly interesting, too, are the recent observations of ω/T scaling for the optical conductivity, as it shows that the critical behavior is not limited to the magnetic degrees of freedom only, but also includes the charge degrees of freedom.

To summarize, the following phenomena seem to be almost universal for the KB–QCP: (i) a sudden jump of n_{H} as the KB–QCP is crossed at $T = 0$; (ii) a sudden reconstruction of the FS as the KB–QCP is crossed at $T = 0$; (iii) a diverging QP mass as the KB–QCP is approached from either side at $T = 0$; (iv) a $\ln(T)$ dependence of $\gamma = C/T$ at finite temperatures above the KB–QCP; (v) a linear-in-T dependence of the resistivity at finite temperatures above the KB–QCP; (vi) ω/T scaling of dynamical susceptibilities at finite temperatures above the QCP. All of these phenomena are not compatible with a magnetic transition in an itinerant electron system. To the best of our knowledge, a full understanding of the KB-QCP has not yet been achieved.

C.   Theory of the KB–QCP: basics and challenges

Below, we introduce the basic models which have been proposed to describe the essentials of HF physics, including the KB–QCP. We further review some basic intuitive, qualitative notions associated with the physics of these models. Then, we give a qualitative overview of the challenges faced when attempting to describe the KB–QCP. Concrete approaches for tackling those challenges are reviewed in the next subsection.

The universal physics of HF systems is believed to be described by the periodic Anderson model (PAM),

$$H_{\mathrm{PAM}} = \sum_{i\sigma} \epsilon_f f_{i\sigma}^\dagger f_{i\sigma} + \sum_i U f_{i\uparrow}^\dagger f_{i\uparrow} f_{i\downarrow}^\dagger f_{i\downarrow}$$
$$+ \sum_{i\sigma} V\left(c_{i\sigma}^\dagger f_{i\sigma} + \mathrm{h.c.}\right) + \sum_{\mathbf{k}\sigma} \epsilon_{c\mathbf{k}} c_{\mathbf{k}\sigma}^\dagger c_{\mathbf{k}\sigma}, \qquad (1)$$

which we consider here on a 3-dimensional cubic lattice. Here, $f_{i\sigma}$ and $c_{i\sigma}$ annihilate an f or c electron with spin $\sigma \in \{\uparrow, \downarrow\}$ at site i, respectively, $c_{\mathbf{k}\sigma}$ is the discrete Fourier transform of $c_{i\sigma}$, while $\epsilon_f = \epsilon_f^0 - \mu$ and $\epsilon_{c\mathbf{k}} = \epsilon_{c\mathbf{k}}^0 - \mu$, with $\epsilon_{c\mathbf{k}}^0 = -2t \sum_{a=x,y,z} \cos(k_a)$, denote the local f energy and c-band dispersion relative to the chemical potential μ, respectively. The f electrons experience a strong local repulsion U, and hybridize with the c electrons with hybridization strength V.

At $U = 0$, the PAM features a two-band structure, with a band gap determined by the hybridization strength V (therefore also often called hybridization gap). The hybridization thereby shifts the FS such that both f and c electrons are accounted for and QP in the vicinity of the FS are hybrid c-f objects. The low-energy physics of the Kondo correlated FL phase can be thought of as a renormalized version of the $U = 0$ case. The interaction does not destroy the low-energy hybridization between c and f electrons, but merely renormalizes it. When approaching the KB–QCP from the Kondo correlated phase, the interaction renormalizes the hybridization to ever smaller values. The point where the hybridization renormalizes to zero and c and f electrons decouple at low energies marks the KB–QCP [71]. In the RKKY correlated phase,

c and f electrons have been argued to remain decoupled, so that the FS is that of the free c electrons, with QP of purely c electron character [3, 71]. Surprisingly, we find a somewhat different scenario. Indeed, we show in the present work that even in the RKKY correlated phase QP close to the FS are c-f hybridized, see Sec. VI C.

Description of the strange metal.— Arguably the most challenging aspect of the KB–QCP is the strange metal behavior at finite temperatures above the QCP. There are by now various routes to microscopically realize NFL behavior, see Ref. 72 for an extensive recent review. Rigorous results on NFL physics can for instance be obtained from Sachdev-Ye-Kitaev (SYK) models [72] or from impurity models featuring quantum phase transitions [73], e.g. multi-channel Kondo impurities [74–77] or multi-impurity models [78–88]. Despite considerable recent progress [89–91], it is to date not fully clarified to what extent known routes to NFL physics connect to the strange metal behavior observed experimentally in HF materials.

Description of the Fermi surface reconstruction.— Another challenging issue is to explain how the FS can change its size in the first place. The volume of the FS is fixed to be proportional to the particle number by the Luttinger sum rule [8, 9], which involves the combined particle number of the c and f electrons [9]. While the FS volume matches the Luttinger sum rule prediction in the Kondo correlated phase, this is not the case in the RKKY correlated phase where the f electrons seem to be missing from the FS volume. A theoretical description of the KB–QCP also needs to correctly describe both the Kondo and RKKY correlated phases, which is far from straight forward especially in the latter case. Nevertheless, this aspect of the KB–QCP is better understood and intuitively more accessible than the strange metal physics.

D. Theory of the KB–QCP: approaches

The KB–QCP has been subject to many theoretical studies in the past, using both analytical and numerical approaches. Below, we briefly list what has been achieved so far and point out the main issues of the corresponding approaches.

Numerically exact methods. — Significant progress on physical phenomena can be made based on exact solutions obtained with controlled numerical methods. The main advantage is that such an approach is highly unbiased: the bare PAM or the closely related Kondo lattice model (KLM) is solved exactly, potentially in some simplified geometry and usually in some constrained parameter regime. Results have so far been obtained with Quantum Monte Carlo (QMC) methods [92–101] and the Density Matrix Renormalization Group (DMRG) [102], some of which have reported evidence of a KB–QCP [98, 99, 102]. Even though reports dynamical or transport properties is scarce, numerically exact studies can provide valuable benchmarks for less controlled approaches.

Slave-particle theories.— Considerable conceptual progress on KB physics has been achieved using slave-particle approaches [103–108]. These approaches decompose the degrees of freedom of the PAM or the KLM in terms of additional fermionic or bosonic degrees of freedom (often called partons) which are subject to gauge constraints, to ensure the mapping is exact [103–106, 108–110]. While the parton decomposition does not render the models solvable, it allows for more flexibility when constructing approximate solutions. For instance, a certain effective low-energy form of the Hamiltonian and some effective dynamics of the gauge fields (which are static after the initial exact mapping) are usually assumed. The effective theory can then be solved by means of approximate methods, for instance by taking certain large N limits and/or resorting to static mean-field theory.

One of the early successes of slave-particle approaches is the prediction of a RKKY phase in which f-electrons are localized and do not contribute to the FS in terms of an orbital selective Mott phase [105, 106, 108]. The missing FS volume in the RKKY phase was linked to emergent topological excitations of fractionalized spins [105, 106, 111], thus coining the term fractionalized FL (FL*). It was further established that a continuous transition between Kondo and RKKY correlated phases can exist [106], including a FS reconstruction accompanied by a sudden jump in the Hall coefficient [112]. Recently, by considering spatially disordered interactions [91, 110], it has been possible to account for a strange-metal-like $\sim T \ln T$ resistivity using a slave particle approach (though to our knowledge, a $\ln T$ correction to the $\sim T$ resistivity has not been reported in YbRh$_2$Si$_2$ [113], which shows the most extensive strange metal regimes of all known HF compounds).

Dynamical mean-field theory.— Dynamical mean-field theory (DMFT) [114, 115] and its extensions [116–118] have been successfully used in many studies on HF systems [119–128] and have lead to valuable new insights. DMFT methods treat lattice models by mapping them on self-consistent impurity models.

The most prominent approach, which has lead to many insights, is the extended DMFT (EDMFT) approach to KLM [119, 120, 129–139]. EDMFT maps the KLM on a self-consistent Bose-Fermi-Kondo (BFK) impurity model and is able to capture a KB–QCP due to the local competition between Kondo screening and magnetic fluctuations. One of the main successes of EDMFT is the explanation of ω/T scaling of the dynamical spin structure factor in CeCu$_{6-x}$Au$_x$ [68] at the KB–QCP. However, to the best of our knowledge, predictions of other thermodynamic and transport properties, like the linear-in-T resistivity or the $T \ln T$ dependence of the specific heat, are lacking to date. It is therefore still unclear whether the EDMFT approach correctly describes the experimentally observed strange metal behavior. We expect though that these gaps in the literature will be filled in future studies.

A downside of the EDMFT approach is that full self-

consistency leads to a first-order phase transition [120, 140] at $T > 0$. A continuous transition can be recovered by insisting on a featureless fermionic density of states (DOS) [141], at the cost of giving up self-consistency of the fermionic degrees of freedom, as is routinely done in KB–QCP studies using EDMFT [132, 133, 135]. This downside of EDMFT has lead to the proposal of using 2-site cellular DMFT (CDMFT) [116] to study Kondo breakdown physics [122]. Using exact diagonalization (ED) as an impurity solver, it was shown that a 2-site CDMFT treatment of the PAM [Eq. (1)] can describe the KB–QCP as an orbital selective Mott transition (OSMT) at $T = 0$ [127, 128], where the f electrons localize while the c electrons remain itinerant. Similar studies with QMC impurity solvers [126, 142, 143] were however not able to find signs of a KB–QCP in the temperature range studied. Since ED suffers from limited frequency resolution while QMC has trouble reaching low temperatures, it is to date not clear to what extent CDMFT can describe KB physics. The ED study was further not able to establish conclusively whether the transition is first or second order.

E. Overview of our main results

In this work, we revisit the CDMFT approach of Refs. 127 and 128, now using the Numerical Renormalization Group (NRG) [144, 145] as an impurity solver. The NRG is numerically exact, produces spectral data directly on the real frequency axis and is able to access arbitrarily low temperatures and frequencies. NRG therefore eliminates the limitations of both ED and QMC for studying quantum critical phenomena. In particular, using NRG, we are able to settle the question of whether a 2-site CDMFT approximation of the PAM on a simple cubic lattice is capable of describing a KB–QCP. Furthermore, leveraging the high resolution of NRG, we find several new features of the RKKY phase which were not accessible to lower resolution methods. Most important, NRG can explore the quantum critical regime governed by the QCP. We stick to the parameters used in Refs. 127 and 128 and vary the c-f hybridization strength V and temperature T [c.f. Eq. (1) and Sec. II]. Similar in spirit as Ref. 127, we focus on purely paramagnetic solutions by artificially preventing the breaking of spin rotation symmetry. This is motivated by experimental observations which suggest that the KB–QCP and magnetic ordering are distinct phenomena [31, 48, 146]. Here, we decide to focus on the paramagnetic KB–QCP and refrain from the additional complications introduced by possible magnetic ordering. The interplay between KB physics and symmetry breaking will be considered in detail in future work.

The main goals of our work are to (i) establish that 2-site CDMFT is able to describes a continuous KB–QCP; (ii) establish that the QCP is governed by a NFL critical fixed point and characterize its properties; (iii) make progress on our understanding of the fate of c-f hybridization in the vicinity of the QCP; and (iv) explore to what extent CDMFT is able to qualitatively capture the experimental phenomena described in Sec. IB. In the process, we reveal several new aspects of the CDMFT solution. The remainder of this subsection is intended as a summary of our main results and a guide to where to find them in our paper.

(i) *The KB–QCP is a continuous OSMT.* — Using NRG, we clearly establish that 2-site CDMFT describes a continuous KB–QCP. First and foremost, this is shown in Sec. III and Fig. 2, where we present the phase diagram obtained with CDMFT-NRG. Here, we establish the presence of two energy scales: the FL scale $T_{\rm FL}$, below which we find FL behavior; and a NFL scale $T_{\rm NFL}(\geq T_{\rm FL})$, which marks the onset of c-f hybridization [c.f. Figs. 11 and 12] and below which we find strange-metal-like NFL behavior in the vicinity of the QCP. We find that as V approaches a critical hybridization strength V_c from either side, $T_{\rm FL}$ continuously decreases to zero while $T_{\rm NFL}$ remains nonzero throughout. We identify V_c as the location of a KB–QCP. While the FS volume in the Kondo correlated phase at $V > V_c$ counts both the c and the f electrons, it only counts the c electrons in the RKKY correlated phase at $V < V_c$ [c.f. Sec. VIII]. The KB–QCP thereby marks a continuous transition between two FL phases, which differ in their FS volumes [c.f. Figs. 13 and 17 and their corresponding sections]. The FS reconstruction, which occurs at the KB–QCP, is accompanied by the appearance of a *dispersive* pole in the f-electron self-energy. This also implies the appearance of a Luttinger surface [10], the locus of points in the Brillouin zone at which the f self-energy pole lies at $\omega = 0$ [c.f. Secs. VI and VII]. Ref. 147 recently suggested that Luttinger surfaces may define spinon Fermi surfaces. The appearance of a Luttinger surface therefore suggests that the f-electron is fractionalized (i.e. spinon degrees of freedom emerge at low energies as stable spin-$1/2$ excitations) in the RKKY phase. In the parlance of Refs. 105 and 106, this suggests that the RKKY phase is a fractionalized FL (FL*). We will explore this more concretely in future work. Following Refs. 127 and 128, *we therefore identify the KB–QCP as a continuous OSMT, in which the f electrons partially localize* while the c electrons do not.

(ii) *NFL physics at intermediate T close to the QCP.* — In the vicinity of the QCP, there is a scale separation between $T_{\rm FL}$ and $T_{\rm NFL}$, giving rise to an intermediate NFL region extending down to $T = 0$ at V_c [c.f. Fig. 2]. Our evidence that this intermediate region is a NFL region is based on NRG finite size spectra [Fig. 3], dynamical correlation functions [Fig. 4] and a $\sim T \ln T$ of the specific heat [Fig. 19]. In a companion paper [148], we will present a detailed analysis of the optical conductivity, showing ω/T scaling, and the temperature dependence of the resistivity, showing linear-in-T behavior in the NFL regime. Moreover, our KB–QCP for the PAM shows several similarities with QCPs found for the 2-impurity and 2-channel Kondo models [c.f. Sec. X]. Very surprisingly, we find a stable
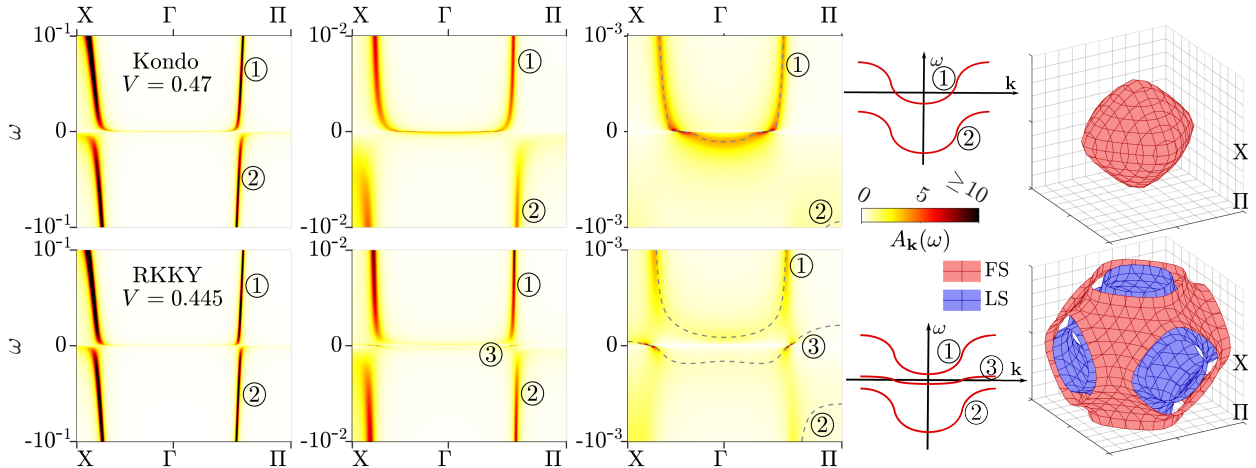
FIG. 1. Three left columns: $\mathbf{k}$ dependent spectral function $A_{\mathbf{k}}(\omega)$ of the PAM at $T = 0$, zooming in on frequencies $|\omega| \leq 10^{-1}$, 10^{-2} and 10^{-3}. V is chosen close to the KB–QCP, in either the Kondo phase (upper row) or the RKKY phase (lower row). At relatively high frequencies (first column), the spectral functions of both phases seem to have a similar structure, involving two bands, labeled ① and ②. However, zooming in to lower frequencies (second and third columns) we find a striking difference: in the RKKY phase, a narrow third band emerges at low frequencies, labeled ③, as indicated by the dashed lines in the third column and in the schematic sketch of the band structure in the fourth column. This difference also leads to different Fermi surfaces, shown on the far right as red surfaces; the blue surface shows the Luttinger surface in the RKKY phase. For more details, see Sec. VII.

NFL fixed point even though the effective 2-impurity model lacks the symmetries necessary to stabilize a NFL fixed point *without* self-consistency [79–82, 84–86, 149–152]. We find that the CDMFT self-consistency conditions are essential for the stability of the NFL fixed point [c.f. Sec. IV and App. A 4].

(iii) *Fate of c-f hybridization across the KB–QCP.—* One of our most surprising findings is that low-energy *c-f* hybridization is not destroyed as the KB–QCP is crossed from the Kondo ($V > V_c$) to the RKKY phase ($V < V_c$). We elaborate this in detail in Sections V, VI, VII and VIII. Indeed, we find that the QP weights for both the *c* and *f* electrons are non-zero in *both* $T = 0$ phases adjacent to the KB–QCP, vanishing only *at* at the KB–QCP [Fig. 9]. This is one of our most surprising results and in stark contrast to previous work. It implies that, contrary to widespread belief [3], the difference between the Kondo and RKKY phase is not due to non-zero versus zero *f*-electron QP weight. Instead, it is caused by a sign change of the effective *f*-level position close to the center of the Brillouin zone [Fig. 9 and its discussion; Sec. VIII]. We connect this sign change to the aforementioned emergence of a dispersive self-energy pole [Fig. 10 and its discussion]. It thus reflects the orbital selective Mott nature of the RKKY phase.

The non-zero *f*-electron QP weight and the dispersive self-energy pole leads to the emergence of a *third* band in the RKKY phase [c.f. Figs. 13 and 14 and their discussion]. The emergence of a third band in a model constructed from only two bands is our most striking and unexpected result. Its emergence is previewed in Fig. 1, showing the total (*c* and *f*) spectral function $A_{\mathbf{k}}(\omega)$: at high frequency ($|\omega| \lesssim 10^{-1}$, measured in terms of the bare *c*-electron half-

band width) its structure remains qualitatively unaltered as the KB–QCP is crossed—it seems as if in both cases, there is a two-band structure characteristic for HF systems. However, as one zooms in further to lower frequencies, it becomes clear that the low frequency physics is entirely different: a third band emerges in the RKKY phase and the FS is shifted relative to that in the Kondo phase. The emergence of the third band is intimately tied to the emergence of a Luttinger surface [c.f. Sec. VII and VIII]. It was concluded in Ref. 147 that Luttinger surfaces may define spinon Fermi surfaces. From that perspective, the third band can be viewed as a direct manifestation of the fractionalization of the *f*-electrons in the RKKY phase: their spinon degrees of freedom become independent, long-lived excitation, giving rise to the third band. A more concrete investigation will be the subject of future work.

(iv) *Relation to experiment.—* We repeatedly make contact to experimental observations in our manuscript. In table I, we provide a list of experimental observations which are qualitatively reproduced by our CDMFT-NRG approach. We include references to the relevant experimental publications and reviews (without claim of completeness) and pointers to where our corresponding CDMFT results appear in this paper.

To conclude our overview, we summarize the structure of the paper: After reviewing CDMFT and NRG in Sec. II, we present and discuss the phase diagram in Sec. III. By detailed discussion of real-frequency dynamical suscepti-bilities and NRG finite size spectra, we demonstrate in Sec. IV that T_{FL} vanishes at the QCP and gives rise to NFL behavior at intermediate temperatures below T_{NFL}. After reviewing expectations on single particle properties in HF systems in Sec. V, a detailed discussion of single-

phenomenon	experiment	PAM, CDMFT
phase diagram	[3, 27, 33]	Fig. 2
sudden FS reconstruction	[29–31, 37, 38]	Figs. 13, 17
jump of Hall coefficient	[25, 31, 36]	Fig. 18, App C
control parameter dependence of T_{Hall}	[25]	Fig. 2
divergent QP mass	[27–29, 32]	Fig. 9, 19
$T_{\mathrm{FL}} \to 0$ at KB–QCP	[3, 27, 33]	Fig. 2
hybridization gap forms at T_{NFL}; $T_{\mathrm{NFL}} \neq 0$ at KB–QCP	[3, 51–59]	Figs. 2, 11, 12
NFL: $\sim T \ln T$ specific heat	[24, 27, 28, 64]	Fig. 19
NFL: linear-in-T resistivity	[24, 31, 60–63]	[148]
NFL: ω/T scaling	[60, 67–70]	[148]

TABLE I. Left: Experimental phenomena associated with heavy-fermion behavior that can be recovered qualitatively from the periodic Anderson model, treated using 2-site CDMFT+NRG. Middle: References and reviews (without claiming completeness) which have inferred these phenomena from experimental data. Right: Figures in this work or a follow-up paper [148] exhibiting these phenomena.

particle properties of the self-consistent 2IAM follows in Sec. VI. Using NRG, we show unambiguously that the f electron QP weight is finite in *both* the Kondo *and* RKKY correlated phases. In Sec. VII, we discuss how the single-particle properties of the self-consistent impurity model translate to lattice properties. There, we show that the FS indeed reconstructs across the KB–QCP. In Sec. VIII, we discuss the details of this FS reconstruction in the context of Luttinger's theorem and present our results for the Hall coefficient. Section IX shows results on the specific heat. Finally, in Section X, we discuss the similarities and differences between the KB–QCP in the PAM studied with 2-site CDMFT and the impurity QCPs in the two-channel and two-impurity Kondo models. Section XI presents our conclusions and an outlook. Several appendices discuss technical details of our methods.

II. MODEL AND METHODS

Although the CDMFT treatment of the PAM is well-established [126–128], we describe it in some detail, to introduce notation and terminology that will be used extensively in subsequent sections.

Before starting, a general remark on notation. Matsubara propagators analytically continued into the complex plane will be denoted $G(z)$, with $z \in \mathbb{C}$. The corresponding retarded propagators are $G(\omega^+)$, with $z = \omega + \mathrm{i}0^+$, $\omega \in \mathbb{R}$. Ditto for self-energies.

A. Periodic Anderson model

We consider the PAM on a three-dimensional cubic lattice, where each lattice site hosts a non-interacting conduction c orbital and an interacting localized f orbital. The Hamiltonian, H_{PAM}, is given by Eq. (1). In this work, we set $t = 1/6$ so that the c-electron half-bandwidth is 1, and use the latter as unit of energy. Following the choices of De Leo, Civelli and Kotliar [127, 128], we set the chemical potential to $\mu = 0.2$, the f-level energy to $\epsilon_f^0 = -5.5$ and the f-level Coulomb repulsion to $U = 10$, so that the system is electron-doped. When exploring the phase diagram in Sec. III, we will vary the c-f hybridization V and temperature T.

In the momentum representation, the lattice propagators can be expressed as

$$
\begin{aligned}
G_{\mathbf{k}}(z) &= \begin{pmatrix} z - \epsilon_f - \Sigma_{f\mathbf{k}}(z) & -V \\ -V & z - \epsilon_{c\mathbf{k}} \end{pmatrix}^{-1} \\
&= \begin{pmatrix} G_{f\mathbf{k}}(z) & G_{fc\mathbf{k}}(z) \\ G_{fc\mathbf{k}}(z) & G_{c\mathbf{k}}(z) \end{pmatrix},
\end{aligned} \tag{2}
$$

The matrix elements in the second line of Eq. (2), defined by computing the matrix inverse stated in the first, are given by

$$
G_{f\mathbf{k}}(z) = \left[z - \epsilon_f - \Delta_{f\mathbf{k}}(z) - \Sigma_{f\mathbf{k}}(z)\right]^{-1}, \tag{3a}
$$

$$
G_{c\mathbf{k}}(z) = \left[z - \epsilon_{c\mathbf{k}} - \Sigma_{c\mathbf{k}}(z)\right]^{-1}, \tag{3b}
$$

$$
G_{fc\mathbf{k}}(z) = \Sigma_{c\mathbf{k}}(z)\, G_{c\mathbf{k}}(z)/V = \Delta_{f\mathbf{k}}(z)\, G_{f\mathbf{k}}(z)/V, \tag{3c}
$$

$$
\Delta_{f\mathbf{k}}(z) = V^2 \left[z - \epsilon_{c\mathbf{k}}\right]^{-1}, \tag{3d}
$$

$$
\Sigma_{c\mathbf{k}}(z) = V^2 \left[z - \epsilon_f - \Sigma_{f\mathbf{k}}(z)\right]^{-1}. \tag{3e}
$$

For brevity, we will often omit momentum and/or frequency arguments. The f-hybridization function Δ_f and the one-particle irreducible f self-energy, Σ_f, describe, respectively, the effects of hybridization and interactions on f electrons. Their effects on c electrons are described by Σ_c, which is not one-particle irreducible and a function of Σ_f. In particular, hybridization leads to so-called hybridization poles in $\Sigma_c(z)$, which in turn cause so-called hybridization gaps in the spectral functions $A_c(\omega) = -\frac{1}{\pi}\mathrm{Im}G_c(\omega^+)$ (discussed in detail in later sections).

B. Two-site cellular DMFT

We study the PAM using a two-site CDMFT approximation, considering a unit cell of two neighboring lattice sites as a cluster impurity and the rest of the lattice as a self-consistent bath. We choose to focus solely on solutions with SU(2) spin rotation symmetry, U(1) total charge symmetry and inversion symmetry, i.e. solutions which treat sites 1 and 2 as equivalent. Enforcing these

symmetries may induce artificial frustration in some regions of the phase diagram; in particular, they exclude the possibility of symmetry-breaking order such as antiferromagnetism. We have two reasons for nevertheless focusing only on non-symmetry-broken solutions. First, in some materials the antiferromagnetic QCP (AF-QCP) and the KB–QCP do not coincide: in YbRh$_2$Si$_2$ they can be shifted apart by applying chemical pressure [48], and in CeCoIn$_5$ they naturally lie apart [31]. This strongly suggests that the onset of antiferromagnetic order is not an intrinsic property of the KB–QCP itself [146]. (The question why the AF-QCP often coincides with the KB–QCP is interesting, but not addressed in this paper.) Second, in experimental studies, symmetry-breaking order is usually absent in the quantum critical region. It is therefore of interest to understand the properties of the KB–QCP and the NFL regime above it in the absence of symmetry breaking. Having chosen to exclude symmetry breaking, we refrain from studying the limit $V \to 0$, where its occurrence is increasingly likely for energetic reasons. Studies of symmetry-broken phases are left for future work.

The CDMFT approximation for the PAM, excluding symmetry breaking, leads to a self-consistent two-impurity Anderson model (2IAM) defined by [126–128]

$$H_{2\mathrm{IAM}} = \sum_{i\sigma} \epsilon_f f_{i\sigma}^\dagger f_{i\sigma} + \sum_i U f_{i\uparrow}^\dagger f_{i\uparrow} f_{i\downarrow}^\dagger f_{i\downarrow} \tag{4}$$
$$+ \sum_{i\sigma} V \big(c_{i\sigma}^\dagger f_{i\sigma} + \mathrm{h.c.} \big) - \sum_{ij\sigma} c_{i\sigma}^\dagger (t\tau^x + \mu\mathbb{1})_{ij} c_{j\sigma}$$
$$- \sum_{ij\lambda\sigma} V_{ij\lambda} \big(c_{i\sigma}^\dagger a_{\lambda j\sigma} + \mathrm{h.c.} \big) + \sum_{\lambda i\sigma} E_{\lambda i} a_{\lambda i\sigma}^\dagger a_{\lambda i\sigma}.$$

Here $i \in \{1,2\}$ labels the two cluster sites in the "position basis", and $\mathbb{1} = \left(\begin{smallmatrix}1 & 0 \\ 0 & 1\end{smallmatrix}\right)$, $\tau^x = \left(\begin{smallmatrix}0 & 1 \\ 1 & 0\end{smallmatrix}\right)$. There are two spinful baths, with annihilation operators $a_{\lambda i\sigma}$. Both baths hybridize with both cluster sites, whose assumed equivalence implies $V_{ij\lambda} = V_{ji\lambda}$. These couplings, chosen to be real, and the bath energies, $E_{i\lambda}$, together define the c-hybridization function

$$(\Delta_c)_{ij}(z) = \sum_{\lambda l} \frac{V_{il\lambda} V_{jl\lambda}}{z - E_{\lambda l}}. \tag{5}$$

The cluster correlators of the 2IAM are 2×2 matrix functions. In the cluster position basis they are given by

$$G_f(z) = [z - \epsilon_f - \Delta_f(z) - \Sigma_f(z)]^{-1}, \tag{6a}$$
$$G_c(z) = [z + \mu + t \cdot \tau^x - \Delta_c(z) - \Sigma_c(z)]^{-1}, \tag{6b}$$
$$G_{fc}(z) = \Sigma_c(z) G_c(z)/V = \Delta_f(z) G_f(z)/V, \tag{6c}$$
$$\Delta_f(z) = V^2 [z + \mu + t \cdot \tau^x - \Delta_c(z)]^{-1}, \tag{6d}$$
$$\Sigma_c(z) = V^2 [z - \epsilon_f - \Sigma_f(z)]^{-1}. \tag{6e}$$

These have to be solved self-consistently, by iteratively computing Σ_f via an impurity solver and re-adjusting the dynamical mean field Δ_c (see App. A and Refs. [116, 117]).

By SU(2) spin symmetry the hybridization function Δ_c is spin-diagonal and spin-independent. The same is true

for Δ_f, which is fully determined by Δ_c. Moreover $1 \leftrightarrow 2$ inversion symmetry ensures that they are linear combinations of $\mathbb{1}$ and τ^x. They can therefore be diagonalized independently of ω using the Hadamard transformation $U_H = \frac{1}{\sqrt{2}}\left(\begin{smallmatrix}1 & 1 \\ 1 & -1\end{smallmatrix}\right)$, which maps τ^x to $\tau^z = \left(\begin{smallmatrix}1 & 0 \\ 0 & -1\end{smallmatrix}\right)$. It is thus convenient to correspondingly transform $H_{2\mathrm{IAM}}$, expressing it through the bonding/antibonding operators

$$f_{\pm,\sigma} = \tfrac{1}{\sqrt{2}}\left(f_{1\sigma} \pm f_{2\sigma}\right), \qquad c_{\pm,\sigma} = \tfrac{1}{\sqrt{2}}\left(c_{1\sigma} \pm c_{2\sigma}\right). \tag{7}$$

After reperiodization (discussed in App. A 3), these modes represent Brillouin zone regions centered at $\Gamma = (0,0,0)$ and $\Pi = (\pi,\pi,\pi)$, respectively [153, 154]. The labels $\alpha \in \{+,-\}$ on $f_{\alpha\sigma}$ and $c_{\alpha\sigma}$ will thus be called "momentum" labels. The $\pm$ modes are only coupled via the Coulomb interaction term, which can only change the total charge in each channel by 0 or ± 2. This implies two $\mathbb{Z}_2$ symmetries: the number parity operators $\hat{P}_\pm = \hat{N}_\pm \bmod 2$ for the $+$ and $-$ channels are both conserved, with eigenvalues $P_\pm \in \{0,1\}$.

C. Numerical renormalization group

We solve the 2IAM using the full-density-matrix NRG [155–157]. Following Wilson [144, 145], the bath's continuous spectrum is discretized logarithmically and the model is mapped onto a semi-infinite Wilson chain. We represent the impurity f and c orbitals by sites $n = -1$ and 0, respectively, and the bath by sites $n \geq 1$. The hopping amplitudes for $n \geq 1$ decay exponentially, $\sim \Lambda^{-n/2}$, where $\Lambda > 1$ is a discretization parameter. This energy-scale separation is exploited to iteratively diagonalize the model, adding one site at a time while discarding high-energy states. For a "length-N" chain (i.e. one with largest site index N), the lowest-lying eigenergies have spacing $\sim \Lambda^{-N/2}$. By increasing N, one can thus zoom in on ever lower energy scales.

We set up the Wilson chain in the momentum basis, in which the $\pm$ modes are coupled only via the interaction term on site -1. To reduce computational costs, we use an interleaved chain [158, 159] of alternating $+$ and $-$ orbitals. (Interleaving slightly lifts degeneracies, if present, of the sites being interleaved—but this is not an issue here, since the $\pm$ modes are non-degenerate due to τ^z contributions to hopping terms. Indeed, we have double-checked, especially close to the QCP, that our interleaved results are reproduced when using a computationally more costly standard Wilson chain geometry.) We exploit the SU(2) spin, U(1) charge and both $\mathbb{Z}_2$ parity symmetries in our NRG calculations using the QSpace tensor library [160, 161], further reducing computational costs. Together with interleaving, this allows us to achieve converged data using a fairly small NRG discretization parameter of $\Lambda = 3$ while keeping $N_{\mathrm{keep}} \leq 20,000$ SU(2) multiplets. Because spectra close to the QCP can be quite sensitive to z-shifting, we refrained from z-averaging.
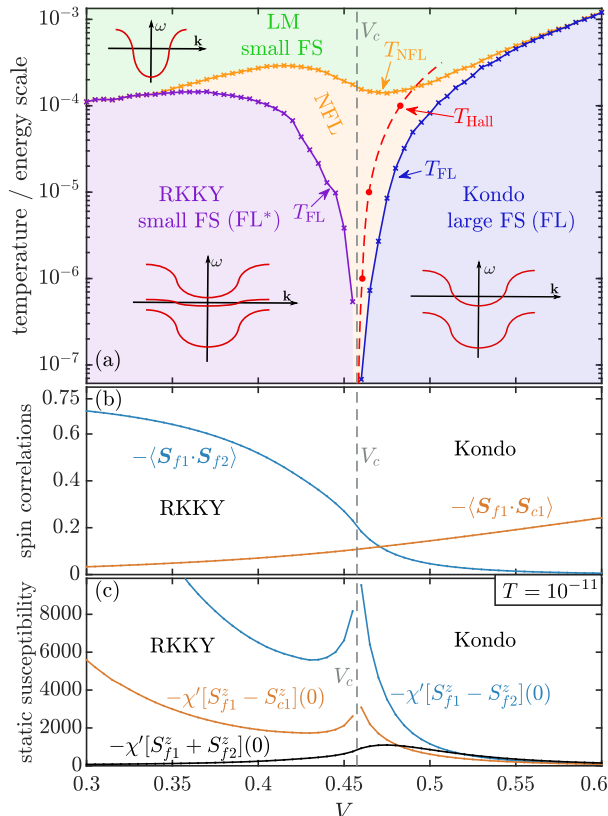
FIG. 2. (a) Paramagnetic phase diagram of the PAM as a function of the c-f hybridization V and temperature T (on a log scale). At $T = 0$, there are two distinct phases, the RKKY phase and the Kondo phase, separated by a QCP at $V_c = 0.4575(25)$. At $T > 0$, we find four different regimes, labeled LM (local moment), RKKY, Kondo and NFL, connected via smooth crossovers. For the first three, associated band structures are depicted schematically in insets. (See Fig. 1 and Figs. 13–15 for the CDMFT band structure results.) The crossovers are charaterized by the temperature scales T_{NFL} (orange solid line) and T_{FL} (purple and blue solid lines) below which NFL and FL behaviors emerge, respectively. The scales $T_{\mathrm{NFL}}(V)$ and $T_{\mathrm{FL}}(V)$ were determined by analyzing dynamical susceptibilities of the self-consistent 2IAM at $T = 0$, as explained in Sec. IV B and App. B. The red dots marked T_{Hall} (and the guide-to-the-eye red dashed line) indicate how the crossover from a large FS in the Kondo phase to the small FS in the RKKY phase evolves with temperature. T_{Hall} was determined by analyzing the Hall coefficient similar to Ref. 25 (see Fig. 18 and App. C). (b) Equal-time intersite f-f spin correlation $\langle \boldsymbol{S}_{f1} \cdot \boldsymbol{S}_{f2} \rangle$ and local c-f spin correlation $\langle \boldsymbol{S}_{f1} \cdot \boldsymbol{S}_{c1} \rangle$, and (c) static susceptibilities for the total f spin $S_{f1}^z + S_{f2}^z$, the intersite staggered f-f spin $S_{f1}^z - S_{f2}^z$ and the local staggered f-c spin $S_{f1}^z - S_{c1}^z$ of the effective 2IAM, all plotted at $T = 10^{-11}$ as a function of V.

For further methodological details on achieving DMFT self-consistency and reperiodization, see App. A.

III. PHASE DIAGRAM

Based on a detailed study of the dynamical properties of various local operators, described in Sec. IV B, we have established a phase diagram for the PAM, shown in Fig. 2(a). While its generic structure has been known for a long time [4, 19, 50, 105, 146], we reach orders of magnitude lower temperatures and better energy resolution than previously possible and characterize the various regimes through a detailed analysis of real-frequency correlators. We first focus on zero temperature, involving two distinct phases separated by a QCP, then discuss finite-temperature behavior, involving smooth crossovers between several different regimes.

Zero temperature: At $T = 0$, we find two phases when tuning V, separated by a QCP at $V_c = 0.4575(25)$. For $V > V_c$, we find a Kondo phase, where the f and c bands are hybridized to form a two-band structure and the correlation between f-orbital local moments in the effective 2IAM is weak, as shown by the blue line in Fig. 2(b) and discussed below. This phase is a FL, with a Fermi surface (FS) whose volume satisfies the Luttinger sum rule [8, 9] when counting both the f and c electrons (see Fig. 17, to be discussed later). We henceforth call a FS *large* or *small* if its volume accounts for both c and f electrons, or only c electrons, respectively. The Kondo phase is adiabatically connected to the case of $U = 0$ and $V > 0$ and is thus a normal FL.

For $V < V_c$, we find a RKKY phase, where the local moments at nearest neighbours have strong antiferromagnetic correlations (see blue line in Fig. 2(b) and its discussion below), while SU(2) spin symmetry is conserved by construction. This phase, too, is a FL, with a small FS accounting only for c electrons. While this phase thus appears to violate Luttinger sum rule, it still obeys a more general version of that rule [10, 35, 105]: we find a surface of poles of $\Sigma_{f\mathbf{k}}(z = 0)$ (Luttinger surface), which, together with the FS, accounts for the total particle number. We will discuss this in detail in Secs. VII and VIII. In the RKKY phase, the FS coincides with the FS of the free c band but the effective band structure differs from that of a free c band: there are *three* bands (see Fig. 1 and Fig. 13 below, to be discussed later), including a narrow QP band crossing the Fermi level. This narrow QP band is responsible for the FL behavior we observe in the RKKY phase. Based on Ref. 147 revealing that Luttinger surfaces may define spinon Fermi surfaces, we conjecture that the RKKY phase is a fractionalized FL (FL*) [105, 106]. We will explore this conjecture in more detail in future work.

Figure 2(b) shows the equal-time f-f intersite spin correlators $\langle \boldsymbol{S}_{f1} \cdot \boldsymbol{S}_{f2} \rangle$ and the local c-f $\langle \boldsymbol{S}_{f1} \cdot \boldsymbol{S}_{c1} \rangle$ of the effective 2IAM at $T = 10^{-11}$, plotted as functions of V. $\langle \boldsymbol{S}_{f1} \cdot \boldsymbol{S}_{f2} \rangle$ smoothly evolves from $\simeq 0$ at $V = 0.6$ deep in the Kondo phase to $\simeq -0.75$ deep in the RKKY phase. On the other hand, the absolute value of $\langle \boldsymbol{S}_{f1} \cdot \boldsymbol{S}_{c1} \rangle$ smoothly decreases when going from the Kondo phase to the RKKY phase. This shows that the Kondo

phase is dominated by local c-f correlations, indicative of spin screening, and only has weak non-local f-f spin correlations. By contrast, the RKKY phase is dominated by non-local antiferromagnetic f-f spin correlations and has only weak local c-f correlations. Note that equal-time spin correlations of the self-consistent 2IAM are continuous across the QCP and do not show non-analytic behavior at V_c. Rather, we will see below that the QCP is characterized by a zero crossing of the effective bonding f level (see discussion of Fig. 9 below). This is accompanied by a sharp jump of the FS and the appearance of a dispersive pole in the f self-energy (see the discussion of Figs. 13, 14 and 17 below).

Figure 2(c) shows static susceptibilities for the total f-spin $S_{f1}^z + S_{f2}^z$, the staggered intersite f-f-spin $S_{f1}^z - S_{f2}^z$, and the staggered local f-c-spin $S_{f1}^z - S_{c1}^z$, plotted versus V at $T = 10^{-11}$. (Susceptibilities are defined in Eq. (8) below.) While the total f-spin susceptibility evolves smoothly across the QCP, both staggered susceptibilities, which are related to intersite f-f singlet formation and Kondo singlet formation, respectively, show singular behavior near the QCP. This suggests that the latter arises from a competition between intersite f-f singlet formation and Kondo singlet formation. Further, both staggered susceptibilities become very large deep in the RKKY phase, reflecting the tendency of this phase towards antiferromagnetic order.

Finite temperature: When the temperature is increased from zero, both FL phases cross over, at a V-dependent scale $T_{\mathrm{FL}}(V)$, to an intermediate NFL critical regime, characterized by the absence of coherent QP (see Fig. 15 and Sec. IV A). Importantly, the scale $T_{\mathrm{FL}}(V)$ vanishes when V approaches V_c from either side, thus the NFL regime extends all the way down to $T = 0$ at the QCP. With increasing temperature, the NFL regime crosses over, at a scale $T_{\mathrm{NFL}}(V)$ (larger than $T_{\mathrm{FL}}(V)$), to a local moment (LM) regime, which is adiabatically connected to $V = 0$. There, free c electrons are decoupled from f orbital local moments, resulting in a one-band structure. The crossover scales T_{NFL} and T_{FL} can be extracted from an analysis of dynamical susceptibilities at $T = 0$ (see Sec. IV B and App. B). To make qualitative contact with experimental results on YbRh$_2$Si$_2$ [25], we also show a scale T_{Hall}, which marks the crossover between large and small FS based on analyzing the Hall coefficient in a way which closely resembles the analysis done in Ref. 25 (see Fig. 18 and App. C). In qualitative agreement with the experimental data of Ref. 25, Fig. 3, T_{Hall} depends on the tuning parameter (V in our case, B-field in Ref. 25) and bends towards the Kondo side of the phase diagram.

IV. TWO-STAGE SCREENING

The presence of two crossover scales, T_{NFL} and T_{FL}, implies that the evolution, with decreasing energy, from unscreened local f moments to a fully-screened FL regime
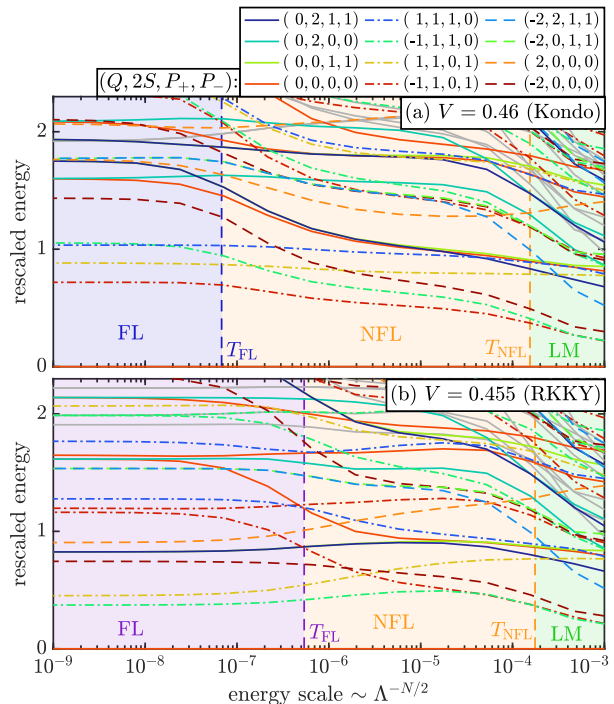
FIG. 3. NRG flow diagrams for the self-consistent effective 2IAM at $T = 0$, in (a) the Kondo phase at $V = 0.46$ and (b) the RKKY phase at $V = 0.455$, both close to the QCP. The rescaled eigenenergies are plotted as functions of the energy scale $\Lambda^{-N/2}$, for odd values of N. The vertical dashed lines indicate the scales T_{FL} and T_{NFL}. Quantum numbers for selected energy levels are indicated in the legend. Energy levels with total charge $|Q| = 0$, 1 or 2 are shown using solid, dash-dotted or dashed lines, respectively.

evolves through two stages. In this section we study this evolution from two perspectives, focusing first on NRG finite-size spectra (Sec. IV A), then on the dynamical properties of various local susceptibilities at $T = 0$ (Sec. IV B).

A. Finite size spectra

We begin our discussion of the physical properties of the different regimes shown in Fig. 2(a) by studying NRG energy-level flow diagrams of the self-consistent effective 2IAM. Such diagrams show the (lowest) rescaled eigenenergies, $\Lambda^{N/2} E_i(N)$, of a length-N Wilson chain as a function of the energy scale $\Lambda^{-N/2}$. Conceptually, the $E_i(N)$ form the finite-size spectrum of the impurity plus bath in a spherical box of radius $R_N \propto \Lambda^{N/2}$, centered on the impurity [144, 162]: with increasing N, the finite-size level spacing, $\sim 1/R_N$, decreases exponentially. The resulting flow of the finite-size spectrum is stationary (N independent) while $\Lambda^{-N/2}$ lies within an energy regime governed by one of the fixed points, but changes when $\Lambda^{-N/2}$ traverses a crossover between two fixed points. We

label eigenenergies by the conserved quantum numbers $(Q, 2S, P_+, P_-)$, where Q is the total charge relative to the ground state, S the total spin, and $P_\pm \in \{0, 1\}$ the number parity eigenvalues in the $\pm$ sectors.

Kondo phase: Fig. 3(a) shows the NRG flow diagram for the self-consistent 2IAM at $T = 0$ and $V = 0.46$, which is in the Kondo phase close to the QCP. The ground state has quantum numbers $(0, 0, 0, 0)$. As already indicated in the discussion of Fig. 2(a), we find a FL at low energy scales and a NFL at intermediate energy scales. In the FL region below $T_{\mathrm{FL}} > V_c$, the low-energy many-body spectrum can be constructed from the lowest particle and hole excitations. These come with quantum numbers $(\pm 1, 1, 1, 0)$ and $(\pm 1, 1, 0, 1)$ for the bonding and anti-bonding channel, respectively, with the $P_\pm$ quantum numbers identifying the channel containing the excitation. The low-energy many-body spectrum can then be generated by stacking these single-particle excitations, leading to towers of equally spaced energy levels, characteristic for FL fixed points [145]. This directly shows that the Kondo phase is a FL featuring a QP spectrum at low energies.

At intermediate energy scales between T_{FL} and T_{NFL}, the effective 2IAM flows through the vicinity of a NFL fixed point. Our calculations strongly suggest that this NFL fixed point also governs the low-energy behavior of the QCP at $T = 0$ and $V = V_c$. We thus identify this NFL fixed point with the critical fixed point of the QCP in the two-site CDMFT approximation. As will be pointed out in subsequent sections and summarized in Sec. X, this fixed point shares several similarities with the NFL fixed points of the two-channel Kondo model (2CKM) [74, 75, 163–167], the two impurity Kondo model (2IKM) [84–86, 149–152] and the 2IAM *without* self-consistency [79–82], which is closely related to the 2IKM. One may therefore argue that it is not surprising to find such a NFL fixed point also in a self-consistent solution of the 2IAM. On the other hand, the NFL fixed points of the 2IKM and the 2IAM are known to be *unstable* to breaking $\pm$ mode degeneracy or particle-hole symmetry [79, 80, 83, 86]. Further, for the 2IKM and the 2IAM, the RKKY interaction has to be inserted by hand as a direct interaction because if $\pm$ mode symmetry and particle-hole symmetries are present (as needed to make the NFL fixed point accessible), then these symmetries prevent dynamical generation of an antiferromagnetic RKKY interaction [168]. It has therefore been argued that this NFL fixed point is artificial and not observable in real systems [168–170]. From this perspective, the behavior found here for our effective *self-consistent* 2IAM is indeed unexpected and remarkable: although it lacks particle-hole symmetry or $\pm$ mode degeneracy and we do not insert the RKKY interaction by hand, it evidently *can* be tuned close to a QCP controlled by a NFL fixed point with 2IKM-like properties.

We note in passing that self-consistency is crucial to reach the NFL fixed point—we checked that naively tuning V without self-consistency leads to a continuous crossover without a QCP (see also App A 4 for more de-

tails). It is not entirely clear to us why the self-consistency stabilizes the NFL fixed point, though we suspect the Luttinger sum rule [8, 9] to play a crucial role. We will discuss the Luttinger sum rule in more detail in Sec. VIII. We also remark that for the non-self-consistent 2IKM mentioned above, frequency-independent or only weakly frequency-dependent hybridization functions were used in the analyses concluding that its NFL fixed point requires some special symmetries. By contrast, for the self-consistent 2IAM studied here, the self-consistent hybridization functions acquire a rather strong frequency dependence in the vicinity of the KB–QCP and appear to become singular at the QCP itself (see App A 4). Regarding the energy level structure of the self-consistent 2IAM, we did *not* find obvious similarities to the NFL fixed point of the 2IKM, i.e. the level structure seems quite different.

RKKY phase: Fig. 3(b) shows the NRG flow diagram for the self-consistent 2IAM at $V = 0.455 < V_c$, which is in the RKKY phase close to the QCP. Again, a NFL is found at intermediate energies and a FL fixed point at low energies. This directly establishes that the RKKY phase, too, is a FL described by a QP spectrum at low energies. However, note that close to the QCP, the level structure of the FL fixed point in the RKKY phase ($V = 0.455$) is quite different from that in the Kondo phase ($V = 0.46$). This suggests that these Fermi liquids are not smoothly connected. Indeed, we will see in Sec. VIII that their FS volumes differ. This implies different scattering phase shifts and hence different NRG eigenlevel structures, consistent with the fact that the level structures of Figs. 3(a) and 3(b) differ strikingly in the FL regimes on the left.

B. Dynamical susceptibilities

The characteristic level structure of RG fixed points governs the behavior of dynamical properties at $T = 0$, causing striking crossovers at the scales T_{FL} and T_{NFL}. In this section, we extract these from the dynamical susceptibilities of local operators.

Let O be a local operator acting non-trivially only on the cluster impurity in the self-consistent 2IAM. We define its dynamical susceptibility as

$$\chi[O](\omega^+) = -\mathrm{i} \int_0^\infty \mathrm{d}t\, e^{\mathrm{i}\omega^+ t} \langle [O(t), O^\dagger(0)] \rangle, \qquad (8)$$

$\langle \cdot \rangle = \mathrm{Tr}(\rho\,\cdot)$ denotes a thermal expectation value. When ω lies within an energy range governed by a specific fixed point, the imaginary part of such a susceptibility typically displays power-law behavior, $\chi''[O](\omega) = -\frac{1}{\pi}\mathrm{Im}\chi[O](\omega^+) \sim \omega^\alpha$. When ω traverses the crossover region between fixed points, the exponent α changes, indicating a change in the degree of screening of the local fluctuations described by O. A log-log plot of χ'' vs. ω thus consists of straight lines with slope α in regions governed by fixed points, connected by peaks or kinks (see
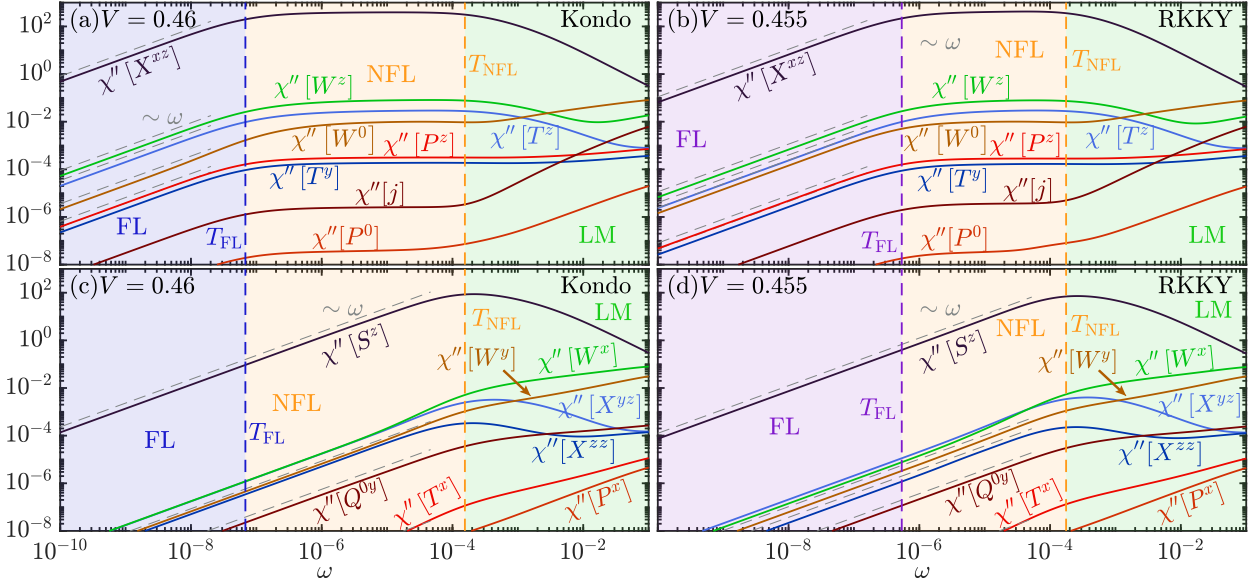
FIG. 4. Dynamical impurity susceptibilities $\chi''(\omega)$ for various operators defined in Eq. (9), computed in (a,c) the Kondo phase, at $V = 0.46$, and (b,d) the RKKY phase at $V = 0.455$, both at $T = 0$, close to the QCP. For the susceptibilities collected in (c,d), the χ'' curves exhibit a maximum around T_{NFL}; for those in (a,b), they instead exhibit a plateau between T_{FL} and T_{NFL}. This plateau indicates that the FL is reached in a two-stage screening process, leading to the emergence of NFL behavior at intermediate energy scales. Grey dashed lines are guides-to-the-eye for $\sim \omega$ behavior.

Fig. 4). We thus define the crossover scales T_{NFL} and T_{FL} via the position of these kinks, as described below. (A systematic method for determining the kink positions is described in App. B.) When discussing finite-temperature properties in later sections, we will see that the scales so obtained also serve as crossover scales separating low-, intermediate- and high-temperature regimes.

We have computed $\chi''[O](\omega)$ for the following local cluster operators, defined in the momentum-spin basis, with indices $\alpha \in \{+, -\}$ and $\sigma \in \{\uparrow, \downarrow\}$:

$$T^a = \tfrac{1}{2} f^\dagger_{\alpha\sigma} \tau^a_{\alpha\alpha'} \delta_{\sigma\sigma'} f_{\alpha'\sigma'} \qquad \text{(momentum)} \tag{9a}$$

$$S^b = \tfrac{1}{2} f^\dagger_{\alpha\sigma} \delta_{\alpha\alpha'} \sigma^b_{\sigma\sigma'} f_{\alpha'\sigma'} \qquad \text{(spin)} \tag{9b}$$

$$X^{ab} = \tfrac{1}{2} f^\dagger_{\alpha\sigma} \tau^a_{\alpha\alpha'} \sigma^b_{\sigma\sigma'} f_{\alpha'\sigma'} \qquad \text{(spin-momentum)} \tag{9c}$$

$$W^a = f^\dagger_{\alpha\sigma} \tau^a_{\alpha\alpha'} \delta_{\sigma\sigma'} c_{\alpha'\sigma'} + \text{h.c.} \qquad \text{(hybridization)} \tag{9d}$$

$$P^a = \tfrac{1}{\sqrt{2}} f_{\alpha\sigma} \tau^a_{\alpha\alpha'} \mathrm{i}\sigma^y_{\sigma\sigma'} f_{\alpha'\sigma'} \qquad \text{(singlet pairing)} \tag{9e}$$

$$Q^{ab} = f_{\alpha\sigma} f_{\alpha'\sigma'} \hat{\tau}^a_{\alpha\alpha'} \hat{J}^b_{\sigma\sigma'} \qquad \text{(triplet pairing)} \tag{9f}$$

$$j = -\mathrm{i} t e (c^\dagger_{1\sigma} c_{2\sigma} - \text{h.c}) \qquad \text{(current)} \tag{9g}$$

Here, sums over repeated indices are implied, τ^a and σ^b are Pauli matrices in the momentum and spin sectors, respectively, $\mathrm{i}\sigma^y = \left(\begin{smallmatrix} 0 & 1 \\ -1 & 0 \end{smallmatrix} \right)$, and $\hat{J}^b$ are SU(2) generators in the triplet representation. These operators can also be expressed in the position spin basis via the Hadamard transformation U_H, which maps $\tau^x \to \tau^z$, $\tau^y \to -\tau^y$ and $\tau^z \to \tau^x$. For example, T^z can be expressed as

$$T^z = \sum_{\alpha,\alpha'=\pm} \tfrac{1}{2} f^\dagger_{\alpha\sigma} \tau^z_{\alpha\alpha'} f_{\alpha'\sigma} = \sum_{i,j=1}^{2} \tfrac{1}{2} f^\dagger_{i\sigma} \tau^x_{ij} f_{j\sigma}, \tag{10}$$

describing f hopping between sites 1 and 2. Similarly, S^z describes the total f-electron spin, $X^{xz} = S^z_{f1} - S^z_{f2}$ the staggered magnetization, $W^z = \sum_{ij} f^\dagger_{i\sigma} \tau^x_{ij} c_{j\sigma} + \text{h.c.}$ nearest-neighbor f-c hybridization, and P^z f-electron nearest-neighbor singlet pairing.

Fig. 4 shows various χ'' susceptibilities at $T = 0$ for the choices $V = 0.46$ [(a,c)] and $V = 0.455$ [(b,d)], in the Kondo and RKKY phases close to the QCP, respectively. For $\omega < T_{\mathrm{FL}}$, all χ'''s decrease linearly with decreasing ω, indicative of FL behavior. Hence all local fluctuations are fully screened in that energy window, leading to well-defined Fermi-liquid QPs. By contrast, for $T_{\mathrm{FL}} < \omega < T_{\mathrm{NFL}}$ only the χ'''s in panels (c) and (d) (e.g. $\chi''[S^z]$) decrease with decreasing ω, while the ones in panels (a) and (b) (e.g. $\chi''[T^z]$, $\chi''[X^{xz}]$, $\chi''[W^z]$ and $\chi''[P^z]$) all traverse plateaus. These plateaus are reminiscent of those found for $\chi''_{\mathrm{2CK}}[S^z]$ of the overscreened, $S = \tfrac{1}{2}$ two-channel Kondo model (2CK), and for $\chi''_{\mathrm{2IKM}}[S^z_1 - S^z_2]$ of the two-impurity Kondo model (2IKM) in their respective NFL regimes (see Fig. 20 below). This implies that the total spin in the $\pm$ basis is screened, whereas the momentum, spin-momentum, pairing and hybridization fluctuations are *overscreened*, yielding the intermediate NFL.

The χ'' curves at $T = 0$ in Fig. 4 clearly demonstrate that when V is close to V_c, the screening process evolves through two stages, characterized by T_{NFL} and T_{FL}. Precisely *at* the critical point, where $T_{\mathrm{FL}} = 0$, the plateaus would extend all the way to zero. Conversely, when V is tuned away from the QCP, T_{FL} tends toward T_{NFL} (see Fig. 2(a)). The two scales merge for $|V - V_c| \gtrsim 0.1$, where
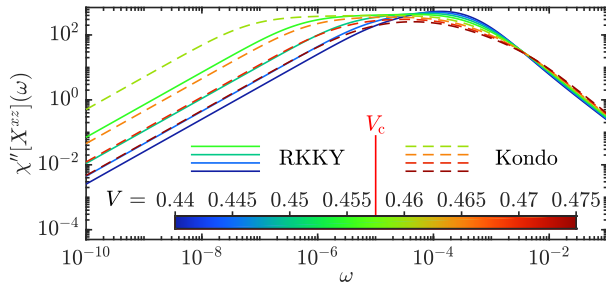
FIG. 5. Evolution of $\chi''[X^{xz}]$ with V across the QCP at $T = 0$. Solid lines: RKKY phase; dashed lines: Kondo phase. As $V \to V_c$ from either above or below such that $T_{\mathrm{FL}} \to 0$, the dashed and dotted plateaus both extend to ever lower scales (they would coincide at V_c, where $T_{\mathrm{FL}} = 0$), demonstrating that the KB–QCP is continuous.

the χ'' plateaus have shrunk to become mere peaks, shown for $\chi''[X^{xz}]$ in Fig. 5. The curves in Fig. 5 further illustrate that the KB–QCP is continuous because $\chi''[X^{xz}]$ evolves smoothly without any discontinuities across the KB–QCP. We find similar behavior for the other dynamical susceptibilities shown in Fig. 4. In a companion paper [148], we show that those χ'' which exhibit a plateau [those shown in Fig. 4(a,b)] exhibit logarithmic ω/T scaling in the NFL region while the corresponding static susceptibilities are singular at the KB–QCP, where the NFL region extends down to $T = 0$. The fact that many static susceptibilities with different symmetries diverge at the QCP suggests that many different, possibly competing symmetry breaking orders may be possible in the vicinity of the QCP. Which order prevails (if any) will be carefully studied in future work.

V. SINGLE-PARTICLE PROPERTIES – PRELIMINARIES

The fact that $T_{\mathrm{FL}} \to 0$ at the QCP (Fig. 2(a)) indicates a breakdown of the FL and QP concepts at the KB–QCP. Experimental evidence for such a breakdown is found in the sudden reconstruction of the FS [25, 36], and the divergence of the effective mass [27] at the KB–QCP. It is to date not fully settled how this should be understood [3, 5]. In the next two sections, Sec. VI and VII, we revisit such questions, exploiting the ability of CDMFT–NRG to explore very low temperatures and frequencies. This will allow us to clarify the behavior of spectral functions and self-energies in unprecedented detail. We discuss their cluster versions for the self-consistent 2IAM in Sec. VI, and the corresponding lattice functions for the PAM in Sec. VII.

In the present section we set the stage for this analysis by summarizing, for future reference, some well-established considerations regarding single-particle properties. We first recall standard expressions for low-frequency expansions of correlators and self-energies in the PAM,

and the definition of its Fermi surface (Sec. V A). Even though our focus here is on the PAM, we note that low-frequency expressions similar to those reviewed in Sec. V A can be obtained for the Kondo lattice using slave particles [3, 71, 105, 106]. In Sec. V B, we discuss possible scenarios how the parameters appearing in the low-frequency expansions in Sec. V A behave in the vicinity of a KB–QCP.

A. Fermi-liquid expansions, Fermi surface, Luttinger surface

In what follows, we will often refer to the low-energy expansions, applicable in conventional FL phases, of the the functions $G_{x\mathbf{k}}(z)$ and $\Sigma_{x\mathbf{k}}(z)$ ($x = f, c$) defined in Eqs. (3). We list them here for future reference.

Fermi-liquid expansions: For z below a characteristic FL scale, $|z| \ll T_{\mathrm{FL}}$, and for $\mathbf{k}$ close to the FS, the self-energies can be expanded as [171]

$$\Sigma_{x\mathbf{k}}(z) = \mathrm{Re}\Sigma_{x\mathbf{k}}(0) + z\mathrm{Re}\Sigma'_{x\mathbf{k}}(0) + \delta\Sigma_{x\mathbf{k}}(z), \quad (11)$$

where $\Sigma'(z) = \partial_z\Sigma(z)$ and $\delta\Sigma_{x\mathbf{k}}(z)$ is of order of $\mathcal{O}(z^2/T_{\mathrm{FL}}^2)$. Moreover, analyticity of $G_{x\mathbf{k}}(z)$ in the upper half-plane requires $\mathrm{Im}\Sigma_{x\mathbf{k}}(z) < 0$ for $\mathrm{Im}\, z > 0$. For $z = \omega^+$ this implies $\mathrm{Im}\Sigma_{x\mathbf{k}}(\omega^+) < 0$ and $\mathrm{Re}\Sigma'_{x\mathbf{k}}(0) \le 0$ (the latter follows since $\delta\Sigma_{x\mathbf{k}}(z) \sim z^2$ implies $\mathrm{Im}\Sigma_{x\mathbf{k}}(0) = 0$).

The expansion coefficients determine the so-called free QP energies, weights and the effective hybridization,

$$\epsilon^*_{x\mathbf{k}} = Z_{x\mathbf{k}}\big[\epsilon_{x\mathbf{k}} + \mathrm{Re}\Sigma_{x\mathbf{k}}(0)\big], \quad (12a)$$

$$Z_{x\mathbf{k}} = \big[1 - \mathrm{Re}\Sigma'_{x\mathbf{k}}(0)\big]^{-1}, \quad (12b)$$

$$V^*_{\mathbf{k}} = \sqrt{Z_{f\mathbf{k}}}V, \quad (12c)$$

with $\epsilon_{x\mathbf{k}} = \epsilon_f$ or $\epsilon_{c\mathbf{k}}$ for $x = f, c$. Since $\mathrm{Re}\Sigma'_{x\mathbf{k}}(0) \le 0$, the QP weights satisfy $Z_{x\mathbf{k}} \le 1$. The QP energies and weights, in turn, appear in the low-frequency expansions of Σ_c and G_c (cf. Eqs. (3)):

$$\Sigma_{c\mathbf{k}}(z) = \frac{(V^*_{\mathbf{k}})^2}{z - \epsilon^*_{f\mathbf{k}}} + \mathcal{O}(z^2/T_{\mathrm{FL}}^2), \quad (13a)$$

$$G_{c\mathbf{k}}(z) = \frac{Z_{c\mathbf{k}}}{z - \epsilon^*_{c\mathbf{k}}} + \mathcal{O}(z^2/T_{\mathrm{FL}}^2). \quad (13b)$$

Evidently, the low-energy expansion of Σ_c is fully determined by that of Σ_f, with

$$\mathrm{Re}\,\Sigma_{c\mathbf{k}}(0) = -\frac{V^{*2}_{\mathbf{k}}}{\epsilon^*_{f\mathbf{k}}}, \quad \mathrm{Re}\,\Sigma'_{c\mathbf{k}}(0) = -\frac{V^{*2}_{\mathbf{k}}}{\epsilon^{*2}_{f\mathbf{k}}}, \quad (14)$$

$$Z_{c\mathbf{k}} = \left[1 + \frac{V^{*2}_{\mathbf{k}}}{\epsilon^{*2}_{f\mathbf{k}}}\right]^{-1} = \frac{\epsilon^{*2}_{f\mathbf{k}}}{\epsilon^{*2}_{f\mathbf{k}} + V^{*2}_{\mathbf{k}}}. \quad (15)$$

These expressions make explicit how c-f hybridization effects c electrons: the sign of the energy shift $\mathrm{Re}\,\Sigma_{c\mathbf{k}}(0)$ is

determined by and opposite to that of $\epsilon_{f\mathbf{k}}^*$; and $\operatorname{Re}\Sigma_{c\mathbf{k}}'(0)$ changes from zero to negative, thereby decreasing $Z_{c\mathbf{k}}$ below 1 and causing c electron mass enhancement [171]. Since $\epsilon_{f\mathbf{k}}^* \sim Z_{f\mathbf{k}}$ and $V_{\mathbf{k}}^* \sim \sqrt{Z_{f\mathbf{k}}}$, Eq. (15) implies $Z_{c\mathbf{k}} \sim Z_{f\mathbf{k}}$ when $Z_{f\mathbf{k}} \ll 1$.

Fermi surface: Next, we recall the definition of the FS. For the PAM, this is not entirely trivial, since the correlators G_c and G_f are not independent, but coupled through Eqs. (3).

We focus on $T = 0$ (else the FS is not sharply defined). If there is no hybridization, $V = 0$, the situation is simple: the partially-filled c band is metallic and the half-filled f band a Mott insulator. Then, the FS comprises essentially only c electrons and is defined by the conditions [12, 171]

$$\epsilon_{c\mathbf{k}}^* = 0\,, \qquad Z_{c\mathbf{k}} > 0\,, \qquad \operatorname{Im}\Sigma_{c\mathbf{k}}(0) = 0\,. \quad (16)$$

The first condition identifies the FS as the locus of $\mathbf{k}$ points in the Brillouin zone for which the free QP energy vanishes; the second states that the QP occupation should exhibit an abrupt jump when this surface is crossed ($Z_{c\mathbf{k}}$ governs the size of this jump); and the third requires the QP scattering rate to vanish at the FS. Together, they imply that the FS is the locus of $\mathbf{k}$ points at which $G_{c\mathbf{k}}^{-1}(0) = 0$.

More generally, for $V \neq 0$, we start from the matrix form, $G_{\mathbf{k}}(z)$, of the combined f and c correlators [Eq. (2)]. Then, the FS is defined as the locus of $\mathbf{k}$ points for which some eigenvalue of $G_{\mathbf{k}}^{-1}(0)$ vanishes. Thus, all points on the FS satisfy the condition $\det\!\left[G_{\mathbf{k}}^{-1}(0)\right] = 0$, or

$$\epsilon_{c\mathbf{k}}\big(\epsilon_f + \Sigma_{f\mathbf{k}}(0)\big) - V^2 = 0\,. \quad (17)$$

For $V \to 0$, either the first or second factor on the left must vanish, implying $\epsilon_{c\mathbf{k}} = 0$ or $\epsilon_f + \Sigma_{f\mathbf{k}}(0) = 0$, respectively. The first condition defines the bare FS for the c band; the second condition is never satisfied for the case of present interest, where the bare f electrons form a half-filled Mott insulator with μ lying within the gap.

If V is non-zero, Eq. (17) implies that *both* of the following inequalities hold on the FS (assuming that $\Sigma_{f\mathbf{k}}(0)$ does not diverge there):

$$\epsilon_{c\mathbf{k}} \neq 0\,, \quad \epsilon_f + \Sigma_{f\mathbf{k}}(0) \neq 0\,. \quad (18)$$

Thus, the bare and actual FS do not intersect. Dividing Eq. (17) by the first or second factor, we obtain [127, 128]

$$G_{f\mathbf{k}}^{-1}(0) = 0\,, \qquad G_{c\mathbf{k}}^{-1}(0) = 0\,. \quad (19)$$

These two conditions are equivalent, in that one implies the other, via Eq. (17). Moreover, the second inequality in (18) ensures that $\Sigma_{c\mathbf{k}}(0)$ does not diverge, hence the second condition in (19) implies Eqs. (16). We thus conclude that Eqs. (16) define the FS also for nonzero V.

Luttinger surface: A second surface of importance is the *Luttinger surface* (LS) [10, 172, 173]. For the PAM it is defined [127] as the locus of $\mathbf{k}$ points for which $\Sigma_{f\mathbf{k}}(z)$ has a pole at $z = 0$. This definition, together with

Eqs. (3a,3e), implies that the following relations hold on the LS:

$$|\Sigma_{f\mathbf{k}}(0)| = \infty\,, \quad G_{f\mathbf{k}}(0) = 0\,, \quad \Sigma_{c\mathbf{k}}(0) = 0\,. \quad (20)$$

The first relation just restates the definition of the LS; the second should be contrasted with the relation $G_{f\mathbf{k}}(0) = \infty$ holding on the FS; and the third implies, via (12a), that $\epsilon_{c\mathbf{k}}^* = Z_{c\mathbf{k}}\epsilon_{c\mathbf{k}}$, i.e. on the LS, the renormalized dispersion is obtained from the bare one purely by rescaling, without any shift. If the LS coincides with the bare FS, then the FS, too, coincides with the bare c-electron FS ($\epsilon_{c\mathbf{k}} = 0$).

Note that $|\Sigma_{f\mathbf{k}}(\omega)|$ can only diverge at isolated frequency values, not on extended frequency intervals, since the frequency integral over its spectral function must be finite. Terefore, when $|\Sigma_{f\mathbf{k}}(0)|$ diverges, $|\Sigma_{f\mathbf{k}}'(0)|$ diverges too. By Eq. (12b), it follows that $Z_{f\mathbf{k}} = 0$ on the LS.

The behavior of $Z_{c\mathbf{k}}$ depends on how strongly $\Sigma_{f\mathbf{k}}(z)$ diverges for $z \to 0$. For example, suppose $\Sigma_{f\mathbf{k}}(z) \sim z^{-\alpha}$ for some $\alpha > 0$. Then, Eq. (3e) implies $\Sigma_{c\mathbf{k}} \sim z^{\alpha}$, $\Sigma_{c\mathbf{k}}' \sim z^{\alpha-1}$. Thus, we obtain $Z_{c\mathbf{k}} \sim z^{1-\alpha} \to 0$ or $\in (0,1)$ or $= 1$ for $\alpha < 1$ or $= 1$ or > 1, respectively, i.e. the c-QP weight may or may not be renormalized.

We show results for the FS and LS in Sec. VII, and discuss their volumes together with Luttinger's sum rule in Sec. VIII.

B. Kondo breakdown

In the introduction, we have qualitatively described the Kondo breakdown scenarios that have been proposed to characterize the KB–QCP. For future reference, we here distinguish KB scenarios of two types: (1) a KB–QCP *with* Kondo destruction (KD), defined below, and (2) a KB-QCP *without* KD. In both scenarios, the f electron quasiparticle weight Z_f decreases to zero when approaching the KB–QCP from the Kondo side. However, in (1) Z_f remains zero on the RKKY side (i.e. all Kondo correlations have been destroyed, hence the monicker "KD"), whereas in (2), Z_f is non-zero on the RKKY side, too (i.e. some Kondo correlations survive there). (Thus, our nomenclature distinguishes between KB, which happens only *at* the critical point, and KD, which, in a type (1) scenario, happens throughout the RKKY phase.) We emphasize that (2) is different from the Hertz–Millis type SDW–QCP where the QP weight is also non-zero at the QCP. Fig. 6 sketches the different scenarios. Most of the scenarios for the KB–QCP proposed in the literature are of type (1), with KD. By contrast, we find a KB–QCP of type (2), without KD. We summarize below the concepts used to describe the HF problem and in particular how type (1) and (2) scenarios differ.

(i) *Hybridization gap:* The hybridization of c and f electrons leads to a well-developed pole in $\Sigma_{c\mathbf{k}}(z)$, called hybridization pole (h-pole), lying at energies well above the FL scale T_{FL}. It manifests itself as a strong peak in
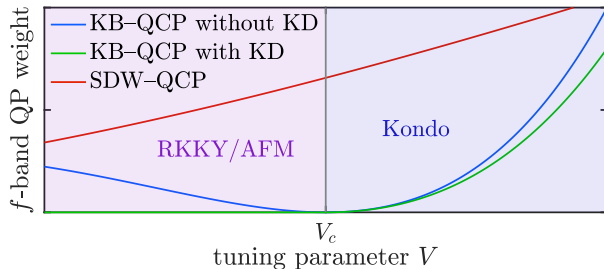
FIG. 6. Sketch of the generic f-band QP weight in different scenarios for quantum criticality. In the conventional SDW–QCP (red), the QP weight is finite at the QCP. At a KB–QCP, it is zero at the QCP. In a type (1) scenario with KD (green), it remains zero in the RKKY phase; in a type (2) scenario without KD (blue), it is finite there.

$-\mathrm{Im}\Sigma_{c\mathbf{k}}(z)$, causing the corresponding c-electron spectral functions to exhibit distinctive gaps or pseudogaps, called hybridization gaps (h-gaps). It occurs irrespective of whether the $T = 0$ phase is Kondo or RKKY correlated and is present for temperatures both above and below T_{FL}. The formation of a h-gap has been observed in many experiments, as reviewed in the introduction. Note that while in the non-interacting PAM ($U = 0$), the h-gap is positioned at $\epsilon_{f\mathbf{k}}^*$, this is not the case in the interacting case: the h-gap forms at scales which can much larger than the FL scale (in our case, it forms at T_{NFL}, see next section), i.e. $\epsilon_{f\mathbf{k}}^*$ and the position of the h-gap are renormalized differently by interactions.

(ii) *Kondo phase:* In the Kondo phase, $Z_{f\mathbf{k}}$ is non-zero for all $\mathbf{k}$. The presence of Kondo correlations is phenomenologically described [3, 71] by Eq. (13a). This situation can phenomenologically be interpreted as arising through an effective hybridization with strength $V_{\mathbf{k}}^*$ (sometimes referred to as "amplitude of static Kondo correlations" [3, 71]) of c electrons with an effective f band with dispersion $\epsilon_{f\mathbf{k}}^*$. This effective hybridization shifts the c-electron Fermi surface from its $V = 0$ form, defined by $\epsilon_{c\mathbf{k}} = 0$, to a form defined by $\epsilon_{c\mathbf{k}}^* = 0$, i.e.

$$\epsilon_{c\mathbf{k}} - \frac{V_{\mathbf{k}}^{*2}}{\epsilon_{f\mathbf{k}}^*} = 0 \,. \tag{21}$$

Therefore the FS volume changes, reflecting the influence of f orbitals. Within the Kondo phase, $V_{\mathbf{k}}^*$ remains non-zero but continuously approaches zero as the KB–QCP is approached. Moreover, in the Kondo phase the ratio $(V_{\mathbf{k}}^*)^2/\epsilon_{f\mathbf{k}}^*$ remains essentially constant as long as $V_{\mathbf{k}}^*$ is finite because both $(V_{\mathbf{k}}^*)^2 \sim Z_{f\mathbf{k}}$ and $\epsilon_{f\mathbf{k}}^* \sim Z_{f\mathbf{k}}$ (c.f. Eq. (12a)). Therefore, the FS will remain basically unchanged in the Kondo phase, even very close to the KB–QCP.

Two comments are in order. First, in general, the first term in Eq. (13a) usually does not represent an actual pole of $\Sigma_{c\mathbf{k}}$: it was derived assuming $|z| \ll T_{\mathrm{FL}}$ and $\mathbf{k}$ close to the FS, whereas $\epsilon_{f\mathbf{k}}^*$ typically lies outside that window (i.e. for $z \to \epsilon_{f\mathbf{k}}^*$, Eqs. (11) and (13a) no longer apply). Second, $\epsilon_{f\mathbf{k}}^*$ is not directly related to the hybridization

gaps, as already mentioned in point (i) above: the latter are determined by pseudogaps of $G_{c\mathbf{k}}$ of (3b), and since these lie at high energies of order $\pm T_{\mathrm{NFL}}$, their positions are not governed by Eq. (13a), but rather by the general form (3e) of $\Sigma_{c\mathbf{k}}$ (see Sec. VII below).

(iii) *Kondo breakdown:* As summarized in Refs. [3, 71], the following behavior is expected when approaching the KB–QCP from the Kondo phase: $V_{\mathbf{k}}^*$, or equivalently $Z_{f\mathbf{k}}$, decreases continuously to zero, hence the low-energy hybridization becomes weaker, while the ratio $(V_{\mathbf{k}}^*)^2/\epsilon_{f\mathbf{k}}^*$ and thus the FS remain constant, and different from the bare c-electron FS. Since $Z_{c\mathbf{k}} \sim Z_{f\mathbf{k}}$ if $Z_{f\mathbf{k}} \ll 1$ [c.f. Eq. (15) and its discussion], e.g. close to the KB–QCP, both QP weights are expected to continuously decrease to zero when approaching the KB–QCP. At the KB–QCP, V^* vanishes, i.e. low-energy hybridization and thus Kondo correlations break down.

(iv) *RKKY with Kondo destruction:* In the type (1) KD scenario [3, 71], $V_{\mathbf{k}}^*$, or equivalently $Z_{f\mathbf{k}}$, *remains* zero in the RKKY phase, i.e. Kondo correlations remain absent, i.e. they have been destroyed. By Eq. (21), that implies the FS reduces to the bare c-electron one, accounting for c electrons only. All in all, the FS jumps across the KB–QCP due to Kondo destruction. Since $Z_{f\mathbf{k}} = 0$ in this scenario, Eq. (11) for the f-electrons and therefore also Eq. (13a) does not apply anymore. Eq. (11) may however still apply for the c-electrons [see also the discussion below Eq. (20)], leading to QP mass enhancement due to the existence of c-f hybridization at finite frequencies. This is sometimes referred to as "dynamical Kondo correlations" [26, 174]. The type (1) KD scenario emerges from the Kondo lattice model both in a slave-particle [105, 106] or an EDMFT treatment [119, 131–133].

(v) *RKKY without Kondo destruction:* Here, we describe the type (2) scenario of a Kondo breakdown without Kondo destruction in the RKKY phase. We emphasize that also in this scenario, the QP weights become zero at the KB–QCP and the FS is small in the RKKY phase. Nevertheless, in the RKKY phase the f-electron QP weight is non-zero at the FS. In the type (2) scenario, $Z_{f\mathbf{k}}$ becomes zero only at a LS [see Eq. (20)], where the f-electron self-energy diverges. If the LS does not coincide with the FS (the converse would require significant fine-tuning), this implies non-zero $Z_{f\mathbf{k}}$ at the FS and c-f hybridized QPs also in the RKKY phase.

The type (2) scenario described above is not so unusual: there is growing evidence that Mott insulators described beyond the single-site DMFT approximation generically feature momentum-dependent Mott poles [175–177], with a singular part of the f self-energy of the form [177],

$$\Sigma_{f,\mathrm{singular}} \sim \frac{1}{z - \epsilon_{\Sigma\mathbf{k}}^*} \,. \tag{22}$$

Here, $\epsilon_{\Sigma\mathbf{k}}^*$ is related to the free dispersion with renormalized parameters and opposite sign of the hopping amplitudes [177]. Such a self-energy therefore features a LS, defined by $\epsilon_{\Sigma\mathbf{k}}^* = 0$. It has been suggested that the LS is the defining feature of Mott phases and that this

feature is stable to perturbations [178–180]. The LS of a Mott phase should therefore in principle be stable to small hybridization with a metal, provided the hybridization strength is not too large, resulting in a OSMP. $Z_{f\mathbf{k}}$ is only zero at the LS where Σ_f diverges. If the LS and the FS do not coincide, it follows that $Z_{f\mathbf{k}}$ is non-zero at the FS.

A comment is in order regarding single-site DMFT or EDMFT, where the Mott pole is not momentum dependent and the QP weight is zero throughout the whole BZ. In single-site DMFT, this phase is not stable to inter-orbital hybridization [121, 181]. As a result, single-site DMFT will always describe a Kondo phase at $T = 0$ [121]. By contrast, OSMPs described by EDMFT seem to be stable to inter-orbital hybridization [182], leading to the type (1) scenario described above.

In our own CDMFT-NRG studies of the PAM, we find a KB scenario of type (2). In Sec. VI, we will establish this by a detailed study the low-energy behavior of the self-consistent effective 2IAM. There, the role of $\mathbf{k}$ is taken by $\alpha = \pm$, i.e. we will show that

$$\Sigma_{c\alpha}(z) = \frac{V_\alpha^{*2}}{z - \epsilon_{f\alpha}^*} + \mathcal{O}\big(z^2/T_{\mathrm{FL}}^2\big) \qquad (23)$$

is valid, with $V_\alpha^* \neq 0$ on both sides of the QCP. When V approaches V_c from either side, V_α^* approaches 0, leading to a breakdown of Kondo correlations at the KB–QCP. We will find that the FS reconstruction at V_c is caused by a sign change of ϵ_{f+}^*, as explained in the Sec. VI. The consequences for the lattice model are established in Sec. VII, and for the Luttinger sum rule in Sec. VIII.

VI. SINGLE-PARTICLE PROPERTIES – CLUSTER

In this section we discuss the single-particle properties of the self-consistent 2IAM, focusing on the spectral functions and retarded self-energies of both c and f orbitals. A discussion of the corresponding momentum-dependent lattice properties follows in Sec. VII. We will argue that the KB quantum phase transition is a continuous orbital selective Mott transition (OSMT) at $T = 0$. The Kondo phase is a normal metallic phase while in the RKKY phase, the f electrons are in a Mott phase, i.e. this phase is an orbital selective Mott phase (OSMP). The defining feature of the OSMP is a momentum-dependent pole in the f-electron self-energy, *not* a single-particle gap. The RKKY phase is thus *not* an orbital selective Mott *insulator*. Indeed, we find that even in the OSMP, the f electrons exhibit a finite QP weight due to finite hybridization with the c electrons.

In sections VI A and VI B, we discuss spectral functions and self-energies at $T = 0$ on the real-frequency axis, exploiting the capabilities of NRG to resolve exponentially small energy scales. We then investigate QP properties

in more detail in Sec. VI C: we clearly show that both the c and f-electron QP weights are finite in both the Kondo and RKKY phases, but vanish at the KB–QCP. Finally, in Sec. VI D, we discuss finite temperature properties, showing that c-f hybridization is already fully developed around T_{NFL}, whereas QP coherence and self-energy poles are only fully formed at T_{FL}.

A. Cluster spectral functions at $T = 0$: overview

In this subsection, we provide a phenomenological overview over the cluster spectral properties of the self-consistent 2AIM at $T = 0$ as functions of V; details and physical insights follow in Sec. VI B. We adopt the $\pm$ basis, where G_f and G_c from Eq. (6) are both diagonal, and study $A(\omega) = -\frac{1}{\pi}\mathrm{Im}G(\omega^+)$ for both f and c orbitals. (When referring to A_f below, we mean both components, $A_{f\pm}$, and likewise for A_c.) Our results for A_f and A_c are shown in Fig. 7 on a linear frequency scale to provide a coarse overview. We enumerate some of their characteristic features, proceeding from high- to low-frequency features.

(i) *Hubbard peaks, band structure:* Figures 7(a,b,e,f) and (c,d,g,h) show the spectral functions $A_f(\omega)$ and $A_c(\omega)$ for different V on a linear frequency scale for the ranges $\omega \in [-10, 10]$ and $\omega \in [-1.25, 1.25]$, respectively, containing all significant spectral weight. A_f has two Hubbard bands around $\omega \simeq \pm 5 = \pm U/2$. They are almost independent of V. Moreover, they show the same structure for A_{f+} and A_{f-}, implying that these high-energy features are momentum independent. By contrast, A_c has no Hubbard bands since the c electrons do not interact, with spectral weight only in the range of the non-interacting bandwidth, $\omega \in [-1.2, 0.8]$. Its shape mimics that obtained for $V = 0$ (insets of Figs. 7(c,d)), reflecting the bare c-electron band structure, except for some sharp structures at intermediate and low frequencies, discussed below.

(ii) *Center of c band:* For A_c, the highest-frequency sharp feature furthest from $\omega = 0$ lies at $\omega \simeq -0.2$, the middle of the bare c-electron band. This feature is prominently developed deep in the RKKY phase at $V = 0.4$ (Fig. 7(g,h)) but almost invisible deep in the Kondo phase at $V = 0.6$ (Fig. 7(c,d)). It is due to scattering of c electrons by antiferromagnetic fluctuations and reflects a tendency towards antiferromagnetic order in the RKKY phase. Though our CDMFT setup excludes such order, it does find strong antiferromagnetic correlations in the RKKY phase (see $\langle \mathbf{S}_{f1} \cdot \mathbf{S}_{f2} \rangle$ in Fig. 2(b)), causing enhanced scattering of c electrons at the band center.

(iii) *Kondo peaks, hybridization gaps:* Deep in the Kondo phase at $V = 0.6$ (red lines), A_f shows a sharp Kondo peak near $\omega \simeq 0$, while A_c has a distinct dip, known as hybridization gap (h-gap, see also Sec.V), at a small, negative value of ω. Both these features are indicative of strong c-f hybridization and coherent QPs.
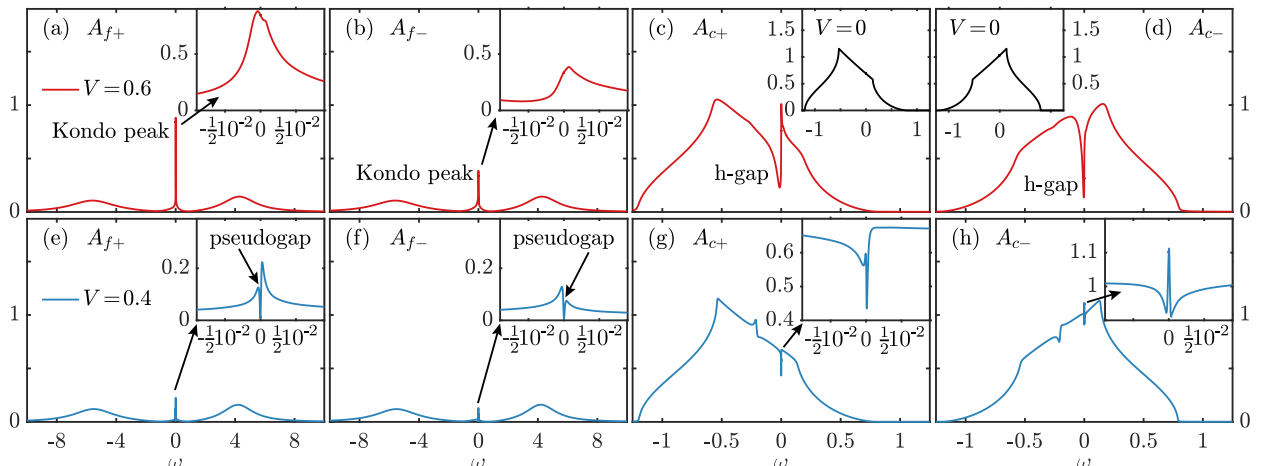
FIG. 7. Cluster spectral functions at $T = 0$, for $V = 0.6$ (top row, deep in the Kondo phase) and for $V = 0.4$ (bottom row, deep in the RKKY phase). Panels (a,b,e,f) and (c,d,g,h) show the f and c-electron spectral functions, respectively. The insets in (c,d) show the c-electron spectral functions at $V = 0$; the insets in all other panels show a zoom into the low-frequency region.

By contrast, deep in the RKKY phase at $V = 0.4$ (blue lines), the Kondo peak in A_f has disappeared, giving rise to a pseudogap (see the insets of Fig. 7(e,f)), and the h-gap in A_c has become very weak. Nevertheless, we will see in Sec. VI B that even deep in the RKKY phase, c-f hybridization is present even at low energies and the f-electron QP weight is finite in this phase. This leads to a sharp peak inside the h-gaps of A_c (see the insets of Fig. 7(g,h)). As will be discussed in more detail in Sec. VII, this sharp feature reflects a narrow QP band with a FS close to $\Pi = (\pi, \pi, \pi)$.

(iv) *Momentum dependence:* The spectral functions and self-energies show several qualitative and/or quantitative differences between the $+$ and $-$ channels (different Kondo peak heights, different h-gap shapes, etc.) Such channel asymmetries reflect the fact that our system is electron-doped—the Fermi surface lies closer to the Γ point than the Π point, causing a stronger c-f hybridization (encoded in $\Sigma_{c\pm}$) for bonding than anti-bonding orbitals. This asymmetry leads to different behavior for momenta near $\Gamma = (0, 0, 0)$ and $\Pi = (\pi, \pi, \pi)$. However, these asymmetries in the *spectral functions* are not necessarily indicative of non-local correlations. Especially deep in the Kondo phase, the channel asymmetries are mostly due to the single-particle dispersion and are not non-local *self-energy* effects. We discuss this in more detail in Sec. VI B.

B. Cluster spectral functions and self-energies at $T = 0$: details

Next, we discuss the main spectral features relevant to KB physics, referring to Fig. 8. It shows both the spectral functions $A_{x\alpha}(\omega)$ and retarded self-energies

$\Sigma_{x\alpha}(\omega^+)$ using a symmetric logarithmic frequency scale with $|\omega| > 10^{-10}$. Figures 8(a–d) show this evolution for A_f and A_c while Figs. 8(e–h) show the corresponding self-energies.

(i) *Self-energy poles for Σ_f:* The most important feature is the pole in Σ_f (denoted as fs-pole), which is present in the RKKY phase but not in the Kondo phase, see Fig. 8(e,f). This fs-pole in the RKKY phase is indicative of Mott physics [127, 128] present in the f band but not in the c band (see also the discussion in Sec. V B). This brings us to one of our main conclusions: *the RKKY phase is an OSMP and the KB quantum phase transition is an OSMT.* Moreover, the fs-pole continuously disappears when approaching the KB–QCP from the RKKY phase. This further shows that the KB quantum phase transition is a *continuous* OSMT (see also Fig. 5 and its discussion). We also note that we found no coexistence region, which further underpins our conclusion of a continuous QPT.

Our conclusion that the KB is an OSMT matches the conclusion of previous CDMFT plus ED studies of the PAM using the same parameters [127, 128]. Nevertheless, the considerably improved accuracy of our NRG impurity solver compared to the ED impurity solver used there yields new conceptional insights and reveals new emergent physics.

The fs-pole in the RKKY phase is positioned at a negative frequency for Σ_{f+} (at $\omega \simeq -T_{\mathrm{FL}}$) and at a positive frequency for Σ_{f-} (at $\omega \simeq T_{\mathrm{FL}}$). Therefore, its position depends on momentum, i.e. it is *dispersive*. A dispersive fs-pole is a generic feature of Mott phases in finite dimensions $d < \infty$ [175, 177] (see also Sec. V B). By contrast in the $d \to \infty$ limit (or equivalently in the single-site DMFT approximation) where the self-energy and thus also the fs-pole is momentum independent, the OSMP is *not* stable against interorbital hopping [181] (i.e. against finite c-f hybridization V in the present context). The
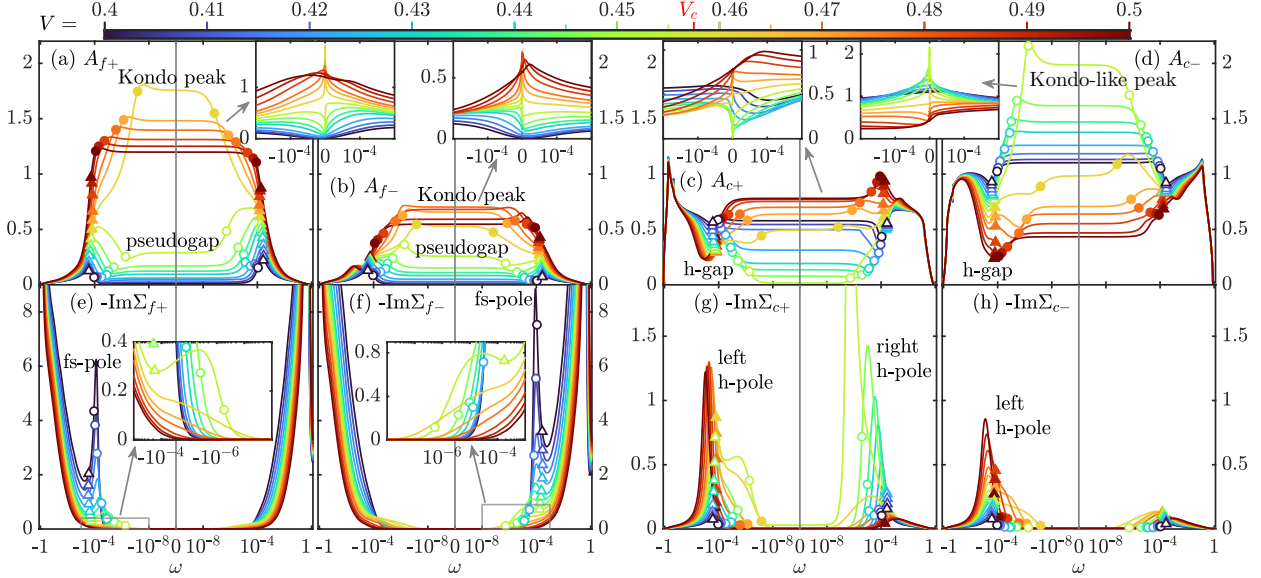
FIG. 8. Evolution of cluster spectral functions $A_{x\alpha}(\omega)$ and retarded self-energies $\Sigma_{x\alpha}(\omega^+)$ at $T = 0$ as V is tuned across the QCP. Colored curves correspond to V values marked by ticks on the color bar. A symmetric log scale with $10^{-10} < |\omega| < 1.25$ is used. On such a scale, the plateaus seen for all curves for very low frequencies, $|\omega| < 10^{-8}$, demonstrate that no new features arise in that range. Triangles and circles mark the crossover scales $\pm T_{\mathrm{NFL}}$ and $\pm T_{\mathrm{FL}}$, respectively, with filled (open) symbols identifying curves in the Kondo (RKKY) phase. The insets in (a-d) show the spectral functions on a linear frequency scale for $|\omega| < 2 \cdot 10^{-4}$.

momentum resolution provided by 2-site CDMFT, though coarse, is therefore a crucial ingredient to stabilize the OSMP. We will show in Sec. VII that after reperiodization of the CDMFT self-energy, the dispersive nature of the fs-pole leads to a reperiodized self-energy with a continuous **k**-dependence of the form of Eq. (22). Based on the results of Ref. 147, the fs-pole can be associated with emergent spinon excitations; its emergence therefore suggests a fractionalization of the f-electron. Since the position of the sf-pole is momentum dependent, the emergent spinon is dispersive.

Even though the dispersive fs-pole is the most pronounced momentum-dependent feature of Σ_f, more subtle momentum-dependent features are responsible for the NFL physics close to the QCP: In the Kondo phase, shoulder-like structures show up in Σ_f below $T_{\mathrm{FL}} < |\omega| < 10^{-4}$ [see insets of Figures 8(e,f)]. These are more pronounced for Σ_{f-} than for Σ_{f+}, leading to momentum-dependent scattering rates at the corresponding energy scales.

The features of A_f [Figs. 8(a,b)], A_c [Figs. 8(c,d)] and Σ_c [Figs. 8(g,h)] can largely be understood in terms of a continuous OSMT. In the following, we enumerate and describe the main spectral and self-energy features and discuss their connection to the presence or absence of fs-poles in Σ_f. We follow the evolution, with decreasing V, from the Kondo phase through the QCP into the RKKY phase, noting the following salient features:

(ii) *From Kondo peak to pseudogap for $A_{f\pm}$:* In the Kondo phase, the Kondo peak of A_{f+} lies slightly below $-T_{\mathrm{FL}}$, that of A_{f-} slightly below T_{FL}. As V decreases to-

wards V_c, the Kondo peaks of both A_{f+} and A_{f-} shift towards zero and become higher and narrower [Figs. 8(a,b)], leaving behind shoulder-like structures at $\pm T_{\mathrm{NFL}}$ (marked by triangles). The Kondo peak of A_{f+} is higher than that of A_{f-}, reflecting the fact that in the Kondo phase, the FS is positioned closer to the Γ point than to the Π point. When V crosses V_c, the Kondo peak abruptly changes into a pseudogap, flanked by the two shoulders. The emergence of the pseudogap in A_f is caused by the appearance of fs-poles in Σ_f in the RKKY phase. A further decrease of V deepens the pseudogap because the poles in Σ_f become stronger. The pseudogap never becomes a true gap (except for $V = 0$) because the poles of Σ_f are positioned away from $\omega = 0$. Thus, the QP weight of the f electrons is finite even in the RKKY phase (see also Sec. VI C). This is one of the crucial differences to the findings of Refs. 127 and 128; there, a charge gap in A_f was found due to the poor energy resolution of the ED impurity solver used in these studies.

(iii) *Pseudogap for A_{c+}, Kondo-like peak for A_{c-}:* Once V drops below V_c, A_{c+} rapidly develops a pronounced pseudogap around $\omega = 0$, which weakens (becomes less pronounced) when V is decreased further. This pseudogap emerges because ϵ_{f+}^* (see Eq. (23)) continuously changes sign at the KB–QCP, from $\epsilon_{f+}^* < 0$ in the Kondo phase to $\epsilon_{f+}^* > 0$ in the RKKY phase (see Fig. 9(b) below). Due to the low energy form of Σ_{c+} shown in Eq. (23), this leads to a h-pole in Σ_{c+} which is close to $\omega = 0$ in the vicinity of the KB–QCP and whose position changes sign across the QCP, in the same way as ϵ_{f+}^*. This h-pole is clearly visible in Fig. 8(g), where we show $-\mathrm{Im}\Sigma_{c+}$. We

discuss the sign change of ϵ_{f+}^* in more detail in Sec. VI C, where we also show that this sign change is intricately connected to the emergence of the fs-pole in Σ_{f+}. The sign change of ϵ_{f+}^* and therefore also the pseudogap in A_{c+} is therefore an integral part of the OSMT. We further show in Sec. VIII that the sign change of ϵ_{f+}^* is ultimately tied to a reconstruction of the FS.

In striking contrast, A_{c-} develops a Kondo-like peak around $\omega = 0$, whose peak height increases rapidly as V drops below V_c, and then decreases when V is decreased further. The emergence of such a peak for *delocalized* electrons is rather unexpected, which is why we call it "Kondo-like" (in contrast to "Kondo peak" for localized electrons). This sharp peak suggests that close to the KB–QCP, the c-electrons become more localized, i.e. that their Fermi velocity is strongly renormalized downward due to the momentum dependence of Σ_c.

(iv) *Hybridization poles for* $\mathrm{Im}\Sigma_c$: The h-gap at negative frequencies for A_c is caused by a corresponding peak in $\mathrm{Im}\Sigma_c$ [Figs. 8(g,h)]. It reflects a c self-energy pole, to be called left hybridization pole (left h-pole). The frequency location of the h-gap and left h-pole is comparable in magnitude to the NFL scale. When V is reduced towards and past V_c into the RKKY phase, the left h-pole in $\mathrm{Im}\Sigma_c$ weakens and almost disappears, causing the same for the h-gap in A_c. At the same time, for the bonding channel a peak in $-\mathrm{Im}\Sigma_{c+}$ at positive frequencies emerges in the RKKY phase. It corresponds to an additional pole of Σ_{c+}, to be called right h-pole, located at $\simeq T_{\mathrm{FL}}$. It causes the h-gap in A_{c+} around $\omega = 0$ close to the KB–QCP. By contrast, for the anti-bonding channel $\mathrm{Im}\Sigma_{c-}$ does not have a second pole—its very weak peak on the right in fact is the tail of its left h-pole (This becomes more clear from the temperature dependence of Σ_c and will be explained in more detail in Sec. VI D.)

(v) *Low-energy Fermi liquid:* For all considered values of V, the $\omega = 0$ quantities $\mathrm{Im}\Sigma_f(i0^+)$ and $\mathrm{Im}\Sigma_c(i0^+)$ all vanish. This implies FL behavior at the lowest energy scales for all $V \neq V_c$ (consistent with the results of Sec. IV A). Moreover, $A_f(0)$ and $A_c(0)$ never vanish, even in the RKKY phase. Thus the pseudogap in A_f never becomes a true gap, implying that f electrons keep contributing to the QPs constituting the low-energy FL.

C. Quasiparticle properties

In this subsection, we substantiate our claims made in the previous subsection regarding QP weights and ϵ_f^*. In particular, we seek to show that the low-frequency form Eq. (23) applies to Σ_c on both sides of the KB–QCP. Note that Eq. (23) is meaningful only if the low-energy physics shows FL behavior; our study of finite-size spectra in Sec. IV A confirmed that this is the case.

We define cluster QP weights and effective level positions for both f and c electrons by replacing $\mathbf{k} \to \alpha$ in
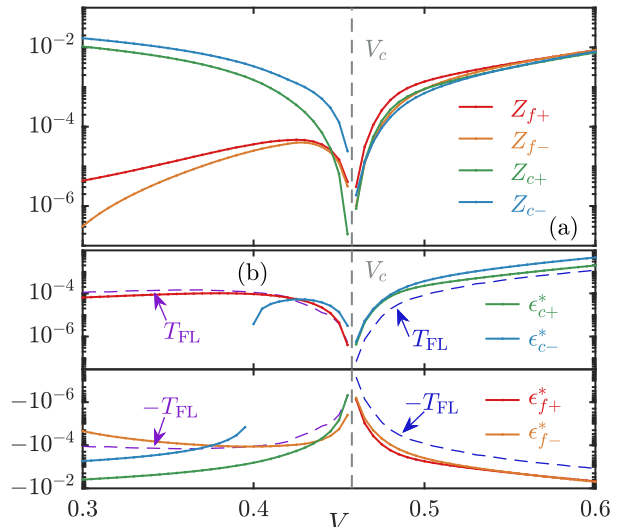
FIG. 9. (a) QP weights and (b) effective level positions of the self-consistent effective 2IAM, computed directly from the NRG finite size spectra at $T = 0$. Blue and purple dashed lines in panel (b) mark $\pm T_{\mathrm{FL}}$ and $\pm T_{\mathrm{FL}^*}$ for reference, respectively.

Eqs. (12a):

$$\epsilon_{x\alpha}^* = Z_{x\alpha}\left[\epsilon_{x\alpha} + \mathrm{Re}\Sigma_{x\alpha}(0)\right], \qquad (24a)$$

$$Z_{x\alpha} = \left[1 - \mathrm{Re}\Sigma_{x\alpha}'(0)\right]^{-1}, \qquad (x = f, c) \quad (24b)$$

with $\epsilon_{f\alpha} = \epsilon_f - \mu$ and $\epsilon_{c\alpha} = -\alpha t - \mu$. The f-electron QP weight is non-zero as long as $\Sigma_{f\alpha}'(0)$ is not infinite, i.e. as long as $\Sigma_{f\alpha}$ has no pole at $z = 0$. In the Kondo phase, there are no low-frequency poles in $\Sigma_{f\alpha}$ at all, while the poles appearing in the RKKY phase are shifted away from $z = 0$.

The QP weights $Z_{x\alpha}$ and effective level positions $\epsilon_{x\alpha}$ can be extracted directly from NRG finite size spectra [183, 184], which avoids fitting frequency dependent data. Figure 9 shows them all. We see that both Z_f and Z_c vanish at the KB–QCP, as expected. However, Z_f is finite not only in the Kondo phase *but also in the RKKY phase*. This further substantiates our claim that
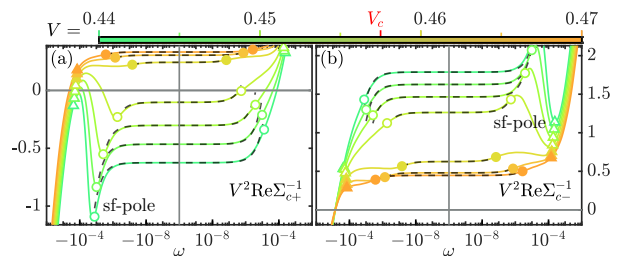
FIG. 10. Evolution of $V^2\mathrm{Re}\Sigma_{c\pm}^{-1}(\omega^+)$ at $T = 0$ as V is tuned in a narrow range across the QCP. As V is lowered, non-monotonic behavior emerges, whose double-wiggle structure (local maximum followed by local minimum) reflects the fs-poles of $-\mathrm{Re}\Sigma_{f\pm}$ (c.f. Eq. (25a)). Circles, triangles and tick marks on the color bar have the same meaning as in Fig. 8. Black dashed lines indicate linear behavior around $\omega = 0$.
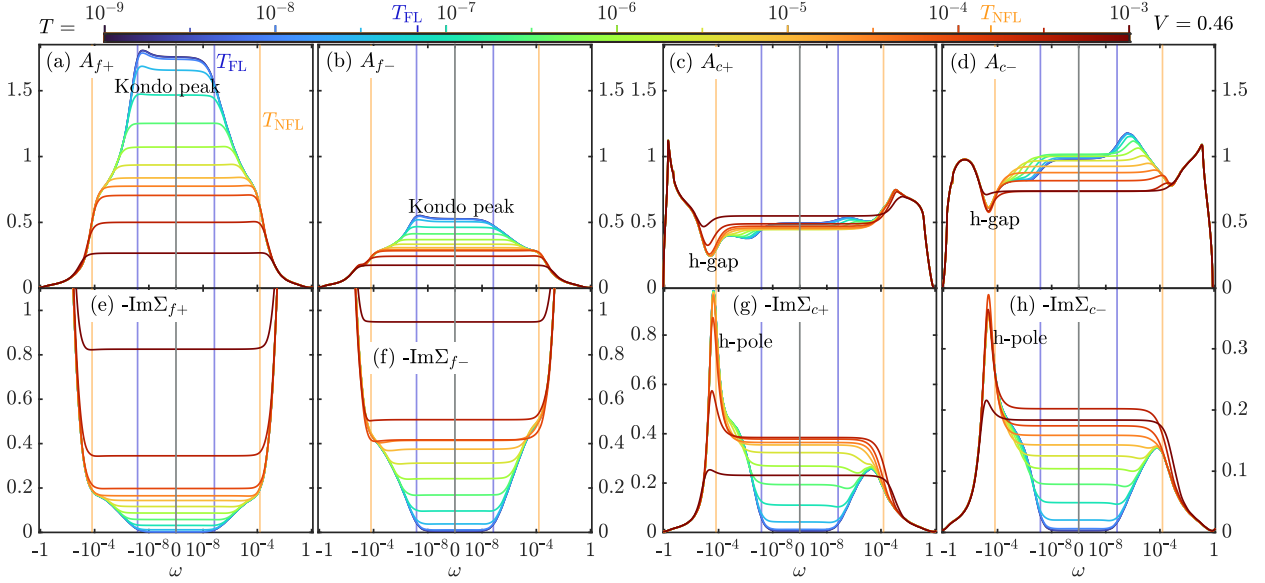
FIG. 11. Evolution of cluster spectral functions and retarded cluster self-energies $\Sigma_{x\alpha}(\omega^+)$ at $V = 0.46 > V_c$ (Kondo phase at $T = 0$) as temperature is increased. Colored curves correspond to T values marked by ticks on the color bar. A symmetric log scale with $10^{-10} < |\omega| < 1.25$ is used. Vertical blue and orange lines mark $\pm T_{\mathrm{FL}}$ and $\pm T_{\mathrm{NFL}}$, respectively.

the f electrons contribute to the low energy QP even for $V < V_c$.

The key difference between the RKKY and Kondo phases therefore is *not* zero versus non-zero Z_f — instead, the key difference turns out to be the sign of ϵ^*_{f+}. Note that our discussion below is applicable for the *electron-doped* case considered in this work; a corresponding discussion of the hole-doped case would follow along the same lines, but with the signs of $\epsilon^*_{f\alpha}$ flipped and the role of bonding and anti-bonding cluster orbitals interchanged. Both ϵ^*_{f+} and ϵ^*_{f-} are negative in the Kondo phase, see Fig. 9(b). The same is true for $U = 0$, and in this sense the non-interacting limit is adiabatically connected to the Kondo phase. However, while ϵ^*_{f-} remains negative in the RKKY phase, ϵ^*_{f+} changes sign at the KB–QCP and becomes positive. Now, Eqs. (6e) and (24a) imply

$$V^2 \Sigma_{c\alpha}^{-1}(z) = z - \epsilon_f - \Sigma_{f\alpha}(z), \qquad (25a)$$

$$\mathrm{sgn}\, \epsilon^*_{f\alpha} = -\mathrm{sgn}\, \mathrm{Re}\,\Sigma_{c\alpha}^{-1}(0). \qquad (25b)$$

Thus, the sign change in ϵ^*_{f+} is also visible in Fig. 10(a) as a sign change of $V^2\mathrm{Re}\Sigma_{c+}^{-1}(0)$. In Sec. VIII, where we perform a careful analysis of the Luttinger sum rule for the PAM, we will show explicitly that this sign change of ϵ^*_{f+} leads to a jump of the FS volume corresponding to exactly one electron per site.

Figure 10(a) also reveals how the sign change of ϵ^*_{f+} is connected to the fs-pole in $\Sigma_{f+}(\omega^+)$. Close to the KB–QCP, in both the Kondo and RKKY phases, when ω is increased (starting from large negative), $V^2\mathrm{Re}\Sigma_{c+}^{-1}(\omega^+)$ increases through zero around $\omega \simeq -T_{\mathrm{NFL}}$. This sign change results in the left h-pole in Σ_{c+}, visible in Fig. 8(g). (Deeper in the RKKY phase, $V^2\mathrm{Re}\Sigma_{c+}^{-1}(\omega^+)$ does not ac-

tually change sign at $\omega \simeq -T_{\mathrm{NFL}}$ but nevertheless becomes almost zero, again causing the left h-pole of Σ_{c+}.) This feature is adiabatically connected to the $U \to 0$ case, where it is also present. It is an intermediate energy feature which characterizes the onset of NFL behavior. (We will show in Sec. VI D that the left h-pole in Σ_c forms around $T \simeq T_{\mathrm{NFL}}$, irrespective of $V > V_c$ or $V < V_c$.)

In the Kondo phase, the sign of $V^2\mathrm{Re}\Sigma_{c+}^{-1}(\omega^+)$ changes only once with increasing ω, remaining positive for $\omega > -T_{\mathrm{NFL}}$ and in particular at $\omega = 0$, so that ϵ^*_{f+} is negative. By contrast, in the RKKY phase the initial increase with ω in $V^2\mathrm{Re}\Sigma_{c+}^{-1}(\omega^+)$ for ω large negative *is counteracted by the fs-pole in* $\Sigma_{f+}(\omega^+)$, which induces a double-wiggle structure in $V^2\mathrm{Re}\Sigma_{c+}^{-1}(\omega^+)$ near $\omega \simeq -T_{\mathrm{FL}}$. As a result, $V^2\mathrm{Re}\Sigma_{c+}^{-1}(i0^+)$ is negative and ϵ^*_{f+} positive in the RKKY phase. The KB-QCP lies in between, at $\epsilon^*_{f+} = 0$.

To summarize: In the Kondo phase, the sign change of $V^2\mathrm{Re}\Sigma_c^{-1}(\omega^+)$ around $\omega \simeq -T_{\mathrm{NFL}}$ leads to the left h-pole and to $V^2\mathrm{Re}\Sigma_c^{-1}(0) > 0$, implying $\epsilon^*_{f+} < 0$. In the RKKY phase, the formation of the fs-pole in $\Sigma_{f+}(\omega^+)$ at energy scales between $-T_{\mathrm{NFL}}$ and $-T_{\mathrm{FL}}$ results in $V^2\mathrm{Re}\Sigma_{c+}^{-1}(0) < 0$ and therefore $\epsilon^*_{f+} > 0$.

D. Temperature dependence close to V_c

We next discuss the temperature dependence of cluster spectral functions and self-energies close to the QCP at $V_c = 0.4575$. We first discuss the case $V = 0.46 > V_c$ (Fig. 11), then $V = 0.455 < V_c$ (Fig. 12), which at $T = 0$ yield the Kondo and RKKY phases, respectively. For
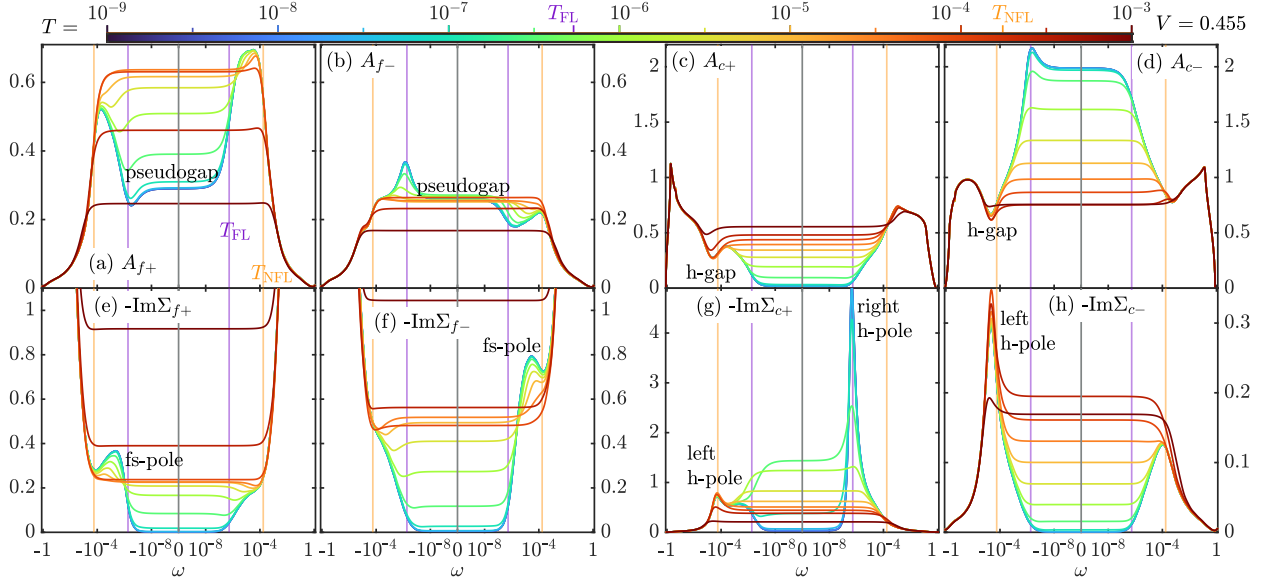
FIG. 12. Same as Fig. 11, but for $V = 0.455 < V_c$ (RKKY phase at $T = 0$).

each we proceed from high to low temperatures.

$V = 0.46$, $T \gtrsim T_{\mathrm{NFL}}$: When the temperature is lowered in the LM regime from $T = 10^{-3}$ towards T_{NFL}, the onset of c-f hybridization leads to the emergence of a hybridization gap in $A_c(\omega)$ (Fig. 11(c,d)) and a left h-pole in $-\mathrm{Im}\Sigma_c(\omega^+)$ (Fig. 11(g,h)), all at $\omega \simeq -10^{-4} \simeq -T_{\mathrm{NFL}}$. This triggers the onset of screening, signified by increased spectral weight in A_f around $\omega = 0$ (Fig. 11(a,b)) and a decrease of $-\mathrm{Im}\Sigma_f$ at $\omega = 0$ (Fig. 11(e,f)). However, at T_{NFL}, no coherent QP have formed yet: both $-\mathrm{Im}\Sigma_f$ and $-\mathrm{Im}\Sigma_c$ have significant spectral weight around $\omega \simeq 0$, implying strong scattering for electrons near the chemical potential.

$V = 0.46$, $T_{\mathrm{FL}} \lesssim T \lesssim T_{\mathrm{NFL}}$: When the temperature is lowered further towards T_{FL}, screening becomes stronger: both $-\mathrm{Im}\Sigma_f$ and $-\mathrm{Im}\Sigma_c$ at $\omega \simeq 0$ decrease, albeit slowly, as $\sim \ln(T)$. (In Figs. 11(e–h), T values equally spaced on logarithmic scale yield $-\mathrm{Im}\Sigma(\mathrm{i}0^+)$ values equally spaced on a linear scale.) At the same time, coherent QPs begin to form: a sharp Kondo peak gradually forms in A_f, and narrow structures A_c emerge.

$V = 0.46$, $T \lesssim T_{\mathrm{FL}}$: Below T_{FL}, coherent QP have formed ($\Sigma_f(\mathrm{i}0^+)$ and $\Sigma_c(\mathrm{i}0^+)$ approach zero), and the T-dependence of the spectral functions becomes weak.

We next consider the case $V < V_c$.

$V = 0.455$, $T \gtrsim T_{\mathrm{NFL}}$: In the LM regime, the behavior for $V < V_c$ is similar to that for $V > V_c$: as T is lowered from 10^{-3} towards T_{NFL}, a hybridization gap emerges in $A_c(\omega^+)$ (Fig. 12(c,d)) , and a left h-pole in $-\mathrm{Im}\Sigma_c$ (Fig. 12(g,h)), all at $\omega \simeq -10^{-4}$. Correspondingly, A_f increases for frequencies near $\omega = 0$, the temperature dependence at $T > T_{\mathrm{NFL}}$ is thus similar to $V > V_c$, as expected.

$V = 0.455$, $T_{\mathrm{FL}} \lesssim T \lesssim T_{\mathrm{NFL}}$: By contrast, below T_{NFL} the temperature dependence is quite different from $V >$

V_c. When T is lowered within the NFL regime from T_{NFL} towards T_{FL}, $\mathrm{Im}\Sigma_f$ develops fs-poles (Fig. 12(e,f)). At the same time, $-\mathrm{Im}\Sigma_{c+}$ develops a right h-pole at a small positive frequency, $\omega \gtrsim T_{\mathrm{FL}}$ (Fig. 12(g)), causing a strong increase of $-\mathrm{Im}\Sigma_{c+}(0)$. The formation of the right h-pole is associated with the formation of the fs-poles in Σ_f, as discussed in Sec. VI C. On the other hand, $-\mathrm{Im}\Sigma_{c-}$ behaves quite similar to its counterpart at $V = 0.46$ in the NFL region, decreasing logarithmically around $\omega = 0$. The appearance of fs-poles in the f-electron self-energies is accompanied by the formation of (somewhat asymmetric) pseudogaps in A_f around $\omega = 0$ (Fig. 12(a,b)). Moreover, the right h-pole in $-\mathrm{Im}\Sigma_{c+}$ in the NFL region causes a pseudogap in A_{c+} in the same temperature window (Fig. 12(c)). A_{c-}, on the other hand, develops a sharp peak around $\omega = 0$ in the NFL region, similarly to the behavior of A_{f+} for $V > V_c$ (Fig. 12(d)).

$V = 0.455$, $T \lesssim T_{\mathrm{FL}}$: When T is lowered below T_{FL}, the imaginary parts of all self-energies quickly tend to zero at $\omega = 0$, as expected in a FL. (Thus, the overall behavior of $-\mathrm{Im}\Sigma_{c+}(\mathrm{i}0^+)$ with decreasing temperature is non-monotonic, first increasing in the NFL regime, then decreasing down to zero in the FL regime.)

No marginal FL phenomenology: In the NFL regime neither the f nor the c electron self-energies show marginal FL phenomenology. The latter would require $-\mathrm{Im}\Sigma(\omega^+, T) \sim \max(|\omega|, T)$ [66]. Instead, the imaginary parts of the self-energies have a much weaker, namely logarithmic frequency and temperature dependence. Nonetheless, the spectral parts of various susceptibilities all show the same phenomenological frequency dependence [66] in the NFL region, namely a plateau for $T \lesssim |\omega| \lesssim T_{\mathrm{NFL}}$ and a $\sim \omega$ dependence for $\omega < T$ [66]. This frequency dependence has already been shown above in Fig. 4; we discuss the temperature dependence in a companion paper [148].

There, we also emphasize that the susceptibilities are not governed by the self-energy alone, as would be the case, in diagrammatic parlance, when evaluating only the bubble contribution—instead, vertex corrections play a crucial role. This especially also concerns the conductivity, which shows a $\sim 1/T$ dependence in the NFL region despite the $\sim \ln(T)$ dependence of $\mathrm{Im}\Sigma(\mathrm{i}0^+)$ [148].

VII. SINGLE PARTICLE PROPERTIES – LATTICE

Having focused on the single-particle properties of the effective 2IAM in the previous section, we now discuss how these translate to the lattice model. Our analysis builds on that of De Leo, Civelli and Kotliar [127, 128], but with our better energy resolution, we uncover much additional detail and new emergent physics at low energies. In particular, we obtain a detailed understanding of the Fermi surface reconstruction occurring when traversing the KB–QCP.

A. Reperiodization

Since the CDMFT artificially breaks translation invariance, the c and f electron self-energies have to be reperiodized before computing lattice spectral functions . To this end, we reperiodize the cluster cumulant [153, 154]

$$M(z) = \left[z + \mu - \Sigma_c(z) \right]^{-1} . \tag{26}$$

It may be viewed as a c-electron propagator excluding bare nearest-neighbor hopping, and in an expansion around the $t = 0$ limit [185] takes the role of the cluster self-energy. Its reperiodized version $M_{\mathbf{k}}(z)$ is defined as

$$M_{\mathbf{k}}(z) = M_{11}(z) + M_{12}(z) \sum_{a=x,y,z} \tfrac{1}{3} \cos(k_a) . \tag{27}$$

Here, M_{11} and M_{12} are the local and nearest-neighbor cluster cumulants, respectively, and the latter is accompanied by the cosine factors arising when diagonalizing a non-interacting hopping Hamiltonian. At the points $\Gamma = (0,0,0)$ and $\Pi = (\pi,\pi,\pi)$, the lattice cumulants reduce to the cluster ones, $M_+ = M_{11} + M_{12} = M_\Gamma$ and $M_- = M_{11} - M_{12} = M_\Pi$. This reflects the correspondence, mentioned in Sec. II, of the BZ points Γ, Π and the bonding, anti-bonding cluster orbitals. The $\mathbf{k}$-dependent self-energies are then defined via the relations

$$M_{\mathbf{k}}(z) = \left[z + \mu - \Sigma_{c\mathbf{k}}(z) \right]^{-1} \tag{28a}$$

$$\Sigma_{c\mathbf{k}}(z) = V^2 \left[z - \epsilon_f^0 + \mu - \Sigma_{f\mathbf{k}}(z) \right]^{-1} . \tag{28b}$$

We will see in Sec. VIII that the CDMFT solution to the PAM must fulfill a generalized version of the Luttinger

sum rule — this sum rule is verifiable via cluster quantities only, i.e. without reperiodization. The reperiodization scheme above is however not guaranteed to preserve this property. We therefore slightly modify the above scheme by adjusting μ in Eq. (26) and Eq. (28a) during the reperiodization only, such that the reperiodized self-energies fulfill this generalized Luttinger sum rule in the same way as the corresponding cluster quantities. We describe our reperiodization procedure and evaluate its validity in detail in App. A 3.

B. Lattice spectral functions

Figure 13 (top row) shows the evolution with V of the ($T = 0$) momentum-dependent spectral function $A_{\mathbf{k}}(\omega) = A_{f\mathbf{k}}(\omega) + A_{c\mathbf{k}}(\omega)$ and of the FS. (Corresponding retarded self-energies $\mathrm{Im}\Sigma_{f\mathbf{k}}(\omega^+)$ and $\mathrm{Im}\Sigma_{c\mathbf{k}}(\omega^+)$ are shown in Fig. 14 below.) To highlight all relevant energy scales and the changes of $A_{\mathbf{k}}(\omega)$ at low frequencies close to the QCP, we use a logarithmic frequency grid for $|\omega| > 10^{-9}$ and a linear grid for $|\omega| < 10^{-9}$ (grey shaded region) to cross $\omega = 0$.

Figure 13 (bottom row) shows three different surfaces, defined in Sec. V A: the free Fermi surface $V = 0$ (FS0, green), where $\epsilon_{c\mathbf{k}} = 0$; the actual Fermi surface (FS, red), where $\mathrm{Re}\, G_{x\mathbf{k}}^{-1}(\mathrm{i}0^+) = 0$ for both $x = f, c$ (numerically, we use $\mathrm{Re}\, G_{c\mathbf{k}}^{-1}(\mathrm{i}0^+) = 0$); and the Luttinger surface (LS, blue), where $|\Sigma_{f\mathbf{k}}(0)| = \infty$, $G_{f\mathbf{k}}(0) = 0$ and $\Sigma_{c\mathbf{k}}(0) = 0$ (numerically, we use $\mathrm{Re}\Sigma_{c\mathbf{k}}(\mathrm{i}0^+) = 0$). To summarize:

$$\text{FS0:} \qquad \epsilon_{c\mathbf{k}} = 0 , \tag{29a}$$

$$\text{FS: } \mathrm{Re}\, G_{x\mathbf{k}}^{-1}(\mathrm{i}0^+) = 0 \;\; \Leftrightarrow \begin{cases} \det G_{\mathbf{k}}^{-1}(\mathrm{i}0^+) \\ \epsilon_{c\mathbf{k}}^* \\ \epsilon_{f\mathbf{k}}^* - \frac{(V_{\mathbf{k}}^*)^2}{\epsilon_{c\mathbf{k}}} \end{cases} = 0 , \tag{29b}$$

$$\text{LS:} \qquad |\Sigma_{f\mathbf{k}}(0)| = \infty \Leftrightarrow \qquad \Sigma_{c\mathbf{k}}(\mathrm{i}0^+) = 0 . \tag{29c}$$

Next, we discuss some salient features of Fig. 13.

Band structures: In the Kondo phase, $A_{\mathbf{k}}(\omega)$ has a two-band structure [186] (marked ① and ② in Fig. 13) with a well-defined QP peak in band ①, as expected in this phase. The dispersion around $\omega = 0$ is clearly shifted away from the $V = 0$ dispersion (indicated by a dashed green line in Fig. 13). As V is lowered towards the QCP at V_c, the upper band develops a broad region of incoherent spectral weight in the NFL energy window $T_{\mathrm{FL}} < |\omega| < T_{\mathrm{NFL}}$.

Interestingly, in the RKKY phase, the spectral function shows a three-band structure (marked ①, ② and ③ in Fig. 13): The top and bottom bands (① and ②) do not cross $\omega = 0$. In addition, there is a third, narrow middle band (③) of width $\sim T_{\mathrm{FL}}$ crossing $\omega = 0$ near Π. The dispersion around $\omega = 0$ of band ③ almost matches the $V = 0$ dispersion. Band ③ is separated from the other two bands by a region of incoherent spectral weight in the NFL window $T_{\mathrm{FL}} < |\omega| < T_{\mathrm{NFL}}$. The additional bandgap
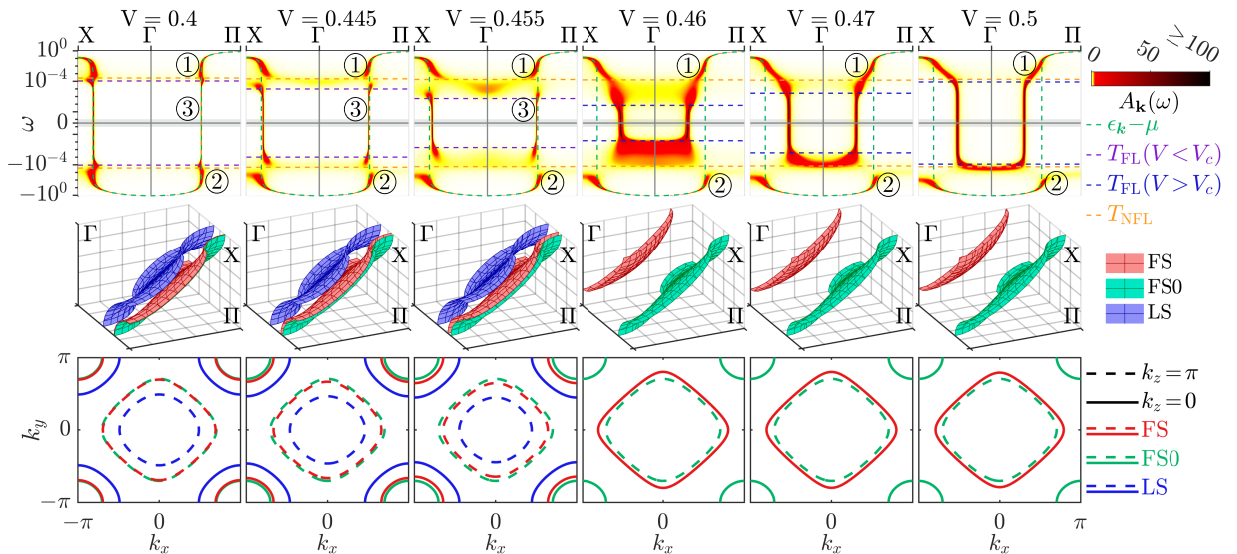
FIG. 13. Top row: Momentum resolved total spectral function $A_{\mathbf{k}}(\omega) = A_{c\mathbf{k}}(\omega) + A_{f\mathbf{k}}(\omega)$ at $T = 0$, for various V crossing the QCP at $V_c = 0.4575(25)$, plotted from $X = (\pi, \pi, 0)$ over $\Gamma = (0, 0, 0)$ to $\Pi = (\pi, \pi, \pi)$. $A_{\mathbf{k}}(\omega)$ is shown on a logarithmic frequency scale for $|\omega| > 10^{-9}$ and on a linear scale for $|\omega| < 10^{-9}$ (grey shaded region). The green dashed line marks the c-electron dispersion at $V = 0$. On the Kondo side ($V > V_c$), $A_{\mathbf{k}}(\omega)$ shows a two-band structure, marked ① and ②, as expected from adiabatic continuation from the $U = 0$, with the upper band intersecting $\omega = 0$ close to Γ. On the RKKY side ($V < V_c$), $A_{\mathbf{k}}(\omega)$ shows a three-band structure, marked ①, ② and ③, with the narrow middle band intersecting $\omega = 0$ close to Π. Middle row: Corresponding FS (red) where $\epsilon^*_{c\mathbf{k}} = 0$, FS at $V = 0$ (green, FS0) where $\epsilon_{c\mathbf{k}} = 0$, and LS where $\Sigma_{f\mathbf{k}}(0) = \infty$ (blue), in an octant of the first Brillouin zone. For $V > V_c$, the FS is centered around Γ. Crossing the QCP towards $V < V_c$, the FS center point jumps to Π and a LS emerges. Bottom row: Brillouin zone cuts showing the FS (red lines), FS0 (green lines) and LS (blue lines) at constant $k_z = 0$ (solid) or $k_z = \pi$ (dashed) versus k_x and k_y.

in the RKKY phase comes from a dispersive fs-pole in Σ_f (see Figs. 8 and 14 and their discussions), associated with orbital selective Mott physics. Ref. 147 suggests that the fs-pole may be interpreted as an emergent coherent spinon excitation [147]. This suggests that the f-electron is fractionalized and the RKKY phase is a fractionalized FL [105, 106]. We will clarify this view in future work. As discussed in Sec. V B, for non-single-site DMFT (as here, where we use 2-site CDMFT), it is natural for a Mott insulator (the f band in the present case) to hybridize with a metal (the c band) and contribute non-zero weight to the low-energy QP, resulting in an OSMP. Because the f band, which is in a (strongly correlated) Mott phase, contributes non-zero QP weight, the QP dispersion is strongly renormalized, leading to the narrow middle band. Its narrow width ($\sim T_{\mathrm{FL}}$) for $V < V_c$ indicates a large effective mass m^*, as observed experimentally e.g. in Refs. 32 and 187 and discussed in detail in Sec. IX below. Note that this strong-correlation effect occurs even though the actual FS lies very close to the free c-electron Fermi surface FS0, for reasons discussed below.

Fermi surface reconstruction: In the Kondo phase, the FS (red) is electron-like and centered around the $\Gamma = (0, 0, 0)$-point, in contrast to the hole-like free FS0 (green) of the c electrons, centered at $\Pi = (\pi, \pi, \pi)$. The FS depends only very weakly on V because it is constrained by the Luttinger sum rule: the latter relates the density $n_f + n_c$ to the FS volume (see Sec. VIII for details), which

depends only very weakly on V (see Fig. 17). As the QCP is crossed, the FS undergoes a sudden reconstruction and becomes centered around Π, positioned close to FS0. This leads to a jump of the Hall coefficient, as discussed with Fig. 18. The FS reconstruction is accompanied by the emergence of a LS (blue), which accounts for the change in the FS volume (see Sec. VIII). The emergence of a LS is the hallmark property of a Mott phase and it has been shown that the LS is stable to small perturbations [178]. This emphasizes again our claim that the RKKY phase is an OSMP. In the RKKY phase, the FS again depends only very weakly on V due to the Luttinger sum rule constraint (the weak V-dependence is again due to a weak V-dependence of the filling).

C. Lattice self-energies

To get a better understanding how the features of the spectral functions in Fig. 13 emerge, Fig. 14 shows the imaginary parts of the momentum-dependent c- and f-electron self-energies. In the Kondo phase at $V > V_c$, $-\mathrm{Im}\Sigma_{f\mathbf{k}}(\omega^+)$ shows only weak momentum dependence. It is large at high frequencies but vanishes towards $\omega = 0$, consistent with the presence of coherent QP. Interestingly, its structure is almost independent of V in the Kondo regime. However, as we have seen in Sec. VI, the
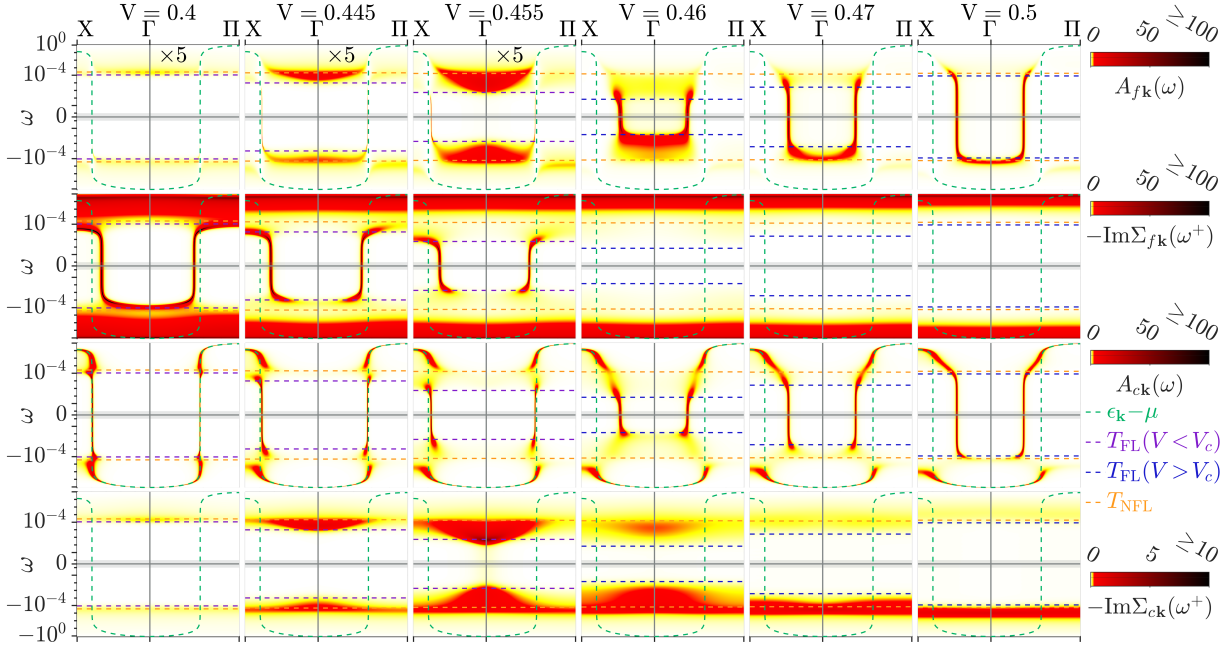
FIG. 14. Momentum resolved f and c spectral functions and imaginary parts of retarded self-energies, $A_{f\mathbf{k}}(\omega)$ (top row), $-\mathrm{Im}\Sigma_{f\mathbf{k}}(\omega^+)$ (second row), $A_{c\mathbf{k}}(\omega)$ (third row), and $-\mathrm{Im}\Sigma_{c\mathbf{k}}(\omega^+)$ (bottom row) at $T = 0$, corresponding to the spectral functions shown in Fig. 13. The three left-most panels ($V < V_c$) of the top row show $5 \times A_{f\mathbf{k}}(\omega)$ to improve the visibility of f-electron spectral features in the OSMP. Note that in the RKKY phase, the spectral weight of $A_{f\mathbf{k}}(\omega)$ close to $\omega = 0$ is underestimated by our reperiodization scheme, as discussed in App. A 3. We have scaled it by a factor of 5 to improve visibility. As discussed in Sec. VI, there is a non-zero f-electron contribution to the FS throughout the RKKY phase.

f-electron self-energy becomes slightly non-local in the Kondo regime close to the QCP (though this is not easily visible in Fig. 14).

Crossing the QCP to the RKKY phase at $V < V_c$, the non-dispersive high frequency structure remains essentially the same as in the Kondo phase. However, additionally a sharp dispersing pole emerges in $\Sigma_{f\mathbf{k}}$ at low frequencies for $|\omega| < T_{\mathrm{FL}}$. As discussed in Sec. V B and VI, this dispersive pole in $\Sigma_{f\mathbf{k}}$ in the RKKY phase is a clear sign of Mott physics present in the f band. Importantly, the fact that the pole is dispersive (c.f. Eq. (22)) results from employing cluster DMFT instead of single-site DMFT. We are therefore not in the $d \to \infty$ limit where the OSMP (i.e. the RKKY phase) would be unstable to finite c-f hybridization V [181].

The c self-energy, shown in the bottom row of Fig. 14, has most of its spectral weight at $\omega \simeq -T_{\mathrm{NFL}}$ deep in the Kondo phase. It is mostly momentum independent and signals the position of the hybridization gap. As V is decreased towards V_c, $-\mathrm{Im}\Sigma_{c\mathbf{k}}(\omega^+)$ becomes increasingly momentum dependent, with more spectral weight at Γ than at Π. Further, at $V = 0.46$ close to the QCP on the Kondo side, spectral weight starts to smear out significantly over the NFL region and significant weight appears at positive frequencies. This suggests that f and c begin to hybridize more strongly at positive frequencies. When the QCP is crossed to $V < V_c$, the spectral weight of $\Sigma_{c\mathbf{k}}$ is now stronger at $\omega > 0$ than at $\omega < 0$, showing that c

and f now hybridize more strongly at positive frequencies than in the Kondo regime. However, significant spectral weight does also remain at $\omega < 0$, reflecting the presence of a left and right h-pole, as discussed already in the previous section. This suggests that in the RKKY regime, the f band is split apart by the pole in $\Sigma_{f\mathbf{k}}$ and the c electrons then hybridize with both of the resulting two f bands, leading to a three-band structure. Thus, the f electrons still hybridize significantly with the c electrons in the RKKY phase close to the QCP, explaining intuitively the strong renormalization of m^* in the RKKY regime mentioned earlier and observed in experiments [188]. Finally, as V is lowered further towards $V = 0$, the overall magnitude of $-\mathrm{Im}\Sigma_{c\mathbf{k}}(\omega^+)$ decreases rapidly, suggesting that f and c bands continuously decouple when $V \to 0$.

D. Finite temperature

In Figure 15 we show the temperature dependence of $A_{\mathbf{k}}(\omega)$ both at $V = 0.46 > V_c$ and $V = 0.455 < V_c$. For $T < T_{\mathrm{FL}}$, the spectral functions are mostly independent of temperature as expected. As T crosses T_{FL} into the NFL region, the incoherent features at $T_{\mathrm{FL}} < |\omega| < T_{\mathrm{NFL}}$ are thermally broadened and the sharp QP features at $\omega = 0$ are smeared out, indicating a thermal destruction of the QP. Deep in the NFL region at $T \simeq 10^{-5}$, spectral
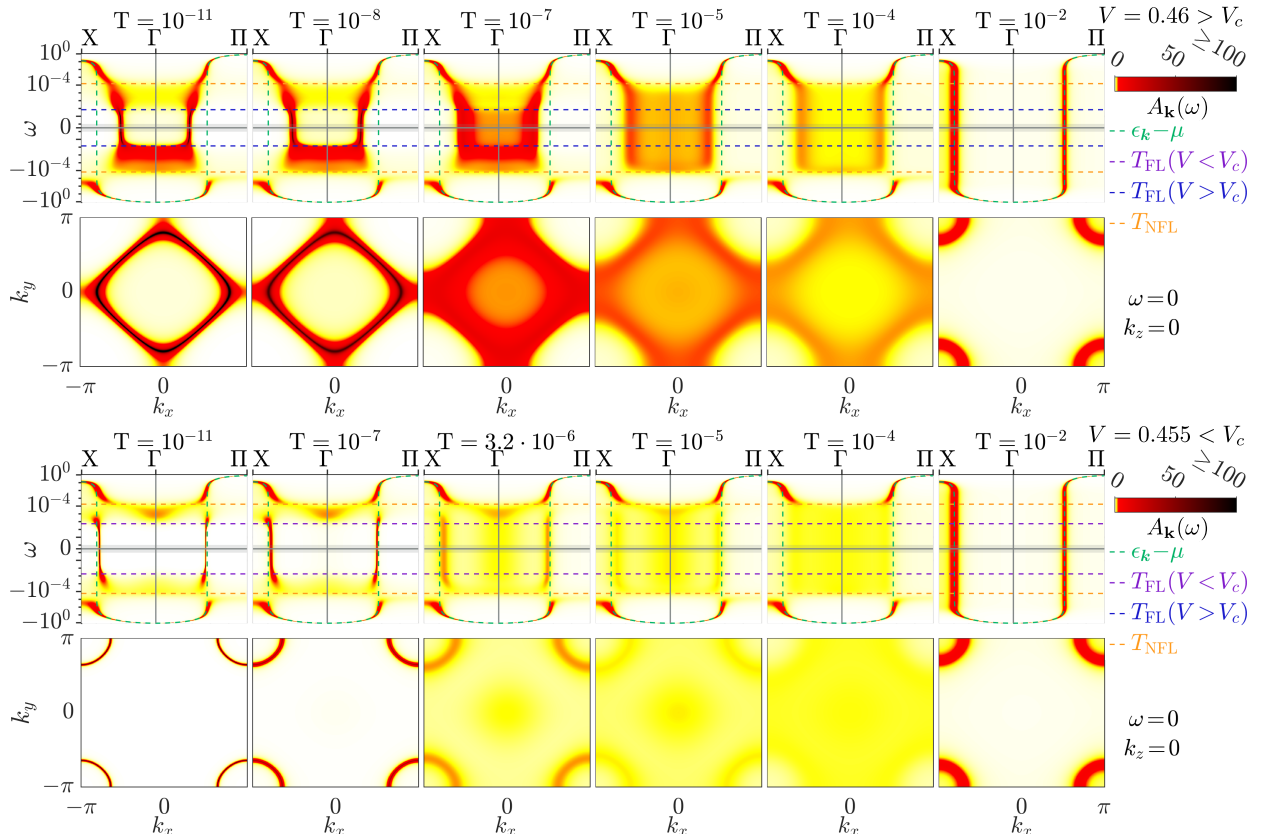
FIG. 15. Temperature dependence of $A_{\mathbf{k}}(\omega)$ at $V = 0.46 > V_c = 0.4575$ (rows 1 and 2) and $V = 0.455 < V_c$ (rows 3 and 4). The layout of rows 1 and 3 mirrors that of the top row of Fig. 13. Rows 2 and 4 show cuts at $\omega = 0$ and $k_z = 0$. These illustrate how the sharp FS at $T = 0$, large for $V > V_c$ and small for $V < V_c$, dissolves as T increases into the NFL regime and finally evolves to a (temperature-broadened) small FS in the LM regime at high T.

weight around $\omega = 0$ is completely incoherent and no FS with sharp QP excitations can be made out. At $T = 10^{-2} > T_{\mathrm{NFL}}$ in the LM region, the features of $A_{\mathbf{k}}(\omega)$ become sharp again around $\omega = 0$ and a single band forms which coincides with the $V = 0$ c-electron dispersion. In this temperature regime, the f electrons can be viewed as free local moments decoupled from the free c electrons. The interaction between c electrons and f moments then leads to scattering, slightly smearing out the features in the spectral function while leaving the qualitative picture of the LM region unaltered.

VIII. GENERALIZED LUTTINGER SUM RULE

In this section, we discuss the FS reconstruction of the previous section from the perspective of the generalized Luttinger sum rule [8–13, 173, 189, 190]. It states that if a Fermi surface exists, the density, n, of electrons in partially-filled bands can be expressed as $n = 2v_{\mathrm{FS}} + 2I_{\mathrm{L}}$, where v_{FS} is the FS volume and I_{L} is an integral known as Luttinger integral. In case of a FL, the generalized

Luttinger sum rule as stated above can be derived from a simple, exact decomposition of the Green's function based on Dyson's equation (we review this decomposition below). The sum rule becomes useful when it is possible to formulate constraints on I_{L}.

For instance, if the interacting and non-interacting ground states are adiabatically connected [8, 191], perturbative arguments can be used to show that $I_{\mathrm{L}} = 0$, leading to the celebrated Luttinger sum rule, $n = 2v_{\mathrm{FS}}$ (also called Luttinger's theorem). Subsequent work [189, 190] has shown that $I_{\mathrm{L}} = 0$ is a consequence of U(1) charge conservation in case Σ is Φ-derivable, i.e. if $\Sigma = \delta\Phi/\delta G$, where Φ is the Luttinger–Ward (LW) functional.

Explicitly, consider a multi-band model with a U(1) total charge symmetry (we assume every band has the same gauge charge). The Green's function $G_{\mathbf{k}}(z)$ is matrix valued, with entries $G_{\alpha\beta\mathbf{k}}(z)$ where α and β label the bands. If the matrix-valued self-energy is Φ-derivable, i.e. $\Sigma_{\mathbf{k}}(z) = \delta\Phi/\delta G_{\mathbf{k}}(z)$, then the Luttinger integral,

$$I_{\mathrm{L}} = \frac{-1}{\pi}\mathrm{Im}\int_{\mathrm{BZ}}\frac{d\mathbf{k}}{\mathcal{V}_{\mathrm{BZ}}}\int_{-\infty}^{0}d\omega\,\mathrm{Tr}\left[G_{\mathbf{k}}(\omega^+)\,\partial_\omega\Sigma_{\mathbf{k}}(\omega^+)\right] \quad (30)$$

equals zero, $I_{\mathrm{L}} = 0$. Note that $I_{\mathrm{L}} = 0$ *only* holds in the

$T \to 0$ limit.

This extends the applicability of Luttinger's theorem beyond the perturbative regime (see also Ref. [9] for a different approach), but requires the existence of the LW functional $\Phi[G]$, at least in the vicinity of the physical Green's function G (note that Φ can be constructed non-perturbatively [192]). However, it has been established that in general, the LW functional is multivalued [193–195] and does not exist for certain physically relevant Green's functions [13, 196], which can lead to $I_L \neq 0$ [13, 173, 196].

A very instructive analysis of a situation where $I_L = 0$ breaks down is provided in Refs. 11 and 12 in terms of a fermionic two-impurity model, where the role of the Luttinger sum rule is taken by the Friedel sum rule [186]. This model exhibits a QPT from a Kondo-type to an RKKY-type phase, with the local density remaining constant while the free QP density changes abruptly. This violates the Friedel sum rule, and the violation was traced to a Luttinger integral abruptly becoming nonzero.

In this section, we perform a similar analysis for the KB–QPT of the PAM. We find that the Luttinger integral is numerically zero in both the RKKY and Kondo phases; the FS reconstruction is due to the appearance of a LS in the RKKY phase and not due to a failure of Luttinger's theorem as formulated in Ref. 189. As a warm-up, we first consider a single partially-filled band of conduction electrons and briefly recall the origin of the generalized Luttinger sum rule. Then we focus on the PAM and derive a generalized Luttinger sum rule for $n_c + n_f$ (there are no useful separate sum rules for only n_c or only n_f, as these are not conserved quantities). It involves not only the FS, comprising all $\mathbf{k}$ points in the Brillouin zone at which $G_{f\mathbf{k}}(i0^+)$ and $G_{c\mathbf{k}}(i0^+)$ have poles, but also the Luttinger surface (LS), at which $\Sigma_{f\mathbf{k}}(i0^+)$ diverges [10]. We then express our results purely through cluster quantities that are directly available from cellular DMFT calculations without requiring reperiodization or interpolation. Thereafter, we show that the discontinuous jump of the FS volume when crossing the QCP into the RKKY phase is accompanied by the emergence of a LS while I_L remains zero throughout. Finally, we discuss this finding together with the Hall coefficient calculated from our data and relate it to experimental findings on YbRh$_2$Si$_2$ and CeCoIn$_5$.

A. Luttinger's theorem for a single band

We begin by recalling standard arguments leading to Luttinger's theorem, following Refs. [8, 12, 171, 189]. We consider a one-band model at $T = 0$, with propagator $G_{\mathbf{k}}(z) = [z - \epsilon_{\mathbf{k}} - \Sigma_{\mathbf{k}}(z)]^{-1}$. The average electron density can be expressed as

$$n = \frac{-2}{\pi} \text{Im} \int_{\text{BZ}} \frac{d\mathbf{k}}{\mathcal{V}_{\text{BZ}}} \int d\omega \, G_{\mathbf{k}}(\omega^+) \, \theta(-\omega) \,, \qquad (31)$$

where the prefactor 2 accounts for spin, $\mathcal{V}_{\text{BZ}}$ is the volume of the Brillouin zone, and the step function $\theta(-\omega)$ is the zero-temperature limit of the Fermi function.

For the next step, we need the identity

$$G_{\mathbf{k}} = \partial_z \ln G_{\mathbf{k}}^{-1} + G_{\mathbf{k}} \, \partial_z \Sigma_{\mathbf{k}} \,, \qquad (32)$$

expressing the correlator through derivates. Using the latter in Eq. (31), together with $\text{Im} \ln G_{\mathbf{k}}^{-1} = \arg G_{\mathbf{k}}^{-1}$, we obtain

$$n = 2v_{\text{FS}} + 2I_L \,, \qquad (33)$$

$$v_{\text{FS}} = \int_{\text{BZ}} \frac{d\mathbf{k}}{\mathcal{V}_{\text{BZ}}} \frac{\delta_{\mathbf{k}}}{\pi} \,, \qquad (34)$$

$$\delta_{\mathbf{k}} = -\text{Im} \int_{-\infty}^{0} d\omega \, \partial_\omega \ln G_{\mathbf{k}}^{-1}(\omega^+) = -\Big[\arg G_{\mathbf{k}}^{-1}(\omega^+)\Big]_{-\infty}^{0} \,,$$

$$I_L = \frac{-1}{\pi} \text{Im} \int_{\text{BZ}} \frac{d\mathbf{k}}{\mathcal{V}_{\text{BZ}}} \int_{-\infty}^{0} d\omega \, G_{\mathbf{k}}(\omega^+) \, \partial_\omega \Sigma_{\mathbf{k}}(\omega^+) \,. \qquad (35)$$

Here, $\delta_{\mathbf{k}}$ is the phase shift of $G_{\mathbf{k}}^{-1}(\omega^+)$ $\omega = -\infty$ and 0; v_{FS} is a shorthand for its integral over the BZ; and I_L is the Luttinger integral (cf. Eq. (30)). Equation (33) is the generalized Luttinger sum rule. It is an exact expression of the electron density n; no assumptions on FL behavior have been made yet. We will show below that in a FL, the average phase shift Eq. (34) is given by the FS volume.

As mentioned above, it can be argued on rather general grounds that $I_L = 0$ in many cases [189]. Conditions are that (i) the interaction preserves the U(1) charge symmetry and (ii) Σ is Φ-derivable, i.e. $\Sigma = \delta\Phi/\delta G$, where Φ is the LW functional. Condition (ii) breaks down if Σ is sufficiently singular, i.e. if no functional Φ exists whose variation w.r.t. G produces Σ [13, 196]; in that case, I_L can become non-zero.

Now, *if* a sharp FS exists, i.e. if the imaginary part of the retarded self-energy vanishes at $\omega = 0$ (cf. Eq. (16)),

$$\text{Im} \Sigma_{\mathbf{k}}(i0^+) = -0^+, \qquad (36)$$

then the integral v_{FS} defined in (34) gives the FS volume. Let us recapitulate why this is the case. Condition (36) holds for regular Fermi liquids, and more generally in the perturbative regime considered by Luttinger and Ward [8, 191]. Now, Eq. (36) implies $\arg G_{\mathbf{k}}^{-1}(i0^+) = \pi\theta\big(-\text{Re}\, G_{\mathbf{k}}^{-1}(i0^+)\big)$, while $\text{Im}\,\Sigma_{\mathbf{k}}(\omega^+) < 0$ implies $\arg G_{\mathbf{k}}^{-1}(-\infty + i0^+) = \pi$. Therefore, the phase shift is

$$\delta_{\mathbf{k}} = \pi - \pi\theta\big(-\text{Re}\, G_{\mathbf{k}}^{-1}(i0^+)\big)$$
$$= \pi\theta\big(-\epsilon_{\mathbf{k}} - \text{Re}\Sigma_{\mathbf{k}}(i0^+)\big) = \pi\theta(-\epsilon_{\mathbf{k}}^*) \,. \qquad (37)$$

By definition, the Fermi surface encloses all $\mathbf{k}$ points in the Brillouin zone having $\epsilon_{\mathbf{k}}^* < 0$. For these, $\delta_{\mathbf{k}}/\pi$ equals 1, for all others it vanishes. Hence, Eq. (34) reduces to

$$v_{\text{FS}} = \int_{\text{BZ}} \frac{d\mathbf{k}}{\mathcal{V}_{\text{BZ}}} \theta(-\epsilon_{\mathbf{k}}^*) \,, \qquad (38)$$

which is the FS volume measured in units of $\mathcal{V}_{\text{BZ}}$ (hence dimensionless). Moreover, in a normal FL, Σ is not singular, hence $I_{\text{L}} = 0$ holds, hence the generalized Luttinger sum rule (33) reduces to the Luttinger sum rule for a FL, $n = 2v_{\text{FS}}$, relating the density to the FS volume.

B. Generalized Luttinger theorem for the PAM

The PAM describes hybridized f and c electrons, the former with local interactions, the latter without. Their correlators, G_f and G_c, are coupled through Eqs. (3). Importantly, because Φ does not depend on propagators involving non-interacting orbitals [171], the LW functional for the PAM depends only on G_f, not on G_c or G_{fc}. Therefore, $\Sigma_f = \delta\Phi/\delta G_f$ is the only Φ-derivable, proper (i.e. 1-particle irreducible) self-energy in the PAM. Σ_c knows about interactions only via its dependence on Σ_f and hence is not a proper self-energy; in particular $\delta\Phi/\delta G_c = \delta\Phi/\delta G_{fc} = 0$. Analogous to the previous subsection, we first derive general formulas for the phase shifts. We then make assumptions on the self-energies compatible with our observations in Sec. VI and VII. These allow us to write down expressions in terms of the FS and LS volumes.

Our starting point again is an identity expressing correlators through derivatives. Equation (2) implies

$$
\begin{aligned}
\text{Tr}\, G_{\mathbf{k}} &= G_{f\mathbf{k}} + G_{c\mathbf{k}} = \text{Tr}\, G_{\mathbf{k}}\partial_z G_{\mathbf{k}}^{-1} + G_{f\mathbf{k}}\,\partial_z\Sigma_{f\mathbf{k}} \\
&= \partial_z \text{Tr}\, \ln G_{\mathbf{k}}^{-1} + G_{f\mathbf{k}}\,\partial_z\Sigma_{f\mathbf{k}} \\
&= \partial_z \ln G_{c\mathbf{k}}^{-1} + \partial_z \ln \Sigma_{c\mathbf{k}}^{-1} + G_{f\mathbf{k}}\,\partial_z\Sigma_{f\mathbf{k}}. \quad (39)
\end{aligned}
$$

To derive the last equality, note that the definitions (2) and (3) for the lattice correlators imply the relation

$$
\begin{aligned}
\det G_{\mathbf{k}}^{-1} &= (z - \epsilon_{c\mathbf{k}})(z - \epsilon_f - \Sigma_{f\mathbf{k}}) - V^2 \\
&= \Big(z - \epsilon_{c\mathbf{k}} - \frac{V^2}{z - \epsilon_f - \Sigma_{f\mathbf{k}}}\Big)(z - \epsilon_f - \Sigma_{f\mathbf{k}}) \\
&= G_{c\mathbf{k}}^{-1}\Sigma_{c\mathbf{k}}^{-1}/V^2 \quad (40)
\end{aligned}
$$

which, together with $\text{Tr}\,\ln G_{\mathbf{k}}^{-1} = \ln \det G_{\mathbf{k}}^{-1}$, yields Eq. (39). Integrating $G_f + G_c$ as in Eq. (31),

$$
n_f + n_c = \frac{-2}{\pi}\text{Im}\int_{\text{BZ}}\frac{d\mathbf{k}}{\mathcal{V}_{\text{BZ}}}\int_{-\infty}^0 d\omega\,\big[G_{f\mathbf{k}}(\omega^+) + G_{c\mathbf{k}}(\omega^+)\big],
$$

and using (39), we obtain

$$
n_f + n_c = 2v_{\text{FS}} + 2v_{\text{LS}} + 2I_{\text{L}}, \quad (41)
$$

with ingredients defined in analogy to Eqs. (34) to (35):

$$
v_{\text{FS}} = \int_{\text{BZ}}\frac{d\mathbf{k}}{\mathcal{V}_{\text{BZ}}}\frac{\delta_{c\mathbf{k}}}{\pi}, \quad v_{\text{LS}} = \int_{\text{BZ}}\frac{d\mathbf{k}}{\mathcal{V}_{\text{BZ}}}\frac{\delta_{\Sigma\mathbf{k}}}{\pi}, \quad (42)
$$

$$
\delta_{c\mathbf{k}} = -\text{Im}\int_{-\infty}^0 d\omega\,\partial_\omega \ln G_{c\mathbf{k}}^{-1}(\omega^+) = -\Big[\arg G_{c\mathbf{k}}^{-1}(\omega^+)\Big]_{-\infty}^0,
$$

$$
\delta_{\Sigma\mathbf{k}} = -\text{Im}\int_{-\infty}^0 d\omega\,\partial_\omega \ln \Sigma_{c\mathbf{k}}^{-1}(\omega^+) = +\Big[\arg \Sigma_{c\mathbf{k}}^{+1}(\omega^+)\Big]_{-\infty}^0,
$$

$$
I_{\text{L}} = \frac{-1}{\pi}\text{Im}\int_{\text{BZ}}\frac{d\mathbf{k}}{\mathcal{V}_{\text{BZ}}}\int_{-\infty}^0 d\omega\, G_{f\mathbf{k}}(\omega^+)\,\partial_\omega\Sigma_{f\mathbf{k}}(\omega^+). \quad (43)
$$

Here, $\delta_{c\mathbf{k}}$ and $\delta_{\Sigma\mathbf{k}}$ describe the phase shifts of $G_{c\mathbf{k}}^{-1}$ and $\Sigma_{c\mathbf{k}}^{+1}$ between $\omega = -\infty$ and 0; v_{FS} and v_{LS} are shorthands for their integrals over the BZ; and I_{L} is the Luttinger integral, now involving only f (no c) functions. Eqs. (41) to (43) are exact and, in the spirit of Refs. 11 and 12, we will refer to (41) as generalized Luttinger sum rule for the PAM, or Luttinger-PAM sum rule, for short. To the best of our knowledge, the existence of such a relation, involving the phase shifts not only of $G_{c\mathbf{k}}^{-1}$ but also of $\Sigma_{c\mathbf{k}}^{+1}$, has so far not been appreciated in the literature. The form (41) is specific to the PAM. For other multiband models, the arguments presented here will have to be suitably adapted.

Now, *if* a sharp FS exists, i.e. if

$$
\text{Im}\,\Sigma_{c\mathbf{k}}(i0^+) = -0^+, \quad (44)
$$

then the integrals v_{FS} and v_{LS} defined in Eqs. (42) give the FS and LS volumes, respectively. The argument proceeds as in the previous subsection. Equation (44) implies $\arg G_{c\mathbf{k}}^{-1}(i0^+) = \pi\theta\big(-\text{Re}\,G_{c\mathbf{k}}^{-1}(i0^+)\big)$ and $\arg \Sigma_{c\mathbf{k}}(i0^+) = -\pi\theta\big(-\text{Re}\,\Sigma_{c\mathbf{k}}(i0^+)\big)$, while $\text{Im}\,\Sigma_{c\mathbf{k}}(\omega^+) < 0$ implies $\arg G_{c\mathbf{k}}^{-1}(-\infty + i0^+) = \pi$ and $\arg \Sigma_{c\mathbf{k}}(-\infty + i0^+) = -\pi$. Therefore, the phase shifts in Eq. (43) yield:

$$
\begin{aligned}
\delta_{c\mathbf{k}} &= \pi - \pi\theta\big(-\text{Re}\,G_{c\mathbf{k}}^{-1}(i0^+)\big) \\
&= \pi\theta\big(-\epsilon_{c\mathbf{k}} - \text{Re}\Sigma_{c\mathbf{k}}(i0^+)\big) = \pi\theta(-\epsilon_{c\mathbf{k}}^*), \quad (45a)
\end{aligned}
$$

$$
\delta_{\Sigma\mathbf{k}} = \pi - \pi\theta\big(-\text{Re}\,\Sigma_{c\mathbf{k}}(i0^+)\big) = \pi\theta\big(\text{Re}\Sigma_{c\mathbf{k}}(i0^+)\big). \quad (45b)
$$

The phase shifts $\delta_{c\mathbf{k}}$ and $\delta_{\Sigma\mathbf{k}}$ are either 0 or π. The jump between these values occurs at the FS, defined by $\text{Re}\,G_{c\mathbf{k}}^{-1}(i0^+) = 0$ and the LS, defined by $\text{Re}\Sigma_{c\mathbf{k}}(i0^+) = 0$, respectively (see Eqs. (29b) and Fig. 16). Thus, Eqs. (42) reduce to

$$
v_{\text{FS}} = \int_{\text{BZ}}\frac{d\mathbf{k}}{\mathcal{V}_{\text{BZ}}}\theta(-\epsilon_{c\mathbf{k}}^*), \quad v_{\text{LS}} = \int_{\text{BZ}}\frac{d\mathbf{k}}{\mathcal{V}_{\text{BZ}}}\theta(\text{Re}\Sigma_{c\mathbf{k}}(i0^+)), \quad (46)
$$

giving the FS and LS volumes in units of $\mathcal{V}_{\text{BZ}}$. Thus, if a sharp FS exists, the Luttinger-PAM sum rule (41) relates the density of c and f electrons to the FS and LS volumes v_{FS} and v_{LS} and the Luttinger integral I_{L}.

The above arguments are directly applicable to our CDMFT+NRG results for the PAM, since the condition (44) is consistent with our results for $0 < V \neq V_c$: indeed, we find that the imaginary part of Σ_c vanishes at $\omega = 0$, both in the effective impurity model (see Sec. VI) and after reperiodization (see Sec. VII).

Since Φ depends only on G_f, so that $\delta\Phi/\delta G_c = 0$ and $\delta\Phi/\delta G_{fc} = 0$, I_{L} as defined in Eq. (43) has the same form as Eq. (30). We therefore expect $I_{\text{L}} = 0$ if the functional Φ exists in the vicinity of G_f, but we will not
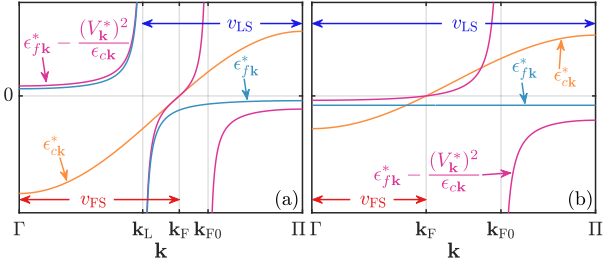
FIG. 16. Sketch of the qualitative behavior of $\epsilon^*_{f\mathbf{k}}$, $\epsilon^*_{c\mathbf{k}}$ and $\epsilon^*_{f\mathbf{k}} - (V^*_{\mathbf{k}})^2/\epsilon_{c\mathbf{k}}$ in (a) the RKKY phase and (b) the Kondo phase. They are related to the Green's functions and the c-electron self-energy via $\operatorname{Re} G^{-1}_{c\mathbf{k}}(0) = -\epsilon^*_{c\mathbf{k}}/Z_{c\mathbf{k}}$, $\operatorname{Re} G^{-1}_{f\mathbf{k}}(0) = -\left[\epsilon^*_{f\mathbf{k}} - (V^*_{\mathbf{k}})^2/\epsilon_{c\mathbf{k}}\right]/Z_{f\mathbf{k}}$ and $\operatorname{Re}\Sigma_{c\mathbf{k}}(0) = -(V^*_{\mathbf{k}})^2/\epsilon^*_{f\mathbf{k}}$. The FS (marked by $\mathbf{k}_{\mathrm{F}}$) is defined by $\epsilon^*_{c\mathbf{k}} = \epsilon^*_{f\mathbf{k}} - (V^*_{\mathbf{k}})^2/\epsilon_{c\mathbf{k}} = 0$; its inside is defined by $\epsilon^*_{c\mathbf{k}} < 0$. $|\epsilon^*_{f\mathbf{k}}| = \infty$ ($\operatorname{Re}\Sigma_{c\mathbf{k}}(0) = 0$) defines the LS (marked by $\mathbf{k}_{\mathrm{L}}$), with its inside defined by $\epsilon^*_{f\mathbf{k}} < 0$. The function $\epsilon^*_{f\mathbf{k}} - (V^*_{\mathbf{k}})^2/\epsilon_{c\mathbf{k}}$ changes sign via a pole both at the LS (due to $\epsilon^*_{f\mathbf{k}}$) and at the free FS (marked by $\mathbf{k}_{\mathrm{F0}}$) due to $\epsilon_{c\mathbf{k}} = 0$. In the Kondo phase, $\epsilon^*_{f\mathbf{k}}$ remains negative everywhere in the BZ while in the RKKY phase, $\epsilon^*_{f\mathbf{k}}$ changes sign between Γ and Π [c.f. also Fig. 9] via a pole at the LS. As a result, $\epsilon^*_{f\mathbf{k}} - (V^*_{\mathbf{k}})^2/\epsilon_{c\mathbf{k}}$ changes sign twice in the Kondo phase (via a zero at $\mathbf{k}_{\mathrm{F}}$ and a pole at $\mathbf{k}_{\mathrm{F0}}$) and three times in the RKKY phase (via a pole at $\mathbf{k}_{\mathrm{L}}$, a zero at $\mathbf{k}_{\mathrm{F}}$ and a pole at $\mathbf{k}_{\mathrm{F0}}$). The pole at $\mathbf{k}_{\mathrm{L}}$ shifts the position of $\mathbf{k}_{\mathrm{F}}$ in the RKKY phase compared to its position in the Kondo phase. Note that the distance between $\mathbf{k}_{\mathrm{F}}$ and $\mathbf{k}_{\mathrm{F0}}$ in (a) is exaggerated in the sketch above.

concern ourselves here with general considerations about the existence of the LW functional. We have, however, checked numerically that $I_{\mathrm{L}} = 0$ holds in our study of the PAM, for all considered values of V at $T = 0$, i.e. both in the Kondo and RKKY regimes. Thus we henceforth assume that $I_{\mathrm{L}} = 0$ throughout.

While n_c and n_f evolve smoothly with V, sudden jumps can occur for v_{FS} and v_{LS}, which must compensate each other appropriately if I_{L} remains zero. In particular, by Eq. (41) a jump in v_{LS} induces a jump in v_{FS}, implying a FS reconstruction, even though $I_{\mathrm{L}} = 0$ remains unchanged.

C. Luttinger's theorem in CDMFT: computing v_{FS}, v_{LS} and I_{L} without reperiodization

The formulas derived in Sec. VIII A require explicit knowledge of the $\mathbf{k}$-dependence of Σ_f to compute v_{FS}, v_{LS} and I_{L}. As CDMFT artificially breaks translation invariance, we have to reperiodize Σ_f if we want to acquire knowledge on its $\mathbf{k}$-dependence. Reperiodization is however a post-processing step which is to some extent ad-hoc. The specific choice of reperiodization will affect the values of the aforementioned quantities. In particular, the question whether $I_{\mathrm{L}} = 0$ holds can therefore not be answered conclusively when relying on some reperiodization scheme. In the following, we therefore provide and

motivate formulas for v_{FS}, v_{LS} and I_{L} which do not require reperiodization.

First, we note that the momentum integrals in the preceding part of this section represent a trace over all quantum numbers. In case of translational invariance, it is convenient to use the momentum basis to perform this trace, as the Green's functions and self-energies are diagonal in this basis. In the 2-site CDMFT approach, it is however more convenient to represent them as 2×2 matrices depending on momenta $\mathbf{K}$ in the cluster BZ (cBZ). This leads to the replacement

$$\int_{\mathrm{BZ}} \frac{d\mathbf{k}}{\mathcal{V}_{\mathrm{BZ}}} \to \frac{1}{2}\operatorname{Tr}\int_{\mathrm{cBZ}} \frac{d\mathbf{K}}{\mathcal{V}_{\mathrm{cBZ}}} \qquad (47)$$

in the formulas presented in Sec. VIII B. Here, $\mathcal{V}_{\mathrm{cBZ}} = \mathcal{V}_{\mathrm{BZ}}/2$ the volume of the cBZ and Tr is the trace of the $\mathbf{K}$-dependent 2×2 matrices.

Now, within the CDMFT approximation, Σ_f and therefore also Σ_c are independent of $\mathbf{K}$,

$$\Sigma_{x\mathbf{K}}(z) = \Sigma_x(z) \quad (x = f, c). \qquad (48)$$

(This $\mathbf{K}$-independence breaks the translation invariance.) Moreover, the cluster propagators of Eq. (6), defined as $\mathbf{K}$-integrated objects, are likewise $\mathbf{K}$-independent:

$$G_x(z) \equiv \int_{\mathrm{cBZ}} \frac{d\mathbf{K}}{\mathcal{V}_{\mathrm{cBZ}}} G_{x\mathbf{K}}(z) \quad (x = f, c). \qquad (49)$$

Using Eqs. (47) to (49), the ingredients (42) to (43) of the Luttinger-PAM sum rule (41) can now readily be transcribed to obtain the following expressions:

$$v_{\mathrm{FS}} = \operatorname{Tr}\int_{\mathrm{cBZ}} \frac{d\mathbf{K}}{\mathcal{V}_{\mathrm{cBZ}}} \frac{\delta_{c\mathbf{K}}}{2\pi}, \quad v_{\mathrm{LS}} = \operatorname{Tr}\int_{\mathrm{cBZ}} \frac{d\mathbf{K}}{\mathcal{V}_{\mathrm{cBZ}}} \frac{\delta_{\Sigma}}{2\pi},$$
$$(50)$$

$$\delta_{c\mathbf{K}} = -\operatorname{Im}\int_{-\infty}^{0} d\omega\, \partial_\omega \ln G^{-1}_{c\mathbf{K}}(\omega^+)$$

$$\delta_{\Sigma} = -\operatorname{Im}\int_{-\infty}^{0} d\omega\, \partial_\omega \ln \Sigma^{-1}_c(\omega^+) = +\Big[\arg\Sigma^{+1}_c(\omega^+)\Big]^0_{-\infty},$$

$$I_{\mathrm{L}} = \frac{-1}{2\pi}\operatorname{Im}\int_{-\infty}^{0} d\omega\, \operatorname{Tr}\left[G_f(\omega^+)\, \partial_\omega \Sigma_f(\omega^+)\right]. \qquad (51)$$

Here, v_{FS}, v_{LS} are expressed as traces of the cBZ integrals of the matrix-valued phase shifts $\delta_{c\mathbf{K}}$, δ_{Σ}. For the latter, which is $\mathbf{K}$-independent δ_{Σ}, the integral is trivial. For the $\mathbf{K}$-dependent $\delta_{c\mathbf{K}}$, we use

$$\partial_z \ln G^{-1}_{c\mathbf{K}}(z) = G_{c\mathbf{K}}(z)(1 - \partial_z\Sigma_c(z)), \qquad (52)$$

such that the $\mathbf{K}$ integral yields a local cluster quantity,

$$\delta_c = \int_{\mathrm{cBZ}} \frac{d\mathbf{K}}{\mathcal{V}_{\mathrm{cBZ}}}\delta_{c\mathbf{K}} = -\operatorname{Im}\int_{-\infty}^{0} d\omega\, G_c(\omega^+)(1 - \partial_\omega\Sigma_c(\omega^+)). \qquad (53)$$

Note that in Eq. (53), $1 - \partial_z\Sigma_c(z) \neq \partial_z G^{-1}_c(z)$ because $G_c(z)$ is a $\mathbf{K}$-integrated quantity, so that $G^{-1}_c(z)$ contains
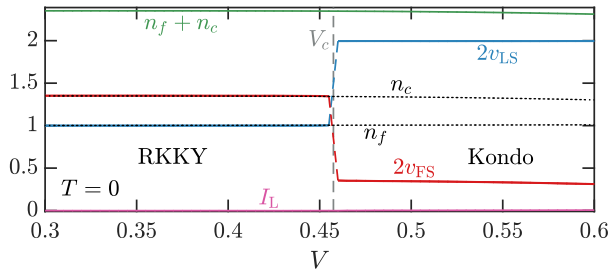
FIG. 17. FS and LS volumes, v_{FS} (red) and v_{LS} (blue), and the Luttinger integral I_{L} (pink), together with the particle numbers n_f and n_c (black dotted) and their sum (green), plotted as functions of V at $T = 0$.

an additional hybridization term $\Delta_c(z)$, c.f. Eq. (6b). Thus, Eqs. (50) reduce to

$$v_{\mathrm{FS}} = \tfrac{1}{2\pi}\operatorname{Tr}\delta_c, \qquad v_{\mathrm{LS}} = \tfrac{1}{2\pi}\operatorname{Tr}\delta_\Sigma. \qquad (54)$$

Equations (54), (53) and (51) achieve our stated goal of expressing v_{FS}, v_{LS} and I_{L} purely through the local Green's functions and self-energies of the effective 2IAM. They can hence can be computed without using reperiodization.

D. Results

Our CDMFT results for v_{FS}, v_{LS} and I_{L} (obtained with the formulas from Sec. VIII C) are shown in Fig. 17, together with the particle numbers n_c and n_f. As mentioned before, we find $I_{\mathrm{L}} = 0$ for all considered values of V. We note that $I_{\mathrm{L}} = 0$ is an empirical numerical finding and may not hold if e.g. different fillings are considered [197, 198]; this will be explored in more detail in future work. Further, we find that the particle numbers n_c and n_f evolve smoothly across the KB–QCP, in contrast to v_{FS} and v_{LS} which exhibit a jump when crossing the KB–QCP. The jumps are such that $2v_{\mathrm{FS}} + 2v_{\mathrm{LS}} = n_f + n_c$ evolves smoothly across the KB–QCP, i.e. the jumps of v_{FS} and v_{LS} compensate each other.

In the Kondo phase, $v_{\mathrm{LS}} = 1$ and v_{FS} is such that together, v_{LS} and v_{FS} account for the total particle number. Note that $v_{\mathrm{LS}} = 1$ means that the LS volume fills the whole BZ, i.e. there is no LS in the Kondo phase. In the RKKY phase on the other hand, $v_{\mathrm{LS}} = \frac{1}{2} \simeq \frac{1}{2}n_f$ while $v_{\mathrm{FS}} \simeq \frac{1}{2}n_c$. v_{LS} takes a fractional value in the RKKY phase, which means the LS volume fills a fraction of the BZ and there is a LS. The presence of a LS can be linked to an emergent spinon FS [147], suggesting that the RKKY phase is a fractionalized FL [105, 106]. We will provide a more detailed analysis of this in future work.

In the Kondo phase, v_{FS} is the same as in the $U = 0$ limit at the same filling (the same is true for v_{LS}). The FS in the Kondo phase is therefore as expected in a normal FL in the PAM. v_{FS} "trivially" (in the sense that one can infer it from the $U = 0$ limit) accounts for both the f and c electrons which is why it is called a "large" FS,

even though the value of v_{FS} is smaller than in the RKKY phase. In the RKKY phase by contrast, $v_{\mathrm{FS}} \simeq \frac{1}{2}n_c$ takes almost the value expected for $V = 0$ with $U \neq 0$. The FS seems to account only for the c electrons and hence is called a "small" FS. Based on the shape and volume of the FS in the RKKY phase, one may be tempted to conclude that c and f electrons have decoupled. However, this is not the case, as elaborated in sections VI and VII above.

We now elaborate how the jump in v_{FS} and v_{LS} is connected to the sign change of ϵ_{f+}^* across the KB–QCP, which we have discussed in Sec. VI C. To make this connection, we examine Eq. (54) for v_{LS} (computed without reperiodization) in more detail, while assuming $\operatorname{Im}\Sigma_c(0) = -0^+$ (Eq. (44)), consistent with our results. Analogously to our discussion of $\delta_{\Sigma\mathbf{k}}$ under the aforementioned assumption (see Eq. (45b)), the corresponding phase shift of the effective 2IAM (see Eq. (51)) is given by $\delta_\Sigma = \pi\theta(\operatorname{Re}\Sigma_c(i0^+))$ (note that both δ_Σ and $\Sigma_c(i0^+)$ are 2×2 matrices which are in our case diagonal in the $\pm$ basis). We can identify three different cases, which lead to distinct values of v_{LS}: both eigenvalues of $\operatorname{Re}\Sigma_c(i0^+)$ are (i) positive, (ii) negative or (iii) the eigenvalues of $\operatorname{Re}\Sigma_c(i0^+)$ have opposite signs, i.e. one is positive, the other negative. Inserting these into $v_{\mathrm{LS}} = \operatorname{Tr}\delta_\Sigma/(2\pi)$ (see Eq. (54)), we find (i) $v_{\mathrm{LS}} = 1$, (ii) $v_{\mathrm{LS}} = 0$ or (iii) $v_{\mathrm{LS}} = \frac{1}{2}$. The value of v_{LS} is therefore connected to the *signs of the eigenvalues* of $\operatorname{Re}\Sigma_c(i0^+)$, which in our case are $\operatorname{Re}\Sigma_{c\pm}(i0^+)$. The signs are related to those of $\epsilon_{f\pm}^*$ via Eq. (25b), namely $\operatorname{sgn}\operatorname{Re}\Sigma_{c\pm}(i0^+) = -\operatorname{sgn}\epsilon_{f\pm}^*$. Thus, we find (i) $v_{\mathrm{LS}} = 1$ if $\epsilon_{f\pm}^*$ are both negative, (ii) $v_{\mathrm{LS}} = 0$ if $\epsilon_{f\pm}^*$ are both positive and (iii) $v_{\mathrm{LS}} = \frac{1}{2}$ if $\epsilon_{f\pm}^*$ come with opposite signs.

In the Kondo phase, both $\epsilon_{f\pm}^*$ are negative (cf. Fig. 9), just as in the $U \to 0$ limit for the parameters we have chosen, which leads to $v_{\mathrm{LS}} = 1$ in the Kondo phase. As discussed in more detail in Sec. VI C, when the KB–QCP is crossed from the Kondo to the RKKY phase, ϵ_{f+}^* changes sign and becomes positive while ϵ_{f-}^* remains negative, which leads to $v_{\mathrm{LS}} = \frac{1}{2}$ in the RKKY phase. Since v_{LS} jumps due to the sign change of ϵ_{f+}^*, v_{FS} exhibits a corresponding jump.

We note that a jump of v_{LS} and v_{FS} is not at odds with a continuous QPT. Indeed, ϵ_{f+}^* changes smoothly across the KB–QCP. The reason why v_{LS} jumps is because it is not sensitive to the absolute value of $\epsilon_{f\pm}^*$, but only to the signs. Signs are by definition discrete quantities and changes can only occur via jumps, which is why both v_{LS} and v_{FS} change via a jump, even though the QPT is continuous. We emphasize that a prerequisite for this sign sensitivity is that $\operatorname{Im}\Sigma_c(i0^+) = 0^-$, i.e. that the $T \to 0$ phase is a FL. If $\operatorname{Im}\Sigma_c(i0^+)$ were finite, v_{LS} and v_{FS} could change continuously. Because finite $\operatorname{Im}\Sigma_c(i0^+)$ would imply that the $T \to 0$ phase is not a FL, v_{LS} and v_{FS} then would not have the interpretations of being volumes in the BZ bounded by sharply defined Fermi or Luttinger surfaces.

Further, our analysis shows that the FS reconstruction
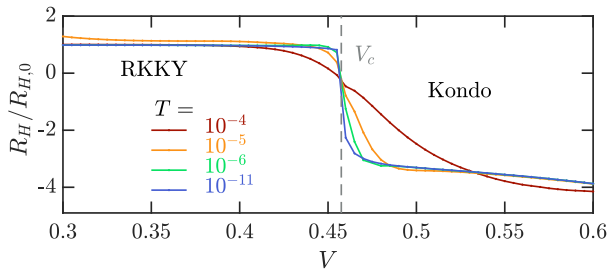
FIG. 18. Hall coefficient versus V for different temperatures.

is a priori independent of possible translation symmetry breaking like antiferromagnetic or charge density wave order. Translation symmetry breaking increases the size of the unit cell and thus reduces the size of the BZ. While this may change the FS volume measured in units of the smaller BZ, it does *not* change the average phase shifts v_{LS} and v_{FS} as they appear in Eqs. (42) and (50). For instance, the onset of antiferromagnetic order without jumps in the phase shifts v_{LS} and v_{FS} marks a SDW–QCP while jumps in the phase shifts v_{LS} and v_{FS} mark a KB–QCP, regardless of whether it is or is not accompanied by the onset of e.g. AFM order.

The generalized Luttinger's theorem also offers a possible explanation why the QCP in the 2IAM is stabilized by the CDMFT self-consistency condition. Without self-consistency, the QCP in the 2IAM is only stable if the scattering phase shifts are constrained by symmetry [84, 86, 170]. The symmetry constraint then prevents a smooth change of the phase shifts, resulting in a QCP where the phase shifts jump between allowed values [84, 86]. However, if such symmetry constraints are *absent*, the phase shifts will simple change without a QCP [86]. In the self-consistent 2IAM, the phase shifts *are* constrained, not by symmetry, but by the Luttinger sum rule, as we have seen in the previous discussions in this section. We conjecture that this Luttinger sum rule constraint is the reason why the self-consistent 2IAM does have a QCP. A more detailed analysis will be presented in future work.

One of the experimental hallmarks of a FS reconstruction at a KB–QCP is a sharp crossover of the Hall coefficient, $R_H \sim 1/n_H$, and thus of the Hall carrier density, n_H [5, 25, 31]. This has been observed in experiments on YbRh$_2$Si$_2$ [25, 36, 199] and CeCoIn$_5$ [31]. A sign change of R_H has also been observed in CeCu$_{6-x}$Au$_x$when increasing x from 0 to 0.1 [200]. To make contact to these experiments, we show the Hall coefficient calculated from our data in Fig. 18, as a function of V at different temperatures. It is calculated using reperiodized self-energies with the formulas shown in App. A 5. At all considered temperatures, we find two qualitatively distinct values of R_H deep in the Kondo regime (high V) and deep in the RKKY regime (low V). It shows a sign change across V_c, reflecting a reconstruction from a particle-like FS in the Kondo regime to a hole-like FS in the RKKY regime. These are connected by a smooth crossover at high temperatures, which becomes sharper as temperature is lowered

and almost step-like at the lowest temperature. This is qualitatively very similar to the experimental findings on YbRh$_2$Si$_2$ [25, 36, 199] and CeCoIn$_5$ [31].

The analysis of generalized Luttinger sum rules for coupled c and f bands presented in this section makes no claims for generality—it focuses solely on the PAM and is based on assumptions consistent with our numerical results for this model. Nevertheless, similar analyses are likely possible for related models hosting QPTs with FS reconstruction, and we expect the LS to play a crucial role, there, too.

IX. SOMMERFELD COEFFICIENT AND ENTROPY

A further quantity showing interesting behavior at a heavy-fermion QCP is the lattice Sommerfeld coefficient,

$$\gamma_{\text{latt}} = C_{\text{latt}}/T = \partial S_{\text{latt}}/\partial T . \tag{55}$$

Here, C_{latt} and S_{latt} are the lattice specific heat and entropy per 2-site cluster (*not* just the impurity contribution). S_{latt} can be computed from the f-electron contribution to the entropy S_f of the effective 2IAM and a correction term S_{corr} [114, 201], as follows:

$$S_{\text{latt}} = S_f + S_{\text{corr}} , \tag{56a}$$

$$S_f = -\left. \frac{\partial \Omega_f}{\partial T} \right|_{\Delta_f = \text{const.}} , \tag{56b}$$

$$\Omega_f = \Phi[G_f] - \frac{2}{\pi} \operatorname{Tr} \int_\omega f_T(\omega)\big(\delta_f - \operatorname{Im}[\Sigma_f G_f]\big) , \tag{56c}$$

$$S_{\text{corr}} = \frac{2}{\pi} \operatorname{Tr} \int_\omega \frac{\partial f_T(\omega)}{\partial T}\big(\delta_c + \delta_\Sigma - \delta_f\big) , \tag{56d}$$

$$\delta_f(\omega^+) = -\operatorname{Im} \ln G_f^{-1}(\omega^+) , \tag{56e}$$

$$\delta_\Sigma(\omega^+) = -\operatorname{Im} \ln \Sigma_c^{-1}(\omega^+) , \tag{56f}$$

$$\delta_c(\omega^+) = -\operatorname{Im} \int_{\text{cBZ}} \frac{d\mathbf{K}}{\mathcal{V}_{\text{cBZ}}} \ln G_{c\mathbf{K}}^{-1}(\omega^+) . \tag{56g}$$

Here, Φ is the Luttinger-Ward functional of the 2IAM, $f_T(\omega) = 1/[\exp(\omega/T) + 1]$ is the Fermi-Dirac distribution, Tr is a trace over the cluster indices and δ_f, δ_Σ and δ_c are matrix-valued phase shifts. The derivative in Eq. (56b), which is evaluated while keeping the hybridization function Δ_f fixed, is accessible via NRG [202]. The correction S_{corr} accounts for the fact that $\Delta_f(T)$ actually depends on temperature [201]. To compute the Sommerfeld coefficient $\gamma_{\text{latt}} = \partial S_{\text{latt}}/\partial T$, we numerically differentiate $S_{\text{latt}}(T)$.

The Sommerfeld coefficient is a measure of the density of states. In a FL, it is proportional to the QP mass (m^*) and QP weight (Z), $\gamma \sim m^* \sim Z^{-1}$ [14] and hence is expected to be independent of temperature. By contrast, a $\gamma_{\text{latt}} \sim \ln(T)$ dependence, indicating NFL behavior, has been observed almost universally for numerous compounds
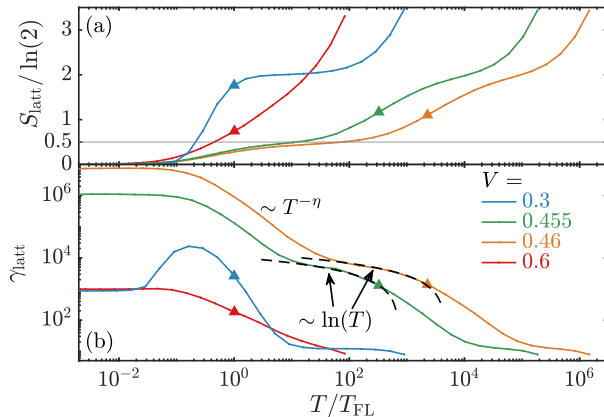
FIG. 19. Temperature dependence of (a) the lattice entropy and (b) the specific heat coefficient per 2-site cluster. Triangles mark the position of $T_{\mathrm{NFL}}/T_{\mathrm{FL}}$.

in strange metallic regimes at finite temperatures above QCPs [4, 6, 203, 204], e.g. for YbRh$_2$Si$_2$ [24, 27, 188, 205], CeCu$_{6-x}$Au$_x$ [28, 61] and CeCoIn$_5$ [64]. Further, γ_{latt} has been observed to diverge when approaching the KB–QCP from either side [27, 187]; this implies a divergent effective mass m^* at the QCP. A divergence of m^* when approaching the KB–QCP from either side has been observed in many HF materials using different measurement techniques [27–29, 32]. This is direct evidence for a breakdown of the FL at the QCP [27]

Our results for $S_{\mathrm{latt}}(T)$ and $\gamma_{\mathrm{latt}}(T)$ are shown Figs. 19(a,b). At very high temperatures ($T \gg T_{\mathrm{NFL}}$), S_{latt} decreases from some high-T value and, for $V < 0.6$, exhibits a shoulder around $2\ln(2)$ (the entropy of two local moments). This shoulder becomes more pronounced for lower V (and is not visible for $V = 0.6$). In the same high-temperature range, γ_{latt} shows a shoulder which is also more pronounced for lower V (and again not visible for $V = 0.6$). Thus, the entropy in this high-temperature regime has a linear T-dependence, $S_{\mathrm{latt}}(T) \simeq 2\ln(2)+a{\cdot}T$, with a slope a which is almost independent of V (since $\gamma_{\mathrm{latt}} = \partial_T S_{\mathrm{latt}}$ is roughly independent of V in the high-T shoulder region). This behavior can be understood in terms of thermally fluctuating f moments (leading to the shoulder of S_{latt}) and unrenormalized thermally excited c electrons, leading to the V-independent linear-in-T dependence and hence a V-independent shoulder in γ_{latt}. Such a temperature dependence is characteristic for the LM regime, which is also expected to be more pronounced for lower V.

As T is lowered, the free moments begin to hybridize with the c electrons. This leads to screening of the moments, both by forming Kondo singlets and inter-impurity singlets, thus reducing the entropy. Far away from V_c (blue, red curves), where $T_{\mathrm{FL}} \simeq T_{\mathrm{NFL}}$, the entropy drops to zero as $T \to 0$ without notable features at intermediate temperatures. Deep in RKKY regime ($V = 0.3$), this entropy decrease reflects the formation of f-electron singlets and is very rapid, leading to a pronounced hump

of γ_{latt} around $T \simeq T_{\mathrm{FL}} \simeq T_{\mathrm{NFL}}$.

However, close to V_c (green, orange curves), $S_{\mathrm{latt}}(T)$ flattens considerably in the intermediate range $T_{\mathrm{FL}} \lesssim T \lesssim T_{\mathrm{NFL}}$, resulting in a second shoulder near $\ln\sqrt{2}$. Concurrently, $\gamma_{\mathrm{latt}}(T)$ shows a logarithmic T dependence (black dashed lines), implying a $T \ln T$ behavior for the specific heat. As mentioned above, this is an almost universal feature of heavy-fermion compounds with KB–QCPs.

The shoulder at $\ln\sqrt{2}$ for the lattice entropy suggests that at the QCP, where $T_{\mathrm{FL}} = 0$, the zero-temperature entropy would be non-zero, $S_{\mathrm{latt}}(T \to 0) = \ln\sqrt{2}$. This value is also found for the zero-temperature impurity entropy of the two-channel Kondo model and the two-impurity Kondo model, where it can be attributed to an unscreened Majorana zero mode at the QCP [76, 162, 206] (see also the next section). For the PAM, this means that 2-site CDMFT predicts a non-zero, extensive entropy at $T = 0$ *at* the QCP. This suggests that the KB–QCP in 2-site CDMFT would be highly unstable to symmetry breaking orders tending to get rid of the non-zero entropy. It remains to be checked in future work (by studying larger cluster sizes) whether this extensive entropy is due to the finite cluster size, i.e. whether the entropy per lattice site at the KB–QCP scales to zero with increasing the cluster size, or whether the nonzero $T \to 0$ entropy per lattice site is robust, independent of cluster size.

When T is decreased to about 1 to 2 orders of magnitude below T_{NFL}, the $\ln T$ dependence of γ_{latt} turns to a $T^{-\eta}$ dependence, with $\eta \simeq 4/3$, before becoming constant below T_{FL}. A somewhat similar power-law T-dependence, with an onset temperature of less than 1 order or magnitude below T_{NFL}, has also been found in YbRh$_2$Si$_2$ [27, 188, 205], albeit with different exponent of $\eta = 1/3 < 1$ [27]. Ref. 27 suggested that for YbRh$_2$Si$_2$, the $T^{-\eta}$ dependence is a property of the NFL. For our PAM however, this cannot be the case: since at V_c the NFL regime reaches down $T \to 0$, it cannot support $T^{-\eta}$ behavior with $\eta > 1$, since its specific heat $C_{\mathrm{latt}} = T\gamma_{\mathrm{latt}} \sim T^{1-\eta}$ would diverge, which is thermodynamically impossible. Further, since $\gamma_{\mathrm{latt}} = \partial_T S_{\mathrm{latt}}$, the $T^{-\eta}$ behavior of γ_{latt} implies $S_{\mathrm{latt}}(T) \sim T^{1-\eta}/(1 - \eta) + \mathrm{const}$ in this regime. If the powerlaw dependence would extend all the way down to $T = 0$, $\eta > 1$ would imply $S_{\mathrm{latt}}(T = 0) = -\infty$, which is clearly nonsense. Therefore, we view the $T^{-\eta}$ power law of γ_{latt} to be a property of the NFL-FL *crossover*, rather than of the NFL regime itself. Since $\gamma_{\mathrm{latt}} \sim \ln T$ in the NFL region is a much weaker singularity than the $T^{-\eta}$ crossover behavior, the latter takes over at a relatively high temperature compared to T_{FL}.

For $T < T_{\mathrm{FL}}$, $\gamma_{\mathrm{latt}}(T)$ is constant for all V values shown, as expected in a FL. It is orders of magnitude larger close to the QCP on either side (green, orange curves) than further away from it (blue, red curves), reflecting the divergence of the QP mass $m^* \sim \gamma_{\mathrm{latt}}(T = 0) \sim Z^{-1}$ at the QCP. It is noteworthy that far from the QCP, the value of $\gamma_{\mathrm{latt}}(T = 0)$ for the RKKY phase is comparable to that in the Kondo phase. This suggests that in the RKKY phase the localized spins, though tending to lock
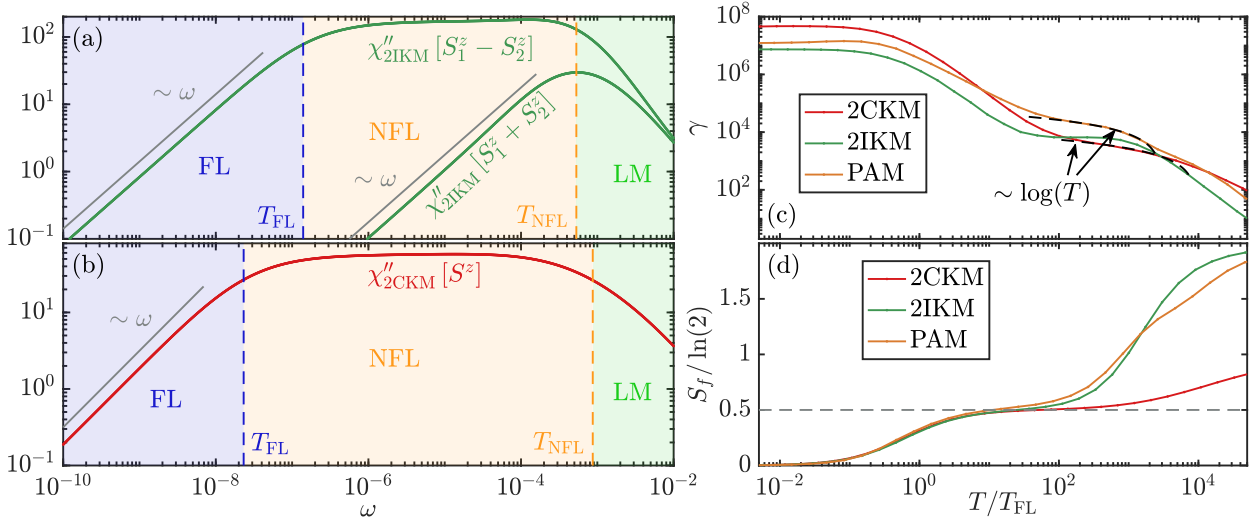
FIG. 20. (a,b) Spectral part of the spin susceptibility of (a) a 2ICK and (b) a 2CKM close to their QCPs. $\chi''_{\text{2IKM}}[S_1^z - S_2^z]$ and $\chi''_{\text{2CKM}}[S^z]$ show similar features as $\chi''[X^{zx}]$ in the PAM close to the KB–QCP (c.f. Fig. 4). (c) Sommerfeld coefficient and (d) impurity contribution to the entropy of the 2IKM, 2CKM and PAM close to their QCPs. The data for the PAM is taken at $V = 0.46$. Most notable, in the NFL region, γ shows a $\ln(T)$ behavior for the 2CKM and the PAM, and $S_f \simeq \frac{1}{2} \cdot \ln(2)$ for all three models.

into nearest-neighbor singlets, nevertheless contribute quite significantly to the density of states. Understanding this aspect in more detail is left as an interesting task for future work.

X. RELATION TO OTHER MODELS

The NFL regime in the PAM shares several similarities with the NFL in the two-impurity Kondo model [84–86, 151, 152] and the two-channel Kondo model [74, 75, 163–167]: (i) The Sommerfeld coefficient γ shows a region of $\ln(T)$-dependence [cf. Fig. 19(b)]; (ii) the entropy takes the value of $\ln\sqrt{2}$; and (iii) plateaus in dynamical susceptibilities imply overscreening.

In this section, we compare the features of the effective 2IAM describing the PAM at $V = 0.46$ close to the QCP to known features of the two-impurity Kondo model (2IKM) close to its QCP. We also include data on the two-channel Kondo model (2CKM) close its QCP [74, 75, 163–167], since its critical behavior is known to be closely related to that of the 2IKM [151, 152].

The Hamiltonian describing the 2IKM is given by

$$H = \sum_{i=1,2} \left[\sum_{k\sigma} \epsilon_k c_{ik\sigma}^\dagger c_{ik\sigma} + J \boldsymbol{S}_i \cdot \boldsymbol{s}_i \right] + K \boldsymbol{S}_1 \cdot \boldsymbol{S}_2 . \quad (57)$$

Here, $c_{ik\sigma}$ destroys an electron in channel $i = 1, 2$ with energy ϵ_k and spin σ, $\boldsymbol{s}_i = \frac{1}{2} \sum_{kk'\sigma\sigma'} c_{ik\sigma}^\dagger \hat{\boldsymbol{\sigma}}_{\sigma\sigma'} c_{ik'\sigma'}$ describes the local spin of channel i at the origin, and $\boldsymbol{S}_i$ describe two impurity spin $1/2$ degrees of freedom at the origin. The impurity spins are coupled antiferromagnetically to the corresponding conduction electrons with

coupling strengths $J > 0$. $\boldsymbol{S}_1$ and $\boldsymbol{S}_2$ are further coupled antiferromagnetically with coupling strength $K > 0$. The 2IKM can be tuned through a QCP from a Kondo regime at $K < K_c$, where $\boldsymbol{S}_i$ is screened by its corresponding bath, to an RKKY regime at $K > K_c$, where $\boldsymbol{S}_1$ and $\boldsymbol{S}_2$ form a singlet. At the QCP, T_{FL} vanishes and an intermediate NFL region emerges, similar to the case of the PAM discussed in the main text.

The NFL in the 2IKM is closely related to the NFL found in the 2CKM, described by the Hamiltonian

$$H = \sum_{i=1,2} \left[\sum_{k\sigma} \epsilon_k c_{ik\sigma}^\dagger c_{ik\sigma} + J_i \boldsymbol{S} \cdot \boldsymbol{s}_i \right] . \quad (58)$$

Here, there is only one impurity spin, coupled antiferromagnetically to two channels, $i = 1, 2$, with coupling strengths $J_i > 0$. The 2CKM has a QCP at $J_1 = J_2$, where the impurity changes from being screened by channel 1 at $J_1 > J_2$ to being screened by channel 2 at $J_1 < J_2$. Close to its QCP, a NFL fixed point is found which extends to $T = 0$ at the QCP and shows features similar to these of the NFL in the 2IKM and in the PAM as presented in the main part.

In the following, we consider a 2IKM and a 2CKM tuned close to their respective QCP's. We compare their Sommerfeld coefficients, impurity contributions to the entropy and dynamical correlation functions to the f electron contribution to the entropy and Sommerfeld coefficient of the self-consistent 2IAM describing the PAM close to its QCP, shown in Fig. 20. For both the 2IKM and the 2CKM, a box shaped, particle-hole symmetric density of states with width 2 and height $1/2$ is used for both channels. As parameters, $J = 0.256$ and $K = 7.2 \cdot 10^{-4}$ where used for the 2IKM and $J_1 = 0.29$, $J_2 = 0.2894$ was chosen for the 2CKM. Both models are

solved with NRG using $\Lambda = 3$ and keeping $N_{\text{keep}} = 2000$ $\text{SU}(2)_{\text{charge}} \times \text{SU}(2)_{\text{charge}} \times \text{SU}(2)_{\text{spin}}$ multiplets at every NRG iteration.

Fig. 20(a) shows $\chi''_{2\text{IKM}}[S_1^z + S_2^z]$ and $\chi''_{2\text{IKM}}[S_1^z - S_2^z]$, together with the NFL and FL scales extracted from the kinks of $\chi''_{2\text{IKM}}[S_1^z + S_2^z]$ and $\chi''_{2\text{IKM}}[S_1^z - S_2^z]$ on the ln-ln scale, respectively, similar as described for the PAM before. In Fig. 20(b), we show the impurity spin susceptibility of the considered 2CKM, $\chi''_{2\text{CKM}}[S^z]$, with the corresponding NFL and FL scales both extracted from $\chi''_{2\text{CKM}}[S^z]$. The similarity of $\chi''_{2\text{IKM}}[S_1^z - S_2^z]$ in Fig. 20(a), $\chi''_{2\text{CKM}}[S^z]$ in Fig. 20(b) and $\chi''[X^{zx}]$ in Fig. 4 is evident.

The Sommerfeld coefficient $\gamma = \mathrm{d}S_f/\mathrm{d}T$, and the impurity contribution to the entropy S_f are shown in Fig. 20(c) and (d), respectively, for the 2IKM, the 2CKM and the PAM at $V = 0.46$. Qualitatively similar behavior is found, most notably a plateau in S_f with $S_f \simeq \frac{1}{2}\ln(2)$ for all three models, and a $\ln(T)$ dependence of γ at intermediate temperatures for the 2CKM and the PAM (the 2IKM shows similar behavior, though without a clean $\ln(T)$ dependence). A further elucidation of the nature of the NFL in the PAM will require an impurity model analysis as done in Refs. [207, 208]. We leave this for future work.

XI. CONCLUSION AND OUTLOOK

We have presented an extensive 2-site CDMFT plus NRG study of the PAM, following up on and considerably extending and refining previous work done with an ED impurity solver [127, 128]. Leveraging the capabilities of NRG to resolve exponentially small energy scales on the real-frequency axis, we confirmed the existence of the KB–QCP found in Refs. 127 and 128, which can be understood in terms of a continuous OSMT at $T = 0$.

Beyond that, we unambiguously showed that the KB–QCP marks a second-order transition between two FL phases [Fig. 3] which differ in their FS volumes [Sec. VIII], leading to a sharp jump of the FS volume [Fig. 17] and the Hall coefficient [Fig. 18]. We found that, in contrast to widespread belief [3], the f-electron QP weight is non-zero both in the Kondo *and* the RKKY phase [Sec. VI, in particular Fig. 9] and only becomes zero at the QCP itself. We showed that the FS reconstruction across the KB–QCP can be understood in terms of a sign change of the effective level position ϵ^*_{f+} [Fig. 9 and Sec. VIII], which is connected to the emergence of a dispersive pole in the RKKY phase [Fig. 10]. An interesting consequence of the non-zero f-electron QP weight is that in the RKKY phase, the band structure consists of *three* bands, with a very narrow band crossing the Fermi level [Sec. VII]. We also showed that both in the Kondo and RKKY phases, the specific heat is linear in T, as expected from a FL; we find that the Sommerfeld coefficient diverges when the KB–QCP is approached from either side [Sec. IX].

We find that the physics at the KB–QCP and at non-zero temperatures in its vicinity is governed by a NFL fixed point [Sec. IV], which has some resemblance to the NFL fixed points in the 2-impurity and 2-channel Kondo models [Sec. X]. In this paper, we reported a strange-metal like $\sim T \ln T$ specific heat in the NFL region [Sec. IX]. A more detailed analysis of the NFL regime is provided in a companion paper [148], where we show data regarding ω/T of the optical conductivity closely resembling experimental data [60] and evidence for linear-in-T resistivity.

We should however also mention some caveats in our work, which may be addressed in future work. For instance, while we provided some extensive formal treatment of Luttinger's theorem [Sec. VIII], we refrained from offering any physical interpretation on how and why the FS in the RKKY phase can be small. Indeed, Oshikawa's non-perturbative treatment of Luttinger's theorem [9] implies that in case of a violation of Luttinger's theorem, additional low-energy degrees of freedom must be present [105, 111]. We leave their identification within the context of the PAM to future work. We expact that this could also lead to a connection to slave particle theories [105, 110]. Further insights could possibly be pursued along the lines of recent work by Fabrizio [147, 172, 209]. As we have pointed out repeatedly in this paper, the work cited above draws a connection between Luttinger surfaces and fractionalized spinon excitations. Our work paves the way to explore this connection in detail in terms of a concrete example.

An unsatisfactory aspect of our 2-site CDMFT treatment is that it yields a non-zero entropy at the KB–QCP at $T = 0$, see Sec. IX. As already mentioned in that section, such a non-zero entropy would render the KB–QCP highly unstable to symmetry breaking. Whether this is a finite cluster size effect or continues to be the case also for larger cluster sizes needs to be checked in future work.

Lastly, our CDMFT treatment requires reperiodization of self-energies to obtain a periodic self-energy with **k**-dependence. Reperiodization is an ad-hoc post-processing procedure. We have checked that our most important claims are consistent with our non-repriodized bare data. Nevertheless, in our view it would be important to cross-check our results in future studies, for instance with numerically exact methods. Such studies will be very useful for establishing the range of applicability of CDMFT for describing KB physics.

Our work motivates several follow-up studies. For instance, as mentioned before, it would be interesting to explore the interplay between KB physics and potential symmetry breaking orders of all kind, e.g. antiferromagnetic or superconducting orders. Similar studies could also be done for models appropriate to other classes of strongly correlated materials. Obvious candidate material classes, which experimentally show quantum critical behavior quite similar to heavy fermions, are cuprates [210–215] or twisted bilayer graphene [216–218].

ACKNOWLEDGMENTS

Appendix A: CDMFT for the PAM

In the two-site CDMFT treatment of the PAM, the three-dimensional lattice is tiled into a superlattice of two-site clusters [116, 126, 128]. An effective action can then be constructed via the cavity method [114]. It takes the form of a 2IAM coupled to an effective bath, describing the rest of the lattice from the point of view of the two-site cluster in the CDMFT approximation. The c electrons can either be treated explicitly, or they can be integrated out and merged with the effective bath, as they are non-interacting. We decided to treat the c electrons explicitly, as this enables us to directly calculate dynamical susceptibilities involving c-electron degrees of freedom. Additional calculations, treating the c electrons together with the bath, confirmed that both methods give the same results. Note that both methods have roughly the same amount of computational complexity for the NRG impurity solver. Since the f electrons only couple to the bath via the c electrons as they do not have any non-local hopping term, one obtains two bands of spinfull bath electrons in both cases. For a detailed description of 2-site CDMFT for the PAM, see Ref. 126.

1. Self-consistency

In the CDMFT approximation, the cluster Green's function is given by

$$G_{\text{loc}}(z) = \int_{\mathbf{k}} \begin{pmatrix} z - \epsilon_f - \Sigma_f(z) & -V \\ -V & \mathcal{G}_{0,c\mathbf{k}}^{-1}(z) \end{pmatrix}^{-1} \quad \text{(A1a)}$$

$$= \begin{pmatrix} G_{\text{loc},f}(z) & G_{\text{loc},fc}(z) \\ G_{\text{loc},fc}(z) & G_{\text{loc},c}(z) \end{pmatrix}, \quad \text{(A1b)}$$

where $\mathcal{G}_{0,c\mathbf{k}}$ is the c-band Green's functions at $V = 0$,

$$\mathcal{G}_{0,c\mathbf{k}}(z) = \frac{1}{(z+\mu)^2 - (\epsilon_{c\mathbf{k}}^0)^2} \begin{pmatrix} z + \mu & e^{ik_x}\epsilon_{c\mathbf{k}}^0 \\ e^{-ik_x}\epsilon_{c\mathbf{k}}^0 & z + \mu \end{pmatrix}, \quad \text{(A2)}$$

and $\Sigma_f(z)$ is the cluster f-electron self-energy (which is a proper, single-particle irreducible self-energy),

$$\Sigma_f(z) = \begin{pmatrix} \Sigma_{f11}(z) & \Sigma_{f12}(z) \\ \Sigma_{f21}(z) & \Sigma_{f22}(z) \end{pmatrix}, \quad \text{(A3)}$$

which is $\mathbf{k}$-independent in CDMFT. $G_{\text{loc},c}(z)$ can be computed by performing a momentum integral (c.f. Sec. A 2),

$$G_{\text{loc},c}(z) = \int_{\mathbf{k}} \left[\mathcal{G}_{0,c\mathbf{k}}^{-1}(z) - \Sigma_c(z) \right]^{-1}, \quad \text{(A4)}$$

while $G_{\text{loc},f}(z)$ and $G_{\text{loc},fc}(z)$ are related to $G_{\text{loc},c}(z)$ via Eq. (6c). $\Sigma_c(z)$ is the cluster c-electron self-energy (which is not single-particle irreducible), related to $\Sigma_f(z)$ via Eq. (6e). $\Sigma_f(z)$ can be computed from an auxiliary self-consistent two-impurity Anderson model (2IAM) [c.f. Eq. (4)] with $G_{\text{loc}}(z) = G_{\text{2IAM}}(z)$, with the corresponding Green's functions of the 2IAM given in Eq. (6).

The self-consistent solution is not known a priori and has to be computed via a self-consistency cycle. For that, the hybridization function of the 2IAM Eq. (5) is initialized with some guess. Then, (i) the self-energies are computed via NRG, (ii) $G_{\text{loc},c}(z)$ is computed via Eq. (A4) and (iii) the hybridization function is updated via

$$\Delta_c(z) = z + \mu + t \cdot \tau^x - \Sigma_c(z) - G_{\text{loc},c}^{-1}(z). \quad \text{(A5)}$$

This cycle is repeated until convergence is reached.

2. Momentum integration

To achieve accurate results, a method for precise momentum integration of propagators is needed in the CDMFT. For this, we employ the tetrahedron method [219, 220], which is applicable for integrals of the form

$$\int_{1.BZ} d\mathbf{k} \frac{f_{\mathbf{k}}}{g_{\mathbf{k}}}, \quad \text{(A6)}$$

where $f_{\mathbf{k}}$ and $g_{\mathbf{k}}$ are smooth functions of $\mathbf{k}$. The Brillouin zone is tiled into tetrahedra and both f and g are interpolated linearly on this tetrahedron. The integral can then be performed analytically, yielding

$$I_{\text{tetra}} = \sum_i f_i w_i(\{g_i\}). \quad \text{(A7)}$$

Here, f_i and g_i are the functions f and g evaluated at the corners of the tetrahedron and $w_i(\{g_i\})$ are integration
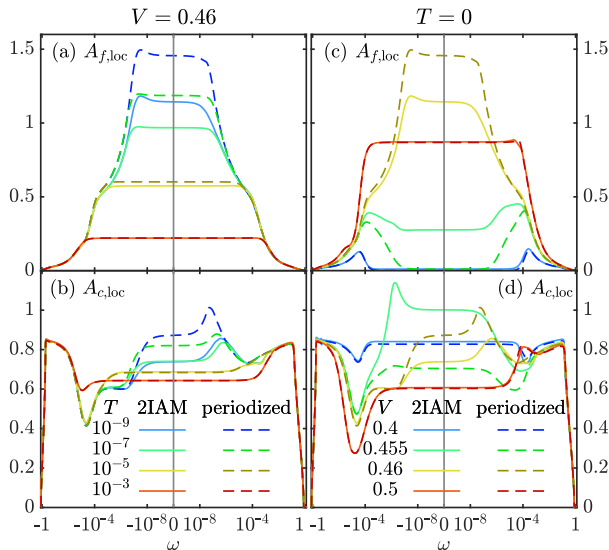
FIG. A.1. Comparison of local cluster spectral functions (solid lines) and local lattice spectral function (dashed lines) after periodization of the self-energies. The upper and lower rows show the f- and c-electron spectral function, respectively. The left panels show data for four different temperatures at fixed $V = 0.46$, close to V_c. The right panels show data for four different V at $T = 0$. The layout mirrors that of Fig. 8.

weights which depend on g only. Formulas for these weights are quite lengthy and can be found in [220] for one-, two- and three-dimensional integration. We further use an adaptive momentum grid to reduce computational effort, adjusting the grid size according to the degree of difficulty of the integral in a certain region. This enables us to evaluate all our integrals with an absolute error less than $5 \cdot 10^{-4}$. For this, the integration domain is tiled into a coarse and a fine grid, and the grid is iteratively refined in regions where the error bound is not fulfilled, until convergence is reached within the error bounds. Using the tetrahedron method, we then calculate $G_{\mathrm{loc},c}(\omega)$ via Eq. (A4). The computational effort for this integral can be reduced by treating the integral over k_y and k_z as a density of states integration, thereby mapping Eq. (A4) to a two dimensional integral:

$$\epsilon(k_x, E) = -2t \left(\cos(k_x) + E \right)$$

$$\mathcal{G}_{0,c}^{-1}(z, k_x, E) = \begin{pmatrix} z + \mu & -e^{ik_x}\epsilon(k_x, E) \\ -e^{-ik_x}\epsilon(k_x, E) & z + \mu \end{pmatrix}$$

$$G_{\mathrm{loc},c}(z) = \int_{k_x} \int_E \rho_{2\mathrm{D}}(E) \left[\mathcal{G}_{0,c}^{-1}(z, k_x, E) - \Sigma_c(z) \right]^{-1}$$

$$\rho_{2\mathrm{D}}(E) = \int_{k_y} \int_{k_z} \delta(E - \cos(k_y) - \cos(k_z)),$$

(A8)

where $\rho_{2\mathrm{D}}$ is the density of states of a square lattice.

3. Reperiodization of the self-energy

To determine transport properties such as the resistivity, the Hall coefficient or the FS, the lattice symmetries have to be restored by reperiodizing the cluster self-energy. We accomplish this via a modified periodization of the cumulant $M(z) = [z + \mu - \Sigma_c(z)]^{-1}$ (M-periodization) [153, 154]. As we discussed in Sec. VIII, the Luttinger integral (at $T = 0$) *without reperiodization* Eq. (51) is zero (c.f. Fig. 17). This property is not respected by conventional M-periodization; the Luttinger integral *with reperiodization* Eq. (43) will generically be non-zero. To ensure that the Luttinger integral vanishes also after reperiodization, we therefore modify the cumulant by a V-dependent shift of the chemical potential in the denominator *only for reperiodization purposes*:

$$\widetilde{M}(z) = \left[z + \mu + \delta\mu(V) - \Sigma_c(z) \right]^{-1} \tag{A9a}$$

$$\widetilde{M}_{\mathbf{k}}(z) = \widetilde{M}_{11}(z) + \widetilde{M}_{12}(z) \sum_{\alpha=1}^{3} \tfrac{1}{3} \cos(k_\alpha) \tag{A9b}$$

$$= \left[z + \mu + \delta\mu(V) - \Sigma_{c\mathbf{k}}(z) \right]^{-1}. \tag{A9c}$$

Here, Eq. (A9a) defines the modified cumulant used for reperiodization, Eq. (A9b) defines the reperiodization of $\widetilde{M}(z)$ and Eq. (A9c) relates it to $\Sigma_{c\mathbf{k}}$, thereby defining $\Sigma_{c\mathbf{k}}$; quantities like $\Sigma_{f\mathbf{k}}$ or $G_{x\mathbf{k}}$ are obtained from $\Sigma_{c\mathbf{k}}$ using the relations Eqs. (3). Note that the shift $\delta\mu(V)$ appears both in Eq. (A9a) and in Eq. (A9c); it therefore does not constitute an *actual* shift in the chemical potential but rather slightly redefines the quantity used for reperiodization (i.e. $\widetilde{M}$ instead of M is reperiodized). The shift $\delta\mu(V)$ is chosen such that the Luttinger integral after reperiodization (Eq. (43)) coincides with that before reperiodization (Eq. (51)) at $T = 0$. The same shift $\delta\mu(V)$ is then used at $T > 0$ for the same V. After reperiodization, we have $\widetilde{M}_\Gamma = \widetilde{M}_{11} + \widetilde{M}_{12} = \widetilde{M}_+$ and $\widetilde{M}_\Pi = \widetilde{M}_{11} - \widetilde{M}_{12} = \widetilde{M}_-$; the same relation also holds between $\Sigma_{x\mathbf{k}}$ and $\Sigma_{x\alpha}$. This establishes a correspondence between Γ/Π point in the lattice model and $+/-$ orbital in the effective cluster model.

To benchmark our reperiodization scheme, we compare the local spectral functions with and without reperiodization, shown in Fig. A.1. For V not too close to $V_c = 0.4575$ and at elevated temperatures, these two functions agree, implying that reperiodization works well here. Close to the QCP (low temperatures, $V \simeq V_c$) however, reperiodized and cluster results show differences. These differences are mostly quantitative, while most of the qualitative features remain similar. For instance, for A_f at $T = 0$, both the Kondo peak height at $V = 0.46$ and the pseudogap at $V = 0.455$ are more pronounced after periodization, but the qualitative behavior is the same before and after periodization [Fig. A.1(c)]. The most severe qualitative mismatch is the $A_{c,\mathrm{loc}}(0)$ for $V < V_c$ [Fig. A.1(d)]: at $T = 0$ in the RKKY phase, as V is increased towards V_c, a Kondo-like peak develops in $A_{c,\mathrm{loc}}$
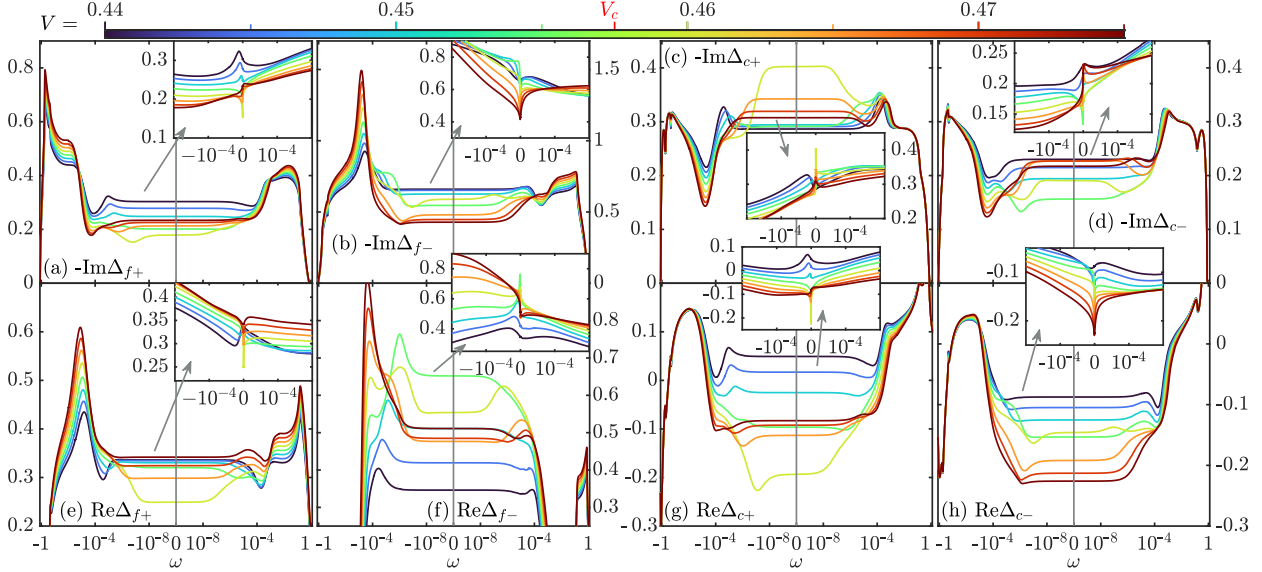
FIG. A.2. Evolution of the self-consistent hybridization functions $\Delta_{x\alpha}(\omega^+)$ at $T = 0$ as V is tuned across the QCP. Colored curves correspond to V values marked by ticks on the color bar. The layout mirrors that of Fig. 8 in the main text. Top row: imaginary parts; bottom row: real parts. The insets show the hybridization functions on a linear frequency scale for $|\omega| < 2 \cdot 10^{-4}$.

before periodization (see our discussion in Sec. VI B), i.e. $A_{c,\text{loc}}(0)$ increases as V approaches V_c (solid green curve lies above solid blue curve at $\omega = 0$); after periodization, the converse happens, i.e. $A_{c,\text{loc}}(0)$ decreases as V approaches V_c (dashed green curve lies below dashed blue curve at $\omega = 0$). Our periodization procedure thus misses the development of the Kondo-like peak in $A_{c,\text{loc}}$.

We emphasize that reperiodization is an ad-hoc post-processing procedure. Features in reperiodized data should always be substantiated by analyzing the raw data before reperiodization. We have done so repeatedly in the main text, for instance for the FS and LS volumes, the dispersive pole in Σ_f or the two and three-band structures in the Kondo and RKKY phases, respectively.

4. Self-consistent hybridization function versus V

In the main text, we emphasized the importance of self-consistency to access the KB–QCP in 2-site CDMFT. Here, we elaborate this aspect by showing that the self-consistent hybridization functions in the vicinity of the KB–QCP show (i) a strong ω-dependence and (ii) a strong V-dependence. This implies that self-consistency is of high importance if one wants to capture the KB–QCP.

Figure A.2 shows the hybridization functions at $T = 0$ on a logarithmic frequency scale, plotted for several different values of V close to the KB–QCP. As seen from the insets, showing the same data on a linear frequency scale, the hybridization functions have sharp features at low frequencies. The sharp features appear stretched out on the log scale of the main panels, which reveal

that for V very close to V_c (green, yellow), they occur at frequencies as low as $|\omega| \simeq 10^{-8}$. This shows that the hybridization functions of the effective 2IAM describing the self-consistent PAM depend strongly on frequency. For a non-self-consistent 2IKM with weakly frequency-dependent hyrbidization functions, it has been shown that the NFL fixed point and thus the QCP is unstable to the breaking of symmetries which are absent in our effective 2IAM [79, 80, 83, 86]. Our work implies that this conclusion does not generalize to the case of hybridization functions displaying a strong frequency dependence.

Figure A.2 shows that the hybridization functions are also strongly V-dependent, especially close to $\omega = 0$. A change of V by $5 \cdot 10^{-3}$ in the vicinity of the KB–QCP induces comparably large changes in the hybridization functions, of the order of 10^{-1} at some frequencies. Thus, close to the KB–QCP, a tiny change in V leads to a considerable readjustment of the self-consistent hybridization
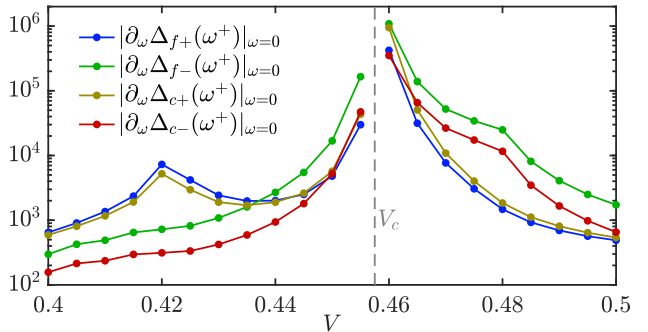
FIG. A.3. Absolute value of the derivative of the hybridization function as zero frequency, $|\partial_\omega \Delta_{x\alpha}(\omega^+)|_{\omega=0}$ at $T = 0$, plotted as a function of V.

function by iterating the CDMFT self-consistency cycle. This shows that self-consistency is of high importance to capture the KB–QCP.

In Figure A.3, we plot the absolute value of the derivative of the hybridization functions at $\omega = 0$, $|\partial_\omega \Delta_{x\alpha}(\omega^+)|_{\omega=0}$, at $T = 0$ as functions of V. The zero frequency derivative of the hybridization functions has a peak at the KB–QCP at V_c, indicative of a divergence. This suggests that the self-consistent hybridization functions become singular at $\omega = 0$ at the KB–QCP. This further emphasizes that (i) results obtained on the 2IAM with weakly frequency dependent hybridization functions are not straightforwardly applicable to the self-consistent 2IAM arising in our CDMFT solution of the PAM; and (ii) self-consistency is important to capture this singular behavior at the KB–QCP. A more detailed study investigating how the self-consistency equations manage to drive the 2IAM to a stable QCP will be subject to future work.

5. Transport properties

For the calculation of the resistivity and the Hall coefficient, the M-reperiodized self-energy is used. The formulas for the optical conductivity $\sigma(\omega)$ ignoring vertex corrections, resistivity $\rho_{xx} = 1/\sigma_{xx}$ and the Hall coefficient $R_\mathrm{H} = \sigma_{xy}/(\sigma_{xx}^2 H)$ are given by [221, 222]

$$\sigma(\omega) = 2\pi e^2 \int d\epsilon\, \Phi_{xx}(\epsilon)\tilde{\sigma}(\epsilon,\omega)\,,$$

$$\tilde{\sigma}(\epsilon,\omega) = \int d\widetilde{\omega}\, \frac{f(\widetilde{\omega}) - f(\widetilde{\omega}+\omega)}{\omega} A_c(\epsilon,\widetilde{\omega}) A_c(\epsilon,\widetilde{\omega}+\omega)\,,$$

$$\sigma_{xx} = \lim_{\omega\to 0}\sigma(\omega)\,,$$

$$\sigma_{xy} = \tfrac{4}{3}\pi^2 e^3 H \int d\epsilon\, \Phi_{xy}(\epsilon) \int d\omega \left[-\frac{\partial f}{\partial \omega}\right] A_c^3(\epsilon,\omega)\,,$$

$$\Phi_{xx}(\epsilon) = \int_{1.\mathrm{BZ}} \frac{d\mathbf{k}}{(2\pi)^3}\, (\epsilon_\mathbf{k}^x)^2\, \delta(\epsilon - \epsilon_{c\mathbf{k}})\,,$$

$$\Phi_{xy}(\epsilon) = \int_{1.\mathrm{BZ}} \frac{d\mathbf{k}}{(2\pi)^3} \begin{vmatrix} \epsilon_\mathbf{k}^x \epsilon_\mathbf{k}^x & \epsilon_\mathbf{k}^{xy} \\ \epsilon_\mathbf{k}^y \epsilon_\mathbf{k}^x & \epsilon_\mathbf{k}^{yy} \end{vmatrix} \delta(\epsilon - \epsilon_{c\mathbf{k}})\,,$$

(A10)

where H denotes the magnetic field, $e < 0$ the charge of the electrons, $f(\omega)$ the Fermi function, $\epsilon_\mathbf{k}^x = \partial_{k_x}\epsilon_{c\mathbf{k}}$ the derivative of the dispersion by k_x (and correspondingly for e.g. $\epsilon_\mathbf{k}^{xy}$) and $|\cdot|$ the determinant. In the above formulas, only the c-electron spectral function appears, as there are no terms involving the f electrons which do not conserve local charge. Note also that the $\mathbf{k}$-dependent spectral function depends on $\mathbf{k}$ only through $\epsilon_{c\mathbf{k}}$ after reperiodization via Eq. (A9).

Eqs. (A10) include only the bubble contribution to the conductivities and ignore vertex corrections. In a companion paper [148], we show that vertex corrections to the conductivity are qualitatively important in order to capture the correct scaling of the optical conductivity in
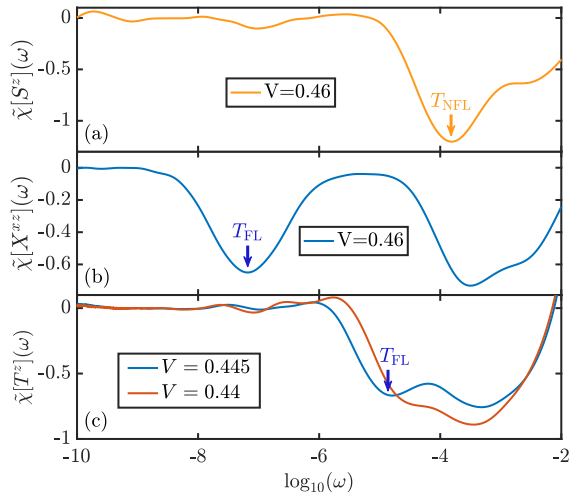
FIG. B.1. (a) $\tilde{\chi}[S^z](\omega)$ plotted versus $\ln_{10}(\omega)$ at $V = 0.46$ and $T = 0$. We extract the NFL scale from the position of the minimum marked by the orange arrow. (b) $\tilde{\chi}[X^{xz}](\omega)$ plotted versus $\ln_{10}(\omega)$ at $V = 0.46$ and $T = 0$. The FL scale is extracted from the position of the minimum marked by the blue arrow. Note that while the other minimum is associated with T_NFL, it is not used to extract this scale. (c) $\tilde{\chi}[T^z](\omega)$ plotted versus $\ln_{10}(\omega)$ at $V = 0.445$ and $V = 0.44$ at $T = 0$. While the FL scale can still be extracted from $\tilde{\chi}[T^z](\omega)$ at $V = 0.445$ because both minima in $\tilde{\chi}[T^z](\omega)$ are still clearly distinguishable, it is not possible any more for $V = 0.44$ as the minima have merged.

the NFL region. A full treatment of vertex corrections is currently computationally unfeasible with our NRG impurity solver because the computation of 4-point correlation functions for the 2IAM at hand is too expensive. To compute the Hall coefficient shown in Fig. 18, we have therefore *not* considered vertex corrections but just used the formulas presented in Eqs. (A10).

Appendix B: Determination of energy scales

To determine the crossover scales T_FL and T_NFL, we exploit the fact that the spectral functions of particular susceptibilities show a well-defined power law dependence in the fixed point regions, which changes when traversing the crossover regions. On a log-log scale this leads to straight lines with kinks in the crossover regions, as can be seen in Fig. 4 in the main text. The second derivative of $\chi''[O](\omega)$ on the log-log scale,

$$\tilde{\chi}[O](\omega) = \frac{\partial^2 \ln_{10}(\chi''[O](\omega))}{\partial \ln_{10}(\omega)^2}\,, \tag{B1}$$

tracks the change in slope at the crossover, enabling us to determine the corresponding scale. We use $\chi''[S^z]$ to determine the NFL scale and $\chi''[X^{xz}]$, $\chi''[T^z]$, $\chi''[T^y]$ and $\chi''[P^z]$ to determine the FL scale. The corresponding
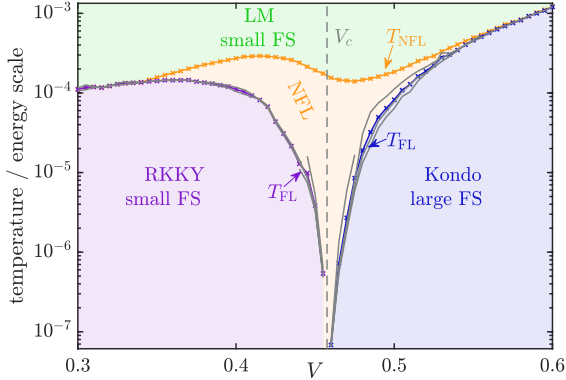
FIG. B.2. FL scales, extracted from different correlators (grey lines). For more information on the energy scales, see Fig. 2 in the main text and the corresponding discussion there.

operators are defined in Eq. (9) in the main text. $\chi''[X^{xz}]$, $\chi''[T^z]$, $\chi''[T^y]$ and $\chi''[P^z]$ are shown in Fig. 2.

Examples for the determination of the NFL scale via $\chi''[S^z]$ and of the FL scale via $\chi''[X^{xz}]$ are shown in Figs. B.1(a) and (b), respectively. While $\chi''[T^y]$ and $\chi''[P^z]$ are much smaller than $\chi''[T^z]$ and $\chi''[X^{xz}]$, they are more suitable than the latter two far away from the QCP, especially for $V < V_c$. The reason for this is shown in Fig. B.1(c) for $\chi''[T^z]$: the second derivative on the ln-ln scale shows two minima, the first related to T_{FL} and the second related to T_{NFL}. The same is true for $\chi''[X^{xz}]$ (not shown). These two minima merge away from the QCP, preventing the determination of T_{FL}. The determination via $\chi''[T^y]$ and $\chi''[P^z]$ is not faced with these difficulties, as they have only one minimum, associated with T_{FL}.

We note that the determination of T_{FL} via $\chi''[X^{xz}]$ works well in the Kondo regime for all V but in the RKKY regime only close to the QCP, while $\chi''[T^z]$ works only close to the QCP both in the Kondo and the RKKY regime. As the FL scale extracted from different correlators in are generally not exactly equal, we define T_{FL} as their geometric mean as shown in Fig. B.2. Each grey line there show a FL scale extracted from a different correlator, while the blue and purple lines show their geometric mean. The grey lines do not exactly lie on top of each other, but they are sufficiently similar to justify the averaging

described above.

Appendix C: Determination of T_{Hall}

Figure 2 includes data points (red dots) marked $T_{\mathrm{Hall}}(V)$, showing how the crossover from a large FS in the Kondo phase to a small FS in the RKKY phase evolve with temperature. Here, we describe how T_{Hall} was determined.

We closely follow the procedure used in Ref. 25. We fit our numerical V-dependent Hall coefficient data (see Fig. 18) at $T = 10^{-4}$, 10^{-5} and 10^{-6} to the form

$$\frac{R_H(V)}{R_{H,0}} \stackrel{\mathrm{fit}}{\simeq} a + \frac{b}{1 + (V/V_{\mathrm{Hall}})^p}, \qquad \text{(C1)}$$

with fit parameters a, b, p and V_{Hall}, i.e. we impose the same functional form as used in Ref. 25 (except for the different tuning parameter, V in our case and B-field in Ref. 25). To closely mirror the procedure used in Ref. 25, we constrain our fit for a given, fixed T to the crossover region from Kondo to RKKY regime by only fitting in a V-region determined by $T > 0.1 \cdot T_{\mathrm{FL}}(V)$ (i.e. we omit datap oints deep in the FL regions). This yields $V_{\mathrm{Hall}}(T)$, and inverting this function yields $T_{\mathrm{Hall}}(V)$. Figure C.1 shows our Hall effect data with the corresponding fits.
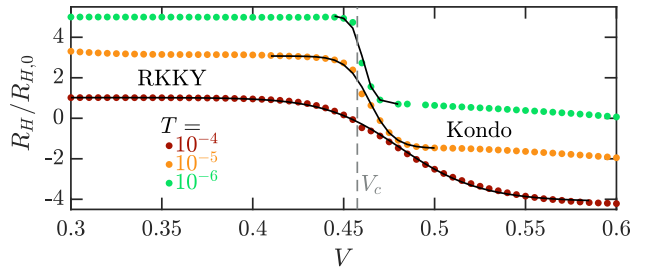
FIG. C.1. Hall coefficient data from Fig. 18 (symbols) and corresponding fits via Eq. (C1) (black lines). To improve visibility, the data for $T = 10^{-5}$ and $T = 10^{-6}$ is offset by 2 and 4, respectively.

[1] H. v. Löhneysen, A. Rosch, M. Vojta, and P. Wölfle, Fermi-liquid instabilities at magnetic quantum phase transitions, Rev. Mod. Phys. **79**, 1015 (2007).

[2] G. R. Stewart, Non-Fermi-liquid behavior in d- and f-electron metals, Rev. Mod. Phys. **73**, 797 (2001).

[3] S. Kirchner, S. Paschen, Q. Chen, S. Wirth, D. Feng, J. D. Thompson, and Q. Si, Colloquium: Heavy-electron quantum criticality and single-particle spectroscopy, Rev. Mod. Phys. **92**, 011002 (2020).

[4] P. Coleman, Heavy Fermions: Electrons at the edge of magnetism, in *Handbook of Magnetism and Advanced Magnetic Materials*, Vol. 1, edited by H. Kronmüller and

S. Parkin (Wiley, 2007) pp. 95–148.

[5] P. Coleman, C. Pépin, Q. Si, and R. Ramazashvili, How do Fermi liquids get heavy and die?, J. Phys. Condens. Matter **13**, R723 (2001).

[6] P. Coleman and C. Pépin, What is the fate of the heavy electron at a quantum critical point?, Physica B: Condensed Matter **312-313**, 383 (2002), the International Conference on Strongly Correlated Electron Systems.

[7] A. C. Hewson, *The Kondo Problem to Heavy Fermions*, Cambridge Studies in Magnetism (Cambridge University Press, 1993).

[8] J. M. Luttinger, Fermi surface and some simple equi-

librium properties of a system of interacting Fermions, Phys. Rev. **119**, 1153 (1960).

[9] M. Oshikawa, Topological approach to Luttinger's theorem and the Fermi surface of a Kondo lattice, Phys. Rev. Lett. **84**, 3370 (2000).

[10] I. Dzyaloshinskii, Some consequences of the Luttinger theorem: The Luttinger surfaces in non-Fermi liquids and Mott insulators, Phys. Rev. B **68**, 085113 (2003).

[11] O. J. Curtin, Y. Nishikawa, A. C. Hewson, and D. J. G. Crow, Fermi liquids and the Luttinger integral, Journal of Physics Communications **2**, 031001 (2018).

[12] Y. Nishikawa, O. J. Curtin, A. C. Hewson, and D. J. G. Crow, Magnetic field induced quantum criticality and the Luttinger sum rule, Phys. Rev. B **98**, 104419 (2018).

[13] J. T. Heath and K. S. Bedell, Necessary and sufficient conditions for the validity of Luttinger's theorem, New J. Phys. (2020).

[14] G. Giuliani and G. Vignale, *Quantum Theory of the Electron Liquid* (Cambridge University Press, 2005).

[15] M. A. Ruderman and C. Kittel, Indirect exchange coupling of nuclear magnetic moments by conduction electrons, Phys. Rev. **96**, 99 (1954).

[16] T. Kasuya, A theory of metallic ferro- and antiferromagnetism on Zener's model, Prog. Theor. Phys. **16**, 45 (1956).

[17] K. Yosida, Magnetic properties of Cu-Mn alloys, Phys. Rev. **106**, 893 (1957).

[18] A. Nejati, K. Ballmann, and J. Kroha, Kondo destruction in RKKY-coupled Kondo lattice and multi-impurity systems, Phys. Rev. Lett. **118**, 117204 (2017).

[19] S. Doniach, The Kondo lattice and weak antiferromagnetism, Physica **91B+C**, 231 (1977).

[20] J. A. Hertz, Quantum critical phenomena, Phys. Rev. B **14**, 1165 (1976).

[21] T. Moriya, *Spin fluctuations in itinerant electron magnetism* (Springer Verlag Berlin, 1985).

[22] A. J. Millis, Effect of a nonzero temperature on quantum critical points in itinerant Fermion systems, Phys. Rev. B **48**, 7183 (1993).

[23] S. Sachdev, *Quantum Phase Transitions*, 2nd ed. (Cambridge University Press, 2011).

[24] O. Trovarelli, C. Geibel, S. Mederle, C. Langhammer, F. M. Grosche, P. Gegenwart, M. Lang, G. Sparn, and F. Steglich, YbRh$_2$Si$_2$: Pronounced non-Fermi-liquid effects above a low-lying magnetic phase transition, Phys. Rev. Lett. **85**, 626 (2000).

[25] S. Paschen, T. Lühmann, S. Wirth, P. Gegenwart, O. Trovarelli, C. Geibel, F. Steglich, P. Coleman, and Q. Si, Hall-effect evolution across a heavy-Fermion quantum critical point, Nature **432**, 881 (2004).

[26] P. Gegenwart, Q. Si, and F. Steglich, Quantum criticality in heavy-Fermion metals, Nat. Phys. **4**, 186 (2008).

[27] J. Custers, P. Gegenwart, H. Wilhelm, K. Neumaier, Y. Tokiwa, O. Trovarelli, C. Geibel, F. Steglich, C. Pépin, and P. Coleman, The break-up of heavy electrons at a quantum critical point, Nature **424**, 524 (2003).

[28] H. Löhneysen, M. Sieck, O. Stockert, and M. Waffenschmidt, Investigation of non-Fermi-liquid behavior in CeCu$_{6-x}$Au$_x$, Physica B: Condensed Matter **223-224**, 471 (1996).

[29] H. Shishido, R. Settai, H. Harima, and Y. Ōnuki, A drastic change of the Fermi surface at a critical pressure in CeRhIn$_5$: dHvA study under pressure, Journal of the Physical Society of Japan **74**, 1103 (2005).

[30] L. Jiao, Y. Chen, Y. Kohama, D. Graf, E. D. Bauer, J. Singleton, J.-X. Zhu, Z. Weng, G. Pang, T. Shang, J. Zhang, H.-O. Lee, T. Park, M. Jaime, J. D. Thompson, F. Steglich, Q. Si, and H. Q. Yuan, Fermi surface reconstruction and multiple quantum phase transitions in the antiferromagnet CeRhIn$_5$, Proc. Natl. Acad. Sci. **112**, 673 (2015).

[31] N. Maksimovic, D. H. Eilbott, T. Cookmeyer, F. Wan, J. Rusz, V. Nagarajan, S. C. Haley, E. Maniv, A. Gong, S. Faubel, I. M. Hayes, A. Bangura, J. Singleton, J. C. Palmstrom, L. Winter, R. McDonald, S. Jang, P. Ai, Y. Lin, S. Ciocys, J. Gobbo, Y. Werman, P. M. Oppeneer, E. Altman, A. Lanzara, and J. G. Analytis, Evidence for a delocalization quantum phase transition without symmetry breaking in CeCoIn$_5$, Science **375**, 76 (2022).

[32] P. Gegenwart, J. Custers, C. Geibel, K. Neumaier, T. Tayama, K. Tenya, O. Trovarelli, and F. Steglich, Magnetic-field induced quantum critical point in YbRh$_2$Si$_2$, Phys. Rev. Lett. **89**, 056402 (2002).

[33] O. Stockert and F. Steglich, Unconventional quantum criticality in heavy-Fermion compounds, Annual Review of Condensed Matter Physics **2**, 79 (2011).

[34] K. Seki and S. Yunoki, Topological interpretation of the Luttinger theorem, Phys. Rev. B **96**, 085124 (2017).

[35] T. Hazra and P. Coleman, Luttinger sum rules and spin fractionalization in the SU(N) Kondo lattice, Phys. Rev. Res. **3**, 033284 (2021).

[36] S. Friedemann, N. Oeschler, S. Wirth, C. Krellner, C. Geibel, F. Steglich, S. Paschen, S. Kirchner, and Q. Si, Fermi-surface collapse and dynamical scaling near a quantum-critical point, Proc. Natl. Acad. Sci. **107**, 14547 (2010).

[37] R. Settai, H. Shishido, S. Ikeda, Y. Murakawa, M. Nakashima, D. Aoki, Y. Haga, H. Harima, and Y. Onuki, Quasi-two-dimensional Fermi surfaces and the de Haas-van Alphen oscillation in both the normal and superconducting mixed states of CeCoIn$_5$, Journal of Physics: Condensed Matter **13**, L627 (2001).

[38] H. Shishido, R. Settai, D. Aoki, S. Ikeda, H. Nakawaki, N. Nakamura, T. Iizuka, Y. Inada, K. Sugiyama, T. Takeuchi, K. Kindo, T. Kobayashi, Y. Haga, H. Harima, Y. Aoki, T. Namiki, H. Sato, and Y. Ōnuki, Fermi surface, magnetic and superconducting properties of LaRhIn$_5$ and CeTIn$_5$ (T: Co, Rh and Ir), Journal of the Physical Society of Japan **71**, 162 (2002).

[39] A. Koitzsch, I. Opahle, S. Elgazzar, S. V. Borisenko, J. Geck, V. B. Zabolotnyy, D. Inosov, H. Shiozawa, M. Richter, M. Knupfer, J. Fink, B. Büchner, E. D. Bauer, J. L. Sarrao, and R. Follath, Electronic structure of CeCoIn$_5$ from angle-resolved photoemission spectroscopy, Phys. Rev. B **79**, 075104 (2009).

[40] A. Koitzsch, S. V. Borisenko, D. Inosov, J. Geck, V. B. Zabolotnyy, H. Shiozawa, M. Knupfer, J. Fink, B. Büchner, E. D. Bauer, J. L. Sarrao, and R. Follath, Hybridization effects in CeCoIn$_5$ observed by angle-resolved photoemission, Phys. Rev. B **77**, 155128 (2008).

[41] Q. Y. Chen, D. F. Xu, X. H. Niu, J. Jiang, R. Peng, H. C. Xu, C. H. P. Wen, Z. F. Ding, K. Huang, L. Shu, Y. J. Zhang, H. Lee, V. N. Strocov, M. Shi, F. Bisti, T. Schmitt, Y. B. Huang, P. Dudin, X. C. Lai, S. Kirchner, H. Q. Yuan, and D. L. Feng, Direct observation of how the heavy-Fermion state develops in CeCoIn$_5$, Phys. Rev. B **96**, 045107 (2017).

[42] S. Jang, J. D. Denlinger, J. W. Allen, V. S. Zapf, M. B.

Maple, J. N. Kim, B. G. Jang, and J. H. Shim, Evolution of the Kondo lattice electronic structure above the transport coherence temperature, Proceedings of the National Academy of Sciences **117**, 23467 (2020).

[43] Q. Y. Chen, D. F. Xu, X. H. Niu, R. Peng, H. C. Xu, C. H. P. Wen, X. Liu, L. Shu, S. Y. Tan, X. C. Lai, Y. J. Zhang, H. Lee, V. N. Strocov, F. Bisti, P. Dudin, J.-X. Zhu, H. Q. Yuan, S. Kirchner, and D. L. Feng, Band dependent interlayer f-electron hybridization in CeRhIn$_5$, Phys. Rev. Lett. **120**, 066403 (2018).

[44] S. Danzenbächer, D. V. Vyalikh, K. Kummer, C. Krellner, M. Holder, M. Höppner, Y. Kucherenko, C. Geibel, M. Shi, L. Patthey, S. L. Molodtsov, and C. Laubschat, Insight into the f-derived Fermi surface of the heavy-Fermion compound YbRh$_2$Si$_2$, Phys. Rev. Lett. **107**, 267601 (2011).

[45] K. Kummer, S. Patil, A. Chikina, M. Güttler, M. Höppner, A. Generalov, S. Danzenbächer, S. Seiro, A. Hannaske, C. Krellner, Y. Kucherenko, M. Shi, M. Radovic, E. Rienks, G. Zwicknagl, K. Matho, J. W. Allen, C. Laubschat, C. Geibel, and D. V. Vyalikh, Temperature-independent Fermi surface in the Kondo lattice YbRh$_2$Si$_2$, Phys. Rev. X **5**, 011028 (2015).

[46] S. Paschen, S. Friedemann, S. Wirth, F. Steglich, S. Kirchner, and Q. Si, Kondo destruction in heavy Fermion quantum criticality and the photoemission spectrum of YbRh$_2$Si$_2$, Journal of Magnetism and Magnetic Materials **400**, 17 (2016).

[47] M. Güttler, K. Kummer, S. Patil, M. Höppner, A. Hannaske, S. Danzenbächer, M. Shi, M. Radovic, E. Rienks, C. Laubschat, C. Geibel, and D. V. Vyalikh, Tracing the localization of $4f$ electrons: Angle-resolved photoemission on YbCo$_2$Si$_2$, the stable trivalent counterpart of the heavy-Fermion YbRh$_2$Si$_2$, Phys. Rev. B **90**, 195138 (2014).

[48] S. Friedemann, T. Westerkamp, M. Brando, N. Oeschler, S. Wirth, P. Gegenwart, C. Krellner, C. Geibel, and F. Steglich, Detaching the antiferromagnetic quantum critical point from the Fermi-surface reconstruction in YbRh$_2$Si$_2$, Nat. Phys. **5**, 465 (2009).

[49] H. Zhao, J. Zhang, M. Lyu, S. Bachus, Y. Tokiwa, P. Gegenwart, S. Zhang, J. Cheng, Y.-f. Yang, G. Chen, Y. Isikawa, Q. Si, F. Steglich, and P. Sun, Quantum-critical phase from frustrated magnetism in a strongly correlated metal, Nat. Phys. **15**, 1261 (2019).

[50] S. J. Yamamoto and Q. Si, Global phase diagram of the Kondo lattice: From heavy Fermion metals to Kondo insulators, J Low Temp Phys **161**, 233 (2010).

[51] P. Aynajian, E. H. da Silva Neto, A. Gyenis, R. E. Baumbach, J. D. Thompson, Z. Fisk, E. D. Bauer, and A. Yazdani, Visualizing heavy Fermions emerging in a quantum critical Kondo lattice, Nature **486**, 201 (2012).

[52] M. Haze, R. Peters, Y. Torii, T. Suematsu, D. Sano, M. Naritsuka, Y. Kasahara, T. Shibauchi, T. Terashima, and Y. Matsuda, Direct evidence for the existence of heavy quasiparticles in the magnetically ordered phase of CeRhIn$_5$, Journal of the Physical Society of Japan **88**, 014706 (2019).

[53] S. Ernst, S. Kirchner, C. Krellner, C. Geibel, G. Zwicknagl, F. Steglich, and S. Wirth, Emerging local Kondo screening and spatial coherence in the heavy-Fermion metal YbRh$_2$Si$_2$, Nature **474**, 362 (2011).

[54] S. Seiro, L. Jiao, S. Kirchner, S. Hartmann, S. Friedemann, C. Krellner, C. Geibel, Q. Si, F. Steglich, and S. Wirth, Evolution of the Kondo lattice and non-Fermi liquid excitations in a heavy-Fermion metal, Nature Communications **9**, 3324 (2018).

[55] S. Kimura, T. Nishi, J. Sichelschmidt, V. Voevodin, J. Ferstl, C. Geibel, and F. Steglich, Optical conductivity of a non-Fermi-liquid material YbRh$_2$Si$_2$, Journal of Magnetism and Magnetic Materials **272-276**, 36 (2004).

[56] S. Kimura, J. Sichelschmidt, J. Ferstl, C. Krellner, C. Geibel, and F. Steglich, Optical observation of non-Fermi-liquid behavior in the heavy Fermion state of YbRh$_2$Si$_2$, Phys. Rev. B **74**, 132408 (2006).

[57] F. P. Mena, D. van der Marel, and J. L. Sarrao, Optical conductivity of CeMIn$_5$ (M = Co, Rh, Ir), Phys. Rev. B **72**, 045119 (2005).

[58] E. J. Singley, D. N. Basov, E. D. Bauer, and M. B. Maple, Optical conductivity of the heavy Fermion superconductor CeCoIn$_5$, Phys. Rev. B **65**, 161101 (2002).

[59] F. Marabelli and P. Wachter, Temperature dependence of the optical conductivity of the heavy-Fermion system CeCu$_6$, Phys. Rev. B **42**, 3307 (1990).

[60] L. Prochaska, X. Li, D. C. MacFarland, A. M. Andrews, M. Bonta, E. F. Bianco, S. Yazdi, W. Schrenk, H. Detz, A. Limbeck, Q. Si, E. Ringe, G. Strasser, J. Kono, and S. Paschen, Singular charge fluctuations at a magnetic quantum critical point, Science **367**, 285 (2020).

[61] H. von Löhneysen, Non-Fermi-liquid behaviour in the heavy-Fermion system, Journal of Physics: Condensed Matter **8**, 9689 (1996).

[62] J. Paglione, M. A. Tanatar, D. G. Hawthorn, E. Boaknin, R. W. Hill, F. Ronning, M. Sutherland, L. Taillefer, C. Petrovic, and P. C. Canfield, Field-induced quantum critical point in CeCoIn$_5$, Phys. Rev. Lett. **91**, 246405 (2003).

[63] T. Muramatsu, N. Tateiwa, T. Kobayashi, K. Shimizu, K. Amaya, D. Aoki, H. Shishido, Y. Haga, and Y. Ōnuki, Superconductivity of CeRhIn$_5$ under high pressure, Journal of the Physical Society of Japan **70**, 3362 (2001).

[64] A. Bianchi, R. Movshovich, I. Vekhter, P. G. Pagliuso, and J. L. Sarrao, Avoided antiferromagnetic order and quantum critical point in CeCoIn$_5$, Phys. Rev. Lett. **91**, 257001 (2003).

[65] L. Chen, D. T. Lowder, E. Bakali, A. M. Andrews, W. Schrenk, M. Waas, R. Svagera, G. Eguchi, L. Prochaska, Y. Wang, C. Setty, S. Sur, Q. Si, S. Paschen, and D. Natelson, Shot noise indicates the lack of quasiparticles in a strange metal 10.48550/arxiv.2206.00673 (2022).

[66] C. M. Varma, P. B. Littlewood, S. Schmitt-Rink, E. Abrahams, and A. E. Ruckenstein, Phenomenology of the normal state of Cu-O high-temperature superconductors, Phys. Rev. Lett. **63**, 1996 (1989).

[67] M. C. Aronson, R. Osborn, R. A. Robinson, J. W. Lynn, R. Chau, C. L. Seaman, and M. B. Maple, Non-Fermi-liquid scaling of the magnetic response in UCu$_{5-x}$Pd$_x$ (x = 1, 1.5), Phys. Rev. Lett. **75**, 725 (1995).

[68] A. Schröder, G. Aeppli, R. Coldea, M. Adams, O. Stockert, H. Löhneysen, E. Bucher, R. Ramazashvili, and P. Coleman, Onset of antiferromagnetism in heavy-Fermion metals, Nature **407**, 351 (2000).

[69] L. Poudel, J. M. Lawrence, L. S. Wu, G. Ehlers, Y. Qiu, A. F. May, F. Ronning, M. D. Lumsden, D. Mandrus, and A. D. Christianson, Multicomponent fluctuation spectrum at the quantum critical point in CeCu$_{6-x}$Ag$_x$, npj Quantum Materials **4**, 52 (2019).

[70] C.-J. Yang, S. Pal, F. Zamani, K. Kliemt, C. Krellner, O. Stockert, H. v. Löhneysen, J. Kroha, and M. Fiebig, Terahertz conductivity of heavy-Fermion systems from time-resolved spectroscopy, Phys. Rev. Research **2**, 033296 (2020).

[71] Q. Si, J. H. Pixley, E. Nica, S. J. Yamamoto, P. Goswami, R. Yu, and S. Kirchner, Kondo destruction and quantum criticality in Kondo lattice systems, Journal of the Physical Society of Japan **83**, 061005 (2014).

[72] D. Chowdhury, A. Georges, O. Parcollet, and S. Sachdev, Sachdev-Ye-Kitaev models and beyond: Window into non-Fermi liquids, Rev. Mod. Phys. **94**, 035004 (2022).

[73] M. Vojta, Impurity quantum phase transitions, Philos. Mag. **86**, 1807 (2006).

[74] A. M. Tsvelick and P. B. Wiegmann, Solution of the n-channel Kondo problem (scaling and integrability), Z. Phys. B **54**, 201 (1984).

[75] A. M. Tsvelick, The thermodynamics of multichannel Kondo problem, J. Phys. C: Solid State Phys. **18**, 159 (1985).

[76] V. J. Emery and S. Kivelson, Mapping of the two-channel Kondo problem to a resonant-level model, Phys. Rev. B **46**, 10812 (1992).

[77] P. Coleman, L. B. Ioffe, and A. M. Tsvelik, Simple formulation of the two-channel Kondo model, Phys. Rev. B **52**, 6611 (1995).

[78] J. Gan, Solution of the two-impurity Kondo model: Critical point, Fermi-liquid phase, and crossover, Phys. Rev. B **51**, 8287 (1995).

[79] O. Sakai, Y. Shimizu, and T. Kasuya, Excitation spectra of two impurity Anderson model, Solid State Communications **75**, 81 (1990).

[80] O. Sakai and Y. Shimizu, Excitation spectra of the two impurity Anderson model. I. Critical transition in the two magnetic impurity problem and the roles of the parity splitting, Journal of the Physical Society of Japan **61**, 2333 (1992).

[81] M. Fabrizio, A. F. Ho, L. D. Leo, and G. E. Santoro, Nontrivial fixed point in a twofold orbitally degenerate Anderson impurity model, Phys. Rev. Lett. **91**, 246402 (2003).

[82] L. D. Leo and M. Fabrizio, Spectral properties of a two-orbital Anderson impurity model across a non-Fermi-liquid fixed point, Phys. Rev. B **69**, 245114 (2004).

[83] J. B. Silva, W. L. C. Lima, W. C. Oliveira, J. L. N. Mello, L. N. Oliveira, and J. W. Wilkins, Particle-hole asymmetry in the two-impurity Kondo model, Phys. Rev. Lett. **76**, 275 (1996).

[84] I. Affleck and A. W. W. Ludwig, Exact critical theory of the two-impurity Kondo model, Phys. Rev. Lett. **68**, 1046 (1992).

[85] I. Affleck, A. W. W. Ludwig, and B. A. Jones, Conformal-field-theory approach to the two-impurity Kondo problem: Comparison with numerical renormalization-group results, Phys. Rev. B **52**, 9528 (1995).

[86] B. A. Jones, Kondo effect, in *Handbook of Magnetism and Advanced Magnetic Materials*, Vol. 1, edited by H. Kronmüller and S. Parkin (Wiley, 2007).

[87] K. P. Wójcik and J. Kroha, Quantum spin liquid in an RKKY-coupled two-impurity Kondo system, Phys. Rev. B **107**, L121111 (2023).

[88] K. P. Wójcik and J. Kroha, Asymmetry effects on the phases of RKKY-coupled two-impurity Kondo systems, Phys. Rev. B **107**, 125146 (2023).

[89] D. V. Else, R. Thorngren, and T. Senthil, Non-Fermi liquids as ersatz Fermi liquids: General constraints on compressible metals, Phys. Rev. X **11**, 021005 (2021).

[90] D. V. Else and T. Senthil, Strange metals as ersatz Fermi liquids, Phys. Rev. Lett. **127**, 086601 (2021).

[91] A. A. Patel, H. Guo, I. Esterlis, and S. Sachdev, Universal theory of strange metals from spatially random interactions, Science **381**, 790 (2023).

[92] F. F. Assaad, Quantum Monte Carlo simulations of the half-filled two-dimensional Kondo lattice model, Phys. Rev. Lett. **83**, 796 (1999).

[93] F. F. Assaad, Coherence scale of the two-dimensional Kondo lattice model, Phys. Rev. B **70**, 020402 (2004).

[94] S. Capponi and F. F. Assaad, Spin and charge dynamics of the ferromagnetic and antiferromagnetic two-dimensional half-filled Kondo lattice model, Phys. Rev. B **63**, 155114 (2001).

[95] E. Berg, S. Lederer, Y. Schattner, and S. Trebst, Monte Carlo studies of quantum critical metals, Annual Review of Condensed Matter Physics **10**, 63 (2019).

[96] F. Parisen Toldin, T. Sato, and F. F. Assaad, Mutual information in heavy-Fermion systems, Phys. Rev. B **99**, 155158 (2019).

[97] B. Danu, M. Vojta, F. F. Assaad, and T. Grover, Kondo breakdown in a spin-1/2 chain of adatoms on a Dirac semimetal, Phys. Rev. Lett. **125**, 206602 (2020).

[98] B. Danu, Z. Liu, F. F. Assaad, and M. Raczkowski, Zooming in on heavy Fermions in Kondo lattice models, Phys. Rev. B **104**, 155128 (2021).

[99] B. Danu, M. Vojta, T. Grover, and F. F. Assaad, Spin chain on a metallic surface: Dissipation-induced order versus Kondo entanglement, Phys. Rev. B **106**, L161103 (2022).

[100] B. Frank, Z. H. Liu, F. F. Assaad, M. Vojta, and L. Janssen, Marginal Fermi liquid at magnetic quantum criticality from dimensional confinement, Phys. Rev. B **108**, L100405 (2023).

[101] Z. H. Liu, B. Frank, L. Janssen, M. Vojta, and F. F. Assaad, Magnetic quantum phase transition in a metallic Kondo heterostructure, Phys. Rev. B **107**, 165104 (2023).

[102] A. Gleis, J.-W. Li, and J. von Delft, Controlled bond expansion for density matrix renormalization group ground state search at single-site costs, Phys. Rev. Lett. **130**, 246402 (2023).

[103] P. Coleman, New approach to the mixed-valence problem, Phys. Rev. B **29**, 3035 (1984).

[104] S. Burdin, D. R. Grempel, and A. Georges, Heavy-fermion and spin-liquid behavior in a Kondo lattice with magnetic frustration, Phys. Rev. B **66**, 045111 (2002).

[105] T. Senthil, S. Sachdev, and M. Vojta, Fractionalized Fermi liquids, Phys. Rev. Lett. **90**, 216403 (2003).

[106] T. Senthil, M. Vojta, and S. Sachdev, Weak magnetism and non-Fermi liquids near heavy-Fermion critical points, Phys. Rev. B **69**, 035111 (2004).

[107] C. Pépin, Fractionalization and Fermi-surface volume in heavy-Fermion compounds: The case of YbRh$_2$Si$_2$, Phys. Rev. Lett. **94**, 066402 (2005).

[108] M. Vojta, Orbital-selective Mott transitions: Heavy Fermions and beyond, Journal of Low Temperature Physics **161**, 203 (2010).

[109] C. Pépin, Kondo breakdown as a selective Mott transition in the Anderson lattice, Phys. Rev. Lett. **98**, 206401 (2007).

[110] E. E. Aldape, T. Cookmeyer, A. A. Patel, and E. Altman,

Solvable theory of a strange metal at the breakdown of a heavy Fermi liquid, Phys. Rev. B **105**, 235111 (2022).

[111] P. Bonderson, M. Cheng, K. Patel, and E. Plamadeala, Topological enrichment of Luttinger's theorem, (2016), arXiv:1601.07902 [cond-mat.str-el].

[112] P. Coleman, J. B. Marston, and A. J. Schofield, Transport anomalies in a simplified model for a heavy-electron quantum critical point, Phys. Rev. B **72**, 245111 (2005).

[113] D. H. Nguyen, A. Sidorenko, M. Taupin, G. Knebel, G. Lapertot, E. Schuberth, and S. Paschen, Superconductivity in an extreme strange metal, Nature Communications **12**, 4341 (2021).

[114] A. Georges, G. Kotliar, W. Krauth, and M. J. Rozenberg, Dynamical mean-field theory of strongly correlated Fermion systems and the limit of infinite dimensions, Rev. Mod. Phys. **68**, 13 (1996).

[115] G. Kotliar, S. Y. Savrasov, K. Haule, V. S. Oudovenko, O. Parcollet, and C. A. Marianetti, Electronic structure calculations with dynamical mean-field theory, Rev. Mod. Phys. **78**, 865 (2006).

[116] G. Kotliar, S. Y. Savrasov, G. Pálsson, and G. Biroli, Cellular dynamical mean field approach to strongly correlated systems, Phys. Rev. Lett. **87**, 186401 (2001).

[117] T. Maier, M. Jarrell, T. Pruschke, and M. H. Hettler, Quantum cluster theories, Rev. Mod. Phys. **77**, 1027 (2005).

[118] G. Rohringer, H. Hafermann, A. Toschi, A. A. Katanin, A. E. Antipov, M. I. Katsnelson, A. I. Lichtenstein, A. N. Rubtsov, and K. Held, Diagrammatic routes to nonlocal correlations beyond dynamical mean field theory, Rev. Mod. Phys. **90**, 025003 (2018).

[119] Q. Si, S. Rabello, K. Ingersent, and J. L. Smith, Locally critical quantum phase transitions in strongly correlated metals, Nature **413**, 804 (2001).

[120] P. Sun and G. Kotliar, Extended dynamical mean field theory study of the periodic Anderson model, Phys. Rev. Lett. **91**, 037209 (2003).

[121] L. de' Medici, A. Georges, G. Kotliar, and S. Biermann, Mott transition and Kondo screening in f-electron metals, Phys. Rev. Lett. **95**, 066402 (2005).

[122] P. Sun and G. Kotliar, Understanding the heavy Fermion phenomenology from a microscopic model, Phys. Rev. Lett. **95**, 016402 (2005).

[123] T. Schäfer, A. Katanin, M. Kitatani, A. Toschi, and K. Held, Quantum criticality in the two-dimensional periodic Anderson model, Phys. Rev. Lett. **122**, 227201 (2019).

[124] H. Hu, A. Cai, and Q. Si, Quantum criticality and dynamical Kondo effect in an SU(2) Anderson lattice model, arxiv:2004.04679 (2020).

[125] Ž. Osolin and R. Žitko, Fine structure of the spectra of the Kondo lattice model: Two-site cellular dynamical mean-field theory study, Phys. Rev. B **95**, 035107 (2017).

[126] D. Tanasković, K. Haule, G. Kotliar, and V. Dobrosavljević, Phase diagram, energy scales, and nonlocal correlations in the Anderson lattice model, Phys. Rev. B **84**, 115105 (2011).

[127] L. De Leo, M. Civelli, and G. Kotliar, $T = 0$ heavy-Fermion quantum critical point as an orbital-selective Mott transition, Phys. Rev. Lett. **101**, 256404 (2008).

[128] L. De Leo, M. Civelli, and G. Kotliar, Cellular dynamical mean-field theory of the periodic Anderson model, Phys. Rev. B **77**, 075107 (2008).

[129] Q. Si, J. L. Smith, and K. Ingersent, Quantum critical behavior in Kondo systems, International Journal of Modern Physics B **13**, 2331 (1999).

[130] J. L. Smith and Q. Si, Spatial correlations in dynamical mean-field theory, Phys. Rev. B **61**, 5184 (2000).

[131] Q. Si, S. Rabello, K. Ingersent, and J. L. Smith, Local fluctuations in quantum critical metals, Phys. Rev. B **68**, 115103 (2003).

[132] J.-X. Zhu, D. R. Grempel, and Q. Si, Continuous quantum phase transition in a Kondo lattice model, Phys. Rev. Lett. **91**, 156404 (2003).

[133] M. T. Glossop and K. Ingersent, Magnetic quantum phase transition in an anisotropic Kondo lattice, Phys. Rev. Lett. **99**, 227203 (2007).

[134] A. Cai, Z. Yu, H. Hu, S. Kirchner, and Q. Si, Dynamical scaling of charge and spin responses at a Kondo destruction quantum critical point, Phys. Rev. Lett. **124**, 027205 (2020).

[135] H. Hu, A. Cai, L. Chen, L. Deng, J. H. Pixley, K. Ingersent, and Q. Si, Unconventional superconductivity from Fermi surface fluctuations in strongly correlated metals (2021), arXiv:2109.13224 [cond-mat.str-el].

[136] H. Hu, A. Cai, L. Chen, and Q. Si, Spin-singlet and spin-triplet pairing correlations in antiferromagnetically coupled Kondo systems (2021), arXiv:2109.12794 [cond-mat.str-el].

[137] A. Kandala, H. Hu, Q. Si, and K. Ingersent, Dynamical Planckian scaling of charge response at a particle-hole-asymmetric quantum critical point with Kondo destruction (2022), arXiv:2206.01174 [cond-mat.str-el].

[138] H. Hu, L. Chen, and Q. Si, Extended dynamical mean field theory for correlated electron models (2022), arXiv:2210.14197 [cond-mat.str-el].

[139] H. Hu, L. Chen, and Q. Si, Quantum critical metals: Dynamical Planckian scaling and loss of quasiparticles (2022), arXiv:2210.14183 [cond-mat.str-el].

[140] P. Sun and G. Kotliar, Consequences of the local spin self-energy approximation on the heavy-Fermion quantum phase transition, Phys. Rev. B **71**, 245104 (2005).

[141] Q. Si, J.-X. Zhu, and D. R. Grempel, Magnetic quantum phase transitions in Kondo lattices, Journal of Physics: Condensed Matter **17**, R1025 (2005).

[142] L. C. Martin and F. F. Assaad, Evolution of the Fermi surface across a magnetic order-disorder transition in the two-dimensional Kondo lattice model: A dynamical cluster approach, Phys. Rev. Lett. **101**, 066404 (2008).

[143] L. C. Martin, M. Bercx, and F. F. Assaad, Fermi surface topology of the two-dimensional Kondo lattice model: Dynamical cluster approximation approach, Phys. Rev. B **82**, 245105 (2010).

[144] K. G. Wilson, The renormalization group: Critical phenomena and the Kondo problem, Rev. Mod. Phys. **47**, 773 (1975).

[145] R. Bulla, T. A. Costi, and T. Pruschke, Numerical renormalization group method for quantum impurity systems, Rev. Mod. Phys. **80**, 395 (2008).

[146] P. Coleman and A. H. Nevidomskyy, Frustration and the Kondo effect in heavy Fermion materials, J Low Temp Phys **161**, 182 (2010).

[147] M. Fabrizio, Spin-liquid insulators can be Landau's Fermi liquids, Phys. Rev. Lett. **130**, 156702 (2023).

[148] A. Gleis, S.-S. B. Lee, G. Kotliar, and J. von Delft, to be published (2023).

[149] B. A. Jones, C. M. Varma, and J. W. Wilkins, Low-temperature properties of the two-impurity Kondo

Hamiltonian, Phys. Rev. Lett. **61**, 125 (1988).

[150] B. A. Jones and C. M. Varma, Critical point in the solution of the two magnetic impurity problem, Phys. Rev. B **40**, 324 (1989).

[151] A. K. Mitchell and E. Sela, Universal low-temperature crossover in two-channel Kondo models, Phys. Rev. B **85**, 235127 (2012).

[152] A. K. Mitchell, E. Sela, and D. E. Logan, Two-channel Kondo physics in two-impurity Kondo models, Phys. Rev. Lett. **108**, 086405 (2012).

[153] T. D. Stanescu, M. Civelli, K. Haule, and G. Kotliar, A cellular dynamical mean field theory approach to Mottness, Ann. Phys. **321**, 1682 (2006).

[154] T. D. Stanescu and G. Kotliar, Fermi arcs and hidden zeros of the Green function in the pseudogap state, Phys. Rev. B **74**, 125110 (2006).

[155] A. Weichselbaum and J. von Delft, Sum-rule conserving spectral functions from the numerical renormalization group, Phys. Rev. Lett. **99**, 076402 (2007).

[156] A. Weichselbaum, Tensor networks and the numerical renormalization group, Phys. Rev. B **86**, 245124 (2012).

[157] S.-S. B. Lee and A. Weichselbaum, Adaptive broadening to improve spectral resolution in the numerical renormalization group, Phys. Rev. B **94**, 235127 (2016).

[158] A. K. Mitchell, M. R. Galpin, S. Wilson-Fletcher, D. E. Logan, and R. Bulla, Generalized Wilson chain for solving multichannel quantum impurity problems, Phys. Rev. B **89**, 121105 (2014).

[159] K. M. Stadler, A. K. Mitchell, J. von Delft, and A. Weichselbaum, Interleaved numerical renormalization group as an efficient multiband impurity solver, Phys. Rev. B **93**, 235101 (2016).

[160] A. Weichselbaum, Non-Abelian symmetries in tensor networks: A quantum symmetry space approach, Ann. of Phys. **327**, 2972 (2012).

[161] A. Weichselbaum, X-symbols for non-Abelian symmetries in tensor networks, Phys. Rev. Research **2**, 023385 (2020).

[162] J. von Delft, G. Zaránd, and M. Fabrizio, Finite-size bosonization of 2-channel Kondo model: A bridge between numerical renormalization group and conformal field theory, Phys. Rev. Lett. **81**, 196 (1998).

[163] N. Andrei and C. Destri, Solution of the multichannel Kondo problem, Phys. Rev. Lett. **52**, 364 (1984).

[164] P. Sacramento and P. Schlottmann, The quadrupolar Kondo effect: Lattice instability and large γ-values, Phys. Lett. A **142**, 245 (1989).

[165] P. D. Sacramento and P. Schlottmann, Low-temperature properties of a two-level system interacting with conduction electrons: An application of the overcompensated multichannel Kondo model, Phys. Rev. B **43**, 13294 (1991).

[166] I. Affleck and A. W. Ludwig, Critical theory of overscreened Kondo fixed points, Nucl. Phys. B **360**, 641 (1991).

[167] I. Affleck and A. W. W. Ludwig, Universal noninteger "ground-state degeneracy" in critical quantum systems, Phys. Rev. Lett. **67**, 161 (1991).

[168] R. M. Fye, "anomalous fixed point behavior" of two Kondo impurities: A reexamination, Phys. Rev. Lett. **72**, 916 (1994).

[169] B. Lechtenberg, F. Eickhoff, and F. B. Anders, Realistic quantum critical point in one-dimensional two-impurity models, Phys. Rev. B **96**, 041109 (2017).

[170] F. Eickhoff and F. B. Anders, Strongly correlated multi-impurity models: The crossover from a single-impurity problem to lattice models, Phys. Rev. B **102**, 205132 (2020).

[171] A. Abrikosov, L. Gorkov, I. Dzyaloshinski, and R. Silverman, *Methods of Quantum Field Theory in Statistical Physics* (Prentice-Hall, Englewood Cliffs, NJ, 1963).

[172] M. Fabrizio, Landau-Fermi liquids without quasiparticles, Phys. Rev. B **102**, 155122 (2020).

[173] J. Skolimowski and M. Fabrizio, Luttinger's theorem in the presence of Luttinger surfaces, Phys. Rev. B **106**, 045109 (2022).

[174] A. Cai, H. Hu, K. Ingersent, S. Paschen, and Q. Si, Dynamical Kondo effect and Kondo destruction in effective models for quantum-critical heavy Fermion metals (2019), arxiv:1904.11471 [cond-mat.str-el].

[175] S. Pairault, D. Sénéchal, and A.-M. S. Tremblay, Strong-coupling expansion for the Hubbard model, Phys. Rev. Lett. **80**, 5389 (1998).

[176] P. Pudleiner, T. Schäfer, D. Rost, G. Li, K. Held, and N. Blümer, Momentum structure of the self-energy and its parametrization for the two-dimensional Hubbard model, Phys. Rev. B **93**, 195134 (2016).

[177] N. Wagner, L. Crippa, A. Amaricci, P. Hansmann, M. Klett, E. König, T. Schäfer, D. D. Sante, J. Cano, A. Millis, A. Georges, and G. Sangiovanni, Mott insulators with boundary zeros (2023), arXiv:2301.05588 [cond-mat.str-el].

[178] E. W. Huang, G. L. Nave, and P. W. Phillips, Discrete symmetry breaking defines the Mott quartic fixed point, Nature Physics **18**, 511 (2022).

[179] J. Zhao, G. L. Nave, and P. Phillips, Proof of a stable fixed point for strongly correlated electron matter, (2023), arXiv:2304.04787 [cond-mat.str-el].

[180] P. Hořava, Stability of Fermi surfaces and k theory, Phys. Rev. Lett. **95**, 016405 (2005).

[181] F. B. Kugler and G. Kotliar, Is the orbital-selective Mott phase stable against interorbital hopping?, Phys. Rev. Lett. **129**, 096403 (2022).

[182] R. Yu and Q. Si, Orbital-selective Mott phase in multiorbital models for iron pnictides and chalcogenides, Phys. Rev. B **96**, 125110 (2017).

[183] A. C. Hewson, Renormalized perturbation expansions and Fermi liquid theory, Phys. Rev. Lett. **70**, 4007 (1993).

[184] A. C. Hewson, A. Oguri, and D. Meyer, Renormalized parameters for impurity models, Eur. Phys. J. B **40**, 177 (2004).

[185] T. D. Stanescu and G. Kotliar, Strong coupling theory for interacting lattice models, Phys. Rev. B **70**, 205112 (2004).

[186] R. M. Martin, Fermi-surface sum rule and its consequences for periodic Kondo and mixed-valence systems, Phys. Rev. Lett. **48**, 362 (1982).

[187] P. Gegenwart, J. Custers, T. Tayama, K. Tenya, C. Geibel, O. Trovarelli, F. Steglich, and K. Neumaier, Divergence of the heavy quasiparticle mass at the antiferromagnetic quantum critical point in $YbRh_2Si_2$, Acta Physica Polonica Series B **B34**, 323 (2003).

[188] C. Krellner, S. Hartmann, A. Pikul, N. Oeschler, J. G. Donath, C. Geibel, F. Steglich, and J. Wosnitza, Violation of critical universality at the antiferromagnetic phase transition of $YbRh_2Si_2$, Phys. Rev. Lett. **102**, 196402 (2009).

[189] P. Coleman, I. Paul, and J. Rech, Sum rules and Ward identities in the Kondo lattice, Phys. Rev. B **72**, 094430 (2005).

[190] S. Powell, S. Sachdev, and H. P. Büchler, Depletion of the Bose-Einstein condensate in Bose-Fermi mixtures, Phys. Rev. B **72**, 024534 (2005).

[191] J. M. Luttinger, Analytic properties of single-particle propagators for many-Fermion systems, Phys. Rev. **121**, 942 (1961).

[192] M. Potthoff, Non-perturbative construction of the Luttinger-Ward functional, Condens. Mat. Phys. **9**, 557 (2006).

[193] E. Kozik, M. Ferrero, and A. Georges, Nonexistence of the Luttinger-Ward functional and misleading convergence of skeleton diagrammatic series for Hubbard-like models, Phys. Rev. Lett. **114**, 156402 (2015).

[194] W. Tarantino, P. Romaniello, J. A. Berger, and L. Reining, Self-consistent Dyson equation and self-energy functionals: An analysis and illustration on the example of the Hubbard atom, Phys. Rev. B **96**, 045124 (2017).

[195] O. Gunnarsson, G. Rohringer, T. Schäfer, G. Sangiovanni, and A. Toschi, Breakdown of traditional many-body theories for correlated electrons, Phys. Rev. Lett. **119**, 056402 (2017).

[196] K. B. Dave, P. W. Phillips, and C. L. Kane, Absence of Luttinger's theorem due to zeros in the single-particle Green function, Phys. Rev. Lett. **110**, 090403 (2013).

[197] B. L. Altshuler, A. V. Chubukov, A. Dashevskii, A. M. Finkel'stein, and D. K. Morr, Luttinger theorem for a spin-density-wave state, Europhysics Letters **41**, 401 (1998).

[198] A. Rosch, Breakdown of Luttinger's theorem in two-orbital Mott insulators, Eur. Phys. J. B **59**, 495 (2007).

[199] S. Friedemann, Electrical transport and quantum criticality in pure and substituted YbRh$_2$Si$_2$, Ph.D. Thesis (Technische Universität Dresden) (2009).

[200] T. Namiki, H. Sato, J. Urakawa, H. Sugawara, Y. Aoki, R. Settai, and Y. Anuki, Hall effect and thermoelectric power in CeCu$_{5.9}$Au$_{0.1}$ and CeCu$_6$, Physica B: Condensed Matter **281-282**, 359 (2000).

[201] A. Gleis, G. Kotliar, and J. von Delft, to be published (2023).

[202] T. A. Costi, A. C. Hewson, and V. Zlatić, Transport coefficients of the Anderson model via the numerical renormalization group, J. Phys. C **6**, 2519 (1994).

[203] M. B. Maple, M. C. de Andrade, J. Herrmann, Y. Dalichaouch, D. A. Gajewski, C. L. Seaman, R. Chau, R. Movshovich, M. C. Aronson, and R. Osborn, Non Fermi liquid ground states in strongly correlated f-electron materials, Journal of Low Temperature Physics **99**, 223 (1995).

[204] M. Maple, R. E. Baumbach, N. P. Butch, J. J. Hamlin, and M. Janoschek, Non-Fermi liquid regimes and superconductivity in the low temperature phase diagrams of strongly correlated d- and f-electron materials, Journal of Low Temperature Physics **161**, 4 (2010).

[205] P. Gegenwart, Y. Tokiwa, T. Westerkamp, F. Weickert, J. Custers, J. Ferstl, C. Krellner, C. Geibel, P. Kerschl, K.-H. Müller, and F. Steglich, High-field phase diagram of the heavy-Fermion metal YbRh$_2$Si$_2$, New J. Phys. **8**, 171 (2006).

[206] A. M. Sengupta and A. Georges, Emery-Kivelson solution of the two-channel Kondo problem, Phys. Rev. B **49**, 10020 (1994).

[207] Y. Wang, E. Walter, S.-S. B. Lee, K. M. Stadler, J. von Delft, A. Weichselbaum, and G. Kotliar, Global phase diagram of a spin-orbital Kondo impurity model and the suppression of Fermi-liquid scale, Phys. Rev. Lett. **124**, 136406 (2020).

[208] E. Walter, K. M. Stadler, S.-S. B. Lee, Y. Wang, G. Kotliar, A. Weichselbaum, and J. von Delft, Uncovering non-Fermi-liquid behavior in Hund metals: Conformal field theory analysis of an SU(2)×SU(3) spin-orbital Kondo model, Phys. Rev. X **10**, 031052 (2020).

[209] M. Fabrizio, Emergent quasiparticles at Luttinger surfaces, Nature Communications **13**, 1561 (2022).

[210] B. Michon, C. Girod, S. Badoux, J. Kačmarčík, Q. Ma, M. Dragomir, H. A. Dabkowska, B. D. Gaulin, J.-S. Zhou, S. Pyon, T. Takayama, H. Takagi, S. Verret, N. Doiron-Leyraud, C. Marcenat, L. Taillefer, and T. Klein, Thermodynamic signatures of quantum criticality in cuprate superconductors, Nature **567**, 218 (2019).

[211] B. Keimer, S. A. Kivelson, M. R. Norman, S. Uchida, and J. Zaanen, From quantum matter to high-temperature superconductivity in copper oxides, Nature **518**, 179 (2015).

[212] B. Michon, C. Berthod, C. W. Rischau, A. Ataei, L. Chen, S. Komiya, S. Ono, L. Taillefer, D. van der Marel, and A. Georges, Reconciling scaling of the optical conductivity of cuprate superconductors with Planckian resistivity and specific heat, Nature Communications **14**, 3033 (2023).

[213] S. Badoux, W. Tabis, F. Laliberté, G. Grissonnanche, B. Vignolle, D. Vignolles, J. Béard, D. A. Bonn, W. N. Hardy, R. Liang, N. Doiron-Leyraud, L. Taillefer, and C. Proust, Change of carrier density at the pseudogap critical point of a cuprate superconductor, Nature **531**, 210 (2016).

[214] A. Legros, S. Benhabib, W. Tabis, F. Laliberté, M. Dion, M. Lizaire, B. Vignolle, D. Vignolles, H. Raffy, Z. Z. Li, P. Auban-Senzier, N. Doiron-Leyraud, P. Fournier, D. Colson, L. Taillefer, and C. Proust, Universal T-linear resistivity and Planckian dissipation in overdoped cuprates, Nature Physics **15**, 142 (2019).

[215] X. Li, J. Kono, Q. Si, and S. Paschen, Is the optical conductivity of heavy fermion strange metals Planckian?, Frontiers in Electronic Materials **2** (2023).

[216] Y. Cao, V. Fatemi, S. Fang, K. Watanabe, T. Taniguchi, E. Kaxiras, and P. Jarillo-Herrero, Unconventional superconductivity in magic-angle graphene superlattices, Nature **556**, 43 (2018).

[217] Y. Cao, D. Chowdhury, D. Rodan-Legrain, O. Rubies-Bigorda, K. Watanabe, T. Taniguchi, T. Senthil, and P. Jarillo-Herrero, Strange metal in magic-angle graphene with near Planckian dissipation, Phys. Rev. Lett. **124**, 076801 (2020).

[218] A. Jaoui, I. Das, G. Di Battista, J. Díez-Mérida, X. Lu, K. Watanabe, T. Taniguchi, H. Ishizuka, L. Levitov, and D. K. Efetov, Quantum critical behaviour in magic-angle twisted bilayer graphene, Nature Physics **18**, 633 (2022).

[219] P. E. Blöchl, O. Jepsen, and O. K. Andersen, Improved tetrahedron method for Brillouin-zone integrations, Phys. Rev. B **49**, 16223 (1994).

[220] S. Kaprzyk, An algebraic formulation and implementation of the tetrahedron linear method for the Brillouin zone integration of spectral functions, Comput. Phys. Commun. **183**, 347 (2012).

[221] P. Voruganti, A. Golubentsev, and S. John, Conductivity

and Hall effect in the two-dimensional Hubbard model, Phys. Rev. B **45**, 13945 (1992).

[222] E. Lange and G. Kotliar, Magnetotransport in the doped Mott insulator, Phys. Rev. B **59**, 1800 (1999).

Dynamical scaling and Planckian dissipation due to heavy-fermion quantum criticality

Andreas Gleis,[1, *] Seung-Sup B. Lee,[1, 2, 3, †] Gabriel Kotliar,[4, 5, ‡] and Jan von Delft[1, §]

[1]*Arnold Sommerfeld Center for Theoretical Physics, Center for NanoScience, and Munich Center for
Quantum Science and Technology, Ludwig-Maximilians-Universität München, 80333 Munich, Germany*
[2]*Department of Physics and Astronomy, Seoul National University, Seoul 08826, Korea*
[3]*Center for Theoretical Physics, Seoul National University, Seoul 08826, Korea*
[4]*Department of Physics and Astronomy, Rutgers University, Piscataway, NJ 08854, USA*
[5]*Condensed Matter Physics and Materials Science Department, Brookhaven National Laboratory, Upton, NY 11973, USA*
(Dated: April 23, 2024)

We study dynamical scaling associated with a Kondo-breakdown quantum critical point (KB-QCP) of the periodic Anderson model, treated by two-site cellular dynamical mean-field theory (2CDMFT). In the quantum critical region, the staggered spin exhibits SYK-like slow dynamics and its dynamical susceptibility shows ω/T scaling. We propose a scaling Ansatz that describes this behavior. It also implies Planckian dissipation for the longest-lived excitations. The current susceptibility follows the same scaling ansatz, leading to strange-metal scaling. This demonstrates that the KB-QCP described by 2CDMFT is an *intrinsic* (i.e., disorder-free) strange-metal fixed point. Surprisingly, the SYK-like dynamics and scaling are driven by strong vertex contributions to the susceptibilities. Our results for the optical conductivity match experimental observations on YbRh$_2$Si$_2$ and CeCoIn$_5$.

Introduction.—Strange metals are enigmatic states of matter which, despite extensive theoretical and experimental effort, still defy clear and unified understanding [1–5]. They are found in the phase diagrams of a large number of strongly correlated materials, such as cuprate superconductors [6–9], iron based superconductors, twisted bilayer graphene [10–12] or heavy fermion metals [13–18].

The phenomenology of strange metals is incompatible with our current understanding of conventional metals. Most prominently, they show T-linear resistivity [9] down to temperatures too low to be of phononic origin (current record: ~ 15 mK in YbRh$_2$Si$_2$ [19]) and a $\sim T \ln T$ specific heat. Both are incompatible with the $\sim T^2$ resistivity and $\sim T$ specific heat expected in normal Fermi liquids [20]. In many materials, ω/T scaling of dynamical susceptibilities [21–23] and more recently also of the optical conductivity [8, 16, 18, 24] is observed. Dynamical scaling is incompatible with Fermi liquids, where quasiparticles with $\sim T^2$ decay rates lead to Lindhard-type susceptibilities and to a Drude peak with width $\sim T^2$ in the optical conductivity. A recent experiment on a strange-metal YbRh$_2$Si$_2$ nanowire further found an almost complete suppression of the shot noise, indicating the absence of well-defined quasiparticles [25].

Despite the ubiquity of materials and experiments showing strange metallicity, even basic questions are to date not fully settled [1]. Do strange metals arise due to quantum critical points and quantum critical phases, or are they intimately connected to quantum criticality at all? Do intrinsic strange metals, i.e., ones without disorder, exist [26, 27]? Recent work showed that many of the features of strange metals can arise from a critical boson coupled to fermions [28, 29], provided that the boson-fermion coupling is disordered. On the other hand, measurements on cuprates suggest that disorder only affects the residual

resistivity, while the linear-in-T slope is unaffected [30]. Further, there exist many stochiometric strange-metal compounds with comparably small residual resistivities.

In this Letter, we show that intrinsic strange-metal scaling can arise due to a heavy-fermion quantum critical point (QCP), described via cellular dynamical mean-field theory (CDMFT) [31, 32]. We study the periodic Anderson model (PAM). It exhibits a so-called Kondo breakdown (KB) QCP [33–35] arising as a continuous orbital-selective Mott transition [36–39]. Its hallmark is a partial localization of electrons, accompanied by a Fermi surface reconstruction, experimentally observable, e.g., via Hall effect or quantum oscillation measurements. Experimental studies in the quantum critical region of KB–QCPs at $T > 0$ often show strange-metal behavior.

In a long companion paper, Ref. [39], we showed that two-site CDMFT (2CDMFT) combined with the numerical renormalization group (NRG) [40] describes many experimental features of the KB–QCP. This includes a novel quantum critical point (stabilized by DMFT self-consistency) and strange-metal behavior, such as a $\sim T \ln T$ specific heat in the non-Fermi liquid (NFL) quantum critical region. Here, we focus on quantum critical dynamical scaling. We find (i) SYK-like slow dynamics; (ii) ω/T scaling of dynamical susceptibilities; (iii) Planckian dissipation; (iv) strange-metal-like ω/T scaling of the optical conductivity $\sigma(\omega)$; and (v) results for $\sigma(\omega)$ consistent with measurements on YbRh$_2$Si$_2$ and CeCoIn$_5$.

Model and methods.—We consider the PAM on a three-dimensional cubic lattice, consisting of an itinerant c band and a localized f band, described by the Hamiltonian

$$H_{\text{PAM}} = \sum_{\mathbf{k}\sigma} (\epsilon_f - \mu) f_{\mathbf{k}\sigma}^\dagger f_{\mathbf{k}\sigma} + U \sum_i f_{i\uparrow}^\dagger f_{i\uparrow} f_{i\downarrow}^\dagger f_{i\downarrow}$$
$$+ V \sum_{\mathbf{k}\sigma} (c_{\mathbf{k}\sigma}^\dagger f_{\mathbf{k}\sigma} + \text{h.c.}) + \sum_{\mathbf{k}\sigma} (\epsilon_{c\mathbf{k}} - \mu) c_{\mathbf{k}\sigma}^\dagger c_{\mathbf{k}\sigma}. \quad (1)$$
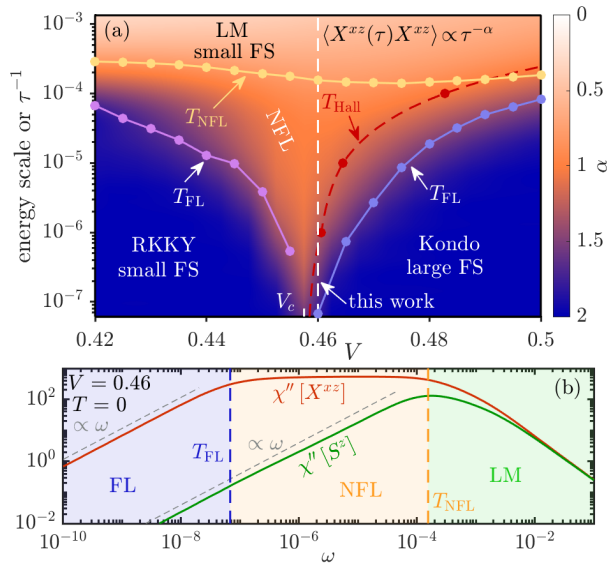
FIG. 1. (a) Phase diagram of the PAM obtained by 2CDMFT+NRG. The dots (connected by lines as guides to the eye) denote relevant energy scales T_{FL} and T_{NFL} below which we observe FL and NFL behavior, respectively, and T_{Hall}, the crossover scale between a large and small FS [see Ref. [39] for details]. The color scale denotes the exponent α of the imaginary-time correlator $\langle X^{xz}(\tau)X^{xz}\rangle \propto \tau^{-\alpha}$. The white dashed line denotes $V = 0.46$, used for all subsequent plots in this work. (b) Spectra of X^{xz} and S^z at $T = 0$.

Here, $f_{\mathbf{k}\sigma}^{\dagger}$ $[c_{\mathbf{k}\sigma}^{\dagger}]$ creates a spin-σ f $[c]$ electron with momentum $\mathbf{k}$, and $\epsilon_{c\mathbf{k}} = -2t\sum_{a=x,y,z}\cos(k_a)$ is the c-electron dispersion. We set the c-electron hopping $t = 1/6$ as an energy unit (half bandwidth $= 1$) and fix the f-orbital level $\epsilon_f = -5.5$, the interaction strength $U = 10$, and the chemical potential $\mu = 0.2$, as chosen in prior 2CDMFT studies [37–39]. We tune the c-f hybridization V and the temperature T as control parameters.

We study the PAM using 2CDMFT, which maps the lattice model to an effective two-impurity Anderson model (2IAM) with a self-consistent bath (cf. Refs. [36–39] for more details). The 2CDMFT approach allows us to study the competition between local Kondo correlations and nonlocal RKKY correlations, which is believed to drive quantum criticality in heavy fermion systems [33, 41–43]. We solve the effective 2IAM using NRG [40], enabling us to reach exponentially small frequency and energy scales. We exploit and enforce U(1) charge and SU(2) spin symmetries (using the QSpace tensor library [44, 45]), thereby excluding the possibility of symmetry-breaking order by hand. We thus study KB quantum criticality in the absence of symmetry breaking [46–49], as can be observed, e.g., in experiments on YbRh$_2$Si$_2$ [50] and CeCoIn$_5$ [51]. We do not find tendencies towards symmetry breaking (divergent susceptibilities) for $V > V_c$ or anywhere within the quantum critical region emanating from the KB-QCP.

Phase diagram.—Figure 1(a) shows our 2CDMFT+NRG phase diagram in the (V, T) plane close to the KB–

QCP. At $T = 0$, we find two Fermi liquid (FL) phases, separated by a KB–QCP located at $V_c = 0.4575(25)$, featuring a sudden Fermi surface (FS) reconstruction [39]. At finite excitation energies, we find two crossover scales, $T_{\text{FL}}(V)$ and $T_{\text{NFL}}(V)$ [39]. FL behavior emerges below T_{FL}, which decreases towards and vanishes at V_c. The high-energy region above T_{NFL} is characterized by thermally fluctuating f-electron local moments decoupled from the c electrons. T_{NFL} does not decrease for V near V_c, hence strong scale separation between T_{NFL} and T_{FL} occurs close to the QCP. For excitation energies between T_{FL} and T_{NFL}, we find NFL behavior—the main subject of this work.

Dynamical susceptibilities.—The different regions can be most conveniently distinguished in terms of the dynamical behavior of response functions. For now, we focus on the staggered f-electron spin on a two-site cluster, $X^{xz} = S_1^z - S_2^z$, with $S_i^z = \frac{1}{2}\left[f_{i\uparrow}^{\dagger}f_{i\uparrow} - f_{i\downarrow}^{\dagger}f_{i\downarrow}\right]$. The color scale in Fig. 1(a) shows the exponent α of the imaginary-time autocorrelation function of X^{xz}, $\langle X^{xz}(\tau)X^{xz}\rangle \propto \tau^{-\alpha}$, obtained via log-derivative. For long times, $\tau^{-1} < T_{\text{FL}}$, we find $\alpha = 2$, consistent with FL behavior and the presence of long-lived quasi-particles (QP) [3] and thus quickly decaying, localized spin excitations. For short times, $\tau^{-1} > T_{\text{NFL}}$, staggered spin excitations decay very slowly with an exponent $\alpha < 0.5$, consistent with local moment behavior. For intermediate times, $T_{\text{FL}} < \tau^{-1} < T_{\text{NFL}}$, we find an SYK-like exponent $\alpha \simeq 1$ in the NFL region, indicative of the absence of coherent QP [3]. For at $V = 0.46$, our data closest to V_c, this behavior extends over almost 4 orders of magnitude: in fact, our data suggests that it extends down to $\tau^{-1} \to 0$ at V_c, where $T_{\text{FL}} = 0$. We note that we do *not* find $\propto \tau^{-1/2}$ behavior of the single-electron Green's function $G(\tau)$, in contrast to the SYK model [3]. Thus, $\langle X^{xz}(\tau)X^{xz}\rangle$ is not $\propto G(\tau)^2$, i.e., the τ^{-1} behavior is governed by vertex contributions.

To understand the origin of the τ^{-1} dependence, we consider the spectral representation of bosonic correlators,

$$\langle \mathcal{A}^{\dagger}(\tau)\mathcal{B}\rangle = \int_{-\infty}^{\infty} d\omega\, \frac{e^{-\tau\omega}}{1 - e^{-\beta\omega}}\, \chi''[\mathcal{A},\mathcal{B}](\omega)\,. \quad (2)$$

Here, the spectrum $\chi''(\omega)$ is obtained from the dynamical susceptibility $\chi(\omega) = \chi'(\omega) - i\pi\chi''(\omega)$,

$$\chi[\mathcal{A},\mathcal{B}](\omega) = -i\int_0^{\infty} dt\, e^{i(\omega+i0^+)t}\,\langle\left[\mathcal{A}^{\dagger}(t),\mathcal{B}\right]\rangle\,. \quad (3)$$

We use the shorthand $\chi[\mathcal{A}](\omega) = \chi[\mathcal{A},\mathcal{A}](\omega)$.

The spectra for X^{xz} and for the total spin $S^z = S_1^z + S_2^z$ are shown in Fig. 1(b) at $V = 0.46$ and $T = 0$. The spectra $\chi''[X^{xz}]$ and $\chi''[S^z]$ both show $\propto \omega$ behavior below T_{FL}, indicating that these fluctuations are screened in the FL, as expected. For long times, $\tau^{-1} < T_{\text{FL}}$, the corresponding imaginary time correlation function Eq. (2) therefore decays as τ^{-2}, as shown for X^{xz} in Fig. 1(a).

In the NFL region ($T_{\text{FL}} < \omega < T_{\text{NFL}}$) the spectra differ qualitatively: while $\chi''[S^z] \propto \omega$ still holds, $\chi''[X^{xz}]$ has an
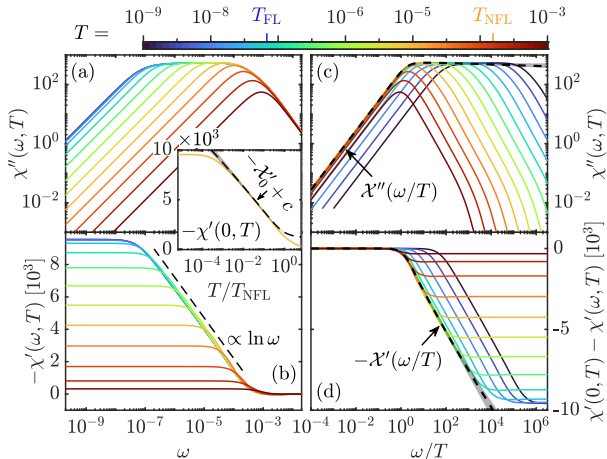
FIG. 2. Dynamical susceptibility $\chi[X^{xz}](\omega,T)$: (a) spectral part and (b) corresponding real part; (c,d) scaling collapse of spectral and real parts. Black dashed lines show the scaling functions $\mathcal{X}''(\omega/T)$ and $\mathcal{X}'(\omega/T)$, respectively [cf. Eq. (5)]. Inset: $\chi'(0,T)$ (orange) and $\mathcal{X}_0'(T/T_{\rm NFL})+c$ [black dashed, cf. Eq. (5)]. The constant shift c accounts for spectral weight at $|\omega|>T_{\rm NFL}$. Grey areas indicate fitting uncertainties [56].

ω-independent plateau; hence S^z fluctuations are screened, X^{xz} fluctuations are over-screened (reminiscent of the two-channel or two-impurity Kondo models [52–54]). For intermediate times $\langle S^z(\tau)S^z\rangle$ thus decays as τ^{-2} (not shown) whereas $\langle X^{xz}(\tau)X^{xz}\rangle$ decays as τ^{-1} [cf. Fig. 1(a)]. We note that besides X^{xz}, many other operators also have plateaus in their spectra, see Fig. 4 in Ref. [39]. Thus, the FL is reached via a two-stage screening process: as ω drops below $T_{\rm NFL}$, some excitations are screened, others over-screened; below $T_{\rm FL}$, the latter are screened, too.

Dynamical scaling.—We now turn to the $T>0$ behavior, focusing on $V=0.46$ and $\chi[X^{xz}]$, whose spectrum shows a plateau in the NFL region at $T=0$. The T-dependent spectra $\chi''(\omega,T)$ and the corresponding real parts $\chi'(\omega,T)$ are shown in Figs. 2(a) and (b), respectively. As T is decreased from around $T_{\rm NFL}$ to $T_{\rm FL}$, the aforementioned plateau in $\chi''(\omega,T)$ emerges between $T<\omega<T_{\rm NFL}$, crossing over to $\propto\omega$ behavior for $\omega<T$. For $T<T_{\rm FL}$, the spectrum becomes T-independent, taking the same form as already shown in Fig. 1(b) for $T=0$.

$\chi'(\omega,T)$ is related to $\chi''(\omega,T)$ via a Kramers–Kronig relation. It thus shows a logarithmic [55] ω-dependence for $\max(T,T_{\rm FL})<\omega<T_{\rm NFL}$ where $\chi''(\omega,T)$ has a plateau, and is constant for $\omega<\max(T,T_{\rm FL})$ where $\chi''(\omega,T)\propto\omega$. As a result, $\chi'(0,T)$ [inset of Fig. 2] has a $\propto\ln T$ dependence for $T_{\rm FL}<T<T_{\rm NFL}$ and is constant for $T<T_{\rm FL}$, where X^{xz} fluctuations are screened.

Figure 2(c) shows $\chi''(\omega,T)$ vs. ω/T. In the NFL region $(T_{\rm FL}<T<T_{\rm NFL},|\omega|<T_{\rm NFL})$, the spectra all collapse onto a single curve. This demonstrates that the T-dependent spectra show dynamical scaling in the sense that in the NFL region, $T^\alpha\chi''(\omega,T)=\mathcal{X}''(\omega/T)$ with $\alpha=0$. Thus, $\chi''(\omega,T)$ depends on ω only via the ratio ω/T, implying

that T is the only scale in this region. The scaling function $\mathcal{X}''(x)$ is flat for $x>1$ and $\propto x$ for $x<1$ (we discuss a phenomenological fit below). The real part also shows ω/T scaling, $\chi'(\omega,T)-\chi'(0,T)\simeq\mathcal{X}'(\omega/T)$.

Scaling function and Planckian dissipation.—In the NFL region $(T_{\rm FL}<T<T_{\rm NFL},|\omega|<T_{\rm NFL})$, the spectra of dynamical susceptibilities showing plateaus (e.g., $\chi[X^{xz}]$) can be fitted with a phenomenological ansatz for $\omega>0$:

$$\widetilde{\chi}''(\omega,T)=\chi_0\int_T^{T_{\rm NFL}}\frac{d\epsilon}{\pi}\frac{(1-e^{-\frac{\omega}{T}})(\frac{\epsilon}{T})^\nu bT}{(\omega-a\epsilon)^2+(bT)^2}. \quad (4)$$

$\omega<0$ follows from anti-symmetry of $\widetilde{\chi}''$, the real part $\widetilde{\chi}'$ is determined through a Kramers–Kronig relation. χ_0, a, b, and ν are determined by fits to our spectra in the NFL region [56]. We find $a\simeq10^{-1}$, $b\simeq1$ and $\nu\simeq0$; χ_0 determines the plateau value. (These parameters are V-independent within our fitting accuracy.) When Eq. (4) is evaluated for $|\omega|,T\ll T_{\rm NFL}$ one finds the scaling form

$$\widetilde{\chi}(\omega,T)\simeq\mathcal{X}_0'\Big(\frac{T}{T_{\rm NFL}}\Big)+\mathcal{X}'\Big(\frac{\omega}{T}\Big)-i\pi\mathcal{X}''\Big(\frac{\omega}{T}\Big). \quad (5)$$

An explicit T-dependence, due to the high-energy cutoff $T_{\rm NFL}$, only enters via $\mathcal{X}_0'(T/T_{\rm NFL})\simeq\widetilde{\chi}'(0,T)$; otherwise, $\widetilde{\chi}(\omega,T)$ only depends on the ratio ω/T (for more information on the scaling functions $\mathcal{X}_0'$, $\mathcal{X}'$ and $\mathcal{X}''$, see Ref. [56]). In Fig. 2(c,d), we show that the scaling function $\mathcal{X}$ captures $\chi[X^{xz}]$ well in the NFL region (black dashed lines).

The ansatz (4) is motivated by a fit of $\langle X^{xz}(t)X^{xz}\rangle$ to a superposition of coherent excitations with mean energy $a\epsilon$, decay rate bT and density of states $(\epsilon/T)^\nu$ [56]. Since $b\simeq1$, these coherent excitations have a decay rate $\gamma\simeq T$ or correspondingly a lifetime $\tau\simeq1/T$, i.e., *the longest-lived X^{xz} excitations have a Planckian lifetime.* By contrast, we do *not* observe a Planckian lifetime for single-particle excitations [cf. Fig. 3(d) and its discussion].

Optical conductivity.—Our 2CDMFT approximation allows us to compute the *local* current susceptibility $\chi[j_i^a](\omega,T)$ of the lattice model from the effective impurity model. Here, $j_i^a=-ite\sum_\sigma(c_{i\sigma}^\dagger c_{i+\mathbf{a}\sigma}-c_{i+\mathbf{a},\sigma}^\dagger c_{i\sigma})$ is the current operator in a-direction, where i and $i+\mathbf{a}$ are nearest neighbors on the lattice, chosen to also correspond to the two sites of the self-consistent impurity model.

For optical experiments and electronic transport, the *uniform* current susceptibility $\chi[j_{\mathbf{q=0}}^a](\omega,T)$ is relevant, where $j_\mathbf{q}^a$ is the $\mathbf{q}$-dependent current in a-direction, $j_\mathbf{q}^a=\frac{1}{N}\sum_{i\sigma}e^{-i\mathbf{q}\cdot\mathbf{r}_i}j_i^a$. Assuming translation symmetry, $\chi[j_\mathbf{0}^a]$ can be expressed as a sum $\chi[j_i^a]+\chi_{\rm nl}[j]$ of local and non-local parts, with $\chi_{\rm nl}[j]=\frac{1}{N}\sum_{\ell\neq i}\chi[j_\ell^a,j_i^a]=\chi[j_\mathbf{0}^a]-\chi[j_i^a]$. The computation of $\chi_{\rm nl}[j]$ would require four-point correlators [63, 64] for the self-consistent two-impurity model, which currently exceeds our computational resources. Hence we approximate it by its bubble contribution, $\chi_{\rm nl,B}[j]=\chi_{\rm B}[j_\mathbf{0}^a]-\chi_{\rm B}[j_i^a]$. Thus, we use

$$\chi[j_\mathbf{0}^a]\approx\chi[j_i^a]+\chi_{\rm nl,B}[j]=\chi_{\rm B}[j_\mathbf{0}^a]+\chi_{\rm vtx}[j_i^a], \quad (6)$$
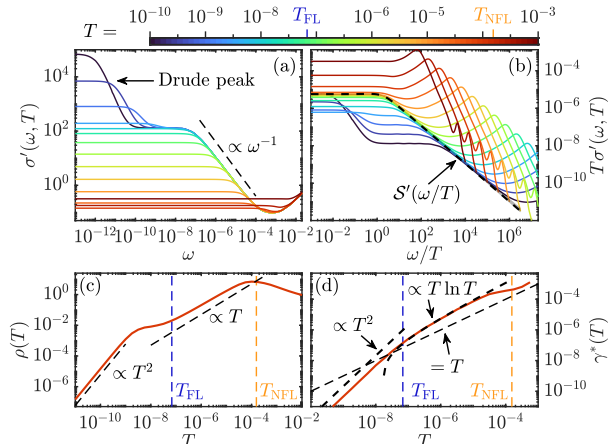
FIG. 3. (a) Real part of the optical conductivity, $\sigma'(\omega, T)$. (b) ω/T scaling of $T\sigma'(\omega, T)$; black dashed line: the scaling function $\mathcal{S}'$ of Eq. (7). (c) The resistivity $\rho(T)$. (d) The single-particle decay rate at the Fermi level, $\gamma^*(T)$.

where $\chi_{\mathrm{vtx}}[j_i^a] = \chi[j_i^a] - \chi_{\mathrm{B}}[j_i^a]$ is the *vertex* contribution to the local current susceptibility.

The uniform current spectrum determines the real part of the optical conductivity, $\sigma'(\omega, T) = \frac{\pi}{\omega}\chi''[j_\mathbf{0}^a](\omega, T)$. It is shown in Fig. 3(a). At $T \ll T_{\mathrm{FL}}$ (blue/black), it features a hybridization gap around $\omega \simeq T_{\mathrm{NFL}}$, ω^{-1} behavior for $T_{\mathrm{FL}} < \omega < T_{\mathrm{NFL}}$, and a Drude peak at low frequencies below T_{FL}. These features emerge as the temperature is lowered from $T \gg T_{\mathrm{NFL}}$: The hybridization gap forms around $T \simeq T_{\mathrm{NFL}}$ (red), the ω^{-1} feature emerges between $T_{\mathrm{FL}} < T < T_{\mathrm{NFL}}$ (yellow/green) and the Drude peak finally emerges for $T < T_{\mathrm{FL}}$ (blue/black).

The most interesting feature is the ω^{-1} behavior in the NFL region. This feature is due to the fact that $\chi''[j_i^a]$ (Fig. S2 in Ref. [56]) exhibits a plateau similar to that of $\chi''[X^{xz}]$ [Fig. 2(a,c)] for $|\omega|, T < T_{\mathrm{NFL}}$. This plateau is entirely due to the vertex contribution $\chi''_{\mathrm{vtx}}[j_i^a]$, which in the NFL region completely dominates the bubble contribution, $|\chi''_{\mathrm{vtx}}[j_i^a]| \gg |\chi''_{\mathrm{B}}[j_\mathbf{0}^a]|$ [56]. (The same is true for $\chi[X^{xz}]$.) Remarkably, $\chi''[j_i^a]$, just as $\chi''[X^{xz}]$, is well described by the ansatz (4) (see Fig. S6 of Ref. [56]), implying ω/T scaling and Planckian dissipation of current fluctuations. This implies that in the NFL region $T_{\mathrm{FL}} < T < T_{\mathrm{NFL}}$, $\sigma'(\omega, T)$ is governed by a scaling function $\mathcal{S}'$:

$$T\sigma'(\omega, T) = (T/\omega)\pi\mathcal{X}''(\omega/T) = \mathcal{S}'(\omega/T). \quad (7)$$

Figure 3(b) shows that $T\sigma'(\omega, T)$ is indeed well described by this scaling function (black dashed line). We discuss scaling of the imaginary part $\sigma''(\omega, T)$ in Ref. [56].

The scaling behavior (7) has two striking implications for the NFL region $T_{\mathrm{FL}} < T < T_{\mathrm{NFL}}$: First, a scaling collapse is achieved for $T^\alpha\sigma'(\omega, T)$ with $\alpha = 1$, an exponent which is also found experimentally [16, 18, 24]. Second, the static conductivity $\sigma(T) = \sigma'(0, T) = \mathcal{S}'(0)/T$ scales as $1/T$, implying T-linear behavior for the resistivity, $\rho(T) = 1/\sigma(T) \propto T$. This is born out in Fig. 3(c): $\rho(T)$

has a maximum around T_{NFL}, where the hybridization gap forms, then decreases with T approximately $\propto T$ for $T_{\mathrm{FL}} < T < T_{\mathrm{NFL}}$, before finally becoming $\propto T^2$ below T_{FL}. In Ref. [56], we analyze the complex optical conductivity, see Sec. S-IV, Fig. S10. In the high-T part of the NFL region $T_{\mathrm{NFL}}/10 \lesssim T \lesssim T_{\mathrm{NFL}}$, it shows qualitative similarities to data on CeCoIn$_5$ of Ref. [65]: a dynamical transport scattering rate $\propto \omega^2$, and a renormalized transport scattering rate $\propto T^2$.

In the FL region, on the other hand, the Drude peak and $\rho(T) \propto T^2$ behavior are due to the nonlocal bubble part $\chi_{\mathrm{nl,B}}[j]$. These features can be understood from the single-particle decay rate [66],

$$\gamma^* = Z\gamma, \quad \gamma = \mathrm{Im}\, G_{\mathbf{k}_\mathrm{F}}^{-1}(0), \quad Z^{-1} = \partial_\omega \mathrm{Re}\, G_{\mathbf{k}_\mathrm{F}}^{-1}(0), \quad (8)$$

shown in Fig. 3(d). In the FL region, $\gamma^* \propto T^2$ as expected, leading to a Drude peak of width $\propto T^2$ and $\rho(T) \propto T^2$, i.e., these features are due to long-lived coherent QP carrying the current. Since we neglect *nonlocal* vertex contributions, the transport relaxation rate, and thus the T^2 prefactor of $\rho(T)$, is set purely by the QP decay rate and is therefore very likely overestimated [67].

In the NFL region, we find $Z \propto T$ and $\gamma \propto \ln T$, leading to $\gamma^* \propto T\ln T$. The latter is also found in the marginal FL (MFL) [68] approach, but there, by contrast, one has $Z \propto \ln T$ and $\gamma \propto T$. Further, Fig. 3(d) shows $\gamma^*(T) > T$ in the NFL region, i.e., single-particle excitations are *not* Planckian and decay faster than, for instance, current or X^{xz} fluctuations. We emphasize that in the NFL region (in contrast to the FL region), the transport relaxation rate is *not* set by the single-particle decay rate: there, $\sigma(\omega, T)$ and thus $\rho(T)$ are qualitatively influenced by the vertex contribution $\chi''_{\mathrm{vtx}}[j_i^a]$, as discussed above.

We conjecture that the following two features in Fig. 3(c) are artifacts of neglecting *nonlocal* vertex contributions: First, $\rho(T)$ shows a slight deviation from perfect T-linear behavior. This deviation results from the fact that the *bubble* part of the nonlocal current susceptibility, $\chi_{\mathrm{B,nl}}[j]$, does not show ω/T scaling [not visible in Fig. 3(b)]. In Sec. S-II D of Ref. [56], we provide indications that the full $\chi_{\mathrm{nl}}[j]$ does show scaling of the same type as $\chi''[j_i^a](\omega)$, which would imply perfect T-linear behavior. Second, $\rho(T)$ has a shoulder somewhat below T_{FL}. This likely reflects the above-mentioned overestimation of the T^2 prefactor of $\rho(T)$ in the FL region.

Discussion and Outlook.—Our work provides a promising route towards an intrinsic strange metal. However, we have not yet achieved a full understanding of the current decay mechanism. An inherent feature of (C)DMFT is that the interaction vertex does not ensure conservation of crystal momentum [32, 69]. Therefore, electron-electron scattering does not conserve crystal momentum, leading to current decay. This mechanism usually manifests as a dominant bubble contribution (in single-site DMFT, this is the only contribution). A dominant bubble contribution

is also key to the Yukawa–SYK approach [28] to strange metals. There, a disordered Yukawa coupling leads to non-conserved momentum in scattering processes. The result is a MFL where strange-metal scaling arises in the bubble contribution and interaction disorder is needed to avoid its cancellation by the vertex contribution. By contrast, in our 2CDMFT approach the strange-metal scaling in the NFL region arises *entirely from the vertex contribution*, and not at all from the (much smaller) bubble contribution. This strongly suggests that the current decay mechanism is not due to the non-conservation of crystal momentum at the interaction vertex. Our 2CDMFT approach also includes crystal momentum conserving Umklapp scattering processes between momenta around $\mathbf{k} = (0,0,0)$ and $\mathbf{k} = (\pi,\pi,\pi)$ which flip the current. We conjecture that these cause our observed strange-metal scaling.

A detailed analysis of the current decay mechanism is left for future work. This will involve studying (i) the frequency and temperature dependence of three- and four-point vertices in the NFL region and (ii) the relevance of Umklapp scattering in 2CDMFT.

---

* andreas.gleis@lmu.de
† sslee@snu.ac.kr
‡ kotliar@physics.rutgers.edu
§ vondelft@lmu.de

[1] P. W. Phillips, N. E. Hussey, and P. Abbamonte, Stranger than metals, Science **377**, eabh4273 (2022).

[2] S. A. Hartnoll and A. P. Mackenzie, Colloquium: Planckian dissipation in metals, Rev. Mod. Phys. **94**, 041002 (2022).

[3] D. Chowdhury, A. Georges, O. Parcollet, and S. Sachdev, Sachdev-Ye-Kitaev models and beyond: Window into non-Fermi liquids, Rev. Mod. Phys. **94**, 035004 (2022).

[4] J. Zaanen, Why the temperature is high, Nature **430**, 512 (2004).

[5] J. G. Checkelsky, B. A. Bernevig, P. Coleman, Q. Si, and S. Paschen, Flat bands, strange metals and the Kondo effect, Nat. Rev. Mater. 10.1038/s41578-023-00644-z (2024).

[6] B. Keimer, S. A. Kivelson, M. R. Norman, S. Uchida, and J. Zaanen, From quantum matter to high-temperature superconductivity in copper oxides, Nature **518**, 179 (2015).

[7] B. Michon, C. Girod, S. Badoux, J. Kačmarčík, Q. Ma, M. Dragomir, H. A. Dabkowska, B. D. Gaulin, J.-S. Zhou, S. Pyon, T. Takayama, H. Takagi, S. Verret, N. Doiron-Leyraud, C. Marcenat, L. Taillefer, and T. Klein, Thermodynamic signatures of quantum criticality in cuprate superconductors, Nature **567**, 218 (2019).

[8] B. Michon, C. Berthod, C. W. Rischau, A. Ataei, L. Chen, S. Komiya, S. Ono, L. Taillefer, D. van der Marel, and A. Georges, Reconciling scaling of the optical conductivity of cuprate superconductors with Planckian resistivity and specific heat, Nat. Commun. **14**, 3033 (2023).

[9] A. Legros, S. Benhabib, W. Tabis, F. Laliberté, M. Dion, M. Lizaire, B. Vignolle, D. Vignolles, H. Raffy, Z. Z. Li, P. Auban-Senzier, N. Doiron-Leyraud, P. Fournier, D. Colson, L. Taillefer, and C. Proust, Universal T-linear resistivity and Planckian dissipation in overdoped cuprates, Nat. Phys. **15**, 142 (2019).

[10] Y. Cao, V. Fatemi, S. Fang, K. Watanabe, T. Taniguchi, E. Kaxiras, and P. Jarillo-Herrero, Unconventional superconductivity in magic-angle graphene superlattices, Nature **556**, 43 (2018).

[11] Y. Cao, D. Chowdhury, D. Rodan-Legrain, O. Rubies-Bigorda, K. Watanabe, T. Taniguchi, T. Senthil, and P. Jarillo-Herrero, Strange metal in magic-angle graphene with near Planckian dissipation, Phys. Rev. Lett. **124**, 076801 (2020).

[12] A. Jaoui, I. Das, G. Di Battista, J. Díez-Mérida, X. Lu, K. Watanabe, T. Taniguchi, H. Ishizuka, L. Levitov, and D. K. Efetov, Quantum critical behaviour in magic-angle twisted bilayer graphene, Nat. Phys. **18**, 633 (2022).

[13] H. von Löhneysen, Non-Fermi-liquid behaviour in the heavy-fermion system $CeCu_{6-x}Au_x$, J. Phys. Condens. Matter **8**, 9689 (1996).

[14] O. Trovarelli, C. Geibel, S. Mederle, C. Langhammer, F. M. Grosche, P. Gegenwart, M. Lang, G. Sparn, and F. Steglich, $YbRh_2Si_2$: Pronounced non-Fermi-liquid effects above a low-lying magnetic phase transition, Phys. Rev. Lett. **85**, 626 (2000).

[15] J. Paglione, M. A. Tanatar, D. G. Hawthorn, E. Boaknin, R. W. Hill, F. Ronning, M. Sutherland, L. Taillefer, C. Petrovic, and P. C. Canfield, Field-induced quantum critical point in $CeCoIn_5$, Phys. Rev. Lett. **91**, 246405 (2003).

[16] L. Prochaska, X. Li, D. C. MacFarland, A. M. Andrews, M. Bonta, E. F. Bianco, S. Yazdi, W. Schrenk, H. Detz, A. Limbeck, Q. Si, E. Ringe, G. Strasser, J. Kono, and S. Paschen, Singular charge fluctuations at a magnetic quantum critical point, Science **367**, 285 (2020).

[17] M. Taupin and S. Paschen, Are heavy fermion strange metals Planckian?, Crystals **12**, 251 (2022).

[18] X. Li, J. Kono, Q. Si, and S. Paschen, Is the optical conductivity of heavy fermion strange metals Planckian?, Front. Electron. Mater **2**, 934691 (2023).

[19] D. H. Nguyen, A. Sidorenko, M. Taupin, G. Knebel, G. Lapertot, E. Schuberth, and S. Paschen, Superconductivity in an extreme strange metal, Nat. Commun. **12**, 4341 (2021).

[20] G. Giuliani and G. Vignale, *Quantum Theory of the Electron Liquid* (Cambridge University Press, 2005).

[21] M. C. Aronson, R. Osborn, R. A. Robinson, J. W. Lynn, R. Chau, C. L. Seaman, and M. B. Maple, Non-Fermi-liquid scaling of the magnetic response in UCu$_{5-x}$Pd$_x$($x = 1, 1.5$), Phys. Rev. Lett. **75**, 725 (1995).

[22] A. Schröder, G. Aeppli, R. Coldea, M. Adams, O. Stockert, H. Löhneysen, E. Bucher, R. Ramazashvili, and P. Coleman, Onset of antiferromagnetism in heavy-fermion metals, Nature **407**, 351 (2000).

[23] L. Poudel, J. M. Lawrence, L. S. Wu, G. Ehlers, Y. Qiu, A. F. May, F. Ronning, M. D. Lumsden, D. Mandrus, and A. D. Christianson, Multicomponent fluctuation spectrum at the quantum critical point in CeCu$_{6-x}$Ag$_x$, npj Quantum Mater. **4**, 52 (2019).

[24] C.-J. Yang, S. Pal, F. Zamani, K. Kliemt, C. Krellner, O. Stockert, H. v. Löhneysen, J. Kroha, and M. Fiebig, Terahertz conductivity of heavy-fermion systems from time-resolved spectroscopy, Phys. Rev. Research **2**, 033296 (2020).

[25] L. Chen, D. T. Lowder, E. Bakali, A. M. Andrews, W. Schrenk, M. Waas, R. Svagera, G. Eguchi, L. Prochaska, Y. Wang, C. Setty, S. Sur, Q. Si, S. Paschen, and D. Natelson, Shot noise in a strange metal, arXiv:2206.00673.

[26] D. V. Else, R. Thorngren, and T. Senthil, Non-Fermi liquids as ersatz Fermi liquids: General constraints on compressible metals, Phys. Rev. X **11**, 021005 (2021).

[27] D. V. Else and T. Senthil, Strange metals as ersatz Fermi liquids, Phys. Rev. Lett. **127**, 086601 (2021).

[28] A. A. Patel, H. Guo, I. Esterlis, and S. Sachdev, Universal theory of strange metals from spatially random interactions, Science **381**, 790 (2023).

[29] E. E. Aldape, T. Cookmeyer, A. A. Patel, and E. Altman, Solvable theory of a strange metal at the breakdown of a heavy Fermi liquid, Phys. Rev. B **105**, 235111 (2022).

[30] F. Rullier-Albenque, P. A. Vieillefond, H. Alloul, A. W. Tyler, P. Lejay, and J. F. Marucco, Universal T_c depression by irradiation defects in underdoped and overdoped cuprates?, Europhys. Lett. **50**, 81 (2000).

[31] G. Kotliar, S. Y. Savrasov, G. Pálsson, and G. Biroli, Cellular dynamical mean field approach to strongly correlated systems, Phys. Rev. Lett. **87**, 186401 (2001).

[32] T. Maier, M. Jarrell, T. Pruschke, and M. H. Hettler, Quantum cluster theories, Rev. Mod. Phys. **77**, 1027 (2005).

[33] Q. Si, S. Rabello, K. Ingersent, and J. L. Smith, Locally critical quantum phase transitions in strongly correlated metals, Nature **413**, 804 (2001).

[34] P. Coleman, C. Pépin, Q. Si, and R. Ramazashvili, How do Fermi liquids get heavy and die?, J. Phys. Condens. Matter **13**, R723 (2001).

[35] P. Coleman and C. Pépin, What is the fate of the heavy electron at a quantum critical point?, Phys. B Condens. Matter **312-313**, 383 (2002), the International Conference on Strongly Correlated Electron Systems.

[36] D. Tanasković, K. Haule, G. Kotliar, and V. Dobrosavljević, Phase diagram, energy scales, and nonlocal correlations in the Anderson lattice model, Phys. Rev. B **84**, 115105 (2011).

[37] L. De Leo, M. Civelli, and G. Kotliar, Cellular dynamical mean-field theory of the periodic Anderson model, Phys. Rev. B **77**, 075107 (2008).

[38] L. De Leo, M. Civelli, and G. Kotliar, $T = 0$ heavy-fermion quantum critical point as an orbital-selective Mott transition, Phys. Rev. Lett. **101**, 256404 (2008).

[39] A. Gleis, S.-S. B. Lee, G. Kotliar, and J. von Delft, Emergent properties of the periodic Anderson model: a high-resolution, real-frequency study of heavy-fermion quantum criticality, arXiv:2310.12672.

[40] R. Bulla, T. A. Costi, and T. Pruschke, Numerical renormalization group method for quantum impurity systems, Rev. Mod. Phys. **80**, 395 (2008).

[41] S. Doniach, The Kondo lattice and weak antiferromagnetism, Physica **91B+C**, 231 (1977).

[42] T. Senthil, S. Sachdev, and M. Vojta, Fractionalized Fermi liquids, Phys. Rev. Lett. **90**, 216403 (2003).

[43] T. Senthil, M. Vojta, and S. Sachdev, Weak magnetism and non-Fermi liquids near heavy-fermion critical points, Phys. Rev. B **69**, 035111 (2004).

[44] A. Weichselbaum, Non-Abelian symmetries in tensor networks: A quantum symmetry space approach, Ann. Phys. (N. Y.) **327**, 2972 (2012).

[45] A. Weichselbaum, X-symbols for non-Abelian symmetries in tensor networks, Phys. Rev. Research **2**, 023385 (2020).

[46] M. Vojta, Orbital-selective Mott transitions: Heavy fermions and beyond, J. Low Temp. Phys. **161**, 203 (2010).

[47] S. J. Yamamoto and Q. Si, Global phase diagram of the Kondo lattice: From heavy fermion metals to Kondo insulators, J. Low Temp. Phys. **161**, 233 (2010).

[48] Q. Si, Quantum criticality and global phase diagram of magnetic heavy fermions, Phys. Status Solidi B **247**, 476 (2010).

[49] P. Coleman and A. H. Nevidomskyy, Frustration and the Kondo effect in heavy fermion materials, J. Low Temp. Phys. **161**, 182 (2010).

[50] S. Friedemann, T. Westerkamp, M. Brando, N. Oeschler, S. Wirth, P. Gegenwart, C. Krellner, C. Geibel, and F. Steglich, Detaching the antiferromagnetic quantum critical point from the Fermi-surface reconstruction in YbRh$_2$Si$_2$, Nat. Phys. **5**, 465 (2009).

[51] N. Maksimovic, D. H. Eilbott, T. Cookmeyer, F. Wan, J. Rusz, V. Nagarajan, S. C. Haley, E. Maniv, A. Gong, S. Faubel, I. M. Hayes, A. Bangura, J. Singleton, J. C. Palmstrom, L. Winter, R. McDonald, S. Jang, P. Ai, Y. Lin, S. Ciocys, J. Gobbo, Y. Werman, P. M. Oppeneer, E. Altman, A. Lanzara, and J. G. Analytis, Evidence for a delocalization quantum phase transition without symmetry breaking in CeCoIn$_5$, Science **375**, 76 (2022).

[52] P. Nozières, A "Fermi-liquid" description of the Kondo problem at low temperatures, J. Low Temp. Phys. **17**, 31 (1974).

[53] B. A. Jones, C. M. Varma, and J. W. Wilkins, Low-temperature properties of the two-impurity Kondo Hamiltonian, Phys. Rev. Lett. **61**, 125 (1988).

[54] B. A. Jones and C. M. Varma, Critical point in the solution of the two magnetic impurity problem, Phys. Rev. B **40**, 324 (1989).

[55] We call frequency dependencies $(\omega^a - 1)/a$ with $a \simeq 0$ logarithmic if the exponent a cannot be reasonably distinguished from $a \to 0$ based on our numerical data. Ditto for temperature dependencies. Similarly, "plateau" means ω^a with $a \simeq 0$ and "linear" ω^a with $a \simeq 1$.

[56] See Supplemental Material at [url] for additional information on basic formulas involving the optical conductivity; the numerical computation of the optical conductivity; the role of vertex contributions; the Drude weight; the scaling functions; scaling of the imaginary part of the optical conductivity and an analysis on the complex optical conductivity, including a comparison to data on CeCoIn$_5$.

The Supplemental Material includes Refs. [57–62].

[57] R. Resta, Drude weight and superconducting weight, J. Phys. Condens. Matter **30**, 414001 (2018).

[58] D. J. Scalapino, S. R. White, and S. Zhang, Insulator, metal, or superconductor: The criteria, Phys. Rev. B **47**, 7995 (1993).

[59] A. K. Mitchell, M. R. Galpin, S. Wilson-Fletcher, D. E. Logan, and R. Bulla, Generalized Wilson chain for solving multichannel quantum impurity problems, Phys. Rev. B **89**, 121105 (2014).

[60] K. M. Stadler, A. K. Mitchell, J. von Delft, and A. Weichselbaum, Interleaved numerical renormalization group as an efficient multiband impurity solver, Phys. Rev. B **93**, 235101 (2016).

[61] F. B. Kugler, Improved estimator for numerical renormalization group calculations of the self-energy, Phys. Rev. B **105**, 245132 (2022).

[62] S.-S. B. Lee and A. Weichselbaum, Adaptive broadening to improve spectral resolution in the numerical renormalization group, Phys. Rev. B **94**, 235127 (2016).

[63] S.-S. B. Lee, F. B. Kugler, and J. von Delft, Computing local multipoint correlators using the numerical renormalization group, Phys. Rev. X **11**, 041007 (2021).

[64] F. B. Kugler, S.-S. B. Lee, and J. von Delft, Multipoint correlation functions: Spectral representation and numerical evaluation, Phys. Rev. X **11**, 041006 (2021).

[65] L. Y. Shi, Z. Tagay, J. Liang, K. Duong, Y. Wu, F. Ronning, D. G. Schlom, K. Shen, and N. P. Armitage, Low energy electrodynamics and a hidden Fermi liquid in the heavy-fermion $CeCoIn_5$, arXiv:2310.10916.

[66] In the PAM, $\mathbf{G_k}(\omega)$ is matrix-valued in the orbital space, with orbital index $\alpha \in \{f, c\}$. $G_{\mathbf{k}_F}^{-1}(\omega)$ is defined in terms of the eigenvalue which fulfils $\mathrm{Re}\,G_{\mathbf{k}_F}^{-1}(0) = 0$. To determine the single-particle decay rate γ^*, the ω-dependence of the corresponding eigenvalue is fitted to a Lorentzian lineshape around $\omega = 0$, $G_{\mathbf{k}_F}(\omega) \simeq Z/(\omega + \mathrm{i}\gamma^*)$, as usual.

[67] P. Coleman, *Introduction to Many-Body Physics* (Cambridge University Press, Cambridge, 2015).

[68] C. M. Varma, P. B. Littlewood, S. Schmitt-Rink, E. Abrahams, and A. E. Ruckenstein, Phenomenology of the normal state of Cu-O high-temperature superconductors, Phys. Rev. Lett. **63**, 1996 (1989).

[69] A. Georges, G. Kotliar, W. Krauth, and M. J. Rozenberg, Dynamical mean-field theory of strongly correlated fermion systems and the limit of infinite dimensions, Rev. Mod. Phys. **68**, 13 (1996).

Supplemental Material for
"Dynamical scaling and Planckian dissipation due to heavy-fermion quantum criticality"

Andreas Gleis,[1, *] Seung-Sup B. Lee,[1, 2, 3, †] Gabriel Kotliar,[4, 5, ‡] and Jan von Delft[1, §]

[1] *Arnold Sommerfeld Center for Theoretical Physics, Center for NanoScience, and Munich Center for Quantum Science and Technology, Ludwig-Maximilians-Universität München, 80333 Munich, Germany*
[2] *Department of Physics and Astronomy, Seoul National University, Seoul 08826, Korea*
[3] *Center for Theoretical Physics, Seoul National University, Seoul 08826, Korea*
[4] *Department of Physics and Astronomy, Rutgers University, Piscataway, NJ 08854, USA*
[5] *Condensed Matter Physics and Materials Science Department, Brookhaven National Laboratory, Upton, NY 11973, USA*
(Dated: April 23, 2024)

In Sec. S-I, we provide basic definitions and expressions regarding the Fourier transforms of operators and regarding the optical conductivity. Section S-II provides additional information on the numerical computation of the optical conductivity, the role of vertex contributions, and to what extent the Drude term vanishes. Section S-III provides more information on the scaling functions $\mathcal{X}$ and $\mathcal{S}$. In Sec. S-IV, we discuss scaling of the imaginary part of the optical conductivity and provide an analysis of the complex optical conductivity similar in spirit to the analysis of experimental data on CeCoIn$_5$ of Ref. [65].

S-I. OPTICAL CONDUCTIVITY

In this section, we state some textbook [67] formulas that are important in the context of the optical conductivity for the PAM.

A. Fourier transforms of operators

We define the Fourier transform of fermionic creation and annihilation operators in a unitary fashion,

$$c_{\mathbf{k}\sigma} = \frac{1}{\sqrt{N}} \sum_i e^{-i\mathbf{k}\cdot\mathbf{r}_i} c_{i\sigma} \,, \qquad (S1)$$

ensuring $\{c_{\mathbf{k}\sigma}^\dagger, c_{\mathbf{k}'\sigma'}\} = \delta_{\sigma\sigma'}\delta_{\mathbf{k}\mathbf{k}'}$. For bosonic observables $\mathcal{O}_i$ like the current density, on the other hand, we define it as an orthogonal but non-unitary transformation,

$$\mathcal{O}_{\mathbf{q}} = \frac{1}{N} \sum_i e^{-i\mathbf{q}\cdot\mathbf{r}_i} \mathcal{O}_i \,. \qquad (S2)$$

This ensures that the expectation values $\langle\mathcal{O}_{\mathbf{q}}\rangle$ and $\langle\mathcal{O}_i\rangle$ scale the same way with N in the thermodynamic limit. (if we had used a unitary Fourier transforms for bosonic observables, $\langle\mathcal{O}_{\mathbf{q}}\rangle \sim \sqrt{N}$ would not be well-defined in the thermodynamic limit). The same goes for source fields like the vector potential.

B. Current and conductivity

In presence of a vector potential $\mathbf{A}$, the Hamiltonian (1) is modified by replacing the hopping between site i and $i + \mathbf{a}$ by $t \to t \exp(-ieA_i^a)$, where $\mathbf{a}$ is some unit lattice vector. The current density is

$$j_i^a = -\frac{\partial H}{\partial A_i^a} = -ite \sum_\sigma \left(e^{-ieA_i^a} c_{i\sigma}^\dagger c_{i+\mathbf{a}\sigma} - \text{h.c.} \right) \,. \quad (S3)$$

If no lattice symmetry is broken, the current response to a $\mathbf{q}$- and ω-dependent electric field $\mathbf{E}_{\mathbf{q}}(\omega) = i\omega^+ \mathbf{A}_{\mathbf{q}}(\omega)$ (where $\omega^+ = \omega + i0^+$) takes the form $\langle j_{\mathbf{q}}^a \rangle(\omega) = \sigma_{\mathbf{q}}(\omega)E_{\mathbf{q}}^a(\omega)$, where the dynamical conductivity is given by

$$\sigma_{\mathbf{q}}(\omega) = \frac{1}{i\omega^+} \left[\langle \hat{K} \rangle - \chi[j_{\mathbf{q}}^a](\omega) \right] \,, \qquad (S4)$$

$$\hat{K} = -\frac{te^2}{N} \sum_{i\sigma} \left(c_{i\sigma}^\dagger c_{i+\mathbf{a}\sigma} + \text{h.c.} \right) \,,$$

and $j_{\mathbf{q}}^a = \frac{1}{N} \sum_i e^{-i\mathbf{q}\cdot\mathbf{r}_i} j_i^a$. In a d-dimensional hypercubic lattice, $\langle \hat{K} \rangle$ is proportional to the kinetic energy density $\epsilon_{\text{kin}} = \frac{d}{e^2} \langle \hat{K} \rangle$.

The optical conductivity $\sigma(\omega) = \sigma_{\mathbf{q}=\mathbf{0}}(\omega)$ is the response to a uniform electric field. It can be decomposed as [57, 58] $\sigma(\omega) = \sigma^{\text{D}}(\omega) + \sigma^{\text{reg}}(\omega)$, with

$$\sigma^{\text{D}}(\omega) = D \left[\delta(\omega) + \mathcal{P}\frac{i}{\pi\omega} \right] \,, \qquad (S5)$$

$$D = \pi \left[\chi'[j_{\mathbf{0}}^a](0) - \langle \hat{K} \rangle \right] \,, \qquad (S6)$$

$$\sigma^{\text{reg}}(\omega) = \mathcal{P}\frac{1}{i\omega} \left[\chi'[j_{\mathbf{0}}^a](0) - \chi[j_{\mathbf{0}}^a](\omega) \right] \,, \qquad (S7)$$

where $\mathcal{P}$ denotes the principal part. The regular term $\sigma^{\text{reg}}(\omega)$ describes currents that decay at long times; the Drude term $\sigma^{\text{D}}(\omega)$ with Drude weight D describes persistent currents. For a non-superconducting, thermodynamically large lattice model at non-zero temperature, one expects $D = 0$.

The optical conductivity fulfills the f-sum rule,

$$\int_{-\infty}^{\infty} \frac{d\omega}{\pi} \sigma'(\omega) = -\langle \hat{K} \rangle \,, \qquad (S8)$$

which follows when evaluating $\chi'[j^a_0](0)$ using the Kramers–Kronig relation for general susceptibilities,

$$\chi'[\mathcal{O}](\omega') = -\mathcal{P}\int_{-\infty}^{\infty} d\omega \, \chi''[\mathcal{O}](\omega)/(\omega - \omega'). \qquad (S9)$$

C. Bubble contribution

The bubble contribution to the current susceptibility is defined as the susceptibility of a free system but with the Green's functions replaced by the Green's function of the interacting system. We shortly outline the corresponding formulas for the bubble contribution to the local current susceptibility, $\chi_B[j^a_i]$ and to the uniform $\mathbf{q} = 0$ susceptibility, $\chi_B[j^a_0]$. Since the current operator in Eq. (S3) consists only of c-electron operators, the formulas for the bubble contribution only involve c-electron Green's functions. For brevity, we suppress the c labels on all Green's functions, spectral functions and self-energies in this section and in Sec. S-II A. The current operators can be written in terms of the bare current vertex $\mathcal{J}^a$,

$$j^a_i = \sum_{\ell\ell'\sigma} \mathcal{J}^a_{i\ell\ell'} c^\dagger_{\ell\sigma} c_{\ell'\sigma}, \qquad (S10a)$$

$$\mathcal{J}^a_{i\ell\ell'} = -\mathrm{i}te\,(\delta_{i\ell}\delta_{i+\mathbf{a}\ell'} - \delta_{i+\mathbf{a}\ell}\delta_{i\ell'}), \qquad (S10b)$$

$$j^a_{\mathbf{q}} = \frac{1}{N}\sum_i e^{-\mathrm{i}\mathbf{q}\cdot\mathbf{r}_i} j^a_i = \sum_{\mathbf{k}\mathbf{k}'\sigma} \mathcal{J}^a_{\mathbf{q}\mathbf{k}\mathbf{k}'} c^\dagger_{\mathbf{k}\sigma} c_{\mathbf{k}'\sigma} \qquad (S10c)$$

$$\mathcal{J}^a_{\mathbf{q}\mathbf{k}\mathbf{k}'} = \frac{-2te}{N}\delta_{\mathbf{q},\mathbf{k}-\mathbf{k}'} e^{\mathrm{i}\frac{\mathbf{q}\cdot\mathbf{a}}{2}} \sin\left[\left(\mathbf{k}-\frac{\mathbf{q}}{2}\right)\cdot\mathbf{a}\right]. \qquad (S10d)$$

We define the polarization bubble (with $\mathrm{Im}\,z > 0$),

$$\mathcal{P}_{g,g'}(z) = T\sum_m G_g(\mathrm{i}\omega_m)G_{g'}(\mathrm{i}\omega_m + z) \qquad (S11)$$

$$= \int_{-\infty}^{\infty} d\omega \, f(\omega)[A_g(\omega)G_{g'}(\omega + z) \qquad (S12)$$
$$+ A_{g'}(\omega)G_g(\omega - z)],$$

where $G(z)$ is the Masubara Green's function, $A(\omega)$ the corresponding spectral function, $f(\omega)$ the Fermi-Dirac distribution function and g and g' are quantum numbers like momentum, spin or spatial distance, $\mathbf{r}_{ij} = \mathbf{r}_i - \mathbf{r}_j$ and we assume G depends on $|\mathbf{r}_i - \mathbf{r}_j|$ only.

The bubble contribution to the $\mathbf{q} = 0$ current susceptibility is

$$\chi_B[j^a_0](z) = \frac{8t^2e^2}{N}\sum_{\mathbf{k}} \sin^2(\mathbf{k}\cdot\mathbf{a})\mathcal{P}_{\mathbf{k},\mathbf{k}}(z)$$
$$= \frac{8t^2e^2}{N}\sum_{\mathbf{k}} \sin^2(\mathbf{k}\cdot\mathbf{a})\int_{-\infty}^{\infty} d\omega \, f(\omega)\times \quad (S13)$$
$$[A_{\mathbf{k}}(\omega)G_{\mathbf{k}}(\omega + z) + A_{\mathbf{k}}(\omega)G_{\mathbf{k}}(\omega - z)].$$

The corresponding spectral function is ($\nu^\pm = \nu \pm \mathrm{i}0^+$)

$$\chi''_B[j^a_0](\nu) = \frac{\mathrm{i}}{2\pi}\left[\chi_B[j^a_0](\nu^+) - \chi_B[j^a_0](\nu^-)\right]$$

$$= \frac{8t^2e^2}{N}\sum_{\mathbf{k}} \sin^2(\mathbf{k}\cdot\mathbf{a})I_{\mathbf{k}}(\nu) \qquad (S14a)$$

$$I_{\mathbf{k}}(\nu) = \int_{-\infty}^{\infty} d\omega \, [f(\omega) - f(\omega + \nu)]\, A_{\mathbf{k}}(\omega)A_{\mathbf{k}}(\omega + \nu). \qquad (S14b)$$

The bubble contribution to the local current-current susceptibility (involving one link in the lattice, i.e., two sites) is then

$$\chi_B[j^a_i](z) = 2\sum_{mm'}\sum_{nn'} \mathcal{J}^a_{imm'}\mathcal{J}^a_{inn'}\mathcal{P}_{\mathbf{r}_{mn'},\mathbf{r}_{m'n}}(z)$$

$$= -4t^2e^2\int_{-\infty}^{\infty} d\omega \, f(\omega)\times \qquad (S15)$$
$$[[A_{\mathbf{r}_{i,i+\mathbf{a}}}(\omega)G_{\mathbf{r}_{i+\mathbf{a},i}}(\omega + z) - A_{\mathbf{r}_{i,i}}(\omega)G_{\mathbf{r}_{i,i}}(\omega + z)]$$
$$+ [A_{\mathbf{r}_{i+\mathbf{a},i}}(\omega)G_{\mathbf{r}_{i,i+\mathbf{a}}}(\omega - z) - A_{\mathbf{r}_{i,i}}(\omega)G_{\mathbf{r}_{i,i}}(\omega - z)]].$$

The local current-current spectral function is

$$\chi''_B[j^a_i](\nu) = \frac{\mathrm{i}}{2\pi}\left[\chi_B[j^a_i](\nu^+) - \chi_B[j^a_i](\nu^-)\right] \qquad (S16)$$

$$= 4t^2e^2\int_{-\infty}^{\infty} d\omega \, [f(\omega) - f(\omega + \nu)]\times \qquad (S17)$$
$$[A_{\mathbf{r}_{i,i}}(\omega)A_{\mathbf{r}_{i,i}}(\omega + \nu) - A_{\mathbf{r}_{i,i+\mathbf{a}}}(\omega)A_{\mathbf{r}_{i+\mathbf{a},i}}(\omega + \nu)].$$

S-II. OPTICAL CONDUCTIVITY: NUMERICAL COMPUTATION

In this section, we describe how we compute the bubble contribution $\chi''_B[j^a_0](\nu)$ [Eq. (S14a)] in a numerically efficient way, how we treat the electronic self-energy close to zero frequency and temperature, and how we deal with vertex contributions and fulfillment of the f sum rule. We further discuss the potential role of vertex contributions for short-ranged nonlocal current fluctuations.

A. Bubble contribution

Computing the bubble contribution to the optical conductivity requires numerical evaluation of Eq. (S14a). This is challenging, especially close to $\nu = 0$ or $T = 0$, due to the close-to-singular behavior of $A_{\mathbf{k}}(\omega)A_{\mathbf{k}}(\omega+\nu)$ in the integrand.

To deal with this, we exploit our knowledge of $G^{-1}_{\mathbf{k}}(\omega^+) = \omega^+ + \mu - \epsilon_{\mathbf{k}} - \Sigma_{\mathbf{k}}(\omega^+)$. It is a smooth function of ω and known on a predetermined frequency grid $\omega \in \{\omega_i\}$. Since $G^{-1}_{\mathbf{k}}(\omega^+)$ is a smooth function, we represent it by linear interpolation, $G^{-1}_{\mathbf{k}}(\omega^+) = a_i + b_i\omega$, for $I_i = [\omega_i, \omega_{i+1}]$. Due to the logarithmic resolution of NRG, we use a logarithmic frequency grid with $10^{-12} \le |\omega_i| \le 10^4$ and 200 grid points per decade.

By writing

$$A_{\mathbf{k}}(\omega)A_{\mathbf{k}}(\omega+\nu) =$$
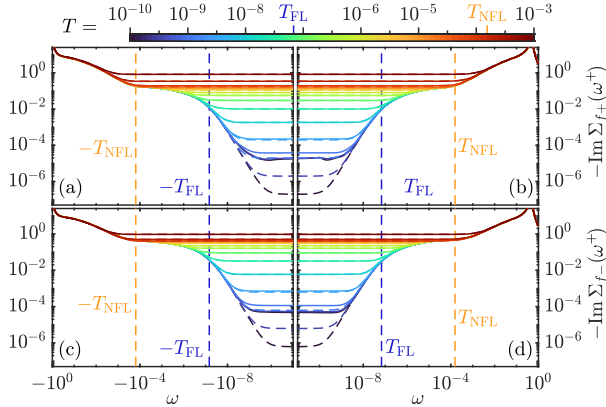
FIG. S1. Self-energy of the f electrons for the self-consistent 2IAM at different temperatures. (a,b) Bonding orbital $(+)$ and (c,d) anti-bonding orbital $(-)$. Solid lines denote the numerical data, dashed lines (not visible whenever they coincide with solid lines) denote the extrapolated self-energy. Visible differences occur only for $|\omega|, T < 10^{-1}T_{\mathrm{FL}}$, i.e., well below the FL scale T_{FL}.

$$\tfrac{1}{\pi}\mathrm{Im}\left[G_{\mathbf{k}}(\omega^+)\frac{G_{\mathbf{k}}(\omega+\nu^+)-G_{\mathbf{k}}(\omega+\nu^-)}{2\pi\mathrm{i}} \right] , \quad \text{(S18)}$$

the frequency integral in Eq. (S14b) can be computed by evaluating the integrals,

$$\begin{aligned} I_{\mathbf{k}}^{\pm}(\nu) &= \int_{-\infty}^{\infty}\mathrm{d}\omega\left[f(\omega)-f(\omega+\nu)\right]G_{\mathbf{k}}(\omega^+)G_{\mathbf{k}}(\omega+\nu^{\pm}) \\ &= \sum_i \int_{I_i}\mathrm{d}\omega\,\frac{\alpha_i+\beta_i\omega}{(a_i+b_i\omega)(c_{i,\pm}+d_{i,\pm}\omega)} \end{aligned} \quad \text{(S19)}$$

where $\alpha_i+\beta_i\omega$ is a linear interpolation of $f(\omega)-f(\omega+\nu)$ on the interval I_i and $a_i+b_i\omega$ and $c_{i,\pm}+d_{i,\pm}\omega$ are the linear interpolations of $G_{\mathbf{k}}^{-1}(\omega^+)$ and $G_{\mathbf{k}}^{-1}(\omega+\nu^{\pm})$, respectively. The integral over every interval I_i in Eq. (S19) is very simple to evaluate exactly, summing up the contributions from all intervals gives $I_{\mathbf{k}}^{\pm}(\nu)$.

The $\mathbf{k}$ sum/integral in Eq. (S14a) is finally computed using a standard integrator. (We use MATLAB's `integral` function.) We use the periodized self-energy when computing Eq. (S14a), cf. App. A.3 of Ref. [39]. In our case, this allows us to reduce the three-dimensional $\mathbf{k}$ integral in Eq. (S14a) to a one-dimensional one, cf. Eq. (A10) of Ref. [39].

B. Self-energy at $\omega, T \simeq 0$

The Drude peak which emerges in the optical conductivity at $T < T_{\mathrm{FL}}$ for small frequencies arises due to $-\mathrm{Im}\Sigma(\omega^+) = a\omega^2 + bT^2$ behavior for $|\omega|, T < T_{\mathrm{FL}}$. Capturing this ω, T-dependence for very small T_{FL} $(\ll T_{\mathrm{NFL}})$, as is the current case close to the QCP, is highly challenging. To achieve this, we keep a large number of states—up to 40,000 $U(1)\times SU(2)$ symmetry multiplets—in iterative diagonalization and use an interleaved Wilson

chain [59, 60] to keep the computational cost manageable. We compute the f-electon self-energy by using the symmetric improved estimator of Ref. [61] which significantly reduces numerical artifacts and leads to state-of-the-art accuracy. This accuracy allows us to obtain $-\mathrm{Im}\Sigma_{f\pm}(\omega^+) = a\omega^2 + bT^2$ behavior for $|\omega|, T \in (T_{\mathrm{FL}}/10, T_{\mathrm{FL}})$ (but not for $|\omega|, T \in (0, T_{\mathrm{FL}}/10)$, because there $-\mathrm{Im}\Sigma_{f\pm}(\omega^+)$ becomes smaller than 10^{-4}, and numerical inaccuracies become significant). Therefore, we fit the coefficients a and b with the data for $(T_{\mathrm{FL}}/10, T_{\mathrm{FL}})$ then extrapolate $-\mathrm{Im}\Sigma_{f\pm}(\omega^+)$ to $(0, T_{\mathrm{FL}}/10)$ based on the fitting. Figure S1 shows the low T and ω behavior of $-\mathrm{Im}\Sigma_{f\pm}(\omega^+)$ before (solid) and after (dashed) extrapolation. The c-electron self-energy $\Sigma_{c\pm}(\omega^+) = V^2/\left(\omega^+ - \epsilon_f - \Sigma_{f\pm}(\omega^+)\right)$ (which is not one-particle irreducible) follows from $\Sigma_{f\pm}(\omega^+)$.

Note that in an FL, $a\pi^2/b = 1$ should hold. On the other hand, our fits yield $a\pi^2/b = \mathcal{O}(2\text{–}3)$ due to the broadening used in NRG, which overestimates a. We have checked that $a \to b/\pi^2$ when we lower the broadening width. This however comes at the expense of severe discretization artifacts. Since the exact value of a is irrelevant to the present work, we preferred to adopt the procedure described above.

C. Local vertex contributions

We stated several times in the main text that vertex contributions are crucial for the current-current correlation functions to capture the strange metallicity and Planckian dissipation. As described in the main text, we have included vertex contributions only for the local contribution, $\chi[j_i^a]$, to the uniform current susceptibility, $\chi[j_{\mathbf{0}}^a] = \chi[j_i^a] + \chi_{\mathrm{nl}}[j_{\mathbf{0}}^a]$, where $j_i^a = -\mathrm{i}te\sum_{\sigma}(c_{i\sigma}^{\dagger}c_{i+\mathbf{a}\sigma} - \mathrm{h.c.})$ is the current between lattice sites i and $i+\mathbf{a}$, the neighbor of i in a-direction. The main reason is that we do not currently have access to three- or four-point correlation functions. By choosing sites i and $i + \mathbf{a}$ as the two sites of our self-consistent two-impurity model, we can compute $\chi[j_i^a]$ directly as a two-point correlation function using NRG. Here, we provide supplemental data that shows to what extent the full local susceptibility $\chi[j_i^a]$ is influenced by its vertex contribution $\chi_{\mathrm{vtx}}[j_i^a] = \chi[j_i^a] - \chi_{\mathrm{B}}[j_i^a]$. To this end, we compare $\chi[j_i^a]$ to its bubble contribution $\chi_{\mathrm{B}}[j_i^a]$, computed via Eq. (S17). The integrand of the latter is *not* close-to-singular [in contrast to that of Eq. (S14b)] and can therefore be efficiently evaluated via a standard integrator.

The bare output of NRG are discrete spectra for $\chi''[j_i^a]$, which are subsequently broadened through log-Gaussian broadening kernels, see Ref. [62] for more details. The spectral functions used in Eq. (S17) to compute $\chi_{\mathrm{B}}''[j_i^a]$ on the other hand are obtained by computing the *self-energy* via the symmetric improved estimators of Ref. [61]; $\chi_{\mathrm{B}}''[j_i^a]$ therefore contains finer high-frequency details than achievable with NRG for $\chi''[j_i^a]$. To compare the full
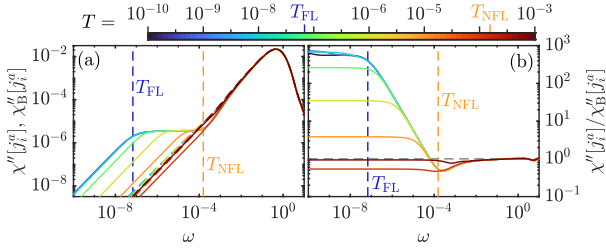
FIG. S2. (a) Spectrum of the local current susceptibility $\chi''[j_i^a](\omega, T)$. Solid lines are full susceptibilities $\chi''[j_i^a]$, dashed lines are the bubble contributions $\chi''_B[j_i^a]$. $\chi''_B[j]$ is almost temperature independent, which is why the $\chi''_B[j_i^a]$ curves for $T < 10^{-3}$ are covered by the $T = 10^{-3}$ curve. $\chi''_B[j_i^a]$ and $\chi''[j_i^a]$ are almost identical at $T = 10^{-3}$. (b) The ratio between full susceptibility and bubble contribution.

FIG. S3. (a,b) Absolute values of the spectra of different nonlocal current susceptibilities, $\chi''[j_i^a, j_1](\omega, T)$ and $\chi''[j_1, j_2](\omega, T)$. Solid lines are full susceptibilities, dashed lines are the bubble contributions. Cusps indicate sign changes in the spectra. (c,d) Ratios between the spectra of the full susceptibility and the bubble contribution. The cusps at $|\omega| > 10^{-1}$ arise due to a slight misalignment between the sign changes in χ'' and χ''_B.

$\chi''[j_i^a]$ and its bubble contribution $\chi''_B[j_i^a]$ [computed from Eq. (S17)], we, therefore, smear out the continuous curve of $\chi''_B[j_i^a]$ by further applying the log-Gaussian kernel used to broaden the discrete data for $\chi''[j_i^a]$, to match their resolution levels. We emphasize here that this broadening of $\chi''_B[j_i^a]$ only affects high-frequency details at $|\omega| > T_{NFL}$, the basic features remain the same.

Figure S2(a) shows the spectrum of the full local current susceptibility $\chi''[j_i^a]$ and of the corresponding bubble contribution $\chi''_B[j_i^a]$, while Fig. S2(b) shows their ratio. The bubble contribution captures only the high-frequency behavior at $|\omega|, T > T_{NFL}$ well: the spectra in Fig. S2(a) almost coincide and the ratios in Fig. S2(b) are close to 1.

On the other hand, the plateau emerging below $|\omega|, T < T_{NFL}$ is not captured at all by the bubble contribution, i.e., both the ω/T scaling and the Planckian dissipation discussed in the main text and in Sec. S-III result from vertex contributions. The ratio shown in Fig. S2(b) increases dramatically in the NFL region ($T_{FL} < |\omega|, T < T_{NFL}$) by several orders of magnitude and saturates close to 10^3 in the FL region ($|\omega|, T < T_{FL}$).

D. Estimate of nonlocal vertex contributions

To estimate what to expect for nonlocal current fluctuations in terms of scaling and vertex contributions, we define "current" operators that lie across the cluster boundaries,

$$j_i = (-1)^i \frac{ite}{\sqrt{5}} \left(c_{i\sigma}^\dagger a_{i\sigma} - \text{h.c.} \right), \quad (S20)$$

where $a_{i\sigma}$ annihilates a spin-σ electron in the first bath orbital (within the Wilson chain) that directly couples to the c orbital of the cluster site $i = 1, 2$. According to the effective medium construction of DMFT (which defines bath sites by replacing the interaction on the original lattice sites by the self-energy, cf. Sec. III D of Ref. [69]), the Green's function of $a_{i\sigma}$ is the same as

that of a symmetric superposition of the five nearest neighbors (on the lattice) of site i which are not located on the same cluster. Due to that, we can interpret these orbitals as a proxy for the aforementioned symmetric superposition. The current operators in Eq. (S20) can therefore be interpreted as a proxy for the average (hence normalization by $\sqrt{5}$) current between these five nearest-neighbor sites and the corresponding cluster site. Since there is no specific direction in the lattice associated with these currents, we did not specify a superscript a in Eq. (S20). We emphasize that this correspondence is *not* exact since the first bath sites are non-interacting orbitals that belong to the dynamical mean field. Correlators involving j_1 or j_2 do not enter the results shown in the main text.

We compute $\chi[j_i^a, j_1]$ and $\chi[j_1, j_2]$ to estimate the behavior of nearest-neighbor and next-nearest-neighbor current susceptibilities, respectively. Their spectra, including the corresponding bubble contribution, are shown in Fig. S3(a,b). The spectra of the full susceptibilities again show a similar plateau as observed for the local current susceptibility. Figure S3(c,d) shows the ratio between full susceptibility and bubble contribution. Similarly to the local current susceptibility, the ratio is somewhat close to 1 for $|\omega|, T > T_{NFL}$ and becomes large for $|\omega|, T < T_{NFL}$, suggesting that vertex contributions are important also on the nonlocal level in this region.

In Fig. S4, we further illustrate that $\chi''[j_i^a, j_1]$ and $\chi''[j_1, j_2]$ show ω/T scaling very similar to $\chi''[j_i^a]$. Since the behavior of the nonlocal susceptibilities is qualitatively similar to that of the local susceptibility, we expect that the full nonlocal current susceptibility $\chi''_{nl}[j]$, in contrast to its bubble contribution $\chi''_{B,nl}[j]$, will show similar ω/T scaling as $\chi''[j_i^a]$. As discussed in the main text, we expect
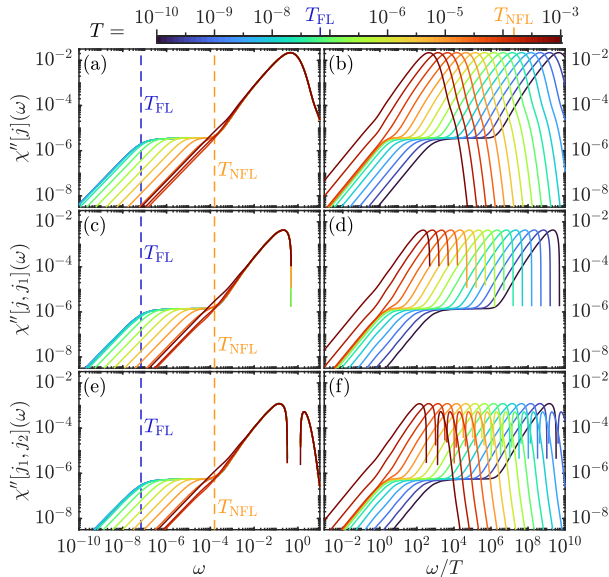
FIG. S4. Current spectra versus frequency (left columns) and versus ω/T (right columns). (a,b) Local current spectrum. (c,d) Proxy to the nearest-neighbor current spectrum. (e,f) Proxy to the next-nearest-neighbor current spectrum.

that the full inclusion of vertex contributions in $\chi''_{\mathrm{nl}}[j]$ will ameliorate or fully avoid the artifacts seen in Fig. 3(c) for the resistivity $\rho(T)$: (i) in the NFL region, the nearly-T-linear behavior will become fully-T-linear; and (ii) in the FL-to-NFL crossover region, the shoulder will become less prominent or disappear.

E. Drude weight

In this section, we discuss the Drude weight of Eq. (S6), $D/\pi = \chi'[j_{\mathbf{0}}^a](0) - \langle \hat{K} \rangle$. According to Eq. (S5), if $D \neq 0$ that would imply (i) a $\delta(\omega)$ contribution to $\sigma'(\omega)$ and therefore zero resistivity (i.e., persistent currents), and (ii) a $1/\omega$ contribution in $\sigma''(\omega)$. Since our study of $\sigma(\omega)$ considers only non-superconducting solutions at $T > 0$, we expect that our system does not support persistent currents and $D = 0$. Accordingly, we have set $D = 0$ for all results shown in this manuscript.

As a consistency check, we have also computed the Drude weight directly. This is a difficult task, since the numerical challenges involved in computing $\chi'[j_{\mathbf{0}}^a](0)$, a *uniform, zero-frequency* susceptibility, and $\langle \hat{K} \rangle$, a *local, equal-time* expectation value, are quite different. Moreover, our computation of $\chi'[j_{\mathbf{0}}^a]$ involves a rather crude approximation [Eq. (6) of the main text]. Nevertheless, we find $|D|/\pi$ to be remarkably small, $\lesssim 10^{-3}$, with an estimated numerical uncertainty that is likewise of the order of 10^{-3}. This justifies our choice to set $D = 0$. Below, we describe how we obtained these values.

Figure S5 shows the Drude weight D/π, with the static current response $\chi'[j_{\mathbf{0}}^a](0)$ computed via Eq. (6) in the
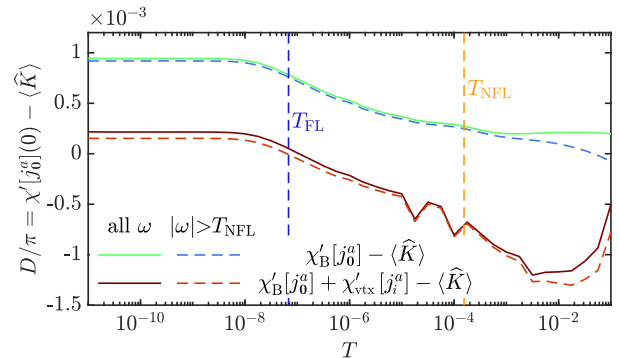
FIG. S5. The Drude weight $D/\pi = \chi'[j_{\mathbf{0}}^a](0) - \langle \hat{K} \rangle$ vs. temperature. For the upper (or lower) row of the legend, $\chi'[j_{\mathbf{0}}^a](0)$ was approximated as $\chi'_{\mathrm{B}}[j_{\mathbf{0}}^a](0)$ (or $\chi'_{\mathrm{B}}[j_{\mathbf{0}}^a](0) + \chi'_{\mathrm{vtx}}[j_i^a](0)$), i.e., using only the bubble contribution (or including also the local vertex contribution). When computing these $\chi'[j](0)$ terms via the Kramers–Kronig transformation (S9), we either integrated over all $\omega \in \mathbb{R}$ (solid lines) or only high frequencies $|\omega| > T_{\mathrm{NFL}}$ (dashed lines). Since solid and dashed lines almost match, $\chi'[j](0)$ is governed by high-frequency contributions, where NRG has poorer frequency resolution. From that perspective, the values for the Drude weight found here, $D/\pi \lesssim 10^{-3}$, are remarkably close to the expected value of zero.

main text. Both the bubble contribution $\chi'_{\mathrm{B}}[j_{\mathbf{0}}^a](0)$ and our locally vertex-corrected result $\chi'_{\mathrm{B}}[j_{\mathbf{0}}^a](0) + \chi'_{\mathrm{vtx}}[j_i^a](0)$ show a deviation from $\langle \hat{K} \rangle$ of the order of 10^{-3}. The inclusion of $\chi'_{\mathrm{vtx}}[j_i^a](0)$ slightly reduces this deviation at low T but slightly increases it at high T. The solid and dashed lines in Fig. S5 compare results obtained by computing the $\chi'[j_{\mathbf{0}}^a](0)$ contributions via the Kramers–Kronig transform (S9) in two ways, either including the spectral weight from all frequencies, $\omega \in \mathbb{R}$ (solid), or only from large frequencies, $|\omega| > T_{\mathrm{NFL}}$ (dashed). Since the solid and dashed lines almost match, the contribution to D from low frequencies $|\omega| < T_{\mathrm{NFL}}$ (including the contribution from the plateau in $\chi''_{\mathrm{vtx}}[j_i^a](\omega)$) is negligible. Therefore, the non-fulfillment of $D = 0$ is mainly due to inaccuracies at high frequencies.

High-frequency inaccuracies are to be expected in NRG spectra, due to the use of logarithmic discretization and an asymmetric log-Gaussian broadening kernel (cf. Eqs. (17) and (21) from Ref. [62]), which can lead to slight shifts in spectral weight. The broadened spectral function is evaluated on a logarithmic frequency grid and approximated by linear interpolation between grid points. In practice, this means that if a discrete spectrum of the form $\chi''(\omega) = \sum_j \chi''_j \delta(\omega - E_j)$ is broadened, the integral of the broadened spectrum can differ slightly from the actual weight, $\sum_j \chi''_j$, typically by an amount $\sim \mathcal{O}(10^{-3})$. As a result, the Kramers–Kronig transformation used to compute $\chi'(0) = -\mathcal{P} \int \chi''(\omega)/\omega$ usually induces an error $\sim \mathcal{O}(10^{-3})$, compared to the result directly computed from the discrete data, $\chi'(0) = -\sum_j \chi''_j/E_j$. Since our approximation of $\chi''[j_{\mathbf{0}}^a](\omega)$ involves the bubble contributions $\chi''_{\mathrm{B}}[j_{\mathbf{0}}^a](\omega)$ and $\chi''_{\mathrm{B}}[j_i^a](\omega)$ which are only available as broad-

ened spectral functions, direct computation of $\chi'_\mathrm{B}[j_\mathbf{0}^a](0)$ from discrete data is not possible. All of the aforementioned issues, on top of the approximation (6), can lead to inaccuracies in the spectral weights and their corresponding frequencies. We have checked that shifting spectral positions by $\mathcal{O}(1\%)$, i.e., $\omega \to (1\pm10^{-2})\omega$ and normalizing the spectra accordingly, i.e., $\chi''(\omega) \to (1\pm 10^{-2})^{-1}\chi''(\omega)$, is sufficient to change $\chi'[j_\mathbf{0}^a](0)$ by $\mathcal{O}(10^{-3})$. For all these reasons, we estimate the numerical uncertainty of our determination of the Drude weight D to be at least of the order of 10^{-3}.

S-III. SCALING FUNCTION

In the main text, we proposed the phenomenological ansatz $\widetilde{\chi}''(\omega, T)$ to capture the X^{xz} and current spectra in the NFL region. In the limit of $|\omega| \ll T_\mathrm{NFL}$, the ansatz is governed by the scaling function (5), $\mathcal{X}(x) = \mathcal{X}'(x) - \mathrm{i}\pi\mathcal{X}''(x)$. To ease future referencing, we duplicate the ansatz (4) and its relation (5) to the scaling function here:

$$\widetilde{\chi}''(\omega, T) = \chi_0 \int_T^{T_\mathrm{NFL}} \frac{\mathrm{d}\epsilon}{\pi} \frac{(1-\mathrm{e}^{-\frac{\omega}{T}})(\frac{\epsilon}{T})^\nu bT}{(\omega - a\epsilon)^2 + (bT)^2}, \qquad \text{(S21)}$$

$$\widetilde{\chi}(\omega, T) \simeq \mathcal{X}_0'\Big(\frac{T}{T_\mathrm{NFL}}\Big) + \mathcal{X}'\Big(\frac{\omega}{T}\Big) - \mathrm{i}\pi\mathcal{X}''\Big(\frac{\omega}{T}\Big), \quad \text{(S22)}$$

In this Section, we motivate the ansatz, derive the scaling function, and provide the detail of the fitting, for the X^{xz} susceptibility. The discussion for other susceptibilities showing a plateau and scaling in the NFL region (e.g., the current susceptibility) is analogous.

We start with representing the greater correlation function $\chi_>[X^{xz}]$ in terms of a superposition of coherent excitations,

$$\chi_>[X^{xz}](t) = -\mathrm{i}\theta(t)\langle X^{xz}(t)X^{xz}\rangle \qquad \text{(S23)}$$

$$\simeq \widetilde{\chi}_>[X^{xz}](t) = -\mathrm{i}\int_T^{T_\mathrm{NFL}} \mathrm{d}\epsilon \left(\frac{\epsilon}{T}\right)^\nu \mathrm{e}^{-\mathrm{i}(a\epsilon - \mathrm{i}bT)t}.$$

These coherent excitations have mean energy $a\epsilon$, decay rate bT, and a power-law density of states with exponent ν. We assume that the spectrum of this ansatz,

$$\widetilde{\chi}_>[X^{xz}](\omega) = -\mathrm{i}\int_0^\infty \mathrm{d}t \, \langle X^{xz}(t)X^{xz}\rangle \mathrm{e}^{\mathrm{i}\omega^+ t}, \qquad \text{(S24)}$$

$$\widetilde{\chi}_>''[X^{xz}](\omega) = -\frac{1}{\pi}\mathrm{Im}\,\widetilde{\chi}_>[X^{xz}](\omega),$$

captures the low-frequency behavior, $|\omega| < T_\mathrm{NFL}$. High frequencies $|\omega| > T_\mathrm{NFL}$ are not governed by the quantum critical point and contain information on the local-moment behavior which is not of interest here. The spectrum should also fulfill the fluctuation-dissipation theorem,

$$\widetilde{\chi}_>''[X^{xz}](-\omega) = -\frac{1-\mathrm{e}^{-\omega/T}}{1-\mathrm{e}^{\omega/T}}\widetilde{\chi}_>''[X^{xz}](\omega), \qquad \text{(S25)}$$

which mainly affects and constrains the very low-frequency spectrum, $|\omega| \lesssim T$. We therefore use our ansatz (S23) to compute the $\omega > 0$ part of the spectrum (S24) and we then determine the $\omega < 0$ part via Eq. (S25), i.e., we enforce Eq. (S25).

The spectrum of the corresponding retarded correlator is given by

$$\widetilde{\chi}''[X^{xz}](\omega) = (1 - \mathrm{e}^{-\omega/T})\widetilde{\chi}_>''[X^{xz}](\omega), \qquad \text{(S26)}$$

which leads to the ansatz (S21) for $\omega > 0$. The $\omega < 0$ side is given by the oddity, $\widetilde{\chi}''[X^{xz}](-\omega) = -\widetilde{\chi}''[X^{xz}](\omega)$. The real part is obtained via the Kramers–Kronig relation,

$$\widetilde{\chi}'[X^{xz}](\omega) = \mathcal{P}\int_{-\infty}^\infty \mathrm{d}\omega' \frac{\widetilde{\chi}''[X^{xz}](\omega')}{\omega - \omega'}. \qquad \text{(S27)}$$

To get the scaling function $\mathcal{X}''$, we take the limit of $T_\mathrm{NFL} \to \infty$ in Eq. (S21). (This limit exists for $\nu < 1$, while our data shows $\nu \simeq 0$.) Equation (S21) is then a function of $x = \omega/T$,

$$\mathcal{X}''(x) = \chi_0\int_1^\infty \frac{\mathrm{d}y}{\pi} \frac{(1-\mathrm{e}^{-x})y^\nu b}{(x-ay)^2 + b^2}, \, x > 0, \quad \text{(S28)}$$

$$\mathcal{X}''(-x) = -\mathcal{X}''(x).$$

In Eq. (S27), $\widetilde{\chi}'[X^{xz}](\omega)$ is singular in $T_\mathrm{NFL}/T \to \infty$ if $\nu \geq 0$. Therefore, we split the real part into a potentially singular static part, $\widetilde{\chi}'[X^{xz}](0)$, and a non-singular part, $\widetilde{\chi}'[X^{xz}](\omega) - \widetilde{\chi}'[X^{xz}](0)$. Using

$$\frac{1}{\omega-\omega'} - \frac{1}{-\omega'} = \frac{\omega}{(\omega-\omega')\omega'},$$

we can take the $T_\mathrm{NFL}/T \to \infty$ limit of the non-singular $\widetilde{\chi}'[X^{xz}](\omega) - \widetilde{\chi}'[X^{xz}](0)$ part,

$$\mathcal{X}'(x) = \mathcal{P}\int_{-\infty}^\infty \mathrm{d}x' \frac{x\mathcal{X}''(x')}{(x-x')x'}. \qquad \text{(S29)}$$

This defines the scaling function $\mathcal{X}(x) = \mathcal{X}'(x) - \mathrm{i}\pi\mathcal{X}''(x)$.

For the potentially singular static contribution $\widetilde{\chi}'[X^{xz}](0)$, we cannot safely take the $T_\mathrm{NFL} \to \infty$ limit. In the $T_\mathrm{NFL}/T \gg 1$ limit, the spectral part $\widetilde{\chi}''[X^{xz}](\omega)$ sharply drops to zero for $|\omega| > T_\mathrm{NFL}$, so that we can approximate $\widetilde{\chi}'[X^{xz}](0) \simeq \mathcal{X}_0'(T/T_\mathrm{NFL})$, with

$$\mathcal{X}_0'(y) = -\mathcal{P}\int_{-y}^y \mathrm{d}x' \frac{\mathcal{X}''(x')}{x'}. \qquad \text{(S30)}$$

$\mathcal{X}_0'(T)$ describes the contribution of the excitations within the NFL region to the static response,

$$\chi_\mathrm{NFL}'(0) = -\mathcal{P}\int_{-T_\mathrm{NFL}}^{T_\mathrm{NFL}} \mathrm{d}\omega' \frac{\chi''(\omega')}{\omega'}. \qquad \text{(S31)}$$

The remaining contribution from high-energy excitations,

$$\chi_\mathrm{high}'(0) = \chi'(0) - \chi_\mathrm{NFL}'(0), \qquad \text{(S32)}$$
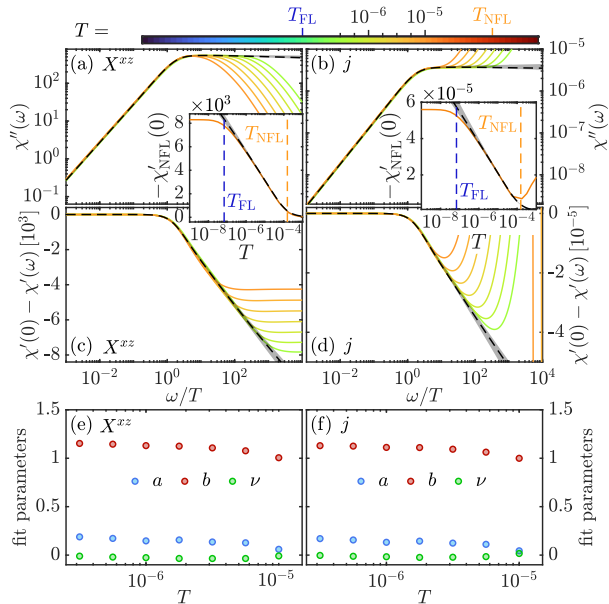
FIG. S6. (a) $\chi''[X^{xz}](\omega)$ and (b) $\chi''[j](\omega)$ (solid lines) versus scaling function $\mathcal{X}''(x)$ (black dashed line). The grey shaded area indicates the deviation when fitting at different temperatures. Only curves used in the fitting process are shown, the ticks on the color bar at the top indicate the temperature, and the color range is the same as in Fig. 3 of the main text. (c,d) Corresponding real parts. Insets: NFL contribution to the static susceptibility. (e,f) Fit parameters at different temperatures. The 95% confidence interval is smaller than the symbol size.

may dominate the temperature dependence of $\chi'(0)$. In that case, $\mathcal{X}_0'(T/T_{\mathrm{NFL}})$ only governs $\chi_{\mathrm{NFL}}'(0)$ but *not* $\chi'(0)$. This is for instance the case for the static current susceptibility, where only $\chi_{\mathrm{NFL}}[j]'(0)$ follows $\mathcal{X}_0'(T)$. On the other hand, $\chi'[X^{xz}](0)$ is well described by $\mathcal{X}_0'(T)$ up to an additive constant.

We determine the parameters a, b, ν and χ_0 in Eq. (S28) by fitting logarithms of $\chi_>''(\omega)$ to the logarithm of our scaling ansatz (S28). We employ a least-square fit on a logarithmic frequency grid with 20 grid points per decade and frequencies between $\omega_{\min} = 10^{-9}$ and $\omega_{\max} = T_{\mathrm{NFL}}/4$, i.e., we stay well below the crossover temperature T_{NFL}. Our fits are done for seven logarithmically spaced temperatures between $(T_{\mathrm{FL}} \ll)10^{-6.5}$ and $10^{-5}(\ll T_{\mathrm{NFL}})$, i.e., for temperatures well separated from the crossover temperatures T_{FL} and T_{NFL}. We then determine a scaling curve by the geometric average over the fitted curves at different temperatures. The largest deviations from the geometric average serve as an error bar. $\mathcal{X}'(x)$ and $\mathcal{X}_0'(T)$ are determined via Eqs. (S29) and (S30), respectively.

Figure S6(a–d) shows the fitting result for $\chi''[X^{xz}](\omega)$ and $\chi''[j](\omega)$. In both cases, our ansatz fits our data very well, with all temperatures yielding very similar curves (the grey area, indicating the largest deviations from the geometric mean, is relatively small). Fig. S6(e,f)
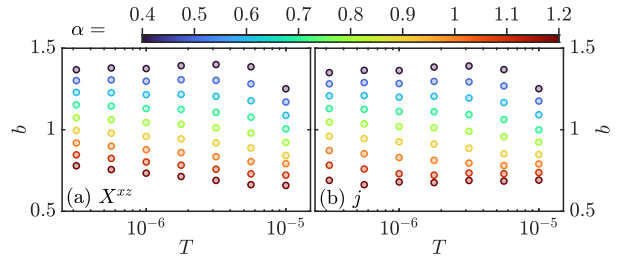
FIG. S7. Effect of log-Gaussian broadening width $\sigma = \alpha \ln \Lambda$ on the fit parameter b for (a) $\chi''[X^{xz}](\omega)$ and (b) $\chi''[j](\omega)$.

shows the results for the fit parameters a, b and ν. The fitting parameters for both $\chi''[X^{xz}](\omega)$ and $\chi''[j](\omega)$ are very similar and the variation with temperature is small. We note that the fits for the highest temperatures are a little less reliable because the plateau in $\chi''(\omega)$ is not that well developed yet. Most important to us is the result for b, which varies between 1.153 at $T = 10^{-6.5}$ and 1.005 at $T = 10^{-5}$ for $\chi''[X^{xz}](\omega)$ and between 1.130 at $T = 10^{-6.5}$ and 0.999 at $T = 10^{-5}$ for $\chi''[j](\omega)$. Thus, our results are consistent with Planckian dissipation, i.e., the lifetime of X^{xz} or current excitations is $\tau \simeq 1/T$, up to a prefactor close to 1.

The fit parameters also depend on how the discrete spectral data from NRG is broadened. For our scaling analysis, we used both a log-Gaussian broadening kernel (cf. Eq. (17) of Ref. [62]) with width $\sigma = 0.7 \ln \Lambda$ ($\Lambda = 3$) and the derivative of the Fermi-Dirac distribution with width $\gamma = T/10$ (cf. Eq. (21) of Ref. [62]) as linear broadening kernel. The broadening parameters are chosen such that the data is almost underbroadened (i.e., discretization artifacts become visible for smaller broadening width). In Fig. S7, we show the effect on b of varying the width $\sigma = \alpha \ln \Lambda$ of the log-Gaussian broadening kernel. Most importantly, b remains of order 1 and changes from $b \simeq 1.4$ for $\alpha = 0.4$ (underbroadened) to $b \simeq 0.66$ for $\alpha = 1.2$ (overbroadened). Interestingly, the parameter b which determines the decay rate *decreases* with *increasing* broadening width. The linear broadening parameter γ (not shown) appears to have the converse effect, i.e., lower γ leads to lower b and vice versa.

The scaling function $\mathcal{S}(x)$ for the optical conductivity follows from the scaling function $\mathcal{X}(x)$ for the current susceptibility,

$$T\sigma(\omega) = \mathcal{S}(x) = -\frac{1}{\mathrm{i}x}\mathcal{X}(x) = \mathcal{S}'(x) + \mathrm{i}\mathcal{S}''(x)\,,$$
$$\mathcal{S}'(x) = \frac{\pi}{x}\mathcal{X}''(x)\,,$$
$$\mathcal{S}''(x) = \frac{1}{x}\mathcal{X}'(x) = \mathcal{P}\int_{-\infty}^{\infty}\mathrm{d}x'\,\frac{\mathcal{X}''(x')}{(x-x')x'}\,. \quad (S33)$$

We show and discuss the scaling of the real part of σ in the main text; the scaling of the imaginary part is shown in Fig. S8(b).
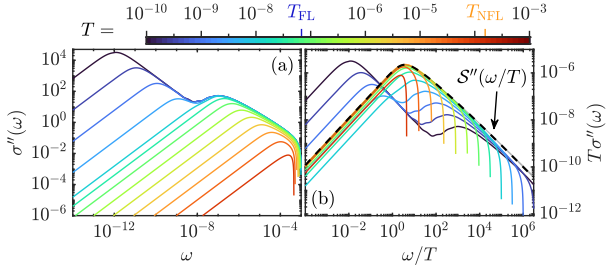
FIG. S8. (a) Imaginary part of the optical conductivity at different temperatures. $\sigma''(\omega)$ becomes negative around $\omega \lesssim 10^{-3}$. (b) Dynamical scaling of the imaginary part. In the NFL region, all curves fall onto the scaling curve $\mathcal{S}''(\omega/T)$. Data at $\omega > 10^{-3}$ has been omitted for clarity.

S-IV. COMPLEX OPTICAL CONDUCTIVITY

In this section, we provide data on the imaginary part of the optical conductivity. Further, we make contact with recent experimental data on CeCoIn$_5$ from Ref. [65], where the dynamical scattering rate $\tau^{-1}(\omega)$ and the dynamical effective mass $m^*(\omega)$ were studied. Even though CeCoIn$_5$ has a strange-metal-like $\tau^{-1}(0) \propto \rho(T) \propto T$, the authors of Ref. [65] found that both the frequency dependence of $\tau^{-1}(\omega)$ and the temperature dependence of the renormalized scattering rate $\tau^{*-1} = \tau^{-1}(0)/m^*(0)$ show FL-like ω^2 and T^2 behavior, respectively. We make contact with these surprising experimental findings by showing that in our CDMFT+NRG data, (i) $\tau^{-1}(\omega) \propto \omega^2$ holds at low frequencies ($|\omega| \lesssim T$) throughout the strange-metal region $T_{\rm FL} < T < T_{\rm NFL}$; and (ii) $\tau^{*-1} \propto T^2$ holds for $T_{\rm NFL}/10 \lesssim T < T_{\rm NFL}$ while deep in the strange metal, $\tau^{*-1} \propto T$ holds.

The imaginary part $\sigma''(\omega) = \operatorname{Im}\sigma(\omega)$ is shown in Fig. S8. As expected from our discussion on σ', also σ'' exhibits ω/T scaling in the NFL region, where it is well described by the scaling curve $\mathcal{S}''(x)$.

Following Ref. [65], we define the ω-dependent transport scattering rate $\tau^{-1}(\omega)$ and effective mass $m^*(\omega)$,

$$\tau^{-1}(\omega) = \operatorname{Re}\left[\frac{1}{\sigma(\omega)}\right], \; m^*(\omega) = -\frac{1}{\omega}\operatorname{Im}\left[\frac{1}{\sigma(\omega)}\right], \; \text{(S34)}$$

$$\sigma(\omega) = \frac{1}{\tau^{-1}(\omega) - \mathrm{i}\omega\, m^*(\omega)}. \quad \text{(S35)}$$

Since we are interested in the qualitative frequency and temperature dependence of these quantities, we omitted the constant prefactors in Eq. (1) of Ref. [65]. Note that $\tau^{-1}(0) = \tau_0^{-1} = \rho(T)$, which is shown in Fig. 3(c) of the main text. In a normal FL (without disorder) exhibiting a usual Drude peak in $\sigma(\omega)$, we expect $\tau_0^{-1} \sim T^2$, $\tau^{-1}(\omega) = \tau_0^{-1} + a\omega^2$, while $m^*(\omega) \simeq m^*(0) = m_0^*$ is expected to be a temperature-independent constant.

Figure S9(a) shows our results for $\tau^{-1}(\omega)$. It shows a peak around $|\omega| = T_{\rm NFL}$ where the hybridization gap forms and then decreases towards $\omega = 0$. There, $\tau^{-1}(0) = \tau_0^{-1} = \rho(T) \propto T$ for $T_{\rm FL} < T < T_{\rm NFL}$. At intermediate
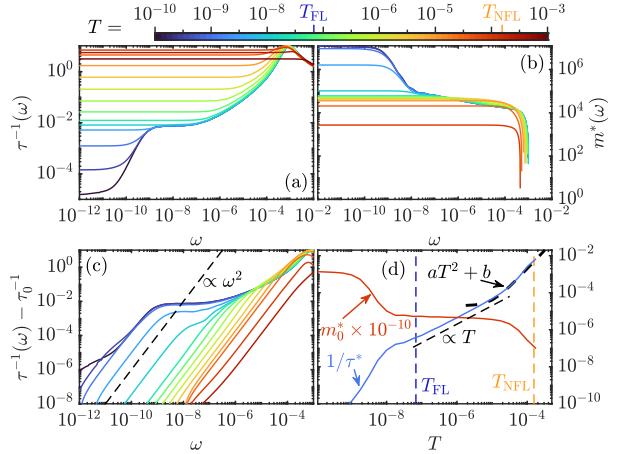
FIG. S9. Frequency dependence of (a) the transport scattering rate $\tau^{-1}(\omega)$, (b) the effective mass $m^*(\omega)$, and (c) $\tau^{-1}(\omega) - \tau_0^{-1}$, where $\tau_0^{-1} = \tau^{-1}(0) = \rho$. (d) Temperature dependence of $\tau^{*-1} = \tau_0^{-1}/m_0^*$ and $m_0^* = m^*(0)$.

frequencies within the NFL region ($\max(T_{\rm FL}, T) < |\omega| < T_{\rm NFL}$), $\tau^{-1}(\omega)$ has a non-trivial ω- and T-dependence and does not seem to follow a simple power law with possible logarithmic corrections. In this region, the optical conductivity does not fit to a usual Drude peak. This non-Drude behavior is most clearly visible from our data for $\sigma'(\omega, T)$ [Fig. 3(a) in the main text], which shows a ω^{-1} dependence in the NFL region, while a usual Drude peak would imply an ω^2 dependence. Similar non-Drude behavior of the optical conductivity has been observed in YbRh$_2$Si$_2$ [16, 18].

Remarkably, in the NFL region ($T_{\rm FL} < T < T_{\rm NFL}$) at low frequencies $|\omega| \lesssim T$, we also find $\tau^{-1}(\omega) - \tau_0^{-1} \sim \omega^2$ similar to a FL, cf. Fig. S9(c). An $\sim \omega^2$ dependence of $\tau^{-1}(\omega)$ has also been found in CeCoIn$_5$, cf. Fig, 4(a,c) of Ref. [65] and its discussion. However, an important difference to normal FL behavior lies in the temperature dependence of the ω^2 prefactor of $\tau^{-1}(\omega) - \tau_0^{-1} = a(T)\,\omega^2$: in the NFL strange-metal region, $a(T)$ is temperature dependent, which is not the case in a normal FL phase. At low frequencies, $m^*(\omega) \simeq \text{const.}$ [c.f. Fig. S9(b)] and $\tau_0^{-1} \sim 1/T$, hence the ω/T scaling of $\sigma(\omega, T)$ we have shown in this work dictates $a(T) \sim 1/T$. This is in line with the data shown in Fig. S9(c).

We emphasize that in our results, $\tau^{-1}(\omega)$ is *not* proportional to $-\operatorname{Im}\Sigma(\omega)$ (*without* vertex contributions, a proportionality would be expected). In our CDMFT+NRG approach to the PAM, $-\operatorname{Im}\Sigma(\omega)$ has a logarithmic frequency and temperature dependence, cf. Figs. 11 and 12 of Ref. [39]. The frequency and temperature dependence $\tau^{-1}(\omega)$ discussed above is different from that. This again directly illustrates the importance of vertex contributions. In an MFL [68] as it appears for instance in the Yukawa–SYK approach [28] with interaction disorder, the strange-metal behavior arises due to a dominant bubble contribution and therefore $\tau^{-1}(\omega) \sim -\operatorname{Im}\Sigma(\omega) \sim \max(T, |\omega|)$
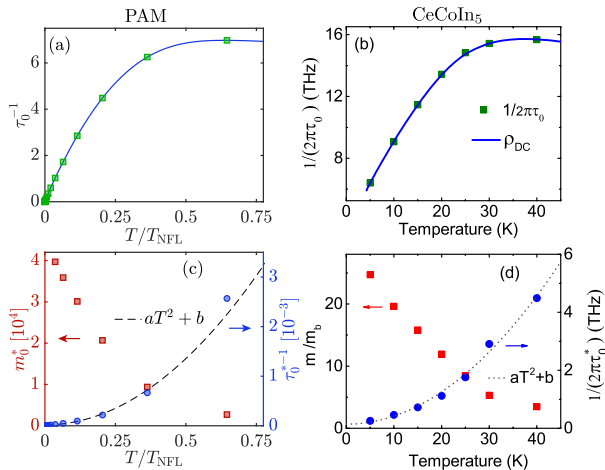
FIG. S10. (a) Scattering rate $\tau_0^{-1} = \rho(T)$ versus temperature for $T \lesssim T_{\mathrm{NFL}} \simeq 1.5 \cdot 10^{-4}$ for the PAM. Green squares are data points, and the blue line is a spline interpolation that serves as a guide to the eye. (b) Scattering rate τ_0^{-1} (green squares) and rescaled resistivity (blue line) for CeCoIn$_5$ close to its coherence temperature $T^* = 40K$. The data in (b) is adapted from Fig. 4(b) of Ref. [65]. (c) Renormalized scattering rate (blue circles) and effective mass (red squares) versus temperature for the PAM. The black dashed line is a quadratic fit to the renormalized scattering rate in this temperature region. (d) Renormalized scattering rate (blue circles) and effective mass (red squares) versus temperature for CeCoIn$_5$, adapted from Fig. 4(d) of Ref. [65].

would be *linear* in frequency.

Figure S9(b) shows $m^*(\omega)$. In the NFL region ($T_{\mathrm{FL}} < T < T_{\mathrm{NFL}}$), $m^*(\omega)$ is strongly frequency dependent around the NFL scale, $\omega \simeq 10^{-3}$–$10^{-4} \simeq T_{\mathrm{NFL}}$, and then saturates to an almost frequency and temperature-independent value $m^*(\omega) \simeq m^*(0) = m_0^*$. The weak frequency and temperature dependence of $m^*(\omega)$ does not seem to follow a simple power law. Interestingly, even though there are no well-defined QPs in the strange-metal region, there nevertheless seems to be a somewhat well-defined effective

mass m_0^*. We emphasize though that in the NFL region, $m_0^* \simeq 5 \cdot 10^4 \sim 10/T_{\mathrm{NFL}}$ is orders of magnitude smaller than in the FL region, where $m_0^* \simeq 1.5 \cdot 10^7 \sim 1/T_{\mathrm{FL}}$, cf. Fig. S9(d). The effective mass in the NFL region is therefore decisively distinct from the QP mass in the low-temperature FL region.

In Fig. S9(d), we show the temperature dependence of the renormalized scattering rate $\tau^{*-1} = \tau_0^{-1}/m_0^*$ (blue), together with m_0^* (red). Deep in the NFL region, we find $\tau^{*-1} \sim T$, since $\tau_0^{-1} \sim T$ and $m_0^* = $ const. Interestingly, in the crossover region between $T \simeq T_{\mathrm{NFL}}$ and $T \simeq 10^{-1}T_{\mathrm{NFL}}$, τ^{*-1} deviates from the linear-in-T behavior and is consistent with FL-like T^2 behavior.

A similar T^2 behavior was reported for CeCoIn$_5$ in Ref. [65], where this behavior was interpreted as evidence for a hidden Fermi liquid. Our calculations suggest that the T^2 behavior is rather a crossover behavior and measurements at lower temperatures are necessary for a definite conclusion. Such measurements are presumably not possible in CeCoIn$_5$ due to its relatively high T_c. A promising candidate material to clarify whether $\tau^{*-1} \sim T$ or $\sim T^2$ may be YbRh$_2$Si$_2$. To emphasize the similarity between the experimental data on CeCoIn$_5$ and our results on the PAM more visually, we show the resistivity $\rho(T)$ of the PAM in Fig. S10(a) on a linear scale in the crossover region, next to the corresponding experimental data on CeCoIn$_5$ [Figs. S10(b)], adapted from Fig. 4(b) of Ref. [65]. In Figs. S10(c) and (d), we further show the data for the renormalized scattering rate and the effective mass for both the PAM and CeCoIn$_5$, respectively (adapted from Fig. 4(d) of Ref. [65] for the latter). The experimental data on CeCoIn$_5$ and our numerical data on the PAM show remarkable qualitative agreement in the crossover region: (i) the resistivity has a broad maximum and turns to linear-in-T; (ii) the renormalized scattering rate $\tau^{*-1} \propto T^2$; and (iii) the effective mass m_0^* increases with temperature in a remarkably similar fashion.

4 Conclusion and Outlook

In this thesis, we have presented results relevant to Kondo breakdown (KB) quantum criticality in heavy fermions (HF). We obtained these results by conducting numerical studies of two toy models, the Kondo-Heisenberg model (KHM) and the periodic Anderson model (PAM).

In the first part of this thesis, we developed a controlled bond expansion (CBE) scheme for matrix product state (MPS) algorithms. CBE offers an update scheme for MPS methods that mirrors the favorable convergence properties of 2-site updates with a computational cost that is only marginally higher than that of 1-site updates. We applied CBE to the density matrix renormalization group (DMRG) for ground state search in Ref. [P2] and to the time-dependent variational principle (TDVP) for MPS in Ref. [P3]. Due to the reduced computational cost, we were able to tackle the KHM on a 4-leg cylinder using CBE–DMRG in Ref. [P2]. This allowed us to show that this model exhibits two phases that differ in their Fermi surface (FS) volumes, a large FS Kondo phase and a small FS RKKY phase. The study of a putative KB quantum critical point (QCP) separating these two phases is left for future work.

In the second part, we obtained an extensive set of results on the PAM using 2-site cellular dynamical mean-field theory (2CDMFT) with the numerical renormalization group (NRG) as an impurity solver. There, we identified and studied a KB–QCP and its vicinity in detail, facilitated by the exceptional frequency and temperature resolution of NRG. In Ref. [P4], we were able to answer numerous questions or uncertainties that were left open by previous studies [DLCK08a, DLCK08b, MBA10, THKD11]. We confirmed the findings in Refs. [DLCK08a, DLCK08b] where a KB–QCP was found and interpreted as an orbital selective Mott transition (OSMT) and we confirmed that this OSMT is continuous. Further, we showed that the FS undergoes a discrete jump as the system is tuned through the QCP. We were able to unambiguously connect this FS jump to a *continous*, momentum selective sign change of the effective f-electron level position. This sign change results in the emergence of a dispersive pole in the f-electron self-energy and a Luttinger surface (LS) at the momenta where this pole crosses the Fermi level. Remarkably, in contrast to previous results based on auxiliary particle approaches [SSV03, SVS04, Voj10, Sac23] and extended dynamical mean-field theory (EDMFT) [SRIS01, ZGS03], we find that c and f electrons retain their low-energy hybridization in the small FS RKKY phase, i.e. the QP in this phase are also hybrid c-f objects. Further, we find that the RKKY phase exhibits a three-band structure, which is surprising since the PAM only hosts two orbitals per lattice site.

We were further able to show that the 2CDMFT self-consistency conditions stabilize a novel non-Fermi liquid (NFL) fixed point that governs the QCP and the quantum critical region at non-zero temperatures. The existence of such an NFL fixed point is unexpected since similar fixed points found in impurity models are unstable to perturbations [FHLS03] which are present in the 2CDMFT approach to the PAM. In Ref. [P5], we extensively studied the properties of this NFL fixed point and showed that it exhibits many features that are found in the strange metal regions of several HF compounds. These include a $\propto T \ln T$ specific heat a $\propto T$ resistivity and ω/T scaling of the optical conductivity, in good qualitative agreement with experimental data on $YbRh_2Si_2$ and $CeCoIn_5$.

Despite considerable progress, our work left many questions to be answered in future studies. Most important is a better understanding of the nature of the small FS phase and

the strange metal region. Possible future directions to achieve this are discussed in Sec. 4.1 and 4.2, respectively. Section 4.3 briefly comments on the possibility of symmetry breaking in the vicinity of the KB–QCP.

4.1 Nature of the small Fermi surface phase

A major open question concerns the nature of the RKKY phase which features a small FS. To a large extent, this boils down to the question of what the effective low-energy degrees of freedom are in this phase. Because the FS is small, the low-energy physics of the RKKY phase cannot be described entirely by gapless degrees of freedom associated with the small FS since that would be inconsistent with either charge or momentum conservation [Osh00]. Possible scenarios could be a topologically degenerate ground state (i.e. topological order) or the presence of additional gapless degrees of freedom which are not associated with the small FS [Sac23]. Since it is rather unlikely that 2CDMFT can describe topological order, we currently conjecture the presence of gapless excitations in addition to the small FS.

Because the RKKY phase in 2CDMFT is characterized by a dispersive pole in the f-electron self-energy and a Luttinger surface, it seems natural to try to associate those with such gapless excitations. Conceptional work in this direction has been published by M. Fabrizio, who argued that Luttinger surfaces may be associated with spinon Fermi surfaces hosting gapless spinon excitations [Fab22]. So far, we have not been able to confirm the presence of gapless spinons at the Luttinger surface we find in our 2CDMFT study.

Another important direction of future work is to benchmark the 2CDMFT results against other approaches, which would help to establish to what extent 2CDMFT describes universal features. This could either be done by increasing the cell size in CDMFT or by comparing to results obtained by MPS methods. The latter is preferable since that would provide a perspective from an entirely different class of methods (in contrast to CDMFT with just increased cell size). However, to compare to 2CDMFT plus NRG, it is necessary to compute spectral functions and self-energies with MPS. These are typically obtained through time evolution methods like TDVP, which is however unfeasible if the ground state calculation using DMRG is already borderline challenging (this is the case for the doped KHM on a cylinder). In a project together with Sasha Kowalska and Jan von Delft, we are currently working on a method based on the excitation ansatz [VDVH+21] to overcome these limitations. This may render such comparisons feasible in the near future.

4.2 Nature of the strange metal

Another highly interesting open question regards the nature of the strange metal which we find in the 2CDMFT approach in the quantum critical region. In Ref. [P5], we have shown that vertex corrections to the optical conductivity are highly important to achieve a qualitatively correct description. However, we were only able to compute vertex corrections to the local cluster contribution by computing the current susceptibility of the effective impurity model. Longer-range vertex corrections would require the computation of three- or four-point correlation functions of the effective impurity model. This is in principle possible with NRG [KLvD21, LKvD21], but currently computationally too expensive for the effective impurity model which arises in the 2CDMFT approach to the PAM. This will hopefully change in the near future, by improving the efficiency of NRG for multipoint correlation functions [KLvD21, LKvD21] and/or decreasing the computational cost for solving the effective impurity model, e.g. by choosing a larger discretization parameter in NRG.

Obtaining data on three- or four-point correlation functions is not only desirable to obtain

more reliable data for the optical conductivity but also to understand the current decay mechanism in the strange metal. This is for instance important to establish whether 2CDMFT describes an intrinsic strange metal [ETS21, ES21], i.e. a strange metal that does not rely on disorder and which features the linear-in-T resistivity as a property of the quantum critical fixed point. In Ref. [P5], we have conjectured that the strange metal described by 2CDMFT is intrinsic, but we were not able to make a definitive claim. Note that such an intrinsic resistivity would be in stark contrast to Fermi liquids, whose intrinsic resistivity is zero,[1] and to a recent universal theory of strange metals [PGES23] which relies on interaction disorder to account for a linear-in-T resistivity.

If the resistivity of the quantum critical fixed point described by 2CDMFT is indeed intrinsic, it would mean that this fixed point is not stable in free space and requires a lattice or some other preferred reference system to exist (in stark contrast to e.g. an FL). This naturally raises the question of what property the lattice exhibits that is absent in free space. An obvious candidate would be (crystal momentum conserving) Umklapp scattering. Since coarse-grained Umklapp scattering is included in the 2CDMFT description [P5], it would be interesting in future studies to artificially suppress the Umklapp scattering terms in 2CDMFT and explore whether this destabilizes the strange metal.

4.3 Symmetry breaking

Finally, it would be highly interesting to explore whether the quantum critical fixed point that arises in the 2CDMFT description triggers some secondary symmetry-breaking instabilities in its vicinity. Possible candidates are magnetic order or superconductivity. The QCP we find in the 2CDMFT description of the PAM bears some striking similarities to an impurity QCP in the two-impurity Anderson model [FHLS03]. Since the latter is unstable to pairing or magnetism, it seems natural that such instabilities may also arise near the former. Similar conjectures have also been put forward in Ref. [DLCK08a]. Further, we find several divergent local susceptibilities in the vicinity of the KB–QCP [P4]. A thorough study of symmetry breaking in the PAM from a 2CDMFT perspective should consider different possible instabilities on equal footing.

---

[1]The usual T^2 correction is due to perturbations that are irrelevant to the FL fixed point, i.e. do not destabilize it. Such corrections would for instance not arise in free space.

Bibliography

[P1]   Andreas Gleis, Jheng-Wei Li, and Jan von Delft, *Projector formalism for kept and discarded spaces of matrix product states*, Phys. Rev. B **106** (2022), 195138. See pages: 16, 30, 31, 32, 36, and 37

[P2]   Andreas Gleis, Jheng-Wei Li, and Jan von Delft, *Controlled bond expansion for density matrix renormalization group ground state search at single-site costs*, Phys. Rev. Lett. **130** (2023), 246402. See pages: 14, 16, 35, 36, 52, and 147

[P3]   Jheng-Wei Li, Andreas Gleis, and Jan von Delft, *Time-dependent variational principle with controlled bond expansion for matrix product states*, 2022. See pages: 16, 36, 52, and 147

[P4]   Andreas Gleis, Seung-Sup B. Lee, Gabriel Kotliar, and Jan von Delft, *Emergent properties of the periodic Anderson model: a high-resolution, real-frequency study of heavy-fermion quantum criticality*, 2023. See pages: 10, 11, 13, 16, 84, 147, and 149

[P5]   Andreas Gleis, Seung-Sup B. Lee, Gabriel Kotliar, and Jan von Delft, *Dynamical scaling and Planckian dissipation due to heavy-fermion quantum criticality*, 2024. See pages: 11, 16, 84, 147, 148, and 149

[AC00]   Ar. Abanov and Andrey V. Chubukov, *Spin-fermion model near the quantum critical point: One-loop renormalization group results*, Phys. Rev. Lett. **84** (2000), 5608–5611. See page: 9

[AC04]   Ar. Abanov and A. Chubukov, *Anomalous scaling at the quantum critical point in itinerant antiferromagnets*, Phys. Rev. Lett. **93** (2004), 255702. See page: 9

[ACPA22]   Erik E. Aldape, Tessa Cookmeyer, Aavishkar A. Patel, and Ehud Altman, *Solvable theory of a strange metal at the breakdown of a heavy Fermi liquid*, Phys. Rev. B **105** (2022), 235111. See pages: 14 and 15

[AdSNG$^+$12] Pegor Aynajian, Eduardo H. da Silva Neto, András Gyenis, Ryan E. Baumbach, J. D. Thompson, Zachary Fisk, Eric D. Bauer, and Ali Yazdani, *Visualizing heavy Fermions emerging in a quantum critical Kondo lattice*, Nature **486** (2012), no. 7402, 201–206. See page: 12

[AGD63]   A.A. Abrikosov, L.P. Gorkov, and I.E. Dzyaloshinski, *Methods of quantum field theory in statistical physics*, Prentice-Hall, Englewood Cliffs, NJ, 1963. See page: 18

[AGO75]   K. Andres, J. E. Graebner, and H. R. Ott, $4f$-*virtual-bound-state formation in* ceal$_3$ *at low temperatures*, Phys. Rev. Lett. **35** (1975), 1779–1782. See pages: 1 and 4

[AKLV13]   Itai Arad, Alexei Kitaev, Zeph Landau, and Umesh Vazirani, *An area law and sub-exponential algorithm for 1d systems*, 2013. See page: 30

[AL92]   Ian Affleck and Andreas W. W. Ludwig, *Exact critical theory of the two-impurity Kondo model*, Phys. Rev. Lett. **68** (1992), 1046–1049. See page: 13

[ALJ95]   Ian Affleck, Andreas W. W. Ludwig, and Barbara A. Jones, *Conformal-field-theory approach to the two-impurity Kondo problem: Comparison with numerical renormalization-group results*, Phys. Rev. B **52** (1995), 9528–9546. See page: 13

[AM76]   N.W. Ashcroft and N.D. Mermin, *Solid state physics*, HRW international editions, Holt, Rinehart and Winston, 1976. See page: 10

[AOR$^+$95]   M. C. Aronson, R. Osborn, R. A. Robinson, J. W. Lynn, R. Chau, C. L. Seaman, and M. B. Maple, *Non-Fermi-liquid scaling of the magnetic response in $UCu_{5-x}Pd_x(x = 1, 1.5)$*, Phys. Rev. Lett. **75** (1995), 725–728. See page: 12

[AS05]   Frithjof B. Anders and Avraham Schiller, *Real-time dynamics in quantum-impurity systems: A time-dependent numerical renormalization-group approach*, Phys. Rev. Lett. **95** (2005), 196801. See pages: 28 and 29

[AS06]   Frithjof B. Anders and Avraham Schiller, *Spin precession and real-time dynamics in the kondo model: Time-dependent numerical renormalization-group study*, Phys. Rev. B **74** (2006), 245113. See pages: 28 and 29

[AS10]   Alexander Altland and Ben D. Simons, *Condensed matter field theory*, 2 ed., Cambridge University Press, 2010. See pages: 6 and 8

[Ass99]   F. F. Assaad, *Quantum Monte Carlo simulations of the half-filled two-dimensional Kondo lattice model*, Phys. Rev. Lett. **83** (1999), 796–799. See page: 13

[Ass04]   F. F. Assaad, *Coherence scale of the two-dimensional Kondo lattice model*, Phys. Rev. B **70** (2004), 020402. See page: 13

[Bay62]   Gordon Baym, *Self-consistent approximations in many-body systems*, Phys. Rev. **127** (1962), 1391–1401. See page: 18

[BBLG$^+$23] Max Bramberger, Benjamin Bacq-Labreuil, Martin Grundner, Silke Biermann, Ulrich Schollwöck, Sebastian Paeckel, and Benjamin Lenz, *Formation of CuO_2 sublattices by suppression of interlattice correlations in tetragonal CuO*, SciPost Phys. **14** (2023), 010. See page: 30

[BCP08]   Ralf Bulla, Theo A. Costi, and Thomas Pruschke, *Numerical renormalization group method for quantum impurity systems*, Rev. Mod. Phys. **80** (2008), no. 2, 395–450. See pages: 27 and 28

[BCPP16]   Parsa Bonderson, Meng Cheng, Kaushal Patel, and Eugeniu Plamadeala, *Topological enrichment of Luttinger's theorem*. See page: 14

[BGG02]   S. Burdin, D. R. Grempel, and A. Georges, *Heavy-fermion and spin-liquid behavior in a Kondo lattice with magnetic frustration*, Phys. Rev. B **66** (2002), 045111. See page: 14

[BH15]   Fernando G. S. L. Brandão and Michał Horodecki, *Exponential decay of correlations implies area law*, Communications in Mathematical Physics **333** (2015), no. 2, 761–798. See page: 30

[BHP98]   R Bulla, A C Hewson, and Th Pruschke, *Numerical renormalization group calculations for the self-energy of the impurity Anderson model*, Journal of Physics: Condensed Matter **10** (1998), no. 37, 8365. See pages: 26 and 28

[BJA94]   Peter E. Blöchl, O. Jepsen, and O. K. Andersen, *Improved tetrahedron method for Brillouin-zone integrations*, Phys. Rev. B **49** (1994), no. 23, 16223–16233. See page: 23

[BK61]   Gordon Baym and Leo P. Kadanoff, *Conservation laws and correlation functions*, Phys. Rev. **124** (1961), 287–299. See page: 18

[BLJF70]   D. W. Bloom, Douglas H. Lowndes Jr., and Leonard Finegold, *Low temperature specific heat of copper: Comparison of two samples of high purity*, Review of Scientific Instruments **41** (1970), no. 5, 690–695. See page: 1

[BLST19]   Erez Berg, Samuel Lederer, Yoni Schattner, and Simon Trebst, *Monte Carlo studies of quantum critical metals*, Annual Review of Condensed Matter Physics **10** (2019), no. 1, 63–84. See page: 13

[BMV$^+$03]   A. Bianchi, R. Movshovich, I. Vekhter, P. G. Pagliuso, and J. L. Sarrao, *Avoided antiferromagnetic order and quantum critical point in* CeCoIn$_5$, Phys. Rev. Lett. **91** (2003), 257001. See page: 12

[BSB22]   Steffen Backes, Jae-Hoon Sim, and Silke Biermann, *Nonlocal correlation effects in fermionic many-body systems: Overcoming the noncausality problem*, Phys. Rev. B **105** (2022), 245115. See page: 26

[BZT$^+$17]   Daniel Bauernfeind, Manuel Zingl, Robert Triebl, Markus Aichhorn, and Hans Gerd Evertz, *Fork tensor-product states: Efficient multiorbital real-time DMFT solver*, Phys. Rev. X **7** (2017), 031013. See page: 30

[CA01]   S. Capponi and F. F. Assaad, *Spin and charge dynamics of the ferromagnetic and antiferromagnetic two-dimensional half-filled Kondo lattice model*, Phys. Rev. B **63** (2001), 155114. See page: 13

[CBC$^+$24]   Joseph G. Checkelsky, B. Andrei Bernevig, Piers Coleman, Qimiao Si, and Silke Paschen, *Flat bands, strange metals and the Kondo effect*, Nature Reviews Materials (2024). See page: 12

[CGPS22]   Debanjan Chowdhury, Antoine Georges, Olivier Parcollet, and Subir Sachdev, *Sachdev-Ye-Kitaev models and beyond: Window into non-Fermi liquids*, Rev. Mod. Phys. **94** (2022), 035004. See pages: 12 and 13

[CGW$^+$03]   J. Custers, P. Gegenwart, H. Wilhelm, K. Neumaier, Y. Tokiwa, O. Trovarelli, C. Geibel, F. Steglich, C. Pépin, and P. Coleman, *The break-up of heavy electrons at a quantum critical point*, Nature **424** (2003), no. 6948, 524. See pages: 9, 10, 11, and 12

[CHZ94]   T. A. Costi, A. C. Hewson, and V. Zlatić, *Transport coefficients of the Anderson model via the numerical renormalization group*, J. Phys. C **6** (1994), 2519. See page: 28

[CIT95]   P. Coleman, L. B. Ioffe, and A. M. Tsvelik, *Simple formulation of the two-channel Kondo model*, Phys. Rev. B **52** (1995), 6611–6627. See page: 13

[CLB+22]   Liyang Chen, Dale T. Lowder, Emine Bakali, Aaron M. Andrews, Werner
           Schrenk, Monika Waas, Robert Svagera, Gaku Eguchi, Lukas Prochaska, Yim-
           ing Wang, Chandan Setty, Shouvik Sur, Qimiao Si, Silke Paschen, and Douglas
           Natelson, *Shot noise indicates the lack of quasiparticles in a strange metal*. See
           page: 12

[CLSP24]   Xiaodong Cao, Yi Lu, E. Miles Stoudenmire, and Olivier Parcollet, *Dynamical
           correlation functions from complex time evolution*, 2024. See page: 30

[CMS05]   P. Coleman, J. B. Marston, and A. J. Schofield, *Transport anomalies in a
           simplified model for a heavy-electron quantum critical point*, Phys. Rev. B **72**
           (2005), 245111. See page: 14

[CNHC18]   O J Curtin, Y Nishikawa, A C Hewson, and D J G Crow, *Fermi liquids and the
           Luttinger integral*, Journal of Physics Communications **2** (2018), no. 3, 031001.
           See page: 4

[Col84]   Piers Coleman, *New approach to the mixed-valence problem*, Phys. Rev. B **29**
           (1984), 3035–3044. See page: 14

[Col07]   Piers Coleman, *Heavy Fermions: Electrons at the edge of magnetism*, Handbook
           of Magnetism and Advanced Magnetic Materials (H. Kronmüller and S. Parkin,
           eds.), vol. 1, Wiley, 2007, pp. 95–148. See pages: 1, 4, and 7

[Col15]   Piers Coleman, *Introduction to many-body physics*, Cambridge University Press,
           Cambridge, 2015. See pages: 1, 2, 3, 4, 5, and 7

[CP02]   P. Coleman and C. Pépin, *What is the fate of the heavy electron at a quantum
           critical point?*, Physica B: Condensed Matter **312-313** (2002), 383–389, The
           International Conference on Strongly Correlated Electron Systems. See pages:
           8 and 9

[CPGSV21] J. Ignacio Cirac, David Pérez-García, Norbert Schuch, and Frank Verstraete,
           *Matrix product states and projected entangled pair states: Concepts, symmetries,
           theorems*, Rev. Mod. Phys. **93** (2021), 045003. See page: 30

[CPSR01]   P. Coleman, C. Pépin, Qimiao Si, and R. Ramazashvili, *How do Fermi liquids
           get heavy and die?*, J. Phys. Condens. Matter **13** (2001), no. 35, R723–R738.
           See pages: 8 and 9

[CXN+17]   Q. Y. Chen, D. F. Xu, X. H. Niu, J. Jiang, R. Peng, H. C. Xu, C. H. P. Wen,
           Z. F. Ding, K. Huang, L. Shu, Y. J. Zhang, H. Lee, V. N. Strocov, M. Shi,
           F. Bisti, T. Schmitt, Y. B. Huang, P. Dudin, X. C. Lai, S. Kirchner, H. Q. Yuan,
           and D. L. Feng, *Direct observation of how the heavy-Fermion state develops in*
           CeCoIn$_5$, Phys. Rev. B **96** (2017), 045107. See page: 11

[CXN+18]   Q. Y. Chen, D. F. Xu, X. H. Niu, R. Peng, H. C. Xu, C. H. P. Wen, X. Liu,
           L. Shu, S. Y. Tan, X. C. Lai, Y. J. Zhang, H. Lee, V. N. Strocov, F. Bisti,
           P. Dudin, J.-X. Zhu, H. Q. Yuan, S. Kirchner, and D. L. Feng, *Band dependent
           interlayer f-electron hybridization in* CeRhIn$_5$, Phys. Rev. Lett. **120** (2018),
           066403. See page: 11

[CYH+20]   Ang Cai, Zuodong Yu, Haoyu Hu, Stefan Kirchner, and Qimiao Si, *Dynamical
           scaling of charge and spin responses at a Kondo destruction quantum critical
           point*, Phys. Rev. Lett. **124** (2020), 027205. See page: 15

[DC21]   Angus J. Dunnett and Alex W. Chin, *Efficient bond-adaptive approach for finite-temperature open quantum dynamics using the one-site time-dependent variational principle for matrix product states*, Phys. Rev. B **104** (2021), 214302. See page: 36

[Dir30]   P. A. M. Dirac, *Note on exchange phenomena in the Thomas atom*, Math. Proc. Camb. Philos. Soc. **26** (1930), no. 3, 376. See page: 35

[DLAR21]   Bimla Danu, Zihong Liu, Fakher F. Assaad, and Marcin Raczkowski, *Zooming in on heavy Fermions in Kondo lattice models*, Phys. Rev. B **104** (2021), 155128. See page: 13

[DLCK08a]   Lorenzo De Leo, Marcello Civelli, and Gabriel Kotliar, *Cellular dynamical mean-field theory of the periodic Anderson model*, Phys. Rev. B **77** (2008), no. 7, 075107. See pages: 15, 83, 84, 147, and 149

[DLCK08b]   Lorenzo De Leo, Marcello Civelli, and Gabriel Kotliar, $T = 0$ *heavy-Fermion quantum critical point as an orbital-selective Mott transition*, Phys. Rev. Lett. **101** (2008), no. 25, 256404. See pages: 15, 83, 84, and 147

[dMGKB05]   L. de' Medici, A. Georges, G. Kotliar, and S. Biermann, *Mott transition and Kondo screening in f-electron metals*, Phys. Rev. Lett. **95** (2005), 066402. See page: 15

[Don77]   S. Doniach, *The Kondo lattice and weak antiferromagnetism*, Physica **91B+C** (1977), 231–234. See page: 8

[DVAG20]   Bimla Danu, Matthias Vojta, Fakher F. Assaad, and Tarun Grover, *Kondo breakdown in a spin-$1/2$ chain of adatoms on a Dirac semimetal*, Phys. Rev. Lett. **125** (2020), 206602. See page: 13

[DVGA22]   Bimla Danu, Matthias Vojta, Tarun Grover, and Fakher F. Assaad, *Spin chain on a metallic surface: Dissipation-induced order versus Kondo entanglement*, Phys. Rev. B **106** (2022), L161103. See page: 13

[DVK+11]   S. Danzenbächer, D. V. Vyalikh, K. Kummer, C. Krellner, M. Holder, M. Höppner, Yu. Kucherenko, C. Geibel, M. Shi, L. Patthey, S. L. Molodtsov, and C. Laubschat, *Insight into the f-derived Fermi surface of the heavy-Fermion compound* $YbRh_2Si_2$, Phys. Rev. Lett. **107** (2011), 267601. See page: 11

[Dzy03]   Igor Dzyaloshinskii, *Some consequences of the Luttinger theorem: The Luttinger surfaces in non-Fermi liquids and Mott insulators*, Phys. Rev. B **68** (2003), 085113. See page: 4

[ECP10]   J. Eisert, M. Cramer, and M. B. Plenio, *Colloquium: Area laws for the entanglement entropy*, Rev. Mod. Phys. **82** (2010), 277–306. See page: 30

[EK92]   V. J. Emery and S. Kivelson, *Mapping of the two-channel Kondo problem to a resonant-level model*, Phys. Rev. B **46** (1992), 10812–10817. See page: 13

[EKK+11]   S. Ernst, S. Kirchner, C. Krellner, C. Geibel, G. Zwicknagl, F. Steglich, and S. Wirth, *Emerging local Kondo screening and spatial coherence in the heavy-fermion metal* $YbRh_2Si_2$, Nature **474** (2011), no. 7351, 362–366. See page: 12

[ES21]   Dominic V. Else and T. Senthil, *Strange metals as ersatz Fermi liquids*, Phys. Rev. Lett. **127** (2021), 086601. See pages: 13 and 149

[ETS21]   Dominic V. Else, Ryan Thorngren, and T. Senthil, *Non-Fermi liquids as ersatz Fermi liquids: General constraints on compressible metals*, Phys. Rev. X **11** (2021), 021005. See pages: 13 and 149

[Fab22]   Michele Fabrizio, *Emergent quasiparticles at Luttinger surfaces*, Nature Communications **13** (2022), no. 1, 1561. See page: 148

[FH17]   Y. Núñez Fernández and K. Hallberg, *Solving the multi-site and multi-orbital dynamical mean field theory using density matrix renormalization*, 2017. See page: 30

[FHLS03]   Michele Fabrizio, Andrew F. Ho, Lorenzo De Leo, and Giuseppe E. Santoro, *Nontrivial fixed point in a twofold orbitally degenerate Anderson impurity model*, Phys. Rev. Lett. **91** (2003), 246402. See pages: 13, 83, 84, 147, and 149

[FLA$^+$23] Bernhard Frank, Zi Hong Liu, Fakher F. Assaad, Matthias Vojta, and Lukas Janssen, *Marginal Fermi liquid at magnetic quantum criticality from dimensional confinement*, Phys. Rev. B **108** (2023), L100405. See pages: 13 and 14

[FO86]   H. O. Frota and L. N. Oliveira, *Photoemission spectroscopy for the spin-degenerate Anderson model*, Phys. Rev. B **33** (1986), 7871–7874. See page: 28

[FOW$^+$10] Sven Friedemann, Niels Oeschler, Steffen Wirth, Cornelius Krellner, Christoph Geibel, Frank Steglich, Silke Paschen, Stefan Kirchner, and Qimiao Si, *Fermi-surface collapse and dynamical scaling near a quantum-critical point*, Proc. Natl. Acad. Sci. **107** (2010), no. 33, 14547–14551. See page: 10

[FWB$^+$09] S. Friedemann, T. Westerkamp, M. Brando, N. Oeschler, S. Wirth, P. Gegenwart, C. Krellner, C. Geibel, and F. Steglich, *Detaching the antiferromagnetic quantum critical point from the Fermi-surface reconstruction in $YbRh_2Si_2$*, Nat. Phys. **5** (2009), no. 7, 465–469. See page: 12

[Gan95]   Junwu Gan, *Solution of the two-impurity Kondo model: Critical point, Fermi-liquid phase, and crossover*, Phys. Rev. B **51** (1995), no. 13, 8287–8309. See page: 13

[GCG$^+$02] P. Gegenwart, J. Custers, C. Geibel, K. Neumaier, T. Tayama, K. Tenya, O. Trovarelli, and F. Steglich, *Magnetic-field induced quantum critical point in $YbRh_2Si_2$*, Phys. Rev. Lett. **89** (2002), 056402. See pages: 10 and 11

[GI07]   Matthew T. Glossop and Kevin Ingersent, *Magnetic quantum phase transition in an anisotropic Kondo lattice*, Phys. Rev. Lett. **99** (2007), 227203. See page: 15

[GK92]   Antoine Georges and Gabriel Kotliar, *Hubbard model in infinite dimensions*, Phys. Rev. B **45** (1992), 6479–6483. See page: 17

[GKKR96]   Antoine Georges, Gabriel Kotliar, Werner Krauth, and Marcelo J. Rozenberg, *Dynamical mean-field theory of strongly correlated Fermion systems and the limit of infinite dimensions*, Rev. Mod. Phys. **68** (1996), no. 1, 13–125. See pages: 15, 17, and 18

[GKP⁺14] M. Güttler, K. Kummer, S. Patil, M. Höppner, A. Hannaske, S. Danzenbächer, M. Shi, M. Radovic, E. Rienks, C. Laubschat, C. Geibel, and D. V. Vyalikh, *Tracing the localization of $4f$ electrons: Angle-resolved photoemission on* $YbCo_2Si_2$*, the stable trivalent counterpart of the heavy-Fermion* $YbRh_2Si_2$, Phys. Rev. B **90** (2014), 195138. See page: 11

[Gle19] Andreas Gleis, *Cluster dynamical mean-field + numerical renormalization group approach to strongly correlated systems*, Masters thesis, Ludwig-Maximilians-Universität München, 2019. See page: 23

[GSS08] Philipp Gegenwart, Qimiao Si, and Frank Steglich, *Quantum criticality in heavy-Fermion metals*, Nat. Phys. **4** (2008), no. 3, 186–197. See pages: 9 and 10

[GV05] Gabriele Giuliani and Giovanni Vignale, *Quantum theory of the electron liquid*, Cambridge University Press, 2005. See pages: 1 and 4

[GWK⁺24] M. Grundner, P. Westhoff, F. B. Kugler, O. Parcollet, and U. Schollwöck, *Complex time evolution in tensor networks and time-dependent green's functions*, Phys. Rev. B **109** (2024), 155124. See page: 30

[Has07] M B Hastings, *An area law for one-dimensional quantum systems*, Journal of Statistical Mechanics: Theory and Experiment **2007** (2007), no. 08, P08024. See page: 30

[HB20] Joshuah T. Heath and Kevin S. Bedell, *Necessary and sufficient conditions for the validity of Luttinger's theorem*, New J. Phys. (2020). See page: 4

[HCC⁺21] Haoyu Hu, Ang Cai, Lei Chen, Lili Deng, Jedediah H. Pixley, Kevin Ingersent, and Qimiao Si, *Unconventional superconductivity from Fermi surface fluctuations in strongly correlated metals*, 2021. See page: 15

[HCCS21] Haoyu Hu, Ang Cai, Lei Chen, and Qimiao Si, *Spin-singlet and spin-triplet pairing correlations in antiferromagnetically coupled Kondo systems*, 2021. See page: 15

[HCO⁺11] Jutho Haegeman, J. Ignacio Cirac, Tobias J. Osborne, Iztok Pižorn, Henri Verschelde, and Frank Verstraete, *Time-dependent variational principle for quantum lattices*, Phys. Rev. Lett. **107** (2011), 070601. See page: 35

[HCS20] H. Hu, A. Cai, and Q. Si, *Quantum criticality and dynamical Kondo effect in an SU(2) Anderson lattice model*, arxiv:2004.04679 (2020). See page: 15

[HCS22a] Haoyu Hu, Lei Chen, and Qimiao Si, *Extended dynamical mean field theory for correlated electron models*, 2022. See page: 15

[HCS22b] Haoyu Hu, Lei Chen, and Qimiao Si, *Quantum critical metals: Dynamical Planckian scaling and loss of quasiparticles*, 2022. See page: 15

[HDH21] Markus Hauru, Maarten Van Damme, and Jutho Haegeman, *Riemannian optimization of isometric tensor networks*, SciPost Phys. **10** (2021), 040. See page: 34

[Her76] John A. Hertz, *Quantum critical phenomena*, Phys. Rev. B **14** (1976), no. 3, 1165–1184. See pages: 8 and 9

[Hew93]   Alexander Cyril Hewson, *The Kondo problem to heavy Fermions*, Cambridge Studies in Magnetism, Cambridge University Press, 1993. See pages: 4 and 7

[HHS18]   C. Hubig, J. Haegeman, and U. Schollwöck, *Error estimates for extrapolations with matrix-product states*, Phys. Rev. B **97** (2018), 045125. See page: 37

[HLO$^+$16] Jutho Haegeman, Christian Lubich, Ivan Oseledets, Bart Vandereycken, and Frank Verstraete, *Unifying time evolution and optimization with matrix product states*, Phys. Rev. B **94** (2016), 165116. See pages: 32, 35, and 36

[HM22]   Sean A. Hartnoll and Andrew P. Mackenzie, *Colloquium: Planckian dissipation in metals*, Rev. Mod. Phys. **94** (2022), 041002. See page: 12

[HMJK00]   M. H. Hettler, M. Mukherjee, M. Jarrell, and H. R. Krishnamurthy, *Dynamical cluster approximation: Nonlocal dynamics of correlated electron systems*, Phys. Rev. B **61** (2000), 12739–12756. See pages: 17 and 20

[HMOV14]   Jutho Haegeman, Michaël Mariën, Tobias J. Osborne, and Frank Verstraete, *Geometry of matrix product states: Metric, parallel transport, and curvature*, Journal of Mathematical Physics **55** (2014), no. 2, 021902. See pages: 32 and 34

[HMSW15]   C. Hubig, I. P. McCulloch, U. Schollwöck, and F. A. Wolf, *Strictly single-site DMRG algorithm with subspace expansion*, Phys. Rev. B **91** (2015), 155115. See page: 35

[Hof00]   Walter Hofstetter, *Generalized numerical renormalization group for dynamical quantities*, Phys. Rev. Lett. **85** (2000), 1508–1511. See page: 28

[HOV13]   Jutho Haegeman, Tobias J. Osborne, and Frank Verstraete, *Post-matrix product state methods: To tangent space and beyond*, Phys. Rev. B **88** (2013), 075133. See page: 32

[HP21]   Johannes Halbinger and Matthias Punk, *Quenched disorder at antiferromagnetic quantum critical points in two-dimensional metals*, Phys. Rev. B **103** (2021), 235157. See page: 9

[HPT$^+$19] Masahiro Haze, Robert Peters, Yohei Torii, Tomoka Suematsu, Daiki Sano, Masahiro Naritsuka, Yuichi Kasahara, Takasada Shibauchi, Takahito Terashima, and Yuji Matsuda, *Direct evidence for the existence of heavy quasiparticles in the magnetically ordered phase of CeRhIn$_5$*, Journal of the Physical Society of Japan **88** (2019), no. 1, 014706. See page: 12

[HTZJ$^+$98] M. H. Hettler, A. N. Tahvildar-Zadeh, M. Jarrell, T. Pruschke, and H. R. Krishnamurthy, *Nonlocal dynamical correlations of strongly interacting electron systems*, Phys. Rev. B **58** (1998), R7475–R7479. See pages: 17 and 20

[HYK10]   Kristjan Haule, Chuck-Hou Yee, and Kyoo Kim, *Dynamical mean-field theory within the full-potential methods: Electronic structure of CeIrIn$_5$, CeCoIn$_5$, and CeRhIn$_5$*, Phys. Rev. B **81** (2010), 195107. See pages: 1 and 2

[JCK$^+$15] Lin Jiao, Ye Chen, Yoshimitsu Kohama, David Graf, E. D. Bauer, John Singleton, Jian-Xin Zhu, Zongfa Weng, Guiming Pang, Tian Shang, Jinglei Zhang, Han-Oh Lee, Tuson Park, Marcelo Jaime, J. D. Thompson, Frank Steglich, Qimiao Si, and H. Q. Yuan, *Fermi surface reconstruction and multiple quantum phase transitions in the antiferromagnet CeRhIn$_5$*, Proc. Natl. Acad. Sci. **112** (2015), no. 3, 673–678. See pages: 1, 9, and 10

[JDA+20]   Sooyoung Jang, J. D. Denlinger, J. W. Allen, V. S. Zapf, M. B. Maple, Jae Nyeong Kim, Bo Gyu Jang, and Ji Hoon Shim, *Evolution of the Kondo lattice electronic structure above the transport coherence temperature*, Proceedings of the National Academy of Sciences **117** (2020), no. 38, 23467–23476. See page: 11

[JFD77a]   R. Jullien, J. Fields, and S. Doniach, *Kondo lattice: Real-space renormalization-group approach*, Phys. Rev. Lett. **38** (1977), 1500–1503. See page: 8

[JFD77b]   R. Jullien, J. N. Fields, and S. Doniach, *Zero-temperature real-space renormalization-group method for a Kondo-lattice model Hamiltonian*, Phys. Rev. B **16** (1977), 4889–4900. See page: 8

[JGK+22]   Bo Gyu Jang, Beomjoon Goh, Junwon Kim Jae Nyeong Kim, Hanhim Kang, Kristjan Haule, Gabriel Kotliar, Hongchul Choi, and Ji Hoon Shim, *Orbital anisotropy of heavy fermion ce_2irin_8 under crystalline electric field and its energy scale*, 2022. See pages: 1 and 2

[Jon07]   Barbara A. Jones, *Kondo effect*, Handbook of Magnetism and Advanced Magnetic Materials (H. Kronmüller and S. Parkin, eds.), vol. 1, Wiley, 2007. See page: 13

[KAH+18]   Ilia Khait, Patrick Azaria, Claudius Hubig, Ulrich Schollwöck, and Assa Auerbach, *Doped Kondo chain, a heavy Luttinger liquid*, Proceedings of the National Academy of Sciences **115** (2018), no. 20, 5140–5144. See page: 14

[Kap12]   S. Kaprzyk, *An algebraic formulation and implementation of the tetrahedron linear method for the Brillouin zone integration of spectral functions*, Comput. Phys. Commun. **183** (2012), no. 2, 347–362. See page: 23

[Kas56]   Tadao Kasuya, *A theory of metallic ferro- and antiferromagnetism on Zener's model*, Prog. Theor. Phys. **16** (1956), no. 1, 45–57. See page: 7

[KBB+23]   Jason Kaye, Sophie Beck, Alex Barnett, Lorenzo Van Muñoz, and Olivier Parcollet, *Automatic, high-order, and adaptive algorithms for Brillouin zone integration*, SciPost Phys. **15** (2023), 062. See pages: 21 and 24

[KBI+08]   A. Koitzsch, S. V. Borisenko, D. Inosov, J. Geck, V. B. Zabolotnyy, H. Shiozawa, M. Knupfer, J. Fink, B. Büchner, E. D. Bauer, J. L. Sarrao, and R. Follath, *Hybridization effects in* $CeCoIn_5$ *observed by angle-resolved photoemission*, Phys. Rev. B **77** (2008), 155128. See page: 11

[KHSI22]   Ananth Kandala, Haoyu Hu, Qimiao Si, and Kevin Ingersent, *Dynamical Planckian scaling of charge response at a particle-hole-asymmetric quantum critical point with Kondo destruction*, 2022. See page: 15

[KK22]   Fabian B. Kugler and Gabriel Kotliar, *Is the orbital-selective Mott phase stable against interorbital hopping?*, Phys. Rev. Lett. **129** (2022), 096403. See page: 26

[KLvD21]   Fabian B. Kugler, Seung-Sup B. Lee, and Jan von Delft, *Multipoint correlation functions: Spectral representation and numerical evaluation*, Phys. Rev. X **11** (2021), 041006. See page: 148

[KNS+04]   S Kimura, T Nishi, J Sichelschmidt, V Voevodin, J Ferstl, C Geibel, and
            F Steglich, *Optical conductivity of a non-Fermi-liquid material YbRh$_2$Si$_2$*,
            Journal of Magnetism and Magnetic Materials **272-276** (2004), 36–37. See
            page: 12

[KOE+09]   A. Koitzsch, I. Opahle, S. Elgazzar, S. V. Borisenko, J. Geck, V. B. Zabolotnyy,
            D. Inosov, H. Shiozawa, M. Richter, M. Knupfer, J. Fink, B. Büchner, E. D.
            Bauer, J. L. Sarrao, and R. Follath, *Electronic structure of CeCoIn$_5$ from
            angle-resolved photoemission spectroscopy*, Phys. Rev. B **79** (2009), 075104. See
            page: 11

[KPC+15]   K. Kummer, S. Patil, A. Chikina, M. Güttler, M. Höppner, A. Generalov,
            S. Danzenbächer, S. Seiro, A. Hannaske, C. Krellner, Yu. Kucherenko, M. Shi,
            M. Radovic, E. Rienks, G. Zwicknagl, K. Matho, J. W. Allen, C. Laubschat,
            C. Geibel, and D. V. Vyalikh, *Temperature-independent Fermi surface in the
            Kondo lattice* YbRh$_2$Si$_2$, Phys. Rev. X **5** (2015), 011028. See page: 11

[KPC+20]   Stefan Kirchner, Silke Paschen, Qiuyun Chen, Steffen Wirth, Donglai Feng,
            Joe D. Thompson, and Qimiao Si, *Colloquium: Heavy-electron quantum criti-
            cality and single-particle spectroscopy*, Rev. Mod. Phys. **92** (2020), 011002. See
            pages: 8, 10, 11, and 12

[KSF+06]   S. Kimura, J. Sichelschmidt, J. Ferstl, C. Krellner, C. Geibel, and F. Steglich,
            *Optical observation of non-Fermi-liquid behavior in the heavy Fermion state of
            YbRh$_2$Si$_2$*, Phys. Rev. B **74** (2006), 132408. See page: 12

[KSH+06]   G. Kotliar, S. Y. Savrasov, K. Haule, V. S. Oudovenko, O. Parcollet, and C. A.
            Marianetti, *Electronic structure calculations with dynamical mean-field theory*,
            Rev. Mod. Phys. **78** (2006), 865–951. See pages: 15 and 17

[KSPB01]   Gabriel Kotliar, Sergej Y. Savrasov, Gunnar Pálsson, and Giulio Biroli, *Cellular
            dynamical mean field approach to strongly correlated systems*, Phys. Rev. Lett.
            87 (2001), no. 18, 186401. See pages: 15, 17, and 20

[Kug22]   Fabian B. Kugler, *Improved estimator for numerical renormalization group
            calculations of the self-energy*, Phys. Rev. B **105** (2022), 245132. See pages: 26
            and 28

[LF04]   Lorenzo De Leo and Michele Fabrizio, *Spectral properties of a two-orbital
            Anderson impurity model across a non-Fermi-liquid fixed point*, Phys. Rev. B
            69 (2004), 245114. See page: 13

[LFJ+23]   Zi Hong Liu, Bernhard Frank, Lukas Janssen, Matthias Vojta, and Fakher F.
            Assaad, *Magnetic quantum phase transition in a metallic Kondo heterostructure*,
            Phys. Rev. B **107** (2023), 165104. See pages: 13 and 14

[P3]   Jheng-Wei Li, Andreas Gleis, and Jan von Delft, *Time-dependent variational
            principle with controlled bond expansion for matrix product states*, 2022. See
            pages: 16, 36, 52, and 147

[LIK07]   A. M. Leushin, V. A. Ivanshin, and I. N. Kurkin, *Crystal field of Yb^{3+} tetragonal
            centers in the YbRh$_2$Si$_2$ intermetallic compound*, Physics of the Solid State **49**
            (2007), no. 8, 1417–1421. See page: 2

[LKvD21]   Seung-Sup B. Lee, Fabian B. Kugler, and Jan von Delft, *Computing local multipoint correlators using the numerical renormalization group*, Phys. Rev. X **11** (2021), 041007. See page: 148

[LO13]   Christian Lubich and Ivan V. Oseledets, *A projector-splitting integrator for dynamical low-rank approximation*, BIT Numer. Math. **54** (2013), no. 1, 171. See page: 35

[LOV15]   Christian Lubich, Ivan V. Oseledets, and Bart Vandereycken, *Time integration of tensor trains*, SIAM Journal on Numerical Analysis **53** (2015), no. 2, 917–941. See page: 32

[LRVW07]   Hilbert v. Löhneysen, Achim Rosch, Matthias Vojta, and Peter Wölfle, *Fermi-liquid instabilities at magnetic quantum phase transitions*, Rev. Mod. Phys. **79** (2007), no. 3, 1015–1075. See page: 8

[LSSW96]   H.v Löhneysen, M Sieck, O Stockert, and M Waffenschmidt, *Investigation of non-Fermi-liquid behavior in $CeCu_{6-x}Au_x$*, Physica B: Condensed Matter **223-224** (1996), 471–474. See pages: 9, 11, and 12

[Lut60]   J. M. Luttinger, *Fermi surface and some simple equilibrium properties of a system of interacting Fermions*, Phys. Rev. **119** (1960), no. 4, 1153–1163. See pages: 4 and 13

[LV84]   Ph. Lambin and J. P. Vigneron, *Computation of crystal green's functions in the complex-energy plane with the use of the analytical tetrahedron method*, Phys. Rev. B **29** (1984), 3430–3437. See page: 23

[LvDW17a]   Seung-Sup B. Lee, Jan von Delft, and Andreas Weichselbaum, *Doublon-holon origin of the subpeaks at the Hubbard band edges*, Phys. Rev. Lett. **119** (2017), 236402. See page: 29

[LvDW17b]   Seung-Sup B. Lee, Jan von Delft, and Andreas Weichselbaum, *Generalized Schrieffer-Wolff transformation of multiflavor Hubbard models*, Phys. Rev. B **96** (2017), 245106. See page: 3

[LW60]   J. M. Luttinger and J. C. Ward, *Ground-state energy of a many-fermion system. ii*, Phys. Rev. **118** (1960), 1417–1427. See page: 18

[LW16]   Seung-Sup B. Lee and Andreas Weichselbaum, *Adaptive broadening to improve spectral resolution in the numerical renormalization group*, Phys. Rev. B **94** (2016), no. 23, 235127. See page: 29

[MA08]   L. C. Martin and F. F. Assaad, *Evolution of the Fermi surface across a magnetic order-disorder transition in the two-dimensional Kondo lattice model: A dynamical cluster approach*, Phys. Rev. Lett. **101** (2008), 066404. See page: 15

[MBA10]   L. C. Martin, M. Bercx, and F. F. Assaad, *Fermi surface topology of the two-dimensional Kondo lattice model: Dynamical cluster approximation approach*, Phys. Rev. B **82** (2010), 245105. See pages: 15, 83, and 147

[McL64]   A.D. McLachlan, *A variational solution of the time-dependent Schrodinger equation*, Molecular Physics **8** (1964), no. 1, 39. See page: 35

[MEC+22]   Nikola Maksimovic, Daniel H. Eilbott, Tessa Cookmeyer, Fanghui Wan, Jan
            Rusz, Vikram Nagarajan, Shannon C. Haley, Eran Maniv, Amanda Gong,
            Stefano Faubel, Ian M. Hayes, Ali Bangura, John Singleton, Johanna C. Palm-
            strom, Laurel Winter, Ross McDonald, Sooyoung Jang, Ping Ai, Yi Lin, Samuel
            Ciocys, Jacob Gobbo, Yochai Werman, Peter M. Oppeneer, Ehud Altman,
            Alessandra Lanzara, and James G. Analytis, *Evidence for a delocalization
            quantum phase transition without symmetry breaking in* CeCoIn$_5$, Science **375**
            (2022), no. 6576, 76–81. See pages: 1, 2, 9, 10, and 12

[MGWF+14]   Andrew K. Mitchell, Martin R. Galpin, Samuel Wilson-Fletcher, David E.
            Logan, and Ralf Bulla, *Generalized Wilson chain for solving multichannel
            quantum impurity problems*, Phys. Rev. B **89** (2014), no. 12, 121105. See page:
            30

[MH89]   E. Müller-Hartmann, *Correlated fermions on a lattice in high dimensions*,
            Zeitschrift für Physik B Condensed Matter **74** (1989), no. 4, 507–512. See page:
            21

[Mil93]   A. J. Millis, *Effect of a nonzero temperature on quantum critical points in
            itinerant Fermion systems*, Phys. Rev. B **48** (1993), no. 10, 7183–7196. See
            pages: 8 and 9

[MJPH05]   Thomas Maier, Mark Jarrell, Thomas Pruschke, and Matthias H. Hettler,
            Quantum cluster theories, Rev. Mod. Phys. **77** (2005), no. 3, 1027–1080. See
            pages: 15, 17, 19, and 21

[MJRG01]   I. P. Mcculloch, A. Juozapavicius, A. Rosengren, and M. Gulácsi, *Ferromag-
            netism in Kondo lattice models*, Philosophical Magazine Letters **81** (2001),
            no. 12, 869–875. See page: 14

[MJRG02]   I. P. McCulloch, A. Juozapavicius, A. Rosengren, and M. Gulacsi, *Localized
            spin ordering in kondo lattice models*, Phys. Rev. B **65** (2002), 052410. See
            page: 14

[Mor85]   Toru Moriya, *Spin fluctuations in itinerant electron magnetism*, Springer Verlag
            Berlin, 1985. See page: 8

[MS10a]   Max A. Metlitski and Subir Sachdev, *Quantum phase transitions of metals in
            two spatial dimensions. i. Ising-nematic order*, Phys. Rev. B **82** (2010), 075127.
            See page: 9

[MS10b]   Max A. Metlitski and Subir Sachdev, *Quantum phase transitions of metals in
            two spatial dimensions. ii. spin density wave order*, Phys. Rev. B **82** (2010),
            075128. See page: 9

[MTK+01]   Takaki Muramatsu, Naoyuki Tateiwa, Tatsuo C. Kobayashi, Katsuya Shimizu,
            Kiichi Amaya, Dai Aoki, Hiroaki Shishido, Yoshinori Haga, and Yoshichika
            Ōnuki, *Superconductivity of CeRhIn$_5$ under high pressure*, Journal of the Phys-
            ical Society of Japan **70** (2001), no. 11, 3362–3367. See page: 12

[MV89]   Walter Metzner and Dieter Vollhardt, *Correlated lattice fermions in* $d = \infty$
            dimensions, Phys. Rev. Lett. **62** (1989), 324–327. See page: 17

[MvdMS05]   F. P. Mena, D. van der Marel, and J. L. Sarrao, *Optical conductivity of* Ce*M*In$_5$
            (M = Co*, Rh, Ir)*, Phys. Rev. B **72** (2005), 045119. See page: 12

[MW90]   F. Marabelli and P. Wachter, *Temperature dependence of the optical conductivity of the heavy-Fermion system* $CeCu_6$, Phys. Rev. B **42** (1990), 3307–3311. See page: 12

[NCHC18]   Y. Nishikawa, O. J. Curtin, A. C. Hewson, and D. J. G. Crow, *Magnetic field induced quantum criticality and the Luttinger sum rule*, Phys. Rev. B **98** (2018), 104419. See page: 4

[Nor05]   M. R. Norman, *Hall number in* $ybrh_2si_2$, Phys. Rev. B **71** (2005), 220405. See page: 2

[OO94]   Wanda C. Oliveira and Luiz N. Oliveira, *Generalized numerical renormalization-group method to calculate the thermodynamical properties of impurities in metals*, Phys. Rev. B **49** (1994), 11986–11994. See page: 29

[OR95]   Stellan Östlund and Stefan Rommer, *Thermodynamic limit of density matrix renormalization*, Phys. Rev. Lett. **75** (1995), 3537–3540. See page: 33

[ORFS83]   H. R. Ott, H. Rudigier, Z. Fisk, and J. L. Smith, Ube_{13}: *An unconventional actinide superconductor*, Phys. Rev. Lett. **50** (1983), 1595–1598. See page: 1

[Osh00]   Masaki Oshikawa, *Topological approach to Luttinger's theorem and the Fermi surface of a Kondo lattice*, Phys. Rev. Lett. **84** (2000), no. 15, 3370–3373. See pages: 4, 13, and 148

[Ov17]   Žiga Osolin and Rok Žitko, *Fine structure of the spectra of the Kondo lattice model: Two-site cellular dynamical mean-field theory study*, Phys. Rev. B **95** (2017), no. 3, 035107. See page: 15

[Ṕ05]   Catherine Pépin, *Fractionalization and Fermi-surface volume in heavy-Fermion compounds: The case of YbRh$_2$Si$_2$*, Phys. Rev. Lett. **94** (2005), no. 6, 066402. See page: 14

[Ṕ07]   C. Pépin, *Kondo breakdown as a selective Mott transition in the Anderson lattice*, Phys. Rev. Lett. **98** (2007), 206401. See page: 14

[PFW$^+$16] S. Paschen, S. Friedemann, S. Wirth, F. Steglich, S. Kirchner, and Q. Si, *Kondo destruction in heavy Fermion quantum criticality and the photoemission spectrum of YbRh$_2$Si$_2$*, Journal of Magnetism and Magnetic Materials **400** (2016), 17–22. See page: 11

[PGES23]   Aavishkar A. Patel, Haoyu Guo, Ilya Esterlis, and Subir Sachdev, *Universal theory of strange metals from spatially random interactions*, Science **381** (2023), no. 6659, 790–793. See pages: 13, 14, 15, and 149

[PHA22]   Philip W. Phillips, Nigel E. Hussey, and Peter Abbamonte, *Stranger than metals*, Science **377** (2022), no. 6602, eabh4273. See page: 12

[PKS$^+$19] Sebastian Paeckel, Thomas Köhler, Andreas Swoboda, Salvatore R. Manmana, Ulrich Schollwöck, and Claudius Hubig, *Time-evolution methods for matrix-product states*, Ann. Phys. **411** (2019), 167998. See page: 35

[PLM$^+$20] L. Prochaska, X. Li, D. C. MacFarland, A. M. Andrews, M. Bonta, E. F. Bianco, S. Yazdi, W. Schrenk, H. Detz, A. Limbeck, Q. Si, E. Ringe, G. Strasser, J. Kono, and S. Paschen, *Singular charge fluctuations at a magnetic quantum critical point*, Science **367** (2020), no. 6475, 285–288. See page: 12

[PLW⁺04]   S. Paschen, T. Lühmann, S. Wirth, P. Gegenwart, O. Trovarelli, C. Geibel, F. Steglich, P. Coleman, and Q. Si, *Hall-effect evolution across a heavy-Fermion quantum critical point*, Nature **432** (2004), no. 7019, 881. See pages: 9 and 10

[PLW⁺19]   Lekh Poudel, Jon M. Lawrence, Liusuo S. Wu, Georg Ehlers, Yiming Qiu, Andrew F. May, Filip Ronning, Mark D. Lumsden, David Mandrus, and Andrew D. Christianson, *Multicomponent fluctuation spectrum at the quantum critical point in $CeCu_{6-x}Ag_x$*, npj Quantum Materials **4** (2019), no. 1, 52. See page: 12

[PMTM09]   Frank Pollmann, Subroto Mukerjee, Ari M. Turner, and Joel E. Moore, *Theory of finite-entanglement scaling at one-dimensional quantum critical points*, Phys. Rev. Lett. **102** (2009), 255701. See page: 30

[PTH⁺03]   Johnpierre Paglione, M. A. Tanatar, D. G. Hawthorn, Etienne Boaknin, R. W. Hill, F. Ronning, M. Sutherland, Louis Taillefer, C. Petrovic, and P. C. Canfield, *Field-induced quantum critical point in* $CeCoIn_5$, Phys. Rev. Lett. **91** (2003), 246405. See page: 12

[PTSA19]   Francesco Parisen Toldin, Toshihiro Sato, and Fakher F. Assaad, *Mutual information in heavy-Fermion systems*, Phys. Rev. B **99** (2019), 155158. See page: 13

[RA20]   Marcin Raczkowski and Fakher F. Assaad, *Phase diagram and dynamics of the* SU(N) *symmetric Kondo lattice model*, Phys. Rev. Res. **2** (2020), 013276. See page: 13

[RDA22]   Marcin Raczkowski, Bimla Danu, and Fakher F. Assaad, *Breakdown of heavy quasiparticles in a honeycomb Kondo lattice: A quantum Monte Carlo study*, Phys. Rev. B **106** (2022), L161115. See page: 13

[RHT⁺18]   G. Rohringer, H. Hafermann, A. Toschi, A. A. Katanin, A. E. Antipov, M. I. Katsnelson, A. I. Lichtenstein, A. N. Rubtsov, and K. Held, *Diagrammatic routes to nonlocal correlations beyond dynamical mean field theory*, Rev. Mod. Phys. **90** (2018), 025003. See pages: 15 and 19

[RK54]   M. A. Ruderman and C. Kittel, *Indirect exchange coupling of nuclear magnetic moments by conduction electrons*, Phys. Rev. **96** (1954), no. 1, 99–102. See page: 7

[RML⁺08]   P. M. C. Rourke, A. McCollam, G. Lapertot, G. Knebel, J. Flouquet, and S. R. Julian, *Magnetic-field dependence of the* $YbRh_2Si_2$ *Fermi surface*, Phys. Rev. Lett. **101** (2008), 237205. See page: 10

[RO97]   Stefan Rommer and Stellan Östlund, *Class of ansatz wave functions for one-dimensional spin systems and their relation to the density matrix renormalization group*, Phys. Rev. B **55** (1997), 2164–2181. See page: 33

[SAB⁺79]   F. Steglich, J. Aarts, C. D. Bredl, W. Lieke, D. Meschede, W. Franz, and H. Schäfer, *Superconductivity in the presence of strong pauli paramagnetism: $Cecu_2si_2$*, Phys. Rev. Lett. **43** (1979), 1892–1896. See page: 1

[SAC⁺00]   A. Schröder, G. Aeppli, R. Coldea, M. Adams, O. Stockert, H.v. Löhneysen, E. Bucher, R. Ramazashvili, and P. Coleman, *Onset of antiferromagnetism in*

heavy-Fermion metals, Nature **407** (2000), no. 6802, 351–355. See pages: 12 and 15

[Sac11] Subir Sachdev, *Quantum phase transitions*, 2 ed., Cambridge University Press, 2011. See pages: 8, 9, and 12

[Sac23] Subir Sachdev, *Quantum phases of matter*, Cambridge University Press, 2023. See pages: 5, 6, 7, 14, 147, and 148

[SAS+19] M. Sundermann, A. Amorese, F. Strigari, B. Leedahl, L. H. Tjeng, M. W. Haverkort, H. Gretarsson, H. Yavaş, M. Moretti Sala, E. D. Bauer, P. F. S. Rosa, J. D. Thompson, and A. Severing, *Orientation of the ground-state orbital in* $CeCoIn_5$ *and* $CeRhIn_5$, Phys. Rev. B **99** (2019), 235143. See page: 2

[SBBM02] E. J. Singley, D. N. Basov, E. D. Bauer, and M. B. Maple, *Optical conductivity of the heavy Fermion superconductor* $CeCoIn_5$, Phys. Rev. B **65** (2002), 161101. See page: 12

[Sch05] U. Schollwöck, *The density-matrix renormalization group*, Rev. Mod. Phys. **77** (2005), 259–315. See page: 33

[Sch11] Ulrich Schollwöck, *The density-matrix renormalization group in the age of matrix product states*, Annals of Physics **326** (2011), no. 1, 96–192, January 2011 Special Issue. See pages: 30, 31, 33, and 34

[SFW84] G. R. Stewart, Z. Fisk, and M. S. Wire, *New ce heavy-fermion system:* $cecu_6$, Phys. Rev. B **30** (1984), 482–484. See page: 1

[Si06] Qimiao Si, *Global magnetic phase diagram and local quantum criticality in heavy Fermion metals*, Physica B: Condensed Matter **378-380** (2006), 23–27, arxiv: cond-mat/0601001. See page: 12

[Si10] Qimiao Si, *Quantum criticality and global phase diagram of magnetic heavy fermions*, physica status solidi (b) **247** (2010), no. 3, 476–484. See page: 12

[SJK+18] S. Seiro, L. Jiao, S. Kirchner, S. Hartmann, S. Friedemann, C. Krellner, C. Geibel, Q. Si, F. Steglich, and S. Wirth, *Evolution of the Kondo lattice and non-Fermi liquid excitations in a heavy-Fermion metal*, Nature Communications **9** (2018), no. 1, 3324. See page: 12

[SK03] Ping Sun and Gabriel Kotliar, *Extended dynamical mean field theory study of the periodic Anderson model*, Phys. Rev. Lett. **91** (2003), no. 3, 037209. See page: 15

[SK05a] Ping Sun and Gabriel Kotliar, *Consequences of the local spin self-energy approximation on the heavy-Fermion quantum phase transition*, Phys. Rev. B **71** (2005), 245104. See page: 15

[SK05b] Ping Sun and Gabriel Kotliar, *Understanding the heavy Fermion phenomenology from a microscopic model*, Phys. Rev. Lett. **95** (2005), no. 1, 016402. See page: 15

[SKF+06] O. Stockert, M.M. Koza, J. Ferstl, A.P. Murani, C. Geibel, and F. Steglich, *Crystalline electric field excitations of the non-fermi-liquid* $YbRh_2Si_2$, Physica B: Condensed Matter **378-380** (2006), 157–158, Proceedings of the International Conference on Strongly Correlated Electron Systems. See page: 2

[SKK$^+$19]   T. Schäfer, A. Katanin, M. Kitatani, A. Toschi, and K. Held, *Quantum criticality in the two-dimensional periodic Anderson model*, Phys. Rev. Lett. **122** (2019), no. 22, 227201. See pages: 15 and 19

[SLO$^+$96]   J. B. Silva, W. L. C. Lima, W. C. Oliveira, J. L. N. Mello, L. N. Oliveira, and J. W. Wilkins, *Particle-hole asymmetry in the two-impurity Kondo model*, Phys. Rev. Lett. **76** (1996), 275–278. See page: 13

[SMvDW16]   K. M. Stadler, A. K. Mitchell, J. von Delft, and A. Weichselbaum, *Interleaved numerical renormalization group as an efficient multiband impurity solver*, Phys. Rev. B **93** (2016), no. 23, 235101. See page: 30

[SRIS01]   Qimiao Si, Silvio Rabello, Kevin Ingersent, and J. Lleweilun Smith, *Locally critical quantum phase transitions in strongly correlated metals*, Nature **413** (2001), no. 6858, 804–808. See pages: 8, 9, 15, and 147

[SRIS03]   Qimiao Si, Silvio Rabello, Kevin Ingersent, and J. Lleweilun Smith, *Local fluctuations in quantum critical metals*, Phys. Rev. B **68** (2003), 115103. See page: 15

[SS92]   Osamu Sakai and Yukihiro Shimizu, *Excitation spectra of the two impurity Anderson model. I. Critical transition in the two magnetic impurity problem and the roles of the parity splitting*, Journal of the Physical Society of Japan **61** (1992), no. 7, 2333–2347. See page: 13

[SS00]   J. Lleweilun Smith and Qimiao Si, *Spatial correlations in dynamical mean-field theory*, Phys. Rev. B **61** (2000), 5184–5193. See page: 15

[SS11]   O. Stockert and F. Steglich, *Unconventional quantum criticality in heavy-Fermion compounds*, Annual Review of Condensed Matter Physics **2** (2011), no. 1, 79–99. See pages: 10 and 11

[SSA$^+$02]   Hiroaki Shishido, Rikio Settai, Dai Aoki, Shugo Ikeda, Hirokazu Nakawaki, Noriko Nakamura, Tomoya Iizuka, Yoshihiko Inada, Kiyohiro Sugiyama, Tetsuya Takeuchi, Kouichi Kindo, Tatsuo C. Kobayashi, Yoshinori Haga, Hisatomo Harima, Yuji Aoki, Takahiro Namiki, Hideyuki Sato, and Yoshichika Ōnuki, *Fermi surface, magnetic and superconducting properties of $LaRhIn_5$ and $CeTIn_5$ (T: Co, Rh and Ir)*, Journal of the Physical Society of Japan **71** (2002), no. 1, 162–173. See page: 10

[SSHO05]   Hiroaki Shishido, Rikio Settai, Hisatomo Harima, and Yoshichika Ōnuki, *A drastic change of the Fermi surface at a critical pressure in* CeRhIn$_5$: *dHvA study under pressure*, Journal of the Physical Society of Japan **74** (2005), no. 4, 1103–1106. See pages: 1, 9, 10, and 11

[SSI99]   Qimiao Si, J. Lleweilun Smith, and Kevin Ingersent, *Quantum critical behavior in Kondo systems*, International Journal of Modern Physics B **13** (1999), no. 18, 2331–2342. See page: 15

[SSI$^+$01]   R Settai, H Shishido, S Ikeda, Y Murakawa, M Nakashima, D Aoki, Y Haga, H Harima, and Y Onuki, *Quasi-two-dimensional Fermi surfaces and the de Haas-van Alphen oscillation in both the normal and superconducting mixed states of $CeCoIn_5$*, Journal of Physics: Condensed Matter **13** (2001), no. 27, L627. See page: 10

[SSK90]   O. Sakai, Y. Shimizu, and T. Kasuya, *Excitation spectra of two impurity Anderson model*, Solid State Communications **75** (1990), no. 2, 81–87. See page: 13

[SSMS09]   Sebastian Smerat, Ulrich Schollwöck, Ian P. McCulloch, and Herbert Schoeller, *Quasiparticles in the Kondo lattice model at partial fillings of the conduction band using the density matrix renormalization group*, Phys. Rev. B **79** (2009), 235107. See page: 14

[SSV03]   T. Senthil, Subir Sachdev, and Matthias Vojta, *Fractionalized Fermi liquids*, Phys. Rev. Lett. **90** (2003), 216403. See pages: 8, 14, and 147

[Sta19]   Katharina M. Stadler, *A model study of strong correlations in hund metals*, Ph.D. thesis, Ludwig-Maximilians-Universität München, January 2019. See page: 28

[Ste84]   G. R. Stewart, *Heavy-fermion systems*, Rev. Mod. Phys. **56** (1984), 755–787. See page: 1

[Ste01]   G. R. Stewart, *Non-Fermi-liquid behavior in d- and f-electron metals*, Rev. Mod. Phys. **73** (2001), no. 4, 797–855. See page: 8

[SVS04]   T. Senthil, Matthias Vojta, and Subir Sachdev, *Weak magnetism and non-Fermi liquids near heavy-Fermion critical points*, Phys. Rev. B **69** (2004), no. 3, 035111. See pages: 14 and 147

[SW66]   J. R. Schrieffer and P. A. Wolff, *Relation between the Anderson and Kondo Hamiltonians*, Phys. Rev. **149** (1966), 491–492. See page: 3

[SW12]   E.M. Stoudenmire and Steven R. White, *Studying two-dimensional systems with the density matrix renormalization group*, Ann. Rev. Cond. Mat. Phys. **3** (2012), 111–128. See page: 35

[SZG05]   Qimiao Si, Jian-Xin Zhu, and D R Grempel, *Magnetic quantum phase transitions in Kondo lattices*, Journal of Physics: Condensed Matter **17** (2005), no. 37, R1025. See page: 15

[SZK+20]   Bin Shen, Yongjun Zhang, Yashar Komijani, Michael Nicklas, Robert Borth, An Wang, Ye Chen, Zhiyong Nie, Rui Li, Xin Lu, Hanoh Lee, Michael Smidman, Frank Steglich, Piers Coleman, and Huiqiu Yuan, *Strange-metal behaviour in a pure ferromagnetic Kondo lattice*, Nature **579** (2020), no. 7797, 51–55. See page: 12

[TGM+00]   O. Trovarelli, C. Geibel, S. Mederle, C. Langhammer, F. M. Grosche, P. Gegenwart, M. Lang, G. Sparn, and F. Steglich, $YbRh_2Si_2$*: Pronounced non-Fermi-liquid effects above a low-lying magnetic phase transition*, Phys. Rev. Lett. **85** (2000), no. 3, 626–629. See pages: 1, 9, and 12

[THKD11]   D. Tanasković, K. Haule, G. Kotliar, and V. Dobrosavljević, *Phase diagram, energy scales, and nonlocal correlations in the Anderson lattice model*, Phys. Rev. B **84** (2011), no. 11, 115105. See pages: 15, 83, and 147

[TKH07]   A. Toschi, A. A. Katanin, and K. Held, *Dynamical vertex approximation: A step beyond dynamical mean-field theory*, Phys. Rev. B **75** (2007), 045118. See page: 19

[Tsv85]   A M Tsvelick, *The thermodynamics of multichannel Kondo problem*, J. Phys. C: Solid State Phys. **18** (1985), no. 1, 159–170. See page: 13

[TW84]   A. M. Tsvelick and P. B. Wiegmann, *Solution of the n-channel Kondo problem (scaling and integrability)*, Z. Phys. B **54** (1984), no. 3, 201–206. See page: 13

[VC06]   F. Verstraete and J. I. Cirac, *Matrix product states represent ground states faithfully*, Phys. Rev. B **73** (2006), 094423. See page: 30

[VDVH+21]   Maarten Van Damme, Robijn Vanhove, Jutho Haegeman, Frank Verstraete, and Laurens Vanderstraeten, *Efficient matrix product state methods for extracting spectral information on rings and cylinders*, Phys. Rev. B **104** (2021), 115142. See page: 148

[vL96]   Hilbert von Löhneysen, *Non-Fermi-liquid behaviour in the heavy-Fermion system*, Journal of Physics: Condensed Matter **8** (1996), no. 48, 9689–9706. See page: 12

[VLSR+89]   C. M. Varma, P. B. Littlewood, S. Schmitt-Rink, E. Abrahams, and A. E. Ruckenstein, *Phenomenology of the normal state of Cu-O high-temperature superconductors*, Phys. Rev. Lett. **63** (1989), 1996–1999. See page: 12

[Voj06]   Matthias Vojta, *Impurity quantum phase transitions*, Philos. Mag. **86** (2006), no. 13-14, 1807–1846. See page: 13

[Voj10]   Matthias Vojta, *Orbital-selective Mott transitions: Heavy Fermions and beyond*, Journal of Low Temperature Physics **161** (2010), no. 1, 203–232. See pages: 14 and 147

[VPC04]   F. Verstraete, D. Porras, and J. I. Cirac, *Density matrix renormalization group and periodic boundary conditions: A quantum information perspective*, Phys. Rev. Lett. **93** (2004), 227205. See page: 33

[Wei12]   Andreas Weichselbaum, *Tensor networks and the numerical renormalization group*, Phys. Rev. B **86** (2012), no. 24, 245124. See pages: 28, 29, 30, and 33

[Wei20]   Andreas Weichselbaum, *X-symbols for non-Abelian symmetries in tensor networks*, Phys. Rev. Research **2** (2020), 023385. See page: 28

[Wei24]   Andreas Weichselbaum, *Qspace - an open-source tensor library for Abelian and non-Abelian symmetries*, 2024. See page: 28

[WGM+15]   F. Alexander Wolf, Ara Go, Ian P. McCulloch, Andrew J. Millis, and Ulrich Schollwöck, *Imaginary-time matrix product state impurity solver for dynamical mean-field theory*, Phys. Rev. X **5** (2015), 041032. See page: 30

[Whi92]   Steven R. White, *Density matrix formulation for quantum renormalization groups*, Phys. Rev. Lett. **69** (1992), 2863–2866. See page: 33

[Whi93]   Steven R. White, *Density-matrix algorithms for quantum renormalization groups*, Phys. Rev. B **48** (1993), 10345–10356. See page: 33

[Whi05]   Steven R. White, *Density matrix renormalization group algorithms with a single center site*, Phys. Rev. B **72** (2005), 180403. See page: 35

[Wil75] Kenneth G. Wilson, *The renormalization group: Critical phenomena and the Kondo problem*, Rev. Mod. Phys. **47** (1975), no. 4, 773–840. See pages: 27, 28, and 29

[WK23a] Krzysztof P. Wójcik and Johann Kroha, *Asymmetry effects on the phases of RKKY-coupled two-impurity Kondo systems*, Phys. Rev. B **107** (2023), 125146. See page: 13

[WK23b] Krzysztof P. Wójcik and Johann Kroha, *Quantum spin liquid in an RKKY-coupled two-impurity Kondo system*, Phys. Rev. B **107** (2023), L121111. See page: 13

[WMPS14] F. Alexander Wolf, Ian P. McCulloch, Olivier Parcollet, and Ulrich Schollwöck, *Chebyshev matrix product state impurity solver for dynamical mean-field theory*, Phys. Rev. B **90** (2014), 115124. See page: 30

[WMS14] F. Alexander Wolf, Ian P. McCulloch, and Ulrich Schollwöck, *Solving nonequilibrium dynamical mean-field theory using matrix product states*, Phys. Rev. B **90** (2014), 235131. See page: 30

[WvD07] Andreas Weichselbaum and Jan von Delft, *Sum-rule conserving spectral functions from the numerical renormalization group*, Phys. Rev. Lett. **99** (2007), no. 7, 076402. See pages: 28 and 29

[XXX+22] Yihe Xu, Zhaoxuan Xie, Xiaoyu Xie, Ulrich Schollwöck, and Haibo Ma, *Stochastic adaptive single-site time-dependent variational principle*, JACS Au **2** (2022), 335. See page: 36

[Yos57] Kei Yosida, *Magnetic properties of Cu-Mn alloys*, Phys. Rev. **106** (1957), no. 5, 893–898. See page: 7

[YPZ+20] Chia-Jung Yang, Shovon Pal, Farzaneh Zamani, Kristin Kliemt, Cornelius Krellner, Oliver Stockert, Hilbert v. Löhneysen, Johann Kroha, and Manfred Fiebig, *Terahertz conductivity of heavy-Fermion systems from time-resolved spectroscopy*, Phys. Rev. Research **2** (2020), 033296. See pages: 12 and 36

[YS10] Seiji J. Yamamoto and Qimiao Si, *Global phase diagram of the Kondo lattice: From heavy Fermion metals to Kondo insulators*, J Low Temp Phys **161** (2010), no. 1, 233–262. See page: 12

[Zaa04] Jan Zaanen, *Why the temperature is high*, Nature **430** (2004), no. 6999, 512–513. See page: 12

[ZGS03] Jian-Xin Zhu, D. R. Grempel, and Qimiao Si, *Continuous quantum phase transition in a Kondo lattice model*, Phys. Rev. Lett. **91** (2003), 156404. See pages: 15 and 147

[Žit09a] Rok Žitko, *Adaptive logarithmic discretization for numerical renormalization group methods*, Computer Physics Communications **180** (2009), no. 8, 1271–1276. See page: 28

[Žit09b] Rok Žitko, *Convergence acceleration and stabilization of dynamical mean-field theory calculations*, Phys. Rev. B **80** (2009), 125125. See page: 19

[ŽP09]   Rok Žitko and Thomas Pruschke, *Energy resolution and discretization artifacts in the numerical renormalization group*, Phys. Rev. B **79** (2009), 085106. See pages: 28 and 29

[ZSVF+18]   V. Zauner-Stauber, L. Vanderstraeten, M. T. Fishman, F. Verstraete, and J. Haegeman, *Variational optimization algorithms for uniform matrix product states*, Phys. Rev. B **97** (2018), 045145. See page: 34

[ZZL+19]   Hengcan Zhao, Jiahao Zhang, Meng Lyu, Sebastian Bachus, Yoshifumi Tokiwa, Philipp Gegenwart, Shuai Zhang, Jinguang Cheng, Yi-feng Yang, Genfu Chen, Yosikazu Isikawa, Qimiao Si, Frank Steglich, and Peijie Sun, *Quantum-critical phase from frustrated magnetism in a strongly correlated metal*, Nat. Phys. **15** (2019), no. 12, 1261–1266. See page: 12